2016
Cosmology

Sponsored by

. CNRS (Centre National de la Recherche Scientifique)
. CEA (Commissariat à l'Energie Atomique et aux Energies Alternatives)
. FNRS (Fond National de la Recherche Scientifique)
. BSP (Belgian Science Policy)

51st Rencontres de Moriond
La Thuile, Aosta Valley, Italy – March 19-26, 2016

2016 Cosmology

© Published by ARISF, 2016

ISBN : 979-10-968-7901-4

web

All rights reserved. This book, or parts thereof, may not be reproduced in any form or by any means, electronic or mechanical, including photocopying, recording or any information storage and retrieval system now known or to be invented, without written permission from the publisher.

Proceedings of the 51st RENCONTRES DE MORIOND

Cosmology

La Thuile, Aosta Valley Italy *March 19-26, 2016*

2016

Cosmology

edited by

Etienne Augé,
Jacques Dumarchez
and
Jean Trân Thanh Vân

The 51st Rencontres de Moriond

2016 Cosmology

was organized by :

Etienne Augé (IN2P3, Paris)
Jacques Dumarchez (LPNHE, Paris)

with the active collaboration of :

P. Astier (Paris)
C. Burgess (Toronto)
K. Ganga (Paris)
Y. Giraud-Héraud (Paris)
J.-M. Le Goff (Saclay)
H. McCracken (Paris)
O. Perdereau (Orsay)
J. Silk (Oxford)
F. Vernizzi (Saclay)
B. Wandelt (Paris)

2016 RENCONTRES DE MORIOND

The 51st Rencontres de Moriond were held in La Thuile, Valle d'Aosta, Italy.

The first meeting took place at Moriond in the French Alps in 1966. There, experimental as well as theoretical physicists not only shared their scientific preoccupations, but also the household chores. The participants in the first meeting were mainly french physicists interested in electromagnetic interactions. In subsequent years, a session on high energy strong interactions was added.

The main purpose of these meetings is to discuss recent developments in contemporary physics and also to promote effective collaboration between experimentalists and theorists in the field of elementary particle physics. By bringing together a relatively small number of participants, the meeting helps develop better human relations as well as more thorough and detailed discussion of the contributions.

Our wish to develop and to experiment with new channels of communication and dialogue, which was the driving force behind the original Moriond meetings, led us to organize a parallel meeting of biologists on Cell Differentiation (1980) and to create the Moriond Astrophysics Meeting (1981). In the same spirit, we started a new series on Condensed Matter physics in January 1994. Meetings between biologists, astrophysicists, condensed matter physicists and high energy physicists are organized to study how the progress in one field can lead to new developments in the others. We trust that these conferences and lively discussions will lead to new analytical methods and new mathematical languages.

The 51st Rencontres de Moriond in 2016 comprised three physics sessions:

- March 12 - 19: "Electroweak Interactions and Unified Theories"
- March 19 - 26: "QCD and High Energy Hadronic Interactions"
- March 19 - 26: "Cosmology"

We thank the organizers of the 51st Rencontres de Moriond:

- A. Abada, E. Armengaud, J. Conrad, P. Fayet, J.-M. Frère, P. Hernandez, L. Iconomidou-Fayard, P. Janot, M. Knecht, J. P. Lees, S. Loucatos, F. Montanet, J. Orloff, A. Pich, S. Pokorski, V. Tisserand, D. Wood for the "Electroweak Interactions and Unified Theories" session,
- E. Augé, E. Berger, S. Bethke, A. Capella, A. Czarnecki, D. Denegri, N. Glover, B. Klima, M. Krawczyk, N. Mahmoudi, L. McLerran, B. Pietrzyk, L. Schoeffel, Chung-I Tan, J. Trân Thanh Vân, U. Wiedemann for the "QCD and High Energy Hadronic Interactions" session,
- P. Astier, C. Burgess, J. Dumarchez, K. Ganga, Y. Giraud-Héraud, J.-M. Le Goff, H. McCracken, O. Perdereau, J. Silk, F. Vernizzi, B. Wandelt for the "Cosmology" session

and the conference secretariat and technical staff:

V. de Sá-Varanda and C. Bareille, I. Cossin, G. Dreneau, D. Fliegel, F. Legrand, G. Perrin, S. Vydelingum.

We are also grateful to Giorgio Palmucci, Francesco Cante, Ida Liseno, Francesco Quinto and the Planibel Hotel staff who contributed through their hospitality and cooperation to the well-being of the participants, enabling them to work in a relaxed atmosphere.

The Rencontres were sponsored by the Centre National de la Recherche Scientifique, the Commissariat à l'Energie Atomique (CEA-Irfu), the Fonds de la Recherche Scientifique (FRS-FNRS) and the Belgium Science Policy. We would like to express our thanks for their encouraging support.

It is our sincere hope that a fruitful exchange and an efficient collaboration between the physicists and the astrophysicists will arise from these Rencontres as from previous ones.

These Rencontres offered us the possibility to celebrate the 50th anniversary of this event, founded in 1966 by Jean Trân Thanh Vân. We had some dedicated talks by some of the pillars of Moriond, giving their personnal recollections or panoramic views of the evolution of physics ideas along these years, and we also had the chance to celebrate the discovery of gravitational waves 100 years after their prediction by A. Eistein. We would like to warmly thank J. Lefrançois, J. Iliopoulos, B. Sathyaprakash and P. Binétruy. Videos of these moments can be viewd on: `https://webcast.in2p3.fr/events-rencontres_de_moriond_`*, thanks to the webcast services at LAL, and particularly to G. Perrin and G. Dreneau. The 51st Rencontres were also the occasion of renewing some long-standing traditions of Moriond, like the slalom: tens of participants of all ages skied down the track in all times and styles to eventually win ... a glass of mulled wine! And delving into the archives we have produced a list of the nearly 10000 participants along these 50 years, which has been put up as wallpaper along the corridor leading to the bar, resulting in persistant traffic jams!*

E. Augé, J. Dumarchez and J. Trân Thanh Vân

Table of Contents

1. Cosmological Microwave Background

Planck results 2015	S. Galli	3
The Hillipop likelihood and the $A_{\rm L}$ parameter using Planck data	S. Henrot-Versille	7
Testing significance of the large angular scale CMB anomalies using Planck data	P. Bielewicz	11
Cosmological Parameters from CMB Maps without Likelihood Approximation	B. Racine	15
Measurements of degree-scale B-mode polarization with BICEP2, KECK ARRAY, and BICEP3	C. Bischoff	19
Instrumentation development for spectroscopic observation of the Cosmic Microwave Background	G. D'Alessandro	27
QUBIC experiment	M. Stolpovskiy	31
Data analysis and cosmological results from the first observational campaigns of the POLARBEAR experiment	J. Peloton	35
Future CMB polarization observatory in the presence of foregrounds and gravitational lensing: the Simons Array	J. Errard	43
SPIDER: Probing The Dawn Of Time From Above The Clouds	L. Moncelsi	47
CMB foregrounds - A brief overview	C. Dickinson	53
Simulating the polarised galaxy	F. Vansyngel	63
Constraining Multiplicative Bias in CFHTLenS Weak Lensing Shear Data	J. Liu	67
Multiple lensing of CMB anisotropies	G. Fabbian	71
A bias to CMB lensing from the bispectrum of large-scale structure	V. Böhm	77
Beam systematics in CMB polarisation measurements	R. Banerji	81

2. Dark Energy

BAO Correlations at $z = 2.3$ with SDSS DR12 Lyman-alpha forests	J. Bautista	85
Quasar-Lyman α Forest Cross-Correlation from SDSS-III BOSS survey: Baryon Acoustic Oscillations	H. du Mas des Bourboux	91
Constraining cosmological parameters using BOSS data: Power Spectrum and Bispectrum.	H. Gil-Marín	95
Measuring BAO scale with quasar clustering in EBOSS	P. Laurent	99
The Dark Energy Spectroscopic Instrument	J. Guy	103
Local environment of SNLS5 Type IA supernovæ	M. Roman	109
SUGAR : when spectra help standardizing supernovae	E. Gangler	113
On the dark contents of the Universe: a Euclid survey approach	I. Tutusaus Lleixa	117
Dark Energy constraints from the ESPRESSO Fundamental Physics GTO	A. Leite	121
Weak Lensing with the Square Kilometre Array	I. Harrison	125
The Homogeneity Scale of the Universe	P. Ntelis	129
Constraining $N_{\rm eff}$ with the Lyman-α Forest	G. Rossi	135
Formation and evolution of heavy sub-structures in the centre of galaxy clusters: the local effect of dark energy	M. Arca Sedda	137

3. Dark Matter

The XENON1T Dark Matter experiment	A. Di Giovanni	141
Dark matter search in the inner Galactic Centre halo with H.E.S.S	V. Lefranc	149
Dark matter distribution and indirect detection in dwarf spheroidal galaxies	C. Combet	153
The DarkSide program at LNGS	S. Davini	157
The weak equivalence principle with antimatter: the AEgIS experiment at CERN	D. Pagano	161
Directional detection of Dark Matter with the MIcro-tpc MAtrix of Chambers	C. Couturier	165
The magnitude-redshift relation for type IA supernovae, locally inhomogeneous cosmological models, and the nature of dark matter	P. Helbig	171
New Solar metallicity measurements	S. Vagnozzi	175

4. Theory

Generalised Dark Matter: Imprints on the CMB and mapping to non-perturbative models	M. Kopp	181
The very best limits on cosmological magnetic fields	F. Urban	185
Universal predictions of screened modified gravity on cluster scales	D. Mota	189
Cosmology with vector distortion	J. Beltrán Jiménez	193
Bumpy Inflation: Subleading Effects in Axion Inflation	I. Zavala	197
The holiest grail	P. Meerburg	201
Probing inflation models with gravitational waves	V. Domcke	205
Gravitational Waves in the Early Universe from Gauge Field Production	I. Ben-Dayan	209
Statistical Decoupling of Lagrangian Fluid Parcel in Newtonian Cosmology	X. Wang	213
Constraints On Gravity from CMB data: an Effective Field Theory approach	V. Salvatelli	217
Cosmology of Massive Gravity and its Extensions	K. Hinterbichler	223
Living with ghosts in Hořava–Lifshitz gravity	S. Ramazanov	233
Cosmological constraints on Lorentz Invariance violation in gravity and dark matter	M. Ivanov	237
Fine-structure constant constraints on dark energy and the Weak Equivalence Principle	C. Martins	241
Expectation of lepton hierarchy and absolute neutrino masses in a microscopic cosmological model	T. Vo Van	245
Randall-Sundrum vs. holographic braneworld	N. Bilic	249
Running vacuum versus the ΛCDM	A. Gómez-Valent	251
General features of single-scalar field dark energy models	L. Perenon	253
Under Pressure: constraining extensions of cold dark matter	D. Thomas	255
The acceleration of the Moon and the Universe	G. Henriksson	259
Bianchi type V viscous fluid dark energy cosmological model with gauge function	B. Mishra	261
Static and Oscillating Universes	J. Kehayias	267

5. Neutrinos and Cosmology

Constraints on the neutrino mass from the Lyman-α forest power spectrum	C. Yèche	271
Cosmic Neutrinos and Other Light Relics	J. Meyers	279
Interplay between cosmology and laboratory experiments: two examples from neutrino physics	M. Gerbino	283

6. Clusters

High angular resolution SZ observations with NIKA and NIKA2	B. Comis	289
Thermal Sunyaev Zel'dovich effect from high redshift ($z > 2$) structures	L. Verdier	297
The mass accretion rate of galaxy clusters: a measurable quantity	C. De Boni	301
Can dark energy explain the observed outflow in galaxy clusters?	M. Donnari	303

7. 21 cm.

Cosmology with the 21cm signal	M. Santos	307
Tianlai: a 21cm radio telescope array for BAO and dark energy, status and progress	F. Wu	315
Update on the BINGO 21cm intensity mapping experiment	R. Battye	319
Simulated Effects of $1/f$ Noise on an SKA Intensity Mapping Survey	S. Harper	327
The Multi-Tracer Technique To Detect Horizon-Scale Effects	S. Camera	331
HI intensity mapping: extracting the 21 cm signal in the presence of foregrounds	L. Collis Olivari	337
The quest for Dusty Primeval Galaxies	C. Mancuso	341

8. Others

Study of Big Bang Nucleosynthesis deep underground	C. Gustavino	347
Non Linear electrodynamics contributing to minimum vacuum energy (a cosmological constant), allowed in Early Universe cosmology	A. Beckwith	349
United Nature of Dark Energy and Low Energy Nuclear Reactions	M. Ivanov	351
The apparent motions of the extragalactic sources images due to astrometric gravitational microlensing in the galaxy: a role of the DM substructure	E. Fedorova	353

Authors Index 357

List of participants 363

1. Cosmological Microwave Background

Planck results 2015

S. Galli
CNRS, UMR 7095, Institut dAstrophysique de Paris, F-75014, Paris, France

Planck is an ESA satellite aimed at the observation of the Cosmic Microwave Background. In 2015, the Planck collaboration released the second round of cosmological results based on the so-called "full mission data" (more than ~ 30 months of observation) both in temperature and, for the first time, in polarization. I will review a few of the most interesting cosmological results of this year release and highlight the power of polarization data to constrain possible extentions of the LCDM model.

1 Introduction

Planck is an ESA satellite that operated between 2009-2013. It is the third generation of satellites observing the CMB after COBE and WMAP. In March 2013, the Planck collaboration published the first release of Planck data based on the so called "Nominal" mission, (~ 1 year of observations), and used temperature data alone . In 2015, the collaboration published the second data release based on the so-called "full" mission, which uses almost all of the data collected by the High Frequency Instrument (HFI) (about 2.5 years) and by the Low Frequency Instrument (LFI) (about 4 years), both in temperature and polarization . In this proceeding, I describe a few of the cosmological results obtained from the second Planck data release. In particular, I present the Planck constraints on the sum of neutrino masses, the number of relativistic species and dark matter annihilation. I will show results using the following datasets:

- Planck TT: the TT temperature spectrum at multipoles $\ell = 2 - 2508$;
- lowP: the TE and EE polarization power spectra at $\ell < 30$;
- Planck TTTEEE: the TT, TE and EE power spectra at $\ell = 2 - 2508$;
- lensing: the reconstructed lensing power spectrum inferred from the 4-point correlation function of the Planck maps as described here [3];
- BAO (Baryon Acustic Oscillation) data from the 6dFGS, SDSS-MGS and BOSS-LOWZ BAO measurements and the CMASS-DR11 anisotropic BAO measurements.

Further details can be found in [1] and [2].

2 Constraints on the total mass of active neutrinos

Allowing for a neutrino mass different from zero is perhaps one of the best motivated extensions of the base ΛCDM model. From neutrino oscillation experiments we know that neutrinos have mass. In a normal-hierarchy scenario, with two light and one heavy mass eigenstates, the sum of the masses is expected to be larger than $\sum m_\nu \sim 0.06\,eV$, while in an inverted scenario, with two heavy and one light mass eigenstates, the sum is expected to be larger than $\sum m_\nu \sim 0.1\,eV$.

The constraints on $\sum m_\nu$ that can be obtained from cosmology are model dependent, but they are currently much stronger than the ones obtained in laboratory, such as the ones from tritium beta decay experiments. For the Planck constraints, we assume three species of degenerate massive neutrinos, which is an accurate approximation at the level of sensitivity of Planck.

The constraints obtainable with the Planck data derive from the impact neutrino mass have on the early and late Integrated Sachs-Wolfe (ISW) effect and on the amplitude of the gravitational lensing that distorts the path of the CMB photons.

Using the datasets described in Sect. 1, the Planck constraints at 95 % c.l. are:

$$\sum m_\nu < 0.72\,eV \quad Planck\ TT + lowP\,; \tag{1}$$
$$\sum m_\nu < 0.21\,eV \quad Planck\ TT + lowP + BAO\,; \tag{2}$$
$$\sum m_\nu < 0.49\,eV \quad Planck\ TTTEEE + lowP\,; \tag{3}$$
$$\sum m_\nu < 0.17\,eV \quad Planck\ TTTEEE + lowP + BAO\,. \tag{4}$$

Adding the BAO data substantially tightens the constraints on $\sum m_\nu$ by breaking the acoustic scale degeneracy. Additionally, including the Planck polarization data at high multipoles produces a relatively small improvement to the Planck TT+lowP+BAO constraint so we consider the TT results to be our most reliable constraints.

3 Constraints on $N_{\rm eff}$

The energy density of relativistic species in the early Universe is usually parameterized by the parameter $N_{\rm eff}$, defined so that the total relativistic energy density in neutrinos and any other dark radiation is given in terms of the photon density ρ_γ at $T \ll 1\ MeV$ by

$$\rho = N_{\rm eff}\frac{7}{8}\left(\frac{4}{11}\right)^{4/3}\rho_\gamma. \tag{5}$$

The numerical factors in this equation are included so that $N_{\rm eff} = 3$ for three standard model neutrinos that were thermalized in the early Universe and decoupled well before electron-positron annihilation. The standard cosmological prediction is actually $N_{\rm eff} = 3.046$, since neutrinos are not completely decoupled at electron-positron annihilation and are subsequently slightly heated.

In addition to massless sterile neutrinos, a variety of other particles could contribute to $N_{\rm eff}$. Also, a non-standard thermal history of the universe can also change the value of $N_{\rm eff}$.

The Planck constraints at 68 % c.l. are:

$$N_{\rm eff} = 3.13 \pm 0.32 \quad Planck\ TT + lowP\,; \tag{6}$$
$$N_{\rm eff} = 3.15 \pm 0.23 \quad Planck\ TT + lowP + BAO\,; \tag{7}$$
$$N_{\rm eff} = 2.99 \pm 0.20 \quad Planck\ TTTEEE + lowP\,; \tag{8}$$
$$N_{\rm eff} = 3.04 \pm 0.18 \quad Planck\ TTTEEE + lowP + BAO\,. \tag{9}$$

Note the significantly tighter constraint with the inclusion of Planck high-ℓ polarization, with $\Delta N_{\rm eff} < 1$ at over $4\,\sigma$ from Planck alone. The strong limit from polarization is also consistent with the joint Planck TT+lowP+BAO result, so Eq. 7 leads to the robust conclusion that $\Delta N_{\rm eff} < 1$ at over $3\,\sigma$. The addition of Planck lensing has very little effect on this constraint.

4 Resuls on Dark Matter annihilation

Energy injection from dark matter (DM) annihilation can alter the recombination history, leading to changes in the temperature and polarization power spectra of the CMB. Thus, CMB anisotropies offer the opportunity to constrain the nature of DM. Furthermore, CMB experiments such as Planck can achieve limits on the annihilation cross-section that are relevant to the interpretation of anomalies in other indirect search experiments, such as the rise in the cosmic-ray positron fraction at energies $> 10\,$GeV observed by PAMELA, *Fermi*, and AMS. The CMB constraints are complementary to those determined from other astrophysical probes, such as the gamma-ray observations of dwarf galaxies by the Fermi satellite.. The rate of energy release per unit volume by annihilating DM can be written as

$$\frac{dE}{dtdV}(z) = 2\,g\,\rho_{\rm crit}^2 c^2 \Omega_{\rm c}^2 (1+z)^6 p_{\rm ann}(z), \tag{10}$$

where $p_{\rm ann}$ is defined as

$$p_{\rm ann}(z) \equiv f(z)\frac{\langle\sigma\rangle}{m_\chi}, \tag{11}$$

$\rho_{\rm crit}$ the critical density of the Universe today, m_χ is the mass of the DM particle, and $\langle\sigma v\rangle$ is the thermally-averaged annihilation cross-section times velocity. In Eq. 11, g is a degeneracy factor that is equal to 1/2 for Majorana particles and 1/4 for Dirac particles. In this paper, the constraints will refer to Majorana particles. The fraction of the rest mass energy that is injected into the gaseous background can be modelled by an "efficiency factor, $f(z)$. Both the amplitude and redshift dependence of $f(z)$ depend on the details of the annihilation process. However to a first approximation the redshift dependence of $f(z)$ can be ignored, since current CMB data (including Planck) are sensitive to energy injection over a relatively narrow range of redshift. The effects of DM annihilation can therefore be reasonably well parameterized by a single constant parameter, $p_{\rm ann}$, with $f(z)$ set to a constant $f_{\rm eff} = f(z = 600)$, since the effect of dark matter annihilation peaks at $z \approx 600$. Table 1 shows the Planck constraints for various data combinations.

Table 1: Constraints on $p_{\rm ann}$ in units of $\rm cm^3\,s^{-1}\,GeV^{-1}$.

TT+lowP	$< 5.7 \times 10^{-27}$
EE+lowP	$< 1.4 \times 10^{-27}$
TE+lowP	$< 5.9 \times 10^{-28}$
TT+lowP+lensing	$< 4.4 \times 10^{-27}$
TTTEEE+lowP	$< 4.1 \times 10^{-28}$
TTTEEE+lowP+lensing	$< 3.4 \times 10^{-28}$

The constraints on $p_{\rm ann}$ from the Planck TT+lowP spectra are about 3 times weaker than the 95 % limit of $p_{\rm ann} < 2.1 \times 10^{-27}\,{\rm cm}^3\,{\rm s}^{-1}\,{\rm GeV}^{-1}$ derived from WMAP9, which includes WMAP polarization data at low multipoles. However, the Planck TE or EE spectra improve the constraints on $p_{\rm ann}$ by about an order of magnitude compared to those from Planck TT alone. This is because the main effect of dark matter annihilation is to increase the width of last scattering, leading to a suppression of the amplitude of the peaks both in temperature and polarization. As a result, the effects of DM annihilation on the power spectra are degenerate with other parameters of base Λ CDM, such as $n_{\rm s}$ and $A_{\rm s}$.

At large angular scales ($\ell \lesssim 200$), however, dark matter annihilation can produce an enhancement in polarization caused by the increased ionization fraction in the freeze-out tail following recombination. As a result, large-angle polarization information is crucial in breaking the degeneracies between parameters.. The strongest constraints on $p_{\rm ann}$ therefore come from the full Planck temperature and polarization likelihood and there is little improvement if other astrophysical data, or Planck lensing, are added.

References

1. Planck Collaboration, Ade, P. A. R., Aghanim, N., et al. 2015, arXiv:1502.01589
2. Planck Collaboration, Aghanim, N., Arnaud, M., et al. 2015, arXiv:1507.02704
3. Planck Collaboration, Ade, P. A. R., Aghanim, N., et al. 2015, arXiv:1502.01591

The Hillipop likelihood and the $A_{\rm L}$ parameter using Planck data

S. Henrot-Versillé for the Hillipop/CAMEL team
Laboratoire de l'Accélérateur Linéaire, Centre scientifique d'Orsay, Bâtiment 200 - BP34, 91898 ORSAY Cedex

The consistency of the cosmological data with the ΛCDM concordance model can be assessed through the estimation of the $A_{\rm L}$ parameter. We will show that a 2.6σ discrepancy with the expected unity value is measured using the profile likelihood method applied to the Planck public likelihoods. $A_{\rm L}$ is highly correlated to the reionisation optical depth τ and one also observes a $\simeq 2\sigma$ discrepancy between the high-ℓ and the low-ℓ Planck results on this parameter. We address those points using Hillipop, a high-ℓ likelihood, built from temperature Planck data. It makes use of foreground templates derived from the Planck data themselves, and has the interesting feature to point to a lower τ value than the official one, fully in agreement with the low-ℓ likelihood results. While the $A_{\rm L}$ value is still high using Planck data alone, we have combined Hillipop with the ACT and SPT data to further constrain the foreground nuisance parameters. We will show that this combination permits to recover an $A_{\rm L}$ value in agreement with one, keeping a τ value fully compatible between all the considered datasets and to get a coherent picture of the ΛCDM scenario. This work is further detailed in [1].

1 Appetizer: Profile likelihoods

The wide-spread approach used in Cosmology for parameter estimation is based on Bayesian inference using Monte Carlo Markov chains algorithms to explore the likelihood function. In contrast, in Particle Physics, the frequentist profile likelihood method is used in most cases[a].

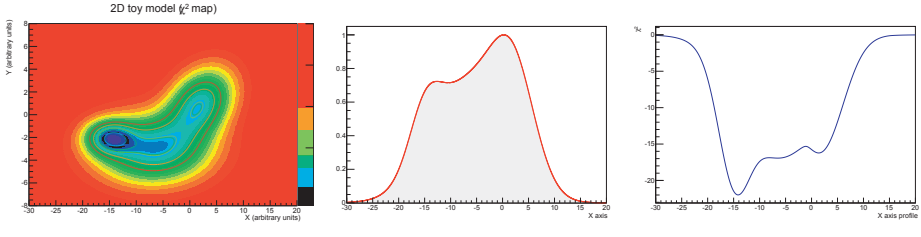


Figure 1 – χ^2 distribution in the (X, Y) plane (left), and corresponding posterior distribution (middle), and profile likelihood for X (right).

Beyond philosophical matters, a potential difference between both approaches is the so-called volume effect. Consider a problem for which we want to infer two parameters (X and Y), which likelihood function $\mathcal{L}$, or more precisely the χ^2 defined as:

$$\chi^2 = -2 \ln \mathcal{L} \tag{1}$$

[a] One can also considered the Neyman CL construction as in [5].

is shown on figure 1, and present two minima (around $X \simeq -15$ and $X \simeq 2$), and a banana shape. If one wants to estimate the mean and error on X using the Bayesian method, one would build the marginal posterior such that:

$$P(X) = \int \mathcal{L}(X,Y)p(X,Y)dY \tag{2}$$

which is represented on the middle of the figure. On the other hand, the profile likelihood (on the right hand side), is simply built for each X value as the point in the Y dimension which maximises the likelihood function:

$$\mathcal{L}(\mathcal{X}) = \max_{\mathcal{Y}} \mathcal{L}(\mathcal{X},\mathcal{Y}) \ . \tag{3}$$

One can straigforwardly show, in this precise example, that, in the Bayesian case, the mean value of the posterior distribution (around $X \simeq 1$) is far from matching the one of the best fit (blueish zone in the 2D distribution corresponding to the points where the likelihood is maximum), while, by construction, the mean value deduced from the profile likelihood method is exactly degenerated with the best fit (as the higher likelihood area of the parameter space is the "most likely" to be the true one).

Hopefully for the Planck data and the standard ΛCDM cosmology, such case does not show up [3] [2] [4], but when considering extensions to ΛCDM one should be aware that such situations may occur. To ensure that the physics results do not depend on the statistical method (or at least to understand the discrepancies if any), we have build a sofware in which both approaches can be tested in a unique framework (CAMEL) that can be found here: `camel.in2p3.fr`. It makes use of CLASS [6] as Boltzman solver.

2 Planck Likelihoods

We first remind the two Planck released likelihoods [2], which are considered in the following: lowTEB, the lowℓ temperature and polarisation map based likelihood, and Plik: a gaussian high-ℓ temperature likelihood. On top of Plik, to better constrain the SZ sector (thermal and kinetic), a constraint has been used, derived from ACT data which writes:

$$A^{SZ} = Z^{kSZ} + 1.6A^{tSZ} = 9.5\mu K^2 \tag{4}$$

with a dispersion of $3\mu K^2$.

Hillipop [2] is another high-ℓ Planck likelihood ($\ell > 50$) based on cross-spectra at 100, 143, 217 and 353GHz, with temperature data, which can be used as an alternative to Plik. The main differences between them occur from the choice we have made in the likelihood building: we use 15 cross-spectra from 6 maps [7], the intercalibration coefficients are defined at the map level, we use different masks to further reduce the contamination from the foregrounds and the parameterization of the foregrounds is based on templates derived from the Planck data themselves.

3 Parameter estimation

3.1 Hillipop combined with lowTEB

Table 1 shows a comparison of the ΛCDM parameters infered from Plik and Hillipop, using the lowTEB likelihood for the low-ℓ part.

The main differences that show up are for τ and A_s (not suprisingly since both are correlated through the fact that the measured C_ℓ spectrum scales as $\propto A_s e^{-2\tau}$). As the estimation of those parameters is mainly driven by the low-ℓ data, one may therefore wonder why they are so different.

Table 1: ΛCDM parameters estimated with the Plik+lowTEB likelihoods (middle column) and with Hillipop+lowTEB (last column).

ΛCDM parameter	Plik+lowTEB	Hillipop+lowTEB
$\Omega_b h^2$	0.02222 ± 0.00023	0.02221 ± 0.00023
$\Omega_c h^2$	0.1197 ± 0.0022	0.1192 ± 0.0022
H_0	67.31 ± 0.96	67.51 ± 0.97
τ	0.078 ± 0.019	0.072 ± 0.020
$\ln(10^{10} A_s)$	3.089 ± 0.036	3.068 ± 0.038
n_s	0.9655 ± 0.0062	0.9645 ± 0.0071
σ_8	0.829 ± 0.014	0.816 ± 0.015

The τ value derived from the lowTEB likelihood using the profile likelihood method reads:

$$\tau = 0.067^{+0.023}_{-0.021} \quad \text{lowTEB} \quad , \tag{5}$$

2.2σ away from the Plik only value:

$$\tau = 0.172^{+0.038}_{-0.042} \quad \text{Plik} \quad , \tag{6}$$

while we have with Hillipop $\tau = 0.134^{+0.038}_{-0.048}$, with similar errors than Plik, but a mean value closer to the lowTEB estimate (1.2σ). Having shown that Hillipop seems to be more coherent with the lowTEB likelihood, one can go one step further and open the ΛCDM parameter space to another parameter: $A_{\rm L}$.

3.2 $A_{\rm L}$

In Boltzman codes, weak lensing enters the prediction of the CMB spectrum through a convolution of the unlensed spectrum with the lensing potential power spectrum C_ℓ^Ψ, which, at first order, smoothes the peaks. A fudge factor $A_{\rm L}$ has been introduced [9] [10], which scales C_ℓ^Ψ in the C_ℓ estimation. If its fitted value is 1, the weak lensing is well modeled and the data are in agreement with ΛCDM, on the other hand, if we found $A_L = 0$ this would lead to the conclusion that the data do prefer a theory where the weak lensing is ignored. When measuring $A_{\rm L}$ different from 1 indicates either a problem in the model, or remaining systematics in the data.

Results are summarized in table 2 for different configurations for Plik: the first line corresponds to the published result, while the second line shows the systematics linked to the MCMC and the Boltzman solver, finally a comparison between the last and second lines shows the impact of the profile analysis wrt the Bayesian one, pushing $A_{\rm L}$ to even higher values.

Table 2: $A_{\rm L}$ values obtained for different Boltzman solvers and/or statistical methods as stated in the last column for the Plik+lowTEB likelihoods.

$A_{\rm L} = 1.22 \pm 0.10$	Plik+lowTEB, camb/MCMC [8]
$A_{\rm L} = 1.24 \pm 0.10$	Plik+lowTEB, CLASS/MCMC
$A_{\rm L} = 1.26^{+0.11}_{-0.10}$	Plik+lowTEB, CLASS/profile

One can go through the same exercise with Hillipop, and one would get:

$$A_{\rm L} = 1.22^{+0.11}_{-0.10} \quad [\text{Hillipop} + \text{lowTEB}, \text{CLASS/profile}]. \tag{7}$$

This result is of the same order of magnitude than the Plik result, still with a lower τ value as shown before. It has to be noted also that, at this stage, one observes a correlation between $A_{\rm L}$ and A^{kSZ}. For this reason, instead of using an ad-hoc prior to mimic the very-high-ℓ ACT and SPT data (as in Eq. 4), we do prefer to directly use those data to further consider the full correlation matrix of cosmological and nuisance parameters.

3.3 Combining SPT and ACT data with Hillipop

The data considered here are the following ones: ACT [11], SPTHigh [12] and SPTLow [13], with the corresponding nuisance parameters (cf. [1] for more details). They are called VHL in the following. When extending the foreground templates up to those high-ℓ regions and proceeding with a profile likelihood fit, we end up with:

$$A_{\rm L} = 1.03 \pm 0.08 \quad \text{Hillipop} + \text{lowTEB} + \text{VHL} \tag{8}$$

fully compatible with 1, and passing successfully the test. This allows to get a coherent picture of ΛCDM which parameters are shown in table 3.

Table 3: Estimates of cosmological parameters using MCMC techniques for the six ΛCDM parameters, when combining lowTEB, Hillipop, and VHL likelihoods.

Parameter	Hillipop+lowTEB+VHL
$\Omega_b h^2$	0.02200 ± 0.00019
$\Omega_c h^2$	0.1200 ± 0.0020
$100\theta_{\rm s}$	1.04200 ± 0.00040
τ	0.059 ± 0.017
n_s	0.9630 ± 0.0054
$\ln(10^{10} A_s)$	3.045 ± 0.032
σ_8	0.811 ± 0.013

References

1. Couchot, F., Henrot-Versillé, S., Perdereau, O., et al. 2015, arXiv:1510.07600
2. Planck Collaboration, Aghanim, N., Arnaud, M., et al. 2015, arXiv:1507.02704
3. Planck Collaboration, Ade, P. A. R., Aghanim, N., et al. 2014, A&A, 566, A54
4. Henrot-Versillé, S., Robinet, F., Leroy, N., et al. 2015, Classical and Quantum Gravity, 32, 045003
5. Palanque-Delabrouille, N., Yèche, C., Lesgourgues, J., et al. 2015, J. Cosmology Astropart. Phys., 2, 045
6. Lesgourgues, J. 2011, arXiv:1104.2932
7. Tristram, M., Macías-Pérez, J. F., Renault, C., & Santos, D. 2005, MNRAS, 358, 833
8. Planck Collaboration, Ade, P. A. R., Aghanim, N., et al. 2015, arXiv:1502.01589
9. Lewis, A., & Challinor, A. 2006, Phys. Rep., 429, 1
10. Calabrese, E., Slosar, A., Melchiorri, A., Smoot, G. F., & Zahn, O. 2008, Phys. Rev. D, 77, 123531
11. Das, S., Louis, T., Nolta, M. R., et al. 2014, J. Cosmology Astropart. Phys., 4, 014
12. Reichardt, C. L., Shaw, L., Zahn, O., et al. 2012, ApJ, 755, 70
13. Story, K. T., Reichardt, C. L., Hou, Z., et al. 2013, ApJ, 779, 86

TESTING SIGNIFICANCE OF THE LARGE ANGULAR SCALE CMB ANOMALIES USING PLANCK DATA

P. BIELEWICZ
Nicolaus Copernicus Astronomical Center, ul. Bartycka 18,
00-716 Warszawa, Poland

Since the COBE and WMAP data releases, considerable effort has been spent on analysing the statistical properties of the CMB maps at large angular scales. Remarkably, this effort has resulted in several reports of a breaking of statistical isotropy, as established by many qualitatively different methods. Recently, these observations has been confirmed for the Planck data. I will present studies of the anomalously weak large scale correlations and hemispherical asymmetry for the 2015 Planck CMB maps. I will assess robustness of statistical significance of the anomalies using various statistics and pay special attention to the interpretation of the anomalies.

1 Introduction

In the standard cosmological model the Universe spacetime on the largest scales is described by the Friedmann-Robertson-Walker (FRW) metric. It is solution of Einstein's equations given assumptions of spatial isotropy and homogeneity. Fluctuations of curvature generated during inflationary epoch are described by perturbations around the FRW metric and isotropy and homogeneity are interpreted in a statistical sense. Validity of isotropy around us can be quite easily tested using cosmological observations. The strongest constraints come from observation of CMB which, apart from a dipole anisotropy of order 10^{-3} due to small peculiar velocity, shows anisotropy merely of order 10^{-5} of the mean CMB temperature. However, few tests of statistical properties of the CMB maps revealed lack of correlations seen in the 2-point angular correlation function and breaking of statistical isotropy at large angular scales. These anomalies, first reported for WMAP temperature maps (Bennett *et al.*[1], Spergel *et al.*[2]), have been recently confirmed for the 2013 Planck maps (Planck collaboration[3], Copi *et al.*[4]). We reassess the lack of correlation at large angular separations and hemispherical asymmetry for the 2015 Planck temperature maps (Planck collaboration[5]).

2 Lack of large-angle correlation

We attempt to quantify the lack of structure using the statistic proposed by Spergel *et al.*[2]:

$$S(x) = \int_{-1}^{x} \left[\hat{C}_2(\theta)\right]^2 \mathrm{d}(\cos\theta) \ , \tag{1}$$

where $\hat{C}_2(\theta)$ is our estimate of the 2-point correlation function. For consistency with previous work we compute the statistic $S_{1/2}$, for the upper limit on the integral $x \equiv \cos 60^\circ = \frac{1}{2}$. The results are presented in Table 1. We find that the data indeed shows a lack of correlations on large angular scales, with a significance consistent with that found by Copi *et al.*[4].

Possible criticisms of the $S_{1/2}$ statistic include that it has been designed a posteriori to test for a lack of large-angle correlations, and that it does not account for the high degree of correlation between bins at different angular scales. We can at least, in part, address these concerns by considering a modified version of the commonly used and well understood χ^2 statistic used in previous studies. In order to test the same hypothesis as the $S_{1/2}$ statistic — that there no correlations on scales larger than some angular cut-off — we do not subtract an averaged 2-point function when computing the χ^2, i.e., we use a statistic defined as

$$\chi^2_0(\theta_{\rm min}, \theta_{\rm max}) = \sum_{i,j=i_{\rm min}}^{i_{\rm max}} \hat{C}_2(\theta_i) M^{-1}_{ij} \hat{C}_2(\theta_j) \ , \tag{2}$$

where $i_{\rm min}$, $i_{\rm max}$ denote the index of the bins corresponding to the minimum and maximum value of the separation angles $\theta_{\rm min}$ and $\theta_{\rm max}$, respectively. In this analysis, we adopt $\theta_{\rm min} = 60^\circ$ and $\theta_{\rm max} = 180^\circ$. M_{ij} is the covariance matrix estimated using Monte Carlo simulations corresponding to the fiducial ΛCDM model. The results are shown in Table 1. The significance level of the anomaly is slightly smaller for the χ^2_0 statistic than that derived with $S_{1/2}$.

Table 1: Probabilities of obtaining values for the $S_{1/2}$ and χ^2_0 statistics for the `Planck` fiducial ΛCDM model at least as large as the observed values of the statistic for the `Planck` 2015 temperature CMB maps with resolution parameter $N_{\rm side} = 64$, estimated using the `Commander`, `NILC`, `SEVEM`, and `SMICA` maps. We show also the corresponding estimation of the global p-value for the $S(x)$ statistic.

Statistic	`Comm.`	`NILC`	`SEVEM`	`SMICA`
$S_{1/2}$	99.5	99.6	99.5	99.6
$S(x)$ (global)	97.7	97.8	97.8	97.9
$\chi^2_0(\theta > 60^\circ)$	98.1	98.8	98.1	98.4

A further potential criticism of the $S_{1/2}$ statistic relates to the a posteriori choice of 60° for the separation angle that delineates the interesting region of behaviour of the correlation function. We therefore consider the generalized statistic $S(x)$ and compute its value for all values of x both for the data and simulations. Then, for each value of x, we determine the number of simulations with a higher value of $S(x)$, and hence infer the most significant value of the statistic and the separation angle that it corresponds to. However, since such an analysis is sensitive to the look-elsewhere-effect, we define a global statistic to evaluate the true significance of the result. Specifically, we repeat the procedure for each simulation, and search for the largest probability irrespective of the value of x at which it occurs. The fraction of these probabilities lower than the maximum probability found for the data defines a global p-value. As seen in Table 1, this corresponds to values of order 98 % for the all of the CMB estimates.

Overall, the tests indicate an unusually good fit of the observed 2-point function to both zero or the predictions for the ΛCDM model for angles above 60°. This problem may be related to the fact that the theoretical variance for the best-fit model is larger than the observed value at large scales, thus the simulations based on this model that have been used in all of the statistical tests may overestimate the variance of the 2-point function.

To assess the look-elsewhere-effect related with the choice of specific mask we repeated the analysis for the more narrow mask than used in the baseline analysis. Use of minimal masking is especially important since the claimed anomalies are on large angular scales. We considered confidence mask associated with the Planck low-ℓ likelihood analysis map retaining 92% of the sky as compared to 67% retained by the mask corresponding to the component-separated maps used in the baseline analysis. It is evident from Table 2 that the 2-point function is more consistent with simulations when analysing a larger sky fraction.

Table 2: Probabilities of obtaining values for the $S_{1/2}$ and χ^2_0 statistics for the simulations at least as large as the observed values of the statistic estimated from the `Lkl-Commander` and `Commander` maps using the low-ℓ likelihood and baseline common masks, respectively. We also show corresponding estimation of the global p-value for the $S(x)$ statistic.

Statistic	`Lkl-Comm.`	`Comm.`
$S_{1/2}$	97.1	99.5
$S(x)$ (global)	90.9	97.7
$\chi^2_0(\theta > 60^\circ)$	95.7	98.1

3 Hemispherical asymmetry

We reassess the asymmetry between the real-space N-point correlation functions computed on hemispheres reported previously for the WMAP (Eriksen *et al.*[6]) and Planck 2013 temperature maps (Planck collaboration[3]). We focus the analysis on the hemispheres determined in the ecliptic coordinate frame and frames defined by the Doppler boost (DB) and the dipole modulation (DM) directions. If we consider that the χ^2 statistic itself can act as a measure of fluctuation level, then asymmetry between the two measured hemispheres can be quantified by the ratio of the corresponding χ^2 values.

The probabilities of obtaining values of the χ^2 statistic or ratio for the Planck fiducial ΛCDM model at least as large as the observed values are given in Table 3.

Table 3: Probabilities of obtaining values for the χ^2 statistic and ratio of χ^2 of the N-point functions for the `Planck` fiducial ΛCDM model at least as large as the observed values of the statistic for the `SMICA` map on hemispheres defined by the ecliptic (first column), Doppler boost (DB, second column), and dipolar modulation (DM, third column) reference frames.

Hemisphere	Ecl.	DB	DM
2-point function			
Negative	88.0	86.9	61.8
Positive	77.6	91.1	59.9
χ^2-ratio	22.3	5.1	7.7
Pseudo-collapsed 3-point function			
Negative	99.7	64.1	95.9
Positive	31.4	79.3	48.3
χ^2-ratio	98.4	23.3	78.6
Equilateral 3-point function			
Negative	98.4	54.8	>99.9
Positive	42.6	95.0	78.4
χ^2-ratio	86.7	67.7	88.2
Rhombic 4-point function			
Negative	99.6	46.4	97.5
Positive	20.1	86.3	23.2
χ^2-ratio	97.0	57.9	92.5

Since we do not have any predictions concerning the behaviour of a given hemisphere, in the case of the χ^2 ratios we provide the complementary probabilities of the 2-tailed statistic. Proper interpretation of results requires that one recognize that the analysis is affected by a posteriori choices for the smoothing scale and reference frame defining the hemispheres. This typically leads to an overestimation of the significance of the results. Accounting for such effects requires the repetition of the analysis for all possible reference directions and also for data at other resolutions. Unfortunately, because of computational limitations, such an extended analysis is not possible for these higher-order statistics. Nevertheless, the observed properties of the Planck data are consistent with a clear lack of fluctuations in a direction towards the north ecliptic pole.

However, the χ^2-ratio statistic indicates a slightly smaller significance level for the asymmetry, not exceeding 99 % for any of the N-point functions.

4 Conclusions

Observed large angular scales CMB anomalies do not provide conclusive proofs that anything nonstandard is going on as they may be just a result of a posteriori inference. However, they may also indicate places to look for interesting nonstandard phenomena on large scales. Because the anomalies were observed also in WMAP temperature data, it effectively rules out residual systematic artifacts as possible origin of these features. Proposed cosmological explanations like anisotropic Bianchi VII_h model and wide class of universes with multi-connected topology are not confirmed for CMB temperature and polarisation data. Next generation of cosmological experiments devoted to observations of CMB polarisation and tracers of the large scale structure such as galaxies and radio sources will enable to avoid problem of a posteriori inference and give opportunity to explain nature of the anomalies.

Acknowledgments

We acknowledge use of the HEALPIX[a] software and analysis package (Górski *et al.*[7]) for deriving the results in this paper. We acknowledge the use of the Planck data. Support for Planck mission is provided by ESA; CNES and CNRS/INSU-IN2P3-INP (France); ASI, CNR, and INAF (Italy); NASA and DoE (USA); STFC and UKSA (UK); CSIC, MINECO, JA, and RES (Spain); Tekes, AoF, and CSC (Finland); DLR and MPG (Germany); CSA (Canada); DTU Space (Denmark); SER/SSO (Switzerland); RCN (Norway); SFI (Ireland); FCT/MCTES (Portugal); ERC and PRACE (EU).

References

1. C. L. Bennett, M. Halpern, G. Hinshaw, N. Jarosik, A. Kogut, M. Limon, S. S. Meyer, L. Page, D. N. Spergel, G. S. Tucker, E. Wollack, E. L. Wright, C. Barnes, M. R. Greason, R. S. Hill, E. Komatsu, M. R. Nolta, N. Odegard, H. V. Peiris, L. Verde, and J. L. Weiland. First-Year Wilkinson Microwave Anisotropy Probe (WMAP) Observations: Preliminary Maps and Basic Results. ApJS, 148:1–27, September 2003.
2. D. N. Spergel, L. Verde, H. V. Peiris, E. Komatsu, M. R. Nolta, C. L. Bennett, M. Halpern, G. Hinshaw, N. Jarosik, A. Kogut, M. Limon, S. S. Meyer, L. Page, G. S. Tucker, J. L. Weiland, E. Wollack, and E. L. Wright. First-Year Wilkinson Microwave Anisotropy Probe (WMAP) Observations: Determination of Cosmological Parameters. ApJS, 148:175–194, September 2003.
3. Planck Collaboration, P. A. R. Ade, N. Aghanim, C. Armitage-Caplan, M. Arnaud, M. Ashdown, F. Atrio-Barandela, J. Aumont, C. Baccigalupi, A. J. Banday, and et al. Planck 2013 results. XXIII. Isotropy and statistics of the CMB. A&A, 571:A23, November 2014.
4. C. J. Copi, D. Huterer, D. J. Schwarz, and G. D. Starkman. Lack of large-angle TT correlations persists in WMAP and Planck. MNRAS, 451:2978–2985, August 2015.
5. Planck Collaboration, P. A. R. Ade, N. Aghanim, Y. Akrami, P. K. Aluri, M. Arnaud, M. Ashdown, J. Aumont, C. Baccigalupi, A. J. Banday, and et al. Planck 2015 results. XVI. Isotropy and statistics of the CMB. *ArXiv e-prints*, June 2015.
6. H. K. Eriksen, A. J. Banday, K. M. Górski, and P. B. Lilje. The N-Point Correlation Functions of the First-Year Wilkinson Microwave Anisotropy Probe Sky Maps. ApJ, 622:58–71, March 2005.
7. K. M. Górski, E. Hivon, A. J. Banday, B. D. Wandelt, F. K. Hansen, M. Reinecke, and M. Bartelmann. HEALPix: A Framework for High-Resolution Discretization and Fast Analysis of Data Distributed on the Sphere. ApJ, 622:759–771, April 2005.

[a] http://healpix.jpl.nasa.gov

Cosmological Parameters from CMB Maps without Likelihood Approximation

B. Racine
Institute of Theoretical Astrophysics, Sem Sælands vei, 0371 Oslo, Norway



A primary goal of modern cosmology is to measure cosmological parameters. Given the sensitivity of current and future CMB surveys, the most important systematic effect is due to astrophysical foreground contamination. Here we present a new method that allows for joint estimation of cosmological parameter and the CMB map[1]. Combining this algorithm with parametric separation of astrophysical components, and thereby marginalizing over physically motivated foreground models, is straightforward, and will be done in future work.

1 Introduction

Recent cosmological surveys (Planck, WMAP, SDSS etc) are in good agreement with predictions from the ΛCDM model, and seem to confirm the standard picture of the Big Bang model starting with an inflationary phase[2].

The current and next generation of CMB experiments are aiming for the detection of B-modes, which are a signature of inflationary gravitational waves in the polarization of the CMB. It will then be of uttermost importance to carefully handle the polarized galactic foregrounds.

The parameters measured by the Planck collaboration are obtained via the maximum likelihood method[3]. There are two caveats to this method as is currently implemented: first, the computation of the likelihood is not exact, they are made in the fiducial Gaussian approximation; in addition, the foreground are modeled at the power spectrum level, whereas there is much more information to be used in the phases. These approximations have been shown to have negligible impact in the Planck analysis, but for future datasets, the use of the full map information might be a great improvement.

2 Component separation and Gibbs Sampling.

Our goal is to recover cosmological information from data $\boldsymbol{d}$ provided for example by experiments like Planck. We want to estimate the CMB map $\boldsymbol{s}$, Gaussian signal with covariance $\mathbf{S}$ as well as the angular power spectrum C_ℓ cleaned from the microwave foreground emissions $\boldsymbol{f_\nu}$, and other instrumental effects $\boldsymbol{I_\nu}$. Our model can then be written in pixel space as $\boldsymbol{d} = \mathbf{A}\boldsymbol{s} + \boldsymbol{n} + \boldsymbol{f_\nu} + \boldsymbol{I_\nu}$, where $\mathbf{A}$ is basically the convolution with the instrumental beam, and $\boldsymbol{n}$ is the Gaussian instrumental noise, of covariance $\mathbf{N}$.

Ideally, we would like to reconstruct the exact joint posterior of all these observables: $P(\boldsymbol{s}, C_\ell, \boldsymbol{f_\nu}, \boldsymbol{I_\nu} | \boldsymbol{d})$. That would allow to mitigate and propagate systematic uncertainties to the cosmological results. It is possible to explore this huge multi-dimensional object in an optimal way using Gibbs Sampling[4,5,6], where we explore the conditional distributions in a series of iterative Markov chain moves, i.e.

$$\begin{aligned}
\boldsymbol{s}^{i+1} &\leftarrow P(\boldsymbol{s}|C_\ell^i, \boldsymbol{f_\nu}^i, \boldsymbol{I_\nu}^i, \boldsymbol{d}) && (1)\\
C_\ell^{i+1} &\leftarrow P(\boldsymbol{C_\ell}|\boldsymbol{s}^{i+1}, \boldsymbol{f_\nu}^i, \boldsymbol{I_\nu}^i, \boldsymbol{d}) && (2)\\
\boldsymbol{f_\nu}^{i+1} &\leftarrow P(\boldsymbol{f_\nu}|\boldsymbol{s}^{i+1}, C_\ell^{i+1}, \boldsymbol{I_\nu}^i, \boldsymbol{d}) && (3)\\
\boldsymbol{I_\nu}^i &\leftarrow P(\boldsymbol{I_\nu}|\boldsymbol{s}^{i+1}, C_\ell^{i+1}, \boldsymbol{f_\nu}^i, \boldsymbol{d}) && (4)
\end{aligned}$$

This method was extensively used in the Planck analysis by the Commander method[7].

3 Sampling $P(\boldsymbol{s}, C_\ell|\boldsymbol{d})$

The central part of the posterior sampling is the joint estimation of the CMB map and the power spectrum $P(\boldsymbol{s}, C_\ell|\boldsymbol{d})$. For this, we then have to sample from two conditional distributions, $P(\boldsymbol{s}|C_\ell, \boldsymbol{d})$ and $P(C_\ell|\boldsymbol{s}, \boldsymbol{d})$. Using Bayes theorem, we have

$$\begin{aligned}
P(\boldsymbol{s}|C_\ell, \boldsymbol{d}) &\propto P(\boldsymbol{d}|\boldsymbol{s}, C_\ell)P(\boldsymbol{s}|C_\ell) \propto e^{-\frac{1}{2}(\boldsymbol{d}-\mathbf{A}\boldsymbol{s})^t\mathbf{N}^{-1}(\boldsymbol{d}-\mathbf{A}\boldsymbol{s})}e^{-\frac{1}{2}\boldsymbol{s}^t\mathbf{S}^{-1}\boldsymbol{s}} && (5)\\
&\propto e^{-\frac{1}{2}(\boldsymbol{s}-\hat{\boldsymbol{s}})^t(\mathbf{S}^{-1}+\mathbf{A}^t\mathbf{N}^{-1}\mathbf{A})(\boldsymbol{s}-\hat{\boldsymbol{s}})} && (6)
\end{aligned}$$

where we introduced the mean field map $\hat{\boldsymbol{s}} \equiv (\mathbf{S}^{-1} + \mathbf{A}^t\mathbf{N}^{-1}\mathbf{A})^{-1}\mathbf{A}\mathbf{N}^{-1}\boldsymbol{d}$. This means that we need Gaussian realizations of mean $\hat{\boldsymbol{s}}$, with covariance $(\mathbf{S}^{-1} + \mathbf{A}^t\mathbf{N}^{-1}\mathbf{A})^{-1}$. These can be done by generating $\boldsymbol{\omega_0}$ and $\boldsymbol{\omega_1}$, vectors from a Gaussian $\mathcal{N}(0, 1)$, with a dimension of a map in pixel space, and then solve

$$[\mathbf{S}^{-1} + \mathbf{A}^t\mathbf{N}^{-1}\mathbf{A}]\boldsymbol{s} = \mathbf{A}\mathbf{N}^{-1}\boldsymbol{d} + \mathbf{S}^{-\frac{1}{2}}\boldsymbol{\omega_0} + \mathbf{A}\mathbf{N}^{-\frac{1}{2}}\boldsymbol{\omega_1}. \quad (7)$$

Solving this equation can be fairly expensive when a mask and realistic anisotropic noise are used. In this work, we simplify by using Gaussian isotropic noise and the full sky, and the equation is then trivial to solve. We show samples drawn with this method in figure 1.

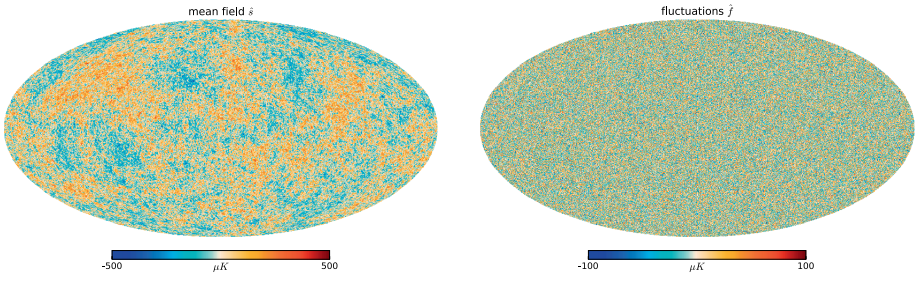


Figure 1 – Samples of $P(\boldsymbol{s}|C_\ell, \boldsymbol{d})$. The mean field map $\hat{\boldsymbol{s}}$, which corresponds to solving (7) for the first left hand side term only, is shown on the left, and the fluctuations $\hat{\boldsymbol{f}}$, solving for the other two terms, is on the right. Each sample is the sum of the two.

Once we have this sample of the CMB map, we need to sample on the power spectrum. First, let's define the power spectrum of the previous estimation's $\boldsymbol{s}$ map: $\sigma_\ell = \frac{1}{2\ell+1}\sum_m |a_{\ell m}|^2$. Using Bayes theorem, we can then show that samples of C_ℓ can be drawn from an inverse Wishart distribution as follows,

$$P(C_\ell|\boldsymbol{s}) \propto P(C_\ell)\frac{e^{-\frac{1}{2}\boldsymbol{s}\mathbf{S}^{-1}\boldsymbol{s}}}{\sqrt{|\mathbf{S}|}} = P(C_\ell)\frac{e^{-\frac{2\ell+1}{2}\frac{\sigma_\ell}{C_\ell}}}{C_\ell^{\frac{2\ell+1}{2}}}. \quad (8)$$

We can generate such samples by drawing a $(2\ell+1)$-vector ρ_ℓ from $\mathcal{N}(0,1)$, and computing $C_\ell = \frac{(2\ell+1)\sigma_\ell}{|\rho_\ell|^2}$. The problem with these normal Gibbs steps, is that the C_ℓ samples then follow cosmic variance, as can be seen in figure 2. Exploring the full posterior will then be hard in the noise dominated regime. Jewell et al. introduced a solution[8], but it is not efficient in the signal dominated regime. Until now, exploring the CMB data sets in both signal and noise dominated regimes was done in an hybrid way, using standard Gibbs sampling at low-ℓ and Jewell's method at high-ℓ. In the next section, we explain an evolution of this method to solve this issue.

4 New deterministic Metropolis-Hasting step.

We show a schematic representation of the standard Gibbs steps in figure 2: in the high signal-to-noise regime, the signal map is tightly constrained and the C_ℓ posterior is dominated by cosmic variance. In the low signal-to-noise regime, C_ℓ and σ_ℓ are strongly correlated, whereas successive Gibbs steps are orthogonal. We would ideally move diagonally in this space.

In this work[1], we propose to rescale the fluctuation maps, i.e. adding a deterministic step after solving the mapmaking equation (7):

$$\boldsymbol{f}^{i+1}_{\ell m} = \sqrt{\frac{C^{i+1}_\ell}{C^i_\ell}}\hat{\boldsymbol{f}}^i_{\ell m}, \tag{9}$$

where the i and $i+1$ indices represent the consecutive states in the Metropolis-Hasting chain. With such a rescaling, in the low signal-to-noise regime, $\boldsymbol{s}^i \simeq \hat{\boldsymbol{f}}^i$ and we are able to do diagonal moves in the $(C_\ell, \boldsymbol{s})$ space. In the high signal-to-noise regime, $\boldsymbol{s}^i \simeq \hat{\boldsymbol{s}}^i$, and the rescaling as a negligible effect, so the steps are similar to standard Gibbs sampling.

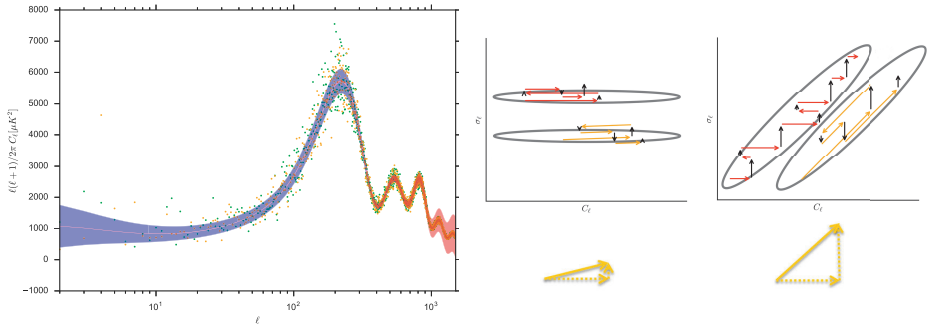


Figure 2 – Left: samples of $P(C_\ell|\boldsymbol{s},\boldsymbol{d})$. We show the cosmic variance as the blue band, whereas instrumental noise is the red band. With our specifications, these two noises are equivalent for $\ell \sim 600$. We also show two samples in green and yellow. As we can see, their variance is given by the cosmic variance, and not the instrumental one. Right: sketch of the sampling in the two regimes. In red we show the standard orthogonal Gibbs sampling steps, where we need many steps in the high signal-to-noise regime to explore the full posterior. In yellow, we show the new algorithm, where we can have diagonal moves in this regime. Below, we sketch the C_ℓ proposal (horizontal dashed arrow) is followed by a rescaling of the fluctuation map using (9) (vertical dashed arrow).

5 Parameter sampling.

This rescaling provides a solution working both at low-ℓ (high signal-to-noise) and high-ℓ (low signal-to-noise). It allows us to sample directly at the cosmological parameter level, i.e., instead of sampling C_ℓ, we draw a vector parameters $\theta = [\Omega_b h^2, \Omega_c h^2, \tau, A_s, n_s, H_0]$, with baryon density $\Omega_b h^2$, cold dark matter density $\Omega_c h^2$, optical depth at reionization τ, amplitude and tilt of the

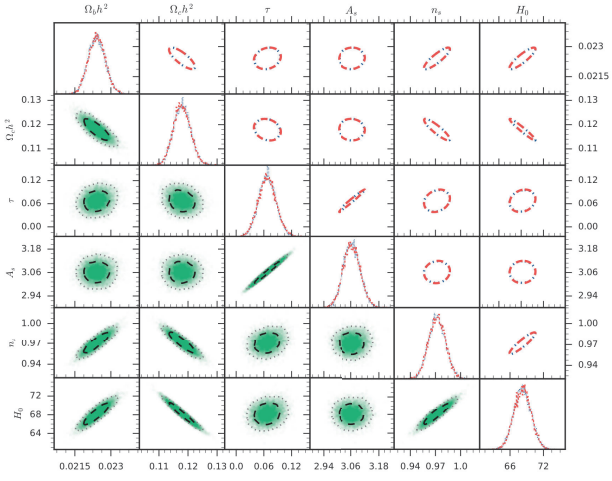


Figure 3 – Recovered parameter distribution using 10^6 samples (green ellipses, and blue dotted) and Gaussian kernel density estimation (black), as well as a comparison with exact solution (red dashed).

primordial power spectrum A_s and n_s, and the Hubble parameter H_0. We use a proposal function $w(\theta)$, and we call a Boltzmann code (here CAMB[9]) to get the corresponding C_ℓ.

We can then show that the Metropolis-Hasting acceptance rate is given by:

$$A = \min\left[1, \frac{\pi(\theta^{i+1})}{\pi(\theta^i)} \frac{w(\theta^i|\theta^{i+1})}{w(\theta^{i+1}|\theta^i)} \frac{P(\theta^{i+1})}{P(\theta^i)}\right], \tag{10}$$

where

$$\pi(\theta^{i+1}) = e^{-\frac{1}{2}(\boldsymbol{d}-\mathbf{A}\hat{\boldsymbol{s}})^{\mathrm{t}}\mathbf{N}^{-1}(\boldsymbol{d}-\mathbf{A}\hat{\boldsymbol{s}})} e^{-\frac{1}{2}\hat{\boldsymbol{s}}^t\mathbf{S}^{-1}\hat{\boldsymbol{s}}} e^{-\frac{1}{2}\hat{\boldsymbol{f}}^t\mathbf{A}^{\mathrm{t}}\mathbf{N}^{-1}\mathbf{A}\hat{\boldsymbol{f}}}. \tag{11}$$

With an adapted proposal function described in the paper, we recover the underlying probability distribution of the parameters, with a correlation length of the same order as standard samplers. The next step will be to include such a sampler in Commander and apply it to simulations and data within component separation.

Acknowledgments

I acknowledge fundings from the Research Council of Norway. I want to thank the organizers of this 51st Rencontres de Moriond, and congratulate all of them for this highly stimulating and pleasant conference.

References

1. Racine, B., Jewell, J. B., Eriksen, H. K., & Wehus, I. K. 2016, ApJ, 820, 31
2. Planck Collaboration, 2015, arXiv:1502.01589
3. Planck Collaboration 2015, arXiv:1507.02704
4. Jewell, J., Levin, S., & Anderson, C. H. 2004, Apj, 609, 1
5. Wandelt, B. D., Larson, D. L., & Lakshminarayanan, A. 2004, PRD, 70, 083511
6. Eriksen, H. K., O'Dwyer, I. J., Jewell, J. B., et al. 2004, Apj Supplement, 155, 227
7. Planck Collaboration 2015, [arXiv:1502.01588]
8. Jewell, J. B., Eriksen, H. K., Wandelt, B. D., et al. 2009, ApJ, 697, 258
9. Lewis, A., Challinor, A., & Lasenby, A. 2000, ApJ, 538, 473

MEASUREMENTS OF DEGREE-SCALE B-MODE POLARIZATION WITH BICEP2, KECK ARRAY, AND BICEP3

C. A. BISCHOFF for the BICEP/Keck Collaboration
Harvard-Smithsonian Center for Astrophysics, 60 Garden St, Cambridge MA, 02138, U.S.A.

BICEP2, the Keck Array, and BICEP3 are a series of small-aperture Cosmic Microwave Background (CMB) polarimeters operating from the South Pole. These telescopes search for evidence of inflation by targeting the recombination peak in the BB spectrum. BICEP2 reported the first detection of degree-scale B modes at 150 GHz, but the cross-correlation with high frequency polarization maps from the Planck satellite shows that most or all of this signal is due to Galactic dust foregrounds. New deep observations from the Keck Array at 95 GHz have significantly improved our ability to distinguish between CMB and foreground signals; these constraints will improve further with 220 GHz data from Keck Array and 95 GHz data from BICEP3. Future B-mode constraints on inflation will be boosted with multi-frequency data at large angular scales from the proposed BICEP Array and delensing in conjunction with the South Pole Telescope.

1 Constraining Cosmological Inflation with B-mode Polarization

While the Standard Model of Cosmology, ΛCDM, is extremely successful at explaining a wide range of observations, it is notably incomplete as we lack understanding of either the cosmological constant (Λ) or cold dark matter (CDM). Another unanswered question in ΛCDM is the origin of the Big Bang itself. The theory of inflation posits a period of exponential expansion of the space-time metric, which would explain the observed homogeneity of our universe, the source of initial perturbations, and other initial conditions.[1] An unverified prediction of inflation is the existence of a stochastic background of gravitational waves, created from quantum fluctuations of the metric that were stretched to macroscopic length scales. The search for this Cosmic Gravitational Wave Background (CGB) is one of the most exciting topics in cosmology.

Direct detection of the CGB is likely impossible, but we may be able to measure the tensor perturbation (gravitational wave) contribution to the Cosmic Microwave Background anisotropies. The amplitude of the CGB is parametrized by r, the ratio of power between tensor and scalar (density) perturbations. The current best upper limit is $r_{0.05} < 0.07$ at 95% confidence, from BICEP2 and Keck Array data in combination with maps from the Planck and WMAP satellites.[2] For such small ratios, sample variance from the dominant scalar perturbations limits our ability to detect tensors in the temperature or E-mode polarization fields, even with full sky observations. Fortunately, the odd parity of the B-mode polarization field means that it receives no contribution from scalar perturbations, making it an ideal "low background" channel to search for gravitational waves.[3,4,5] The B-mode signal induced by gravitational waves at the time of recombination peaks at multipoles near $\ell = 80$,[a] which corresponds to angular scales of 2–4 degrees.

[a] This is referred to as the recombination bump. The reionization bump, present at very large scales $\ell < 10$, is due to gravitational waves scattering after the universe reionizes at lower redshift.

There are several obstacles to detection of gravitational waves via the degree-scale CMB BB spectrum. First, the amplitude of the signal is very small,[b] requiring large arrays of background-limited detectors integrating deeply from an excellent terrestrial site, high altitude balloon, or satellite. Our vantage point in the Milky Way means that all lines of sight must pass through some column of diffuse Galactic matter. In the microwave part of the electromagnetic spectrum, the two most important types of Galactic emission are synchroton emission from free electrons (brighter at low frequencies) and thermal emission from dust (brighter at high frequencies). Both synchrotron and dust emission are partially polarized due to the Galactic magnetic field. Multicolor observations allow us to distinguish between the CMB blackbody spectrum and foregrounds, but we have only just begun to understand the properties of polarized foreground emission in the cleanest regions of the sky. Finally, the E-mode polarization pattern of the CMB, sourced by scalar perturbations, is distorted by gravitational lensing from large scale structure between us and the surface of last scattering, leaking part of that signal into B modes.[6] While techniques have been developed to identify and remove these lensing B modes,[7,8,9] a resulting improvement in sensitivity to r has not yet been demonstrated on real data.

2 The BICEP/Keck Observational Program

BICEP2, the Keck Array, and BICEP3 make up a long-running program of microwave polarimeters operating at the Amundsen-Scott South Pole Station that have produced the best constraints to date on B-mode polarization from inflation. Beyond a common observing site, these experiments share similar optical designs, detector technology, survey strategy, and their data are analyzed jointly. The BICEP/Keck experimental strategy is to maximize sensitivity by packing a large number of detectors into high optical throughput telescopes with the minimum aperture size needed to target the signature of inflation at angular scales of a few degrees. Figure 1 summarizes the progression from BICEP2 and the Keck Array through BICEP3 and the planned BICEP Array. As the program proceeds, we have increased the number of deployed detectors and distributed them across three observing frequencies (95, 150, and 220 GHz) to improve our ability to separate CMB and foreground signals.

BICEP2 observed from 2010–2012 from the Dark Sector Laboratory (DSL), making use of a three-axis mount that was originally built for BICEP1. BICEP2 consisted of a single small-aperture telescope with a focal plane array of 512 transition edge sensor (TES) bolometers arranged into 256 dual-polarization pixels. All BICEP2 detectors operated in the 150 GHz observing window. Papers describing the cryostat, optics, and detectors[10,11] and the optical calibrations[12] contain further details.

The Keck Array was designed to use existing South Pole infrastructure by multiplying the successful BICEP2 design into a five telescope array on the mount originally built for the DASI experiment. The main design change was to upgrade the liquid Helium cooled BICEP2 cryostat to a more compact, pulse tube cooled design.[13] A major advantage of the Keck Array's modular design has been the ability to update the observing frequencies of individual telescopes from year to year. Table 1 summarizes the distribution of deployed detectors between 95, 150, and 220 GHz observing bands across seven years of the BICEP/Keck observing program.

BICEP3 represents a significant upgrade over BICEP2 and Keck Array, with a combination of larger telescope aperture and faster optics that yield five times the focal plane area.[14] While the 95 GHz detectors in BICEP3 use a similar design to those from BICEP2 or Keck Array, the BICEP3 detector tiles have been packaged into modular units that can be individually installed on the focal plane. BICEP3 began full operations in 2016.

[b] Theory doesn't provide a lower bound for r, but there is significant interest in the large-field regime, $r \gtrsim 10^{-3}$.

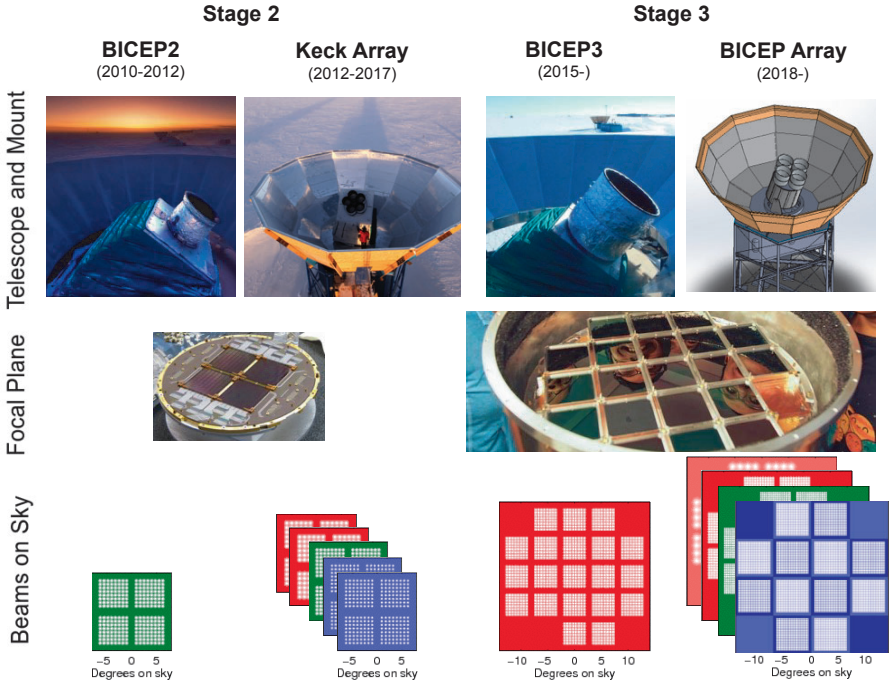


Figure 1 – Summary of the BICEP/Keck observing program. From left to right, the columns summarize BICEP2, the Keck Array, BICEP3, and the planned BICEP Array. The top row shows a photo of each instrument (CAD rendering for BICEP Array). The second row shows photos representing the focal planes of each instrument. These photos have approximately the same scale, demonstrating that BICEP3 and BICEP Array feature much larger focal planes. The bottom row contains diagrams of the focal planes projected on the sky. The focal plane projections are color coded to show various observing frequencies. Red represents 95 GHz; green represents 150 GHz; blue represents 220 GHz. For BICEP Array, we additionally include light red (35 GHz) and dark blue (270 GHz).

Table 1: Number of detectors deployed by year and observing frequency for BICEP2, Keck Array, and BICEP3. Each of the five Keck Array telescopes can field 288 detectors at 95 GHz or 528 detectors at 150 or 220 GHz. This table reflects the design detector count, not achieved yield. The right hand columns show the accumulated survey weight at each frequency. The 2012 survey weight includes BICEP2 only. The 2015 and 2016 survey weight values (in parentheses) are preliminary.

	Detector count					Survey weight $[\mu K^{-2}]$		
	BICEP2		Keck Array		BICEP3			
Year	150 GHz	95 GHz	150 GHz	220 GHz	95 GHz	95 GHz	150 GHz	220 GHz
2010	512							
2011	512							
2012	512		2560				100,000[15]	
2013			2560				250,000[16]	
2014		576	1536			47,000[2]	310,000[2]	
2015		576	512	1024		(94,000)	(340,000)	(4,000)
2016			512	2048	2560	(233,000)	(370,000)	(12,000)

In addition to showing deployed detector counts, Table 1 shows the accumulated survey weight by year for each observing frequency. Survey weight increases linearly with effort and is

calculated as

$$\text{Survey weight} = 2 \times \frac{\text{map area}}{(\text{map depth})^2}\,, \tag{1}$$

with the factor of two included to count both the Q and U polarization maps. Survey weight represents the total sensitivity to signals with a CMB-like $3K$ blackbody spectrum; the 220 GHz data will provide considerable sensitivity to Galactic dust foregrounds, despite its apparently low weight.

3 Current Constraints on Cosmology and Foregrounds

Since the initial BICEP2 results publication[15] in 2014, we have made significant progress on our understanding of Galactic foreground polarization. High frequency (353 GHz) polarization maps from the Planck satellite provided the first hints[17,18] that the BICEP2 signal is dominated by Galactic dust emission. A joint analysis of BICEP2, Keck Array (2012–2013, 150 GHz only), and Planck data detected dust at 5.1σ and set an upper limit on tensors, $r_{0.05} < 0.12$ at 95% confidence.[19] This joint analysis was ultimately limited by the noise level in the Planck 353 GHz map; further improvement requires better multi-frequency data. As shown in Table 1, Keck Array and BICEP3 are busy producing deep maps covering the same region of sky at 95 and 220 GHz to address this problem.

The first results including 95 GHz data from Keck Array[2] were published this year (referred to here as BK14). This paper represents a milestone, as the constraint on r from the BB spectrum has exceeded the CMB temperature-derived constraint[c] for the first time. Figure 2 summarizes the BK14 constraints on r as well as foreground nuisance parameters. To derive these results, we compute all BB auto and cross-spectra between a set of multi-frequency maps and calculate the likelihood of a parametrized model, using the Hamimeche-Lewis approximation for the likelihood of correlated Gaussian fields.[21] Prior to calculating the BB spectra, these maps have been purified by a matrix operation that removes the "ambiguous modes" that occur when an E-mode map is filtered and apodized in the data reduction process.[22] This highly effective purification step is critical to fully take advantage of the deep BICEP2/Keck maps.

The data used in this analysis are:

- BICEP2 + Keck Array 150 GHz map, including all observations through 2014.
- Keck Array 95 GHz map (2014 data only).
- Planck full mission polarization maps[23] at 30, 44, 70, 100, 143, 220, and 353 GHz. These maps have been smoothed to BICEP2/Keck resolution and reobserved with the same coverage as the BICEP2/Keck 150 GHz map.
- WMAP nine-year polarization maps[24] at 23 and 33 GHz, which have been likewise reobserved.

The parametrized model includes the following components:

- Lensing B modes, calculated assuming a standard ΛCDM model.
- Tensor B modes with amplitude proportional to r.
- A dust component with spectral behavior corresponding to a modified blackbody with emissivity power law index β_d. The dust is assumed to scale with ℓ as $\ell(\ell+1)\mathcal{C}_\ell \sim \ell^{\alpha_d}$. We define A_d, the amplitude of the dust power spectrum, at $\nu = 353$ GHz and $\ell = 80$. We apply a Gaussian prior on β_d that is centered at 1.59 with width 0.11. There is a weak

[c] Planck TT+lowP+lensing+ext yields $r_{0.002} < 0.11$ ($r_{0.05} < 0.12$) at 95% confidence.[20]

uniform prior on the ℓ scaling, $-1 < \alpha_d < 0$, but the analysis is fairly insensitive to this parameter.

- A synchrotron component with power law spectral behavior governed by parameter β_s. We also assume power law scaling in ℓ for this component, with index α_s. The synchrotron amplitude, A_s, is defined at $\nu = 23$ GHz and $\ell = 80$. The Gaussian prior on β_s is centered at -3.1 with width 0.3. The prior on α_s is the same as for α_d.

- We allow for spatial correlation between the dust and synchrotron foreground components. The correlation coefficient, ϵ, is assumed to be constant in ℓ. We apply a uniform prior between 0 and 1 for ϵ (positive correlation).

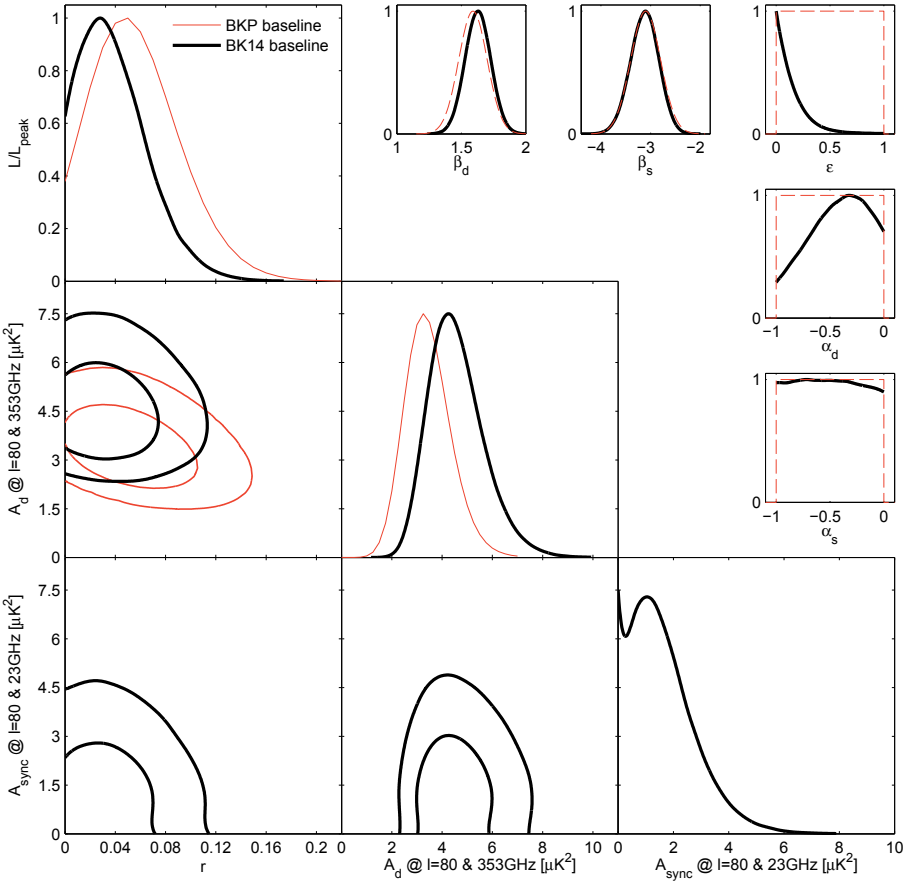


Figure 2 – Likelihood figure reproduced from the BK14 results paper.[2] Solid black lines show the BK14 results; solid red lines show previous results from the BICEP2/Keck Array/Planck joint analysis.[19] One-dimensional marginalized posteriors are shown along the main diagonal for r, A_d, and A_s. We also show the two-dimensional marginalized posteriors between these three parameters. The small panels in the upper right show posteriors for auxiliary parameters, β_d, β_s, ϵ, α_d, and α_s, with dashed red lines to indicate the priors that were applied on these parameters.

From Figure 2, we see that the dust component is detected at high significance (center panel). No synchrotron component is detected (bottom right panel), which suggests that deeper 95 GHz observations from BICEP3 will yield significant returns. As noted above, these data provide the tightest upper limit to date on r (upper left panel). Comparing the BK14 result (solid black) with the previous BICEP2/Keck Array/Planck joint analysis (solid red) for the two-dimensional r vs A_d posterior (middle left panel), we can see the power of the Keck Array 95 GHz data; the red contours show a significant degeneracy between r and A_d, which is broken with the new data.

4 Future Prospects

The last two lines of Table 1 promise great improvements in the foreground separation and constraint on r for upcoming BICEP/Keck publications. The current experimental strategy employs Keck Array as a high frequency dust monitor while BICEP3 provides very high mapping speed at 95 GHz. For the 2017 observing season, we plan to experiment with 270 GHz focal planes in two of the Keck Array telescopes. South Pole atmospheric properties are less well known at that frequency, but models suggest that higher sky temperatures will be more than compensated by increased brightness of the dust signal. Additional high frequency channels will also increase the robustness of the component separation against foreground complexities, such as decorrelation of the dust signal.

To surpass the currently operating instruments, we are building the BICEP Array (right column of Figure 1), which will deploy to South Pole for observations starting in 2018. BICEP Array will be an upgrade of the Keck Array to four BICEP3-like telescopes. With this upgrade, we will retain the modularity of Keck Array but increase the throughput of the telescopes to match BICEP3. BICEP Array will operate at 35, 95, 150, 220, and 270 GHz.

While this summary of the BICEP/Keck program focuses on separation of CMB and foreground components, it will soon be equally important to be able to remove the lensing B modes, which would otherwise contribute irreducible sample variance to attempts to measure tensors. With an estimate of the lensing-mass map, ϕ, and maps of the CMB E modes, it is possible to reconstruct a template of the lensing-induced B modes. The auto and cross-spectra derived from this template can be folded into our likelihood analysis to help reduce lensing sample variance while simultaneously constraining foregrounds and tensors.

In the short term, our best estimate of ϕ might come from the Cosmic Infrared Background, which measures high redshift galaxies that are imperfect tracers of the lensing potential. A collaborative effort is currently underway to use a CIB-derived ϕ map together with E modes from SPTpol[25] (which are complete to much higher ℓ than the BICEP/Keck E-mode map) to delens BICEP/Keck B modes. While this delensing exercise is expected to yield only a small improvement on the r constraint, it will be an important first demonstration of the technique.

Ultimately, the best measurements of ϕ will be derived from the higher order statistics of the CMB maps themselves. There have already been publications demonstrating CMB-derived lensing maps from Planck,[26] SPTpol,[27] ACTpol,[28] POLARBEAR,[29,30] and BICEP/Keck,[31] but the signal-to-noise per mode is still rather low. The South Pole Telescope 3rd Generation camera (SPT-3G), scheduled for deployment at the end of 2016, represents a huge upgrade in sensitivity which will provide critical assistance in delensing the BICEP Array data.[32]

Acknowledgments

The BICEP/Keck team acknowledges our intrepid winter-overs: Steffen Richter (BICEP2, 2010–2012), Robert Schwarz (Keck Array, started in 2011 and still going!), Sam Harrison (BICEP3, 2015), and Hans Boenish (BICEP3, 2016).

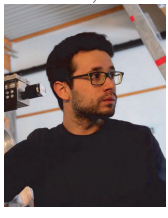
References

1. A. R. Liddle and D. H. Lyth. *Cosmological Inflation and Large-Scale Structure*. Cambridge University Press, 2000.
2. BICEP2 and Keck Array Collaborations. *Phys. Rev. Lett.*, 116(3):031302, January 2016.
3. U. Seljak. *Astrophys. J.*, 482(1):6, Jun 1997.
4. M. Kamionkowski, A. Kosowsky, and A. Stebbins. *Phys. Rev. Lett.*, 78:2058, Mar 1997.
5. U. Seljak and M. Zaldarriaga. *Phys. Rev. Lett.*, 78:2054, Mar 1997.
6. M. Zaldarriaga and U. Seljak. *Phys. Rev. D*, 58(2):023003, July 1998.
7. W. Hu and T. Okamoto. *Astrophys. J.*, 574:566, August 2002.
8. A. Cooray, M. Kamionkowski, and R. R. Caldwell. *Phys. Rev. D*, 71(12):123527, June 2005.
9. T. Namikawa, D. Yamauchi, and A. Taruya. *J. Cosmol. Astropart. Phys.*, 1:007, January 2012.
10. BICEP2 Collaboration. *Astrophys. J.*, 792:62, September 2014.
11. BICEP2, Keck Array, and SPIDER Collaborations. *Astrophys. J.*, 812:176, October 2015.
12. BICEP2 and Keck Array Collaborations. *Astrophys. J.*, 806:206, June 2015.
13. C. D. Sheehy, P. A. R. Ade, R. W. Aikin, et al. In *Millimeter, Submillimeter, and Far-Infrared Detectors and Instrumentation for Astronomy V*, volume 7741 of *Proc. SPIE*, page 77411R, July 2010.
14. Z. Ahmed, M. Amiri, S. J. Benton, et al. In *Millimeter, Submillimeter, and Far-Infrared Detectors and Instrumentation for Astronomy VII*, volume 9153 of *Proc. SPIE*, page 91531N, August 2014.
15. BICEP2 Collaboration. *Phys. Rev. Lett.*, 112(24):241101, June 2014.
16. BICEP2 and Keck Array Collaborations. *Astrophys. J.*, 811:126, October 2015.
17. Planck Collaboration. Intermediate results. xix. *A&A*, 576:A104, Apr 2015.
18. Planck Collaboration. Intermediate results. xxx. *A&A*, 586:A133, Feb 2016.
19. BICEP2/Keck and Planck Collaborations. *Phys. Rev. Lett.*, 114(10):101301, March 2015.
20. Planck Collaboration. 2015 results. xiii. *arXiv e-prints*, 1502.01589, February 2015.
21. S. Hamimeche and A. Lewis. *Phys. Rev. D*, 77(10):103013, May 2008.
22. Keck Array and BICEP2 Collaborations. *arXiv e-prints*, 1603.05976, March 2016.
23. Planck Collaboration. 2015 results. i. *arXiv e-prints*, 1502.01582, February 2015.
24. C. L. Bennett, D. Larson, J. L. Weiland, et al. *Astrophys. J. Suppl.*, 208:20, October 2013.
25. A. T. Crites, J. W. Henning, P. A. R. Ade, et al. *Astrophys. J.*, 805:36, May 2015.
26. Planck Collaboration. 2015 results. xv. *arXiv e-prints*, 1502.01591, February 2015.
27. K. T. Story, D. Hanson, P. A. R. Ade, et al. *Astrophys. J.*, 810:50, September 2015.
28. A. van Engelen, B. D. Sherwin, N. Sehgal, et al. *Astrophys. J.*, 808:7, July 2015.
29. POLARBEAR Collaboration. *Phys. Rev. Lett.*, 113(2):021301, July 2014.
30. POLARBEAR Collaboration. *Phys. Rev. Lett.*, 112(13):131302, April 2014.
31. Keck Array and BICEP2 Collaborations. *arXiv e-prints*, 1606.01968, June 2016.
32. B. A. Benson, P. A. R. Ade, Z. Ahmed, et al. In *Millimeter, Submillimeter, and Far-Infrared Detectors and Instrumentation for Astronomy VII*, volume 9153 of *Proc. SPIE*, page 91531P, July 2014.



Instrumentation development for spectroscopic observations of the Cosmic Microwave Background

D'Alessandro G. *on behalf OLIMPO collaboration*
Department of Physics, University Sapienza of Rome,
Piazzale Aldo Moro 5, 00185 Roma, Italy



The Sunyaev-Zel'dovich (SZ) effect is a powerful tool for studying clusters of galaxies and cosmology. Large mm-wave telescopes are now routinely detecting and mapping the SZ effect in a number of clusters, measure their comptonisation parameter and use them as probes of the large-scale structure and evolution of the universe. By using accurate simulations of observations, we show that estimates of the physical parameters of clusters (optical depth, plasma temperature, peculiar velocity, non-thermal components etc.) obtained from multi-band SZ photometry can be significantly biased, owing to the reduced frequency coverage, to the degeneracy between the parameters and to the presence of a number of independent components larger than the number of frequencies measured. By demonstrating that low-resolution spectroscopic measurements of the SZ effect that are effective in removing the degeneracy [1]. I describe an imaging, efficient, differential Fourier transform spectrometer (FTS), optimized for measurements of faint brightness gradients at millimeter wavelengths [2]. The instrument is based on a Martin-Puplett interferometer (MPI) configuration. We combined two MPIs working synchronously to use the whole input power. In our implementation the observed sky field is divided into two halves along the meridian, and each half-field corresponds to one of the two input ports of the MPI. In this way, each detector in the FTS focal planes measures the difference in brightness between two sky pixels, symmetrically located with respect to the meridian. Exploiting the high common mode rejection of the MPI, we can measure low sky brightness gradients over a high isotropic background. This unique feature makes the MPI an optimal zero instrument, able to detect small brightness gradients embedded in a large common background. We investigate experimentally the common-mode rejection achievable in the MPI at mm wavelengths, and discuss the use of the instrument to measure the spectrum of cosmic microwave background (CMB) anisotropy [3,4].

1 Thermal Sunyaev-Zel'dovich effect

Galaxy clusters are rich in hot ionized gas. A typical galaxy cluster mass is $3 \cdot 10^{14} M_{\odot}$, with a gravitational effective radius of the order of one Mpc. A gas in hydrostatic equilibrium in the gravitational field of the cluster should have an electronic temperature $T_e \sim KeV$ The thermal emission at this temperature is in the X ray range, so that the galaxy cluster becomes a strong source of X-rays. When CMB photons cross this hot gas they can interact with hot electrons,

undergoing inverse Compton scattering. A small fraction of the kinetic energy of the electron is transferred to the photon, shifting its frequency higher. This phenomenon is called Thermal Sunyev Zel'dovich effect (SZ), from the scientists who theorized it in the '70s [5].

2 OLIMPO Experiment

The OLIMPO experiment [5] consists of a mm-wave telescope, with 2.6m diameter aperture, designed to operate aboard of a stratospheric balloon, at an altitude around 40 km, to avoid atmospheric contamination of the measurements. The telescope is equipped with 4 arrays of detectors, covering the frequency range between 140 GHz and 450 GHz, and optimized to measure cosmological signals. The first target for OLIMPO is the cosmic microwave background (CMB), in particular its anisotropy, and in particular the Sunayaev-Zel'dovich effect, through the observation of a selected sample of clusters of galaxies. The angular resolution of OLIMPO is a factor 2.5 better than the one of the Planck satellite at 340 GHz, and the number of detectors in the same band is 4 times larger; moreover the angular resolution of OLIMPO in the sub-mm bands (around 1 arcmin) matches the angular resolution of the large ground based telescopes devoted to SZ surveys, thus providing much needed complementary high-frequency information. The experiment will allow to measure the spectrum of CMB anisotropy up to multipoles $\ell \sim 2500$.

3 The Murtin Pupplet interferometer plug-in

In 2010 we have started the design of a Fourier transform spectrometer for the OLIMPO experiment. The main purpose was to transform the experiment from a standard 4-band photometer into something no one had ever done: a differential spectrometer on a stratospheric balloon. The main problem was technical: where and how to place an optically and mechanically complex component as a Fourier transform spectrometer in the already crowded OLIMPO instrument. The optical design was made by dr. Alessandro Schillaci and ended in late 2010.

3.1 The spectral resolution advantage

OLIMPO as a balloon-borne multiband photometer would be just another one among many high performance instruments devoted to SZ measurements. So it was decided do build a low-resolution differential spectrometer for OLIMPO, multiplying the number of independent frequency bands by a factor 5-10 with respect to multiband photometers. This would allow full control of the different components contributing to the measured signal, and to fully exploit the advantage of the operation from the highly transparent stratosphere.

Including such a complex optical system in an experiment already built required years of work and use of very significant resources, so first of all we need to demonstrate how much this plug-in would improve the capabilities of the OLIMPO experiment.

In the paper Low-resolution spectroscopy of the Sunyaev-Zel'dovich effect and estimates of cluster parameters (de Bernardis et al. A&A 538, A86 (2012)), we used accurate simulations of observations with lines-of-sight through clusters of galaxies with different experimental configurations (4-band photometers, 6-band photometer, multi-range differential spectrometer, full coverage spectrometers) and different intracluster plasma stratifications. We found that measurements carried out with ground-based few-band photometers are biased towards high electron temperatures and low optical depths, and require coverage of high frequency and/or independent complementary observations to produce unbiased information. Instead, a differential spectrometer that covers 4 bands with a resolution of $\sim$ 6 GHz eliminates most if not all of the bias; full-range differential spectrometers are the ultimate resource that allows a full recovery of all parameters.

For each experimental configuration we simulated 3000 measurements and fitted each simulated measurement with a theoretical spectrum including the SZ and all the other possible

contributions. In table 1 of the paper [1] we show the best-fit parameters and their standard deviations. In the following table we select the results for a 4-band balloon-borne photometer.

3.2 Maximum resolution

Interferogram obtained moving one roof mirror up to the maximum stroke of +2cm from the zero path difference (ZPD), and the other symmetrically to a maximum offset -2cm from the ZPD, producing a maximum optical path difference (OPD) of 8 cm. This is to be compared to interferograms for shorter maximum optical path differences. For the longest possible optical path difference introduced by our DFTS (8 cm), the width of the 140 GHz line is 1.87 GHz, consistent with the expectation $\Delta\sigma \sim 1/(2OPD_{max})$ (the interferogram was apodized with a triangular window). Decreasing the OPD, the spectral resolution degrades as expected, while the signal-to-noise ratio for the measurement of continuum sources improves as $1/\Delta\sigma$ [2].

3.3 Continuum measurements and FTSs characterization

In order to test the performance at higher frequency, we coupled the DFTS to a thermal source, an Hg lamp producing a $\sim 5000K$ gray body, and we filtered the emission using different mesh filters.

These measurements were used to evaluate the inherent characteristics of the FTS. Having 2 FTSs allows you to recover a 50% of the signal that would be lost otherwise. But it is important to evaluate how the two FTS are balanced. To do this, you can exclude a FTS by placing a sheet of Eccosorb on its beamsplitter. Using the lamp and a bandpass filter at 600GHz ww produced the two interferograms for the two FTSs; in Fig.3 the algebraic sum of the two interferograms was then compared with the signal of the whole DFTS. Same measurements were made using other filters to 220GHz, 375GHz and 450GHz and producing similar results [2].

Another important measurement to characterize the DFTS is the balance between the two inputs. The measurement was made by measuring the signal at the center of the A-side of the wedge and at center of the other side. This measurement is used to see if the instrument outputs correctly the difference between the two fields on the wedge or if a branch is more efficient than the other. We obtain a difference less then 1%

3.4 Efficiency of the instrument

Comparing the ZPD signal transmitted by our instrument to the ZPD signal measured with the same detector, when the spectrometer is bypassed, we can assess the optical efficiency of the instrument. We find that this is dominated by the alignment of the mirrors and wiregrids of the interferometers. After careful alignement, we measured that for unpolarized sources, the ratio between the two signals is $> 90\%$ at 150 GHz, $> 95\%$ at 220 GHz and 375 GHz, and $> 80\%$ at 600 GHz. Given the sensitivity of these numbers to alignment of the mirrors, and the fact that when the alignment is not perfect, the efficiency is reduced by the same factor for all frequencies, we conclude that the slight inefficiency is mainly due to edge rays that are lost in case of inaccurate alignment. In the spectroscopic configuration we compared the height of the ZPD peak (above the baseline) with the baseline amplitude to assess the interferometric modulation efficiency of the instrument. This is $> 98\%$ at 145 GHz and $> 80\%$ at 600 GHz, demonstrating that the instrument features a good efficiency in the whole frequency range useful for SZ measurements [2].

3.5 Common mode rejection

By using dedicated black body calibrators we perform intensity measurement at several temperature differences. We obtain a zero-signal, corresponding a common mode residual, of $7mK$, showing as we can separate the S-Z signal to common mode [4].

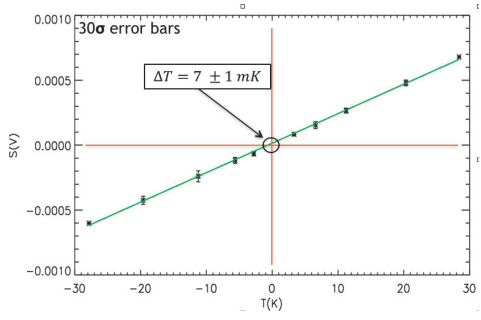


Figure 1 – Fit for all bolometers. The error bars are at 30σ; the measures are relative to the total 4.5 hours of integration for a total of 13 bolometers

4 Conclusion

The experimental study of the Cosmic Microwave Background, started about 50 years ago, and is continuing today with increasing ambitions and complexity in the experiments.

Most of the instruments used are few-bands photometers/polarimeters. The spectral study of CMB anisotropy is a still relatively unexplored, and should be carried out using efficient spectrometers mounted on balloons and other space carriers to avoid atmospheric disturbance and fully exploit the spectral information content.

A differential spectrometer like the one studied in this thesis work has many benefits:

- it can directly difference the brightness of two separate fields of view, with high rejection of the common mode, even gaining a factor of 2 in integration time since the source and the reference field are observed simultaneously.
- It can separate better the CMB from foreground emissions, since it produces a large number independent spectral elements. For example, a space-based photometer like Planck has 9 frequency bands, approximately 10% wide, producing 9 spectral data points; a spectroscopic instrument instead, with 5 GHz resolution produces ~ 70 independent spectral data points. It is clear how much the measure analysis is better with 70 data points. This low-resolution is easily achieved with an FTS with just $3cm$ of mechanical path difference.
- The benefits in a Sunyaev Zel'dovich spectral measurement are even larger, since due to the low contrast of the signal it is mandatory to compare the line of sight with the cluster to a clean reference region (where there is only CMB and foregrounds brightness); moreover for the same reason it is mandatory to have a large number of differential spectral measurements to separate the SZ signal from overwhelming foregorunds.

References

1. de Bernardis *et. al.*, A&A 538 A86 (2012).
2. Schillaci *et. al.*, A&A 565 A125 (2014).
3. Schillaci *et. al.*, Infrared Physics and Technology Vol.58 pp64-67 (2012).
4. D'Alessandro *et. al.*, Applied optics Vol.54 pp 9269-9276 (2015).
5. Sunyaev, R. A., Ya. B. Zel'dovich, Astrophysics and Space Science 7 p3 (1970).
6. Masi *et al.*, memsai Vol.74 p 96 (2003).

QUBIC EXPERIMENT

M. STOLPOVSKIY on behalf of the QUBIC collaboration
Universit Paris Diderot-Paris 7 Laboratoire APC Btiment Condorcet Case 7020
75205 Paris Cedex 13, France



QUBIC is a ground-based experiment, currently under construction, that uses the novel bolometric interferometry technology. It is dedicated to measure the primordial B-modes of CMB. As a bolometric interferometer, QUBIC has high sensitivity and good systematics control. Dust contamination is controlled by operating with two bands – 150 and 220 GHz. There are two possible sites for QUBIC: either Concordia station in Antarctic or in the Argentinian Puna desert. It is planned to see the first light in 2018-2019.

1 Introduction

The QUBIC experiment is described in the white paper [1]. The QUBIC abbreviation stands for "Q and U Bolometric Interferometer for Cosmology". It is a ground-based cryogenic experiment, currently in construction phase, dedicated to measure the primordial B-modes of the CMB polarisation. In the last decade scientists have been chasing the primordial B-modes. As they can only be induced by the gravitational waves produced during the inflation epoch, the B-modes are often considered as the smoking gun of inflation [2].

QUBIC uses a novel concept called bolometric interferometry: the instrument combines the advantages of imagers and interferometers. From imagers it inherits a high sensitivity – for the focal planes the bolometric detectors are used. These are background limited transition edge sensitive NbSi detectors with measured noise equivalent power $NEP \sim 4 \times 10^{-17} W Hz^{-1/2}$. QUBIC is a millimetric equivalent of the Fizeau interferometer with 400 elements, which gives very good systematics control. QUBIC works on two frequency bands – 150 and 220 GHz, which allows to efficiently control the dust contamination.

The QUBIC collaboration consists of more than 80 scientists from 15 institutes around the globe. The baseline site is in Antarctic at Concordia station. We also consider an alternative site in Argentina, in Puna desert. Both sites have good atmospheric conditions for CMB observations. But the seasonal changes are much stronger in Argentina and the air humidity is higher, which implies factor of 1–3 worse sensitivity on the tensor to scalar ratio r, depending on the observational efficiency. The difficult logistics in Antarctica would shift the timeline to about a year in comparison with Argentinian site. The approximate timeline for QUBIC is the

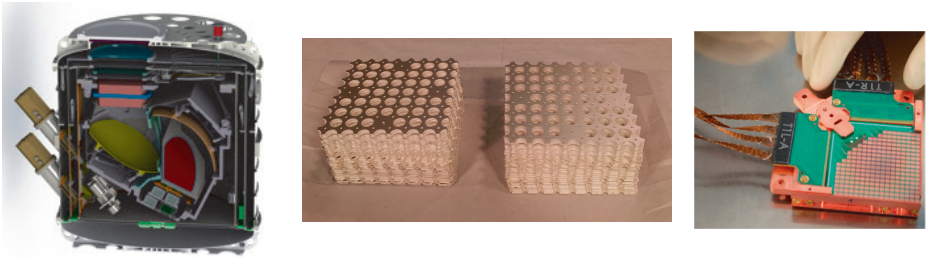


Figure 1 – The QUBIC complete design as a 3-d model (left), the horns array for the technical demonstrator (center) and a quarter of the focal plane (right)

following: in 2016 we test the focal plane and the produce the technological demonstrator, which would test the detection capabilities of the bolometric interferometry concept. Then from the end of 2016 till the end of 2017 the construction phase starts. If the Puna site will be chosen, then the installation on the site starts right away and first light will occur in 2018. In case of the Concordia station the installation and operation are postponed by one year. The final decision on the site must be made in the middle of 2016.

Currently the QUBIC instrument is fully designed, see figure 1, left panel. The two tubes on the left are the pulse tubes for the cryostat. Light comes through the window on the top. The pink box below the window is the horns array, which is the array of 400 pairs of horn antennas. One can consider each pair of horns as a diffractive pupil of an interferometer. The blue stripe on the horns array represents the switches that can open and close each pair of horns separately. Horns array is made of aluminium platelets. The 8×8 horns array, produced for the technological demonstrator, is shown on the middle panel of figure 1. The light from the horns is focused by two mirrors (yellow shells) on two focal planes. Mirrors act as an optical equivalents of the correlator devices in usual interferometer concept. One of the focal planes is shown on the bottom centre of the image, another one is not shown. The light is separated by a dichroic (red panel) to two bands – 150 and 220 GHz. One quarter of the focal plane has been produced and tested in APC, France (see right panel of figure 1). The readout system consists of time-domain SQUIDs and custom ASIC. The total multiplexing factor is 32:1 per SQUIDs and 4:1 per ASIC, thus 128:1 multiplexing in total [3].

2 QUBIC concept

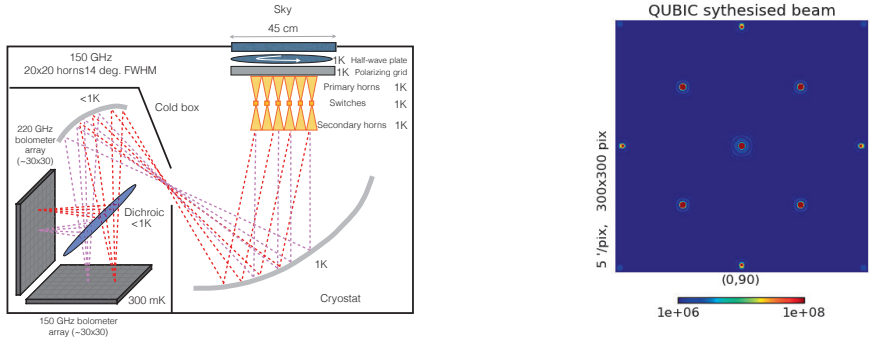


Figure 2 – Left: schematic sketch of the QUBIC instrument. Right: QUBIC synthesised beam.

The QUBIC working principle is schematically shown on the picture 2, left panel. The input radiation from the sky falls on the 45 cm wide window, that also includes filters. Next to it is the cold half-wave plate, which rotates stepwise on the magnetic friction. After that there is the polarising grid and the horns array. The full width on half maximum of the primary beam is 13 degrees. The half-wave plate, polarising grid, horns array and the primary mirror are situated inside 1K cryostat. If we describe the incoming radiation in terms of electric field on two orthogonal orientations E_x and E_y, then after the half-wave plate the radiation will be

$$S_{hwp} = \begin{pmatrix} E_x cos2\phi(t) + E_y sin2\phi(t) \\ E_x cos2\phi(t) - E_y sin2\phi(t) \end{pmatrix}, \quad (1)$$

where $\phi(t)$ is the angle of rotation of the half-wave plate, that depends on time. The polarizing grid simply removes one component of S_{hwp} and the total signal, that falls on the horns array, expressed in terms of Stocks I, Q and U parameters is $S = I + Qcos4\phi(t) + Usin4\phi(t)$. This signal remains unchanged in the following components of the instrument. And even if there is cross-polarisation in, for example, horns array, it doesn't change the S. The QUBIC detectors are not sensitive to polarisation, thus the signal, registered by the detectors is indeed S. As ϕ depends on time, it is possible to reconstruct I, Q and U of incoming radiation. The secondary mirror and the dichroic are inside the cold box and are cooled down below 1K. The focal planes operate at temperature 300 mK.

2.1 Self-calibration

With 400 horn pairs the synthesised beam of QUBIC has a complex shape, shown on the figure 2. It has the main peak with full width on half maximum 23.5 arcmin and number of secondary peaks around it. The fraction of power in the secondary peaks is around 70%. The idea of the self-calibration is the following: for a perfect instrument with zero systematics all the redundant baselines would give the same interferometric pattern on the focal planes. Using the switches one can close all the horn pairs except one baseline. One can perform measurement of an artificial point source with one baseline open. Then the same repeated with all the redundant baselines. The differences between actual interferometric patterns from redundant baselines could be fitted with systematics imperfections as parameters. As shown in the work by M-A. Bigot-Sazy et al. [4], the systematic errors could be reduced by factor of order 10^3 with about 30% of time dedicated to self-calibration.

3 QUBIC map-making

Due to it bolometric interferometer nature, QUBIC requires a special treatment for data analysis, particularly for map-making. In the QUBIC software the synthesised beam is modelled as the sum of gaussians, centered on the positions of the synthesised beam peaks. It means, that on the time ordered data (TOD) not only the main peak is present, but also all its secondary replications. QUBIC map-making is able to resolve signal from different directions and accurately reconstructs the original signal, see fig. 3.

When the instrument is pointed to the edge of the coverage field, it observes signal from secondary peaks from the part of the sky, never swept by the main peak. Thus one can expect poor signal to noise ratio on the edge of the QUBIC patch. To prevent it, QUBIC map-making uses Planck maps as starting guess to reduce noise on the edge of the reconstructed map.

4 QUBIC sensitivity

Running realistic simulations, that include atmospheric and detector noise, one can obtain sensitivity limits for QUBIC. It is below the peak from the primordial gravitational wave on the

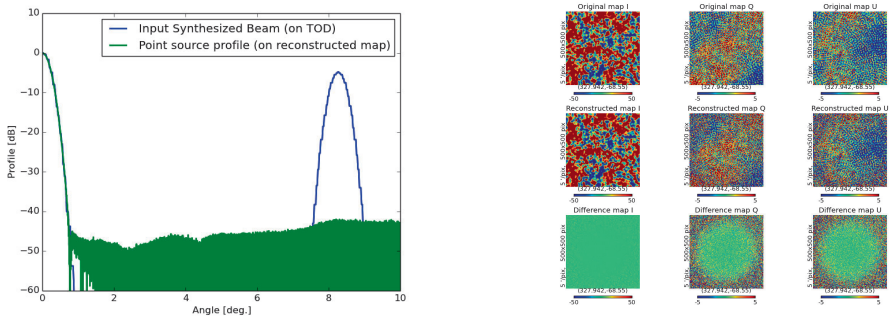


Figure 3 – Left: point source observation. Blue – direct projection of TOD to the sky, that includes all the secondary peaks. Green – reconstruction of the original map with a single point source. Note, that the secondary peak has been deconvolved. Right: from the top row to the bottom – the input maps, used for simulations, the reconstructed maps and the difference between the two. From the left column to the right – the I, Q and U maps.

BB-spectrum for the value of $r = 0.02$ (see figure 4, left). The Chi-square analysis for dual band observations during two years of operation, including the Planck 353 GHz data, gives constraint for sensitivity on $r < 0.016$ at 95% confidence level assuming a single power law for dust and the level of the dust emission measured by Planck [5] (figure 4, right).

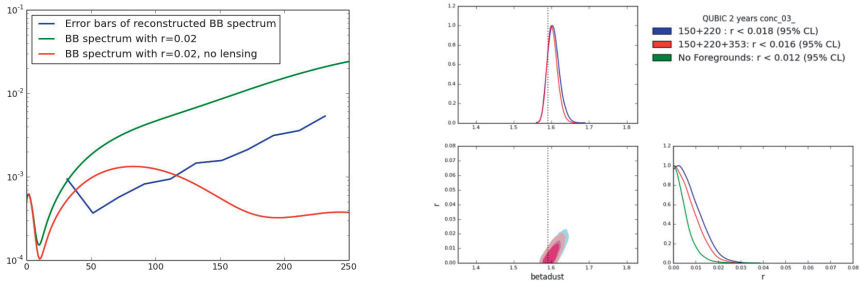


Figure 4 – QUBIC sensitivity after 2 years of operation on Concordia station. Left: error-bars on BB-spectrum (blue), in comparison with BB-spectrum with $r = 0.02$ with lensing (green) and without lensing (red). Right: Chi-square estimation of QUBIC sensitivity on r and dust emission. The blue lines and contour is for QUBIC-alone (150 and 220 are designations for two QUBIC bands). The red lines and contour includes the Planck data of 353 GHz channel. The green line is estimated in no-foregrounds case, it is the ultimate limitation of QUBIC sensitivity.

References

1. E Battistelli et al. *Astroparticle Physics*, 34(9):705–716, 2011.
2. Ade et al. *Astronomy & Astrophysics*, 571:A22, 2014.
3. A Ghribi et al. *Journal of Low Temperature Physics*, 176(5-6):698–704, 2014.
4. M-A Bigot-Sazy et al. *Astronomy & Astrophysics*, 550:A59, 2013.
5. Ade et al. *Astronomy & Astrophysics*, 576:A104, 2015.

Data analysis and cosmological results from the first observational campaigns of the POLARBEAR experiment

Julien Peloton for the POLARBEAR Collaboration
Department of Physics and Astronomy, University of Sussex, Brighton BN1 9QH, UK

In this proceeding, I describe data analysis of the first data sets produced by one of the most advanced, current CMB experiments, POLARBEAR and the major results it produced. The POLARBEAR experiment is a leading CMB B-mode polarization experiment aiming at detection and characterization of the so-called B-mode signature of the CMB polarization. This is one of the most exciting topics in the current CMB research, which only just has started yielding new insights onto cosmology in part thanks to the results discussed hereafter.

1 The Polarbear experiment

POLARBEAR is a new generation CMB B-mode polarization experiment. It consists of the POLARBEAR receiver and the Huan Tran Telescope (HTT). Since the beginning of 2012, POLARBEAR is located at the James Ax Observatory in the Atacama Desert in Chile. During the first half of the first campaign of observations (2012-2014), it focused on small patches on the sky (10 $\deg^2$ each) with approximately 3.5 arcminute resolution and precise control and mitigation of systematic effects. These regions on the sky were scanned repetitively at constant elevation with the polarization of the incident radiation modulated by a cold stepped half-wave plate (HWP). The observations were performed with 1,274 bolometric detectors operating simultaneously all along the first campaign. In order to handle such a huge flow of data (about 10 times more than PLANCK), POLARBEAR instrument includes a complex detector/readout system. Its operation involved multiple modulations on different timescales to allow for discrimination of the sky signals from the instrumental or atmospheric ones. Mid-2014 to the end of 2015, we switched to the observation of a bigger patch on the sky (roughly 400 $\deg^2$), and the cold stepped HWP was replaced by a warm (outside the receiver) and continuously rotated HWP. During observations, the instrument is observing the sky with the initial array at 150 GHz.

POLARBEAR is dedicated to characterize the B-mode polarization of the CMB on both large and small angular scales. Its relatively small angular resolution (3.5 arcminutes) allows to probe the small scales down to $\ell \sim 2500$ while its location in Chile gives in practice access to more than half-sky coverage revealing the largest scales. In its first campaign, POLARBEAR focused on small patches on the sky, and integrated deeply to quickly achieve a very low level of noise. This strategy was devised in order to characterize first the gravitational lensing signal. This strategy has been a success, and based on one year of the data the signal has been detected using three different observables as described in three major papers [1,2,3]. Combining all probes (galaxy cross-correlation, deflection field power spectrum, and direct B-power measurement), POLARBEAR achieved a 4.7σ rejection of the null hypothesis of no B-modes. The second season focused also on the small patches, while the third season seen a change of scanning strategy. A large portion

of the sky is now under observations ($\sim$ 400 sq. degrees), in order to also probe larger scales. POLARBEAR and its successor, so-called SIMONS ARRAY, are projected to achieve a 2σ detection of $r = 0.001$ and will also continue to characterize the gravitational lensing signals in an attempt to measure properties of cosmological neutrinos and dark energy properties.

2 Low level data processing

The POLARBEAR instrument is a complex system, operating in a complex and changing environment. The calibration of the data is the first step, and at this early stage of the experiment, it's one of the longest in order to have the cleanest data possible. In order to do any meaningful analysis, we need to calibrate the data taken by the instrument. Calibrating the data consists in building a coherent data model in which we can compare and combine different measurements of the same quantity. This means establishing a relation between reference measurements with uncertainties and any "real life" measurements with their uncertainty used to derive the scientific results. Ideally, the reference measurements (calibrator) have smaller uncertainties than the measurements used for scientific purposes, so that the calibration should only be a small part of the total error budget in the final results. In order to maintain the quality of measurement as well as to monitor the performance of the instrument, we perform some of the calibration steps recurrently.

There are four primary instrument properties to be modeled: individual detector pointing, thermal-response calibration, the instrument effective beam, and the polarization angle. In addition, specifically to ground-based experiment, one needs to take into account the influence of the atmosphere through its transmission, the weather and the surrounding environment: POLARBEAR is set on the ground and surrounded by mountains! There are few and rather general recipes available in the literature given that each experiment is unique and requires a unique treatment, and so we need the in-depth knowledge of the instrument and its environment in order to clean the data at best. We often process iteratively, by refining models and testing new hypotheses.

2.1 Individual detector pointing

A five-parameter pointing model characterizes the relationship between the telescope's encoder readings and its true boresight pointing on the sky. Of the parameters described in this reference, POLARBEAR uses IA, the azimuth encoder zero offset, IE, the elevation encoder zero offset, CA, the collimation error of the electromagnetic axis, AN, the azimuth axis offset/misalignment (north-south) and AW, the azimuth offset/misalignment (east-west). We experimented with extending and modifying this parameter set, by adding more parameters and/or splitting the data as a functions of different criteria (distance to the Sun/Moon, weather, temperature of the ground, etc.). So far we did not find substantial improvements to the model reported above and used in [3]. The pointing model is created by observing bright extended and point-like millimeter sources that were selected from known source catalogs to span a wide range in azimuth and elevation. These pointing observations occurred several times per week during observations. For the first release of data, the best-fit pointing model recovers the source positions for the sources that were used to create it with an accuracy of 25" RMS. Individual detector beam offsets are determined relative to the boresight using raster scans across Saturn and Jupiter and offsets are then combined with the boresight pointing model to determine the absolute pointing of each bolometer. In order to characterize the fluctuations, we made offset measures several times per week during observations for both seasons, and we found an RMS fluctuation of less than 6" over time. The offsets show arcsecond-level differential pointing between the two detectors in a pixel, which is shown to be a negligible contaminant.

2.2 Thermal-response calibration

While performing observations, we register the bolometer Time-Ordered Data (TOD), which are the electrical current in the detector. However we would like to convert this current into temperature units. There are two issues : the absolute gain calibration and the relative gain calibration between detectors. To perform the gain calibration, we used different relative calibrators such as astrophysical and ground-based calibrators. The determination of the gain for each bolometer is done in two ways: from observations of planets (main method) or from observations of the atmosphere (cross-check method). This section describes how we use observations of planets in combination with measurements from the *stimulator* to derive the gain model (bootstrapping). The stimulator is a thermal calibration source of known temperature of 700°C located behind the secondary mirror of the telescope. The light runs from the stimulator to the focal plane *via* a small hole in the secondary mirror, and the effective intensity of the source varies across the focal plane from about 35-85 mK.

Once we have made measurements from the stimulator, the gain pipeline proceeds in three steps to do the gain calibration. The first step is to determine the intensity template used to perform an absolute calibration. The intensity template is computed individually for each channel from stimulator measurements without accounting for stimulator polarization. So in a second step we characterize the polarization of the thermal source by computing a polarization template(s) using measurements of different astrophysical sources at different Half Wave Plate (HWP) rotation angles. The last step consists in gathering those two informations - intensity and polarization - and generate the effective temperature template which is used to recover the absolute gain in $\mathrm{ADC/K}_{RJ}$ of each pixel for all the observations. In addition to those 3 steps, we have a two iteration process to take into account the impact of the atmosphere on the detectors.

2.3 Instrument effective beam

When a detector is observing, the signal received is not exactly the same as the one sent due to the diffraction-limited optics in the telescope. As a consequence, all the scales undergo a suppression of signal, and the smaller the scales the bigger is the suppression. The effect start to be non-negligible at the level of the beam size, that is at scales equal to the effective Full Width Half Maximum (FHWM) if the beam would have been represented by a circular 2D Gaussian. On the observed map level m, the effect of the beam can be represented by a convolution with the sky signal S

$$m(\theta,\phi) = (S * B)(\theta,\phi) = \int\int d\theta_1 d\phi_1 S(\theta-\theta_1,\phi-\phi_1)B(\theta_1,\phi_1), \tag{1}$$

where B is the effective beam of the instrument. Currently, the estimation of each detector beam is made in two steps. We first make use of observations of Jupiter to determine the beam profile, and then we modify the beam profile to account for blurring in the maps due to pointing model inaccuracies, evaluated using point sources in the different sky patches.

2.4 Polarization angle calibration

Each of the POLARBEAR detectors' response to polarized signal, including its polarization angle, polarization efficiency, and leakage due to relative-gain miscalibration, is modeled. Also modeled are non-idealities in the HWP, which may vary for different detectors across the focal plane. We developed the polarization model using two astrophysical calibrators: Tau A and Cen A. The polarization model is based on a hierarchical understanding of our polarization calibration, consisting of a global reference polarization angle, the wafer-averaged polarization angles relative to that global angle, and the individual pixel angles relative to the wafer-averaged angle.

3 Mapmaking

This section focuses on the mapmaking step, that is the estimation of the sky maps from the cleaned and calibrated Time Ordered Data (TOD). POLARBEAR scans the sky with roughly a thousand detectors at a rate of 190 Hz, and for the first two years of data we downsampled the data down to 30 Hz. Observations are performed every day, and after cleaning and performing the data selection, the data set collected is of the order of few Terabytes per year (time samples), and we want to make sky maps with $\mathcal{O}(10^5)$ pixels. While recording the sky signal, we also record the pointing information of the telescope which is the position on the sky $p(t) = (\theta(t), \phi(t))$ as a function of the time. From the pointing, we associate each time sample value d to a pixel s on the sky. In addition to be sensitive to the intensity of the CMB, the detectors of POLARBEAR are polarization sensitive (linearly), that is any time sample value contains information from the three Stokes parameters of interest (I, Q, and U) convolved with the instrumental beam of the instrument. We can model such a detector as a (partial) polarizer followed by a total power detector, and the timestream data d as a function of time t for *one detector* may be expressed in its simplest form as a linear combination of the Stokes parameter maps

$$d(t) = I(p(t)) + Q(p(t))\cos 2\Theta(t) + U(p(t))\sin 2\Theta(t) + n(t), \tag{2}$$

where $n(t)$ represents usually the instrumental noise, and Θ the polarization angle. The scanning strategy of POLARBEAR is such that we come back to the same pixel very frequently to have a lot of redundancy. The optimal solution for the map is given by the maximum-likelihood estimate $\hat{\mathbf{s}}$ which is obtained by solving the generalized least-squares equation for all detectors and all Stokes parameters

$$\hat{\mathbf{s}} = \left(\mathbf{A}^T\mathbf{N}^{-1}\mathbf{A}\right)^{-1}\mathbf{A}^T\mathbf{N}^{-1}\mathbf{d}, \tag{3}$$

where $\mathbf{A}$ is the pointing matrix, and $\mathbf{N}$ is the noise matrix. However, since we are basically now solving for the model of a sky that is constant in time for every pixel in the map, the estimate $\hat{\mathbf{s}}$ is not a simple projection from time to pixel domain but a map solution. The form of the maximum likelihood solution suggests the two main considerations: removing correlated noise components ($\mathbf{N}^{-1}\mathbf{d}$) and undoing the transfer function of those filters, $\left(\mathbf{A}^T\mathbf{N}^{-1}\mathbf{A}\right)^{-1}$. However, in experiments with a large number of detectors and long time-scale correlations in the timestream data, it is computationally intensive, and even impossible in practice, to invert or even build the $[n_p n_{Stokes} \times n_p n_{Stokes}]$ full $\mathbf{A}^T\mathbf{N}^{-1}\mathbf{A}$ matrix (the inverse of the pixel-pixel covariance matrix of the resulting map). The goal is then to find some filters or models that optimally capture noise and correlations between detectors. In practice, we also filter the timestreams in order to get rid of the correlated component of the noise, that is the data model and the mapmaking equation read

$$\left(\mathbf{A}^T\mathbf{F}\mathbf{A}\right)\hat{\mathbf{s}} = \mathbf{A}^T\mathbf{F}\mathbf{d}. \tag{4}$$

$\mathbf{z}$ is the amplitudes of the modes we want to remove from the data, and $\mathbf{Z}$ is the corresponding pointing matrix which defines where we have to filter the data. The matrix $\mathbf{F}$ contains the effect of the time-domain filters and the noise weights ($\mathbf{N}^{-1}$). The different mapmakers developed to analyze the data of POLARBEAR make use of different assumption to solve Eq. 4.

4 Power-spectrum estimation

In order to estimate the angular power spectra from the maps, we use a pseudospectrum technique. The idea is to estimate directly the pseudospectrum from the data, and correct in the harmonic domain the different biasing effects such as the mode-mode couplings induced by the small and irregular size of the patch, the beam function, and the pixelization. The pseudospectrum technique is very fast (requiring $\mathcal{O}(N^{3/2})$ operations) and it is frequently near-optimal for temperature in

practice. The estimation of polarized spectra however suffers from a spurious mixing of E and B modes, called E-to-B leakage, which has to be taken into account carefully to obtain the near optimality of the estimator [4].

5 Instrumental systematics

As of 2012 when we started the analysis of the first season of observation, the B-modes were not measured. Both lensing B-modes and primordial B-modes remained theoretical. The difficulty of the B-mode measurement mainly comes from the weakness of the signal. The POLARBEAR experiment is designed to reach high enough sensitivity to detect it. But such a high sensitivity means that we are also more prone to detect any spurious signals, which were considered until now too weak to matter. Therefore we decided to adopt a blind-analysis framework, which is a standard technique to minimize observer bias, frequently employed in particle and nuclear physics, but also recently in cosmology. In our framework, no one in the team viewed the measured BB power-spectrum values, the deflection power spectra based on B-modes, or the corresponding maps, until we eliminated possible sources of observer bias by finalizing calibration, filtering, data selection, data validation and showed that all systematic uncertainties were small. This framework bring us to develop quantitative tools, including null tests and simulations, that convincingly argued for analysis choices and constraints without showing the BB angular power-spectrum, thus removing the possibility that people within the team would be more convinced by an argument or method because of the BB spectrum that it produced. Other power spectra and maps were used as subsidiary information in this work, and they were unblinded in stages during the analysis procedure.

6 Evidence for Gravitational Lensing of the CMB Polarization from Cross-correlation with the CIB

This section is a summary of the results published by the POLARBEAR Collaboration in [1]. In this paper, we measure the gravitational lensing of CMB polarization by cross-correlating CMB polarization lensing convergence κ from POLARBEAR with maps of the cosmic infrared background from HERSCHEL. The purpose of this work is threefold: first, to measure the gravitational lensing of polarization and the lensing B-mode polarization and test that the data agree with the prediction of the standard ΛCDM cosmological model; second, to support the concurrent direct detection of the polarized lensing deflection power spectrum by POLARBEAR with an independent measurement of polarized lensing via the robust cross-correlation channel; third (and probably most importantly), to demonstrate the new, promising technique of polarization lensing reconstruction in practice. Recently, a similar cross-correlation result was published by the SPTPOL collaboration [5]. This work differs in some aspects (for example, our lensing maps have higher signal-to-noise per mode on a smaller area), but it essentially confirms the SPTPOL results. This is a non-trivial check of a challenging observation, using an independent experiment with potentially different systematic errors (e.g., due to differences in map depth, scan strategy, observing location or experiment design).

We use the observations of HERSCHEL H-ATLAS survey at 500 μm as an estimate of the CIB emission in the RA23 and RA12 regions[a] and the convergence extracted from POLARBEAR maps in the same fields. We use POLARBEAR data from the first season of observation. The POLARBEAR maps come from the primary pipeline (biased maps), and the cut-sky and filter effects are corrected in the harmonic domain. Gravitational lensing by large-scale structure results in a remapping of the CMB photons by the lensing deflection field $\mathbf{d}$ – typically few arcminutes in magnitude – which points from the direction in which a CMB photon is received to the direction in which it was originally emitted. Lensing converts E modes into B modes and thus induces a correlation between the lensing B modes and E modes; similar correlations are also introduced between

[a] HERSCHEL maps and LST do not overlap.

formerly independent pairs of E polarization modes. The optimal polarized quadratic estimators for lensing make use of these changes in the statistical properties of the CMB sky, and estimate lensing by measuring the characteristic lensing-induced correlation between different polarized Fourier modes. In this work, we focus only on the so-called EB and EE estimators which are given by:

$$\hat{\kappa}_{EB}(\mathbf{L}) = \int \frac{\mathrm{d}^2\mathbf{l}}{(2\pi)^2} g^{EB}(\mathbf{L},\mathbf{l}) E(\mathbf{l}) B(\mathbf{L}-\mathbf{l}) \tag{5}$$

$$\hat{\kappa}_{EE}(\mathbf{L}) = \int \frac{\mathrm{d}^2\mathbf{l}}{(2\pi)^2} g^{EE}(\mathbf{L},\mathbf{l}) E(\mathbf{l}) E(\mathbf{L}-\mathbf{l}) \tag{6}$$

where g is a function chosen as in [6] to normalize and optimize the estimator, and κ is the lensing convergence, defined from the lensing deflection field $\mathbf{d}$ by $\kappa = -\nabla \cdot \mathbf{d}/2$. In the estimators, we only use scales $500 \leq \ell \leq 2700$ in the polarization maps. Using these estimators, we calculate a noisy map of the lensing convergence field κ which can be correlated with the Herschel submillimeter background maps. The correlation with the EB reconstruction channel in all the patches provides evidence at 2.3σ level of the presence of lensing generated B-modes. The combination of the EE and EB channels in all the patches provides a 4σ measurement of polarized lensing. We also perform different tests to estimate the effects of potential sources of systematic error (astrophysical and instrumental) on the polarization lensing – CIB cross-correlation. The data were analyzed using a blind analysis framework and checked for spurious systematic contamination using null tests and specific combinations of the data (curl and swap-field null-tests). No evidence of contamination was found.

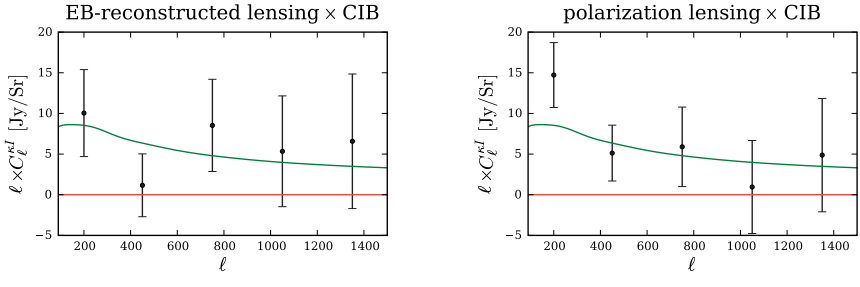


Figure 1 – Cross-power spectra of CMB polarization lensing and the 500μm Herschel CIB flux. *Left panel*: the cross power of EB-reconstructed lensing with the Herschel maps; constructed from the EB estimator applied to both Polarbear maps, this result corresponds to 2.3σ evidence for lensing B-modes. *Right panel*: the minimum variance combination of all polarization lensing measurements cross-correlated with the Herschel maps; this result corresponds to 4σ evidence for gravitational lensing of CMB polarization.

7 Measurement of the CMB Polarization Lensing Power Spectrum with the Polarbear experiment

This section is a summary of the results published by the Polarbear Collaboration in [2]. A companion paper to this one has shown the evidence of the CMB lensing – Cosmic Infrared Background cross-correlation results using Polarbear data [1], finding good agreement with the SPTpol measurements [5]. This cross-correlation is immune to several instrumental systematic effects but the cosmological interpretation of this measurement requires assumptions about the relation of sub-mm galaxies to the underlying mass distribution [7]. In this work, we present the first direct evidence for gravitational lensing of the polarized CMB using first season data from the Polarbear experiment. The maps are computed from the primary pipeline, and the cut-sky and filter effects are corrected in the harmonic domain.

The gravitational lensing of large-scale structure on CMB changes the statistical properties of the primordial CMB signal. Lensing in fact acts as a convolution in harmonic domain and correlates different Fourier modes which are otherwise independent. This off-diagonal non-Gaussian feature can be exploited to reconstruct the underlying deflection field $\mathbf{d}$ from the observed CMB. Quadratic estimators take advantage of this feature to measure CMB lensing. The channels chosen for the reconstruction are the so-called EE and EB channels. The power-spectrum of these estimators are given by

$$\langle d_\alpha(\mathbf{L}) d^*_\beta(\mathbf{L}')\rangle = (2\pi)^2\delta(\mathbf{L}-\mathbf{L}')(C_L^{dd} + N^{(0)}_{\alpha\beta}(L) + \text{higher-order terms}). \quad (7)$$

Here, C_L^{dd} is the deflection power spectrum and $N^{(0)}_{\alpha\beta}$ is the lensing reconstruction noise, α and β are chosen from $\{EE, EB\}$, however we do not use $\alpha = \beta = EE$ as our focus is on the direct probe of CMB lensing represented by the conversion of E-to-B patterns. The BB estimator also probes B-modes, but it does not make a substantial contribution to the deflection power spectrum [6], so it is not used in this work. The estimator is affected by the presence of the so-called lensing Gaussian bias term $N^{(0)}_{\alpha\beta}$, which is the disconnected part in the four-point correlation, and by higher order biases that depend on the lensing field itself. Though higher order terms are found to be negligible, the $N^{(0)}_{\alpha\beta}$ has to be subtracted as often it is larger than the deflection field power spectrum. We create 500 simulated lensed and unlensed maps to estimate the Gaussian bias and establish the lensing transfer function. In addition, the data were analyzed using a blind analysis framework and checked for spurious systematic contamination using null tests, simulations, and specific combinations of data (curl and swap-field null-tests). No evidence of contamination was found. The rejection of the hypothesis of no lensing on CMB polarization has a significance of 4.2σ combining statistical and systematic errors in quadrature. We note however that since the lensing reconstruction exploits peculiar off-diagonal correlation, it is less sensitive to systematics than standard CMB analysis. The $\langle$EEEB$\rangle$ channel used alone provides an evidence of lensing generated B-modes at 3.2σ level. If we include the presence of lensing in our data set, the measured lensing amplitude is consistent at 2σ level with ΛCDM predictions (see Fig. 2).

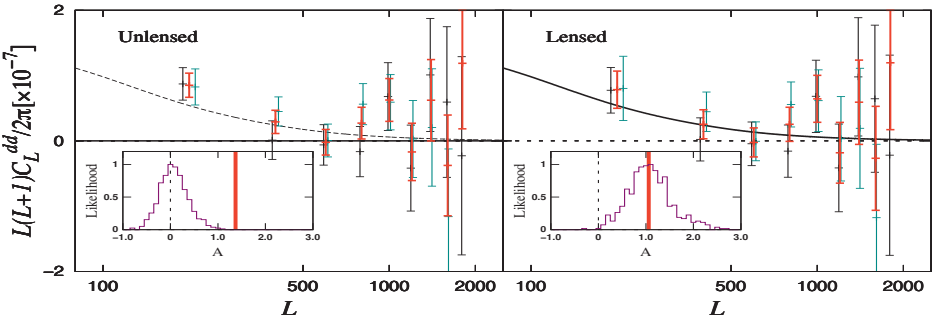


Figure 2 – Polarization lensing power spectra co-added from the three patches and two estimators (in red). The lensing signal predicted by the ΛCDM model is shown in black dashed curve and solid curve in the left and right panel respectively. The reconstructed lensing potential from $\langle$EEEB$\rangle$ and $\langle$EBEB$\rangle$ is shown in blue and green respectively. *Left* A 4.2σ rejection of the null hypothesis of no lensing. *Right*: The same data, assuming the existence of gravitational lensing to calculate error bars, including sample variance and including the covariance between the two reconstruction channels $\langle$EEEB$\rangle$ and $\langle$EBEB$\rangle$. The histograms of the expected amplitudes of $\mathcal{A}$ from 500 unlensed and lensed simulations are shown in the inset boxes.

8 A Measurement of the CMB B-Mode Polarization Power Spectrum at Sub-Degree Scales with Polarbear

This proceeding describes the different steps (calibration, mapmaking, instrumental systematic control, power-spectrum estimation) used to achieve the results described in [3]: the first measurement of the CMB's B-mode angular power spectrum, C_ℓ^{BB}, over the multipole range $500 < \ell < 2100$ with a significance about 2σ. We previously presented evidence for gravitational lensing of the CMB in POLARBEAR data using the non-Gaussianity imprinted in the CMB by large-scale structure [1,2]. We can calculate the combined significance with which those measurements of non-Gaussian B-modes and the C_ℓ^{BB} measurements reported here reject the hypothesis that there are no CMB lensing B-modes. In this null hypothesis, the signals are uncorrelated (when using a realization-dependent lensing bias subtraction to calculate the deflection field), so a simple quadrature sum of the rejection significance is appropriate. This calculation results in a rejection of the hypothesis that there are no lensing B-modes with 4.7σ confidence for a normal distribution.

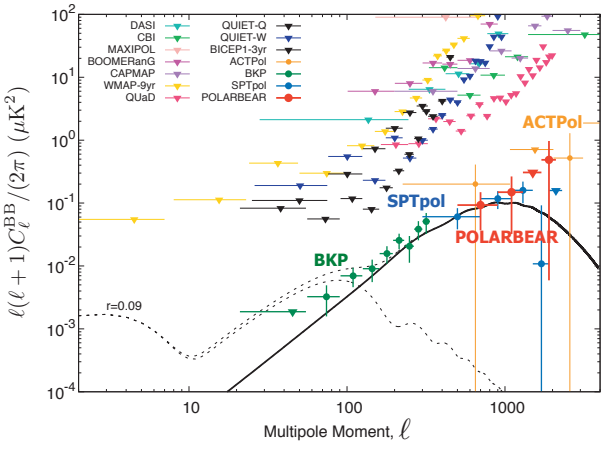


Figure 3 – Constraints on CMB B-modes from many CMB experiments as of June 2015. Measurements from POLARBEAR SPTPOL and ACTPOL are highlighted. The major challenges when reaching small multipoles from the ground will be foreground contamination, atmosphere contamination, and to have access to a large portion of sky (after cuts). The results of the joint analysis between PLANCK and BICEP2 (BKP) is also shown. All results with high significance have been announced between the previous year and now.

Acknowledgments

JP acknowledges support from the Science and Technology Facilities Council [Grant No. ST/L000652/1]. The research leading to these results has received funding from the European Research Council under the European Union's Seventh Framework Programme (FP/2007-2013) / ERC Grant Agreement No. [616170].

References

1. POLARBEAR Collaboration (a) *Phys. Rev. Lett.* **112**, 131302 (2014).
2. POLARBEAR Collaboration (b) *Phys. Rev. Lett.* **113**, 021301 (2014).
3. POLARBEAR Collaboration (c) *The Astrophysical Journal* **794**, 171 (2014).
4. Grain, J and Tristram, M and Stompor, R *Phys. Rev.* D **79**, 123515 (2009).
5. Hanson, D and Hoover, S and Crites, A and Ade, PAR and Aird, KA and Austermann, JE and Beall, JA and Bender, AN and Benson, BA and Bleem, LE and others *Phys. Rev. Lett.* **111**, 141301 (2013).
6. Hu, Wayne and Okamoto, Takemi *The Astrophysical Journal* **574**, 566 (2002).
7. Abazajian, KN and Carlstrom, JE and Lee, AT, and others *arXiv preprint arXiv:1309.5383*, 2013.

Future CMB polarization observatory in the presence of foregrounds and gravitational lensing: the Simons Array

Josquin Errard
Sorbonne Universités, Institut Lagrange de Paris (ILP),
98 bis Boulevard Arago, 75014 Paris, France
LPNHE, CNRS-IN2P3 and Universités Paris 6 & 7,
4 place Jussieu, F-75252 Paris Cedex 05, France

We present a new forecasting method for future CMB instruments, as well as an overview of the design and status of the Simons Array experiment. CMB4CAST is a new code allowing the CMB community to estimate the scientific performance of a given instrumental design in the presence of astrophysical foregrounds and gravitational lensing. The Simons Array is a CMB polarimetry experiment which aims at characterizing the arcminute angular scale B-mode signal from weak gravitational lensing and search for the degree angular scale B-mode signal from inflationary gravitational waves. It is composed of three receivers observing at 95, 150, 220 and 280GHz, each of them having a 365 mm diameter focal plane cooled to 270 milli-Kelvin. The entire array has 22,764 polarization sensitive Transition Edge Sensor (TES) detectors, associated with lenslet-antenna coupled pixels that are sensitive to two frequency bands simultaneously. The first receiver, named POLARBEAR-2, will deploy in 2016 in the Atacama desert in Chile. The Simons Array will achieve first light in 2018 and will be able to constrain tensor-to-scalar ratio to $\sigma(r = 0.1) = 6 \times 10^{-3}$, and the sum of neutrino masses to $\sigma\left(\sum m_\nu\right) = 40$ meV when combined with spectroscopic galaxy surveys.

1 Introduction

Measurements of the Cosmic Microwave Background (CMB) temperature and polarization anisotropies open a unique window onto the physics of the early and late Universe, bringing powerful observational constraints on cosmological models. The observation of even parity polarization patterns, E-mode, of the CMB are in agreement with temperature anisotropy observations [15], and fit up to a high level of fidelity the standard cosmological model, ΛCDM. Recently, the first direct and cross-correlated measurements of the odd parity polarization pattern, B-mode, were also reported [12,13,10,11,17,9,18]. The B-mode polarization has two primary sources; First, primordial gravitational waves, if present, would polarize the CMB at degree angular scale [2]. Tighter upper limits or detection of this signal will constrain inflation model and energy level associated to the inflation potential. Second, weak gravitational lensing induced by large scale structures breaks E-mode patterns' symmetry and produces small amounts of B-mode polarization patterns [3]. The B-mode signal from weak gravitational lensing peaks around ten arcmin angular scales. Its characterization could constrain the cosmological parameters governing the formation of large scale structures such as the sum of neutrino masses and the evolution of dark energy equation of state.
In parallel to the contamination from gravitational lensing, detection of primordial B-modes is obscured by astrophysical signals coming from our galaxy. There is now growing evidence that there are no regions of the sky in which B-mode emission from galactic dust can be neglected

when attempting to extract inflationary B-modes at frequencies above $\sim$ 100 GHz. Planck's results suggest that polarized foregrounds such as synchrotron radiation and dust emission need to be carefully subtracted for accurate CMB polarization measurements [16,14]. In this context, as detailed below, the Simons Array uses highly sensitive receivers with a broad frequency coverage which has been optimized for foreground mitigation.

2 Forecasting in the presence of foregrounds and gravitational lensing

Errard et al (2016) [19] presents a new framework to forecast the scientific performance of future CMB observatories in the presence of polarized astrophysical foregrounds (dust, synchrotron) and gravitational lensing – that can potentially be removed using the so-called delensing methods. The parametric maximum likelihood approach (PMLA) uses the following reasoning:

- For each sky pixel p, the observation at a frequency f is given as a linear combination of the sky components s_p, with the weights being encapsulated into a so-called mixing matrix $\mathbf{A}$,
$$d_{f,p} = \sum_c \mathbf{A}_{fc}\, {s_p}^c + n_p \tag{1}$$
where the index c goes over sky components {CMB, dust, synchrotron} and n_p corresponds to the noise in each sky pixel.

- The parametric component separation assumes that the emission laws can be parametrized i.e. that the mixing matrix, $\mathbf{A}$, has a known functional form involving "spectral" parameters that have to be estimated. Given the data model in Eq. 1, the PMLA estimates the spectral parameters via the maximization of a so-called spectral likelihood [1,4,5]. Note that any imperfect estimation of the spectral parameters might lead to the presence of foregrounds residuals in the component-separated CMB map [6,7].

- Once the mixing matrix is estimated, we can "invert" Eq. 1 to disantangle the CMB signal from the other sky components:
$$\tilde{s}_p = \left(\mathbf{A}^T\mathbf{N}^{-1}\mathbf{A}\right)^{-1}\mathbf{A}^T\mathbf{N}^{-1}d \tag{2}$$
Note that the noise variance, after component separation, associated with the reconstructed CMB map is given by $\sigma_{\rm CMB} = \left[\left(\mathbf{A}^T\mathbf{N}^{-1}\mathbf{A}\right)^{-1/2}\right]_{\rm CMB\times CMB}$, which is higher than the simple quadratic combination of sensitivities from each observed frequency map.

CMB4CAST uses the approximation described in Errard et al (2011,2012) [7,8] which evaluates the spectral likelihood at its peak and approximates the error bars on spectral parameters using the curvature of the spectral likelihood [a].
The code also evaluates the delensing performance: given a measurement of E-mode and the reconstruction of the lensing potential, it is possible to estimate and remove the contribution of lensing B-modes from the observed total B-mode signal. In addition, the estimation of the lensing potential can be performed using the observation of the CMB alone, or by exploiting the cross-correlation between CMB and large scale structures observations such as the cosmic infrared background [19].
Finally, CMB4CAST estimates the error bars on cosmological parameters using a Fisher approach, which includes contributions from post-component separation noise, foregrounds residuals and delensing. The code has been applied to many planed ground-based and space-borne instruments, and the numerical efficiency of the implementation has allowed for an optimization of the instrumental designs with respect to the achievable constraints on inflation or on the dark sector. This led, in particular, to the Simons Array's current configuration.

[a] Errard et al (2011) [7] gives a semi-analytical expression for the curvature of the likelihood, which allows for quick numerical evaluation of it.

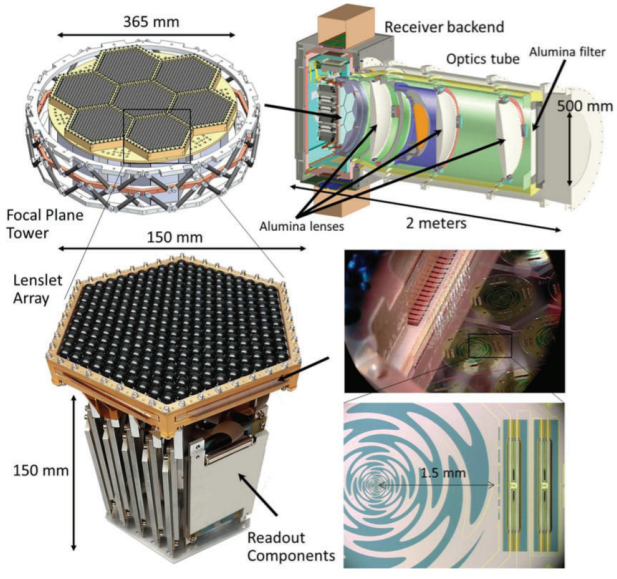


Figure 1 – (Color online) CAD drawing of the POLARBEAR-2 receiver (upper right), and CAD drawing of the focal plane tower (upper left). Three temperature stages (250 milli-Kelvin, 350 milli-Kelvin, 2 Kelvin) are separated by vespel support structures. Photograph of a detector module (bottom left), which consists of a detector wafer, lenslet wafer, Invar holder, and cryogenic readout electronics. Automated wirebonds have $100\,\mu m$ pitch (bottom right). The Sinusoidal circular structure is a broadband antenna. Large rectangular structures are TES bolometers. The RF diplexer filter is visible between the antenna and the bolometers (bottom right). From Suzuki et al (2016) [20].

3 The Simons Array project

The POLARBEAR-2 receiver, first among three involved in the Simons Array, will observe from the James Ax observatory at 5,200 meter altitude in the Chilean Atacama Desert. The site has access to 80% of the sky, which allows for powerful cross-correlation with other experiments (LSST, Euclid, etc.). The POLARBEAR-2 receiver will be mounted on a telescope with the same design as the Huan Tran Telescope (HTT) that is currently observing with the POLARBEAR-I receiver. The HTT features an offset Gregorian design obeying the Mizuguchi-Dragone condition to minimize instrumental cross-polarization. The HTT has co-moving baffles to minimize sidelobes. The 3.5 meter primary mirror produces a 5.2/3.5/2.8/2.2-arcmin FWHM beam at 95/150/220/280 GHz. The POLARBEAR-2 receiver will deploy at 95 and 150 GHz frequencies in 2016. The second receiver will cover 95 and 150 GHz as well, and the third receiver will cover 220 and 280 GHz bands. The second and third receivers will deploy in 2017. Sensitivity of the Simons Array in its final configuration is $8.3\,\mu\mathrm{K_{CMB}}\sqrt{s}$ at both 95 and 150 GHz, $26.9\,\mu\mathrm{K_{CMB}}\sqrt{s}$ at 220 GHz and $57.7\,\mu\mathrm{K_{CMB}}\sqrt{s}$ at 280 GHz. The Simons Array will be able to constrain the tensor-to-scalar ratio r to $\sigma(r = 0.1) = 4 \times 10^{-3}$ when considering only CMB signal, and $\sigma(r = 0.1) = 6 \times 10^{-3}$ when foregrounds are cleaned in combination with Planck data sets [19]. The Simons Array will also be able to constrain the sum of neutrino masses to 19 meV at 1-σ when considering CMB signal alone — and 40 meV when foreground cleaning is considered — and when cross-correlations with spectroscopic galaxy surveys are used. A cross-sectional view of a typical POLARBEAR-2 receiver is shown in Figure 1.

4 Conclusion

We have presented the new forecasting framework for CMB instruments named CMB4CAST, with a world wide accessible interface at `http://portal.nersc.gov/project/mp107/index.html`. The Simons Array experiment will measure and characterize the polarization of the CMB with high sensitivity. Its first receiver, POLARBEAR-2, will deploy in 2016 and the Simons Array will be fully deployed in 2017.

Acknowledgments

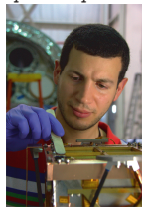
JE acknowledges the Labex ILP (reference ANR-10-LABX-63) part of the Idex SUPER, and received financial state aid managed by the Agence Nationale de la Recherche, as part of the programme Investissements d'avenir under the reference ANR-11-IDEX-0004-02.

References

1. Brandt W. N. et al, Astrophysical Journal, Part 1 (ISSN 0004-637X), vol. 424, no. 1, p. 1-21, 1994.
2. Seljak U. et al, Physical Review Letters, Volume 78, Issue 11, March 17, 1997, pp.2054-2057.
3. Hu W. et al, the Astrophysical Journal, Volume 574, Issue 2, pp. 566-574, 2002.
4. Eriksen H. K. et al, the Astrophysical Journal, Volume 641, Issue 2, pp. 665-682, 2006.
5. Stompor R. et al, Monthly Notices of the Royal Astronomical Society, Volume 392, Issue 1, pp. 216-232, 2009.
6. Stivoli F. et al, Monthly Notices of the Royal Astronomical Society, Volume 408, Issue 4, pp. 2319-2335, 2010.
7. Errard J. et al, Physical Review D, vol. 84, Issue 6, id. 069907, 2011.
8. Errard J. et al, Physical Review D, vol. 85, Issue 8, id. 083006, 2012.
9. Hanson D. et al, Physical Review Letters, vol. 111, Issue 14, id. 141301, 2013.
10. The POLARBEAR collaboration, Physical Review Letters, Volume 112, Issue 13, id.131302, 2014.
11. The POLARBEAR collaboration, Physical Review Letters, Volume 113, Issue 2, id.021301, 2014.
12. The POLARBEAR collaboration, the Astrophysical Journal, Volume 794, Issue 2, article id. 171, 21 pp. (2014).
13. The BICEP2 collaboration, Physical Review Letters, Volume 112, Issue 24, id.241101, 2014.
14. The Planck collaboration, arXiv:1409.5738, 2014.
15. Planck collaboration, arXiv:1502.01582, 2015.
16. The BICEP2/Keck and Planck collaborations, Physical Review Letters, Volume 114, Issue 10, id.101301, 2015.
17. The BICEP2 and Keck Array collaborations, the Astrophysical Journal, Volume 811, Issue 2, article id. 126, 13 pp. (2015).
18. Keisler R. et al, the Astrophysical Journal, Volume 807, Issue 2, article id. 151, 18 pp. (2015).
19. Errard J. et al, Journal of Cosmology and Astroparticle Physics, Issue 03, article id. 052 (2016).
20. Suzuki A. et al, Journal of Low Temperature Physics (2016).

SPIDER: Probing The Dawn Of Time From Above The Clouds

Lorenzo Moncelsi
Division of Physics, Mathematics & Astronomy,
California Institute of Technology, Pasadena, CA, USA
E-mail: moncelsi@caltech.edu
for the SPIDER collaboration
https://spider.princeton.edu/



SPIDER is a balloon-borne microwave polarimeter designed to measure cosmological B-modes on scales larger than $\frac{1}{2}$ degree in the presence of Galactic foregrounds. With six independent telescopes housing a total of 2400 detectors in the 95 and 150 GHz frequency bands, SPIDER is the most instantaneously-sensitive mm-wave polarimeter deployed on the sky to date (total instrument sensitivity of $4\,\mu\mathrm{K}\,\sqrt{s}$). SPIDER was successfully launched from McMurdo Station, Antarctica in January 2015 and acquired science data for 16 days. I will summarize the in-flight performance and present highlights from the ongoing data-analysis. After the recent and successful instrument recovery campaign, the SPIDER team is planning the next flight for Dec 2017, featuring two channels at $\gtrsim 250$ GHz to monitor contamination from Galactic dust, allowing us to constrain the primordial tensor-mode amplitude at the level of $r < 0.03$ (99% confidence level), even in the presence of foregrounds.

1 Introduction

One of the foremost goals in modern physics is to measure the polarization of the Cosmic Microwave Background (CMB) over the entire sky to statistical and astrophysical limits. The CMB may carry a B-mode polarization signature imparted by a tensorial gravitational wave background (GWB) produced by the Inflationary expansion 10^{-32} s after the Big Bang. A detection of this primordial polarization signal would constrain the exotic physics of Inflation, as the amplitude of the GWB depends on the energy scale and properties of Inflation, probing energies up to 10^{12} times higher than those achieved by the Large Hadron Collider. This measurement would have profound implications for cosmology and bears on the current frontiers of fundamental physics, such as the union of general relativity and quantum mechanics.

Recent results from *Planck* LFI confirm that the polarized Galactic synchrotron emission cannot be neglected at frequencies around 90 GHz when making deep maps of CMB polarization. The contribution of dust polarization on and off the Galactic plane has been characterized by the *Planck* HFI instrument, covering six frequency bands spanning 85–1000 GHz. Confusion by

these Galactic foregrounds will likely set the ultimate limit to our ability to measure either the E- or B-modes at large angular scales; accurate treatment of foregrounds in the analysis is thus of primary importance. The HFI has measured the spectrum of the fractional polarization of dust over the whole sky, improving our ability to model and separate the contributions of dust and the CMB on large angular scales. However, the recent joint *Planck* × Bicep2/KECK analysis highlights the need for even deeper maps of the dust component at high Galactic latitudes, where *Planck*'s sensitivity on small patches of sky is limited.[4] The Bicep2/KECK collaboration holds the current best upper limit on the tensor-to-scalar ratio, $r < 0.09$ at 95% confidence (polarization data only).[2]

2 The SPIDER Instrument

SPIDER is a mm-wave balloon-borne CMB polarimeter designed to measure the cosmological B-modes on scales larger than $\frac{1}{2}$ degree in the presence of foregrounds.[9]

The SPIDER payload is comprised mainly of a cryogenic vessel (the largest ever deployed on a balloon platform),[12] and a lightweight carbon-fiber gondola frame,[17] which is equipped with a reaction wheel plus pivot for fast Azimuth scanning,[16] a suite of redundant pointing sensors for in-flight and post-flight attitude reconstruction (star cameras, dGPS, gyroscopes, pinhole sun sensors, magnetometer),[11] as well as sun-shields, and is designed for nearly autonomous observations.[1]

The SPIDER cryostat houses six independent telescopes (Fig. 1),[15] which for the 1st science flight covered the 94 and 150 GHz frequency bands with a total of 2400 bolometers (time-multiplexed arrays of superconducting Transition Edge Sensors [TESs]).[3] A cold half-wave plate at the aperture of each telescope is stepped twice a day to modulate the polarization of incoming light and control instrumental systematics.[7,8,6] SPIDER was successfully launched from McMurdo Station, Antarctica in January 2015 and acquired science data for 16 days. After the successful recovery campaign in November 2015, the SPIDER team is planning the next flight for December 2017, featuring at least one foreground-optimized band (centered at 285 GHz; three telescopes), which will allow us constrain the primordial tensor-mode amplitude at the level of $r < 0.03$ (99% c.l.), even in the presence of foregrounds.[10]

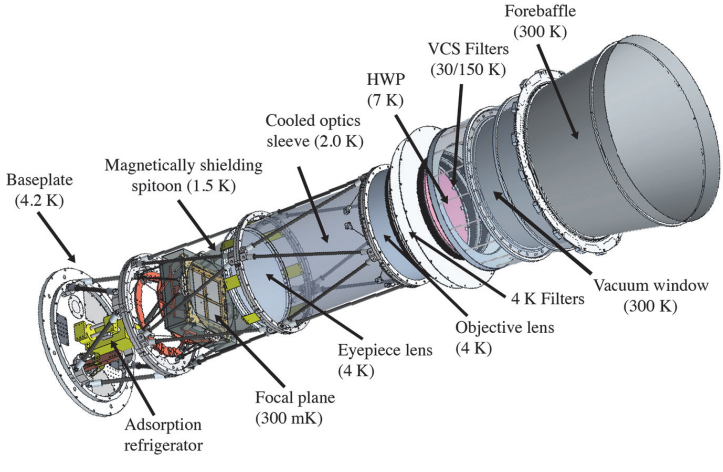


Figure 1 – Solid model of one of the six individual SPIDER telescopes ("inserts"). The overall architecture is common to the 94, 150 and 285 GHz inserts, but the optics of the latter have been re-optimized and modified to accommodate the horn-coupled NIST focal plane (not shown here).

NIST is leading the development of the three 285 GHz platelet-feed,[5] horn-coupled arrays of Al-Mn TESs,[13] which have extensive heritage from ground-based instruments. The device design, fabrication and test program is well underway, while in parallel the optics are being re-optimized and modified accordingly.

Concurrently, SPIDER continues to be engaged with the detector program at CalTech/JPL in pursuing the frequency scalability of the antenna-coupled TES architecture. We are currently developing 25%-bandwidth channels centered at 35 and 270 GHz (for monitoring of the synchrotron and dust foregrounds, respectively), as well as a 40%-bandwidth band centered at 250 GHz for maximum sensitivity to dust; the latter may be flown on SPIDER2 alongside the 285 GHz NIST detectors.

3 In-flight Performance

The SPIDER instrument as a whole performed well throughout its first flight, with no failures in any of the critical sub-systems. Analysis of the data is ongoing. The SPIDER observing region is shown in Fig. 2 (geometric $f_{\rm sky} = 11\%$, hits-weighted $f_{\rm sky} = 6.2\%$), while Fig. 3 shows the CMB temperature map at 150 GHz. One of the major advantages of a sub-orbital platform is the ability to access sky fractions larger than those accessible from the South Pole, as well as the ability to recover large angular scales, both in temperature and in polarization, due to the vastly reduced $1/f$ noise component from the atmosphere compared to any ground-based observatories. "3rd generation" terrestrial instruments currently under development plan to implement fast polarization modulation hardware to address this specific issue, but the effectiveness of this technique in the field has yet to be demonstrated.

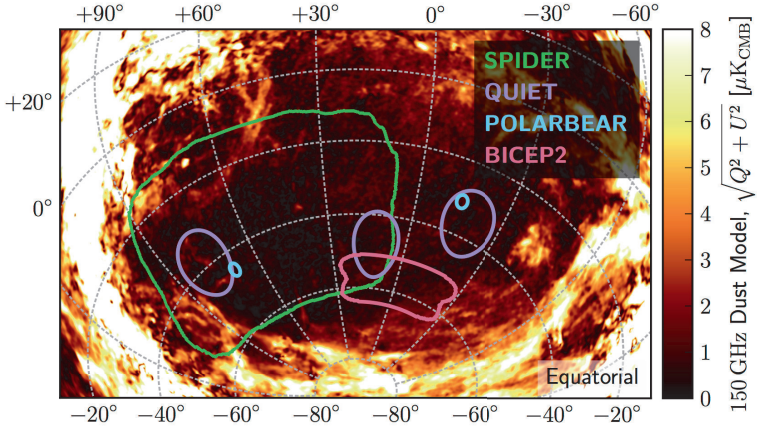


Figure 2 – The SPIDER observing region overlaid on the 150 GHz polarized intensity, estimated using the *Planck* `Commander` model and showing the dust morphology. Also shown are the QUIET, POLARBEAR, and BICEP2 fields; SPIDER mapped $\gtrsim 6\times$ more sky than the latter.

Current estimates of the in-flight sensitivity show that the median detector Noise Equivalent Temperatures (NETs) are consistent with first-principle design calculations and are in line with the expectations from past proposals and publications.[10] With low photon loading (total, in band: ≤ 0.35 pW at 150 GHz and ≤ 0.25 pW at 94 GHz), slow-scanned observations, and a demanding cosmic-ray environment, SPIDER demonstrates the operation of the antenna-coupled TES detector scheme in a space-like environment and raised their technology readiness level (TRL) to 6.

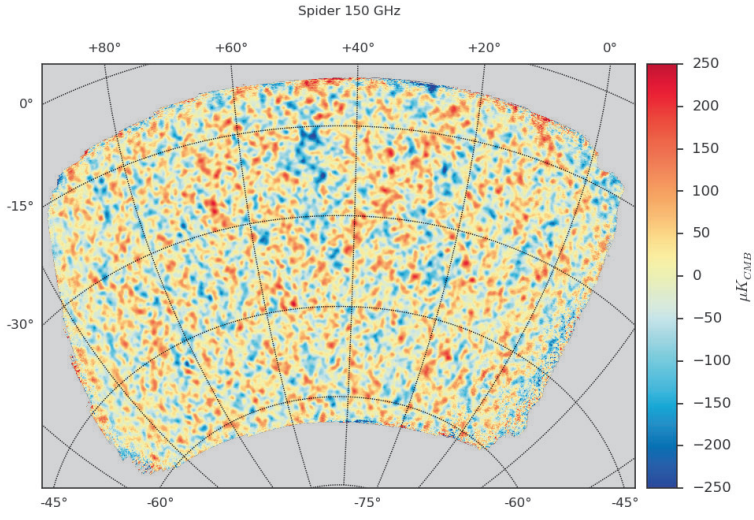


Figure 3 – SPIDER CMB temperature map at 150 GHz. The region covers roughly 4500 square degrees (∼11% of the full sky). The effective $f_{\rm sky}$, accounting for the distribution of integration time, is about 6.2%. The presence of structures on large angular scales is visually evident and constitutes one of the major advantages of a sub-orbital balloon platform over terrestrial observatories.

The SPIDER flight provides the first direct experience of cosmic ray interactions with these detectors in a relevant environment. The in-flight data reveal that the fraction of observing time lost to glitches in the time-ordered data due to particle events is negligible, indicating that the cosmic-ray cross-section is smaller than the spider-web bolometers flown on BLAST and BOOMERanG. Based on a typical 30-minute subset of SPIDER data at float, the median rate is 0.05 hits/minute, significantly lower than the rate in BLAST (1.5–6 hits/minute) and BOOMERanG (0.5 hits/minute) in the same environment. Event amplitudes based on a first-order calibration are 0.1–2 keV, with a median of 0.4 keV. Events that cause a DC-level discontinuity or drive a detector or its SQUID readout unstable are extremely rare.

During its 1st flight, SPIDER suffered from radio frequency interference (RFI) between systems on-board the payload and both the cold detectors/multiplexers and the warm electronics. These transients, which affect approximately 15% of the data, are easily identified and discarded from the analysis. Both JPL and NIST have been incorporating increased RFI mitigation into the design of their detector arrays, both at the chip-level and in the overall focal plane architecture. The NIST focal planes benefit from an RF firewall at the feedhorn array, providing a Faraday cage at the focal plane assembly that will guard against RF that couples through the aperture; a similar arrangement is being developed for the JPL detectors using a high-pass metal-mesh filter mounted directly onto the focal plane and electrically RF-sealing the aperture. In parallel, design modifications to the warm multiplexing electronics are being implemented to improve their RF grounding scheme.

4 Conclusions and Outlook

After its first successful flight and recovery campaigns, the SPIDER program is on track to test or experimentally rule out early Universe models by setting an upper limit of $r < 0.03$ (99% c.l., accounting for the presence of foregrounds) in two flights. The build of the SPIDER2 flight cryostat (not reusable from the first flight) is complete; the design of the three 285 GHz NIST

detector arrays and of the new focal plane architecture, as well as the consequent re-optimization of the optics, is complete; the device fabrication and test program is well underway.

In parallel, efforts are ongoing to re-arrange the existing JPL detectors into two or three focal planes to optimize yield and sensitivity for the 94 and 150 GHz bands. Finally, a 40% broadband channel centered at 250 GHz is under development at JPL and may be ready in time to be flown in one of the six inserts on SPIDER2.

After the successful instrument recovery campaign in November 2015, the second flight of SPIDER is planned for December 2017. Fig. 4 shows the projected per-multipole statistical errors for two flights (based on actual performance from the first flight). The goal for SPIDER is to recover angular modes corresponding to $10 \lesssim \ell \lesssim 300$, which represents a valuable niche in the multi-dimensional parameter space of observing strategies aimed at the measurement of primordial B-modes.

Finally, SPIDER provides a unique platform to qualify new technologies for future space applications. The JPL antenna-coupled bolometer architecture has achieved TRL 6 after the first flight of SPIDER. During our second flight, the NIST horn-coupled detector design can potentially be raised to the same TRL level.

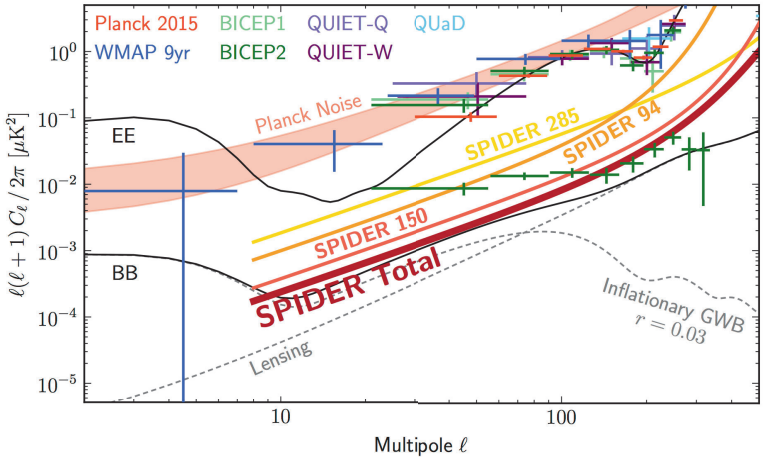


Figure 4 – Theoretical E- and B-mode power spectra and projected per-multipole statistical errors for two flights of SPIDER (based on actual performance from the 1st flight), as well as E-mode detections from the literature. The B-mode spectrum is the sum of two components: inflationary gravitational waves, shown here at a level of $r = 0.03$, and weak gravitational lensing of E-modes.

Acknowledgments

SPIDER is supported in the U.S. by NASA under Grant No. NNX07AL64G and NNX12AE95G issued through the Science Mission Directorate, and by the NSF through PLR-1043515. Logistical support for the Antarctic deployment and operations was provided by the NSF through the U.S. Antarctic Program, and by the British Antarctic Survey for the crucial data and payload recovery campaigns. The collaboration is grateful for the generous support of the David and Lucile Packard Foundation. Support in Canada is provided by the NSERC and the CSA.

References

1. Benton, S. J., Ade, P. A., et al., Proceedings of *SPIE* **9145**, 91450V (2014)
2. BICEP2 & Keck Array Collaborations, *Phys. Rev. Lett.* **116**, 031302 (2016)
3. BICEP2, Keck Array & SPIDER Collaborations, *Astrophys. J.* **812**, 176 (2015)
4. BICEP2/Keck & Planck Collaborations, *Phys. Rev. Lett.* **114**, 101301 (2015)
5. Britton, J. W., Nibarger, J. P., et al., Proceedings of *SPIE* **7741**, 774121 (2010)
6. Bryan, S., Ade, P., et al., *Rev. Sci. Instrum.* **87**, 014501 (2016)
7. Bryan, S. A., Ade, P. A. R., et al., Proceedings of *SPIE* **7741**, 77412B (2010)
8. Bryan, S. A., Montroy, T. E., & Ruhl, J. E., *Appl. Opt.* **49**, 6313 (2010)
9. Filippini, J. P., Ade, P. A. R., et al., Proceedings of *SPIE* **7741**, 77411N (2010)
10. Fraisse, A. A., Ade, P. A. R., et al., *J. Cosmol. Astropart. Phys.* **4**, 47 (2013)
11. Gandilo, N. N., Ade, P. A. R., et al., Proceedings of *SPIE* **9145**, 91452U (2014)
12. Gudmundsson, J. E., Ade, P. A. R., et al., Cryogenics **72**, 65 (2015)
13. Hubmayr, J., Appel, J. W., et al., *J. Low Temp. Phys.* **167**, 904 (2012)
14. Rahlin, A. S., Ade, P. A. R., et al., Proceedings of *SPIE* **9153**, 915313 (2014)
15. Runyan, M. C., Ade, P. A. R., et al., Proceedings of *SPIE* **7741**, 77411O (2010)
16. Shariff, J. A., Ade, P. A. R., et al., Proceedings of *SPIE* **9145**, 91450U (2014)
17. Soler, J. D., Ade, P. A. R., et al., Proceedings of *SPIE* **9145**, 91450T (2014)

CMB foregrounds - A brief overview

Clive Dickinson

Jodrell Bank Centre for Astrophysics, School of Physics & Astronomy, Alan Turing Building, The University of Manchester, Oxford Road, Manchester, M13 9PL, U.K.



CMB foregrounds consist of all radiation between the surface of last scattering and the detectors, which can interfere with the cosmological interpretation of CMB data. Fortunately, in temperature (intensity), even though the foregrounds are complex they can relatively easily be mitigated. However, in polarization, diffuse Galactic radiation (synchrotron and thermal dust) can be polarized at a level of $\geq 10\,\%$ making it more of a challenge. In particular, CMB B-modes, which are a smoking-gun signature of inflation, will be dominated by foregrounds. Component separation will therefore be critical for future CMB polarization missions, requiring many channels covering a wide range of frequencies, to ensure that foreground modelling errors are minimised.

1 Introduction

The Cosmic Microwave Background (CMB) radiation is the most distant source of electromagnetic radiation in our Universe, at a redshift $z \approx 1100$.[1] The CMB is therefore a backlight to all other sources of radiation between the surface of last scattering and the observer, which can contaminate the primordial signal - these sources of contamination are known as "CMB foregrounds". To accurately measure the CMB and its anisotropies, foregrounds must be removed either by a component separation algorithm or marginalised over during power spectrum and/or cosmological parameter estimation.[26,27,28] These methods rely on a prior knowledge of the foregrounds, such as intensity/polarization maps, statistical information on their spatial fluctuations, and most importantly, spectral information.[15,10] Indeed, component separation has become a field in itself with applications in other areas of astronomy such as Epoch of Reionization and Intensity Mapping. The increasing difficulty of dealing with foregrounds, particularly in polarization, has been highlighted by the initial detection of large-scale B-modes from the BICEP2 collaboration, which has been shown to be largely due to thermal dust emission.[2]

In this article, I briefly review the sources of foreground contamination, their basic characteristics, and comment on the difficulties for future CMB missions, particularly for inflationary B-modes on large scales.

2 Review of foregrounds

Table 1 gives examples of common types of foregrounds, many of which can be mitigated by careful design of experiments.

Table 1: Examples of the various types of CMB foregrounds. Some of these can be mitigated by careful design of the experiment, and in particular, by observing from a space satellite. Only a few astrophysical foregrounds are significantly polarized ("low" polarization typically means $< 1\,\%$) - most notably, diffuse Galactic emission, which is polarized at $\geq 10\,\%$, and is dominant on large angular scales ($> 1^\circ$).

Foreground	Polarization	Angular scales	Mitigation technique
Atmosphere	$\approx 0\,\%$	Large scales	Space/Balloon/high altitude sites
Ground	Varies	Large scales	Space/ground shield/low beam sidelobes
Radio Freq. Interference (RFI)	$0 - 100\,\%$	All	Space/remote sites/ground shield
Sun/Moon	Low	All	Space/low beam sidelobes
Planets/solar system objects	Low	Small scales	Low frequencies / high resolution
Zodiacal light	Low	Large scales	Low frequencies
Galactic synchrotron radiation	$\approx 10 - 40\,\%$	Large scales	Spectrum/high freqs.
Galactic free-free radiation	Low	Large scales	Spectrum/Hα/recomb. lines
Galactic thermal dust radiation	$\approx 2 - 20\,\%$	Large scales	Spectrum/low freqs/starlight abs.
Galactic spinning dust radiation	Low	Large scales	Spectrum/FIR templates
Galactic magnetic dust radiation	$0 - 35\,\%$	Large scales	Spectrum
Galactic line emission (e.g. CO)	Low	Large scales	Narrow bandpasses
Radio galaxies	Few %	Small scales	High frequencies/high resolution
Sub-mm/IR galaxies	Low	Small scales	Low frequencies/high resolution
Infrared Background (CIB)	Low	Small/interm. scales	Low frequencies/very high resolution
Secondary Anisotropies	Low	All	Spectrum/spatial

Fig. 1 shows the *Planck* temperature maps from 30 GHz to 857 GHz. The foregrounds are clearly visible, most notably from diffuse Galactic radiation, which dominate at the lowest and highest frequencies.

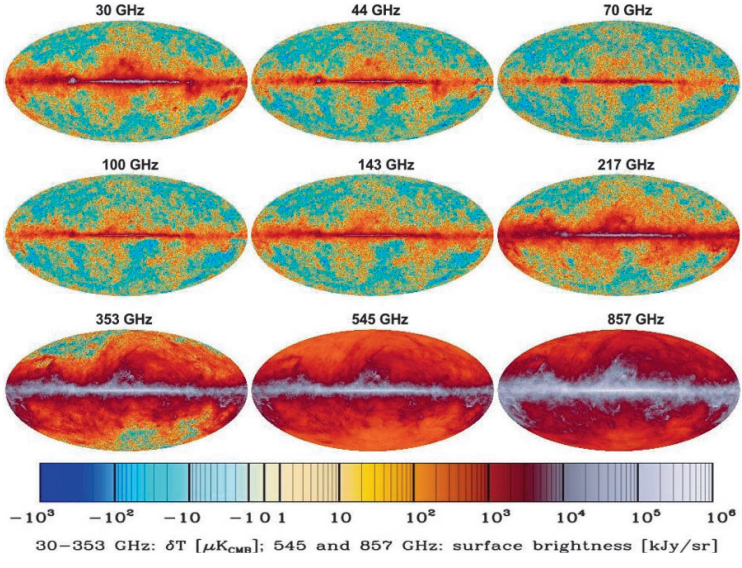


Figure 1 – *Planck* temperature maps, covering frequencies from 30 GHz to 857 GHz.[25] The diffuse Galactic foregrounds are very visible across all the maps, but dominating at the lowest and highest frequencies. The foreground minimum is at ≈ 70 GHz; the exact value depends on angular scale and sky coverage.

Fig. 2 shows the spectra of diffuse foregrounds in temperature and polarization, as derived from *Planck* data.[27] There are at least 4 distinct foregrounds in temperature, each with a different spectral signature. In polarization, there are currently two known foregrounds, in the form of diffuse synchrotron and thermal dust emission.

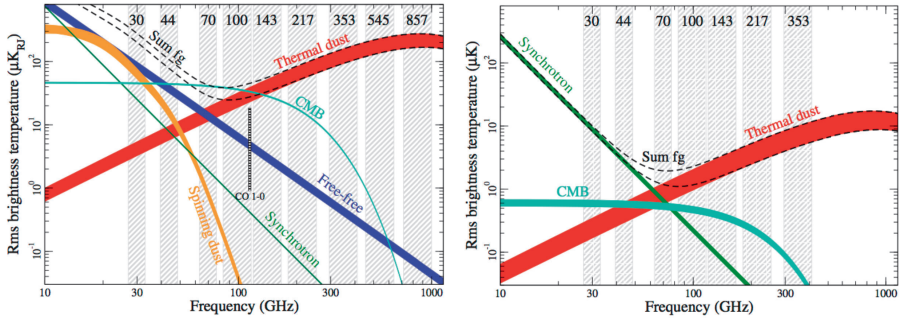


Figure 2 – Spectral characteristics of foregrounds and CMB in temperature (*left*) and polarization (*right*).[27] These estimates represent the average fluctuations on $\approx 1^\circ$ scales over $\approx 80\,\%$ of the sky. The foregrounds in temperature appear to be more complex, but are comparable or below the CMB signal. In polarization, the number of significant components may be less, but their amplitudes are well above the typical level of CMB polarization anisotropies at all frequencies.

In this review, we focus on diffuse Galactic radiation, which is the dominant foreground on large angular scales ($> 1^\circ$) and in polarization.

2.1 Synchrotron radiation

Synchrotron radiation is emitted by relativistic cosmic ray (CR) electrons, which are accelerated by the Galactic magnetic field. In a regular magnetic field, the electrons spiral around the field lines, emitting radiation as they traverse a circular path. The emission depends on the number and energy spectrum of the CR electrons and the strength of the magnetic field. The spectrum of synchrotron radiation is directly dependent on the CR energy spectrum, which can vary across the sky, but is well-approximated by a power-law, at least over a range of frequencies. Most of the information on Galactic synchrotron radiation has come from low-frequency radio surveys. At frequencies above a few hundred MHz, the spectrum is optically thin and is steeply falling with frequency, with typical temperature spectral indices ($T \propto \nu^\beta$) of $\beta \approx -2.7$ at GHz frequencies, with variations $\Delta\beta \approx \pm 0.2$.[32,33] At higher frequencies, the spectrum appears to steepen further, presumably due to radiative losses, which cause spectral ageing, with $\beta \approx -3.0$ at WMAP/*Planck* frequencies.[3,1,28] However, multiple components along the line-of-sight can also flatten the spectrum.

The polarization of synchrotron radiation is less well known, since it can only be directly mapped at frequencies above a few GHz, due to the effect of Faraday Rotation, which is important at frequencies below a few GHz.[35] The best maps to date are CMB data from WMAP and *Planck*, which are limited in S/N ratio and do not allow accurate spectral indices to be derived (except for relatively bright emission). Fig. 3 shows a model of the synchrotron polarization at 30 GHz. Large-scale features are readily visible and contribute significant polarization even at high Galactic latitudes. The polarization fraction of synchrotron radiation can, in principle, be as high as 75 %, in a uniform and regular magnetic field. In practice, depolarization along the line-of-sight and non-regular fields reduces the polarized intensity. Even though we have maps of polarized synchrotron emission, the precise values of polarized fractions are difficult to quantify because the intensity of synchrotron emission is not well-known at frequencies above a few GHz

due to the contributions of free-free and anomalous microwave emission. Nevertheless, at high latitudes, synchrotron emission is polarized at a level of $10 - 40\,\%$.[34,29]

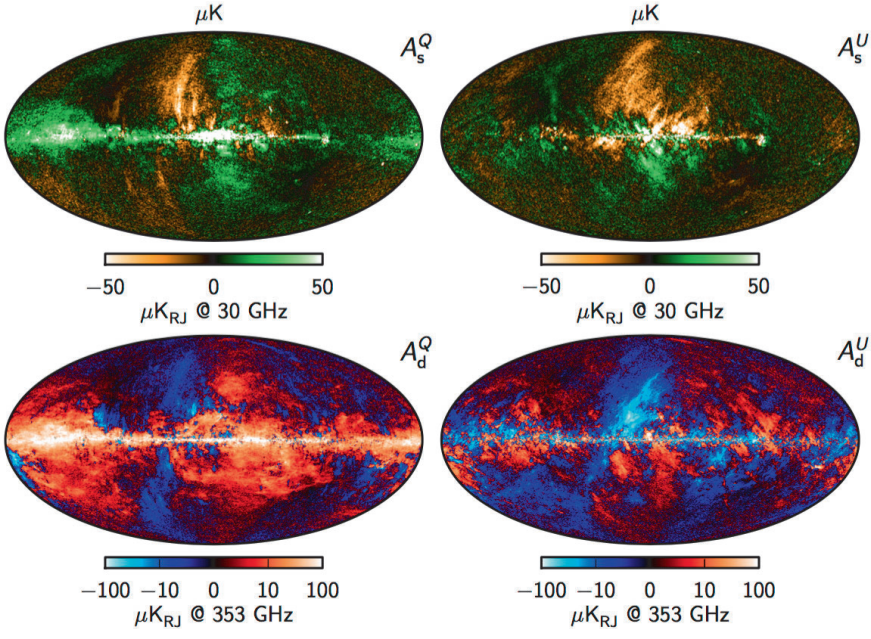


Figure 3 – Amplitude maps of polarization foregrounds in Stokes Q (*left*) and U (*right*) of synchrotron emission at 30 GHz (*top*) and thermal dust emission at 353 GHz (*bottom*). These maps are from the COMMANDER component separation analysis.[27]

2.2 Free-free radiation

Free-free radiation, or thermal bremsstrahlung, is emitted by free electrons interacting with ions, in ionised gas. As electrons are accelerated by ions (usually protons) they emit free-free radiation. Free-free radiation has a well-understood spectrum. At frequencies above a few GHz, where the emission is optically thin, the spectrum has a temperature spectral index of $\beta = -2.1$, with very little variation with electron temperature.[4] At higher frequencies, approaching 100 GHz, the spectrum steepens slightly to $\beta = -2.13$.[21] The relatively flat spectral index means that it could be the dominant foreground near the foreground minimum ($\nu \approx 70$ GHz). The confusion with synchrotron, AME, and thermal dust, means it can be difficult to separate accurately. However, the close correlation with the optical Hα line allows the amplitude to be derived independently.[4] At high Galactic latitudes, free-free emission is relatively weak with $\Delta T \approx 10\,\mu$K at 30 GHz, or $\Delta T \approx 1\,\mu$K at 100 GHz.

Free-free is intrinsically unpolarized. Coulombic interactions are by their nature random in orientation, with no significant alignment with the magnetic field. Residual polarization can occur on sharp edges due to Thomson scattering. At high Galactic latitudes, the polarization is therefore expected to be very low ($\ll 1\,\%$), with current measured upper limits at $< 3\,\%$ [16] for diffuse emission and $\ll 1\,\%$ for compact HII regions. Free-free emission is probably not going to be a major foreground for CMB polarization studies.

2.3 *Thermal dust radiation*

Thermal dust radiation is blackbody emission modified by opacity effects, from interstellar dust grains with typical temperatures $T \approx 20\,\mathrm{K}$. The observed spectrum is often modelled as a modified black-body, $T(\nu) = \tau\nu^{\beta_d}B(\nu, T_d)$, where the ν^{β} term represents the change in emissivity of the grains with wavelength. β_d is referred to as the emissivity index and is generally in the range $\beta = 1 - 2$ although it can be steeper. *Planck* data, combined with IRAS/COBE data, have provided full-sky measurements of the thermal dust spectrum.[20] The thermal dust emission is reasonably well-modelled by a single modified-blackbody with mean temperature $T_d \approx 19\,\mathrm{K}$ and index $\beta_d \approx 1.6$.[24] This value is somewhat flatter than had previously been predicted ($\beta \approx 1.7-2.0$), making it more difficult to observe the CMB at frequencies $\approx 100\,\mathrm{GHz}$.

Thermal dust emission can be significantly polarized. Elongated dust grains emit preferentially along their shortest axes while large dust grains, which are important at sub-mm wavelengths, can align efficiently by the Galactic magnetic field, causing a net polarization. The mean polarization fraction at high latitude is significantly higher than initial estimates and measurements from the Archeops experiment, which were at $\approx 5\,\%$. Recent *Planck* data have allowed the polarization fraction to be measured across the sky, and has found polarization fractions of up to $\approx 20\,\%$ with a mean value at high latitude of $\approx 10\,\%$.[22,31] Fig. 4 shows estimates of the thermal dust polarization fraction across the sky, and as a function of the total column density. The latter was estimated from the optical depth at 353 GHz, which, to first order, is simply the brightness at 353 GHz. It can be seen that a large fraction of the sky has polarization fractions $> 5\,\%$. More worryingly for CMB studies is that the higher polarization fractions tend to occur in regions of low column density, which means low intensity. Higher density regions, including the Galactic plane, tend to have lower polarization fractions due to the effect of line-of-sight depolarization. The power spectrum of thermal dust anisotropies appears to follow a power-law with a slope $\alpha \approx -0.4$;[30] leading to larger fluctuations on large angular scales.

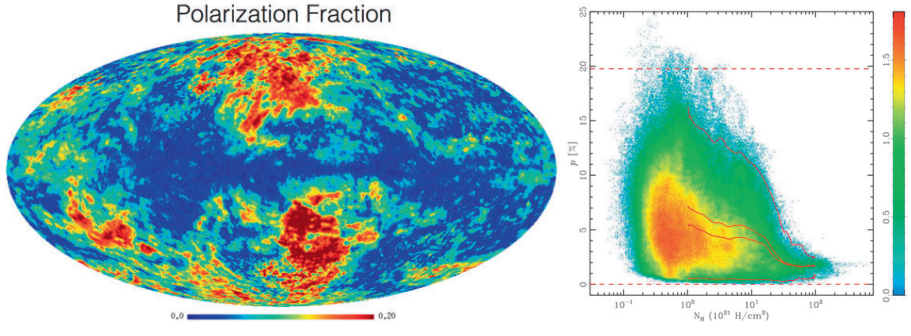


Figure 4 – *Left*: Full-sky map of thermal dust polarization fraction, as seen by *Planck* at 353 GHz.[22] *Right*: Polarization fraction of thermal dust emission, as seen by *Planck* at 353 GHz, against an estimate of the total column density of the interstellar medium along the line-of-sight (which is essentially a scaled version of the intensity at 353 GHz).[22]

2.4 *Spinning dust radiation*

Spinning dust radiation is emitted by the smallest ($\sim 10^{-9}\,\mathrm{m}$) interstellar dust grains and molecules, which can rotate at GHz frequencies. If they have an electric dipole moment, they emit by electric dipole radiation.[6] The spectrum of spinning dust is invariably a highly peaked spectrum, which is dominated by the emission of the smallest grains (since they can spin the fastest due to lower moments-of-inertia). At least in a few Galactic clouds, observations have

shown a good fit to a spinning dust spectrum with a typical peak frequency of $\approx 30\,\mathrm{GHz}$. For the diffuse emission at high Galactic latitudes, the spectrum of spinning dust has not been measured due to the difficulty of component separation.

Theoretical work suggests that spinning dust is not highly polarized at frequencies above a few GHz.[14,13,9] Measurements of the level of polarization of spinning dust, largely consist of upper limits at the level of a few per cent.[5,18] This is one of the major arguments that AME is indeed due to spinning dust, and not magnetic dust (§ 2.5). If all AME is due to spinning dust, then even a low ($\approx 1\,\%$) level of polarization could be problematic for future CMB data.[17] This is because of the very low target on r and the unprecedented sensitivity of large detector arrays.

2.5 Magnetic dust radiation

Magnetic dust (MD) radiation is emitted by interstellar dust grains and/or free-floating ferromagnetic material (e.g., Fe). Thermal fluctuations can change the net magnetization of a collect of grains by perturbing the alignment of spins in the magnetic domain, producing MD radiation.[7] The spectrum of MD is similar to that of thermal dust emission, similar to a blackbody with temperature of order tens of K, depending on the type of magnetic materials and whether they are free-fliers or inclusions within dust grains. This is the main reason why MD emission is difficult to detect unambiguously. The most distinct feature(s) of MD radiation is that it can be highly polarized, and with a potentially distinct polarization signature as a function of frequency. A wide range of signatures can be produced depending on the precise model. The first works[7] predicted, at least for a single-domain magnetic grains a $30-35\,\%$ polarization fraction at frequencies of $> 200\,\mathrm{GHz}$, falling to zero with lower frequency and then increasing again. More recent theoretical work[13] predicts a maximum polarization fraction of $10-15\,\%$ at high ($> 200\,\mathrm{GHz}$) and low ($< 10\,\mathrm{GHz}$) with a sharp transition somewhere in between.

MD radiation has not been definitively detected, although there have been a number of hints. The spectrum of the SMC has been shown to be readily fitted by including a plausible component of Fe particles, without which results in a poorer fit.[8] *Planck* data have shown that the thermal dust spectrum appears to flatten at lower frequencies ($< 350\,\mathrm{GHz}$), which if not taken into account, results in a small excess at frequencies near 100 GHz in intensity. Furthermore, the polarization fraction of the thermal dust emission correlated with thermal emission at 353 GHz, appears to reduce slightly from 353 GHz to 100 GHz and below.[23] These may be hints that a contribution of MD radiation is detectable in *Planck data*, although both of these can be explained by changes in dust grain properties, which affect the thermal dust emission. This complication of the spectrum near frequencies of 100 GHz would clearly be problematic for CMB component separation in polarization.

3 Measuring CMB B-modes

A large fraction of the basic statistical information from the CMB has been extracted already. Although there are still several avenues to pursue (small-scales, SZ, large-scale anomalies, E-modes, lensing etc.), a major goal for the future is to constrain, and if possible detect, large-scale B-modes. The detection of primordial B-modes on scales $\ell < 100$ ($> 2^\circ$) would be a smoking-gun signature of inflation. Furthermore, the amplitude of these B-modes, given by the tensor-to-scalar ratio r, determines the energy scale of inflation. The major obstacles, besides raw sensitivity, are the calibration requirements and component separation. Indeed, several CMB polarization satellite concepts have been put forward (B-pol, PRISM, CORE and CORE+ from ESA, EPIC and PIXIE from NASA, and LiteBIRD from JAXA), which have the sensitivity to detect inflationary B-modes at the level of $r \approx 10^{-3}$ or better.[12,17] To achieve this our knowledge of the foregrounds and performance of component separation algorithms will need to be improved.

Fig. 5 depicts the level of diffuse foregrounds in B-mode polarization, for various sky areas, compared to the CMB, assuming $r = 0.01$.[10] It is clear that foregrounds dominate the CMB signal at all frequencies due to the fact that the foregrounds have a higher polarization fraction and that foregrounds emit similar amounts of E- and B-modes. It is important to note that these estimates were made pre-*Planck*, assuming a 5 % average polarization fraction for thermal dust. Therefore, in reality, the high frequency (> 100 GHz) foregrounds will have a factor of $\approx 2 - 4$ power. This clearly makes the situation worse, and is clearly born out by the BICEP2/Keck results. It also causes the foreground minimum to move to lower frequencies (≈ 70 GHz).

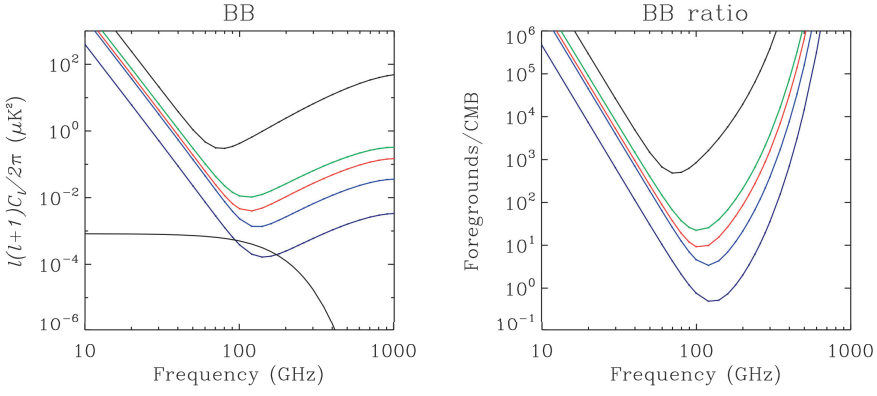


Figure 5 – Foregrounds B-mode power, as a function of frequency (*left*) and ratio of foregrounds-to-CMB B-mode power (*right*). The black curve represents the CMB B-mode power for $r = 0.01$. The curves from top to bottom represent different sky areas (full-sky, 82 %, 50 %,23 %, and 5 %).[10] The data were produced using the Planck Sky Model as of 2009. The low frequency side is accurate to within a factor of 2, primarily based on WMAP data. On the high frequency side, it assumes an average thermal dust polarization fraction of ≈ 5 % since it was made pre-*Planck*. New results from *Planck* show that the foreground power on the high frequency side is ≈ 2 times larger in amplitude, or ≈ 4 times in power.

The *Planck* data have revolutionised our knowledge of the microwave/sub-mm sky, particularly above 100 GHz. However, the sensitivity of *Planck* polarization data, even at 353 GHz (the highest frequency that contains polarization data, and therefore the highest signal-to-noise ratio), is still relatively low, particularly on scales $< 1^\circ$. Future CMB missions will need to incorporate additional high frequency (> 300 GHz) channels as foreground monitors. This will not significantly affect the focal plane design since such detectors will take up a small amount of space because of their small size and only a small number of detectors would be required.

At low frequencies, CMB satellites will be limited by the focal plane area. Having additional low frequency channels uses up a lot of space (they will be physically large, scaling as λ for a given angular resolution since they will likely be diffraction limited), which would reduce the overall sensitivity of the higher frequency "CMB channels". Satellites are unlikely to include frequencies below about 30 GHz. It will therefore be crucial to make high-sensitivity, high-fidelity ground-based surveys. Table 2 lists some of the main low-frequency polarization surveys underway. Foreground surveys should ideally be full-sky, have high signal-to-noise ratios per beam, and have minimal systematic errors.

We note that lensing of E-modes to B-modes by large-scale structure is also a foreground to the inflationary B-modes on the largest angular scales. Since lensing B-modes have the same frequency spectrum as the CMB, other methods are required, either based on spatial correlations or from direct subtraction using high-resolution measurements.

We also note that the Cosmic Infrared Background (CIB) might also be a polarized foreground. The CIB consists of a large number of individual galaxies,[19] which individually are

Table 2: Low-frequency ground-based surveys relevant to large-scale CMB polarized foregrounds.

Survey	Frequency	Angular resolution	Sky	Status
GEM	0.4,1.4,2.3,5,10	≈ 0.5 (10 GHz)	Full-sky	On-going
S-PASS	2.3	0.1	Southern sky	Obs complete
C-BASS	5	0.75	Full-sky	N complete; S started
QUIJOTE	11,13,17,19	≈ 1	Northern sky	On-going

expected to have a low level ($< 1\,\%$) of polarization, one might think that on average, should average to $\approx 0\,\%$ if they are orientated in random directions (as one would expect). This is true for the mean but since we are interested in the *fluctuations* it is the *variance* of the polarized intensity that matters, which does not cancel out.

Finally, we remark on emission lines that can contaminate the detector bands and cause systematic errors in the data. This was a significant problem for *Planck* HFI, which was contaminated by the strongest sub-mm lines of CO (e.g., $J = 1 \rightarrow 0$ at 115 GHz). Bandpasses will need to be carefully chosen to avoid at least the very brightest emission lines. Furthermore, wide bandwidths require colour corrections to take into account the finite bandwidth, which causes the effective frequency to vary with the colour (spectrum) of the source. For ultra-sensitive experiments, this could be a limiting factor.

Fig. 6 shows the posterior probability distributions for r for a range of CMB polarization satellite concepts. This simulation includes polarized thermal dust and synchrotron foregrounds, which were fitted for, using the COMMANDER code.[11] The synchrotron spectrum includes positive curvature (flattening with increasing frequency), which causes a bias in the recovered estimates of r. The LiteBIRD curve is most discrepant in the left-hand panel, due to its lack of frequency coverage. The right panel is the same but with additional frequency channels for the LiteBIRD configuration, which significantly reduces the bias. A bias in the recovered r-value can result either from incorrect foreground modelling or lack of frequencies to remove them.

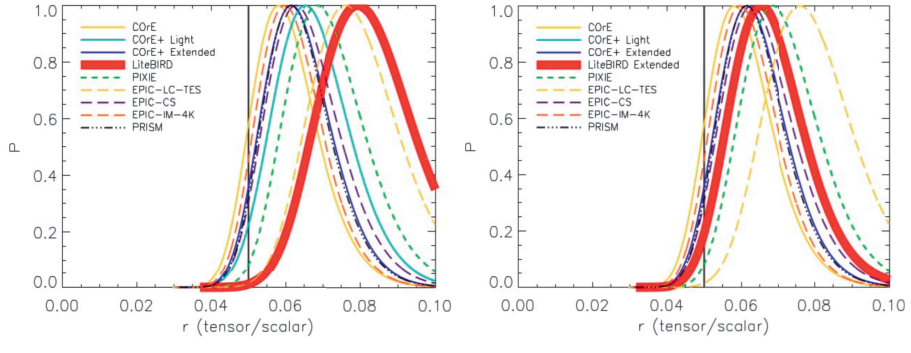


Figure 6 – Simulated posterior probability distributions for the tensor-to-scalar ratio, r, for a range of CMB polarization satellite mission concepts.[17] The input value is $r = 0.05$. The foreground simulation includes synchrotron emission with positive curvature. The *left* panel shows that the results are biased high, due to the mis-modelling of the synchrotron foreground. The *right* panel shows how adding additional low frequency channels to the LiteBIRD experiment, the bias can be reduced.

4 Conclusions and outlook

Foregrounds are a major issue for accurate studies of CMB anisotropies. Fortunately, in temperature, foregrounds appear not to be a major limitation. However, for detailed polarization studies, particularly large-scale B-modes, foregrounds are a more serious problem. It will therefore be vital for future missions to have as many frequency channels and as large a frequency range as possible. There are several proposed CMB polarization satellite mission concept, which typically have 6 or more frequency channels, up to frequencies of 350 GHz and higher. However, at lower frequencies (below the minimum of foregrounds at ≈ 70 GHz) focal plane area limitations mean that satellite configurations can only afford one or two low frequency channels at most. It will therefore be critical to accurately measure the low frequency polarized foregrounds from ground-based telescopes operating at a few GHz up to ≈ 20 GHz. Component separation will likely be the limiting factor in achieving constraints on r down to the $r = 10^{-3}$ level and below. More frequency channels, covering a wide range of frequencies, will be critical in testing foreground mitigation.

Acknowledgments

CD acknowledges support from an ERC Starting Consolidator Grant (no. 307209) and an STFC Consolidated Grant (ST/L000768/1). This review is dedicated to the late Prof. Rodney Deane Davies and Prof. Richard John Davis. They were both mentors and friends to me and many colleagues around the world.

References

[1] Bennett, C. L., Halpern, M., Hinshaw, G., et al. 2003, ApJS, 148, 1
[2] BICEP2/Keck and Planck Collaborations, et al. 2015, PRD Letters, 114, 101301
[3] Davies, R. D., Dickinson, C., Banday, A. J., et al. 2006, MNRAS, 370, 1125
[4] Dickinson, C., Davies, R. D., & Davis, R. J. 2003, MNRAS, 341, 369
[5] Dickinson, C., Peel, M., & Vidal, M. 2011, MNRAS, 418, L35
[6] Draine, B. T., & Lazarian, A. 1998, ApJ, 508, 157
[7] Draine, B. T., & Lazarian, A. 1999, ApJ, 512, 740
[8] Draine, B. T., & Hensley, B. 2012, ApJ, 757, 103
[9] Draine, B. T., & Hensley, B. S. 2016, arXiv:1605.06671
[10] Dunkley, J., et al. 2009, American Inst. of Physics Conf. Series, 1141, 222
[11] Eriksen, H. K., Jewell, J. B., Dickinson, C., et al. 2008, ApJ, 676, 10-32
[12] Errard, J., Feeney, S. M., Peiris, H. V., & Jaffe, A. H. 2016, JCAP, 3, 052
[13] Hoang, T., & Lazarian, A. 2016, ApJ, 821, 91
[14] Lazarian, A., & Draine, B. T. 2000, ApJL, 536, L15
[15] Leach, S. M., Cardoso, J.-F., Baccigalupi, C., et al. 2008, A&A, 491, 597
[16] Macellari, N., Pierpaoli, E., Dickinson, C., & Vaillancourt, J. E. 2011, MNRAS, 418, 888
[17] Remazeilles, M., Dickinson, C., Eriksen, H. K., & Wehus, I. K. 2016, MNRAS, 458, 2032
[18] Rubiño-Martín, J. A., et al., 2012, Advances in Astronomy, 2012, 351836
[19] Planck Collaboration, Ade, P. A. R., Aghanim, N., et al. 2011, A&A, 536, A18
[20] Planck Collaboration, Abergel, A., Ade, P. A. R., et al. 2014, A&A, 571, A11
[21] Planck Collaboration, Ade, P. A. R., Aghanim, N., et al. 2014, A&A, 565, A103
[22] Planck Collaboration, Ade, P. A. R., Aghanim, N., et al. 2015, A&A, 576, A104
[23] Planck Collaboration, Ade, P. A. R., Alves, M. I. R., et al. 2015, A&A, 576, A107
[24] Planck Collaboration, Aghanim, N., Ashdown, M., et al. 2016, arXiv:1605.09387
[25] Planck Collaboration, Adam, R., Ade, P. A. R., et al. 2015, arXiv:1502.01582
[26] Planck Collaboration, Adam, R., Ade, P. A. R., et al. 2015, arXiv:1502.05956
[27] Planck Collaboration, Adam, R., Ade, P. A. R., et al. 2015, arXiv:1502.01588

[28] Planck Collaboration, Aghanim, N., Arnaud, M., et al. 2015, arXiv:1507.02704
[29] Planck Collaboration, Ade, P. A. R., Aghanim, N., et al. 2015, arXiv:1506.06660
[30] Planck Collaboration, Adam, R., Ade, P. A. R., et al. 2016, A&A, 586, A133
[31] Planck Collaboration, Ade, P. A. R., Aghanim, N., et al. 2016, A&A, 586, A141
[32] Platania, P., Bensadoun, M., Bersanelli, M., et al. 1998, ApJ, 505, 473
[33] Platania, P., Burigana, C., Maino, D., et al. 2003, A&A, 410, 847
[34] Vidal, M., Dickinson, C., Davies, R. D., & Leahy, J. P. 2015, MNRAS, 452, 656
[35] Wolleben, M., Landecker, T. L., Reich, W., & Wielebinski, R. 2006, A&A, 448, 411

SIMULATING THE POLARISED GALAXY

Flavien Vansyngel
Institut d'Astrophysique Spatiale, Université Paris Sud, Btiment 121, 91405 Orsay FRANCE

One major goal in experimental cosmology is the detection of the primordial B-modes of the CMB polarisation. The next generation projects will have the sensitivity required to detect the signal predicted by the simplest models of inflation. However, any detection will involve separation from Galactic foregrounds. To optimize observing strategies, assess separation methods, and quantify Galactic residuals left after foreground subtraction, realistic simulations of polarised Galactic, dust and synchrotron, foregrounds are needed. In this proceeding, I present a method to make such simulations, which focusses on dust but could also be applied to synchrotron. It simulates statistically the interplay between dust polarization properties, the density structure of matter and interstellar MHD turbulence. The sky maps match the dust polarization power spectra measured on the Planck data. This approach also allows users to obtain multiple realisations of the dust polarized sky, very much like what is available for simulating CMB maps.

1 Context

The next big step in observational CMB cosmology should be a detection of the imprint that the inflationary period left on the polarisation pattern of the CMB anisotropies. A major issue in CMB data analysis is the presence in the data of many different and complex signals, because we are embedded into the late time object that is our Galaxy.

In the *Planck* intermediate paper XXX[1], the authors show that in the high Galactic latitudes regions, contamination to CMB B-modes due to dust is high. Even in the best case scenarios and in the less contaminated regions, dust and CMB B-modes are present at a same order of magnitude at 353GHz. So dust is not negligible and has to be taken into account carefully during the process of component separation.

The plots from figure 1 are taken from a recent paper by Remazeilles et al.[2]. Using simulations, the authors show that future experiments will have the required sensitivity to achieve a detection if the CMB tensor-to-scalar ratio r is of the order of 10^{-2}. But they also show that there is a good recovery of r only in the case where the dust model used in the simulations is the same than the model used for the analysis. They show that, using the same set of simulation, but this time in the analysis the dust is not correctly modelled, a bias appears on the measurement of r: there is a creation of fake CMB B-modes.

2 Dust of the ISM

What experimental design for optimal cleaning? What level of B-modes can we actually reach? How to quantify the confidence in the cleaning? To answer these questions, we need sky simulations to test analysis methods. These simulations need to be as close as possible to actual complexity of the real sky in order to push the methods to their limits. An ideal model would

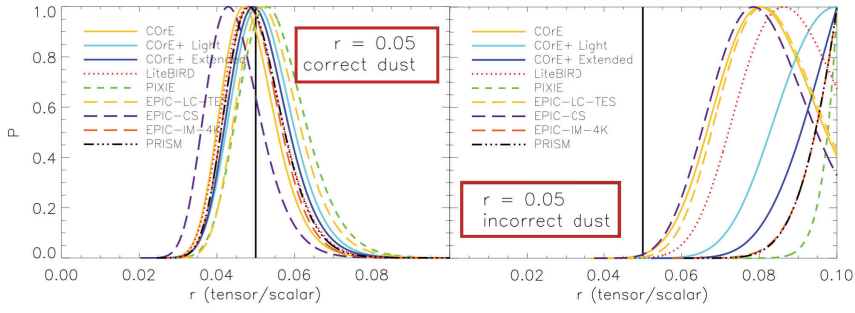


Figure 1 – Bias in CMB B-modes estimation. On each plot, the black line represent the input r value and the curves represent the posterior distributions for the set up of various future experiments.

take into account all physical processes, from the microscopic to the Galactic scale. But this is a too ambitious goal, we have to select the relevant aspects to be modelled.

Polarisation mechanism The accepted mechanism for producing dust polarisation is the following: dust grains are not spherical, one axis is longer than the other. Because of some mechanism, grains align with their local magnetic filed lines such that the longest axis is perpendicular to the field lines. Because of this configuration, the thermal emission of the dust grains is polarised perpendicular to the field lines. Thus, a fundamental piece for building a physical dust model is the Galactic magnetic field.

Line of sight structure It is obvious but the Galaxy is a 3D object. It has not only structure when projected on the plane of the sky but also on the line of sight. One important effect is a large variance in the polarisation fraction and the scatter at high latitudes, due to turbulence, is coherent on the sky. These effect can be explained by an averaging on the line of sight. Thus, if we want to recover these effects in simulations, the line of sight dimension must be taken into account in the modeling.

Matter-field correlation The structure of matter and the magnetic field are correlated. The figure 2 shows in color the total intensity of *Planck* 353GHz channel, and the ripples gives a good idea of the orientation of the magnetic field lines. In many filaments, we can see this striking correlation between the orientations of the filament and of the field. This configuration of the field will then induce E-modes polarisation pattern. This produces correlation between total intensity and polarization, i.e. TE correlation. Also, since E-modes are preferred to B-modes, there is a E-B power asymmetry in dust polarisation.

Dust-synchrotron correlation Dust is not the only emission in the frequency range relevant to CMB observation. For example, the dominant CMB contaminant at low frequencies is the synchrotron emission from free electrons spiralling around the magnetic field lines. In the data, we observe correlation between observations at low and high frequencies. So far, this observation suggests that dust and synchrotron polarized emissions are correlated, but it is not well understood.

3 Simulation method

In this section I present the model that my collaborators and I have been developing and show step by step how we construct our simulations of polarized dust emission.

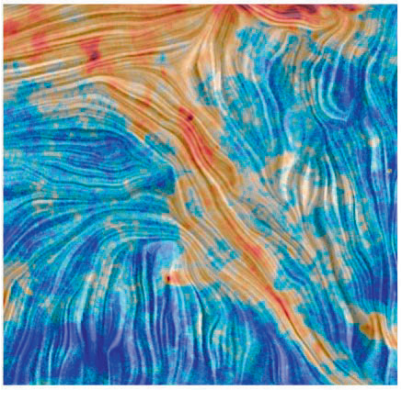


Figure 2 – Matter-field correlation. In filaments, direction of magnetic field (ripples) is correlated with the structure of matter (color).

Magnetic field The starting point of the model is the choice of a model for the Galactic magnetic field. The magnetic field is modelled as the sum of a mean field and a turbulent part, which is stochastic. The most important parameters are that characterising the turbulent field: (1) the relative strength of the turbulent field compared to the mean field, and (2) the slope of the turbulence cascade. These parameters are input parameters of the simulations.

Q/I, U/I Stokes parameters The second step is to derive the observables for linear polarisation, the Q and U Stokes parameters. From a random realisation of the Galactic magnetic field, we can infer the direction of the projected field lines on the plane of the sky. The polarisation direction is then just this direction rotated by 90 degrees. From this angle, we can derive the Q and U Stokes parameters (normalised to intensity) for each direction.

Depolarisation The third step introduces the large scatter in the polarisation fraction observed in the data. The idea is to realize a number N of Galactic field on the plane of the sky, and stack the corresponding Stokes maps. The different directions of the magnetic filed (due to the random turbulent field) creates a different polarisation direction in each of the N layers, such that the total polarisation is partially cancelled. The number of layers N is also a input parameter of the simulations.

I, Q, U Stokes parameters The next step is to multiply the stacked normalised Stokes parameters maps by an intensity map in order to get a triplet of IQU dust maps. Thus by realising many turbulent field, we get many possible realisation of polarised dust maps.

Realistic statistics Because the intensity and the polarisation part are treated independently, the simulations do not feature TE correlation and E-B asymmetry. The last step of the recipe of the simulations is to transform the simulations in order to introduce the correct 2-point statistics. The statistics (power spectrum amplitudes and correlations) are input parameters of the simulations.

4 Properties of the simulations

Power spectra The simulations are able to reproduce the data at the power spectrum level. In Fig. 3, left plot, the blue points represents the mean and the standard deviation of the BB

power spectrum of 1000 simulations and the red line is a fit and the error on the fit to the *Planck* power spectrum. Right plot of Fig. 3 shows the E-B asymmetry and errors on it in the simulations (blue points) and in the *Planck* data (dotted lines). The dash-dotted lines represent the input ratio to the simulations.

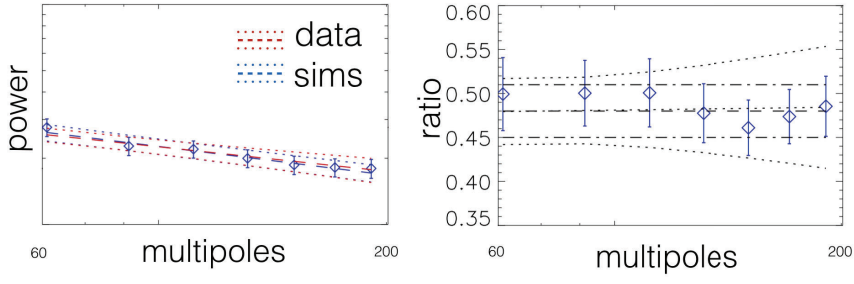


Figure 3 – BB power spectrum and E-B asymmetry in both simulations and *Planck* data.

Power probability distribution function (PDF) We studied the PDF of the power per multipole bin of the simulations. The dispersion is due to both cosmic variance and stochasticity of the turbulent field. The distribution is close to a Gaussian distribution. By looking at the difference with a Gaussian fit, we can see a deviation from Gaussianity. There is a clear pattern showing that the actual distribution of the power per bin is slightly skewed. It is not a big effect, but it might be not negligible for future likelihood analysis.

5 Prospects: simulation on a range of frequency channels

This proceeding discusses a method to simulate structures on the sky. The next big issue to address is the extrapolation of these structures to other observed frequencies. Each line of sight has its own frequency law dependence. This is very important to take into account because it introduces spatial decorrelation between frequencies, meaning that at each frequency the spatial distribution won't be exactly the same. Greater decorrelation is expected in polarisation than in total intensity because decorrelation happens for both intensity and polarisation angle. Because of the noise, this effect is weak in present data but its significance will increase with future sensitivities and component separation techniques will have to struggle with it.

Acknowledgements

The talk of this proceeding has been done on behalf of the authors (F. Vansyngel, F. Boulanger, T. Ghosh, A. Bracco, B. Wandelt, J. Aumont, L. Montier) of the paper "Statistical simulations of the dust foreground to CMB polarisation" to be submitted. The work is funded by the ERC program.

References

1. Planck collab., PIPXXX, *Astron. Astrophys.* Vol. 586 pp. A133 (2016)
2. Remazeilles et al., *Mon. Not. Roy. Astron. Soc.* Vol. 458 pp. 2032 (2016)

Constraining Multiplicative Bias in CFHTLenS Weak Lensing Shear Data

JIA LIU
Department of Astronomy and Astrophysics, Columbia University, New York, NY 10027, USA

Several recent cosmological analyses have found tension between constraints derived from the Canada-France-Hawaii Telescope Lensing Survey (CFHTLenS) data and those derived from other data sets, such as the *Planck* cosmic microwave background (CMB) temperature anisotropies. Similarly, a direct cross-correlation of the CFHTLenS data with *Planck* CMB lensing data yielded an anomalously low amplitude compared to expectations based on *Planck* or WMAP-derived cosmological parameters (Liu & Hill 2015). One potential explanation for these results is a multiplicative bias afflicting the CFHTLenS galaxy shape measurements, from which shears are inferred. We cross-correlate CFHTLenS galaxy density maps with CFHTLenS shear maps and *Planck* CMB lensing maps to calibrate an additional multiplicative shear bias (m) in CFHTLenS (beyond the multiplicative correction that has already been applied to the CFHTLenS galaxy shears). We analyze three magnitude-limited galaxy samples, finding 2–4σ evidence for $m < 1$ using the deepest sample ($i < 24$), while the others are consistent with $m = 1$ (no bias). A value of $m \approx 0.9$ would suffice to reconcile the amplitude of density fluctuations inferred from the CFHTLenS shear two-point statistics with that inferred from *Planck* CMB temperature data. This scenario is consistent with our results.

1 Introduction

Weak gravitational lensing is a promising tool to probe the nature of dark energy, the total mass of neutrinos, and possible deviations from general relativity. Large galaxy lensing datasets, such as the ones from the Large Synoptic Survey Telescope and the Euclid Space Mission, will come online in the next decade. While providing unprecedentedly precise measurements of the large scale structure (LSS), these surveys also present a great challenge, as measurement systematics must be minimized in order to realize the surveys' full statistical power. Major known galaxy lensing systematics include galaxy shape (or "shear") measurements, photometric redshift calibrations, and intrinsic alignments of galaxies.

In this work, we study the impact of one type of shape measurement systematic, the multiplicative bias, in the first large galaxy lensing survey — the 154 deg^2 CFHTLenS. The multiplicative bias originates from the galaxy model bias and pixel noise bias, and is more likely to occur for faint galaxies. The bias can change the overall amplitude of the cosmic shear auto-correlation and its cross-correlation with other probes of the LSS, hence causing a biased estimation of cosmological parameters.

Mild discrepancies between cosmological parameters estimated using galaxy lensing data and those estimated from CMB temperature measurements have been reported by several groups[1,2,3,4,5]. For example, the cosmological parameter $\sigma_8(\Omega_m/0.27)^{0.46}$, which is orthogonal to the Ω_m-σ_8 degeneracy direction for galaxy lensing, is lower by $\approx$ 2–2.5σ when estimated from CFHTLenS cosmic shear two-point statistics than when estimated from *Planck* CMB temperature measurements[1,6,7]. Such a disagreement can potentially be explained by a multiplicative shear bias $m < 1$, where $m = 1$ corresponds to no bias. In this work, we estimate m through a joint analysis of the cross-correlations of (1) maps of galaxy number density and galaxy lensing convergence, and (2) maps of galaxy number density and CMB lensing convergence.

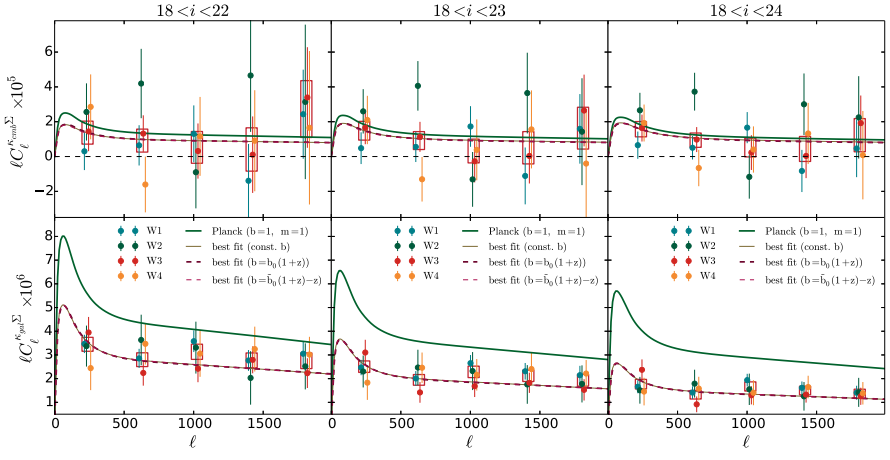


Figure 1 – Angular cross-power spectra of (1) $\kappa_{\rm cmb}$ and Σ (upper panels) and (2) $\kappa_{\rm gal}$ and Σ (lower panels) for three galaxy samples ($18 < i < 22$, $18 < i < 23$, and $18 < i < 24$). Data points are for individual CFHTLenS fields, and errors are estimated using 100 simulated $\kappa_{\rm cmb}$ maps and 100 randomly-rotated $\kappa_{\rm gal}$ maps. The boxes represent the inverse-variance weighted sum of the four fields. The thick-solid, thin-solid, thick-dashed, and thin-dashed curves are the fiducial theoretical model using *Planck* 2015 parameters ($b = 1$), the best-fit model assuming a constant b, the best-fit model assuming $b(z) = b_0(1+z)$, and the best-fit model assuming $b(z) = \tilde{b}_0(1+z) - z$, respectively. The multiplicative shear bias m is held fixed to unity in all models shown here.

2 Formalism

In the Limber approximation, the angular cross-power spectrum of two different probes (denoted α and β) of the LSS can be expressed in general as

$$C_\ell^{\alpha\beta} = \int_0^\infty \frac{dz}{c}\frac{H(z)}{\chi^2(z)} W^\alpha(z) W^\beta(z) P\left(k = \frac{\ell}{\chi(z)}, z\right) \tag{1}$$

where z is the redshift, c is the speed of light, $H(z)$ is the Hubble parameter, $\chi(z)$ is the comoving distance, and $P(k,z)$ is the matter power spectrum at redshift z and wavenumber k. The weighting kernels $W(z)$ for galaxy lensing convergence ($\kappa_{\rm gal}$), CMB lensing convergence ($\kappa_{\rm cmb}$), and galaxy number density (Σ) are

$$W^{\kappa_{\rm gal}}(z) = \frac{3}{2}\Omega_m H_0^2 \frac{(1+z)}{H(z)}\frac{\chi(z)}{c} \times \int_z^\infty dz_s \frac{dn(z_s)}{dz_s}\frac{\chi(z_s)-\chi(z)}{\chi(z_s)}, \tag{2}$$

$$W^{\kappa_{\rm cmb}}(z) = \frac{3}{2}\Omega_m H_0^2 \frac{(1+z)}{H(z)}\frac{\chi(z)}{c}\frac{\chi(z_\star)-\chi(z)}{\chi(z_\star)}, \tag{3}$$

$$W^{\Sigma}(z) = b(z)\frac{dn(z)}{dz}, \tag{4}$$

where Ω_m is the matter density (relative to critical) at $z = 0$, $H_0 = H(z=0)$, z_s is the redshift of the background source, where $z_\star = 1100$ for the CMB, and $b(z)$ is the galaxy bias. The multiplicative bias can be estimated using a combination of auto- and cross-correlations involving $\kappa_{\rm gal}$, $\kappa_{\rm cmb}$, and Σ (see discussions in[8,9]). In this work, we use cross-correlations,

$$C_\ell^{\kappa_{\rm gal}\Sigma,{\rm obs}} = m C_\ell^{\kappa_{\rm gal}\Sigma,{\rm theory}}(b), \quad C_\ell^{\kappa_{\rm cmb}\Sigma,{\rm obs}} = C_\ell^{\kappa_{\rm cmb}\Sigma,{\rm theory}}(b), \tag{5}$$

to isolate the effect of m. While $C_\ell^{\kappa_{\rm gal}\Sigma,{\rm obs}}$ is sensitive to both m and the galaxy bias b, $C_\ell^{\kappa_{\rm cmb}\Sigma,{\rm obs}}$ is sensitive to b alone. Thus, a joint analysis of these probes can break the degeneracy between b and m, yielding robust constraints on both [8,9]. The primary assumption of this method is that all data sets are governed by the same cosmological parameters (we assume minimal ΛCDM). We also must make assumptions regarding the behavior of the galaxy bias $b(z)$, for which we consider three scenarios, a constant b, $b(z) = b_0(1+z)$, and $b(z) = \tilde{b}_0(1+z) - z$. Finally, we assume that the CMB lensing data are not afflicted by a multiplicative bias.

3 Results

We use the publicly available CMB lensing convergence ($\kappa_{\rm cmb}$) map released by the *Planck* collaboration (2015 data release). We use CFHTLenS data to construct $\kappa_{\rm gal}$ and Σ maps. It is important to note that we have already applied to the $\kappa_{\rm gal}$ maps the multiplicative bias correction provided in the CFHTLenS catalogue [10]. The cross-power spectra $C_\ell^{\kappa_{\rm gal}\Sigma}$ and $C_\ell^{\kappa_{\rm cmb}\Sigma}$ for the three galaxy number density samples are shown in Fig. 1, where we also overlay the fiducial theoretical models ($b = 1, m = 1$) and best-fit results. Fig. 2 shows the derived constraints on b and m from these two cross-correlations, assuming a constant b.The marginalized constraints are listed in Table 1.

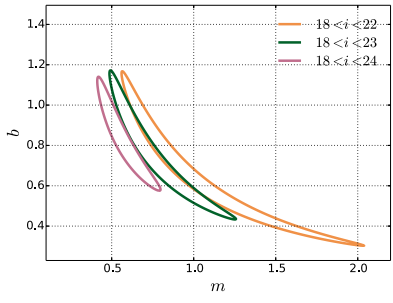


Figure 2 – Error contours (68%) in the m–b plane, assuming a constant b. The different contours correspond to different galaxy samples, as labeled. Marginalized values of m and b are listed in Table 1.

The joint analysis shows that m is statistically consistent with unity (no bias) for the $i < 22$ and $i < 23$ samples, while we obtain 2–4σ evidence for $m < 1$ using the $i < 24$ sample, depending on the galaxy bias model adopted (only the constant bias result is shown here due to the page limit). The m constraints are statistically consistent for the three different galaxy bias models considered. It is not surprising that $m < 1$ is only significant for the deepest sample, as this cross-correlation probes the LSS at a higher redshift than the other two samples. At high redshifts, the $\kappa_{\rm gal}$ signal receives more contributions from faint galaxies, whose shapes are more difficult to measure accurately.

4 Discussion

In this work, we search for evidence of additional multiplicative biases in CFHTLenS weak gravitational lensing shear measurements (beyond the standard multiplicative correction from the CFHTLenS shear catalogue) using joint cross-correlations of CFHTLenS data and *Planck* CMB lensing data. Our results show hints (2–4σ) of a non-vanishing multiplicative bias for the deepest sample of galaxies considered in this analysis. We stress that, despite our focus on biases in shear measurement, other systematics that can change the overall amplitude of $C_\ell^{\kappa_{\rm gal}\Sigma}$ may also partially or even fully account for the discrepancy we see. Possible sources include intrinsic alignment contamination and photometric redshift errors, which are beyond the scope of this work, but must be studied more carefully in the future. Another alternative

Table 1: Marginalized constraints on b and m, where a constant b is assumed. We provide constraints obtained using $C_\ell^{\kappa_{\rm cmb}\Sigma}$ only (column 2), $C_\ell^{\kappa_{\rm gal}\Sigma}$ only (column 3), and their combination (columns 4 and 5).

Σ sample	$C_\ell^{\kappa_{\rm cmb}\Sigma}$	$C_\ell^{\kappa_{\rm gal}\Sigma}$	$C_\ell^{\kappa_{\rm cmb}\Sigma} + C_\ell^{\kappa_{\rm gal}\Sigma}$	
	b	b (m=1)	b	m
$18 < i < 22$	$0.73^{+0.20}_{-0.21}$	$0.69^{+0.02}_{-0.02}$	$0.71^{+0.18}_{-0.19}$	$0.82^{+0.27}_{-0.16}$
$18 < i < 23$	$0.80^{+0.17}_{-0.17}$	$0.59^{+0.02}_{-0.02}$	$0.62^{+0.17}_{-0.16}$	$0.82^{+0.28}_{-0.16}$
$18 < i < 24$	$0.83^{+0.13}_{-0.13}$	$0.49^{+0.02}_{-0.02}$	$0.73^{+0.13}_{-0.13}$	$0.60^{+0.11}_{-0.08}$

would be an unexpectedly complex galaxy bias model — a non-monotonic redshift dependence would be needed to explain the results in Table 1.

To place this work in context, we estimate the level of multiplicative bias needed to reconcile the tension between cosmological parameter constraints derived from CFHTLenS two-point statistics and those derived from *Planck* CMB temperature anisotropy measurements. We use the fact that the auto-power spectrum of $\kappa_{\rm gal}$ scales roughly quadratically with σ_8 and exactly quadratically with m. $\sigma_8(\Omega_m/0.27)^{0.46} = 0.89 \pm 0.03$ (using "*Planck*+WP+highL" data[11]), compared with 0.774 ± 0.04 from CFHTLenS[6]. Therefore, a multiplicative bias $m \approx 0.9$ suffices to bridge the gap between these two measurements. Such a bias would also help reconcile the discrepancy seen in measurements of $C_\ell^{\kappa_{\rm gal}\kappa_{\rm cmb}}$[3], where the amplitude of the best-fit model compared to predictions based on *Planck* CMB-derived parameters is found to be $A_{planck} = 0.44 \pm 0.22$.[a] Our results using shallow galaxy samples ($i < 22$ or $i < 23$) are consistent with such a value, but also with $m = 1$, due to the relatively large error bars. Our best-fit m for the deepest sample ($i < 24$) prefers a lower $m = 0.6 - 0.7$, depending on the galaxy bias model adopted, but is also statistically consistent with a value of m that would bring the CFHTLenS constraints into agreement with *Planck*. Thus, within the uncertainties of current data sets, a multiplicative shear bias remains a feasible option to reconcile the tension between the CFHTLenS and *Planck* cosmological parameter constraints. If more sensitive CMB lensing data were taken on these fields, it would be possible to improve the overall signal-to-noise such that the galaxies in the $\kappa_{\rm gal}$ reconstruction could be split into sub-samples based on different properties (e.g., color or size), perhaps allowing the cause of the multiplicative bias to be isolated. With our current signal-to-noise, such data splits are not feasible.

This study represents the first constraint on a multiplicative shear bias based on a joint cross-correlation analysis with CMB lensing data. As our overall covariance matrix is dominated by the *Planck* CMB lensing noise, galaxy lensing surveys that overlap with CMB lensing surveys with a lower noise level, e.g., the Atacama Cosmology Telescope (ACT) and the South Pole Telescope (SPT), will provide better constraints on the multiplicative bias. Furthermore, a larger sky coverage of the galaxy lensing survey will also enhance the constraint (near-future surveys are typically designed to overlap with CMB surveys). Therefore, the 5000 deg^2 Dark Energy Survey(overlapping ACT and SPT), the 1500 deg^2 Hyper Suprime-Cam survey (entirely within ACT coverage), and the 1500 deg^2 Kilo-Degree Survey (overlapping ACT) will provide an excellent opportunity to study and control the multiplicative shear bias in the future.

Acknowledgments

This summary is based on Liu et al. (2016)[12]. I thank my co-authors for their permission to present our joint work.

References

1. Planck Collaboration *et al.*, ArXiv e-prints (2015), [arXiv:1502.01589].
2. N. Hand *et al.*, *Phys. Rev.* D**91**, 062001 (2015), [arXiv:1311.6200].
3. J. Liu and J. C. Hill, *Phys. Rev.* D**92**, 063517 (2015), [arXiv:1504.05598].
4. M. Raveri, ArXiv e-prints (2015), [arXiv:1510.00688].
5. S. Grandis, S. Seehars, A. Refregier, A. Amara and A. Nicola, ArXiv e-prints (2015), [arXiv:1510.06422].
6. C. Heymans *et al.*, MNRAS **432**, 2433 (2013), [arXiv:1303.1808].
7. J. Benjamin *et al.*, MNRAS **431**, 1547 (2013), [arXiv:1212.3327].
8. A. Vallinotto, ApJ **759**, 32 (2012), [arXiv:1110.5339].
9. S. Das, J. Errard and D. Spergel, ArXiv e-prints (2013), [arXiv:1311.2338].
10. L. Miller *et al.*, MNRAS **429**, 2858 (2013), [arXiv:1210.8201].
11. Planck Collaboration *et al.*, A&A **571**, A16 (2014), [arXiv:1303.5076].
12. J. Liu, A. Ortiz-Vazquez and J. C. Hill, ArXiv e-prints (2016), [arXiv:1601.05720].

[a] Intrinsic alignment contamination is likely to explain a significant fraction of this discrepancy, and has not been corrected for here.

Multiple lensing of CMB anisotropies

G. Fabbian
International School for Advanced Studies (SISSA), Trieste 34014, Italy



We study the gravitational lensing effect on the anisotropies of the Cosmic Microwave Background (CMB) performing a ray-tracing of its photons through intervening large-scale structures (LSS) distribution predicted by N-Body numerical simulations. We discuss differences of CMB lensing observables derived with this method with respect to the standard techniques usually employed in this context that are based on the Born approximation. Finally we analyze the impact of second order lensing effects propagating the full lensing jacobian through cosmic structures.

1 Introduction

The CMB is now firmly established as one of the most important cosmological probe thanks to the accuracy of the measurements of the recent Planck satellite and the current generation of suborbital CMB polarization experiments. In parallel to the studies on the primordial signal for cosmological applications, the attention of the community has swiftly moved towards the weak gravitational lensing of CMB anisotropies. Being sensitive to the whole matter distribution along the line of sight, CMB lensing can be used to infer information about the Large Scale Structure (LSS) distribution and on the parameters that govern the physics of structure formation at intermediate and late time (like, e.g., the dark energy and massive neutrinos properties).

2 Mathematical formalism

In weak lensing calculations, the effect of deflections of photons along the entire line of sight is described by the lens equation, which maps the final position $(\boldsymbol{\beta}, \chi)$ of the photon to the position of its source $\boldsymbol{\theta}$, i.e.

$$\beta_i(\boldsymbol{\theta}, \chi) = \theta_i - \frac{2}{c^2} \int_0^\chi \frac{(\chi - \chi')}{\chi\chi'} \Phi_{,\beta_i} \left(\boldsymbol{\beta}(\boldsymbol{\theta}, \chi'), \chi'\right) \mathrm{d}\chi', \tag{1}$$

where $\Phi(\boldsymbol{\beta}, \chi)$ is a gravitational potential and $\Phi_{,\beta_i}$ its spatial derivative. The relative position of nearby light rays is described by the derivative of the previous equation (lensing jacobian):

$$A_{ij}(\boldsymbol{\theta}, \chi) = \partial_j \beta_i(\boldsymbol{\theta}, \chi) = \delta^K_{ij} - \frac{2}{c^2} \int_0^\chi \frac{f_K(\chi - \chi')}{f_K(\chi) f_K(\chi')} \Phi_{,\beta_i \beta_k} \left(\boldsymbol{\beta}(\boldsymbol{\theta}, \chi'), \chi'\right) A_{kj}(\boldsymbol{\theta}, \chi') \mathrm{d}\chi'. \quad (2)$$

A is usually decomposed into four fields describing how the source at $\chi \equiv \chi_s$ is transformed by its interaction with the matter distribution,

$$A_{ij} = \begin{pmatrix} 1 - \kappa - \gamma_1 & -\gamma_2 + \omega \\ -\gamma_2 - \omega & 1 - \kappa + \gamma_1 \end{pmatrix}, \quad (3)$$

$\kappa(\boldsymbol{\theta}, \chi_s)$ describes image magnification, $\omega(\boldsymbol{\theta}, \chi_s)$ the image rotation while $\gamma(\boldsymbol{\theta}, \chi_s) = \gamma_1(\boldsymbol{\theta}, \chi_s) + i\gamma_2(\boldsymbol{\theta}, \chi_s)$ defines the complex spin-2 shear. The latter describes the shearing of the image, and can be decomposed into E and B-modes in analogy with CMB polarization. In the context of CMB lensing, the lens equation is usually integrated in the Born approximation, i.e. over the unperturbed, unlensed photon paths $(\boldsymbol{\theta}, \chi)$ [a]. Shear B-modes and image rotation are non-zero only if we take into account the full non-linear equation or the coupling between lenses at two different redshifts while are zero in the Born approximation.The overall effect of lensing deflection field can be expressed an effective deflection (vector) field that can be decomposed in a pure gradient of a scalar potential ψ (lensing potential), and a curl-like potential Ω:

$$\boldsymbol{\beta}(\boldsymbol{\theta}, \chi_s) = \boldsymbol{\theta} - \nabla\psi(\boldsymbol{\theta}, \chi_s) - \nabla \times \Omega(\boldsymbol{\theta}, \chi_s), \quad (4)$$

The latter is null in the Born approximation. The exponentially growing quality of CMB observations requires a great effort to simulate and make predictions for the various lensing observables with the highest possible accuracy. One of the major challenges lies in the improvement in the modeling of the LSS distribution to include the non-linear evolution of the dark matter distribution at low redshift as well as to include the multiple deflection of photons along the line of sight. We tried to overcome these last points at the same time implementing a multiple-lens plane (hereafter ML) method first sketched by Das & Bode [3].

3 From particles to surface mass density maps

Starting from an N-Body simulation, we create 3D simulated matter distribution around a chosen observer along the past lightcone. For this work we used the CoDECS [5] and DEMNUni [6] ΛCDM simulations. We overcome the problem of the finite volume of the simulation using box replication and randomization techniques. We then divided the lightcone in shell of $150h^{-1}$Mpc thickness and project all the matter particle inside a given shell over a single 2D spherical map. For each of these surface mass density map at different redshift we then solved the full-sky Poisson equation in the harmonic domain up to a given angular scale ℓ^ψ_{max} and extracted the lensing potential of each shell $\psi^{(k)}$ (see fig. 2). We also computed the effective integrated potential combining the single 2D mass maps with a proper lensing weight. To test that the box replication and randomization procedure did not create spurious effect, we checked that the total mass in each slice was consistent with the amount of mass expected from the cosmology of the N-body simulation. We found that this number agrees with theoretical expectation at sub-percent level at $z > 0.5$ and better than 2% level at $z \lesssim 0.5$ for the CoDECS simulation and is always sub-percent for the DEMNUni simulation. For both simulations we also found that the 1-point PDF of the surface mass density planes is well described by a modified log-normal distribution following the Das & Ostriker [9] model in agreement with previous numerical results.

[a] this is equivalent to drop the dependence over the lensed position $\boldsymbol{\beta}$ in eqs. (1, 2) and replace it with $\boldsymbol{\theta}$.

4 Lensing the CMB

To lens the CMB we first generated a gaussian realization of the unlensed CMB up to a given scale ℓ_{max}^{CMB}. To propagate the CMB photons through the different shells we used the the publicly available code Lenspix. Starting from the $\psi_{\ell m}^{(k)}$ coefficients, we computed the deflection field for each shell $\boldsymbol{\alpha}^{(k)}$ in the harmonic domain[b]. We then assumed that the Born approximation is valid between two consecutive shells. Each time a CMB photon crosses a mass shell in the direction $\hat{\mathbf{n}}^{(k)}$, is remapped into $\hat{\mathbf{n}}'^{(k)}$,

$$\hat{\mathbf{n}}'^{(k)} = \hat{\mathbf{n}}^{(k-1)} + \boldsymbol{\alpha}^{(k)}, \tag{5}$$

where $\hat{\mathbf{n}}^{(k-1)}$ represents the unlensed position of the CMB photons at the previous step. Pixel based method are affected by several numerical effects[2] and therefore we tested the convergence of our results with respect to choices of spatial resolution and cut-off in power in the Fourier domain used to synthesize signals on the sphere (i.e. $\ell_{max}^{CMB}, \ell_{max}^{\psi}$). The baseline choice of these parameters used to obtained the results shown in this proceeding are $\ell_{max}^{CMB} = \ell_{max}^{\psi} = 4096$.

5 Lensed CMB power spectra

In Figure 1 we show the comparison between the expected CMB lensed temperature C_ℓ^{TT} and the lensed B-modes of polarization power spectra C_ℓ^{BB} computed using CAMB, and the spectra extracted from our lensed CMB maps. For both these cases the simulated power spectra follow precisely the analytical signal. After having subtracted the shot-noise induced lensing contribution, the fractional difference between CAMB and the N-Body lensed spectra shows no significant bias up to $\ell \approx 3000$ where we start seeing effects due to the choice of ℓ_{max}^{CMB}. The latter is not high enough to properly resolve power on those scales with high-accuracy. The abrupt decrease in power observed on those scales for the ML approach w.r.t. the Born approximation is due to the effect of polynomial interpolation employed in Lenspix. As the latter tends to smooth the underlying signal, the consecutive application effectively removes more power on small angular scale with respect to the Born approach, for which the interpolation is performed only once. Similar results are obtained for the E-modes power spectrum. The situation however is different for the B-modes of polarization where we found the shot-noise contribution to be important at the percent level at small angular scales. This is expected given that B-modes are very sensitive to non-linear power, which is affected by shot-noise for $\ell >> 2000$.

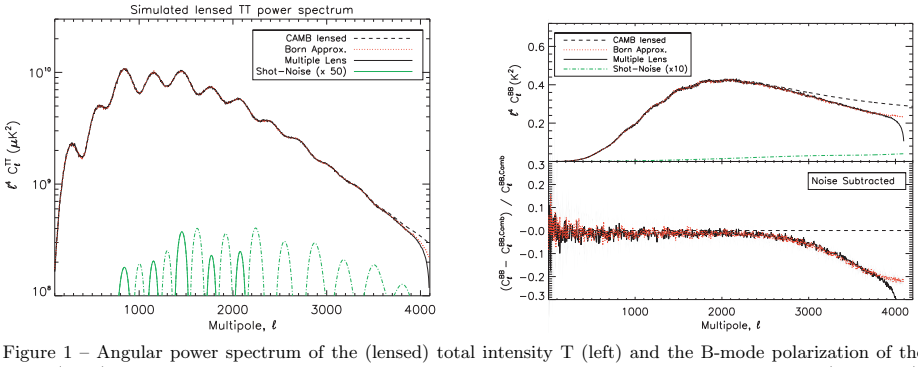


Figure 1 – Angular power spectrum of the (lensed) total intensity T (left) and the B-mode polarization of the CMB (right) compared to the theoretical expectation obtained with the Boltzmann code CAMB (black line). Red dotted line show results obtained in the Born approximation, while for the blue solid line the CMB is lensed through ML method. Green lines in both panels show the shot-noise contribution in the N-body simulation to the lensed spectra; green, dot-dashed lines represent the absolute value of this contribution.

[b] At this step we take into account the incidence angle of the light ray on the lens plane.

The lack of power due to the choice of ℓ_{max}^{CMB} starts to be important on angular scales larger than the ones affected in T and E-modes power spectra. This can be explained considering that at those scales a non-negligible fraction of the contribution to the BB power spectrum starts to come from progressively higher multipoles of both E and ψ that are not included by construction in the setup of our simulation [2,1].

6 CMB lensing jacobian simulation

Recent analytical work [4] claimed that large corrections at small angular scales are expected in the angular power spectrum of CMB lensing potential with respect to the results obtained with the Born approximation. The authors also made the hypothesis that the resolution of numerical simulations implemented in Calabrese et al.[1] were not sufficient to resolve these corrections. Motivated by these arguments, we expanded and improved the previous ray-tracing algorithm to explore and characterize the component of the full CMB lensing jacobian using the ML method [7,8] up to arc-minute scales. In this regime in fact non-linear effects are at most noticeable and beyond the limit of the results presented in the previous section. For this work we used the DEMNUni simulation [6] to produced 62 lens planes. To test these effects at the greatest level of accuracy we improved the raytracing method adopting the LenS^{2}HAT code [2] instead of LensPix. Thanks to its low memory footprint and massively parallelism we were able to propagate the full lensing jacobian together with the CMB light rays at a resolution of roughly 2arcsec over the full sky. In fig. 2 we show the power spectra of the CMB lensing observables extracted from its lensing jacobian at $z = 0$. We recover with high accuracy the consistency relation that exists between the lensing observables [8] while we see an excess of power in $\kappa, \epsilon$and E-mode of the α field with respect to the CAMB result due to the improved modeling of non-linearity and shot noise contribution of the N-body simulation. We also recover a purely second order non-zero ω, β field showing that the method is precise enough to resolve beyond Born corrections. We tested the convergence of the result as a function of the sky pixelization resolution and found it to be of the order of 0.5% for κ and ω fields. We also tested the stability of the result with respect to the number of lensing planes employed in the raytracing. A thinner slicing of the light-cone in shells of $50h^{-1}$Mpc (corresponding to an increase by a factor 3 in number of planes) lead to sub-percent differences in κ a 1% increase in ω.

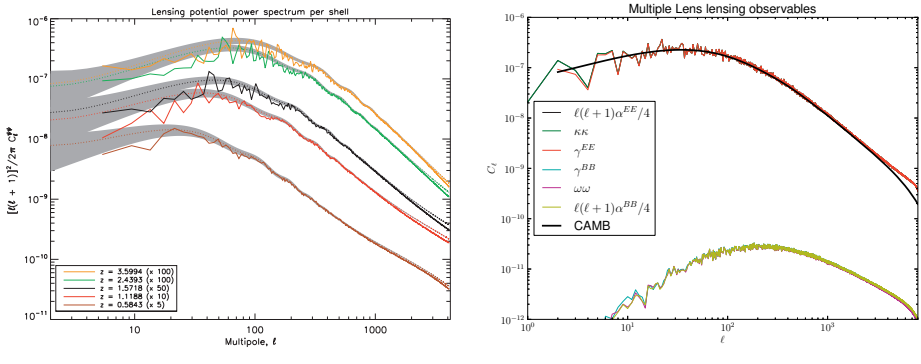


Figure 2 – Left: comparison between the angular power spectrum of the lensing potential computed with our algorithm from the CoDECS simulations (solid lines) and the analytical results in the Limber approximation at different redshifts. The grey area displays the cosmic variance. Right: convergence ($\kappa\kappa$), shear E (γ^{EE}) and B-modes (γ^{BB}) and rotation ($\omega\omega$) angular power spectra for CMB lensing. E and B-modes of the effective photon displacement $\alpha^{E/B}$ have been converted into the power spectra of the effective scalar potentials (see eq. 4).

References

1. Calabrese, M., Carbone, C., Fabbian, G., Baldi, M., & Baccigalupi, C. 2015, *JCAP* , 3, 049
2. Fabbian, G., & Stompor, R. 2013, *A & A*, 556, A109
3. Das, S., & Bode, P. 2008, *Astrophysical Journal*, 682, 1-13
4. Hagstotz, S., Schäfer, B. M., & Merkel, P. M. 2015, *MNRAS* , 454, 831
5. Baldi, M. 2012, *MNRAS* , 422, 1028
6. Castorina, E., Carbone, C., Bel, J., Sefusatti, E., & Dolag, K. 2015, *JCAP* , 7, 043
7. Hilbert, S., Hartlap, J., White, S. D. M., & Schneider, P. 2009, *A & A*, 499, 31
8. Becker, M. R. 2013, *MNRAS* , 435, 115
9. Das, S., & Ostriker, J. P. 2006, *Astrophysical Journal*, 645, 1


LA THUILE
53
50
22
36
37
4
13
27
30
45
8
6
54
52
20
48
40

A BIAS TO CMB LENSING FROM THE BISPECTRUM OF LARGE-SCALE STRUCTURE

V. BÖHM[1], M. SCHMITTFULL[2], and B. D. SHERWIN[2,3]
[1]*Max-Planck-Institut für Astrophysik, Karl-Schwarzschild Strasse 1, 85748 Garching, Germany*
[2]*Berkeley Center for Cosmological Physics, Department of Physics and Lawrence Berkeley National Laboratory, University of California, Berkeley, CA 94720, USA*
[3]*Miller Institute for Basic Research in Science, University of California, Berkeley, CA, 94720, USA*

We identify a new, so far ignored, bias to measurements of gravitational lensing of the cosmic microwave background (CMB). This bias is sourced by a nonzero bispectrum of the CMB lensing potential, which contributes to the lensed CMB four-point function that enters into the standard estimator of the CMB lensing power spectrum. We analytically derive all contributions to this new bias but restrict the numerical evaluation to two terms which are likely among the largest. The bias from these two terms is at the level of a few percent of the signal for temperature-based lensing measurements with CMB Stage-III and Stage-IV experiments. Following further investigations into its exact magnitude, this bias should be accounted for in future lensing analyses.

1 Gravitational Lensing of the CMB

Gravitational lensing remaps the CMB temperature field T at angular position $\mathbf{x}$ on the sky

$$\tilde{T}(\mathbf{x}) = T\left[\mathbf{x} + \alpha(\mathbf{x})\right] = T\left[\mathbf{x} + \nabla\phi(\mathbf{x})\right], \tag{1}$$

where the total deflection angle $\alpha(\mathbf{x})$ depends on the large-scale structures along the line of sight. It can be expressed in terms of the lensing potential ϕ, which is a weighted projection of all gravitational potentials that the photon encounters along its path.

The lensed temperature $\tilde{T}$ can be approximated by perturbing in the lensing potential. We adopt a schematic, short-hand, notation for the perturbation series in Harmonic space

$$\tilde{T}(\mathbf{l}) = T(\mathbf{l}) + \delta T(\mathbf{l}) + \delta^2 T(\mathbf{l}) + \mathcal{O}(\phi^3), \tag{2}$$

where the order in δ labels the order in ϕ of each term.

2 Bispectrum of the CMB Lensing Potential

The CMB lensing potential is commonly assumed to be a Gaussian random field inheriting its Gaussianity from the large-scale matter distribution. However, at low redshifts the matter distribution acquires a nonzero bispectrum due to nonlinear structure formation. This bispectrum of large-scale structure induces a corresponding bispectrum of the lensing potential. In Limber, Born and flat-sky approximation the CMB lensing bispectrum B_ϕ is given by a weighted integral over the bispectrum of matter fluctuations B_δ. Apart from being an interesting signal on its own [1], the CMB lensing bispectrum can be a source of error in measurements that rely on the

Gaussian nature of ϕ. We have investigated the impact of the lensing bispectrum on measurements of the CMB lensing power spectrum and found that it leads to a new, so far neglected, bias [2].

3 Measurements of the CMB Lensing Potential and its Statistics

The commonly applied estimator of the lensing potential is quadratic in the observed lensed CMB field [3,4]

$$\hat{\phi}(\mathbf{L}) = A_L \int_{\mathbf{l}} g(\mathbf{l},\mathbf{L}) \tilde{T}_{\rm expt}(\mathbf{l}) \tilde{T}_{\rm expt}(\mathbf{L}-\mathbf{l}), \tag{3}$$

where $\tilde{T}_{\rm expt}$ denote noisy, beam-deconvolved, lensed temperature fluctuations. A_L is a normalization chosen such that the estimator is unbiased and the weight g is determined such that it minimizes the estimator's variance.

From Eq. 3 one can obtain an estimator of the lensing potential power spectrum

$$\langle \hat{\phi}(\mathbf{L}) \hat{\phi}(-\mathbf{L}) \rangle = A_L^2 \int_{\mathbf{l}_1} \int_{\mathbf{l}_2} g(\mathbf{l}_1,\mathbf{L})\, g(\mathbf{l}_2,\mathbf{L})\, \langle\, \tilde{T}_{\rm expt}(\mathbf{l}_1)\, \tilde{T}_{\rm expt}(\mathbf{L}-\mathbf{l}_1)\, \tilde{T}_{\rm expt}(-\mathbf{l}_2)\, \tilde{T}_{\rm expt}(\mathbf{l}_2-\mathbf{L})\, \rangle, \tag{4}$$

which depends on the lensed temperature four-point function [a]. Unlike the estimator for the lensing potential itself, the estimator of its power spectrum $C^{\hat{\phi}\hat{\phi}}(L) = 2\pi\delta(\mathbf{L}+\mathbf{L}')\langle\hat{\phi}(\mathbf{L})\hat{\phi}(\mathbf{L}')\rangle$ is biased

$$\langle C_L^{\hat{\phi}\hat{\phi}} \rangle = N_L^{(0)} + C_L^{\phi\phi} + N_L^{(1)} + \mathcal{O}[(C^{\phi\phi})^3]. \qquad \text{(Gaussian } \phi\text{)}. \tag{5}$$

The bias terms, denoted by N and labeled with superscripts corresponding to their order in $C^{\phi\phi}$, have been studied in the literature [6,7], can be estimated and are subtracted from CMB lensing measurements.

4 Bias to CMB Lensing Measurements from the Lensing Potential Bispectrum

The presence of a nonzero bispectrum of the lensing potential changes the lensed temperature four-point function in Eq. 4. In the perturbative picture of Eq. 2 one finds four different contributions to the lensed CMB four-point correlator at order $\mathcal{O}(\phi^3)$

$$\begin{aligned} &\text{Type (A)}: \quad \langle \delta T \delta T\, \delta T' T' \rangle \qquad \text{Type (B)}: \quad \langle \delta^2 T \delta T\, T' T' \rangle \\ &\text{Type (C)}: \quad \langle \delta^2 T T\, \delta T' T' \rangle \qquad \text{Type (D)}: \quad \langle \delta^3 T T\, T' T' \rangle, \end{aligned} \tag{6}$$

where we have labeled the last two temperature fields with primes to indicate that they belong to the second reconstruction field $\hat{\phi}(-\mathbf{L})$ in Eq. 4. These four couplings contribute to the estimator of the lensing potential power spectrum. Their sum is a new bias of order $\mathcal{O}[(C_L^{\phi\phi})^{(3/2)}]$, which we denote $N_L^{(3/2)}$. To evaluate their individual contribution to Eq. 4 we treat the unlensed temperature fluctuations as a Gaussian random field and neglect any correlation between ϕ and T. By applying Wick's theorem each correlator in Eq. 6 separates into three subterms, one for every coupling of unlensed CMB fields. For the bias contribution of type A,

$$\text{Type (A)} \sim \langle \overbrace{T_{,i}\underbrace{\phi_{,i} T_{,j}}\phi_{,j}\, \overbrace{T'_{,k}\underbrace{\phi'_{,k} T'}}} \rangle_{A1} \;+\; \langle \overbrace{T_{,i}\underbrace{\phi_{,i} \overbrace{T_{,j}\underbrace{\phi_{,j}\, T'_{,k}}}\phi'_{,k}}T'} \rangle_{A2} \;+\; \langle \overbrace{T_{,i}\underbrace{\phi_{,i} T_{,j}}\underbrace{\phi_{,j}\, T'_{,k}}\phi'_{,k} T'} \rangle_{A3}, \tag{7}$$

and similarly for the remaining types B, C and D, so that the total bias becomes

$$N_{\rm tot}^{(3/2)} = \sum_{i=1}^{3} \left(N_{A_i}^{(3/2)} + N_{B_i}^{(3/2)} + N_{C_i}^{(3/2)} + N_{D_i}^{(3/2)} \right). \tag{8}$$

[a] The expectation value is taken over the joint PDF of CMB lensing potential and unlensed CMB.

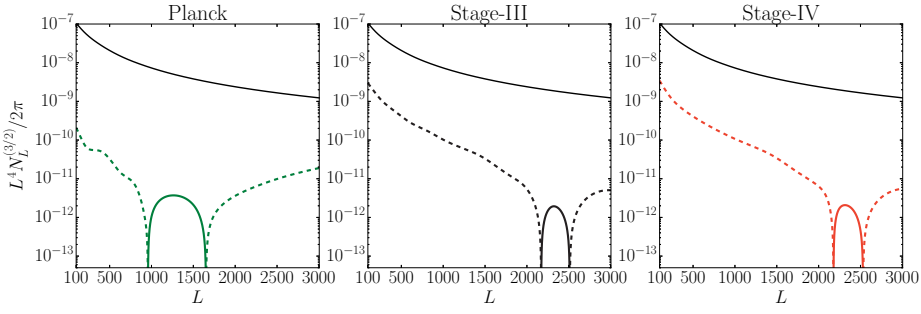


Figure 1 – Bias to a measurement of the CMB lensing power spectrum sourced by a nonzero bispectrum of the lensing potential. The bias plotted here (in color) is the sum of only two contributions to the total bias at $\mathcal{O}(\phi^3)$. We plot a fiducial CMB lensing power spectrum (black line) for comparison. Dashed lines indicate negative signs.

Each of the contributions can be written as a more or less tightly coupled 6D integral over lensing weights g, unlensed temperature power spectra C_l^{TT} and the lensing bispectrum B_ϕ. From closer inspection of the terms we find that all terms of type D as well as one term of type B vanish. One type C term captures contributions from the bispectrum to the lensed temperature power spectrum. It adds to the $N^{(0)}$ bias. Two terms of type A are tightly coupled, which suggests that they are subdominant compared to other, less coupled, contributions. One type C term (type C1) is completely separable, i.e. it can be written as a product of three 2D integrals. This facilitates its numerical evaluation and indicates that it should to be among the largest contributions to $N^{(3/2)}$. The remaining type A contribution (type A1) has a similar structure as type C1 but is of opposite sign. Type A1 is not completely separable, but can be written as a product of a 2D integral times a 4D integral. We restrict numerical evaluation to these two terms and defer a quantification of the remaining (not separable) terms of type B to future work. We also only consider temperature-based measurements but note that the bias can be generalized to CMB lensing measurement from arbitrary combinations of polarization and temperature fields.

5 Numerical Evaluation of Type A1 and Type C1 Contributions to $N^{(3/2)}$

For the numerical evaluation of the two bias terms, we use cosmological parameters from Planck 2013 results [8]. Power spectra are computed with the publicly available CLASS [9] code. The analytic expressions for the bias involve integrals over the bispectrum of large-scale matter fluctuations. We adopt an analytic model for B_δ derived from standard Eulerian perturbation theory (SPT) without loop-corrections in a slightly modified form [b].

Results for the sum of the two bias terms of type A1 and C1 for different experiments are shown in Fig. 1. We consider different experimental setups roughly corresponding to Planck ($\theta_{\rm FWHM}$=7.0 arcmin, σ_N^{TT}=30.0μK arcmin, $f_{\rm sky}$=0.63), CMB Stage-III ($\theta_{\rm FWHM}$=1.4 arcmin, σ_N^{TT}=6.0μK arcmin, $f_{\rm sky}$=0.4) and CMB Stage-IV ($\theta_{\rm FWHM}$=1.0 arcmin, σ_N^{TT}=1.0μK arcmin, $f_{\rm sky}$=0.5) experiments.

For the high resolution Stage-III and Stage-IV experiments the bias is 0.5-3.0% of the signal, slowly decreasing towards smaller scales (see Fig. 2, left panel). The sign of the bias is negative on all relevant scales, i.e. it reduces the measured lensing power. For Planck, the A1 and C1 terms partially cancel each other and the resulting bias is nearly an order of magnitude smaller than for CMB Stage-III and Stage-IV experiments. In the right panel of Fig. 2 we plot the bias over the lensing power spectrum error. We find that the sum of terms A1 and C1 is negligible for

[b] Replacing the linear matter power spectrum in the SPT expression for B_δ by a power spectrum with nonlinear corrections extends the range of validity of this bispectrum model to slightly smaller scales.

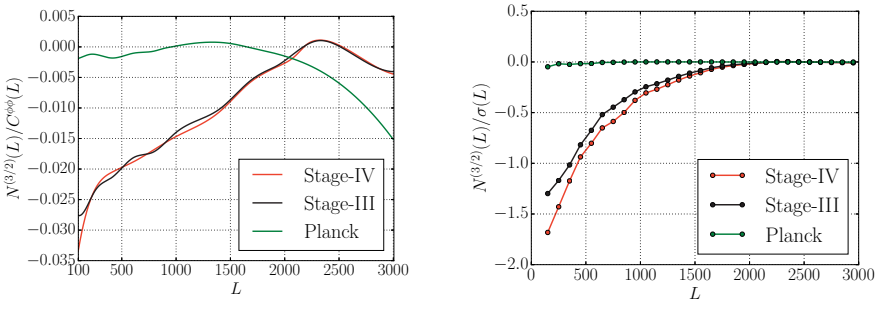


Figure 2 – Left Panel: CMB lensing bias $N^{(3/2)}$ (from two out of several contributing terms) over the signal power spectrum $C_L^{\phi\phi}$. Right Panel: The bias-to-noise ratio $N^{(3/2)}(L)/\sigma(L)$ if the measured lensing power spectrum is binned with bin width $\Delta L = 100$.

Planck but can shift lensing measurements with Stage-III and Stage-IV experiments by multiple standard deviations. More details about the $N^{(3/2)}$ lensing bias can be found in Reference [2].

6 Conclusions and Outlook

We have identified a new bias term to measurements of the CMB lensing potential power spectrum. This bias, denoted $N^{(3/2)}$, arises as a consequence of a nonzero bispectrum of the CMB lensing potential. We have derived analytic expressions of all terms that contribute to the standard estimator for the CMB lensing power spectrum at order $\mathcal{O}(\phi^3)$, but restricted the numerical evaluation to two terms, which are likely among the largest contributions to $N^{(3/2)}$. The magnitude of the bias depends on the experiment under consideration. For Planck it seems negligible. For CMB Stage-III and Stage-IV it is a significant effect, which can change CMB measurements at the percent level. We conclude that this bias needs to be accounted for in future CMB lensing analyses, but caution that the exact magnitude of the bias could be affected by neglected contributions or approximations made in its evaluation. An exact quantification of the $N^{(3/2)}$ bias will require further investigations.

Acknowledgments

We thank Anthony Challinor, Colin Hill, Antony Lewis and Uroš Seljak for numerous crucial discussions. We also thank Jia Liu, Björn M. Schäfer, Alex van Engelen, Martin White and Oliver Zahn for useful comments. VB thanks the organizers of Moriond for the opportunity to present this work.

References

1. T. Namikawa, ArXiv e-prints **1604.08578**, (2016).
2. V. Böhm, M. Schmittfull and B. D.Sherwin, ArXiv e-prints **1605.01392**, (2016).
3. M. Zaldarriaga and U. Seljak, Phys. Rev. D **59**, 123507 (1999), astro-ph/9810257.
4. W. Hu, APJL **557**, L79-L83 (2001), astro-ph/0105424.
5. T. Okamoto and W. Hu, Phys. Rev. D **67**, 083002 (2003), astro-ph/0301031.
6. M. Kesden, A. Cooray and M. Kamionkowski, Phys. Rev. D **67**, 123507 (2003).
7. D, Hanson, A. Challinor, G. Efstathiou and P. Bielewicz, Phys. Rev. D **83**, 043005 (2011).
8. Planck Collaboration, A&A **571**, A16 (2014).
9. D. Blas, J. Lesgourgues and T. Tram, JCAP **7**, 34 (2011), *http://class-code.net/*.

BEAM SYSTEMATICS IN CMB POLARISATION MEASUREMENTS

R. BANERJI
Laboratoire APC, Université Paris Diderot,
Bâtiment Condorcet, 75205 Paris Cedex 13, France

We have developed a new simulation tool for fast real space convolution of a CMB sky with beams of any shape at the timestream level. We use this code to simulate the leakage of signal from Temperature to Polarisation due to beam systematics, especially the case of asymmetric beams. We then attempt at estimating the leaked signal and subtracting it from the observed map to correct for them. The results are promising and motivate considering a next generation CMB space mission with polarisation modulation without a rotating half-wave plate.

1 Motivation

CMB science has come a long way and matured in the last couple of decades owing to the success of many sub-orbital and space missions, especially the recent Planck mission which has been successful in estimating the main cosmological parameters to high precision [1]. The Planck mission has produced exquisite temperature maps over 9 frequency bands and created a legacy for both cosmological and astrophysical research, however, it not optimised for polarisation.

The most promising theory regarding the origin of the universe, as of now, is cosmic inflation. To understand its mechanism it is essential to detect primordial B-modes and get an estimate of the tensor to scalar ratio r. Current efforts have provided an upper bound [2] to the value of r and future missions demand a sensitivity for r of about $\delta r \sim 0.001$ or better. It is thus essential to ensure that systematic effects do not degrade performance, and we optimise the future mission and build analysis techniques to minimise and mitigate such systematics. We present here a study of beam asymmetries in CMB polarisation measurements and how we mitigate the effect.

2 Convolving in the Real Space and Map Making

We developed a simulation package that allows us to simulate the scanning for a future space mission to be submitted to ESA, and provides a fast method of pixel space convolution of the signal by a beam of any shape.

To perform a fast pixel space convolution, we generate a pixelized map of the required normalised beam at a pixel resolution matching our co-scan sampling. This restriction on the resolution frees us from generating redundant data points along the co-scan direction. For a beam map of size $N \times N$ we proceed to generate N independent timestreams for each row of the beam map and convolve them in Fourier space with the corresponding row of the beam map. The final beam-convolved timestream is thus the sum of all the individual N timestreams. This method thus scales as $\sim N$ for a beam map of size $N \times N$.

Our data model is thus simply given by :

$$d_t = A_{tp} S_p + n_t \tag{1}$$

For reconstructing the sky maps we use a maximum likelihood map-maker with a PCG solver (in anticipation of future work involving non-diagonal co-variance matrices) and use a MPI distribution model [3] to solve for S in the following set of linear equations :

$$(A^T N^{-1} A)S = A^T N^{-1} d \tag{2}$$

3 Estimating the Leakage and Results

We have studied several cases of asymmetric beams with our simulation tools. We discuss one such case, where we use four elliptical Gaussian beams of 8' FWHM at the minor-axis, of 5% differential ellipticity, and with the major-axis aligned at 45^0 from the polarisation direction of the bolometer. In this configuration the dominant leakage is to CMB B modes. The four bolometers themselves are in an optimal configuration, at 45^0 from each other, all pointing to the same point in the sky, and this leads to each pixel-pixel covariance matrix to be diagonal.

We employ an iterative technique in estimating the leakage due to beam asymmetry. We deconvolve the reconstructed temperature map and re-observe it with the same scanning and beams to subtract an estimate of the beam-shape induced temperature to polarisation leakage. This method thus assumes knowledge of the scanning and the beam profile.

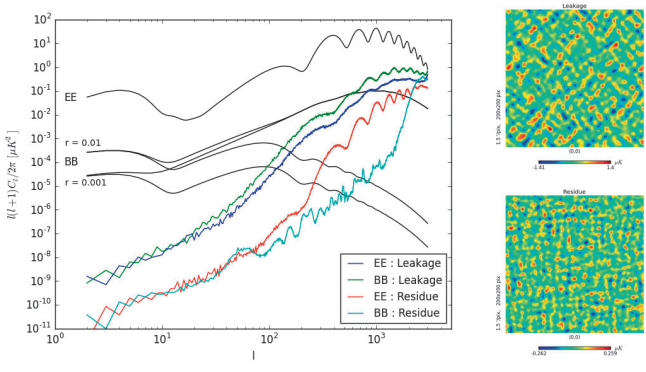


Figure 1 – (Left)Leakage and the residual after subtracting the estimated leakage simulated by the real space convolution, for an 8' beam at 5% differential ellipticity, by a beam map of extent 4 FWHMs and from an input map of nside=4096. (Right)Q maps of the simulated leakage and the residual after subtracting the leakage. This simulation was for half sky coverage over 1 precession period.

With out method we have been able to reduce the leakage due to beam asymmetry by an order of magnitude. The same study for 30' and 4' beams also shows promising results.

Acknowledgments

RB acknowledges CNRS/IN2P3 and CNES for funding his doctoral studies, NERSC for providing their computational facilities used in this work, Pierre Chanial for his help during the initial phases of coding and Jacques Delabrouille for his tireless supervision throughout.

References

1. *Planck 2015 results. XIII. Cosmological parameters*, arXiv:1502.01589
2. *A Joint Analysis of BICEP2/Keck Array and Planck Data*, PRL **114**, 101301 (2015)
3. Chanial and Barbey in *Operators and solvers for high-performance computing*, SF2A 2012

2.
Dark Energy

BAO Correlations at $z = 2.3$ with SDSS DR12 Lyman-alpha forests

Julian E. Bautista
Department of Physics and Astronomy, University of Utah,
115 S 1400 E, Salt Lake City, UT 84112, USA

1 Introduction

Sound waves propagating in the baryon-photon fluid prior to recombination created spherical overdense shells around primordial overdensities. These shells show up as a single peak in the two-point correlation function at a comoving separations $r_d \sim 150$ Mpc, or, equivalently in Fourier space, as oscillation in the matter power-spectrum. This particular separation, known as sound horizon or baryon acoustic oscillations (BAO) scale, has been used as a cosmological statistical standard ruler [1], since its size increases, after recombination, mainly under the effect of the expansion of the Universe.

Observed in the cosmic microwave background (CMB) [2] at redshift $z \sim 1100$, the BAO scale was also measured at percent level precision in galaxy two-point functions at $z < 1.0$ (cite many galaxy BAO papers). Combined, high and lower redshift measurements provide the best constraints on dark energy and curvature, complementary to supernovae Hubble diagram[3].

In the last five years, the Baryon Oscillation Spectroscopic Survey (BOSS [4]) opened a new window for BAO measurements at intermediate redshifts using the two-point correlation function of the flux in the Lyα forest. Using the Sloan Digital Sky Survey 2.5-meter telescope, BOSS observed spectra of more than 190 000 quasars at $z > 2$ and obtained an unique 2.5% measurement of BAO at $z = 2.3$ [5,6].

The paper is organized as follows. In section 2, the main steps of the BAO Lyα analysis are presented. Then, I summarize the previous measurement of BAO using Data Release 11[7] (section 3) and I introduce the main improvements on the data analysis that is currently in progress on the full BOSS data-sample (section 4).

2 Basis of Lyα forest clustering

The Lyα forest is the region of the rest-frame quasar spectrum showing numerous absorption lines due to absorption of quasar light by low density neutral hydrogen in intergalactic medium (IGM), over the quasar line-of-sight.

The fraction F of quasar flux, at a given observed frame wavelength λ, that reaches the telescope depends on the amount of neutral hydrogen at $z = \lambda/\lambda_{Ly\alpha} - 1$. Therefore, fluctuations in the transmitted flux fraction around the mean, defined as $\delta_F = F/\bar{F} - 1$, are tracers of fluctuations of the underlying dark matter field. In other words, denser regions yield more absorption, or less transmission F. Several cosmological hydrodynamical simulations[8,9] have

shown that on sufficiently large scales (above tens of Mpc comoving) the two-point function of δ_F is *linearly* related to the matter two-point function[a].

Past and current analysis of the three-dimensional clustering of the Lyα forest share some common steps:

- Obtaining correct quasar redshifts: visual inspection[10] of all quasar targets provided z estimates and flagged features such as Broad Absorption Systems (BALs) and Damped Lyα systems (DLAs);
- Estimating flux fluctuations over the forests: two automated methods were developed and give consistent BAO results. The main idea is to fit a fixed shape in rest-frame over all forests, tilting them with a linear function to take into account flux calibration errors. The first method assumes Gaussianity of the F field, while the second actually estimates the unabsorbed flux level.
- Estimating the two point function of fluctuations: we compute the flux auto-correlation function, but also use quasars as tracers by computing the quasar-flux cross-correlation. The covariance matrix of our measurements are estimated both using sub-samples of the data or explicitly computing the 4-point functions. Both methods are consistent with each other.
- Fitting for the BAO scale: we use the `baofit`[b] package[11] to find the best-fit two-point function models, scaling the radial and angular BAO peak position by two parameters,

$$\alpha_{\parallel} = \frac{D_H(\bar{z})/r_d}{[D_H(\bar{z})/r_d]_{\rm fid}} \qquad \text{and} \qquad \alpha_{\perp} = \frac{D_A(\bar{z})/r_d}{[D_A(\bar{z})/r_d]_{\rm fid}}, \tag{1}$$

  where D_H and D_A are respectively Hubble and angular diameter distances at effective redshift $\bar{z} \sim 2.3$, r_d is the comoving size of the sound horizon and the subscript "fid" denotes the value at the assumed fiducial cosmology (used to translate redshifts into comoving separations). Nuisance parameters are added to the models to capture any broadband distortions of the correlation function.

Mock catalogs were an essential tool in order to access biases eventually introduced by our analysis procedure, and to test and quantify other sources of systematics. One hundred realizations of DR11 were generated, simulating a realistic correlation function and including instrumental noise and flux calibration errors[12].

3 Current status of Lyα forest BAO measurements

The latest measurements of BAO correlations in the Lyα forest auto-correlation [5] and quasar-Lyα cross-correlation [6] using DR11 data yield the constraints shown in Figure 1. The best-fit values are:

$$\text{Auto}: \qquad D_H(2.3)/r_d = 9.18 \pm 0.28 \qquad D_A(2.3)/r_d = 11.28 \pm 0.65 \tag{2}$$

$$\text{Cross}: \qquad D_H(2.3)/r_d = 9.07 \pm 0.30 \qquad D_A(2.3)/r_d = 10.78 \pm 0.42 \tag{3}$$

If we assume that auto and cross-correlation are independent, these results give a 2.5σ tension with Planck 2013 + WP + SPT + ACT predictions. This tension was reduced to 2.4σ using Planck 2015[2] "TT+lowP+lensing" flat model.

Systematic contributions to errors were computed in these analyses but no evident source of contamination was found at this precision level. Those tests include:

[a] There are assumption in the simulations, such as constant ionizing background, but current observations are not sensitive yet to these second-order effects

[b] `http://darkmatter.ps.uci.edu/baofit`

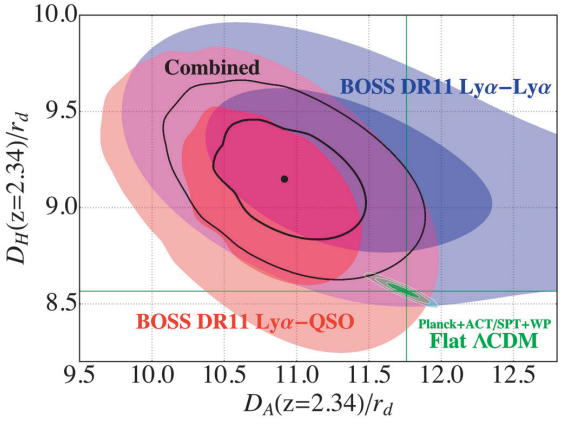


Figure 1 – Constraints on angular and radial BAO, $(D_A/r_d, D_H/r_d)$. Contours show 68.3% ($\Delta\chi^2 = 2.3$) and 95.5% ($\Delta\chi^2 = 6.2$) contours from the auto-correlation (blue), the quasar-Lyα forest cross-correlation (red), and the combined constraints assuming no correlation (black). The green contours are CMB constraints calculated using the Planck+WP+SPT+ACT chains assuming a flat ΛCDM cosmology.

- Varying the functional form of the broadband model, increasing the number of free parameters.
- Simulating the presence of metals in the forests using mock catalogs based on stacked forests[13]. In particular the Si II(1260)-Lyα cross-correlation creates a bump at $r_\parallel \sim 110$ Mpc/h and $r_\perp = 0$ that could bias the BAO measurement. Using 10 mocks, we found no evidence for shifts caused by this metal transition. In section 4, we describe an improvement to this test.
- Computing the contribution of flux calibration residuals that created bumps in flux at observer-frame wavelengths corresponding to Balmer transitions. One pair of these transitions fall over the BAO peak when translated into comoving separations at $z = 2.3$. We found that this signal is negligible compared to the total signal.

4 Towards the final analysis of BOSS DR12 Lyα forest sample

The final BOSS sample, released as part of DR12, contains 15% more quasars than DR11. In terms of pairs of forest pixels, it corresponds to a 18% gain in statistical power. As it is still work in progress, I do not present any cosmological preliminary results in this paper. Instead, I overview the main improvements in the analysis and in the quantification of systematic errors. The bottom line is that no systematic error was found to be significant at this statistical precision level.

Improved spectral reconstruction When extracting 1D spectra from 2D CCD images, the DR12 optimal extraction algorithm would create a bias in the flux counts due to weighting schemes that use the data itself. We re-reduced the data changing the weighting scheme, while correctly propagating errors. This procedure reduced significantly the contamination of sky residuals in quasar spectra.

Spectral throughput corrections To optimize the throughput in the Lyα forest region of spectra ($\lambda \sim 4000$ Å), quasar optical fibers where placed differently in the focal plane than the

standard stars used to calibrate flux. Therefore, the DR12 quasar flux calibration is not correct. Corrections based on these focal plane shifts were computed[14] and applied all quasar spectra[c].

Marginalization over metal correlations in the BAO fitting Using different models of metal contamination in mock spectra, we studied in more detail the impact of the cross-correlation Lyα-metal on the inference of BAO. As mentioned in section 3, the Si II(1260)-Lyα cross-correlation creates a worrying excess of correlation over the BAO peak. In this new analysis, we marginalize over the amplitude of the metal-Lyα and metal-metal cross-correlations in the flux correlation function.

We test this marginalization using noise-free mocks with strong metal absorption (stronger than seen in data). We see a 2% bias in $\alpha_{\parallel}$ and $\alpha_{\perp}$ on these mocks because of metal contamination. When using templates to marginalize over these cross-correlations, the bias on α is successfully corrected on mocks.

Improved modeling of continuum fitting distortions Our methods to compute flux fluctuations use information on the forest itselt, suppressing power on scales comparable to the size of the forest. This power suppression is referred to as distortion by continuum fitting. These distortions are marginalized over in previous analyses through the use of smooth functions of separation and angle with respect to the line of sight while fitting for BAO. The new analysis attempt to model this power suppression differently by transforming the fluctuation field such that the distorted correlation function can be computed theoretically using the distribution of pixels.

Null tests We tested any source of non-physical correlations by building sets of fake forests, cross-correlating them with true forests. Fake forests were built using the quasar flux redwards of the Lyα emission line (where no hydrogen absorption is expected) or galaxy spectral residuals (galaxy spectra with its best-fit model subtracted). A significant non-zero signal is found when cross-correlating pairs of spectra in the same observing plate and same spectrograph. For pairs in different observing plates/spectrographs the correlation is compatible with zero. This non-zero signal is well modeled by correlations induced by noise in the sky modeling and flux calibration, i.e., by the data reduction process itself. While these undesired correlations distort the measured correlation function, these signals do not bias the inference of the BAO peak position, at this precision level.

Other sources of contamination, such as light cross-talk among neighboring optical fibers or interstellar medium absorption, show no impact on the derived cosmological parameters.

5 Conclusion

In this paper, I summarized the current status of the measurement of baryon acoustic oscillations using the complete sample of Lyα forests from BOSS.

Using DR11 data, the combined measurement of BAO using the flux-flux correlation function and the quasar-flux cross-correlation yields a 2.5% precision inference of the Hubble expansion rate at $z = 2.3$. The 2.5σ tension with the CMB predictions inspired careful studies of systematics on the Lyα BAO results.

The currently in-progress analysis of the full BOSS sample, released in DR12, shows confident quantification of many sources of spurious correlations that could in principle bias the BAO measurement. The uncertain amount of contamination by metal-Lyαcross-correlations is now marginalized over when BAO fitting, making the estimates of cosmological parameters more robust. The final results are expected to be published in some months from now.

[c]These corrections are publicly available at `http://darkmatter.ps.uci.edu/tpcorr/`

Acknowledgments

I would like to thank the organizers for the invitation for this wonderful and enriching conference.

References

1. David H. Weinberg, Michael J. Mortonson, Daniel J. Eisenstein, et al. Observational Probes of Cosmic Acceleration. *arXiv:1201.2434*, January 2012.
2. Planck Collaboration. Planck 2015 results. XIII. Cosmological parameters. *arXiv:1502.01589 [astro-ph]*, February 2015. arXiv: 1502.01589.
3. M. Betoule, R. Kessler, J. Guy, et al. Improved cosmological constraints from a joint analysis of the SDSS-II and SNLS supernova samples. *Astronomy and Astrophysics*, 568:22, August 2014.
4. Kyle S. Dawson, David J. Schlegel, Christopher P. Ahn, et al. The Baryon Oscillation Spectroscopic Survey of SDSS-III. *The Astronomical Journal*, 145:10, January 2013.
5. Timothée Delubac, Julian E. Bautista, Nicolás G. Busca, et al. Baryon acoustic oscillations in the Ly-alpha forest of BOSS DR11 quasars. *Astronomy and Astrophysics*, 574:A59, February 2015.
6. Andreu Font-Ribera, David Kirkby, Nicolas Busca, et al. Quasar-Lyman alpha forest cross-correlation from BOSS DR11: Baryon Acoustic Oscillations. *Journal of Cosmology and Astro-Particle Physics*, 05:027, May 2014.
7. Shadab Alam, Franco D. Albareti, Carlos Allende Prieto, et al. The Eleventh and Twelfth Data Releases of the Sloan Digital Sky Survey: Final Data from SDSS-III. *arXiv:1501.00963 [astro-ph]*, January 2015. arXiv: 1501.00963.
8. Jordi Miralda-Escudé, Renyue Cen, Jeremiah P. Ostriker, and Michael Rauch. The Ly alpha Forest from Gravitational Collapse in the Cold Dark Matter + Lambda Model. *The Astrophysical Journal*, 471:582, November 1996.
9. Patrick McDonald. Toward a Measurement of the Cosmological Geometry at z ˜ 2: Predicting Ly-alpha Forest Correlation in Three Dimensions and the Potential of Future Data Sets. *The Astrophysical Journal*, 585:34–51, March 2003.
10. Isabelle Pâris, Patrick Petitjean, Éric Aubourg, et al. The Sloan Digital Sky Survey quasar catalog: tenth data release. *Astronomy and Astrophysics*, 563:A54, March 2014.
11. David Kirkby, Daniel Margala, Anže Slosar, et al. Fitting methods for baryon acoustic oscillations in the Lyman-alpha forest fluctuations in BOSS data release 9. *Journal of Cosmology and Astro-Particle Physics*, 03:024, March 2013.
12. Julian E. Bautista, Stephen Bailey, Andreu Font-Ribera, et al. Mock Quasar-Lyman-alpha forest data-sets for the SDSS-III Baryon Oscillation Spectroscopic Survey. *Journal of Cosmology and Astro-Particle Physics*, 05:060, May 2015.
13. Matthew M. Pieri, Michael J. Mortonson, Stephan Frank, et al. Probing the circumgalactic medium at high-redshift using composite BOSS spectra of strong Lyman alpha forest absorbers. *Monthly Notices of the Royal Astronomical Society*, 441:1718–1740, June 2014.
14. Daniel Margala, David Kirkby, Kyle Dawson, et al. Improved Spectrophotometric Calibration of the SDSS-III BOSS Quasar Sample. *arXiv:1506.04790 [astro-ph]*, June 2015. arXiv: 1506.04790.






QUASAR-LYMAN α FOREST CROSS-CORRELATION FROM SDSS-III BOSS SURVEY: BARYON ACOUSTIC OSCILLATIONS

Hélion du MAS des BOURBOUX
CEA-Saclay, Irfu F-91191 Gif-sur-Yvette, France



We measure the large-scale cross-correlation of quasars with the Lyman-α forest absorption field. We use over 170,000 forests from Data Release 12 (DR12) of the SDSS-III BOSS survey and over 240,000 quasars from DR12 and from DR7 of the SDSS-II survey. This study allows us to measure the Baryonic Acoustic Oscillation (BAO) scale, along and across the line-of-sight, at a mean redshift of z = 2.40. These scales are linked to the Hubble parameter and the angular diameter distance, respectively. We produced a set of 100 Gaussian random field simulations. The covariance of the set is found to agree with the covariance matrix calculated from the data. These simulations will be used in the future to search for a possible bias in the measurement of the BAO scale.

1 Introduction

During the last decade the Baryonic Acoustic Oscillation (BAO) scale has proved itself a very powerful measure of the expansion of the Universe related to the dark matter and dark energy redshift evolution. The Lyman-α auto-correlation [1] and Lyman-α-quasar cross-correlation [2] measure the BAO parameters: $\alpha_{\parallel} = D_H(z)/r_d(z_d)$ and $\alpha_{\perp} = D_A(z)/r_d(z_d)$ at a mean redshift of $z = 2.40$, with r_d the sound horizon.

The Lyman-α (Lyα) forest is the pattern seen in a quasar spectrum between the Lyβ emission line ($\lambda_{R.F.} = 1025.72$ Å) and the Lyα emission line ($\lambda_{R.F.} = 1215.67$ Å). This absorption is mainly induced by the presence of neutral hydrogen in the intergalactic medium. A small fraction of the absorption is also linked to the presence of metals: mainly carbon, magnesium, silicon and iron. A Lyα density fluctuation δ_α is related to a dark matter density fluctuation δ_{DM} by the bias parameter b_α:

$$\delta_\alpha = b_\alpha \cdot \delta_{DM}. \tag{1}$$

In a similar way, quasars (QSO) traces matter fluctuations with a bias b_{QSO}. The matter clustering can then be estimated with the cross-correlation between Lyα forest pixels and quasars:

$$\xi^{qf}(\vec{r}) = < \delta_\alpha(\vec{x}) \cdot \delta_q(\vec{x} + \vec{r}) > . \tag{2}$$

A measurement of this function was done by Font-Ribera et al.[2] using the Data Release 11 (DR11) of the SDSS-III Baryon Oscillation Spectroscopic Survey (BOSS). The study measured $\alpha_{\parallel} = 1.042 \pm 0.034$ and $\alpha_{\perp} = 0.930 \pm 0.036$.
The improvements of this new study are: an increase of statistics with the final quasar catalogue DR12 of BOSS, improvements in the data reduction, and the development of Gaussian random field simulations. These simulations will allow us to validate the measured parameters.

2 BOSS quasar sample and data reduction

The BOSS observations ran from 2009 to 2014 and covered 10^4 deg^2 on the sky. We use over 170,000 forests from DR12 of the SDSS-III BOSS survey and over 240,000 quasars from DR12 and from DR7 of the SDSS-II survey. The Lyα forest is defined for rest frame wavelength $\lambda_{R.F.} \in [1040, 1200]$ Å and for observed wavelength $\lambda_{Obs.} \in [3600, 7235]$ Å. Assuming Lyα to be the main absorber, we cover the redshift range $z \in [1.96, 4.95]$.

A Lyα absorption fluctuation is defined by:

$$\delta_{\alpha}^{l,i} = \frac{f^{l,i}}{\overline{F}(\lambda_{Obs.}^{l,i}) \cdot \overline{C}(\lambda_{R.F.}^{l,i}) \cdot (a^l + b^l \lambda_{R.F.}^{l,i})} - 1, \tag{3}$$

where l is for a given quasar forest and i is for a pixel of this forest, $f^{l,i}$ is the observed flux. $\overline{C}$ is the unabsorbed quasar continuum. It is allowed to vary linearly from forest to forest, with parameters a^l and b^l. Finally, $\overline{F}$ is the mean transmitted flux fraction, giving the evolution of neutral hydrogen density. For the data, Figure 1 shows, in blue, the quasar continuum on the left panel and the mean transmitted flux fraction on the right panel.

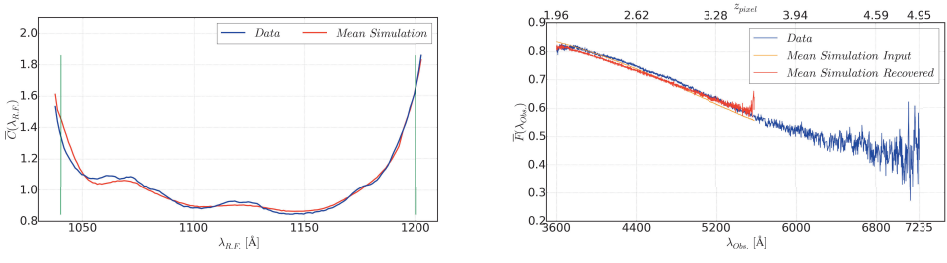


Figure 1 – Left pannel: unabsorbed quasar continuum for data in blue and for simulations in red in the rest frame wavelength range of the Lyα forest. Right pannel: mean transmitted flux fraction for data in blue, for simulations in red and for simulation input in orange.

The quasar catalogue provides us with a boolean information of the matter density field. The Lyα-quasar cross-correlation is then defined by:

$$\xi^{qf}(\vec{s}) = \frac{\sum\limits_{(i,k)\ at\ \vec{s}} w_{\alpha}^{i}\, \delta_{\alpha}^{i}}{\sum\limits_{(i,k)\ at\ \vec{s}} w_{\alpha}^{i}}, \tag{4}$$

where i is a forest pixel, w_{α}^{i} is the pixel weight, k is a quasar and $\vec{s}$ is the comoving redshift space vector between the pixel and the quasar.

Figure 2 shows, in blue, the Lyα-QSO cross-correlation for data as a function of the comoving redshift space separation. The cross-correlation is rescaled by a factor $|s|^2$ in order to see the BAO scale. This scale appears as a dip in the correlation function around $r_s \approx 105$ h^{-1}Mpc. When a Lyα pixel is close to a QSO, it sits in a higher density region and thus absorbs more flux. This explains why the correlation function is negative at small scales. Data error bars are

calculated using 80 sub-samples. In this method, the data set is separated in 80 regions acording to the forests position on the sky. The cross-correlation is calculated in each sub-divisions of the sky. The errors are then given by the covariance of the set.

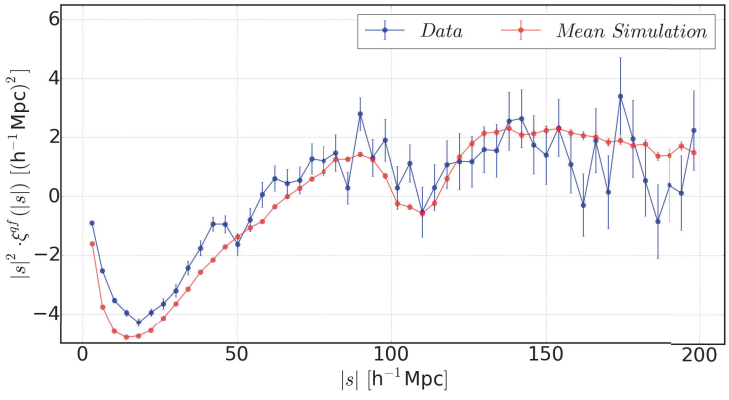


Figure 2 – Lyα-quasar cross-correlation monopole as a function of comoving redshift space coordinate. The monopole is multiplied by a factor $|s|^2$. In blue the data with sub-sampling errors. In red the mean over the 100 simulations with errors given by the variance of the set.

3 Simulation and data comparison

3.1 Description

We have developed simulations of the cross-correlation measurement. They allow us to test our covariance matrix estimation, to look for possible biases in our data extraction process. These simulations have been performed following J.-M. Le Goff et al. [3]. We use the fiducial cosmology of a flat ΛCDM Universe ($h = 0.7$, $\Omega_b h^2 = 0.0227$, $\Omega_c h^2 = 0.1096$, $\sigma_8 = 0.794961$). The linear matter power spectrum is calculated with CAMB. A Gaussian random field is generated over a comoving volume of 11 Gpc^3 with this power spectrum. Pixels have a comoving size $a_{LR} = 3.15$ h^{-1}Mpc. The box center has a redshift of $z = 2.50$.

Quasars are defined to sit in pixels where overdensities are greater than δ_{cut}. In order to have a similar bias as the data, we set this threshold using Padmanabhan and White [4] to get $b_{QSO} = 3.6$ at $z = 2.50$. A random selection of these pixels are rejected in order to reproduce the redshift distribution of quasars in data and their number density. The QSO position is randomly selected within the volume of the pixel. Their redshift is shifted according to the line-of-sight velocity of the pixel.

Forests are drawn along the line-of-sight of these quasars. High resolution boxes of comoving edge length $l_{HR} = 3.15$ h^{-1}Mpc and pixels comoving size $a_{HR} = l_{HR}/16 \approx 0.2$ h^{-1}Mpc are placed in the low resolution box pixels. This process allows us to reproduce the level of noise in the data along with the 1D forest correlation $\xi^{1D,ff}$: the correlation between pixels along the line-of-sight of a quasar. The density fluctuation and the velocity of a pixel is then translated to a transmission field using the Gunn-Peterson approximation:

$$F = \exp[-a(z) f(v) \exp(\gamma g(z)(\delta_{LR} + \delta_{HR}))], \tag{5}$$

where f is a function of the velocity of neighbouring pixels and g is the linear growth factor. The function a and the parameter γ are set to reproduce the mean transmitted flux fraction and

the bias evolution of data. In the right panel of Figure 1, the orange curve shows the evolution of $\overline{F}$ in the simulation as a function of observed wavelength. We can see that it is very similar to the evolution of $\overline{F}$ in the data, in blue on the same graph.

The mock expander, described in J. E. Bautista et al. [5], transforms the transmission $\overline{F}$ in flux ϕ. It adds the resolution of the SDSS-III BOSS spectrograph, the continuum and magnitude properties of the BOSS quasars and the level of noise of the data.
We also add absorbtions of the relevant metals for the cross-correlation: Si-II (1190 Å), Si-II (1193 Å), Si-II (1260 Å) and Si-III (1207 Å). Parameters of the metal absorbtion field are set in order to reproduce the $\xi^{1D,ff}$ measured in data. These are the only relevant transitions for the cross-correlation. Other transitions only induce noise in our measurement.

As a result, we get a set of 100 full simulations, reproducing the most important properties of the data. These are the first simulations with simultaneously three correlations: forests auto-correlation ξ^{ff}, quasar-forest cross-correlation ξ^{qf} and quasar auto-correlation ξ^{qq}. The 1D correlation $\xi^{1D,ff}$ is also reproduced.

In Figure 2, we show, in red, the stack of the 100 simulated cross-correlation monopoles. The error bars are computed from the variance of the set. The BAO scale is the dip at $r_s \approx 105$ h^{-1}Mpc. The differences between the data and the simulations at small scales ($|s| < 50$ h^{-1}Mpc) are caused by two effects: a small difference of biases between the data and the simulations, and other aspects. This is expected to have no effect on the values of the BAO parameters, because biases have no correlations with them.

In practice we fit the cross-correlation $\xi(\vec{s}) = \xi(s_\perp, s_\parallel)$. In Figure 3 we show the covariance matrix normalized to its diagonal (i.e. the correlation matrix). On both plot, the matrix is estimated using sub-samples on data in blue and using simulations in red. The left plot shows the mean of the correlation matrix for bins with same $s_\perp$. The right plot shows the correlation matrix for bins with $|\Delta s_\perp| = 4$ h^{-1}Mpc. We can see that the matrix is nearly diagonal. Sub-samples and simulations give similar results.

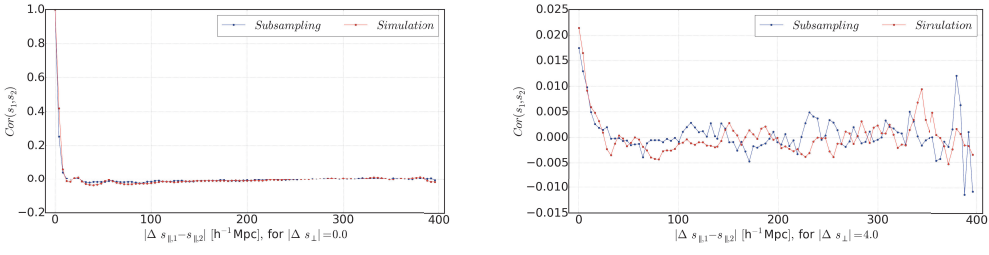


Figure 3 – Correlation matrix of the Lyα-quasar cross-correlation. Left pannel: mean correlation between two bins $\vec{s_1}$ and $\vec{s_2}$ when $|\Delta s_\perp| = 0$ h^{-1}Mpc. Right pannel: mean correlation between two bins when $|\Delta s_\perp| = 4$ h^{-1}Mpc.

References

1. T. Delubac et al. Baryon acoustic oscillations in the Lyα forest of BOSS DR11 quasars. Astronomy and Astrophysics, 574:A59, February 2015.
2. A. Font-Ribera et al. Quasar-Lyman α forest cross-correlation from BOSS DR11: Baryon Acoustic Oscillations. Journal of Cosmology and Astroparticle Physics, 5:027, May 2014.
3. J. M. Le Goff et al. Simulations of BAO reconstruction with a quasar Ly-α survey. Astronomy and Astrophysics, 534:A135, October 2011.
4. N. Padmanabhan and M. White. Calibrating the baryon oscillation ruler for matter and halos. Phys. Rev. *D*, 80(6):063508, September 2009.
5. J. E. Bautista et al. Mock Quasar-Lyman-α forest data-sets for the SDSS-III Baryon Oscillation Spectroscopic Survey. Journal of Cosmology and Astroparticle Physics, 5:060, May 2015.

CONSTRAINING COSMOLOGICAL PARAMETERS USING BOSS DATA: POWER SPECTRUM AND BISPECTRUM

H. GIL-MARÍN

Sorbonne Universités, Institut Lagrange de Paris [a] (ILP), 98 bis Boulevard Arago, 75014 Paris, France
LPNHE, Université Pierre et Marie Curie, 4 Place Jussieu, 75005 Paris, France

We measure and analyse the power spectrum and bispectrum of the data release 12 results of the SDSS-III Baryon Oscillation Spectroscopic Survey, splitting by selection algorithm into LOWZ and CMASS samples. This survey has mapped the spatial distribution of luminous red galaxies and quasars from $z = 0.15$ up to $z = 0.70$, and as today is the largest spectroscopic galaxy survey with an effective volume of $\sim 7.4\,\mathrm{Gpc}^3$. From the redshift space distortion and baryon acoustic oscillation analyses we determine cosmological constrains in the product of the Hubble constant and the co-moving sound horizon at the baryon drag epoch $H(z)r_s(z_d)$, the angular distance parameter divided by the sound horizon $D_A(z)/r_s(z_d)$, and the product of the growth of structure parameter times the amplitude of dark matter density fluctuations, $f\sigma_8(z)$. We measure $f\sigma_8(z_{\rm LOWZ}) = 0.427\pm0.052$, $D_A(z_{\rm LOWZ})/r_s(z_d) = 6.60\pm0.13$, $H(z_{\rm LOWZ})r_s(z_d) = (11.55 \pm 0.38) \cdot 10^3\,\mathrm{kms}^{-1}$ for the LOWZ sample at $z_{\rm LOWZ} = 0.32$; and $f\sigma_8(z_{\rm CMASS}) = 0.426\pm0.023$, $D_A(z_{\rm CMASS})/r_s(z_d) = 9.39\pm0.10$, $H(z_{\rm CMASS})r_s(z_d) = (14.02\pm0.22)\cdot 10^3\,\mathrm{kms}^{-1}$ for the CMASS sample at $z_{\rm CMASS} = 0.57$.

1 Introduction

The large-scale distribution of matter, as observed through galaxy clustering, encodes significant cosmological information. Much of this can be extracted from the shape and amplitude of the galaxy power spectrum multipole moments though an analysis of the redshift space distortions (RSD), and the baryon acoustic oscillation (BAO) peak, whose position depends on the geometry of the Universe. Moreover, the evolution of gravitational instabilities amplifies the initial perturbations and generates a non-Gaussian signal in the distribution of galaxies. In order to fully extract the information contained in the galaxy field, we need to additionally measure statistics of higher order than the power spectrum. The 3-point correlation function, and its Fourier counter part, the bispectrum, add significant additional information to state-of-art analyses based on the 2-point correlation function and power spectrum. For a cosmological over-density field $\delta(\mathbf{x})$, the power spectrum P and bispectrum B are defined,

$$\langle\delta(\mathbf{k})\delta(\mathbf{k}')\rangle = P(\mathbf{k})\delta^D(\mathbf{k}+\mathbf{k}'), \quad (1)$$

$$\langle\delta(\mathbf{k}_1)\delta(\mathbf{k}_2)\delta(\mathbf{k}_3)\rangle = B(\mathbf{k}_1,\mathbf{k}_2)\delta^D(\mathbf{k}_1+\mathbf{k}_2+\mathbf{k}_3), \quad (2)$$

where δ^D is the Dirac delta distribution, $\delta(\mathbf{k}) \equiv \int d^3\mathbf{x}\,\delta(\mathbf{x})\exp(-i\mathbf{k}\cdot\mathbf{x})$ is the Fourier transform of the over-density field $\delta(\mathbf{x}) \equiv \rho(\mathbf{x})/\bar{\rho} - 1$, where $\rho(\mathbf{x})$ is the dark matter density and $\bar{\rho}$ its mean value. The shape and amplitude of the power spectrum and bispectrum depend on the

[a] This work has been done within the Labex ILP (reference ANR-10-LABX-63) part of the Idex SUPER, and received financial state aid managed by the Agence Nationale de la Recherche, as part of the programme Investissements d'avenir under the reference ANR-11-IDEX-0004-02.

geometry and the matter and energy content of the Universe through several parameters such as, the growth of structure times the amplitude of primordial dark matter power spectrum $f\sigma_8(z)$; the product of the Hubble constant and the co-moving sound horizon at the baryon drag epoch $H(z)r_s(z_d)$, the angular distance parameter divided by the sound horizon $D_A(z)/r_s(z_d)$.

In this proceeding we present the power spectrum monopole and quadrupole moments, in addition to the bispectrum monopole calculated from the galaxy sample of the Sloan Digital Sky Survey III [1] Baryon Oscillation Spectroscopic Survey (BOSS [2,3,4]) data release 12 (DR12), splitting by selection algorithm into LOWZ and CMASS samples. We display the main results on $f\sigma_8(z)$, $H(z)r_s(z_d)$ and $D_A(z)/r_s(z_d)$ corresponding to i) a RSD analysis on the power spectrum monopole and quadrupole; ii) a RSD analysis combing the power spectrum multipoles with the bispectrum monopole; iii) a BAO analysis on the post-reconstructed data catalogues; at the effective redshifts of $z = 0.32$ and $z = 0.57$.

2 Data and Mocks

As part of the Sloan Digital Sky Survey III the Baryon Oscillations Spectroscopic Survey (BOSS) measured spectroscopic redshifts for more than 1 million galaxies and over 200 000 quasars on the redshift range of $0.15 < z < 0.70$. The galaxy survey used two primary target algorithms, selecting samples called LOWZ, with 361 762 galaxies in the final data release DR12 between $0.15 < z < 0.43$ and CMASS, with 777 202 galaxies in DR12 between $0.43 < z < 0.70$.

The initial BAO signal in the clustering is damped by the comoving motions of galaxies, potentially reducing the fidelity of BAO measurements. Using the observed density field, we model the galaxy motions, and move the over-density back to its original position, recovering a fraction of this signal. When presenting the results from the BAO analysis they will refer to the measurements made on the data after applying this algorithm (post-recon); whereas RSD analyses will always refer to the data catalogue before applying the algorithm (pre-recon).

Mock samples are a key component in the analysis of precision cosmological data provided by galaxy surveys. They are a fundamental requirement to test and analyse the large-scale structure and they help to determine the statistical errors and the correlation among measurements. Here we use 2048 independent realisations of the MultiDark Patchy mocks [5] (hereafter MD-Patchy), for each galaxy sample. We use the MD-Patchy mocks for estimating the full covariance of the power spectrum and bispectrum, as well as for computing the correlation of different probes, such as RSD and BAO analyses.

The power spectrum multipoles and bispectrum are measured from the CMASS and LOWZ samples using the Yamamoto [6,7] estimator for the power spectrum and the FKP [8] estimator for the bispectrum. Fig. 1 displays the measured pre-recon CMASS power spectrum monopole and quadrupole as a function of k (left panel in blue and red symbols, respectively) and bispectrum monopole as a function of the triangle index (right panel in different colours according to their shape). For the bispectrum panel the different colours display the different shapes as indicated. The error-bars are computed using the MD-Patchy mocks, and stands for 1σ errors. The middle and bottom panels show the performance of the best-fitting theoretical model based on perturbation theory for the dark matter clustering and coherent velocity motions for the RSD. As a general trend we see that the models describe well the observed data, and for most of the bins are within 95.4% confident regions (2σ). The displayed model has a set of free parameters that are adjusted to reproduce the data. Among these free parameters there are the cosmological parameters of interests: $f\sigma_8$, Hr_s and D_A/r_s; as well as some other nuisance parameters such as the shot noise amplitude or the galaxy bias parameters.

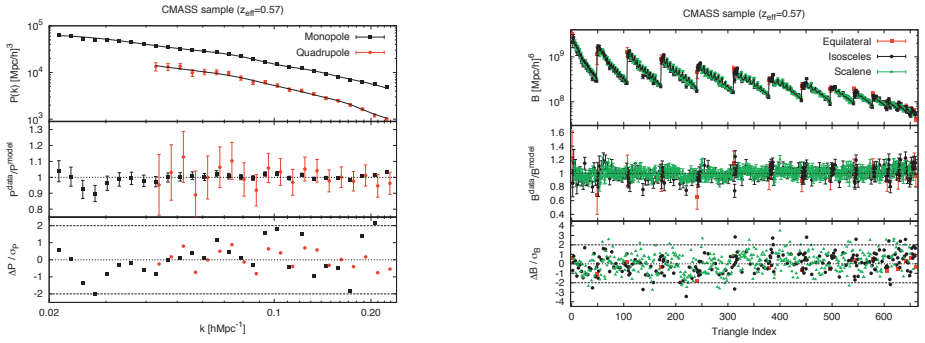


Figure 1 – Power spectrum and bispectrum data measurements (left and right panels, respectively) for the CMASS-DR12 BOSS sample. The top sub-panels display the measured power spectrum monopole (blue symbols in the left panel), quadrupole (red symbols in the left panel) and bispectrum monopole (red, blue and green symbols in the right panel according to the triangle shape). The error-bars correspond to the dispersion among 2048 realisations of the MD-Patchy mocks. The black solid lines correspond to the best-fitting model. The middle sub-panels show the ratio between the measurements and the best-fitting models. In the bottom sub-panel the difference between the data and the model, relative to the statistical error of the data is presented. The black dashed lines represent a 2σ deviation (95.4%) confidence level.

3 Results and Conclusions

In Table 1 we display the best-fitting cosmological parameters, $H(z)r_s(z_d)$, $D_A(z)/r_s(z_d)$ and $f\sigma_8(z)$ to the data, for the LOWZ ($z_{\rm LOWZ} = 0.32$) and CMASS samples ($z_{\rm CMASS} = 0.57$), for 3 complementary analyses:

(i) RSD - P. RSD pre-recon analysis of the power spectrum monopole and quadrupole [9].

(ii) RSD - P+B. RSD pre-recon analysis of the power spectrum multipoles and bispectrum monopole [10].

(iii) BAO - P. BAO post-recon analysis of the power spectrum moments [11].

Table 1: Results on the H/r_s, D_A and $f\sigma_8$ cosmological parameters corresponding to the LOWZ sample, $z_{\rm LOWZ} = 0.32$ (top table) and for the CMASS sample, $z_{\rm CMASS} = 0.57$ (bottom table). The different rows correspond to the different techniques used for measuring these parameters (see text). The last row correspond to the consensus value among the previous 3 analyses. The error-bars stands for 1σ confident levels.

	$H(z_{\rm LOWZ})r_s(z_d)$ $[10^3\,{\rm kms}^{-1}]$	$D_A(z_{\rm LOWZ})/r_s(z_d)$	$f\sigma_8(z_{\rm LOWZ})$
RSD-P	11.33 ± 0.56	6.33 ± 0.19	0.395 ± 0.064
RSD-P+B	11.75 ± 0.55	6.74 ± 0.22	0.460 ± 0.066
BAO-P	11.54 ± 0.55	6.66 ± 0.15	–
Consensus	11.55 ± 0.38	6.60 ± 0.13	0.427 ± 0.052

	$H(z_{\rm CMASS})r_s(z_d)$ $[10^3\,{\rm kms}^{-1}]$	$D_A(z_{\rm CMASS})/r_s(z_d)$	$f\sigma_8(z_{\rm CMASS})$
RSD-P	13.84 ± 0.42	9.42 ± 0.19	0.442 ± 0.037
RSD-P+B	13.78 ± 0.28	9.33 ± 0.15	0.418 ± 0.027
BAO-P	14.55 ± 0.36	9.42 ± 0.13	–
Consensus	14.02 ± 0.22	9.39 ± 0.10	0.426 ± 0.023

The results from the different analyses are compatible within 1σ and expected to be correlated. We re-combine the results of these analyses into a single consensus set of cosmological

parameters using the MD-Patchy mocks to determine their correlations. For simplicity we define the consensus estimator to be a linear combination of the measurements of the individual probes, where the coefficients weight each parameter according to their covariance. We determine the weights by imposing the condition of minimum variance to the consensus estimator.

In Fig. 2 we show the results on the $f\sigma_8(z)$ parameter as a function of redshift for the consensus values presented in Table 1 (black points), along with the results coming from other galaxy surveys: 6DFGS [12], SDSS-MGS [13], SDSS-LRG [14], WiggleZ [15] and VIPERS [16]. We also display the prediction drawn from the cosmological parameters from Planck15 [17] when General Relativity (GR) is assumed.

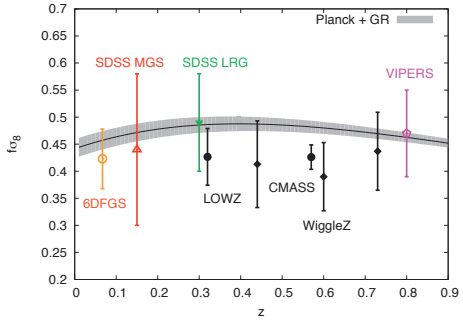


Figure 2 – Constrains on $f\sigma_8(z)$ from several galaxy redshift surveys in the base of a ΛCDM + GR: orange circles (6dFGRS); red triangle (SDSS Main Galaxy Sample); green inverse triangles (SDSS Luminous Red Galaxies); blue diamonds (WiggleZ); and purple pentagon (VIPERS). In black squares the consensus results from BOSS-DR12 according to Table 1. The grey band shows the 1σ confident levels allowed by Planck TT+lowP in the base of a ΛCDM + GR model.

The presented constraints on $f\sigma_8(z_{\rm eff})$, along with $H(z_{\rm eff})r_s(z_d)$ and $D_a(z_{\rm eff})/r_s(z_d)$, will be useful in joint analyses with other cosmological data sets (in particular CMB data) for setting stringent constraints on neutrino mass, dark energy, gravity, curvature as well as number of neutrino species.

References

1. Eisenstein, D. J., Weinberg, D. H., Agol, E., et al. 2011, *AJ*, 142, 72
2. Bolton, A. S., Schlegel, D. J., Aubourg, É., et al. 2012, *AJ*, 144, 144
3. Dawson, K. S., Schlegel, D. J., Ahn, C. P., et al. 2013, *AJ*, 145, 10
4. Smee, S. A., Gunn, J. E., Uomoto, A., et al. 2013, *AJ*, 146, 32
5. Kitaura, F.-S., Rodríguez-Torres, S., Chuang, C.-H., et al. 2016, *MNRAS*, 456, 4156
6. Yamamoto, K., Nakamichi, M., Kamino, A., et al. 2006, *PASJ*, 58, 93
7. Bianchi, D., Gil-Marín, H., Ruggeri, R., & Percival, W. J. 2015, *MNRAS*, 453, L11
8. Feldman, H. A., Kaiser, N., & Peacock, J. A. 1994, *ApJ*, 426, 23
9. Gil-Marín, H., Percival, W. J., Brownstein, J. R., et al. 2016, arXiv:1509.06386
10. Gil-Marín, H., Percival, W. J., Verde, L., et al. in prep.
11. Gil-Marín, H., Percival, W. J., Cuesta, A. J., et al. 2016, arXiv:1509.06373
12. Beutler, F., Blake, C., Colless, M., et al. 2012, *MNRAS*, 423, 3430
13. Howlett, C., Ross, A. J., Samushia, L., et al. 2015, *MNRAS*, 449, 848
14. Oka, A., Saito, S., Nishimichi, T., Taruya, A., & Yamamoto, K. 2014, *MNRAS*, 439, 2515
15. Blake, C., Brough, S., Colless, M., et al. 2012, *MNRAS*, 425, 405
16. de la Torre, S., Guzzo, L., Peacock, J. A., et al. 2013, *A&A*, 557, A54
17. Planck Collaboration, Ade, P. A. R., Aghanim, N., et al. 2015, arXiv:1502.01589

MEASURING BAO SCALE WITH QUASAR CLUSTERING IN EBOSS

P. LAURENT
CEA Saclay/DSM/IRFU/SPP, Building 141,
91191, Gif-sur-Yvette, France

Two years after the beginning of the fourth phase of SDSS programs, the eBOSS quasar sample is already the biggest spectroscopic quasar sample ever observed in the range $0.9 < z < 2.2$, and it will provide the first measurement of the Baryonic Acoustic Oscillation (BAO) scale in this redshift range. This proceeding focuses on the method used to compute the 2-point correlation function of this quasar sample, and on systematic effects that could bias its measurement. We present a preliminary measurement of the quasar bias, along with its evolution with redshift. The statistic of the eBOSS quasar sample is still too limited to provide a measure of the BAO scale, but we present a preliminary study of its significance.

1 Introduction

Primordial sound waves propagate in the early universe, when ionized baryonic matter is coupled to photons. When recombination occured, these waves were frozen after travelling a distance r_s that corresponds to the integrated sound speed between inflation and $z = 1100$. This results in a bump in the 2-point correlation function $\xi(r)$, or oscillations in the power spectrum. The measure of the CMB power spectrum allows to fix the value of r_s, also known as the sound horizon. This distance provides a standard ruler, which only evolves with the expansion of the universe. Measuring this Baryonic Acoustic Oscillation (BAO) scale in the correlation function at lower redshifts can be used to constrain models of the expansion of the universe.

Since the first measurement performed by Eisenstein et al. in 2005 [1], the BOSS collaboration provided accurate measurements of the BAO scale, using the CMASS and LOWZ galaxy sample [2] ($0.2 < z < 0.7$) and the quasar Lyman α forest data [3] [4] ($2.2 < z < 3.5$). The gap between these 2 measurements will be filled using the eBOSS [5] spectroscopic quasar sample.

The sample consists in 97,299 quasar spectra, with a flat redshift distribution from 0.9 to 2.2, distributed in the North and South Galactic Cap. In total, 500,000 quasar spectra should be measured for the final eBOSS quasar sample (on roughly 10,000 deg^2). This will be the biggest quasar sample ever observed in this redshift slice. Quasars are homogeneously selected using SDSS I-II photometry and the XDQSO algorithm, allowing for clustering analysis and $\xi(r)$ measurement. In this proceeding, we give a review of the method used to compute $\xi(r)$, along with a study of systematic effects that could bias the measurement. We also give a preliminary measure of $b_Q(z)$, and a look at the significance of the BAO signal in our data.

2 Measuring $\xi(r)$

For each plate of the eBOSS survey, 1,000 fibers are available to observe the target sample. The observation of quasars in eBOSS is not homogeneous because targets are more likely to be

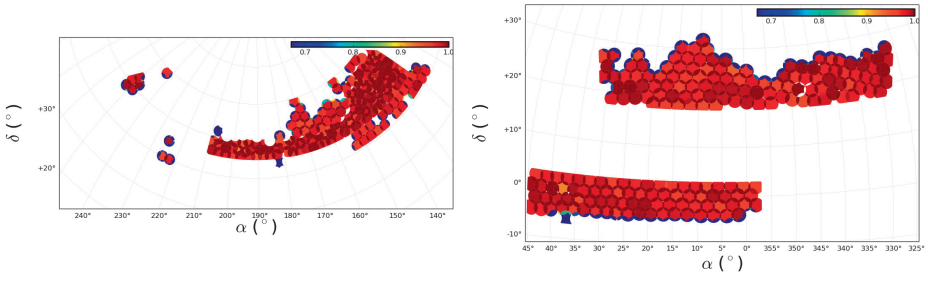


Figure 1 – Current footprint of the eBOSS quasar sample for the NGC (left) and for the SGC (right)

observed when located on areas where plates overlap. First, we defined the completeness of the survey as :

$$C = \frac{N_{\rm obs} + N_{\rm col}}{N_{\rm targets} - N_{\rm known}} \quad . \tag{1}$$

This quantity is defined in each polygon, which are defined as the intersection of the plates on the celestial sphere. N_{obs} is the number of observations, $N_{targets}$ is the number of targets. N_{known} is the number of targets that have already been observed by the SDSS collaboration. Since the number of fibers is limited, it has been choosen not to reobserve these targets : this is the reason why they are removed from the denominator. N_{col} is the number of 'collided' targets. Because of the shielding of the fibers, it is not possible to observed 2 targets separated by less than 62 ". This effect is accounted for by upweighting the closest observed quasar within 62 ", and by adding this target to the numerator of equation 1.

We generate a homogeneous sample of objects with random angular positions over the footprint of the eBOSS survey. The number of objects in each polygon is proportionnal to the polygon area times its completeness. Then, we assign to each object a redshift drawn from the $n(z)$ distribution of the data. The correlation function $\xi(r)$ is then computed using the Landy-Szalay estimator [6]. Statistical uncertainties are obtained from bootstrap realizations. This means that our statistical uncertainties do not account for cosmic variance, but this is not an issue since our survey is shot-noise limited.

3 Correcting systematic effects

We perform a study of systematic effects that can arise when small inhomogeneities appear in target selection. The quasars are selected up to a maximum apparent magnitude of $g < 22$ or $r < 21.85$. The average 5-σ detection limit for point sources (also called depth) of the SDSS photometric survey is $g < 23.1$ or $r < 22.7$. Since SDSS photometry is not perfectly homogeneous, this detection limit varies with seeing, airmass, Galactic extinction and sky brightness. The amplitude of the variations reaches $\pm$ 0.8 magnitude, which means that faint targets can end up very close to the detection limit. These targets are then more likely to be missed by the target selection algorithm.

To study this effect, we use the HEALPix software to generate maps of the depth and the photometric quantity mentionned above, and also of star density. We also produce a map of the ratio of the number of quasars to the number of random objects. The black lines on Figure 2 show that this ratio varies with all quantities but star density. These dependencies are all redshift independent. We fit a linear function to the curve of the dependence with the depth, and recompute the ratio of quasar and random objects after weighting each pixel with

Table 1: Results for the bias fit in different redshift bins for the eBOSS quasar sample. All fits are performed using Minuit and the full covariance matrices, for $10 < r < 90 h^{-1}$Mpc.

z_{min}	z_{max}	z_{eff}	b_Q	χ^2 (9 d.o.f.)
0.9	1.2	1.06	1.82 ± 0.08	9.91
1.2	1.5	1.35	2.08 ± 0.08	5.96
1.5	1.8	1.65	2.54 ± 0.07	6.10
1.8	2.2	1.99	2.93 ± 0.10	4.14
0.9	2.2	1.55	2.42 ± 0.04	10.28

the inverse of the fitted linear function. Most of the dependencies then vanishes, as shown by red lines on Figure 2. We apply the same weighting when computing $\xi(r)$.

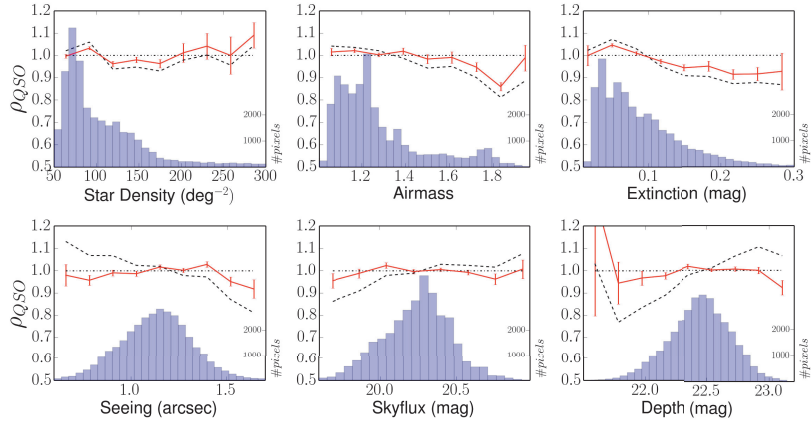


Figure 2 – Dependency of different photometric quantities with respect to the normalized quasar density, corrected for completeness. The black curves show the dependencies before correction, the red ones after the correction by the depth. The histograms give the number of pixels of the Healpix map in each bins.

4 Results

We measure the bias b_Q of the eBOSS quasar sample, and its redshift dependency. We use CAMB to generate a fiducial ΛCDM power spectrum $P_m(k)$, using the cosmological parameters from the PLANCK intermediate results, namely $h = 0.6704$, $\Omega_m = 0.3183$, $\Omega_b h^2 = 0.022032$, $n_s = 0.9619$). We model linear redshift space distortions using Kaiser formula, $P_Q(k, \mu) = b_Q^2(1 + \beta\mu^2)^2 P_m(k)$. The Fourier transform of P_Q gives us the model for ξ_Q. We then fit b_Q in different redshift bins, using the Minuit algorithm. We perform the fit for separations between 10 and 90 h^{-1}Mpc, using the full covariance matrices. The different redshift ranges, effective redshift and b_Q values are displayed in Table 1. Our results are compatible with the results from Croom et al. (2005), but with much better accuracy.

We test the significance of the BAO signal using our full data sample. We use a gaussian as a model for the BAO peak, and we add a broadband to model the excess of correlation on large scales :

$$\xi_r = A_{BAO} \exp(-(r - r_{BAO})^2 / 2\sigma_{BAO}^2) + a r^{-2} + b r^{-1} + c\,. \quad (2)$$

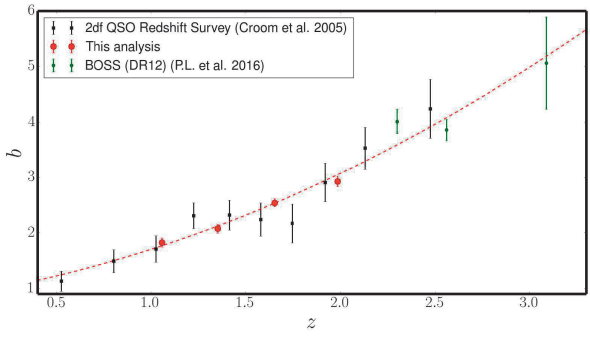


Figure 3 – Evolution of b_Q with redshift. The red dots correspond to this analysis, the green dots to the analysis using the BOSS quasar sample (P.L. et al. 2016) and the black dots correspond to an analysis performed by Croom et al. (2005) [7]

The parameters of the gaussian are tuned to fit the CAMB model in the range of the BAO peak, which yield $A_{BAO} = 0.0031$, $\sigma_{BAO} = 10$, $r_{BAO} = 100.7$, and we leave the broadband parameters a, b and c free. We fit this model over $40 < r < 200h^{-1}$Mpc (see Fig 4), and get $\chi^2 = 12.71$ (for 17 d.o.f.). If we remove the BAO peak from our model by setting $A_{BAO} = 0$, we obtain $\chi^2 = 19.26$. This yields $\Delta\chi^2 = 6.46$, which corresponds to a detection larger than 2σ. Knowing that we only have access to 20% of the final quasar sample, this early result is very promising for the future of the BAO study in this redshift range.

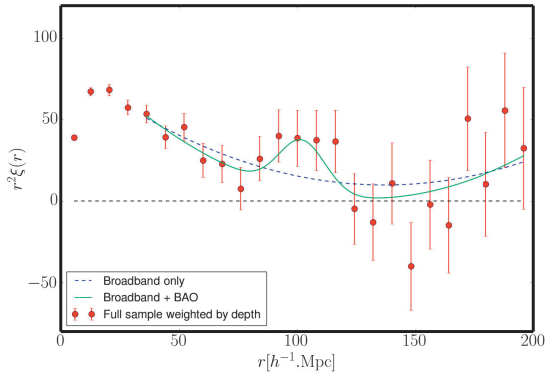


Figure 4 – Green line : fit of a 'BAO peak' tuned on Λ-CDM, with a broadband model given by $ar^{-2} + br^{-1} + c$. Blue dashed line : fit performed after removal of the peak.

References

1. D. J. Eisenstein, I. Zehavi *et al*, *Astrophys. J.* C **633**, 560 (2005)
2. L. Anderson *et al*, *Mon. Not. Roy. Astron. Soc.* C **441**, 24 (2014)
3. T. Delubac *et al*, *Astrophys. J.* C **151**, 44 (2016)
4. A. Font, J. Miralda *et al*, *Astrophys. J.* C **221**, 402 (2013)
5. K. Dawson, J. P. Kneib, W. Percival *et al*, *Astronom. J.* C **151**, 44 (2016)
6. S. D. Landy, A. S. Szalay *et al*, *Astrophys. J.* C **412**, 64 (1993)
7. S. M. Croom *et al*, *Mon. Not. Roy. Astron. Soc.* C **392**, 19 (2005)

The Dark Energy Spectroscopic Instrument

J. GUY
on behalf of the DESI collaboration
LPNHE, CNRS/IN2P3, Université Pierre et Marie Curie Paris 6,
Université Denis Diderot Paris 7, 4 place Jussieu, 75252 Paris CEDEX, France

Baryon Acoustic Oscillations (BAO) are a major probe of the Dark Energy science, with low systematic uncertainties, and an important complementarity with Supernovae Ia for the measurement of the expansion history (absolute distance measurement, measurement of the instantaneous expansion rate, extension of the Hubble diagram to much higher redshifts with the Lyman-α forests, measurement of H_0 with the inverse distance ladder approach). Massive spectroscopic surveys optimized for BAO can also measure the growth rate of structures with redshift space distortions. This provides an independent test of general relativity on cosmological scales, and helps constraining alternative theories of gravitation designed to explain the recent acceleration of expansion. DESI is a large Dark Energy project optimized for those probes. BAO and redshift space distortions will be measured with LRG, ELG, quasars and Lyman-α over a 14,000 square degrees footprint. Observations will be conducted on the 4-m diameter Mayall Telescope at Kitt Peak, Arizona. The survey will begin in 2019 and will last 5 years. DESI will be close to ten times as precise as current BAO surveys, with a combined precision on the radial and longitudinal BAO scales of 0.3% and 0.5% respectively at an effective redshift of $z \sim 1.3$. At $z > 2.1$, with the Lyman-α forest auto-correlation, the integrated precision on the radial and longitudinal BAO scale is expected to be of 0.8% and 0.7%. Cross-correlations of Lyman-α forests with QSO will provide additional BAO constraints. Much more information will also be provided by the correlation function at smaller scales, at the expense of a more demanding accuracy on the modeling of both the clustering and survey efficiency. For instance DESI will measure the sum of neutrino masses with a statistical uncertainty of 0.020 eV (when considering data up to $k_{max} = 0.2\ h\ \mathrm{Mpc}^{-1}$).

1 Scientific context

1.1 Baryon acoustic oscillations

Plasma sound waves that propagate in the early universe are frozen at recombination when matter and radiation decouple. This is imprinted in the correlation function or power spectrum of the cosmic microwave background (CMB) which is an image of the universe at recombination. An excess of correlation is found at a comoving separation that can be accurately predicted from the energy density content of the early universe: it corresponds to the distance covered by sound waves before recombination. This physical process is called baryon acoustic oscillations (BAO), and the preferred comoving separation the sound horizon (or r_s). BAO can also be found in large galaxy redshift catalogs and quasar Lyman-α forests (see Figure 1) that trace the matter density field at later times (or lower redshift). The BAO scale detected in the angular correlation function of matter density tracers is a measurement of the angular diameter distance $d_A(z)$ at the redshifts of the tracers in units of r_s. Measuring it along the line of sight using the source redshifts gives the expansion rate $H(z)$ at the redshifts of the sources (in units of $1/r_s$). Combining CMB and BAO data in the framework of a given cosmological model gives an estimate of r_s and the constraints

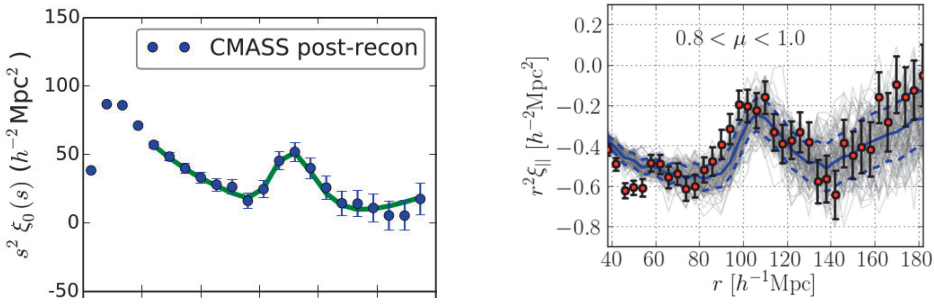


Figure 1 – Left: BOSS DR12 CMASS (LRG sample at $z \simeq 0.57$) auto-correlation function (monopole). This figure is extracted from Cuesta et al. (2016) [2]; see also the DR12 results combining several approaches in Alam et al. (2016) [4]. Right: BOSS DR11 Lyman-α forest correlation function (line of sight angular wedge, red points with error bars) at $z \simeq 2.3$. The gray curves represent the simulations and the blue curve their average for the fiducial cosmology. This figure is extracted from Delubac et al. (2015) [5].

on $d_A(z)$ and $H(z)$ allow us to measure the expansion of the universe at late times and estimate for instance the cosmological constant or the Dark Energy equation of state parameter w.

1.2 BAO in the Lyman-α forests

Each neutral hydrogen cloud at redshift z intersecting the line of sight of a background quasar leaves an absorption line in the quasar spectrum at a wavelength of $(1+z)\times 121$ nm corresponding to the Lyman-α atomic transition. The accumulation of such absorptions in a quasar spectrum at various redshifts is called a Lyman-α forest. It can be measured from the ground at wavelength > 350 nm (because the atmospheric and instrumental UV cutoff) corresponding to a minimal quasar redshift $z > 1.9$.

Lyman-α forests open a new high redshift window for the measurement of the expansion rate. Whereas neither ground-based nor space-borne spectroscopic surveys are providing a sufficient density of high redshifts sources [a] to measure the BAO scale at $z > 2$, this difficulty is overcome with the Lyman-α forests that do not require an equivalent statistics, as each quasar allows a pencil beam mapping of the neutral hydrogen along its line of sight. This has been demonstrated by the BOSS experiment where the BAO peak has been detected and measured in the correlation of Lyman-α forests at an effective redshift of 2.3 (see Figure 1).

1.3 BAO have low systematics uncertainties

The measurement of a peak in the angular and redshift correlation function has very mild instrumental and data reduction systematic uncertainties. This is striking for the galaxy clustering measurement of BOSS (see for instance [1]). The variations of the targeting [b] efficiency on the sky (due to variations of atmospheric transparency, image quality, sky brightness during the imaging observations) imprint a spurious large scale signal in the galaxy correlation function. Those variations of efficiency are corrected for by reweighting the galaxy catalog entries. However, the resulting BAO scale measurement is hardly modified by those important corrections as they modify the broad-band part of the correlation function and not its shape at scales that would affect

[a] Spectroscopic surveys are intrinsically limited at high redshift, because of the brightness and transmission of the atmosphere in the near infra-red for ground-based surveys, and schematically because of the possible collection area (mirror size) for space missions, making it impossible to obtain a sufficient density of bright enough sources at high-z.

[b] The targeting is the selection process of spectroscopic targets from imaging catalogs. It is based on a set of cuts on the magnitudes and colors of galaxies designed to optimize the yield, purity and redshift distribution of the selection.

the peak position. For Lyman-α forests, the source of observational systematics is different but the conclusion is qualitatively the same. Sources of correlated noise are introduced in the spectroscopic observations and data reduction and result in a spurious broad-band contribution to the measured Lyman-α correlation function, however those contaminants also induce negligible shifts ($< 1\%$) on the BAO measurement of BOSS data given the current precision [3]. They can also be corrected, leaving even smaller systematic uncertainties.

The BAO peak is generated in the early universe where density contrasts are such that computations at first order of perturbation yield predictions at a sub-percent precision for the position of the peak. Higher order effects, due to the growth of structures at later times affect the shape of the peak. They are well quantified for galaxies, leading to a correction of 0.3%. For Lyman-α forests, the effect of non-linear clustering is less important, but the correlation signal is contaminated by other atomic transitions, fluctuations of the UV background (and hence the hydrogen neutral fraction) and the presence in the forests of undetected damped Lyman-α systems. Current analyses on BOSS data [3] show that those signals can be corrected for and have a negligible impact on the measurement of the BAO scale. They however limit our ability to understand in detail the broad-band shape of the correlation function.

1.4 Redshift Space Distortions

Despite the fact that the galaxy clustering is statistically isotropic, we observe an increased density contrast along the line of sight in redshift surveys at intermediate scales (~ 40 Mpc, see Figure 2). This is due to the Doppler effect induced by the coherent peculiar velocities of galaxies that tend to fall in gravitational potentials. Because the divergence of the peculiar velocity field is directly related to the time derivative of the density contrasts through conservation of mass, the so-called Redshift Space Distortions (RSD) give us constraints on the growth rate of structures. Measuring this growth rate is a test of General Relativity on cosmological scales, and permits to validate or rule out alternative theories of gravitation that could mimic the expansion history of ΛCDM, and hence be indistinguishable from the standard model of cosmology when constrained only by supernovae or BAO.

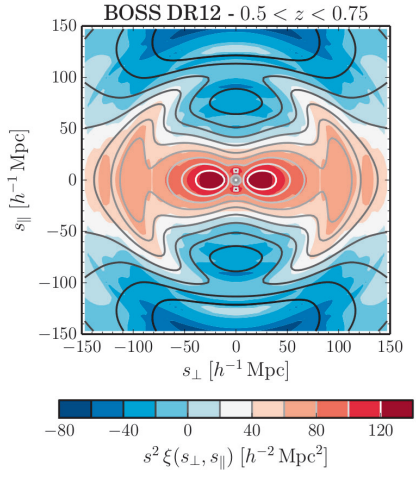


Figure 2 – The two-dimensional correlation function of the BOSS DR12 galaxy sample (North Galactic Cap only) measured perpendicular (x-axis) and parallel (y-axis) to the line of sight. The color scale shows the data and the contours show the prediction of the best-fit model. The BAO ring is clearly visible, as is the characteristic squashing of the correlation function on large scales due to a combination of the RSD and AP effects. We also see the Finger of god effect at $r_\perp \sim 0$ and $|r_\parallel| \sim 10$ Mpc.h^{-1}.

Two other effects give rise to an apparent anisotropic clustering in redshift space. The first is the so-called Alcock-Paczynski (AP) test. Cosmological models that differ in their prediction for the expansion history will have different predictions for the transverse and longitudinal coordinate separation of a pair of galaxies given its observed angular and redshift separation ($D_A(z)\Delta\theta$ and $\Delta z/H(z)$) . A model inconsistent with the true expansion history will lead to an apparent anisotropy in the correlation function. The Alcock-Paczynski test is hence constraining the product $D_A(z) \times H(z)$. BAO also constrain this parameter combination, but the AP measurement in the context of RSD is based on the 2D broad-band shape of the correlation function at smaller scales than BAO, resulting in a nearly independent (or statistically uncorrelated) observable.

The second effect is due to the dispersion of velocities of galaxies in dark matter halos at small scales that induces an apparent elongation of galaxy clusters along the line of sight. This signal is striking in the correlation function. It is however difficult to model and leads to potential systematic uncertainties in the measurement of the growth rate and AP test from the redshift space distortions. The Fingers of god effect is an obvious manifestation of non-linear effects that need to be modeled when trying to interpret the galaxy clustering signal at small scales. Entering the analysis is the ability to model accurately the population of galaxies in dark matter halos that are themselves defined by the method used to select them in dark matter simulations. This is a domain of active research, with many approaches, N-body and/or hydrodynamical simulations, perturbative developments, or more empirical methods.

2 The DESI Project

The Dark Energy Spectroscopic Instrument (DESI) is a DOE Stage IV Dark Energy project aiming at measuring BAO and redshift space distortions with Luminous Red Galaxies (LRGs) , Emission Line Galaxies (ELGs), quasars and Lyman-α forests over a 14,000 square degrees footprint. DESI will also conduct a bright time survey, complementing the galaxy redshift catalog at $z < 0.4$, and measuring the radial velocities and metallicities of millions of stars from the GAIA catalog.

2.1 Instrumentation overview

DESI is very similar to BOSS/eBOSS in its concept but with a considerably increased statistics thanks to major improvements in the instrument system. Observations will be conducted on the 4-m diameter Mayall Telescope (see Figure 3) at Kitt Peak, Arizona. The focal plane will be equiped with a 5000 robotically-actuated fiber system feeding 10 spectrographs located in a temperature-controled room. Each spectrograph receiving 500 fibers is composed of three arms/cameras which optics and CCDs are optimized for blue, red and near infra-red wavelength. The design maximizes the throughput over the wavelength range accessible with CCDs from the ground. The wavelength resolution is tuned for the identification of the two lines of the [O II] doublet, which is a crutial requirement to identify and measure the redshifts of faint ELGs.

Thanks to a larger mirror area ($\times$2.4), a larger number of fibers ($\times$5), an improved throughput ($\times$1.6) and resolution ($\times$2.3 at 7000 $\AA$), DESI will measure redshifts 45 times faster than BOSS for ELGs, and 20 times faster for quasars (for which the gain in resolution is less important). Using fiber positionners instead of drilled plates will allow much more flexibility in the survey design. The use of an Atmospheric Dispersion Compensator will improve the light yield in the fibers. In addition, thanks to their location in a temperature-controlled room, the spectrographs will be much more stable than those of BOSS, potentially resulting in a significantly improved data reduction (CCD spectral extraction, sky background subtraction, wavelength and flux calibration).

2.2 Survey

DESI will measure the redshifts and spectra of 4 millions LRGs at $0.4 < z < 1.0$, 17 million ELGs at $0.6 < z < 1.6$, 1.7 million quasars at $z < 2.1$ and 0.7 million Lyman-α forests quasars at $z > 2.1$

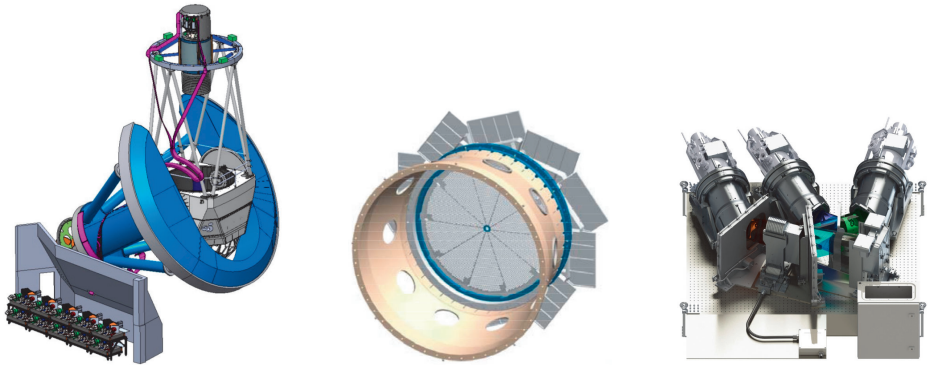


Figure 3 – From left to right: the DESI instrument installed on the Mayall telescope, focal plane system with 10 petals each hosting 500 fiber positioners, one of the 10 spectrographs installed in the Coudé room.

during dark time, along with about 10 million galaxies at lower redshifts and millions of stars during bright time.

The footprint of 14,000 square degrees, as observable from Kitt Peak, will consist of two contiguous regions split by the Galactic plane to avoid regions with high stellar density and Galactic dust extinction. With a field of view of 7.5 square degrees, most of this footprint can be observed with about 2000 pointings (or tiles). In the current design, the footprint will be covered 5 times (once per year), with a total of approximately 10000 pointings, allowing an average number of observations of 5.1, with only 3.5% of the area covered less than 3 times. The average exposure time will be of 1800 seconds, but will vary with pointing and observation conditions, with an expected minimal exposure time of 1200 seconds for the best conditions (at zenith, far from the Galactic plane).

The spectral targets will be selected from on-going imaging surveys that will cover the SDSS g, r and z bands (at a minimal depth of 24.0, 23.4, 22.5 AB respectively), complemented with infrared photometry from the WISE telescope. The southern part of the footprint is being observed with the Blanco/DECam camera [c], and the northern part with the Bok/90Prime camera for the g, r bands and an upgraded MOSAIC-2 camera on the Mayall for the z band. The analysis of the imaging data and the design of selection cuts for the DESI targets is an important on-going activity in the collaboration.

2.3 Scientific forecast

DESI will achieve a Dark Energy Task Force Figure of Merit (FoM) [d] of 169 from BAO alone (galaxy and Lyman-α combined). This number is however quite biased towards surveys efficient at low-redshift where Dark Energy has an important weight, so it is not very favorable for BAO projects. More interesting are the expected precisions on the BAO scale in independent redshift bins given in Table 2.3, 2.5 and 2.7 of the DESI Final Design Report [6]. The results from those tables are reproduced in Figure 4 for the isotropic BAO scale (combined radial and transverse measurements). DESI will be a major experiment for the measurement of the expansion history, in analogy with Planck for the CMB temperature anisotropies.

As an example, DESI will be close to ten times as precise as eBOSS at an effective redshift of $z \sim 1.3$ (when integrating the combined ELG, LRG and quasar forecast over the redshift range

[c] Dark Energy Camera Legacy Survey (DECaLS) `http://legacysurvey.org/decamls/`

[d] The FoM of Dark Energy has been designed to quantify the constraining power of upcoming surveys. It is approximately the inverse of the product of the uncertainties of the mean and time derivative of the Dark Energy equation of state parameter $(\sigma(w_p)\sigma(w_a))^{-1}$ (arranged in the form of uncorrelated quantities), see Albrecht et al. (2009) [7].

probed by the main survey), with a combined precision on the radial and longitudinal BAO scale of 0.3% and 0.5% respectively. At $z > 2.1$, with the Lyman-α forest auto-correlation, the integrated precision on the radial and longitudinal BAO scales is expected to be of 0.8% and 0.7% (compared to 5% and 3% today with BOSS). It is very likely that those statistical predictions will not be dominated by systematic errors.

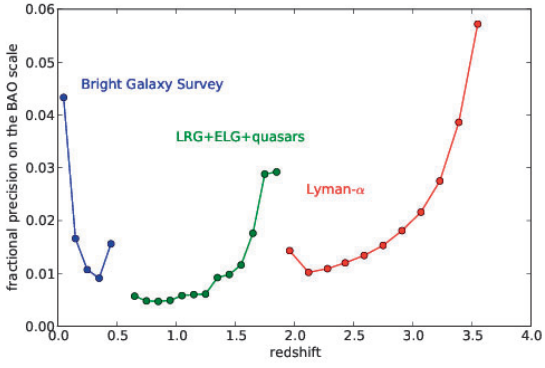


Figure 4 – Fractional precision on the isotropic BAO scale in *independent* redshift bins (from Table 2.3, 2.5 and 2.7 of the DESI FDR [6])

In addition to providing constraints on Dark Energy, DESI will provide new measurements that can constrain theories of modified gravity and inflation, and that will measure the sum of neutrino masses.

2.4 Schedule

DESI passed the DOE CD-3 review in May 2016 and is now in construction phase. The expected first light is for mid-2019. After a few month of commissioning, the science survey will start at the end of 2019. The survey planning is optimized for early science results, with a first pass on the whole sky during the first year. Subsequent years will be dedicated to the re-observation of most targets, with additional targets that could not be allocated a fiber in the previous passes. With this strategy, significant cosmological results are expected after the first year of data taking.

The construction is well advanced, with the first spectrograph fully assembled and being tested in Marseille, France. The telescope pointing, guiding and fiber positioning systems are tested on the Mayall in August-September 2016. The collaboration (with more than 200 members from more than 40 institutions from USA, Canada, China, Columbia, France, Korea, Mexico, Spain, Switzerland and UK) is already very active in the imaging survey analysis, targeting algorithms, spectral data analysis, and science preparation with simulations. A full survey simulation with be conducted in 2017, starting from large scale structure simulations down to CCD image simulations, allowing a test of the whole analysis chain, from CCD spectral extraction to cosmological constraints. Much more information on the project and collaboration can be found on the DESI web site `http://desi.lbl.gov`.

References

1. A.J. Ross et al., MNRAS **424**, 564 (2012).
2. A.J. Cuesta et al., MNRAS **457**, 1770 (2016).
3. J. Bautista et al., BOSS collaboration, in prep.
4. S. Alam et al., BOSS collaboration, `arXiv:1607.03155`.
5. T. Delubac et al., A&A **574**, A59 (2015).
6. DESI Final Design Report, accessible at `http://desi.lbl.gov/`.
7. A. Albrecht et al., `arXiv:0901.0721`.

LOCAL ENVIRONMENT OF SNLS5 TYPE IA SUPERNOVÆ

M. ROMAN
Laboratoire de Physique Nucléaire et des Hautes Energies, UPMC Univ. Paris 6, UPD Univ. Paris 7, CNRS IN2P3, 4 place Jussieu 75005, Paris, France



Type Ia supernovæ constitute a powerful probe of dark energy equation of state and expansion rate, assuming an empirical standardization process. As supernovæ lie in galactic regions that evolve with redshift, we expect that their luminosities depend on local properties. We measure local $U-V$ rest-frame colors in regions of 3 kpc around the explosion location and find that, under the assumption of a bimodal distribution, local color correlates to Hubble diagram residuals at a significance of 7σ. This is more significant than any other global quantity we measure. Local effects must be included in the standardization.

1 Introduction

The first Hubble diagrams constructed using type Ia supernovæ (SNIa) revealed that the expansion of the universe entered a late time phase of acceleration[1,2]. A multitude of supernovae experiments have constrained this acceleration, dubbed "dark energy" with increasing precision, the *Supernova Legacy Survey* (SNLS) chiefly among them. The SNLS has been regularly releasing constraints on the nature of dark energy as it updates both its data sample and analysis methods. The latest such release was a joint analysis between the SNLS and *Sloan Digital Sky Survey* (SDSS) teams called the *Joint Lightcurve Analysis* (JLA[3]), giving rise to the best existing constraint (6%) on the dark energy equation of state parameter.

Type Ia supernovæ have long proved to be a successful probe of dark energy thanks to their property of *standardizable* candle. The standardization process correcting from light-curve width (using the *stretch* parameter) and color reduces the scatter in supernovæ peak magnitudes to ~ 0.15 mag. However, it is believed that the intrinsic dispersion in the supernova population reflects the fact that the standardization process does not entirely capture the physical processes at play during the explosion, leaving plenty of room for a third variable correcting the supernova luminosity. The exact mechanism for how the progenitor system accretes mass is still poorly known and could be different between galaxy types or local stellar population.

Therefore, the search for correlations between SNIa properties and the properties of their parent galaxies is strongly motivated. During the past fifteen years, a large number of independent studies aimed at casting a new light on host galaxies properties, with samples of various sizes and quality. For the first time, a sample using both distant SNIa observed by the SNLS

after a 3 years survey has been gathered and analysed[4]. Completing the sample with nearby SNIa, this work found 4σ evidence that SNIa exploding in massive and passive galaxies are on average brighter. This result has been confirmed by the recent *Joint Lightcurve Analysis*. However, as galaxy stellar mass depends on many other properties of the stellar population (age, stellar formation rate, metallicity, color), it is likely that this observable is a proxy for other local galactic properties.

Recently, a star-formation bias taking into account different supernova local environments traced by Hα emission has been exploited to perform a direct measurement of H_0 making use of a low-redshift sample[5]. It has been shown by another group that, on the contrary, there is little evidence that supernovæ in locally star-forming regions are fainter than in locally passive regions[6]. Therefore, the proposed changes to H_0 measurement would not be significant.

Studying the dependence of SNIa luminosities on their local environment involves a challenging measurement, strongly depending on the size and quality of the sample, subject to systematic errors, and possibly giving rise to opposite conclusions. As cosmological consequences are important (measurement of the present expansion rate of the Universe, nature of dark energy), it is fundamental to shed a new light on the environmental dependence of supernova luminosity.

Here, we consistently measure global and local properties, extending our sample to higher redshifts and significantly increasing its size. We present correlations between the different host variables and Hubble diagram residuals.

2 Host galaxies sample

When discussing the available host galaxies sample, we distinguish redshift categories.

We find 117 nearby host galaxies (with spectroscopic redshift typically below $z = 0.08$) corresponding to type Ia supernovæ detected by the CSP, CfAIII and CfAIV surveys. Among them, **78** galaxies are found in SDSS images. As a consequence, the local photometry around the supernova explosion and the global photometry are directly estimated on the images where those galaxies are located. The remaining 39 have photometry in the 2MASS catalog, so we can use the proportionality relation between galaxy stellar mass and K-band magnitude in order to estimate this specific quantity.

The intermediate redshift range (between $z = 0.04$ and $z = 0.4$) are provided by the SDSS survey. For **291** host galaxies, we also estimate global and local properties on their corresponding SDSS images.

As for distant type Ia supernovæ ($0.12 < z < 1$), we make use of data obtained during the *CFHT Legacy Deep Survey*, corresponding to the SNLS survey. It provides images covering 4 patches of sky, of 1 square degree each. We find identifiable host galaxies for **346** type Ia supernovæ detected by SNLS.

3 From photometry to galaxy properties

We perform our own global and local photometry for distant parent galaxies on SNLS images, and for intermediate distance and nearby host galaxies on SDSS images.

Regarding parent galaxies coming from the SDSS survey, we make use of the tremendous DR12 legacy[7] providing uniform, well-calibrated images in *ugriz* bands of more than 31600 square degrees in the sky, comprising the North Galactic Cap and 3 stripes in the South Galactic Cap. The DR12 release observed about 940000 individual fields resulting in images of size 1361×2048 with pixels subtending 0.396 square arcsec on the sky and a median PSF FWHM of 1.3 arcsec. Those images are dubbed *single-epoch images* in the following. As a result of the SDSS DR7 release[8], all images from the Stripe 82 along the Celestial Equator in the Southern Galactic Cap have also been made available. This release contains a coaddition of 47 South strip and 55 North strip scans into a pair of runs in which objects are detected about 2 magnitudes

Table 1: Repartition of SNIa hosts galaxies in the different available SDSS images. The number between parenthesis corresponds to the situation for which quality cuts are applied.

	SNLS	SDSS	low-redshift surveys
Stacks	–	214 *(118)*	1 *(1)*
Single-epoch	–	77 *(31)*	77 *(66)*
Sub-Total	**346** ***(225)***	**291** ***(149)***	**78** ***(67)***
Total	**715** ***(441)***		

deeper than in any individual Stripe 82 scans. The corresponding images are refered to as *stacks* in the following text. Stacked images are going deeper in magnitude and allow the detection of more objects. We will use them whenever possible. The repartition between stacks and single-epoch images is represented in Table 1.

All images are observed with `SExtractor`[9], considering different blending parameters for low redshift and intermediate redshift supernovæ (the limit is set at $z = 0.05$) in order to better isolate large galaxies. The galaxy having the largest overlap between a given SNIa location and the `SExtractor` segmentation map is defined as the parent galaxy of the supernova. Therefore, the *global* photometry corresponds to the flux integrated in the ellipse associated to the host galaxy using an `Astropy` tool. On the other hand, the *local* photometry is computed with the same tool, inside a radius of proper size 3 kpc. The local photometric radius goes from ~ 1.4 pixel at the highests redshifts to ~ 66 pixels for very low redshift supernovæ.

In order to derive global properties of galaxies such as metallicity, age, color, stellar mass or star formation rate starting from a set of observed magnitudes m_f, we can fit galaxies photometric measurements to a mass-dependent model. `PEGASE`[10] is one such model. It constructs an artifical spectrum based on the observed magnitudes of an object at fixed redshift z and compare it to the `PEGASE` library. With a χ^2 minimization, a model spectrum is found giving all galaxy properties, including stellar masses. The masses are measured in units of $\log_{10} M_\odot$, and to a precision of 9.3% for SNLS, 5.5% for the SDSS survey and 4% for the fraction of hosts of the low-redshift sample for which we have *ugriz* photometry. The `PEGASE` fit takes into account extinction from the Milky Way. To compute rest-frame colors integrated in U and V spectral bands, supposedly good estimates of stellar formation, we use our own template library. Rest-frame $U - V$ colors are measured with 4.7% precision with SNLS, 3.6% and 3.2% respectively for the SDSS survey and the nearby supernova sample.

4 Analysis

To ensure the quality of the correlation we aim at studying, supernovæ host galaxies and the measure of local photometry around the explosion region must satisfy certain conditions. In particular, we make sure that type Ia supernovæ are well enough detected ($\sigma_{x_1} < 0.5$), and that local photometry is well defined ($\sigma_u^{\rm local} < 1$, $\sigma_{g,r,i,z}^{\rm local} < 0.5$). Those cuts allow us to keep about 60% of the whole sample, leaving **225** host galaxies coming from the SNLS survey, **149** from the SDSS and **67** from low redshift surveys (see also Table 1).

We perform both local and global photometry for the full sample corresponding to 715 type Ia supernovæ and compare both quantities after quality cuts are applied. We find on average good correlation between local and global $U - V$ rest-frame colors but we also observe that this correlation depends on the distance to the galactic centre. For a supernova exploding far away from the centre, the region close to the explosion is seen bluer than its host. Conversely, if the explosion region is close to the galactic centre, the local color is redder than the whole galaxy. A few visual examples on SDSS images are shown on the right panel of Figure 1. From this study, we confirm the fact that the local information is dependent on the galaxy size, on the distance between the supernova explosion region and the galactic centre, but also on redshift. Those

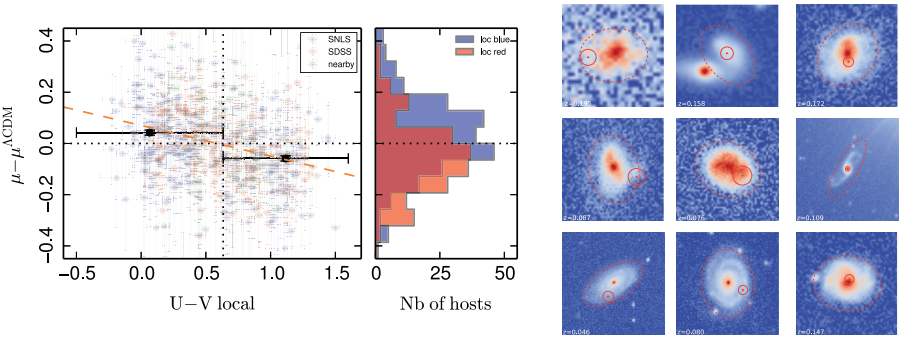


Figure 1 – **Left:** correlation between local $U-V$ color and Hubble diagram residuals for all surveys. The separation between color bins is drawn as the vertical dotted black line. **Right:** examples of g-band images around host galaxies. The local radius is shown as the red solid circle, the host ellipse as the dashed red line.

subtle effects are not yet taken into account when correcting for the supernova light-curve.

We therefore correlate local and global $U-V$ color, but also host galaxy stellar mass estimated from the observed global magnitudes, to Hubble diagram residuals ($\delta = \mu^{\rm obs} - \mu^{\Lambda\rm CDM}$ after light-curve corrections). For that purpose, we assume that the color distribution is bimodal, thus we fit the separation between bins position. When all surveys are combined, we find that the difference between observed distance moduli for the two *local* color bins (separated at $U-V=0.63$) is $\Delta\mu^{\rm obs} = 0.100 \pm 0.014$, corresponding to a 7.1σ significance. Applying the same method to our *global* color distribution, we find the bin separation at $U-V=0.78$ and obtain $\Delta\mu^{\rm obs} = 0.091 \pm 0.016$ (5.8σ). Regarding host stellar mass, the bin separation is set at $10^{10} M_\odot$ since there is no possible bimodal fit. With this value, we get $\Delta\mu^{\rm obs} = 0.079 \pm 0.015$ (5.4σ). The increasing significance when going from global to local variables is valid for the whole sample, as well as for its low redshift part or its high redshift part.

5 Conclusion

We present the first analysis on the local environment of type Ia supernovæ spanning a wide redshift range and significantly increasing the sample size. There is a strong hint at the 7σ level that the remaining luminosity variations in Hubble diagram with type Ia supernovæ can be significantly reduced taking into account local properties, such as the local star formation rate traced by $U-V$ rest-frame color. In the future, significantly decreasing the luminosity variations in supernovæ samples will improve their ability to constrain the dark energy equation of state and will make them a major cosmological probe in the context of the LSST survey.

References

1. S. Perlmutter *et al*, *ApJ* **517**, 565 (1999).
2. B. P. Schmidt *et al*, *ApJ* **507**, 46 (1998).
3. M. Betoule *et al*, *AAP* **568**, A22 (2014).
4. M. Sullivan *et al*, *MNRAS* **406**, 782 (2010).
5. M. Rigault *et al*, *ApJ* **802**, 20 (2015).
6. D. O. Jones, A. Riess *et al*, *ApJ* **812**, 31 (2015).
7. S. Alam *et al*, *ApJS* **219**, 12 (2015).
8. K. N. Abazajian *et al*, *ApJS* **182**, 543 (2009).
9. E. Bertin, S. Arnouts, *A&AS* **117**, 393 (1996).
10. M. Fioc, B. Rocca-Volmerange, *A&A* **326**, 950 (1997).

SUGAR : WHEN SPECTRA HELP STANDARDIZING SUPERNOVAE

E. Gangler & P.-F. Léget
Laboratoire de Physique Corpusculaire de Clermont-Ferrand 4, Avenue Blaise Pascal
F-63178 Aubière Cedex, France



Type Ia supernovae (SNIa) have now a long track record of producing strong constraints on cosmological parameters, and are expected to play still an important role in future stage IV experiments such as LSST. However, our understanding of their variability has gone few alterations through the years: popular spectral energy density (SED) models like SALT-II for instance still describe supernovae as depending mostly on 2 parameters. They however do not reflect the observed spectral diversity of Type Ia supernovae. With the help of the Nearby Supernova Factory data, we revisit the spectral diversity of the SNIa to build a novel SED model, SUGAR (Supernovae Useful Generator And Reconstructor). We will present the derivation of the model, and discuss the perspectives it opens for supernova standardization.

1 Introduction

The cosmological use of Type Ia Supernova (or SNIa) assumes that their luminous flux contain sufficient information in order to reliably deduce their distances. Remarkably, the correction scheme designed in 1998[1] is still in use, one of the modern version being the SALT2 parametrization[2]. The latest refinement come from the introduction of a rather crude correction linked to the mass of host galaxies[3], and can be considered as an acknowledgement that our understanding of SNIa is far from complete. In order to improve the situation, we opt to refine the description of the supernova SED employed to extract the supernovae parameters which will be used in the cosmological corrections. This implies to identify the meaningful parameters affecting the supernova variability, as well as training the model on data which will track precisely enough the variations within the SED.

The data coming from the Nearby Supernova Factory[5] collaboration are well suited for this analysis. Between 2004 and 2013, the SNIFS instrument[6] screened 1123 supernovae, out of which we followed 234 SNIa with an average of 14.9 epochs, and which satisfied photometric quality cuts. This amounts to a total of 3462 spectra with a spectral coverage of 330 – 970 nm and a resolution of 0.565 to 0.754 nm. The photometric precision is of the order of 0.03 mag on synthetic broad-band photometry, with a residual color effect of 0.01 mag[7].

2 Deriving an SED model

With on average 35100 measurements per supernova, some dimensional reduction is needed to derive the most meaningful synthetic quantities describing a given SNIa. Our approach is to perform this reduction in 2 steps: first, we extract a set of specific quantities from supernova spectra called spectral indicators, and inspired by the physics of the line formation. In a second step, we use a dimension reduction technique in order to produce a restricted set of input data, on which the model is trained.

2.1 Selection of spectral indicators

For this analysis, we restricted ourselves to spectral indicators computed at the supernova maximum light (in B band). At this phase, the spectrum can be interpreted in terms of absorption lines over a complex continuum resulting from non local thermodynamics equilibrium physics. We define a set of 13 spectral indicators independent from reddening by dust and present on all supernovae: 9 pseudo-equivalent width and 4 line velocities. To further reduce the dimension, principal component analysis (PCA) is a standard technique. As the uncertainties on spectral indicator measurements are not negligible with respect to their spread, we have however to apply a full treatment where we distinguish natural dispersion from measurement noise. It relies on maximizing the full likelihood of the spectral indicator distribution assuming gaussian statistics and employing expectation-maximization factor analysis formalism [8].

The results exhibit that 3 eigenvectors dominate the intrinsic diversity of SNIa as measured by the spectral indicator space, explaining 71.0% of the observed variance, while the noise explains 13.9% of it. Figure 1 represents the correlation between spectral indicators and the first eigenvectors, which allows to attempt a physical interpretation. The first eigenvector represents a coherent correlation between equivalent widths. The second vector exhibit the independent influence of Ca H&K line as already observed by previous works [9] as well as the corresponding influence on line velocities. The third vector exhibits some anticorrelations between Si equivalent width and velocities, which is expected as PCA tends to orthogonalize vectors and the first vector exhibits a correlation. One has to be careful about attempting physical interpretations of this third vector however.

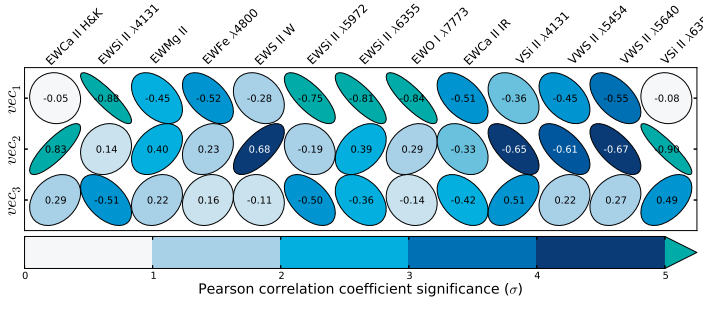


Figure 1 – Interpretation of the 3 first eigenvectors in terms of the underlying spectral indicators

2.2 The SUGAR SED model

The SED model in magnitude $M(\lambda, t)$ then takes the linear expression

$$M(\lambda, t) = M_0(\lambda, t) + \sum_{i=1}^{3} \alpha_i(\lambda, t) q_i + A_V C_L(\lambda) + \Delta_M \quad (1)$$

where $M_0(\lambda, t)$ is the average spectrum at wavelength λ and phase t, α_i the model components corresponding to the variations along the 3 axes defined by eigenvectors, q_i the coordinates in the eigenvector space, A_V the exctinction in V band and $C_L(\lambda)$ a color law. Δ_M is a flux normalization constant allowing to have a modelization independant from the underlying cosmology.

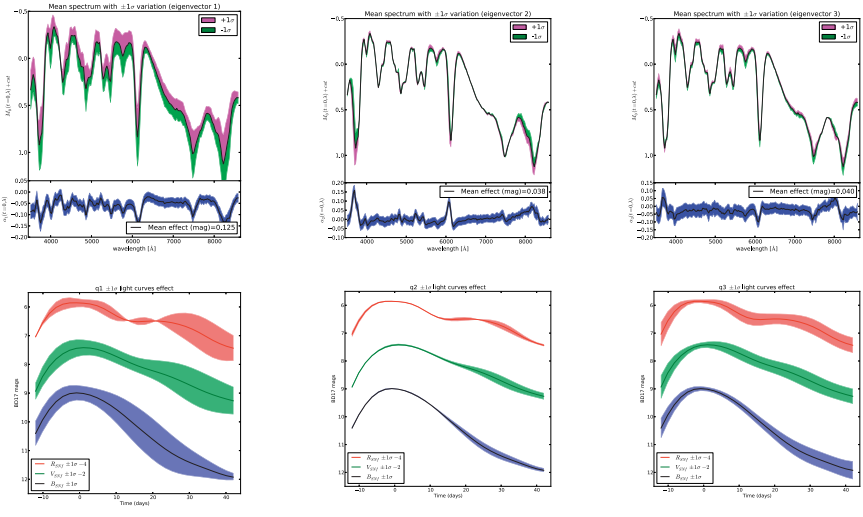


Figure 2 – Spectral and light-curve variation induced by each of the 3 eigenvectors (from left to right). Upper panels exhibit the spectral components considered at maximum light, the lower panels represent the effect integrated in B,V,R synthetic broad band. The shaded areas correspond to $\pm 1\sigma$ variation around the mean value for each q_i parameter.

The resulting model components α_i are represented on figure 2. The first component describes the well known effect of the stretch: fainter supernovae have narrower light-curves in B band, while exhibiting deeper spectral troughs. The second component exhibits a spectral behavior liking together Ca lines, both H&K and the IR triplet, and the Si II 6355 Å line. While having marginal effects on the lightcurves, which explains why this component is not identified by photometricly trained models like SALT2, the inclusion of this component leads to a smooth color law compatible with a CCM law [10] as shown on figure 3. The inclusion of the third vector is a new finding from this analysis: while probably having little physical interpretation, the inclusion of this component exhibits a net effect on the light-curves, with a substantial difference with respect to vector 1 in the R band.

The model as written can also be employed to fit arbitrary supernovae with spectral data, without having to resort on spectral indicator computation. When comparing the spread of data points in synthetic photometry with respect to the underlying model, SUGAR exhibits a consistent improvement with respect to SALT2 in B,V,R, with for instance a normalized absolute deviation going from 0.051 mag in V with SALT2 to 0.035 with SUGAR, for a limit coming from calibration uncertainties estimated at 0.030 mag. After extracting the supernovae properties q_i, A_v and Δ_M, it is possible to perform a Hubble fit in the same way as it is done with SALT2, but with 2 additional components. The resulting description improves by 15% the dispersion of the residuals.

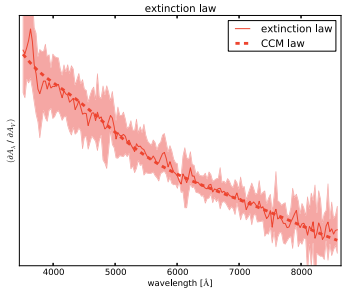


Figure 3 – Spectral color law derived from the model fit, and the associated error bar obtained by jackknifing. In dashed-line, the best-fit Cardelli law. The actual value of R_V is blinded.

3 Concluding remarks

As written, the SUGAR model extends over the SALT2 model with the addition of 2 new components, motivated by a through analysis of spectral variation at maximum light. It confirms that color is compatible with extinction by dust. The model can be employed for supernova simulations, providing a richer variation space than current simulations. It can also be employed as a fitter whenever calibrated spectral data are available, leading to improved results with respect to the state of the art. As one of the vector component has a clear effect on broad band magnitudes, this opens the perspective to recover it from a photometric fit. This will however be difficult to perform for the second component, which may remain as a systematic source of uncertainty for precision cosmology.

As scrutinizing environmental effects of SNIa has become a key to detect new sources of variations, one of the study to be conducted now is to check how the known environmental effects will be affected by the inclusion of the 2 new components in the standardization. The influence of the new parametrization on the w parameter of the dark energy equation of state is also a promising perspective. Lastly, our initial assumption was that the study of spectral variations would lead to dramatic improvements in the standardization. The fact that since many years of study the improvements are marginal at best suggests that an important source of uncontrolled variation does not originate in the physics of the explosion. One intriguing possibility could be that our description of the extinction with a single color law fails to reproduce the observed diversity of magnitudes.

References

1. R. Tripp, *A&A* **331**, 815 (1998).
2. J. Guy *et al*, *A&A* **466**, 11 (2007)
3. A. Conley *et al*, *ApJS* **192**, 1 (2011)
4. M. Rigault *et al*, *ApJ* **802**, 20 (2015)
5. G. Aldering *et al*, in *SPIE Conf. Ser.* 4836, eds. J.A. Tyson and S. Wolff, 61 (2002).
6. B. Lantz *et al*, in *SPIE Conf. Ser.* 5249, eds. L. Mazuray, P. J. Rogers, and R. Wartmann, 146 (2004).
7. R. Pereira *et al A&A* **554**, 27 (2013)
8. Z. Ghahramani and G. E. Hinton *Technical Report* CGR-TR-96-1 (1996)
9. N. Chotard *et al*, *A&A* **529**, 4 (2011)
10. J. Cardelli *et al*, ApJ **345**, 345 (1989)

ON THE DARK CONTENTS OF THE UNIVERSE: A EUCLID SURVEY APPROACH

ISAAC TUTUSAUS, BRAHIM LAMINE, ALAIN BLANCHARD
Université de Toulouse, UPS-OMP, CNRS, IRAP, F-31028 Toulouse, France

In this work we study the consequences of allowing non pressureless dark matter when determining dark energy constraints. We show that present-day dark energy constraints from low-redshift probes are extremely degraded when allowing this dark matter variation. However, adding the CMB we can recover the $w_{DM} = 0$ case constraints. We also show that with the future Euclid redshift survey we expect to largely improve these constraints; but, without the complementary information of the CMB, there is still a strong degeneracy between dark energy and dark matter equation of state parameters.

1 Introduction

The ΛCDM cosmological model is the current standard model in cosmology thanks to its good phenomenological fit to cosmological data like SNIa[1], BAO[2] or CMB[3]. However, neither a dark matter, nor a dark energy candidate have been experimentally detected, so there is still room to study models differing from this ideal case. There has been a great effort in studying models accounting for different dark energy components than a cosmological constant[3] and there has also appeared some studies of models accounting for variations on the dark matter sector[4]. We propose here to study which are the consequences on the dark energy constraints when considering non pressureless dark matter. For this, we use present-day data and we forecast the precision of the Euclid redshift survey.

2 Dark content(s) of the Universe

In this section we use present-day data from type Ia supernovae (SNIa), the baryonic acoustic oscillations (BAO) and the cosmic microwave background (CMB) to constraint cosmological models with perturbations in both the dark matter and the dark energy sector. In all this work a flat Universe is assumed and we consider a Robertson-Walker metric with Friedmann-Lemaître dynamics.

2.1 Method and data samples

In the following we use compressed versions of the different probes likelihood, since they have been shown to be faster and easier to evaluate and still remain accurate for the most common cases.

In order to determine the constraints on the parameters under study we use the common χ^2 minimization procedure and, since we are combining essentially independent probes, we compute the total χ^2 function as the sum of the χ^2 for each probe.

For the SNIa data we use the compressed likelihood of the JLA sample from Betoule *et al.*[1]. Corresponding the BAO data, we use the measurements of the ratio of the comoving sound horizon at the redshift of baryon drag to the BAO distance scale at three different redshifts: $z = 0.106$[6], 0.35[7], 0.57[8], following Planck Collaboration XVI[9]. For the CMB probe we use the values of the so-called reduced parameters (the scaled distance to recombination R, the angular scale of the sound horizon at recombination ℓ_a and the reduced density parameter of the baryons ω_b) provided by the Planck 2015 data release[3], where temperature-temperature fluctuations and the low-ℓ Planck temperature-polarization likelihoods have been used.

2.2 Models

In the standard ΛCDM model there exist a dark matter component with equation of state $P = w_{DM}\rho$, $w_{DM} = 0$, and a dark energy component with equation of state $P = w_{DE}\rho$, $w_{DE} = -1$. In this work we consider that the dark equation of state parameters w_{DM} and w_{DE} are constant but may differ from their standard value. This leads to the Friedmann-Lemaître equation:

$$\frac{H^2(z)}{H_0^2} = \Omega_r(1+z)^4 + \Omega_b(1+z)^3 + (\Omega_m - \Omega_b)(1+z)^{3(1+w_{DM})} + (1-\Omega_r-\Omega_m)(1+z)^{3(1+w_{DE})}\,. \quad (1)$$

We consider three different models: the wCDM model, consisting of standard cold dark matter ($w_{DM} = 0$) and dark energy with constant equation of state parameter($w_{DE} = w$); the ϵCDM model, with constant dark matter equation of state parameter ($w_{DM} = \epsilon$) and a cosmological constant ($w_{DE} = -1$); and the ϵwCDM model, with both dark matter and dark energy constant equation of state parameters ($w_{DM} = \epsilon$ and $w_{DE} = w$). Since in the ϵCDM and ϵwCDM models we are modifying the matter component at the CMB era, we must adapt the computation of the reduced parameters by changing the dark matter density parameter to an effective dark matter density parameter: $\Omega_{DM}^{eff} = \Omega_{DM}(1 + z_{CMB})^{3\epsilon}$.

2.3 Results

The obtained constraints for the cosmological parameters[a] of the different models are shown in columns 1 and 3 of Table 1.

For the wCDM model our results are very similar to those of Betoule *et al.*[1]. Concerning the ϵCDM model we have obtained compatible results with Thomas *et al.*[4]. The values obtained for the ϵwCDM model are slightly worse than the ones obtained for the wCDM and the ϵCDM models due to the introduction of a new degree of freedom.

All the constraints for the proposed models are compatible with the ΛCDM model. However, two points worth to be mentioned: first of all, the CMB probe plays a crucial role here, since SNIa+BAO data alone cannot constraint ϵ and w at the same time. And secondly, the constraints on dark matter and dark energy are not completely independent (see the left panel of Fig. 1); therefore, all the assumptions done in one of the sectors may influence the constraints obtained in the other one.

3 Dark content(s) of the Universe: a Euclid forecast

In this section we study the models departing from the ΛCDM ideal case presented by looking at the expected precision from a galaxy power spectrum Euclid[b] survey forecast. In this work we restrict ourselves to the spectroscopic Euclid redshift survey. Adding the photometry and

[a] The baryon density parameter is not shown because either it is fixed to the Planck 2015[3] value (column 1) or it is very well constrained close to it (column 3). The radiation contribution is fixed following Komatsu *et al.*[5].

[b] http://www.euclid-ec.org

the weak lensing probe we can expect even better constraints than the ones presented in this work.

3.1 Method

In order to perform the forecast, we use a Fisher matrix formalism in a parameterized cosmological model, considering the Hubble parameter and the angular-diameter distance as observables.

The Fisher matrix in a given redshift interval is given by[10]:

$$F_{ij} = \int_{-1}^{1} \int_{k_{min}}^{k_{max}} \frac{\partial \ln P_{obs}(k,\mu)}{\partial p_i} \frac{\partial \ln P_{obs}(k,\mu)}{\partial p_j} V_{eff}(k,\mu) \frac{2\pi k^2 dk d\mu}{2(2\pi)^3} \,, \tag{2}$$

where V_{eff} is the effective volume of the survey (redshift range: 0.7-2.1, area: 15000 sq. deg., number of galaxies: $50{\times}10^6$), p_i and p_j stand for the observables and P_{obs} is the observed power spectrum, which differ from the matter power spectrum because of the biasing of galaxies and their velocity field[11]. We consider the bias given in Amendola *et al.*[12]: $b(z) = \sqrt{1+z}$. We assume that there is no extra noise in this power spectrum relation. We follow Seo & Eisenstein[11] in cutting the integral of eq. (2) at k_{min} and k_{max} to keep the linear part of the power spectrum. Also, we multiply the integrand of the Fisher matrix by an exponential suppression $\exp(-k^2\mu^2\sigma_r^2)$, with $\sigma_r = c\sigma_z/H(z)$, in order to take into account the redshift error $\sigma_z = 0.001(1+z)$ of the galaxy survey. Once we obtain the Fisher matrix for the observables we propagate it to the parameters under study following Wang *et al.*[13]. The final Fisher matrix is obtained as the sum of the different matrices for the different redshift bins.

3.2 Results

The obtained constraints from the forecast on the cosmological parameters[c] of the different models are shown in column 2 of Table 1. The constraints obtained combining the forecast with the CMB probe are shown in column 4 of Table 1. We have used the values obtained in column 3 (SNIa+BAO+CMB) as fiducial model for the forecast.

For the wCDM and the ϵCDM models, the obtained constraints from the forecast alone are extremely better than present-day low-redshift constraints (SNIa+BAO). When adding the CMB to the forecast we obtain constraints between a factor 2 and 6 more precise than the current ones. Given that these results are only for the galaxy clustering probe restricted to the linear scale we expect even better constraints from the full exploitation of the future Euclid data. Concerning the ϵwCDM model, the results obtained with the forecast alone are extremely better than SNIa+BAO data (which do not lead to significant constraints), but they still show a degradation on the dark energy constraints due to the dark matter freedom. When adding the CMB we recover constraints similar to the ones obtained for the wCDM and the ϵCDM models (see right panel of Fig. 1).

4 Conclusions

We have examined the consequences on the obtained constraints of dark energy properties when the pressureless dark matter assumption is relaxed (assuming constant equation of state parameter for both dark matter and the dark energy). We have found that for low redshift present-day data this freedom in the dark matter equation of state parameter completely degrades the constraints on the dark energy sector. When adding the CMB we almost recover the pressureless dark matter case constraints thanks to the tight constraint on the dark matter equation of state parameter from the CMB. We have also seen that the galaxy clustering probe of the Euclid survey will perform extremely better than low redshift present-day data, but in order to reach

[c]The baryon density parameter is not shown because either it is fixed to the Planck 2015[3] value (column 2) or it is very well constrained close to it (column 4). The radiation contribution is fixed following Komatsu *et al.*[5].

the same precision as in the pressureless dark matter case we need to add the CMB. This strong role from the CMB probably comes from assuming a constant equation of state parameter up to the CMB redshift, but focusing in low redshift data or general variations of the dark matter sector we will have to deal with the observed dark matter and dark energy equation of state parameter degeneracy.

Table 1: Cosmological parameter constraints for the different models and the different probes considered. The errors are given at the 1-σ confidence level on 1 parameter ($\Delta\chi^2 = 1$). The dash in the ϵwCDM model using SNIa+BAO data stands for the extreme degeneracies which do not allow to obtain significant constraints on the cosmological parameters.

		SNIa+BAO	Euclid GC	SNIa+BAO+CMB	Euclid GC + CMB
wCDM	Ω_m	≤ 0.28	0.299 ± 0.022	0.299 ± 0.012	0.2990 ± 0.0021
	w	-0.72 ± 0.25	-0.995 ± 0.026	-0.995 ± 0.054	-0.994 ± 0.022
	H_0	53.0 ± 13.3	68.70 ± 0.45	68.7 ± 1.3	68.68 ± 0.40
ϵCDM	Ω_m	≥ 0.31	0.301 ± 0.010	0.301 ± 0.014	0.3001 ± 0.0030
	ϵ	-0.49 ± 0.44	-0.0003 ± 0.0092	-0.0003 ± 0.0011	-0.00024 ± 0.00066
	H_0	50.00 ± 3.83	68.60 ± 0.27	68.6 ± 1.2	68.62 ± 0.12
ϵwCDM	Ω_m		0.301 ± 0.041	0.301 ± 0.014	0.3011 ± 0.0038
	w		-1.01 ± 0.13	-1.010 ± 0.077	-1.010 ± 0.023
	ϵ	–	0.000 ± 0.046	-0.0004 ± 0.0016	-0.00045 ± 0.00066
	H_0		68.6 ± 1.0	68.6 ± 1.3	68.60 ± 0.44

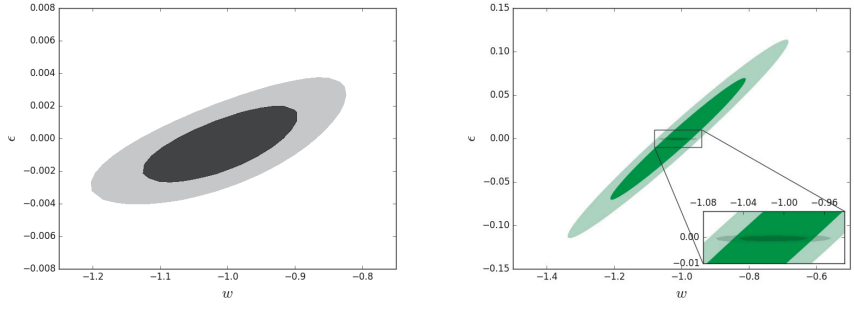


Figure 1 – Confidence contours at 68% and 95% confidence level for the w and ϵ parameters of the ϵwCDM model. Left panel: SNIa+BAO+CMB present-day data. Right panel: Euclid galaxy clustering forecast (green) and Euclid galaxy clustering+CMB (black).

References

1. M. Betoule *et al.*, Astron. Astrophys. **568**, A22 (2014).
2. L. Anderson *et al.*, Mon. Not. Roy. Ast. Soc. **441**, 24 (2014).
3. Planck Collaboration 2015, arXiv:1502.01590 [astro-ph.CO]
4. D. B. Thomas *et al.* 2016, arXiv:1601.05097 [astro-ph.CO]
5. E. Komatsu *et al.*, ApJS **192**, 18 (2011).
6. F. Beutler *et al.*, Mon. Not. Roy. Ast. Soc. **416**, 3017 (2011).
7. N. Padmanabhan *et al.*, Mon. Not. Roy. Ast. Soc. **427**, 2132 (2012).
8. L. Anderson *et al.*, Mon. Not. Roy. Ast. Soc. **427**, 3435 (2012).
9. Planck Collaboration, Astron. Astrophys. **571**, A16 (2014).
10. M. Tegmark, *Phys. Rev. Lett.* **79**, 3806 (1997).
11. H. Seo & D. J. Eisenstein, Astrophys. J. **598**, 720 (2003).
12. L. Amendola *et al.*, Liv. Rev. in Rel. **16**, 6 (2013).
13. Y. Wang *et al.*, Mon. Not. Roy. Ast. Soc. **409**, 737 (2010).

DARK ENERGY CONSTRAINTS FROM THE ESPRESSO FUNDAMENTAL PHYSICS GTO

A. C. O. LEITE[a,b,c], C. J. A. P. MARTINS[a,b,c], P. MOLARO[d], D. CORRE[e]
[a] *Centro de Astrofísica, Universidade do Porto, Rua das Estrelas, 4150-762 Porto, Portugal*
[b] *Instituto de Astrofísica e Ciências do Espaço, CAUP, Rua das Estrelas, 4150-762 Porto, Portugal*
[c] *Faculdade de Ciências da Universidade do Porto, Rua do Campo Alegre, 4150-007 Porto, Portugal*
[d] *INAF-Osservatorio Astronomico di Trieste, Via G.B. Tiepolo 11, I-34143 Trieste, Italy*
[e] *Laboratoire d'Astrophysique de Marseille - LAM, Université d'Aix-Marseille & CNRS, UMR7326, F-13388 Marseille, France*

ESPRESSO is a high-resolution-ultra-stable spectrograph for the VLT, whose commissioning will start in early 2017. One of its key science drivers is to test the stability of fundamental couplings such as the fine structure constant with unprecedented accuracy and control of possible systematics. Specifically, a total of 27 nights of the ESPRESSO Consortium's guaranteed time observations (GTO) will be spent in testing the stability of the fine-structure constant and other fundamental couplings. A set of 14 priority optimal targets have been selected for the GTO period. In this contribution I present the forecasts of the impact that observations will have on fundamental physics and cosmology, focusing on dark energy constraints and further discuss the synergies with future supernova type Ia surveys.

1 Target list for ESPRESSO GTO on Fundamental Physics

ESPRESSO is a high-resolution-ultra-stable spectrograph that will be installed in VLT in early 2017 and will contribute to test the stability of fundamental couplings[1]. The Fundamental Physics Guaranteed time of observation (GTO) to this purpose will have 27 nights and a list of 14 "ideal" targets was put together. In order to achieve higher constrains on the variation of the fine structure constant, α, an ideal target should present simple and strong absorption features of transitions with high sensitivities to variations of α.

To select the list of targets for the GTO of ESPRESSO we considered previous measurements from UVES and Keck spectrographs and took into account the transitions not observed because of the shorter wavelength coverage of ESPRESSO. In Fig 1 this effect is illustrated in redshift coverage for transitions usually used to do variation of α measurements. In the same Figure each transition is colored by the corresponding sensitivity, q, on α variation. In order to have a sensitive measurement on α with a better control of systematics one should ensure to have at least one anchor, one blue and one red shifter, this sets Δq on a given system to be large.

We chose the targets able to be observed from the VLT site with a $\Delta q > 2000$ and a reported uncertainty of $\sigma_{\Delta\alpha/\alpha} < 5ppm$. This last criteria comes from the fact that simple spectra should have already produced measurement with statistically lower uncertainties. The 14 targets selected are presented in Table 1. The first measurement on the table doesn't fulfil the criteria, but is a system where proton to electron mass ratio and the T_{CMB} relation to redshift can also be measured. This fact makes this an interesting target to investigate the nature of the fundamental constants variation testing different theories where a relation between these three constants are predicted.[6] These type of measurements are important by themselves for testing

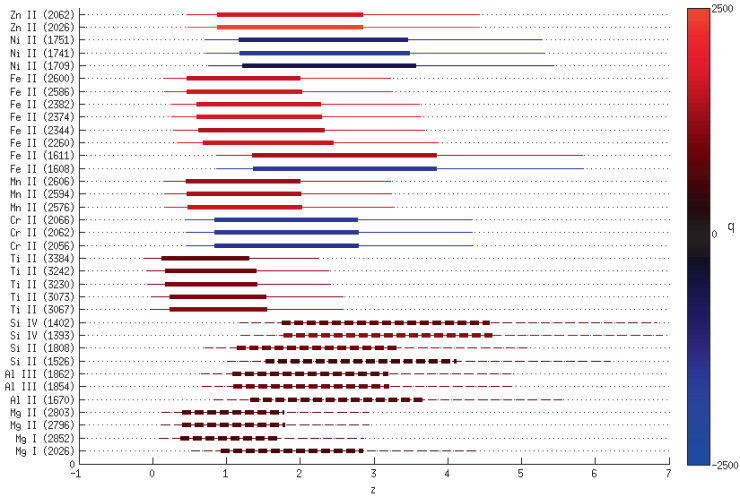


Figure 1 – Redshift coverage of ESPRESSO and UVES of common transitions used to do measurements of the variation of α. Thinner lines represent the coverage of UVES, the thicker part is representative of ESPRESSO's. The colour code is indicative of the q sensitivity parameter, each transition has the colour according to their shift to the blue or red on spectra and by how much. The dashed transitions correspond to anchors, i.e. transitions that don't shift much.

the stability of α but even a non-detection of variation can be used to constrain dark energy. In the next section we will describe the impact that this measurements can have in the study of the properties of Dark Energy

2 Forecasts on Dark Energy constraints

Our formalism to perform the forecast is described in Amendola et al.[7], to which we refer the reader for further details. We consider models for which the variation of α is linearly proportional to the displacement of a scalar field, and further assume that this field is a quintessence type field, i.e. responsible for the current acceleration of the Universe. We take the coupling between the scalar field and electromagnetism to be:

$$\mathcal{L}_{\phi F} = -\frac{1}{4} B_F(\phi) F_{\mu\nu} F^{\mu\nu}, \tag{1}$$

where the gauge kinetic function $B_F(\phi) = 1 - \zeta(\phi - \phi_0)$, $\kappa^2 = 8\pi G$ and ζ is a constant to be marginalized over. This can be seen as the first term of a Taylor expansion, and should be a good approximation if the field is slowly varying at low redshift. Then, the evolution of α is given by

$$\frac{\Delta\alpha}{\alpha} \equiv \frac{\alpha - \alpha_0}{\alpha_0} = \zeta\kappa(\phi - \phi_0)\,. \tag{2}$$

For a flat Friedmann-Lemaïtre-Robertson-Walker Universe with a canonical scalar field, $\dot{\phi}^2 = (1+w(z))\rho_\phi$, hence, for a given dependence of the equation of state parameter $w(z)$ with redshift, the scalar field evolves as

$$\phi(z) - \phi_0 = \frac{\sqrt{3}}{\kappa} \int_0^z \sqrt{1 + w(z)} \left(1 + \frac{\rho_m}{\rho_\phi}\right)^{-1/2} \frac{dz}{1+z}. \tag{3}$$

where we have chosen the positive root of the solution.

Table 1: List of the best measurements of the variation of the fine structure constant considering the wavelength coverage of ESPRESSO. Column 1 gives the quasar name; the redshifts of the absorption system are given in Column 2; Column 3 and 4 gives the value of the measurement and the correspondent uncertainty. The last Column gives the references for each measurement. Flagged measurements - * - mean that the measurement lost transitions due to the wavelength range of ESPRESSO

Name	z_{abs}	$\frac{\Delta\alpha}{\alpha}$ (10^{-6})	$\sigma_{\frac{\Delta\alpha}{\alpha}}(10^{-6})$	Ref.
J034943-381031	3.02	-27.9	34.2	[3]
J040718-441013	2.59	5.7	3.4*	[2]
J043037-485523	1.35	-4.0	2.3*	[2]
J053007-250329	2.14	6.7	3.5*	[2]
J110325-264515	1.84	5.6	2.6	[4]
J115944+011206	1.94	5.1	4.4*	[2]
J133335+164903	1.77	8.4	4.4	[2]
HE1347-2457	1.43	-21.3	3.6	[4]
J220852-194359	1.92	8.5	3.8	[2]
HE2217-2818	1.69	1.3	2.4	[5]
Q2230+0232	1.86	-9.9	4.9	[3]
J233446-090812	2.15	5.2	4.3*	[2]
J233446-090812	2.28	7.5	3.7*	[2]
Q2343+1232	2.43	-12.2	3.8*	[3]

From this, one can calculate the Fisher matrix to infer the precision on the measurement of w using standard techniques[7], obtaining from a set of observables and its uncertainties, the eigenvalues λ_i of the diagonalized Fisher matrix (ordered from best determined modes to worst ones) and the variance of the new parameters, $\sigma_i^2 = 1/\lambda_i$. To reconstruct the fiducial equation only the best determined modes are used.

We will consider three fiducial forms, presented in that same work, for the equation of state parameter: $w_c(z) = -0.9$, $w_s(z) = -0.5 + 0.5tanh(z - 1.5)$ and $w_b(z) = -0.9 + 1.3exp(-(z - 1.5)^{2/0.1})$). In what follows we will refer to these cases as the constant, step and bump fiducial models.

2.1 Results

We applied this Principal Component Formalism to the 14 Targets on α and a set of future Sna Ia Surveys. For the α measurements we assumed two different scenarios: **Baseline**, in which we use measurements with uncertainty of $\sigma_{\Delta\alpha/\alpha} = 0.6ppm$; and **Ideal** in which the measurements are set to have uncertainties of $\sigma_{\Delta\alpha/\alpha} = 0.2ppm$. For Type Ia supernovas we consider the following datasets: **LOW**: A low-redshift sample, of 3000 supernovas uniformly distributed in the redshift range $0 < z < 1.7$, with an uncertainty on the magnitude of $\sigma_m = 0.11$; **MID**: An intermediate redshift sample, of 1700 supernovas uniformly distributed in the redshift range $0.75 < z < 1.5$ and the same σ_m as before.

We assumed 7 redshift bins with 2 α measurements each for the reconstructions with the ESPRESSO GTO Target List (**GTO**), and for the type Ia supernovas we used 20 redshift bins in the covered redshift. In order to quantify gains in sensitivity for each case using the PCA, we counted the number of modes with uncertainty under 0.3. This value is somewhat arbitrary, but serves our purpose comparing this number on different combinations of future datasets.

We present in Table 2 the number of modes with uncertainty under 0.3 for the reconstruction of the different fiducial parametrizations with the 14 Target List for ESPRESSO GTO and the combination with the **LOW** and **MID** Supernovas Type Ia samples. On its own, the reconstruction with the Target List for the GTO is not good compared with the one's from the Supernova data. It should be pointed that the reconstruction using Supernova only gain when

Table 2: The table indicates how many modes have an error below the threshold value $\sigma = 0.3$ considering the constant, step and bump fiducial parametrizations in the baseline and ideal scenarios for the uncertainty on the variation of α measurements expected for ESPRESSO. SNAP, and SNAP+MID are not affected by the baseline vs ideal scenario, since that refers to the uncertainties on α measurements

	Baseline			Ideal		
	constant	step	bump	constant	step	bump
GTO	1	-	1	3	1	2
LOW	4	4	4	4	4	4
GTO + LOW	4	4	4	9	4	5
LOW + MID	4	4	5	4	4	5
GTO + LOW + MID	4	4	5	9	4	6

combined with the GTO target list, and since they probe different redshifts this combination allows to get the behaviour of the equation of state of Dark Energy from redshift 0 to 3.

3 Conclusion

The ESPRESSO target selection for the GTO has been put together, the exploitation of the different modes of operation of the instrument will be explored in the future. The classical way to study the equation of state parameter is using type Ia Supernovas, but they are for now limited in redshift ($z \sim 1.7$) using fine structure constant measurements allows to parametrize it to higher redshifts, and in particular, just from the GTO from ESPRESSO we will be able to do it till $z \sim 3$. Previous work[7,8,9] using the PCA-based forecast technique showed that the reconstruction of dark energy equation of state has improvements when combining the Type Ia Supernovas with measurements on the stability of fine-structure constant. These 14 measurements expected from the GTO of ESPRESSO will not be able to reconstruct the equation of state and distinguish models in a convincing manner by themselves. However, improvements can be achieved by combining these with Supernova type Ia data.

Acknowledgments

This work was done in the context of grant PTDC/FIS/111725/2009 from FCT (Portugal). A.C.L. is supported by the Gulbenkian Foundation through *Programa de Estímulo à Investigação 2014*, grant number 2148613525 and by an FCT PD Program PHD::SPACE(PD/000402012). C.J.M. is also supported by an FCT Research Professorship, contract reference IF/00064/2012, funded by FCT/MCTES (Portugal) and POPH/FSE (EC).

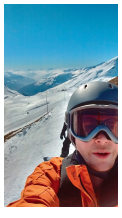
References

1. F. Pepe et al., The Messenger 153, 6 (2013).
2. J.A. King, PhD Thesis (UNSW, 2011), arXiv:1202.6366.
3. M.T. Murphy, Ph.D. Thesis, University of New South Wales (2002).
4. P. Molaro, D. Reimers, I.I. Agafonova & S.A. Levshakov, European Physical Journal Special Topics, 163, 173 (2008).
5. P. Bonifacio, et al., Astronomische Nachrichten, 335, 83 (2014).
6. M.C. Ferreira, O. Frigola, C.J.A.P. Martins, A.M.R.V.L. Monteiro, J. Sol, Phys. Rev. D89, 083011 (2014).
7. L. Amendola et al., Phys. Rev. D 86, 063515 (2012).
8. A.C.O. Leite et al., Phys. Rev. D 90, 063519 (2014).
9. A.C.O. Leite and C.J.A.P. Martins, Phys. Rev. D 91, 103519 (2015).

WEAK LENSING WITH THE SQUARE KILOMETRE ARRAY

I. HARRISON

Jodrell Bank Centre for Astrophysics, School of Physics & Astronomy, The University of Manchester, Manchester M13 9PL, UK



The Square Kilometre Array (SKA) will achieve the necessary galaxy number densities over large areas to be competitive with other Stage IV weak lensing cosmology surveys such as *Euclid*, LSST and WFIRST-AFTA. We identify and summarise the unique and potentially very powerful aspects of surveys facilitated by the SKA which can solve major challenges in the field of weak lensing. We show parameter constraint forecasts for both SKA weak lensing alone and also how cross-correlating shear maps between radio and optical wavebands can complement and enhance these constraints by being more robust to potential systematics. We also describe a sophisticated catalogue-level simulation pipeline for SKA weak lensing experiments and detail its use for optimising the observing strategy for cosmology, finding optimal constraints from a $\sim 10^3\,\mathrm{deg}^2$ survey at $\sim 1\,\mathrm{GHz}$.

1 Introduction

Weak lensing cosmology[1] involves measuring the shapes of millions of distant ($z \sim 1$ and above) galaxies and averaging together their ellipticities to estimate the coherent shearing distortion caused by gravitational lensing. The resultant map of estimated shear gives a measurement of the total mass along the line of sight to the redshift of the source, making such cosmic shear studies excellent probes of structure abundance and physics which affects structure growth (such as the dark energy equation of state and its evolution). Previously, weak lensing has been the near-exclusive preserve of optical wavelength surveys, which are capable of detecting the necessary number density of sources n_{gal} on the sky to average over enough intrinsic shapes of galaxies and isolate the $\sim 1\%$ contribution from weak lensing. However, the mid-frequency dish array component of the Square Kilometre Array (SKA-MID)[a] in both its first phase (SKA1) and full (SKA2) guises will be capable of the necessary kind of wide, deep surveys at radio wavelengths. Here, we will describe the usfulness of such surveys to cosmology and exactly what such surveys may look like.

[a] `https://www.skatelescope.org/`

2 Radio Weak Lensing

Performing weak lensing cosmology at radio wavelengths carries a number of potential advantages[2]. From a source perspective, a higher median redshift z_m is expected and more information on potentially damaging intrinsic galaxy alignments (which can mimic cosmic shear) can be provided by both radio polarisation and resolved rotational velocity measurements. Radio interferometers themselves also carry the advantage of having highly deterministic and stable Point Spread Functions (PSFs), at frequencies high enough to not be affected by the ionosphere and access to significantly more of the sky when compared to optical experiments (the foreground of our galaxy is largely removed by lack of sensitivity to large scale emission). In addition, and potentially powerfully, many sytematic errors on the measured cosmic shear measured by radio interferometers will be uncorrelated with the systematics from optical imaging telescopes, meaning they will be supressed when the cross-correlation is taken.

3 Radio and Radio-Optical Forecasts

In Figure 1[3] we show Markov Chain Monte Carlo (MCMC) forecast constraints for weak lensing surveys conducted with Dark Energy Task Force (DETF) 'Stage III' (left) and 'Stage IV' (right) surveys on the matter clustering and abundance parameters σ_8 and $\Omega_{\rm m}$, showing representative SKA surveys (as defined in Table 1) alongside optical ones.

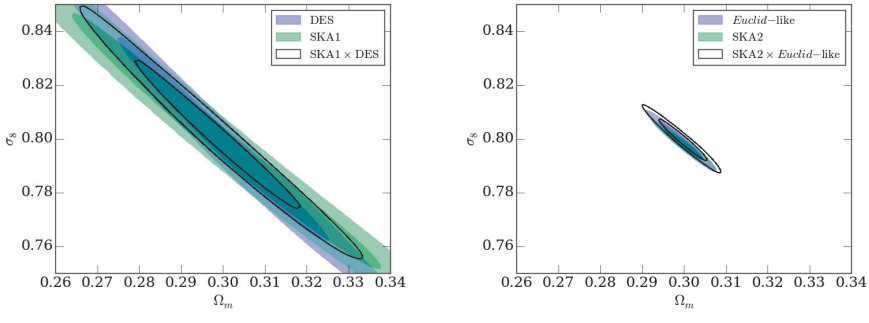


Figure 1 – MCMC forecasts for constraints from weak lensing only with Stage III (*left*) and Stage IV (*right*) radio, optical and radio-optical cross-correlation experiments on matter parameters.

Table 1: Parameters used in the creation of simulated data sets for the representative experiments considered here.

Experiment	$A_{\rm sky}$ [deg^2]	$n_{\rm gal}$ [arcmin^{-2}]	z_m
SKA1	5,000	2.7	1.1
Dark Energy Survey (DES)	5,000	12	0.6
SKA2	30,000	10	1.3
Euclid-like	15,000	30	0.9

In addition to the constraints formed from shear power spectra formed by cross-correlating shear maps made in each experiment individually, we also show those obtained by *cross*-correlation power spectra between experiments. For each experiment we divide sources into ten tomographic redshift bins and form the power spectra for each bin combination between experiments X, Y and bins i, j: $C_\ell^{X_i Y_j}$. For the filled coloured contours we use only information from correlations between bins from the same experiment; as can be seen, the SKA surveys are

capable of matching the optical. In addition, for the unfilled black contours we use only information from spectra which cross-correlate bins from different experiments. These cross-correlation spectra will be far more robust to systematics which are uncorrelated between wavebands, but do not significantly degrade the cosmological constraining power.

In Figure 2 we also show the constraints on the dark energy equation of state parameters w_0 and w_a from the two sets of experiments, again showing the competitiveness of SKA surveys and the comparable power of the radio-optical cross-correlation studies.

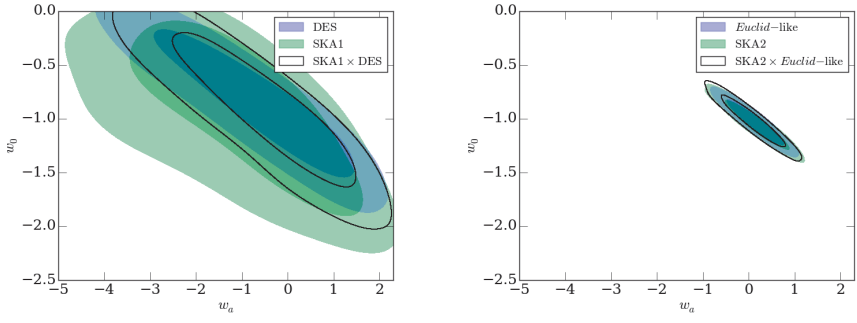


Figure 2 – Same as Figure 1 but for dark energy equation of state parameters.

4 Survey Optimisation

As well as the MCMC forecasts, we have also conducted catalogue-level simulations of SKA weak lensing surveys in order to quantify a number of effects[4]. We consider a number of different SKA configurations given by central observing frequency ν, image-plane PSF size $\theta_{\rm FWHM}$ (which may be tuned, at the expense of sensitivity, by differently weighting different interferometer array baselines), sky area $A_{\rm sky}$ and resultant sensitivity $S_{\rm rms}$. For a chosen configuration we generate a catalogue of galaxy fluxes, sizes and redshifts from the distributions in the S3-SEX simulation[5] and a measured shear including SNR-dependent errors from the shape measurement process. In addition, we include a simple model of ionospheric distortions and discount regions where the ionospheric PSF is larger than that of the instrument. This allows us to explore the sensitivity surface in the left of Figure 3 and convert it into measured tomographic power spectra, such as the left of Figure 3, and subsequently a cosmological figure of merit. We then optimise the survey strategy in order to best recover the power spectra and input cosmology.

The best results are achieved for a $5,000\,{\rm deg}^2$ survey in the lower third of Band 2 of the SKA correlator (centred at 1.4 GHz), corresponding to the constraints shown in the previous section. We see a weak trend in constraints with sky area down to $1,000\,{\rm deg}^2$, with significant decrease in cosmological power for smaller surveys, even with a fixed observing time giving greater depth.

5 Conclusions

We have explored the utility of radio weak lensing with the SKA, showing in particular the power of cross correlations between radio and optical surveys. In order to achieve this success, a number of areas require significant progress. Surveys on the pathfinders and precursors for the SKA will probe the properties of the star-forming galaxy populations expected to be used for radio weak lensing, their counts, sizes and polarisation properties. The relation of this to optical and near-Infra Red populations will also be important, both for the noise properties of cross-correlation surveys and in order to obtain redshift information for the radio galaxies (although this may also

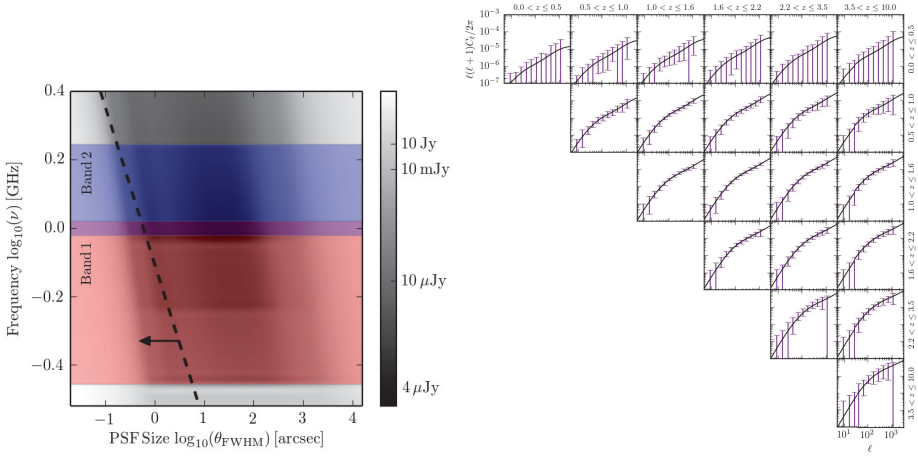


Figure 3 – *Left*: Sensitivity of the SKA1-MID array for a 10,000 hour $5,000\,\mathrm{deg}^2$ survey for different choices of observing frequency and image-plane PSF size. Parts to the left of the dashed line are not considered as the ionospheric PSF dominates. *Right*: The recovered power spectra for a survey at the centre of Band 2 with a 0.5 arcsec image plane PSF, which gives close-to-optimal recovery of the input spectra.

be obtained by novel sub-threshold spectroscopic techniques). In addition, significant work is required to solve the problem of inferring source shapes from interferometer data (which arrives in a poorly-sampled Fourier plane rather than pixelised in the image plane as from a CCD) – see the efforts of the radioGREAT challenge[b].

If these aspects can be understood sufficiently well, the use of radio and radio-optical cross-correlation surveys will maximise the potential of weak lensing experiments, allowing us to more closely approach the full precision available from the data and give the best chance possible of starting to understand the true physical nature of dark matter and dark energy.

Acknowledgments

We thank Michael L. Brown, Anna Bonaldi, Stefano Camera and Joe Zuntz for their collaboration. IH is supported by an ERC Starting Grant (grant no. 280127).

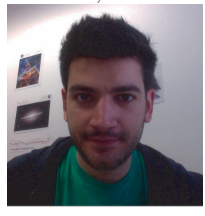
References

1. Schneider, P., Kochanek, C., Wambsganss, J., 2006, Gravitational Lensing: Strong, Weak and Micro, Springer
2. Brown, M., Bacon, D., Camera, S., et al., 2015, Advancing Astrophysics with the Square Kilometre Array (AASKA14), 23, arXiv:1501.03828
3. Harrison, I., Camera, S., Zuntz, J., Brown, M. L., 2016, ArXiv e-prints, arXiv:1601.03947
4. Bonaldi, A., Harrison, I., Camera, S., Brown, M. L., 2016, ArXiv e-prints, arXiv:1601.03948
5. Wilman, R. J., Miller, L., Jarvis, M. J., et al., 2008, MNRAS, 388, 1335, arXiv:0805.3413

[b] `http://radiogreat.jb.man.ac.uk`

THE HOMOGENEITY SCALE OF THE UNIVERSE

P. NTELIS
Astroparticle and Cosmology Group, University Paris-Diderot 7 , 10 rue A. Domon & Duquet, Paris , France



In this study, we probe the cosmic homogeneity with the BOSS CMASS galaxy sample in the redshift region of $0.43 < z < 0.7$. We use the normalised counts-in-spheres estimator $\mathcal{N}(< r)$ and the fractal correlation dimension $\mathcal{D}_2(r)$ to assess the homogeneity scale of the universe. We verify that the universe becomes homogenous on scales greater than $\mathcal{R}_H \simeq 64.3 \pm 1.6\ h^{-1} Mpc$, consolidating the Cosmological Principle with a consistency test of ΛCDM model at the percentage level. Finally, we explore the evolution of the homogeneity scale in redshift.

1 Introduction on Cosmic Homogeneity

The standard model of Cosmology, known as the ΛCDM model is based on solutions of the equations of General Relativity for isotropic and homogeneous universes where the matter is mainly composed of Cold Dark Matter (CDM) and the Λ corresponds to a cosmological constant. This model shows excellent agreement with current data, be it from Type Ia supernovae, temperature and polarisation anisotropies in the Cosmic Microwave Background or Large Scale Structure.

The main assumption of these models is the Cosmological Principle which states that the universe is homogeneous and isotropic on large scales [1]. Isotropy is well tested through various probes in different redshifts such as the Cosmic Microwave Background temperature anisotropies at $z \approx 1100$, corresponding to density fluctuations of the order 10^{-5} [2]. In later cosmic epochs, the distribution of source in surveys the hypothesis of isotropy is strongly supported by in X-ray [3] and radio [4], while the large spectroscopic galaxy surveys such show no evidence for anisotropies in volumes of a few Gpc^3 [5].As a result, it is strongly motivated to probe the homogeneity property of our universe.

In this study, we use a fiducial flat ΛCDM cosmological model using the parameters estimated by Planck [6]:

$$p_{cosmo} = (\omega_{cdm}, \omega_b, h, n_s, ln\left[10^{10} A_s\right]) = (0.1198, 0.02225, 0.6727, 0.9645, 3.094) \qquad (1)$$

2 Methodology

2.1 Dataset Characteristics

The Baryon Oscillation Spectroscopic Survey (BOSS) is a part of Sloan Digital Sky Survey SDSS-III 2.5m telescope located at Apache point Observatory [7]. BOSS is dedicated to study the clustering of $\sim 1.4 \times 10^6$ galaxies and $\sim 10^5$ of Quasars and their Lyman-a forests in an effective area of $\sim 10000 deg^2$ [8]. Using 1000 optical fibers on the focal plane of the telescope the light of each target is led to the spectrograph to allow gather the spectra of 1000 objects per exposure [9]. Using the imaging data in u,g,r,i,z bands, massive galaxy targets are selected [10] through several colour cuts designed to keep targets in redshifts between $0.43 < z < 0.7$ and keeping a constant stellar mass according to a passively evolving model [11]. We divide our sample into North and South galactic Cap and in we show the amount of objects in 5 redshift bins as shown in the left panel of figure [1]. There we show for comparison the amount of objects observed on a previous study [12].

We use an FRW-metric to infer the comoving distances of galaxies from the measured spectra:

$$\chi_{comov}(z) = c \int_0^z \frac{dz'}{H(z')} \tag{2}$$

where $H(z) = H_0 \sqrt{\Omega_{m,0}(1+z)^3 + \Omega_{\Lambda,0}}$ and $H_0 = 100h$ km/s/Mpc.

2.2 Estimators

In order to determine the homogeneity scale we use the estimator for the galaxy density of our BOSS CMASS sample, the *Normalised Count-in-Spheres* which is defined as follows:

$$\mathcal{N}(< r) = \frac{N(< r)}{N_{Random}(< r)} \tag{3}$$

where we have divided by the count-in-spheres of a random distribution ($N_{Random}(< r)$) placed on the same galaxy sample volume in order to correct for geometric effects. A random distribution will have count-in-spheres scaling with the volume ($N_{Random}(< r) \propto r^3$) while for a fractal distribution will scaling with a power-law as ($N(< r) \propto r^{D_2}$). So our main estimator is the *Fractal Correlation Dimension*:

$$\mathcal{D}_2(r) = \frac{d\ ln\ \mathcal{N}(< r)}{d\ ln\ r} + 3 \tag{4}$$

Since this estimator is defined with the total matter distribution, e.i. the biased galaxy sample, we need to convert it using a Redshift Space Distortion Analysis as explained in section 3. The new estimator is corrected for the bias of the galaxy clustering b w.r.t. Total Matter and the peculiar velocities σ_p:

$$\mathcal{D}_2(r; b, \sigma_p) = \frac{d\ ln\ \mathcal{N}(< r; b, \sigma_p)}{d\ ln\ r} + 3 \tag{5}$$

Then we chose to define the Homogeneity Scale as the scale at which the fractal correlation dimension gets the value for a homogeneous distribution at 1%, following WiggleZ [12]:

$$\mathcal{D}_2(\mathcal{R}_H; b, \sigma_p) = 2.97 \tag{6}$$

3 RSD Analysis

3.1 Modelling

We need to reconstruct our estimator *fractal correlation dimension*. To do that we use a simplistic Redshift Space Distortion Model which is the convolution of a factor $F(r; b, \sigma_p)$ with

the 2-point-correlation-function (2ptCF) of total matter in our universe:

$$\xi(r; b, \sigma_p, p_{cosmo}) = F(r; b, \sigma_p) \otimes \xi(r; p_{cosmo}) \tag{7}$$

This model assumes a linear evolution of the power spectrum which is Fourier Transform gives the 2ptCF in the real space $\xi(r; p_{cosmo})$ .To account for non linearities on small scale we include the $F(r; b, \sigma_p)$ factor. This accounts for the Kaiser effect in scales greater that $10h^{-1}Mpc$ and the Finger-of-god effect in scales less than $10h^{-1}Mpc$.

These models assume a non-scale dependent galaxy bias at the corresponding redshifts. We use the CLASS software to obtain the linear power spectrum using our fiducial parameters p_{cosmo} [13].

3.2 Measurement of RSD parameters

We tune our fitting parameters and ranges by using 1000 QPM mocks. These mocks are constructed with quick-particle-mesh algorithm which is faster but almost the same amount accurate as heavy N-body simulations [14]. The result is shown in figure [1] in the middle panel. In the right panel of figure [1], we plot the correlation matrix of the 2ptCF. We obtain a measured galaxy bias $b = 1.826 \pm 0.019$ and a galaxy peculiar velocity parameter of $\sigma_p \simeq 334 \pm 7\ Km.s^{-1}$.

We use these parameters to convert our galaxy *Fractal Correlation Dimension* observable into the one corresponding for the total matter $\mathcal{D}_2^{MM}(r; b, \sigma_p) \rightarrow \mathcal{D}_2^{MM}(r)$ as it is demonstrated in the left panel of figure 2. The conversion of equation 4 is explained analytically in [15] and references therein.

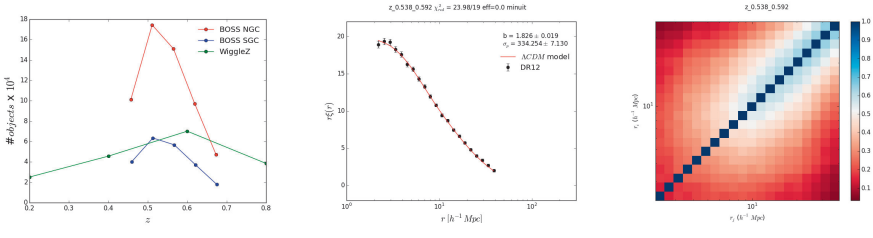


Figure 1 – *Left*: Redshift profile of objects. In red(blue) the NGC(SGC) CMASS sample. In green the WiggleZ galaxy sample [12]. The amount of objects of BOSS survey are 4 times more that the WiggleZ survey. *Center*: RSD analysis determining the galaxy bias and peculiar velocities in the z=0.538-0.592 bin in the NGC. Black error bars correspond to the scaled 2ptCF as a function of scale. With red-line is the best-fit ΛCDM model prediction for the fiducial cosmological parameters with 1% and 2% measurement of galaxy bias and peculiar velocities respectively. *Right:* The corresponding correlation matrix of the 2ptCF built by 1000 QPM mock catalogues.

4 Results with the Homogeneity Scale $\mathcal{R}_H$

4.1 Fractal Correlation Dimension

In figure [2] in the middle panel, the scale dependence of the *fractal correlation dimension* is shown. We show that $\mathcal{D}_2(r)$ is increasing with scale and reaches asymptotically the nominal value 3 which corresponds to a homogeneous universe. This provides us with the information that the universe becomes homogeneous by increasing scale which validates the Cosmological Principle in a consistent way. Furthermore, it is shown that for smaller scales the $\mathcal{D}_2(r)$ deviates from the nominal value implying that the universe presents a clustering or a fractal-like behaviour.

Moreover, we measure the homogeneity scale according to equation 6 by fitting a 5-node spline around the nominal value 2.97. We end up with $\mathcal{R}_H = 64.3 \pm 1.6h^{-1}Mpc$ within 2σ from ΛCDM prediction $\mathcal{R}_H^{th} = 62h^{-1}Mpc$. We also show the performance of 1000 QPM catalogues which gives as the estimation of the covariance matrix needed to our calculation.

4.2 Epoch evolution of Cosmic Homogeneity

In figure [2] in the middle panel, we plot the epoch dependence of the homogeneity scale $\mathcal{R}_H = \mathcal{R}_H(z)$ at $0.43 < z < 7$. We show that the homogeneity scale is increase with the epoch as predicted by ΛCDM.

This evolution can be interpreted by the growth of structure in our universe. We show the accuracy of our method in the 5 redshift bins for the NGC and SGC CMASS sample. And we show the 2σ consistency with ΛCDM.

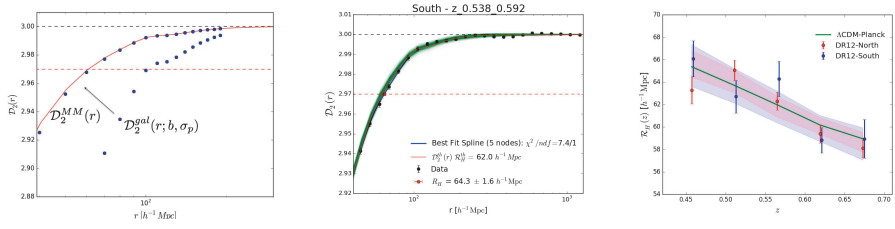


Figure 2 – *Left*: $\mathcal{D}_2^{MM}(r;b,\sigma_p) \rightarrow \mathcal{D}_2^{MM}(r)$ conversion in order to account for the bias and redshift distortion of our cosmic matter tracer. *Center*: *Fractal correlation dimension* scale dependence measurement. By fitting a 5-node spline around the nominal value 2.97 according to equation 6, we measure the homogeneity scale $\mathcal{R}_H = 64.3 \pm 1.6 h^{-1} Mpc$ at the middle z-bin of our galaxy sample. Green-lines correspond to 1000 QPM catalogues. *Right:* Cosmic Homogeneity redshift evolution. Red(Blue) corresponds to NGC(SGC) CMASS galaxy sample in accordance with the ΛCDM prediction. We can infer the growth of structures with time.

5 Conclusion & Discussion

In this study, we perform measurements of the homogeneity scale of our universe on DR12 BOSS CMASS galaxy sample. We measured the *fractal correlation dimension* showing its scale dependence.$\mathcal{D}_2(r)$ reaches the homogeneous value asymptotically behaving as a homogeneous distribution on scales greater than $\mathcal{R}_H = 64.3 \pm 1.6 h^{-1} Mpc$ at $z = 0.538 - 0.592$. On scales less than the distribution behaves as a fractal for different scales.

Moreover, we have shown the consistency of our homogeneity scale measurement for different cuts of our data at the North and South galactic caps we have optimised the measurement of previous studies at 3% level.

Additionally, we present the epoch evolution of the cosmic homogeneity and its accordance with the ΛCDM prediction at percentage level.

Finally, since we assume the ΛCDM model to infer distances and to correct for redshift space distortions, we can only conclude with a consistency test validation of Cosmological Principle.

Acknowledgments

I am grateful for the organisers of the conference for inviting me to present the Homogeneity Scale Measurement of BOSS collaboration at the Moriond's meeting.

References

[1] George FR Ellis. Cosmology and verifiability. *Quarterly Journal of the Royal Astronomical Society*, 16:245–264, 1975.

[2] DJ et al. Fixsen. The cosmic microwave background spectrum from the full cobe firas data set. *The Astrophysical Journal*, 473(2):576, 1996. arXiv:astro-ph/9605054v1.

[3] CA et al. Schärf. The 2-10 kev xrb dipole and its cosmological implications. Technical report, 1999. arXiv:astro-ph/9908187.

[4] Chris Blake and Jasper Wall. Detection of the velocity dipole in the radio galaxies of the nrao vla sky survey. *arXiv preprint astro-ph/0203385*, 2002.

[5] J-Ch Hamilton. What have we learned from observational cosmology? *Studies in History and Philosophy of Science Part B: Studies in History and Philosophy of Modern Physics*, 46:70–85, 2014.

[6] Ade et al. Adam. Planck 2015 results. i. overview of products and scientific results. *arXiv preprint arXiv:1502.01582*, 2015.

[7] James E et al. Gunn. The 2.5 m telescope of the sloan digital sky survey. *The Astronomical Journal*, 131(4):2332, 2006. arXiv:astro-ph/0602326.

[8] S. Alam et al. The eleventh and twelfth data releases of the sloan digital sky survey: final data from sdss-iii. *The Astrophysical Journal Supplement Series*, 219(1):12, 2015. arXiv:1501.00963v3.

[9] Smee S et al. The multi-object, fiber-fed spectrographs for the sloan digital sky survey and the baryon oscillation spectroscopic survey. *The Astronomical Journal*, 146(2):32, 2013. arXiv:1208.2233.

[10] Reid Beth et al. Sdss-iii baryon oscillation spectroscopic survey data release 12: galaxy target selection and large-scale structure catalogues. *Monthly Notices of the Royal Astronomical Society*, 455(2):1553–1573, 2016. arXiv:1509.06529.

[11] Claudia Maraston, G Strömbäck, Daniel Thomas, DA Wake, and RC Nichol. Modelling the colour evolution of luminous red galaxies–improvements with empirical stellar spectra. *Monthly Notices of the Royal Astronomical Society: Letters*, 394(1):L107–L111, 2009.

[12] Morag I et al. Scrimgeour. The wigglez dark energy survey: the transition to large-scale cosmic homogeneity. *Monthly Notices of the Royal Astronomical Society*, 425(1):116–134, 2012. arXiv:1205.6812.

[13] Diego Blas, Julien Lesgourgues, and Thomas Tram. The cosmic linear anisotropy solving system (class). part ii: approximation schemes. *Journal of Cosmology and Astroparticle Physics*, 2011(07):034, 2011.

[14] Martin White, Jeremy L Tinker, and Cameron K McBride. Mock galaxy catalogues using the quick particle mesh method. *Monthly Notices of the Royal Astronomical Society*, 437(3):2594–2606, 2014.

[15] J.M. LeGoff P. Laurent E. Burtin et al. P. Ntelis, J.C. Hamilton. Exploring cosmic homogeneity with the boss dr12 galaxy sample. *to be published*, 2016.


VOLKL
RaG

CONSTRAINING $N_{\rm eff}$ WITH THE LYMAN-α FOREST

GRAZIANO ROSSI
Department of Physics and Astronomy, Sejong University, Seoul, 143-747, Korea



We present joint constraints on the number of effective neutrino species $N_{\rm eff}$ and the sum of neutrino masses $\sum m_\nu$ using a technique based on state-of-the-art hydrodynamical simulations with massive neutrinos, and by exploiting the full information contained in the one-dimensional Lyman-α forest flux power spectrum – complemented by additional cosmological probes. Our results provide strong evidence for the cosmic neutrino background ($N_{\rm eff} = 0$ is rejected at more than 14σ), and rule out the possibility of a sterile neutrino thermalized with active neutrinos at a significance of over 5σ – one of the strongest bounds to date.

1 Massive and Sterile Neutrinos

With the advent of large-volume cosmological surveys such as eBOSS or DESI,[1,2] it is becoming progressively feasible to use the universe as a unique laboratory to study the nature and fundamental properties of neutrinos – especially the mass scale and hierarchy – and place upper bounds on their total mass. Cosmology will then soon provide a better understanding of the neutrino sector, and shed light into leptogenesis, baryogeneis, and the origin of mass.[3] In particular, if $\sum m_\nu < 0.1$ eV, one could in principle exclude the inverted hierarchy scenario, in which two neutrino eigenstates are much heavier than the third one and nearly degenerate. A novel method to place upper bounds on the total neutrino mass from cosmology is to look at the small-scale clustering, such as that inferred from the one-dimensional flux power spectrum measured from the Lyman-α (Lyα) forest. The Lyα forest can also be used to place interesting constraints on the number of effective neutrino species $N_{\rm eff}$, and on the possibility of additional neutrino species (i.e. sterile neutrinos) – beyond the standard model of particle physics.

2 Methods and Results

We used a sophisticated technique to construct the Lyα forest likelihood, based on a second-order Taylor-expansion model for the dependence of the Lyα flux power spectrum on cosmological and astrophysical parameters, complemented by an analytical approximation to include non-standard dark radiation models.[4,5,6] To this end, we devised new cosmological hydrodynamical simulations with massive neutrinos and also considered alternative cosmologies, where $N_{\rm eff}$ is

different from the canonical value of 3.046 expected in the standard three-neutrino framework (see Figure 1).[4,7,8] We finally interpreted the likelihood obtained by combining our simulation-based Taylor-expansion model with data from the BOSS Lyα forest, the BOSS galaxy clustering BAO measurements, and state-of-the-art CMB probes (i.e., WMAP9, ACT, SPT) in the context of the frequentist approach. The main results of our analysis are shown in Figure 2. Specifically, $N_{\rm eff} = 2.91^{+0.21}_{-0.22}$ (95% CL) and $\sum m_\nu < 0.15$ eV (95% CL) without BAO data, and $N_{\rm eff} = 2.88 \pm 0.20$ (95% CL) and $\sum m_\nu < 0.14$ eV (95% CL) with BAO information.[4] We find that a sterile neutrino thermalized with active neutrinos – or more generally of any decoupled relativistic relic with $\Delta N_{\rm eff} \simeq 1$ – is ruled out at a significance of over 5σ, and in addition our constraints provide strong evidence for the CNB from $N_{\rm eff} \sim 3$ by rejecting $N_{\rm eff} = 0$ at more than 14σ.

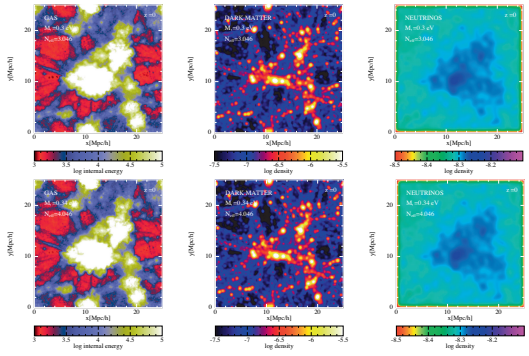


Figure 1 – Snapshots at $z = 0$ of the gas internal energy, dark matter, and neutrino density, from simulations with $25h^{-1}$Mpc box size and resolution $N_{\rm p} = 192^3$ particles/type. Both standard (top) and non-standard (bottom) $N_{\rm eff}$ cosmologies are considered, for different values of $\sum m_\nu$ – related by our analytic remapping.

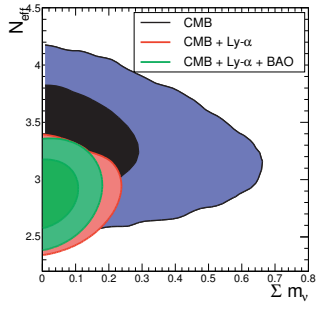


Figure 2 – Joint constraints on $N_{\rm eff}$ and $\sum m_\nu$ from cosmological probes, as specified in the panel with different colors. Our results exclude a sterile neutrino – thermalized with active neutrinos – at a significance of over 5σ, and provide strong evidence for the CNB from $N_{\rm eff} \sim 3$ – as $N_{\rm eff} = 0$ is rejected at more than 14σ (Rossi et al. 2015).

Acknowledgments

This work and the participation to the 'Rencontres de Moriond' (March 2016) in La Thuile, Aosta Valley, Italy, were supported by the National Research Foundation of Korea (NRF) through NRF-SGER 2014055950 funded by MoEST, and by the faculty research fund of Sejong University in 2016. Some numerical simulations presented in this work were performed using the Korea Institute of Science and Technology Information (KISTI) supercomputing infrastructure under allocation KSC-2016-G2-0004. It is a pleasure to thank Jacques Dumarchez, the secretariat, and the scientific and organizing committee, and congratulate for the 50th Moriond anniversary.

Selected References

1. Dawson, K. S., Schlegel, D. J., Ahn, C. P., et al. 2013, AJ, 145, 10
2. Levi, M., Bebek, C., Beers, T., et al. 2013, arXiv:1308.0847
3. Lesgourgues, J., & Pastor, S. 2006, Phys. Rep., 429, 307
4. Rossi, G., Yèche, C., Palanque-Delabrouille, N., et al. 2015, Phys. Rev. D, 92, 063505
5. Palanque-Delabrouille, N., Yèche, C., Lesgourgues, J., et al. 2015, *JCAP*, 2, 045
6. Palanque-Delabrouille, N., Yèche, C., Baur, J., et al. 2015, *JCAP*, 11, 011
7. Rossi, G. 2015, Publication of Korean Astronomical Society, 30, 321
8. Rossi, G., Palanque-Delabrouille, N., Borde, A., et al. 2014, A&A, 567, AA79

Formation and evolution of heavy sub-structures in the centre of galaxy clusters: the local effect of dark energy

M. Arca Sedda[1], M. Donnari[1,2], M. Merafina[1]
[1] *Department of Physics, Sapienza University of Rome*
Piazzale A. Moro 5, I-00185 Rome, Italy
[2] *Department of Physics, University of Rome Tor Vergata*
Via O. Raimondo , I-00173 Rome, Italy

We discuss how the centres of galaxy clusters evolve in time, showing the results of a series of direct N-body simulations. In particular, we followed the evolution of a galaxy cluster with a mass $M_{clus} \simeq 10^{14} M_{\odot}$ in different configurations. The dynamical evolution of the system leads in all the cases to the formation of dense and massive sub-structures in the cluster centre, that form in consequence of a series of collisions and merging among galaxies travelling in the cluster core. We investigate how the structural properties of the main merging product depends on the characteristics of those galaxies that contributed to its formation.

1 Numerical simulations

We modelled the dynamical evolution of a galaxy cluster (GC) under the action of dark energy (DE) [1], in order to understand whether its anti-gravitational term in the equation of motion of each particle may play a significant role in shaping the structure of the GC. We focused our investigation on the role of orbital decay and merging of galaxies moving in the cluster innermost region, aiming at finding whether DE can leave a footprint on the evolution of the cluster core. We simulated GC composed of 240 galaxies using a modified version of a direct N-body code `HiGPUs` [2]. Each galaxy is modelled according to a Dehnen profile, whereas all the galaxies are distributed in the phase-space according to a King density profile. For DE we follow ΛCDM model and for the gaseous component (ICM) we use the so-called β-model. In order to highlight the different role played by each component, we switched on/off alternatively the DE or ICM, as indicated in Tab. 1. We found that galaxies moving within the Zero-Gravity Radius (ZGR), which is the radius within gravity overcomes antigravity, are mostly affected by mutual gravitational interactions, which drive the orbital decay of the most massive galaxies due to the action of dynamical friction (df) [3]. This leads to an accumulation of heavy galaxies in the GC core, favouring their pairing and merging. In Fig. 1 (left panel) is shown how the df time-scale varies at varying galaxy mass and position.

2 Outcomes and conclusions

Concerning the dynamical evolution of the cluster nucleus, we followed the orbits of the central galaxies. Indeed, these galaxies are efficiently affected by df, which drags them toward the cluster centre. Surprisingly, the combined action of DE and ICM seems to facilitate collisions among galaxies. Indeed, the number of merging is much higher in simulation MM2, in which our results show that a sequence of 21 merging and collisions occurs over a time-scale t $\simeq$ 5 Gyr

Table 1: Left: Physical processes considered in simulations and their evolutionary ages. Right: Parameters of the simulated galaxy cluster.

Model	Λ	ICM	$T_{ev}(Gyr)$
MM1	X		3.7
MM2	X	X	5.3
MM3		X	3.5
MM4			3.5

Parameter	Value
M_{clus}	$9.2 \times 10^{13} M_{\odot}$
r_c	0.1 M pc
$M_{g,min}$	$9 \times 10^{10} M_{\odot}$
$M_{g,max}$	$1.0 \times 10^{12} M_{\odot}$

driving the formation of a huge spheroidal structure. This massive central structure (MCS) has a dynamical mass of $6 \times 10^{12} M_{\odot}$ and a central velocity dispersion of 1300 km/s.

Another interesting outcomes of these simulations is the possibility to develop a study of super-massive black holes (SMBHs) dynamics. As widely accepted, the presence of SMBHs are thought to occupy the centre of the majority of obseved galaxies. However, it is not completely clear how they interact during multiple galaxy mergings. To investigate this point, we assumed that an SMBH forms and grows efficiently at the centre of each merging galaxy before the MCS assembly ($\simeq$ 3 Gyr), and we simulated their mutual interactions and subsequent evolution in model MM2. We found that 13 of the 21 SMBHs are ejected away through multiple scatterings, reaching velocities up to 10^3 km/s [4]. On the other hand, 4 SMBH sink to the MCS centre, where they form a bound system. Their subsequent evolution can lead to the formation of a final SMBH with mass $5 \times 10^9 M_{\odot}$ as shown in Fig. 1.

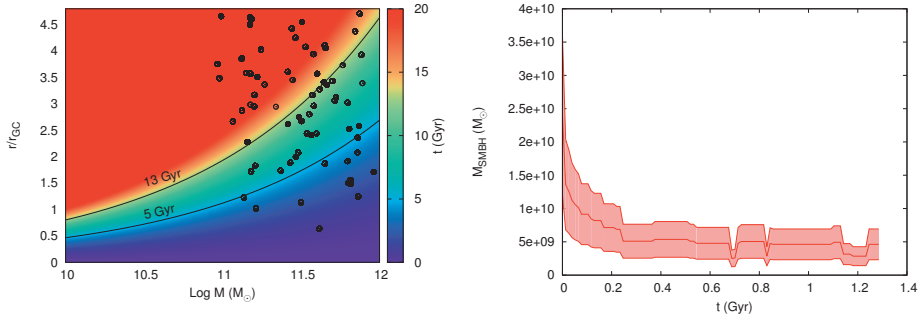


Figure 1 – Left: Surface map of $\tau_{\rm df}$ at varying M_g and r. The open circles represent the galaxies in our models. Right: Mass (with its error) of the SMBHs that move within 10 kpc from the centre of the central structure.

References

[1] M. Donnari, M. Arca-Sedda and M. Merafina, MNRAS , submitted (2016).

[2] R. Capuzzo-Dolcetta, M. Spera and D. Punzo, J. Co. Ph. **236**, 580 (2013).

[3] M. Arca-Sedda and R. Capuzzo-Dolcetta, *ApJ* **785**, 51 (2014).

[4] Y. Miki *et al*, *ApJ* **783**, 87 (2014).

3.
Dark Matter

The XENON1T Dark Matter Experiment

Adriano Di Giovanni on behalf of the XENON1T collaboration.
Department of Physics, NYUAD-New York University Abu Dhabi, Saadiyat Island, UAE

After a brief introduction to the state-of-art of direct detction searches for Dark Matter particles, the paper has been focused at the decription of the main features of the XENON1T detector presently under commissioning at Gran Sasso National Laboratory - Italy. Designed to allow 2 $t \times year$ of exposure, XENON1T will push down the limit on sensitivity to 1.6×10^{-47} cm^2 @ 50GeV, representing the most performing and powerful detector devoted to Dark Matter searches on Earth for the upcoming years.

1 Introduction

The search for Dark Matter (DM) is one of the hottest topics in modern physics. The existence of DM was first pointed out by F. Zwicky [1,2].

The Swiss astronomer demonstrated (with a classical mechanics derivation) that the galaxies of the Coma cluster should have an average mass of 4.5×10^{10} solar masses, corresponding to the mass-luminosity (γ) ratio of about 500, in striking contrast with values of $\gamma = 3$ considered as normal. Several years after, Rubin, Ford, and Thonnard [3] measured the rotational profiles of several spiral galaxies. The shape of those curves (Fig. 1) "implies that the mass is not centrally condensed" and that "the conclusion is inescapable that non-luminous matter exists beyond the optical galaxy" [3]

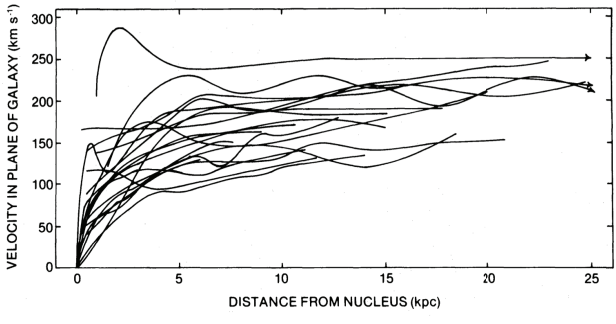


Figure 1 – Rotational curves of 21 spiral galaxies as measured by Rubin, Ford, and Thonnard [3]

Further evidence of the existence of Dark Matter comes from the measurements of the Cosmic Microwave Background (CMB), the well known diffuse radiation that represents the afterglow of the Big Bang. In particular, measurements from the WMAP [4] and Planck experiments [5] have revealed with great detail the anisotropies of the CMB. These anisotropies strongly constrain

the various contributions to the energy and mass content of the Universe. The newest Planck results indicate that the baryonic fraction of the matter of the Universe is 18.3 %, while the density of the DM halo in our galaxy should be of the order $0.3 \div 0.6$ GeV/cm^3 (this conference). According to measurements[6,8], a large percentage of the energy of the Universe is made of cold, non-relativistic, dark matter.

One of the most popular Dark Matter candidate is a massive particles characterised by extremely weak interactions with ordinary matter, normally referred to as 'Weakly Interacting Massive Particles' (WIMPs). A natural candidate for WIMPs is the lightest supersymmetric particle, the neutralino (χ). Many techniques for WIMP search assume a ≈100 GeV neutralino with a χ-nucleon cross section of $\approx 10^{-40}$ cm^2 or less, in accordance with expectations of supersimmetric models.

Experimentalists expect to detect Dark Matter particles through three different search strategies:

- Indirect detection: looking for DM annihilation into Standard Model (SM) particles.
- Particle colliders: direct or by decay production of DM.
- Direct detection: DM scattering off SM particle

XENON1T experiment will be the most promising and sensitive detector in the ''Direct detection" class.

2 Direct Searches

The simple idea of direct detection is based on the possibility the nuclear recoils originated by the rare interactions, if any, of DM particles. Two kinds of interactions can be envisaged, a scalar coupling "spin independent " - SI), where the WIMP couples to the nucleus as a whole ($\propto A^2$), or a vector coupling ($\propto J(J+1)$) normally referred to as "spin dependent" (SD). The expected rate of interaction of these particles scattering off target nuclei as a function of energy recoil can be estimed through the equation:

$$\frac{dR}{dE_r} = N\frac{\rho_0}{M} m_N m_\chi \int_{v_{\min}}^{v_{\rm esc}} v f(v) \frac{d\sigma_\chi}{dE_r} dv^3 \qquad (1)$$

where:

- M is the mass of target;
- ρ_0 the density of DM particles;
- m_N is the mass of a nucleus in the target;
- m_χ the mass of ta WIMP;
- $\int_{v_{\rm esc}}^{v_{\rm esc}} v f(v) dv^3$ takes into account the the velocity distribution with respect to the Earth reference frame;
- $\frac{d\sigma_\chi}{dE_r}$ is the cross section for WIMP interactions as a function of nuclei energy recoil.

Assuming a local density of the DM halo of the order of 0.3 GeV/cm^3, a candidate WIMP with 100 GeV, and a speed of the Earth through the DM halo of 230 km/s (the speed of the Solar System with respect of the center of the Milky Way), a local WIMP flux of about $10^5 \mathrm{cm}^{-2}\mathrm{s}^{-1}$ is obtained.

For values of m_χ and σ_χ still allowed for supersymmetry by LHC[9], the expected rate is of order of one event per 1 t per year, with a typical recoil energy of the order of 10 keV.

By any standards this represents an extremely low rate of extremely low energy events, that would never be detectable in any location above the Earth's surface because of the constant flux of charged cosmic rays. This is why all direct Dark Matter experiments are located in underground laboratories. The underground environment takes advantage of a reduced, but definitely not zero, residual flux of high energy muons [10]. The residual muons and associated neutron flux, and the natural radioactivity of the rocks motivate the need for further shielding of the apparatuses looking for DM interactions. In fact, the typical DM detector has an 'onion-like' shielding structure where each layer targets a specific background. Water or polyethylene, given their hydrogen content, stop neutrons and, if the water shielding is equipped with photo-multipliers, also may tag muons and associated particles through the Cherenkov light emission. High purity copper and lead, typically placed in the inner layers, stop gamma radiation to enter the detector. Finally, discrimination techniques, based either on the shape of the pulses or on the use of multiple detection channels (scintillation light, ionisation charge or phonons) further enhance the signal to noise ratio, allowing to single out samples of nuclear recoil events with high efficiency. Fig. 2 show the discrimination capability between ERs and NRs (see caption) for the XENON100 experiment.

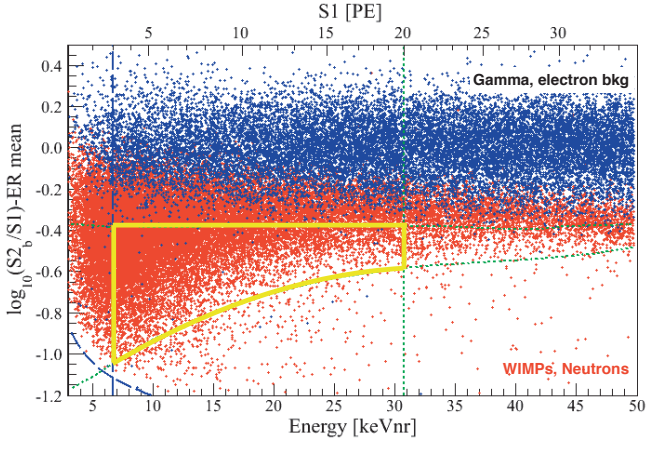


Figure 2 – Discrimination capability between Electroin Recoil (ER) events (mainly γ- and β- induced interactions, reported in blue) and Nuclear Recoil (NR) events (mainly neutron induced, reported in red). A Dark Matter detection would appear within the highlighted yellow countour.

A review of experimental scenario on DM direct search may be found in [16]. The detection technologies utilised are of several kinds: scintillators, bolometers, proportional counters, bubble chambers, etc. All detectors are characterised by the effort of achieving the lowest possible backgrounds in order to enhance their sensitivity and their discovery potential. The present situation can be summarised in fig. 3. This is the usual plot where many experiments compare their results in the space of WIMP-nucleus elastic cross section vs WIMP mass. In this figure there are positive, albeit controversial, detection results along with exclusion curves from other experiments. The discovery contour of DAMA-LIBRA [17] and CDMS-Si [18] are shown, together with the exclusion limits of other experiments: XENON10 [19], SuperCDMS [20], PandaX [21], DarkSide-50 [22], XENON100 [14] and LUX with the 2015 re-analysis [23]. For comparison, with the dashed brown line we plot also the"neutrino discovery limit" [24].

In the following section we focus specifically on a type of detection technology, the one adopted by the XENON collaboration, the 'time projection chamber with noble liquids' (Noble Liquid TPC).

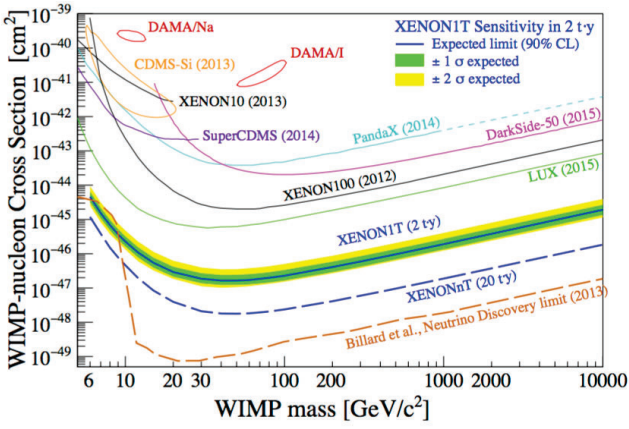


Figure 3 – XENON1T sensitivity (90 % C.L.) to spin-independent WIMP-nucleon interaction, calculated with the LUX2015 emission model: the solid blue line represents the median value, while the 1 σ and 2 σ sensitivity bands are indicated in green and yellow respectively. The XENONnT median sensitivity, also calculated with the LUX2015 model, is shown with the dashed blue line.

3 Noble liquid TPCs

Time projection chambers with noble liquids such as Ar and Xe are powerful and easily scalable detectors. The detector's core system is a cryostat containing the noble liquid with a layer of gas at its top and both of the phases are exploited by this technique. An interaction in the liquid produces direct scintillation photons (S1) and ionization electrons. An electric field is applied across the volume with appropriate potentials on a series of copper rings connected to each other by means of one or more resistor chains, drifting ionization electrons away from the interaction zone.

Electrons which reach the liquid-gas interface are extracted into the gas phase, where another scintillation signal (S2), proportional to the ionisation charge, is produced. Both the S1 and the S2 scintillation signals are detected by photomultiplier tubes. Because of the different ionisation yield, the ratio S2/S1 produced by a WIMP (or neutron) interaction is different from that produced by an electromagnetic interaction. Thus, it allows a rejection of the majority of the gamma and beta particle background. This detection principle has been adopted both with liquid xenon (LXe) and liquid argon (LAr) -based detector.

Xenon is very expensive (more than 1000 USD/kg), but it has the advantages of not having intrinsically radioactive isotopes, although small contaminations of ^{85}Kr should be removed by distillation to allow reaching the highest sensitivities. The scintillating wavelength is around 175 nm; its high atomic number and natural blend of even and odd spin isotopes make it a suitable target for both SI and SD interactions.

4 The XENON dark matter program at the Gran Sasso National Laboratory

The XENON Collaboration started off in 2004 as a group of less than 40 scientists from USA, Portugal and Italy. In the years 2006 - 2007 the collaboration successfully installed and operated a relatively small (15 kg) double phase LXe TPC, XENON10 [19] achieving the best sensitivity for WIMP elastic interaction.

Successively, the Collaboration increased in size and diversity. It now consists of about 110

scientists of 9 countries and 15 institutions. After XENON10, a new TPC with a factor of 10 more mass and a factor of 100 less electromagnetic background was designed to fit inside the improved passive shield of XENON10. The detector, currently taking data, XENON100 [11], is characterised by a careful selection of all detector materials regarding intrinsic radioactivity [12], a xenon target with lower ^{85}Kr contamination, a novel detector design leaving only low radioactive components close to the target, and by an improved passive shield. Furthermore, XENON100 features an active LXe veto: a 3 cm layer of liquid xenon completely surrounding the sensitive volume, and instrumented as well with photomultipliers.

XENON100 has set the most stringent limit for a very large range of WIMP masses [13,14]. The current limit has a minimum of 2×10^{-45} cm^2 at 55 GeV and 90% confidence level (see Fig. 3 [14]). Only recently, this limit has been superseded by the result of the LUX experiment [15].

While the XENON100 detector was still running, the next generation detector, XENON1T, with a fiducial mass of about 1 t, has been designed. XENON1T is presently under commissioning in the Hall B of the Gran Sasso Laboratory, and it is about to start taking data.

5 XENON1T

XENON1T is the lastest detector in the XENON 'legacy'. It's a massive detector, featuring a total mass of 3.3 t of xenon, with 1 t in the fiducial volume. The layout is shown in Fig. 4. Contrary to XENON100, the shielding in XENON1T is made of water. The detector is in fact immersed in a water tank containing about 700 t of ultra-pure water and equipped with 82 8-inches R5912ASSY photomultipliers that allow to veto the detector in coincidence of the passage of muons, minimising the risk of stray neutrons arriving into the fiducial volume and mimicking a WIMP interaction.



Figure 4 – Left: CAD drawing of the whole XENON1T installation in the Hall B of the Gran Sasso Laboratories. On the left, the water tank containing the cryostat and the detector. On the right, the service building with the cryogenics (top floor), electronics (middle floor), and gas storage (ground level). Right: the actual XENON1T Darlk Matter project.

In all other respects, XENON1T works exactly as XENON100, using the principle of double phase TPC, albeit with a larger volume of LXe. However, handling this large volume poses challenges and presents risks, that have to be managed with a complex set of sub-systems. In the following paragraphs we briefly outline the main components of XENON1T, starting from the inside.

5.1 The TPC

The active volume of the XENON1T TPC is defined by a 1 m diameter cylinder with a height of 0.96 m and composed of 74 ultra-radiopure copper rings supported by 24 PTFE pillars connected to the uppermost stainless steel ring and the latest ring.

Photosensors are arranged in two close-packed arrays: a bottom array with 121 PMTs, in the liquid, below the sensitive volume, and a top array, with 127 PMTs, in the gas above the liquid. High optical transparency mesh electrodes close the cylinder and define the liquid xenon drift



Figure 5 – The Time Projection Chamber (TPC) before closing the cryostat. In the close-up, the bottom array of photomultipliers facing the inner detection volume is visible.

volume and the gas 'proportional' region, above the liquid level. The chosen photomultipliers are the 3-inch R11410 from Hamamatsu. A high voltage feedthrough (HVFT) provides up to 100 kV necessary to guarantee the desired field: 2 resistor chains connected to the shaping electrode rings keep the field uniform (up to $\approx$ 1.5 kV/cm) through the drift volume.

5.2 Cryostat and support structures

The XENON1T cryostat is a double-walled vacuum insulated vessel designed to contain the detector assembly with more than 3 t of LXe at a temperature of about 178 K. The inner vessel is supported by the outer vessel by means of three low thermal conductivity fastening assemblies. The inner vessel is covered with a super-insulation blanket, composed of multiple layers of aluminized mylar foil, to substantially reduce the radiative heat transfer. The upper domes have a central port from which the cryostat is connected to the XENON1T cryogenics system, via a long double-walled vacuum insulated tube: the main cryogenic pipe. The main cryogenic pipe, filled with GXe, contains five independent lines (for LXe and GXe transfer and recirculation) and one larger tube.The structure which supports the XENON1T cryostat consists of an open frame which reaches almost to the top of the water tank. From the top of the structure three stainless steel rods are designed to suspend a maximum load of 7.5 t. The rods are attached to three leveling arms, which allow to adjust the length of the rods to achieve the parallelism between the LXe level and the TPC's anode. The leveling system is designed such that fine adjustments can be made to the length of the rods, to fulfil the requirement to have the liquid level adjusted to 100 μm.

5.3 Cryogenics system

The cryogenics system uses two redundant pulse tube refrigerator (PTR) cooling systems and an additional emergency liquid nitrogen cooling system. The cryogenics system interfaces with the cryostat through the main cryogenic pipe. Xenon gas from the inner vessel flows to the cryogenics system, is liquefied by the PTR and flows back into the detector via a tube that runs inside the main cryogenic pipe. One of the tubes contained in the main pipe carries liquid xenon out of the detector's vessel to a heat exchanger where it is evaporated before exiting the cryogenics system to the purification system. The xenon gas from the purification system enters the cryogenics system, is liquefied in the heat exchanger, and flows back to the detector. This system allows circulation at flow rates in excess of 100 standard liter per minutes (SLPM) .The total thermal load of the XENON1T cryostat and its long cryogenic pipe is estimated at 50 W.

5.4 LXe Storage and Recovery

Operating a detector that contains several tonnes of LXe poses serious challenges regarding the storage, recovery and purification of the xenon. A simple and reliable solution for these challenges has been studied and developed within the XENON program, as it moves towards multi-tonne scale LXe TPCs. The ReStox (Recovery and Storage of Xenon) system is able to:

- Store a maximum of 7.6 t of Xe in gas, liquid or solid phase;
- Condense the gas and allow fast filling of LXe into the detector;
- Recover the LXe from the detector in 1 - 2 h, in case of emergency;
- Purify the stored LXe during periods of detector's maintenance, via its connection to the Purification system.

The system is based on a 2 m diameter spherical double walled SS pressure vessel which can safely store 62 bar of GXe, which correspond to 7.6 tonnes at 289 K, the average temperature of Hall B, where the detector is installed. The sphere is vacuum insulated and designed to have a maximum heat leak of 50 W.

5.5 Water Cherenkov Muon Veto

The water shield with 4π coverage moderates and attenuates the external neutron and gamma radiation. Pure water, contained in a stainless steel tank, is instrumented to enable its additional role as an active muon anti-coincidence veto detector. By detecting the Cherenkov emission from cosmic muons traversing the water volume, the muon-induced neutron background is reduced to negligible levels in the WIMP search region. The cylindrical tank has a radius of 4.8 m and about 9 m height plus a truncated cone-shaped top for a maximum height of 10.5 m. The water fills the tank to a height of 10.2 m.

With an arrangement of photomultipliers (PMTs) on the tank's walls and floor, optical Cherenkov photons, produced by cosmic muons and their secondary showers during their passage through water, are detected with high efficiency. The PMTs selected for the muon veto are the high quantum efficiency (QE) 8" Hamamatsu R5912ASSY (order of 30 % for Cherenkov light spectrum), already provided with a water-proof enclosure.

6 Conclusions

XENON1T is presently under commissioning and is about to start taking data. The detector is the most sensitive detector ever built for the direct search for WIMPS and meant to push down the sensitivity to 1.6×10^{-47} cm^2 @ 50GeV (Spin-Independent model). All the relevant subsystems have been designed to allow for a rapid upgrade to XENONnT with minor changes on the infrastructure. With the next upgrade to XENONnT, planned for the beginning of the next decade, the XENON Dark Matter Project will further improve the detection sensitivity of one order of magnitude (1.6×10^{-48} cm^2 @ 50 GeV, Spin-Independent model).

Acknowledgments

The XENON project is realized with funds from US National Science Foundation, Max Planck Gesellschaft, Schweizerischer Nationalfonds, Research Center Elementary Forces and Mathematical Foundations, Bundesministerium fur Bildung und Forschung, Weizmann Institute of Science, Stichting voor Fundamenteel Onderzoek der Materie, Knut and Alice Wallenberg Foundation, Deutsche Forschungsgemeinschaft, Initial Training Network Invisibles, Fundação para a Ciência e a Tecnologia, Helmholtz Alliance for Astroparticle Physics, ISF-ICORE, Region des Pays de la Loire, Nordrhein-Westfalen, the Istituto Nazionale di Fisica Nucleare as well as the participating institutions.

References

1. F. Zwicky, Helv. Phys. Acta 6, 110, (1933), reprinted in Gen Relativ Gravit 41 (1), 203-206 (2009)
2. F. Zwicky, ApJ 86, 217, (1937)
3. V. Rubin et al., ApJ **238**, 471-487, (1980).
4. http://lambda.gsfc.nasa.gov/product/map/current/map_bibliography.cfm
5. Planck Collaboration, A&A 571, A15 (2014)
6. G. R. Blumenthal, S. Faber, J. R. Primack and M. J. Rees, Formation of Galaxies and Large Scale Structure with Cold Dark Matter, Nature 311 (1984) 517525
7. M. Davis, G. Efstathiou, C. S. Frenk and S. D. White, The Evolution of Large Scale Structure in a Universe Dominated by Cold Dark Matter, Astrophys.J. 292 (1985) 371394
8. **CDMS** R. Agnese et al., Silicon Detector Dark Matter Results from the Final Exposure of CDMS II, Phys. Rev. Lett. 111 (2013), no. 25 251301
9. A. Fowlie et al., arXiv:1206.0264v3.
10. M. Aglietta et al., Phys. Rev. D, **58** (9) 092005 (1998).
11. **XENON** Collaboration, E. Aprile et al., The XENON100 Dark Matter Experiment, Astr. Phys. Vol. 35 Issue 9, April 2012 (573-590).
12. E. Aprile et al., XENON100 Collaboration, Astropart. Phys. **35** 43 (2011)
13. E. Aprile et al., XENON100 Collaboration, Phys. Rev. Lett. **107** 131302 (2011).
14. **XENON** Collaboration, E. Aprile et al., Dark Matter Results from 225 Live Days of XENON100 Data, Phys.Rev.Lett. 109 (2012) 181301.
15. **LUX** Collaboration, D.S. Akerib et al., Improved Limits on Scattering of Weakly Interacting Massive Particles from Reanalysis of 2013 LUX Data, Phys. Rev. Lett. 116 (2016), no. 16 161301
16. T.M. Undagoitia and L. Rauch, Dark matter direct-detection experiments, J. Phys. G: Nucl. Part. Phys. 43 (2016) 013001
17. C. Savage, G. Gelmini, P. Gondolo and K. Freese, Compatibility of DAMA/LIBRA dark matter detection with other searches, Journal of Cosmology and Astroparticle Physics 2009 (2009), no. 04 010.
18. **CDMS** R. Agnese et al., Silicon Detector Dark Matter Results from the Final Exposure of CDMS II, Phys. Rev. Lett. 111 (2013), no. 25 251301
19. **XENON10** Collaboration, J. Angle, Erratum: Search for Light Dark Matter in XENON10 Data [Phys. Rev. Lett. 107 , 051301 (2011)], Phys. Rev. Lett. 110 (Jun, 2013)
20. **SuperCDMS** Collaboration, R. Agnese et al., Search for Low-Mass Weakly Interacting Massive Particles with SuperCDMS, Phys. Rev. Lett. 112 (2014), no. 24 241302
21. **PandaX** Collaboration, M. Xiao et al., First dark matter search results from the PandaX-I experiment, Science China Physics, Mechanics & Astronomy 57 (2014), no. 11 20242030.
22. **DarkSide-50** DarkSide-50 Collaboration, P. Agnes et al., Low radioactivity argon dark matter search results from the DarkSide-50 experiment
23. **LZ** Collaboration, D. S. Akerib et al., LUX-ZEPLIN (LZ) Conceptual Design Report
24. J. Billard, L. Strigari and E. Figueroa-Feliciano, Implication of neutrino backgrounds on the reach of next generation dark matter direct detection experiments, Phys.Rev. D89 (2014) 023524

DARK MATTER SEARCH IN THE INNER GALACTIC CENTER HALO WITH H.E.S.S.

V. LEFRANC and E. MOULIN. for the H.E.S.S. collaboration

DRF/Irfu, Service de Physique des Particules, CEA Saclay, F-91191 Gif-Sur-Yvette Cedex, France

The presence of dark matter in the universe is nowadays supported by a substantial set of astronomical and cosmological observations. A large amount of dark matter is expected in the Galactic Center (GC) region. Thanks also to its proximity, it is one of the best targets to look for dark matter particle self-annihilation into very high energy gamma-rays. We perform a search for annihilating dark matter in the central 300 parsecs around the GC with the H.E.S.S. array of ground-based Cherenkov telescopes. Using the full H.E.S.S.- I dataset (2004-2014) of GC observations, new constraints are derived on the velocity-weighted annihilation cross section $\langle \sigma v \rangle$ with a 2D likelihood method using spectral and spatial morphologies of the DM signal compared to background. These constraints are the strongest obtained so far in the TeV mass range and improve the previous constraints by a factor of 5. Considering an Einasto profile, the constraints reach $\langle \sigma v \rangle$ values of $6 \times 10^{-26}\mathrm{cm}^3\mathrm{s}^{-1}$ for a DM particle mass of 1.5 TeV annihilation into $\mathrm{W}^+\mathrm{W}^-$ pairs. In the $\tau^+\tau^-$ channel, the constraints probe the natural scale for thermal relic cross section for DM particles of masses between 400 GeV and 2 TeV.

1 Introduction

The presence of Dark Matter (DM) in the Universe is supported by numerous of astrophysical and cosmological measurements, taking part of about 85% of its mass content [1]. Many well-motivated elementary particle candidates arising in extensions of the Standard Model of particle physics are proposed. One of the most promising class of models is the Weakly Interactive Massive Particles (WIMPs). They are stable particle with masses and couplings at the electroweak scale produced in a standard thermal history of the Universe has the relic density that corresponds to that of DM, $\langle \sigma v \rangle = 3 \times 10^{-26}\mathrm{cm}^3\mathrm{s}^{-1}$. The self-annihilation of DM particles is expected to create Standard Model particles, including gamma-rays that can be detected by ground-based Cherenkov telescopes. Overdense regions of the universe are the best place to look for a DM signal because the annihilation rate is proportional to the square of the DM density along the line of sight. The Galactic Center (GC) is one of the favorite target for indirect detection due to its proximity and the high expected DM density. Currently, the best constraints on the velocity weighted cross section above 800 GeV are obtained by H.E.S.S. and reach 3×10^{25} $\mathrm{cm}^3\mathrm{s}^{-1}$ at 1 TeV for 112 hours of observation toward the GC [2]. In this study we present an update this analysis using 10 years of data and a two dimensional likelihood to make use of the spectral and spatial characteristics of the DM compared to background

2 Dark Matter search with H.E.S.S. in the Galactic halo

2.1 Galactic Center observations

The H.E.S.S. array, located in the Khomas Highland of Namibia, is made of 4 telescopes of 12 m in diameter with a total field of view of 5°, and a larger one of 28 m diameter located at the center of the array aiming at lowering the energy threshold down to a few tens of GeV. Only the observation using the 4 12-m telescopes will be use in this analysis. We used for this analysis 254 hours of observations of the GC taken between 2004 and 2014. All data pass the standard H.E.S.S. quality criteria [3] and lead to an average zenith angle off 18°. The data analysis is done in a circular region of interest (RoI) of 1° radius centered on the GC excluding the Galactic latitudes $|b| < 0.3°$ to avoid any contamination by standard astrophysical sources [4,5,3,6,7]. We then subdivise the ON region into seven spatial bins corresponding to sub RoIs defined as annuli of 0.1° width centered on the GC with inner radii from 0.3° to 0.9°.

2.2 Dark matter annihilation flux

The differential γ-ray flux, produced by the annihilation of self-conjugated DM particles of mass m_{DM}, in a solid angle in the sky $d\Omega = 2\pi \sin\theta d\theta$, is given by:

$$\frac{d\Phi_\gamma^P}{d\Omega dE_\gamma} = \frac{1}{8\pi m_{DM}^2} \sum_f \langle \sigma v \rangle_f \frac{dN_\gamma^f}{dE_\gamma}(E_\gamma) \times J(\theta) \ , \qquad J(\theta) = \int_{l.o.s.} ds \ \rho^2(r(s,\theta)) \tag{1}$$

where $\langle \sigma v \rangle_f$ and dN_γ^f/dE_γ are the thermally-averaged velocity-weighted annihilation cross section and the energy spectrum of photons in a given the channel for a finale state f, respectively. The coordinate r writes $r(s,\theta) = (r_\odot^2 + s^2 - 2r_\odot s\cos\theta)^{1/2}$, where s is the distance along the line of sight. θ is the aperture between the direction of observation and the GC plane, and $r_\odot = 8.5$ kpc is the Sun location with respect to the GC. The function $J(\theta)$, or *J-factor*, integrates the square of the DM density ρ along the line of sight. For the computation of the *J-factor*, we will assume an Einasto and an NFW profile parametrized by:

$$\rho(r) = \rho_s \exp\left[-\frac{2}{\alpha_s}\left(\left(\frac{r}{r_s}\right)^{\alpha_s} - 1\right)\right] \ , \quad \rho_{NFW}(r) = \rho_s \left(\frac{r}{r_s}\left(1 + \frac{r}{r_s}\right)^2\right)^{-1} \ , \tag{2}$$

The Einasto and NFW profile parameters, (ρ_s, α_s, r_s) and (ρ_s, r_s), are extracted from Ref. [2] assuming a local DM density of $\rho_\odot = 0.39$ GeVcm^{-3}. The J-factors computed in the RoI, gives $J_E = 4.92 \times 10^{21}$ GeV^{2}cm^{-5} and $J_{NFW} = 2.67 \times 10^{21}$ GeV^{2}cm^{-5} for the Einasto and NFW profiles, respectively. An alternative parametrization of the Einasto profile [8] leads to $J_{E_2} = 1.51 \times 10^{21}$ GeV^{2}cm^{-5}.

2.3 Analysis methodology

The analysis is based on a two-dimensional likelihood ratio test which uses the spatial and spectral characteristics of the DM signal versus background. For a given DM mass m_{DM}, the total likelihood is obtained by the product over the spatial bins i and the energy bins j of the individual Poisson likelihoods. It writes $\mathcal{L}(m_{DM}, \langle \sigma v \rangle) = \prod_{i,j} \mathcal{L}_{ij}$, with the individual likelihood is then given by [9]:

$$\mathcal{L}_{ij}(N_S, N_B | N_{ON}, N_{OFF}, \alpha) = \frac{(N_{S,ij} + N_{B,ij})^{N_{ON,ij}}}{N_{ON,ij}!} e^{-(N_{S,ij}+N_{B,ij})} \ . \tag{3}$$

$N_{S,ij}+N_{B,ij}$ is the expected total number of events in the spatial bin i and spectral bin j in the ON regions. $N_{S,ij}$ is the expected number of signal events and $N_{B,ij}$ the number of background events expected in the spatial bin i and spectral bin j. $N_{ON,ij}$ and $N_{OFF,ij}$ are the number of observed

events in the ON and OFF regions, respectively. $N_{\rm B,ij}$ is extracted from the OFF regions and given by $N_{\rm B,ij} = \alpha_i N_{\rm OFF,ij}$. The parameter $\alpha_i = \Delta\Omega_i/\Delta\Omega_{\rm OFF}$ refers to the ratio between the angular size of the ON region i and the OFF region. In our case, this ratio is equal to one since each OFF region is taken symmetrically to the ON region for each run pointing position. Consequently they have the same angular size and exposure. Constraints on $\langle\sigma v\rangle$ are obtained from the likelihood ratio test statistic given by TS $= -2\ln(\mathcal{L}(m_{\rm DM}, \langle\sigma v\rangle)/\mathcal{L}_{\rm max}(m_{\rm DM}, \langle\sigma v\rangle))$, which, in the high statistics limit, follows a χ^2 distribution with one degree of freedom [10]. Values of $\langle\sigma v\rangle$ for which TS is higher than 2.71 are excluded at 95% confidence level (C.L.).

3 Results

No γ-ray excess is found in any of the RoIs. We compute the upper limits on $\langle\sigma v\rangle$ with 95 % C. L. for WIMPs with masses between 160 GeV and 70 TeV annihilating into quark ($b\bar{b}$, $t\bar{t}$), gauge bosons (W^+W^-) and leptons ($\mu^+\mu^-$, $\tau^+\tau^-$) channels. The γ-ray spectrum coming from DM annihilation is computed using the tools available in Ref [8]. The left panel of Fig. 1 shows the observed 95% C. L. upper limits for the W^+W^- channel and the Einasto profile in black solid line. The expectations are obtained from 1000 Poisson realizations of the background measured in blank-field observations at high Galactic latitudes. The mean expected limit (black dotted line) together with the 68% (green band) and 95% (yellow band) C. L. containment bands are shown. We obtain a factor 5 improvement in total compare to the previous H.E.S.S. results [2] (blue solid line). In the right panel the same results are shown for the $\tau^+\tau^-$ channel. For the first time a ground based telescope array is able to probe the thermal relic density.

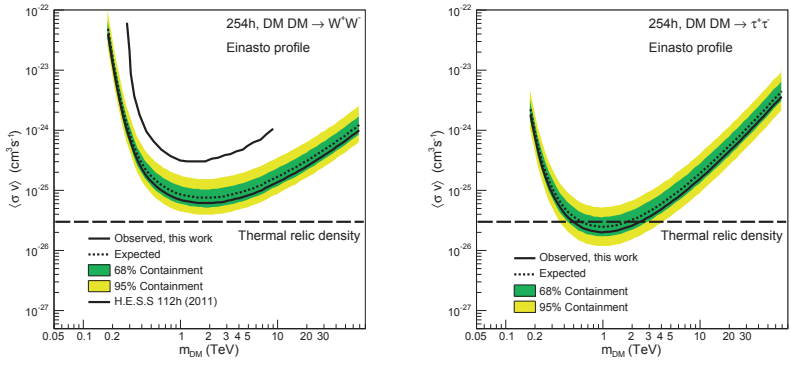


Figure 1 – Constraints on the velocity-weighted annihilation cross section $\langle\sigma v\rangle$ for the W^+W^- (left panel) and $\tau^+\tau^-$ (right panel) channels derived from 10 years of observations of the inner 300 pc of the GC region with H.E.S.S. as a function of the DM mass $m_{\rm DM}$. The observed limit is shown as black solid line.The mean expected limit (black dotted line) together with the 68% (green band) and 95% (yellow band) C. L. containment bands are shown. The blue solid line corresponds to the limits derived in a previous analysis of 4 years (112 h of live time) of GC observations by H.E.S.S.. The horizontal black long-dashed line corresponds to the thermal relic velocity-weighted annihilation cross section.

In the left panel of Fig. 2, the impact of the assumption on the DM distribution on the upper limit is shown for the three previous defined profile (see Eq. (2)). Finally, the right panel of Fig. 2 shows the comparaison with the more recents constraints obtain in indirect detection. We represent for the ground based telescope: MAGIC towards the dwarf galaxy Segue 1 [11], the combined observation of 4 dwarfs galaxies by H.E.S.S. [12] and the combined observations of 15 dwarfs galaxies by the Fermi satellite [13].

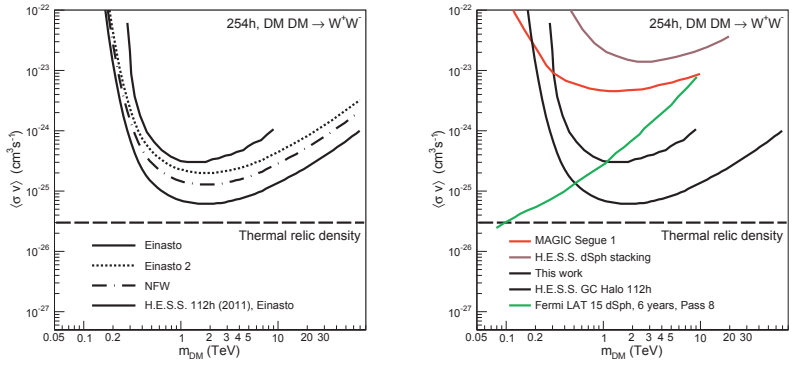


Figure 2 – Left: Impact of the DM density distribution on the constraints on the velocity-weighted annihilation cross section $\langle\sigma v\rangle$. The constraints expressed in terms of 95% C. L. upper limits are shown as a function of the DM mass m_{DM} in the W^+W^- channels for the Einasto profile (solid black line), another parametrization of the Einasto profile (dotted black line), and the NFW profile (long dashed-dotted black line), respectively. Right: Comparison of constraints on the W^+W^- channels with the previous published H.E.S.S. limits from 112 hours of observations of the GC (blue line), the limits from the observations of 15 dwarf galaxy satellites of the Milky Way by the Fermi satellite (green line), the limits from 157 hours of observations of the dwarf galaxy Segue 1 (red line), and the combined analysis of observations of 4 dwarf galaxies by H.E.S.S. (brown line).

4 Summary

We performed a search for a signal of self-annihilating dark matter particles in the inner Galactic halo using the full dataset of the first phase of H.E.S.S. available. With 10 years of observations of the GC we obtained 254 hours of data. In this dataset, no significant gamma-ray excess is found in the considered RoIs, thus we derived 95% C.L. upper limits on $\langle\sigma v\rangle$ for DM annihilations into several channels. Together with higher statistics and a two dimensional likelihood analysis method we improve the limits by a factor 5 compare to previous H.E.S.S. results reaching 6×10^{-26} cm^{3}s^{-1} for a 2 TeV DM mass in the W^+W^- channel. The strongest limits are obtained in the $\tau^+\tau^-$ channel at 2×10^{-26} cm^{3}s^{-1} for a DM particle mass of 1 TeV. For the first time, observations with a ground-based array of imaging atmospheric Cherenkov telescopes are able to probe the thermal relic annihilation cross section in the TeV DM mass range.

References

1. R. Adam et al. 2015. arxiv:1502.01582.
2. A. Abramowski et al. *Phys. Rev. Lett.*, 106:161301, 2011.
3. F. Aharonian et al. *Astron. Astrophys.*, 457:899–915, 2006.
4. F. Aharonian et al. *Astron. Astrophys.*, 425:L13–L17, 2004.
5. F. Aharonian et al. *Astron. Astrophys.*, 432:L25–L29, 2005.
6. F. Aharonian et al. *Nature*, 439:695–698, 2006.
7. F. Aharonian et al. *Astron. Astrophys.*, 503:817, 2009.
8. M. Cirelli et al. *JCAP*, 1103:051, 2011.
9. G. Cowan, Cranmer K., E. Gross, and O. Vitells. *EPJ C*, 71:1554, 2011.
10. W. A. Rolke, A. M. Lopez, and J. Conrad. *Nucl. Instrum. Meth.*, A551:493–503, 2005.
11. J. Aleksic et al. *JCAP*, 1402:008, 2014.
12. A. Abramowski et al. *Phys. Rev.*, D90:112012, 2014.
13. M. Ackermann et al. *Phys. Rev. Lett.*, 115(23):231301, 2015.

DARK MATTER DISTRIBUTION AND INDIRECT DETECTION IN DWARF SPHEROIDAL GALAXIES

C. COMBET, V. BONNIVARD, D. MAURIN
LPSC, Université Grenoble-Alpes, CNRS/IN2P3, 53 avenue des Martyrs, 38026 Grenoble Cedex, France

Dwarf spheroidal (dSph) galaxies are prime targets for present and future gamma-ray telescopes hunting for indirect signals of dark matter (DM). The interpretation of the data requires a careful assessment of their dark matter content in order to derive robust constraints on candidate relic particles. We present a data-driven DM profile determination that is based on the Jeans analysis, which we have "optimised" using a set of mock dSph kinematic datasets, testing for the various systematics that may affect the results (choice of DM, light and anisotropy profile parametrizations, binned versus unbinned datasets, stellar contamination, triaxiality). We have used this optimised setup to re-analyse the 8 classical and 13 ultrafaint dSphs, as well as Ret 2 (an ultrafaint dSph newly discovered by DES in 2015), and provide a new ranking of the best dSphs candidates w.r.t their expected signal and associated error bars. Notably, we find Segue I (often considered the best target) to be among the most uncertain candidates. This analysis illustrates the challenges that still need to be addressed when inferring the dark matter content of the new ultrafaint satellites recently discovered in the DES data.

1 Introduction

A careful determination of the DM distribution in dwarf spheroidal galaxies is mandatory if they are to be used as robust targets for DM indirect detection. Indeed, the differential γ-ray flux (at energy E and integrated over the solid angle $\Delta\Omega$) from DM annihilation is written as

$$\begin{aligned} \frac{d\Phi}{dE}(E,\vec{k}) &= \frac{d\Phi^{\rm PP}}{dE}(E)\times J(\vec{k}) \\ &= \frac{1}{4\pi}\frac{\langle\sigma v\rangle}{m_\chi^2\delta}\sum_f \frac{dN_\gamma^f}{dE}B_f \times \int_{\Delta\Omega}\int_{\rm l.o.s}\rho^2 dl\, d\Omega\,, \end{aligned} \tag{1}$$

where i) the particle physics term $d\Phi^{\rm PP}/dE$ provides the spectrum for a given mass m_χ, annihilation cross-section $\langle\sigma v\rangle$ and annihilation channels f of the DM candidate, and ii) the so-called J-factor depends on the DM density squared ρ^2, integrated along the line-of-sight direction $\vec{k}$.

Two broad types of approaches have been developed to estimate the DM distributions, and therefore J-factors, of the known dSph of the Milky Way. All studies generally require some fit to the kinematic data of the dSph galaxies and use more or less severe assumptions. On the one hand, several authors have used strong cosmological priors, or have used pre-defined DM profile parametrizations (e.g. core or NFW profiles), e.g. Pieri *et al.*[1]. These strong assumptions could however bias the results. On the other hand, data-driven analyses (i.e. relying on little underlying assumptions) have also been developed and generally yield more robust results despite larger error bars (Essig *et al.*[2], Geringer-Sameth *et al.*[3]).

In a recent series of articles (Bonnivard *et al.*[4,5,6]), we have revisited the data-driven approach we originally developed in Charbonnier *et al.*[7] by optimising the Jeans analysis using a set of

mock dSph galaxies (§2) and applying this optimised setup to the classical and ultrafaint dSph galaxies whose data were available at the time (§3). From the dSph J-factors, we obtained a new ranking of the best targets and briefly conclude in §4.

2 Optimisation of the Jeans analysis using mock data

Assuming spherical symmetry, steady-state and negligible rotational support the so-called Jeans equation links the dynamics of a tracer population to the underlying gravitational potential as

$$\frac{1}{\nu}\frac{d}{dr}(\nu\bar{v_r^2}) + 2\frac{\beta_{\rm ani}(r)\bar{v_r^2}}{r} = -\frac{GM(r)}{r^2}\,, \tag{2}$$

where ν is the numerical density of the tracer population, $\bar{v_r^2}$ is the radial velocity dispersion, $\beta_{\rm ani}(r) \equiv 1 - \bar{v_\theta^2}/v_r^2$ is the velocity parameter, and $M(r)$ is the total mass enclosed in radius r. Neglecting the stellar mass, the latter is simply written from the DM density ρ as

$$M(r) = 4\pi \int_0^r \rho(s) s^2 ds\,. \tag{3}$$

The quantities $\nu(r)$ and $\bar{v_r^2}$ are linked to the surface brightness of the object $\Sigma(R)$ and to its projected velocity dispersion $\sigma_P(R)$ through Abel transforms. These projected quantities are observables of the dSph galaxies, obtained by photometric and spectroscopic observations respectively. Therefore, given a set of observations one may solve the Jeans equation to constrain the DM density profile $\rho(r)$, and subsequently the J-factors.

To do so, parametric functions must be assumed for $\rho(r)$, $\Sigma(R)$, and $\beta(r)$ and it is not straightforward to decide what choice constitutes an adequate parametrizations and what choice would lead to biased results. Parametrizations of these quantities, using different numbers of free parameters have been proposed in the literature. In Bonnivard *et al.*[4], we make use of a set of mock dSph galaxies (for which the true underlying DM distribution is known) to systematically explore these various parametrizations and identify which combination yields the most accurate and robust reconstruction of the J-factors. This has been done using the CLUMPY code (Bonnivard *et al.*[8]) which allows us to solve the Jeans equation using a Markov Chain Monte Carlo (MCMC) and to propagate the error budget to the J-factors. Our main findings are the following:

- The light profile $\Sigma(R)$ is the first quantity to be fitted prior to the Jeans MCMC analysis. We find that a proper fit of the outer regions sampled by the light profile is indispensable to a good reconstruction of the J-factors. An underestimation of the light could lead to a biased reconstruction, with an overestimation of the J by a factor of a few. We conclude that the 5-parameter Zhao parametrization is a fexible enough choice to fit the light profile.

- Concerning the anisotropy $\beta_{\rm ani}(r)$, and given the lack of any constraining data, the choice $\beta_{\rm ani} = {\rm cst}$ is often made. We find that this assumption is safe when dealing with *ultrafaint* objects (in which only a few stars are measured); in this case, the error budget is dominated by the little statistic available rather than by anything else. This is not true for *classical* dSph galaxies where this choice could bias the reconstruction of the J-factors, as illustrated by the blue contours in Fig. 1. In that case, we recommend the use of the more flexible Baes & Van Hese parametrizations.

- For the DM profile parametrizations $\rho(r)$, we have tested the Einasto (3 parameters) and Zhao (5 parameters) parametrizations. As far as the J-factor is concerned, both these choices yield similar results and we therefore recommend the Einasto parametrizations as the default, as the smaller number of parameters allows for a faster run of the MCMC analysis.

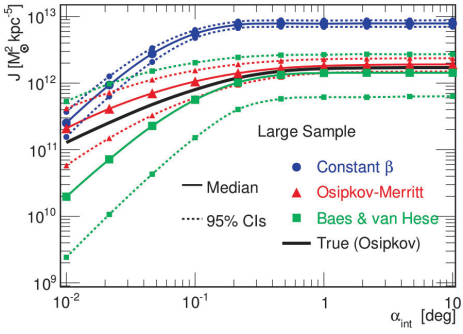


Figure 1 – Reconstructed J-factor as a function of the integration angle for a mock dSph galaxy with a large number of stars, using various parametrizations for $\beta_{\rm ani}(r)$. The mock data was generated using an Osipkov-Merritt profile. Assuming a constant $\beta_{\rm ani}$ (blue) biases the reconstruction. The more generic Baes & van Hese description (green) encompasses the true value (black).

These parametrisation choices are associated to a careful selection of the priors used to run the MCMC analysis, in order to avoid nonphysical models and limit the effect of the degeneracy between the dark matter and anisotropy profiles.

Finally, the spherical symmetry assumption of the Jeans equation may not hold as numerical simulations have shown DM halos to be triaxial. Using two triaxial mock dSph galaxies, we find that DM projection effects alone yield a $\sim$ 30% increase of the uncertainties. Furthermore, reconstructing the J-factors, assuming spherical symmetry (for both the light and DM) for these triaxial objects could bias the results by a factor of a few. For more details and the exhaustive analysis, we refer the reader to Bonnivard *et al.*[4].

3 Application to classical and ultrafaint dSph galaxies

We have applied the optimised Jeans analysis described above to real dSph galaxy data (Bonnivard *et al.*[5,6]). The set of objects consist of the 8 *classical* dSph galaxies discovered prior to SDSS and of 14 *ultrafaint* objects discovered since, for which kinematic data were available at the time of the study. The J-factors obtained for a 0.5° integration angle are gathered in Fig. 2, ordered by increasing values. Blue symbols correspond to this study and are compared to the results of other works.

Our results are generally consistent with those of other studies, but we note that using the more flexible Zhao profile for the light (and not the generally used Plummer parametrizations) may slightly increase the J-factors of a few dSphs, but as we have shown, this choice is necessary to mitigate possible biases. Furthermore, the error bars we obtained for this data-driven analysis are, as one would expect, larger for the ultrafaint dSphs, where only a small number of stars are measured spectroscopically.

We find Draco and Ursa Minor to be the best targets among the classical dSphs, as they combine relatively large J-factor values and small errors. More uncertain, but possibly more promising are the ultrafaint objects Ursa Major 2, Coma and Reticulum 2.

Finally, we find Segue I to be the most uncertain object, with a median J-factor much lower than what was previously considered. While this object has generally been considered to be one of the most promising dSph target to place limits on DM candidate, our results suggest that it may not be the case due to possible stellar contamination of the data (Bonnivard *et al.*[9]).

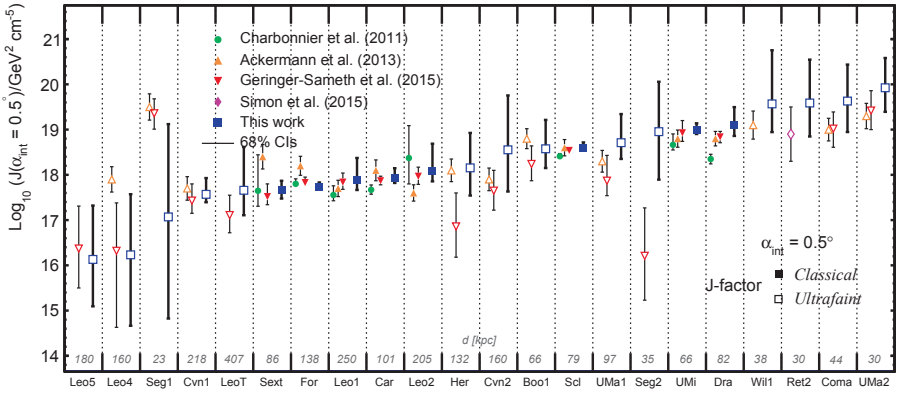


Figure 2 – J-factors of the classical (filled symbols) and ultrafaint dSph galaxies (open symbols), ordered by increasing values. Error bars denote the 68% confidence intervals. Results from the optimised Jeans analysis developed here (blue squares) are compared to those of other studies (other symbols).

4 Conclusion

Robust values of the J-factors of dSph galaxies are necessary to place constraints on the DM candidates. We make use of a set of mock dSph galaxies to determine what is the best setup to run the Jeans analysis in order to obtain unbiased J-factors with robust error bars. This setup has then been applied to the 8 classical and 14 ultrafaint dSph galaxies to provide a new ranking, where Draco, Ursa Minor, Ursa Major 2, Coma and Reticulum 2 appear as the most promising targets. Conversely to what was generally assumed before, our results suggest that Segue I is possibly one of the most uncertain targets to place robust limits on the DM candidates.

Finally, we note that since this work was performed, a few other ultrafaint objects have been identified and more kinematic data have become available. In particular, the recently discovered Triangulum II galaxy, not included in this study, could have one of the highest J-factors among the known dSph galaxies (Hayashi *et al.*[10]).

Acknowledgments

This work has been supported by the "Investissements d'avenir Labex ENIGMASS", and by the French ANR, Project DMAstro-LHC, ANR-12-BS05-0006.

References

1. L. Pieri, M. Lattanzi, and J. Silk. *MNRAS*, 399, 2033 (2009).
2. R. Essig, N. Sehgal, and L. E. Strigari. *Phys. Rev. D.*, 80(2), 023506, (2009).
3. A. Geringer-Sameth, S. M. Koushiappas, and M. G. Walker. *ApJ*, 801, 74 (2015).
4. V. Bonnivard, *el al. MNRAS*, 446, 3002 (2015).
5. V. Bonnivard, *el al. MNRAS*, 453, 849 (2015).
6. V. Bonnivard, *el al. ApJL*, 808, L36 (2015).
7. A. Charbonnier, *el al. MNRAS*, 418, 1526 (2011).
8. V. Bonnivard, *el al. Computer Physics Communications*, 200, 336 (2016).
9. V. Bonnivard, *el al. ArXiv e-prints*, 1506.08209 (2015).
10. K. Hayashi, *el al. ArXiv e-prints*, 1603.08046 (2016).

The DarkSide program at LNGS

S. Davini, M. Bossa, A. Mandarano, C. Savarese
Gran Sasso Science Institute, L'Aquila AQ 67100, Italy

A. Razeto, G. Bonfini, A. Candela, M. Carlini, P. Cavalcante, M. De Deo, M. D'Incecco, F. Gabriele, A. M. Goretti, A. Ianni, M. Orsini, N. Rossi, D. Sablone, R. Tartaglia
Laboratori Nazionali del Gran Sasso, Assergi AQ 67010, Italy

M. Pallavicini, G. Testera, B. Bottino, M. Cariello, L. Marini, P. Musico, L. Pagani
Istituto Nazionale di Fisica Nucleare, Sezione di Genova, Genova 16146, Italy

S. M. Mari, F. Budano, S. Bussino, M. De Vincenzi, I. James
Istituto Nazionale di Fisica Nucleare, Sezione di Roma Tre, Roma 00146, Italy

G. Fiorillo, S. Catalanotti, A. G. Cocco, G. Covone, F. Granato, B. Rossi, P. Trinchese, S. Walker
Istituto Nazionale di Fisica Nucleare, Sezione di Napoli, Napoli 80126, Italy

A. Devoto, M. Cadeddu, M. Cadoni, M. Lissia
Istituto Nazionale di Fisica Nucleare, Sezione di Cagliari, Cagliari 09042, Italy

G. Ranucci, A. Brigatti, D. D'Angelo, P. Lombardi, S. Parmeggiano, P. Saggese
Istituto Nazionale di Fisica Nucleare, Sezione di Milano, Milano 20133, Italy

D. Franco, P. Agnes, A. Tonazzo
APC, Université Paris Diderot, CNRS/IN2P3, CEA/Irfu, Obs. de Paris, Sorbonne Paris Cité, Paris 75205, France

S. De Cecco, C. Giganti
LPNHE Paris, Université Pierre et Marie Curie, Université Paris Diderot, CNRS/IN2P3, Paris 75252, France

C. Galbiati, P. D. Meyers, I. F. M. Albuquerque, J. Brodsky, H. Cao, F. Calaprice, G. Koh, X. Li, H. Qian, W. Sands, E. Shields, C. Stanford, M. Wada, S. Westerdale, X. Xiang, J. Xu, C. Zhu
Department of Physics, Princeton University, Princeton, NJ 08544, USA

S. Pordes, K. Biery, G. Forster, K. Herner, Y. Guardincerri, C. L. Kendziora, J. Yoo
Fermi National Accelerator Laboratory, Batavia, IL 60510, USA

H. Wang, A. Fan, Y. Suvorov
Department of Physics and Astronomy, University of California, Los Angeles, CA 90095, USA

A. Pocar, A. Monte, K. Randle
Amherst Center for Fundamental Interactions and Dept. of Physics, University of Massachusetts, Amherst, MA 01003, USA

J. Maricic, E. Edkins, B. R. Hackett, R. Milincic, B. Reinhold
Department of Physics and Astronomy, University of Hawai'i, Honolulu, HI 96822, USA

E. V. Hungerford, A. L. Renshaw, N. Canci, A. Empl, G. Korga, P. N. Singh
Department of Physics, University of Houston, Houston, TX 77204, USA

C. J. Martoff, J. Napolitano, T. Miletic, A. W. Watson
Department of Physics, Temple University, Philadelphia, PA 19122, USA

E. Pantic, T. Johnson
Department of Physics, University of California, Davis, CA 95616, USA

A. Chepurnov, M. Gromov
Skobeltsyn Institute of Nuclear Physics, Lomonosov Moscow State University, Moscow 119991, Russia

O. Smirnov, K. Fomenko, D. Korablev, A. Sotnikov, A. Wishneva
Joint Institute for Nuclear Research, Dubna 141980, Russia

M. M. Wojcik, K. Pelczar, G. Zuzel
Smoluchowski Institute of Physics, Jagiellonian University, Krakow 30348, Poland

(The DarkSide Collaboration)

The DarkSide program at Laboratori Nazionali del Gran Sasso aims to perform background-free WIMP searches using double phase liquid argon time projection chambers, with the ultimate goal of covering all parameters down to the so-called neutrino floor. One of the distinct features of the program is the use of underground argon with has a reduced content of the radioactive ^{39}Ar compared to atmospheric argon. The DarkSide Collaboration is currently operating the DarkSide-50 experiment, the first such WIMP detector using underground argon, resulting in the best WIMP limits obtained with argon. The results obtained with DarkSide-50 and the plans for the next steps of the DarkSide program, the 20 t fiducial mass DarkSide-20k detector and the 200 t fiducial Argo, are reviewed in this proceedings.

1 Introduction

The existence of dark matter, postulated since 1930, is today widely accepted among particle physicists and cosmologists. Among a wide range of theories and dark matter candidates, one hypothesis is that dark matter could be constituted of weakly interacting massive particles (WIMP) with masses in the GeV/c^2 or TeV/c^2 range. There are many WIMP candidates from different theoretical models, but all sharing these common features: WIMPs are electrically neutral and stable over cosmological times, they interact through gravitational force and eventually with other unknown interactions of weak intensity (elastic scattering cross sections below the 10^{-44} cm^2 ballpark). According to these properties, WIMPs could interact with the nuclei of detectors releasing kinetic energies of few tens of keV. Very low interaction rates are expected, based on existing detection limits. Ultra-low background detectors with target masses of 0.1 – 10 tons may be required to discover WIMPs.

The DarkSide project at Laboratori Nazionali del Gran Sasso (LNGS) aims to perform background-free WIMP searches using double phase liquid argon time projection chambers (LAr TPCs). One of the advantages of argon is the powerful pulse-shape discrimination (PSD) between electron recoils (such as β and γ decays) and nuclear recoils (such as an elastic scattering interaction between a WIMP and a nucleus). One of the distinctive features of the program is the use of underground argon (UAr), which has a lower content of the radioactive ^{39}Ar compared to atmospheric argon (AAr).

2 DarkSide-50

The DarkSide-50 experiment is running at LNGS since November 2013. The DarkSide-50 detector system is described in Ref. [1] and in several proceedings of the collaboration. The apparatus consists of three nested detectors. Innermost is the cylindrical LAr TPC, with an active UAr mass of 46.4(7) kg observed by 38 3" PMTs. The design of the DarkSide-50 TPC is based upon

the successful prototype DarkSide-10 [2]. The LAr TPC is mounted and operated at the center of a liquid scintillator veto (LSV), described in Ref. [4], consisting of a 4.0 m diameter stainless steel sphere instrumented with 110 PMTs and filled with boron-loaded liquid scintillator. The scintillator is a solution of pseudocumene (PC), with 5% by volume trimethylborate (TMB). Surrounding the LSV is a 1 kilo-ton water Cerenkov veto (WCV) instrumented with 80 PMTs to veto the residual cosmic-ray muons present at the LNGS depth. Signals from the LSV and WCV are used to reject events in the LAr TPC caused by cosmogenic neutrons or by neutrons and γ-rays from radioactive contamination in the detector components.

An interaction in the LAr target generates primary scintillation light (S1 pulse) and ionization electrons. The electrons escaping recombination drift in the TPC electric field to the surface of the LAr, where a stronger electric field extracts them into the gaseous region, where they induce further light emission (S2 pulse) via proportional scintillation. The S1 and S2 signals together allow the interaction vertex to be localized in 3D. The time profile of the scintillation signal S1 allows rejection of backgrounds from γ-ray- and β-decay-induced events by using PSD. The PSD parameter used in the WIMP searches is f_{90}, the fraction of S1 light in the first 90 ns of the scintillation pulse.

The DarkSide-50 detectors have been calibrated during 2014, 2015, and 2016, using a series of γ and neutron radioactive sources placed inside the LSV next to the TPC. Data taken with ^{57}Co, ^{133}Ba, and ^{137}Cs γ-ray sources were used to validate Monte Carlo (MC) simulations. Data taken with AmBe and AmC neutron sources were used to validate the transfer of the nuclear recoil response from SCENE [5] to DarkSide-50, as described in Ref. [3], and also to study the response of the LSV to neutron captures and neutron recoils.

The DarkSide-50 collaboration published two null WIMP search results in 2015 [1] and 2016 [3]. A first run of DarkSide-50, with data taken during 2014 with a 1422(67) kg-day exposure of AAr, produced a null result for the WIMP search with zero backgrounds from ^{39}Ar decays [1]. A total of 15 million events in the LAr TPC, mostly originating from ^{39}Ar, were collected. All but two of the events falling within the WIMP region of interest were rejected using the PSD. The two remaining events in the WIMP search region had a signal in coincidence with the LSV and were therefore discarded.

After the AAr run, the TPC was drained and filled with low radioactivity UAr in April 2015. The low radioactivity UAr was extracted from the Doe Canyon (Colorado, USA) CO_2 wells. A total of 155 kg of low radioactivity UAr has been obtained. The ^{39}Ar activity of the UAr corresponds to a depletion by a factor of $1.4(2) \times 10^3$ relative to AAr [3].

The first WIMP search in DarkSide-50 using UAr has been reported in Ref. [3], where it is shown that the combination of the electron recoil background rejection observed in the AAr run, and the reduction of ^{39}Ar from the use of UAr would allow DarkSide-50 to be free from ^{39}Ar background for several tens of years. A non-blind physics analysis was performed. The TPC and veto physics cuts applied, as well as their efficiency and acceptance, are described in Refs. [3 4]. The distribution of events in the f_{90} vs. S1 plane, after all quality and physics cuts, is shown in the left panel of Fig. 1. No events are present within the WIMP search region, shown in Fig. 1, which is defined as a region in the f_{90} vs. S1 plane with known high acceptance for nuclear recoils and low leakage of single-scatter ER events between 20–460 PE (13–201 $\mathrm{keV_{nr}}$).

Dark matter limits from the present exposure are determined from the WIMP search region using the standard isothermal galactic WIMP halo parameters. When combined with the null result of the previous AAr exposure in DarkSide-50, a 90% CL upper limit on the WIMP-nucleon spin-independent cross section of $2.0 \times 10^{-44}\,\mathrm{cm^2}$ ($8.6 \times 10^{-44}\,\mathrm{cm^2}$, $8.0 \times 10^{-43}\,\mathrm{cm^2}$) for a WIMP mass of $100\,\mathrm{GeV/c^2}$ ($1\,\mathrm{TeV/c^2}$, $10\,\mathrm{TeV/c^2}$) is obtained. Fig. 2 compares these limits to those obtained by other experiments. A detailed description of the procedure can be found in Ref. [3].

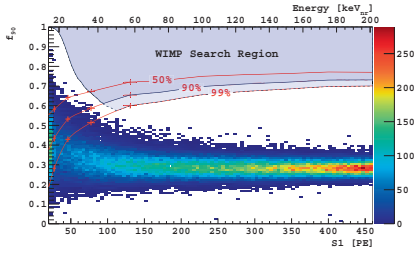


Figure 1 – Distribution of events in the f_{90} vs S1 plane which survive all physics cuts. Shaded blue with solid blue outline: WIMP search region.

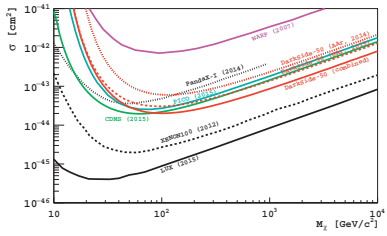


Figure 2 – Spin-independent WIMP-nucleon cross section 90% C.L. exclusion plot for DarkSide-50, compared to other experiments.

3 The future steps of the DarkSide program

The combination of the AAr and UAr results in DarkSide-50 leads to the expectation that a background-free result can also be obtained from a much larger exposure with a multi-tonne detector. On this basis, an enlarged DarkSide Collaboration has proposed the construction of DarkSide-20k, a direct WIMP search using a LAr TPC with a fiducial mass of 20 t of depleted argon (DAr). DAr is UAr which has been further depleted in ^{39}Ar by means of isotopic separation. DarkSide-20k is designed to achieve a background-free exposure of 100 t yr accumulated during a run of 5 years, giving a sensitivity to WIMP-nucleon interaction cross sections of $1 \times 10^{-47}\,\mathrm{cm}^2 (1 \times 10^{-46}\,\mathrm{cm}^2)$ for WIMPs of $1\,\mathrm{TeV/c}^2$ ($10\,\mathrm{TeV/c}^2$) mass.

In the longer term, the aim of the DarkSide collaboration is to develop a path towards a WIMP detector to be built and operated at LNGS with a 200 t DAr fiducial mass. For now, this ultimate experiment is called Argo. Argo is planned to accumulate an exposure of 1000 t yr, free of backgrounds other than those induced by coherent scattering of neutrinos, and thus be sensitive to WIMP cross sections below the neutrino floor.

Procurement of the necessary quantity of low radioactivity UAr for DarkSide-20k is the critical technical challenge for the experiment, and will be addressed within the framework of the Urania and Aria projects. The Urania project will provide a plant capable of extracting 100 kg/d of UAr from the same wells that yielded the UAr for DarkSide-50. The Aria project will provide a cryogenic distillation plant capable of reducing the residual ^{39}Ar in the UAr by a factor of 10 per pass, at a rate of 150 kg/d, by exploiting the small difference in vapor pressure between ^{39}Ar and ^{40}Ar. The Urania and Aria projects will ultimately supply the DAr for the DarkSide-20k experiment.

4 Conclusions and Outlook

The DarkSide collaboration reported the first WIMP search using low radioactivity UAr [3], resulting in the best WIMP limits obtained with argon. The combination of PSD in argon and low radioactivity UAr lead to the expectation that a background-free result can also be obtained with a multi-tonne detector. The DarkSide collaboration has proposed the construction of the 20 t fiducial mass DarkSide-20k detector.

References

1. P. Agnes *et al*, *Phys. Lett.* B **743**, 456-466 (2015)
2. T. Alexander *et al*, ASTROPARTICLE PHYSICS **49**, 44-51 (2013)
3. P. Agnes *et al*, *Phys. Rev.* D **93**, 081101 (2016)
4. P. Agnes *et al*, JINST **11**, P03016 (2016)
5. H. Cao *et al*, *Phys. Rev.* D **91**, 092007 (2015)

THE WEAK EQUIVALENCE PRINCIPLE WITH ANTIMATTER: THE AEgIS EXPERIMENT AT CERN

D. Pagano[b,c], C. Amsler[a], T. Ariga[a], G. Bonomi[b,c], P. Bräunig[d], R. S. Brusa[f,g], L. Cabaret[h], M. Caccia[i,j], R. Caravita[k,l], F. Castelli[i,m], G. Cerchiari[n], D. Comparat[h], G. Consolati[o,i], A. Demetrio[o,i], L. Di Noto[k,l], M. Doser[e], A. Ereditato[a], C. Evans[o,i], R. Ferragut[o,i], J. Fesel[e], A. Fontana[c], S. Gerber[e], M. Giammarchi[i], A. Gligorova[p], F. Guatieri[f,g], S. Haider[e], H. Holmestad[r], T. Huse[r], A. Kellerbauer[n], D. Krasnický[k,l], V. Lagomarsino[k,l], P. Lansonneur[s], P. Lebrun[s], C. Malbrunot[e,t], S. Mariazzi[t], V. Matveev[u,v], Z. Mazzotta[i,m], G. Nebbia[w], P. Nedelec[s], M. Oberthaler[d], N. Pacifico[p], L. Penasa[f,g], V. Petracek[q], C. Pistillo[a], F. Prelz[i], M. Prevedelli[x], L. Ravelli[l], B. Rienaecker[e], O.M. Røhne[e], A. Rotondi[c,y], M. Sacerdoti[i,m], H. Sandaker[e], R. Santoro[i,j], P. Scampoli[a,z], L. Smestad[e,aa], F. Sorrentino[k,l], I. M. Strojek[q], G. Testera[l], I. C. Tietje[e], S. Vamosi[t], E. Widmann[t], P. Yzombard[h], J. Zmeskal[t], N. Zurlo[c,ab]

[a] *Laboratory for High Energy Physics, Albert Einstein Center for Fundamental Physics, University of Bern, 3012 Bern, Switzerland*
[b] *Department of Mechanical and Industrial Engineering, University of Brescia, via Branze 38, 25123 Brescia, Italy*
[c] *INFN Pavia, via Bassi 6, 27100 Pavia, Italy*
[d] *Kirchhoff-Institute for Physics, Heidelberg University, Im Neuenheimer Feld 227, 69120 Heidelberg, Germany*
[e] *Physics Department, CERN, 1211 Geneva 23, Switzerland*
[f] *Department of Physics, University of Trento, via Sommarive 14, 38123 Povo, Trento, Italy*
[g] *TIFPA/INFN Trento, via Sommarive 14, 38123 Povo, Trento, Italy*
[h] *Laboratoire Aimé Cotton, Université Paris-Sud, ENS Cachan, CNRS, Université Paris-Saclay, 91405 Orsay Cedex, France*
[i] *INFN Milano, via Celoria 16, 20133, Milano, Italy*
[j] *Department of Science, University of Insubria, Via Valleggio 11, 22100 Como, Italy*
[k] *Department of Physics, University of Genova, via Dodecaneso 33, 16146 Genova, Italy*
[l] *INFN Genova, via Dodecaneso 33, 16146 Genova, Italy*
[m] *Department of Physics, University of Milano, via Celoria 16, 20133 Milano, Italy*
[n] *Max Planck Institute for Nuclear Physics, Saupfercheckweg 1, 69117 Heidelberg, Germany*
[o] *Politecnico of Milano, Piazza Leonardo da Vinci 32, 20133 Milano, Italy*
[p] *Institute of Physics and Technology, University of Bergen, Allégaten 55, 5007 Bergen, Norway*
[q] *Czech Technical University, Prague, Brehov 7, 11519 Prague 1, Czech Republic*
[r] *Department of Physics, University of Oslo, Sem Slandsvei 24, 0371 Oslo, Norway*
[s] *Institute of Nuclear Physics, CNRS/IN2p3, University of Lyon 1, 69622 Villeurbanne, France*
[t] *Stefan Meyer Institute for Subatomic Physics, Austrian Academy of Sciences, Boltzmanngasse 3, 1090 Vienna, Austria*
[u] *Institute for Nuclear Research of the Russian Academy of Science, Moscow 117312, Russia*
[v] *Joint Institute for Nuclear Research, 141980 Dubna, Russia*
[w] *INFN Padova, via Marzolo 8, 35131 Padova, Italy*
[x] *University of Bologna, Viale Berti Pichat 6/2, 40126 Bologna, Italy*
[y] *Department of Physics, University of Pavia, via Bassi 6, 27100 Pavia, Italy*
[z] *Department of Physics "Ettore Pancini", University of Napoli Federico II, Complesso Universitario di Monte S. Angelo, 80126, Napoli, Italy*
[aa] *The Research Council of Norway, P.O. Box 564, NO-1327 Lysaker, Norway*
[ab] *Department of Civil Engineering, University of Brescia, via Branze 43, 25123 Brescia, Italy*

The AEgIS experiment at CERN's Antiproton Decelerator (AD) aims at performing a direct measurement of the gravitational force on antimatter to probe the Weak Equivalence Principle of General Relativity with antimatter. The idea is to measure the vertical displacement of a cold antihydrogen beam, due to the gravitational force, by using a moiré deflectometer. Antihydrogen will be formed through the reaction of charge exchange between cold antiprotons and Rydberg positronium. An overview of the physics goals, experimental setup and preliminary results is presented.

1 Introduction

Since the XVI century, it is experimentally known that objects fall in the gravitational field of the Earth with the same acceleration, regardless their mass or composition. This led Newton to conclude, in his *Philosophiae Naturalis Principia Mathematica* [1], that inertial and gravitational mass must be necessarily equivalent. Today this equivalence is know as *Weak Equivalence Principle* (WEP). In 1916 Einstein formulated a *stronger* version of the WEP [2], the *Einstein Equivalence Principle* (EEP), which is not only a pillar of General Relativity but, more in general, of all metric theories of gravity[3]. The WEP is a necessary condition for the EEP and it has been widely tested experimentally, resulting in very stringent limits on its possible violation with *ordinary* matter [3].

At present, several experimental and theoretical arguments seem to suggest that the WEP should also hold for antimatter [5,6,7]. However, not only all these arguments are indirect and rely on some theoretical assumptions, but, on the other hand, most of the attempts for a quantum theory of gravity tipically predict interactions which could violate the WEP for antimatter [8].

The AEgIS experiment aims at performing a direct test of the WEP on antimatter by measuring the acceleration g of a cold beam of antihydrogen in the Earth's gravitational field. The idea is to measure the vertical displacement, due to gravity, of a beam of antihydrogen crossing a moiré deflectometer coupled to a position sensitive detector (see Section 2). The goal is to reach a precision of the order of some percent on g. In the following section an overview of the AEgIS experiment is given.

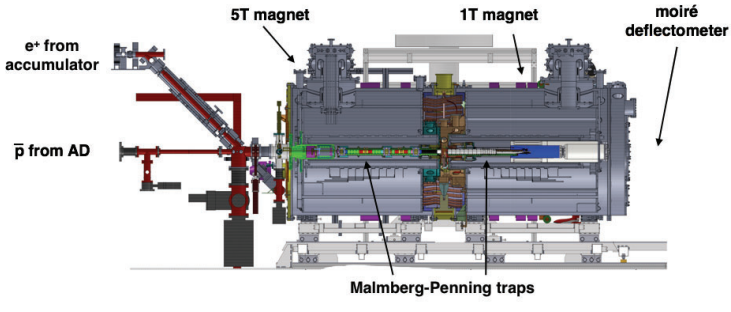


Figure 1 – Scheme of the experimental setup of the AEgIS experiment (moiré deflectometer not reported).

2 Overview of the AEgIS experiment

The AEgIS apparatus is schematically shown in Fig. 1 and consists of a 5 T and a 1 T superconducting solenoids, which house a Malmberg-Penning trap each [9]. The CERN's *Antiproton Decelerator* provides AEgIS with bunches of $\sim 3\times10^7$ antiproton, with 5 MeV of kinetic energy, every ∼100 s. The antiprotons loose their energy down to few keV by crossing a set of thin aluminum foils (degrader) and a fraction of them are caught by the trap in the 5 T magnet. They are then cooled to few K with sympathetic electron cooling and transferred to the 1 T trap for the $\bar{H}$ production. Rydberg antihydrogen atoms $\bar{H}^*$ will be produced from cold $\bar{p}$ and Rydberg ortho-positronium Ps^* via by the so-called *charge-exchange process* [10] $Ps^* + \bar{p} \rightarrow \bar{H}^* + e^-$, which is sketched in Fig. 2a . The positronimum is produced by sending pulses of positrons, emitted by a Na^{22} source and bunched in a Surko-type accumulator, toward a nanoporous silica target and exciting the emerging positronium to Rydberg states by two laser pulses. The charge-exchange process allows the production of ultra cold Rydberg $\bar{H}$ atoms, which, thanks to

their large electric dipole moment, can be accelerated by electric field gradients to form a beam.

The beam of $\bar{H}$ atoms passes through the so-called *gravity module*, which is composed by a classical moiré deflectometer [11] with two gratings, coupled to a position sensitive detector, as shown in Fig. 2b. For simple geometrical arguments, as the beam crosses the gratings it produces a fringe patter on the sensitive detector. Because of the gravity, this pattern is vertically shifted with respect to the one produced using light (Fig. 2b). This vertical displacement h is:

$$h = g_{\bar{H}} \left(\frac{L}{v}\right)^2, \tag{1}$$

where $g_{\bar{H}}$ is the modulus of the gravitational acceleration experienced by the $\bar{H}$ atoms, v is component of their velocity along the direction perpendicular to the grating period, and L is the distance between gratings. As Eq. 1 shows, this strategy allows a direct measurement of $g_{\bar{H}}$, with a resolution which mainly depends on the number of reconstructed $\bar{H}$ atoms and the detector resolution.

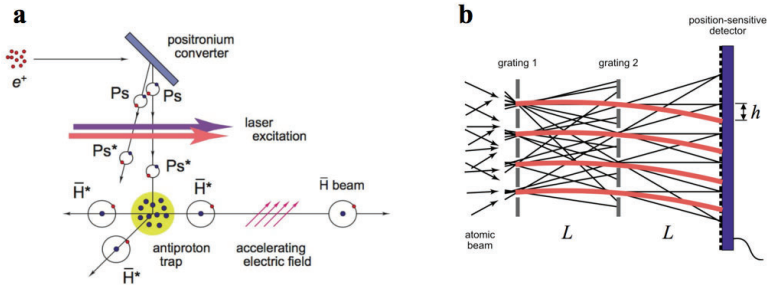


Figure 2 – a) Scheme of the Rydberg antihydrogen production via charge-exchange in AEgIS; b) Scheme of the AEgIS gravity module.

3 First results with a small-scale Moiré deflectometer

A proof of principle of the measurement technique has been performed [12] by exposing a small-scale moiré deflectometer ($L = 25$ mm), coupled to an emulsion detector, to a beam of antiprotons coming from AD, whose energy at the gravity module was estimated to be ~ 0.1 MeV from MC simulations. The sensitive detector was composed by two different regions, as shown in Fig. 3a: one with only the emulsion, and one with an additional grating in direct contact to it. The goal of the contact grating was to align the measurements with antiprotons and visible light, being the latter used to create the reference frame.

A total of 241 annihilation stars were recorded on the nuclear emulsions. Their positions were reconstructed, with an accuracy of ~ 2 μm, and then compared to the reference light pattern. Fig. 3b shows the reconstruction of the annihilation vertexes from data (blue dots), superimposed to the reference pattern (red band), as produced without (left) and with (right) the contact grating. The periodicity of data was extracted using a Rayleigh test and the y-coordinates of the reconstructed vertexes were compared (in grating units d) to what expected from the reference frame, as shown in Fig. 3c. The period of the moiré pattern of the $\bar{p}$ beam was found to be the same as the reference light pattern, shifted by $9.8 \pm 0.9(stat) \pm 6.4(syst)$ μm. The observed shift of the moiré pattern is consistent with a mean force acting on the antiprotons of $530 \pm 50(stat) \pm 350(syst)$ aN. This force can be explained in terms of the Lorentz force of a 7.4 G

magnetic field, consistent with the residual magnetic field of ∼10 G measured at the location of the moiré deflectometer. Although a measurement of the gravitational force on the antiprotons cannot be inferred from data, the results prove that the use of a moiré deflectometer, coupled to a position detector, allows the measurement of a micrometric phase shift due to a magnetic force. Moreover, according to Eq. 1, this measured phase shift is expected to be comparable to the one to be produced by the gravitational force on antihydrogen, in the full-scale deflectometer ($L = 1$ m) and with $v \sim 500\ ms^{-1}$.

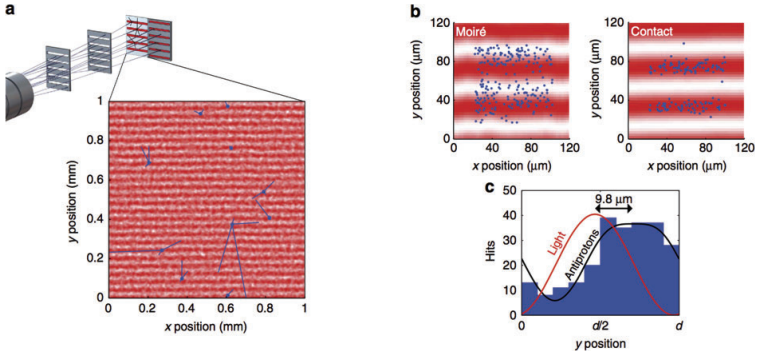


Figure 3 – a) Schema of the small-scale gravity module used [12]; b) Shadow fringe pattern on the emulsion detector produced by the moiré deflectometer (left) and the contact grating (right) [12]; c) Vertical displacement of the $\bar{p}$ fringe with the respect to reference one created with light (in grating units d) [12].

4 Conclusions

The main goal of the AEgIS experiment is to probe the WEP with antimatter, by measuring the gravitational acceleration of a $\bar{H}^*$ beam with an accuracy of some percents. The experimental setup is almost fully in place, with the exception of the full-scale gravity module, which is still under development. A proof of principle has been performed, using a small-scale prototype of the moiré deflectometer and a beam of antiprotons. The results showed that a micrometric shift is observable, proving the feasibility of the proposed detection method. At present, the $\bar{H}^*$ production is expected to be achieved by the end of this year, while the first measurement of $g_{\bar{H}}$ is planned for the following years.

References

1. I. Newton, Philosophiae Naturalis Principia Mathematica, **1**, (1687).
2. A. Einstein, Annalen Phys., **49**, 769 (1916).
3. C. M. Will, Living Rev. Rel. **17**, 4 (2014).
4. T. A. Wagner *et al.*, Class. Quantum Grav. **29**, 184002 (2012).
5. S. Pakvasa, W. A. Simmons and T. J. Weiler, Phys. Rev. D **39**, 1761-1763 (1989).
6. A. Apostolakis *et al.*, Phys. Lett. B **452**, 425-433 (1999).
7. M. M. Nieto and T. Goldman, Phys. Rep. **205**, 221-281 (1991).
8. J. Ponce de Leon Int. J. Mod. Phys. D **18**, 251273 (2009)
9. M. Amoretti *et al.*, CERN-SPSC-2007-017 (2007).
10. B. I. Deutch *et al.*, Proc. 1st Workshop on Antimatter Physics at Low Energies `http://lss.fnal.gov/conf/C860410/` (1986).
11. M. K. Oberthaler *et al.*, Phys. Rev. A **54**, 4 (1996).
12. S. Aghion *et al.*, Nat. Commun. **7**, 5 (2014).

Directional detection of Dark Matter with the MIcro-tpc MAtrix of Chambers

C. COUTURIER[a1], J. BRUNNER[3], J. BUSTO[3], P. COLAS[2], D. FOUCHEZ[3], I. GIOMATARIS[2], O. GUILLAUDIN[1], F. NARAGHI[1], Q. RIFFARD[1], D. SANTOS[1], C. TAO[3]

[1] *LPSC, Université Grenoble-Alpes, CNRS/IN2P3, 38026 Grenoble, France*
[2] *IRFU, CEA Saclay, 91191 Gif-sur-Yvette, France*
[3] *Aix Marseille Université, CNRS/IN2P3, CPPM UMR 7346, 13288 Marseille, France*



The hypothesis of the existence of non-baryonic dark matter in our galactic halo is supported by many astrophysical observations at local to cosmological scales. Particles interacting weakly with ordinary matter, with an associated mass of the order of an atomic nucleus (aka WIMPS), are credible candidates for Dark Matter (DM). The direct detection of an elastic collision of a target nuclei on one of these WIMPs has to be discriminated from the signal produced by the neutrons, which leaves the same signal in a detector. Initiating a new generation of directional detectors, the MIMAC (MIcro-tpc MAtrix of Chambers) collaboration has developed an original prototype detector which combines a large pixelated Micromegas coupled with a fast, self-triggering, electronics. A two-chamber module has been in operation in the Underground Laboratory of Modane (LSM) for the past four years. Aspects of the Modane prototype are presented: calibration, characterization of the ^{222}Rn progeny. A new test bench combining a MIMAC chamber with the COMIMAC portable quenching line has been installed at LPSC (Grenoble) so as to characterize the 3D tracks of low energy ions in the MIMAC gas mixture: the setup and the preliminary results thereof will be presented. Future steps and how a low-pressure gaseous TPC like MIMAC compare with other directionnal strategies will be briefly discussed.

1 Directional detection of Dark Matter

The movement of matter in observed galaxies suggests the presence of a roughly spherical halo of dark matter that encompasses the galactic disc of visible matter. The density of the local dark matter has been determined, from "tracers" (nearby stars) or rotation curves to be between 0.3 and 0.4 GeV/cm^3. In the framework of the WIMP (weakly interacting massive particle) hypothesis, *ie* if we assume Dark Matter interacts weakly with ordinary matter, we can try to look for recoils due to the elastic scattering of these WIMPs: this is called *direct detection.* The kinetic energy of the recoiling nucleus E_R depends on the mass of the WIMP M_χ, its velocity

[a] ccouturi@lpsc.in2p3.fr

v, the mass of the target nucleus M_R, and the angle of scattering θ :

$$E_R = \frac{2\mu^2 v^2 \cos^2\theta}{M_R}$$

with $\mu = M_\chi M_R/(M_\chi + M_R)$ the reduced mass of the system {WIMP - nucleus}. For instance, for a fluorine nucleus ^{19}F, a WIMP mass of 100 GeV/c^2 and a relative WIMP velocity of 300 km/s, the maximum ($\theta = 0°$) expected kinetic energy of the recoiling ^{19}F is 26 keV.

The kinetic energy of the recoil is deposited in the detector medium in multiple channels: ionization, scintillation, heat. To recover the kinetic energy of the recoil, it is necessary to understand what proportion of the kinetic energy is deposited in the relevant channel, for instance the charge yield or quenching factor IQF = E_{ioni}/E_{kin} and the light yield. Detectors often use two channels to distinguish electronic recoils from nuclear recoils. Once the electronic/nuclear recoil separation is efficient enough, the next challenge is to discriminate the direct detection of an elastic collision of a target nuclei on a WIMP from the signal produced by the neutrons; both indeed leave the same energy signal in a detector. Standard, non directional, direct detectors cannot directly distinguish recoils originating from WIMP scattering and those from neutron scattering. They usually estimate the *probability* of the neutron-induced recoils, thanks to Monte Carlo simulations ; however there is a lack of available data for low-energy neutrons. As the sensitivity of the direct detectors improve, elastic scattering from neutrinos will represent an even tougher background noise to discern. Directional detection proposes to use the anisotropy arising from the motion of the Earth through the galaxy is used to get an unambiguous signature of WIMP signal, clearly separated from all earthly background noise. In fact, the WIMP velocity with respect to the Earth comes primarily from the rotation of the solar system around the galactic center, approximately in the direction of the constellation Cygnus. The angular distribution of the recoils in the galactic reference frame should show a preferential direction toward the movement of the solar system in the halo.

⋆ ⋆ ⋆

In the next section, we will introduce the MIMAC detector. As a directional detector, MIMAC provides observables to retrieve both the kinetic energy and the initial direction of the WIMP-induced recoiling ions: we will detail how the kinetic energy is determined in section 3 and present ongoing studies of the directionality in section 4. In the last section, we briefly discuss the ongoing developments and mention the comparison with other directional strategies.

⋆ ⋆ ⋆

2 The MIMAC detector

The MIMAC (MIcro-tpc MAtrix of Chambers) collaboration has developed an original directional detector. The project started in 2006 as the successor of MACHe3 [1]. The idea was to use a low-pressure gaseous TPC to improve the electron/recoils discrimination and to observe tracks long enough to provide the sought for direction of the recoils. A specific gas mixture has been developed in order to precisely control the gain and the velocity of the primary electrons in the drift chamber : 70% CF_4+28% CHF_3+2% C_4H_{10}. The few dozens of primary electrons produced by ionization along the recoil track are collected by an electric field of 180 V/cm toward the anode. These electrons are amplified at the anode level by a 256 mum-gap pixelated Micromegas [REF] which has been specifically designed to allow a working pressure of 50 mbar. The Micromegas has 256×256 pixels placed on 424 μm wide pitches in both X and Y directions, leading to a 10.8 cm × 10.8 cm total area. The signal is retrieved by a total of 512 channels – 256 in X-axis and 256 in Y-axis; each of these has a calibrated threshold above the background noise. A coincidence between a X and a Y strip/channel defines a triggered pixel. An additional channel measures the integrated signal on the grid of the Micromegas, over the whole detecting

area, to retrieve the ionization energy of the events. An electronic card, developed at LPSC, allows a sampling of the channels at 50 MHz. The performance of this card, detailed in [REF], gives a clear advantage over other directional detectors [REF-REF: Drift, DMTPC, Newage].

In order to discriminate the background events at the cathode level (see section [REF]) and to optimize the chamber volume, two detectors are combined, facing each other in a single gas compartment and sharing a common cathode. A first two-chamber module was installed in the Underground Laboratory of Modane (LSM) in June 2012, followed by upgrades in June 2013 and June 2014.

The discrimination between electronic and nuclear recoils is obtained by applying selection cuts on the different MIMAC observables. For instance, the pulse shape from the preamplifier is more asymetric and present a longer rise-time for electron events; at the track level, it has been observed that electrons tend to lead to more diluted ionization electron clouds, leading to "holes" in the track reconstruction. A selection of the symmetric charge pulses and denser track will increase the nuclear-over-electronic recoils ratio. A multivariate analysis has been implemented recently, making the best use of the 20+ available MIMAC observables: a boosted decision tree was trained on data taken using monochromatic neutron field [REF Riffard]. The electron rejection power of this technique was estimated on simulations: 10^5 with a 85.1% nuclear recoil efficiency.

Data taken in LSM have been analyzed in order to characterize the ^{222}Rn progeny [REF Riffard b]. The results are stunning: MIMAC is not only able to provide a neat spectrum of the ^{214}Pb and ^{210}Pb daughters emitted at the cathode level (Figure 1a), it also provides the track information of each individual events (Figure 1b).

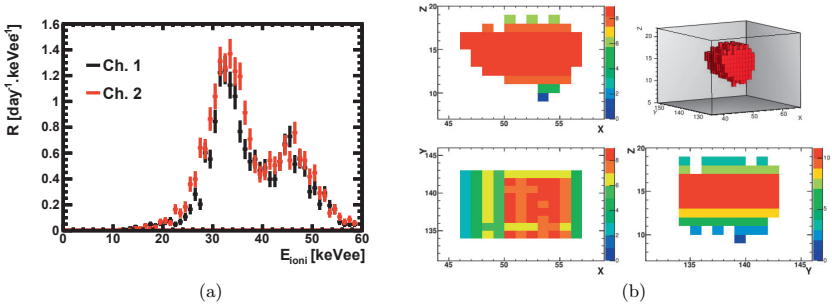


Figure 1 – (a) Energy spectra of the volume and cathode nuclear recoils measured in both chambers (1 and 2). The two peaks at 33 and 46 keV correspond to the ^{214}Pb and ^{210}Pb events respectively. (b) Track reconstruction of a cathode event.

3 Energy calibration

A charge preamplifier connected to the grid of the Micromegas delivers the charge integration on the whole anode area every 20 ns. The total ionization energy of an event is the baseline-subtracted integration over the total duration of the track event. This ionization energy is given in terms of ADC units. Two steps are needed to bring back the kinetic energy of the event: obtain ADC-to-keV parameters and the quenching factor.

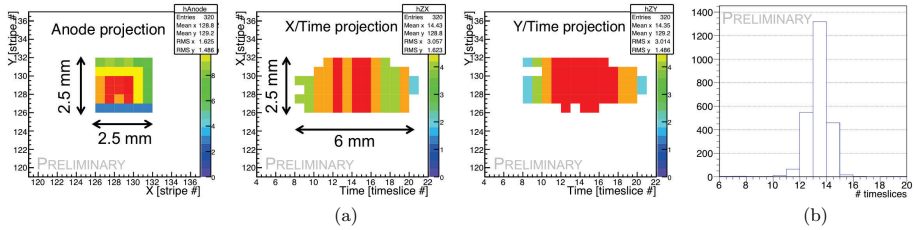
We get the ADC-to-keV parameters by measuring electrons with a known kinetic energy. Electrons above 1 keV indeed leave all their kinetic energy in ionization [REF ?]. These electrons can be produced for instance by radioactive sources. In Modane, this calibration is performed by producing, in the two chambers, fluorescence photons from inox, cadmium and copper foils bombarded by an X-ray generator. This calibration is done weekly and has shown a remarkable stability of the gas quality for more than two years of operation with the circulating pump.

Unlike electrons, ions do not leave all their energy in the ionization channel. Hence the need of a specific study of the ionization quenching factor (IQF), *ie* the proportion of the kinetic energy released in ionization. This proportion depends on the considered nucleus, on the value of its initial kinetic energy, on the composition and pressure of the gas mixture. Analytical [REF Lindard] and semi-analytical [REF SRIM] models proposing quenching factors for a given configuration exist, but previous measurements have shown that these models fail to reconcile with data at energies below 50 keV [REF Santos 2008, Guillaudin 2012]. The only way to retrieve the initial kinetic energy of an ion in a gas mixture from its measured ionization energy is to measure the IQF as a function of the kinetic energy for each specific configuration (ion species, gas composition and pressure).

To do so, a portable ion beam facility has been designed at LPSC to make IQF measurements: COMIMAC [REF Muraz 2016]. It uses an COMIC plasma source to produce both ions and electrons beams up to kinetic energies of 50 keV. In ion configuration, a Wien filter makes for an efficient charge-over-mass separation. As such, it can both be used to calibrate the ADC-to-keV coefficients – in electron mode – and measure the IQF – in ion mode. Although primarily designed to measure the IQF for MIMAC related gas mixture and ion targets, it can be used to measure the IQF in any gas mixture for any pressure up to 3 bar.

4 Reconstruction of tracks with a controlled direction and energy

In order to characterize the 3D tracks of low energy ions in the MIMAC gas mixture, the COMIMAC line was coupled to a MIMAC detector at LPSC. The two chambers are connected by a hole diameter 1 μm diameter hole which limits, at the molecular level, leakage from the TPC (50 mbar) onto COMIMAC (10^{-5} mbar). Several data taking campaigns have been conducted to send electrons, protons and ^{19}F in the MIMAC gas mixture of with energies from a few keV to 12 keV (electrons) and 30 keV (fluorine ions). We have been able to measure tracks of fluorine ions down to 5 keV. Figure 2a shows the projection of a track of a $^{19}F^{+}$ ion sent by COMIMAC with a controled kinetic energy of 25 keV into a MIMAC chamber; we measured a ionization energy of 9 keV for this event. The distribution of the number of timeslices (*ie* multiples of 20 ns) of 25 keV kinetic energy fluorine tracks is presented on Figure 2b. The maximum occurrence corresponds to 6.5 mm tracks. Going to lower energies is possible, yet the lower part of the energy spectrum is filled with other species and fluorescence photos. Also, the gain is very sensitive to the purity of the gas: the pumping system plays here a key role in removing unwanted species (e.g. SF_6) from previous experimental setups. Further optimizations and data taking are ongoing to try to observe ^{19}F tracks down to 1 keV. The detailed performance of the MIMAC reconstruction, *e.g.* in terms of track length and angular distribution as a function of the energy, will be detailed in a separate publication [REF "in preparation" ?].



(a) (b)

Figure 2 – (a) Projection of the track of a $^{19}F^{+}$ ion sent by COMIMAC with a controled kinetic energy of 25 keV into a MIMAC chamber filled with 70% CF_4+28% CHF_3+2% C_4H_{10} at 50 mbar. (b) Distribution of the number of timeslices (*ie* multiples of 20 ns) of 25 keV kinetic energy fluorine tracks. The maximum occurrence value of 13 timeslices corresponds to 6.5 mm.

5 Discussion

Ongoing R&D The prototype presented in section 2 is an element of the final matrix. Developments are going on to design high radio purity, low cost and larger ($35\times35\,\mathrm{cm}^2$) Micromegas detectors. The next step of $1\,\mathrm{m}^3$ of effective volume, to be installed at LSM, will thus require only 16 bi-chamber modules, assembled in one big vessel. After the commissioning and characterization of the performances of MIMAC-$1\,\mathrm{m}^3$ at LSM, a $50\,\mathrm{m}^3$ extension is foreseen to be built in Jinping underground facility.

Comparison with other directional detection strategies Other directional techniques have been proposed, *e.g.* using emulsion [REF] or crystal [REF] detectors. Simple simulations using the SRIM [REF] software show that only a gas TPC can achieve the measurement of the direction of WIMP-induced nuclear recoils. Indeed, after a WIMP collision, the nuclei recoils with typical energies of 1-100 keV, travel distances of the order of few 100 Å in solids losing the directional information very rapidly, while in gases this distance can be up to the mm scale, leading to a description of the track event by event. A new figure of merit is proposed to measure the preservation of the initial direction information in a given detecting material, allowing a quantitative comparison of the different directional detection strategies [REF].

Acknowledgments

CC acknowledges support from the Labex ENIGMASS.

References

1. Mayet, F., Santos, D., Perrin, G., Bunkov, Y. M., & Godfrin, H. 2000, Nuclear Instruments and Methods in Physics Research A, 455, 554






50




RENCONTRES DE MORIOND
50

THE MAGNITUDE-REDSHIFT RELATION FOR TYPE IA SUPERNOVAE, LOCALLY INHOMOGENEOUS COSMOLOGICAL MODELS, AND THE NATURE OF DARK MATTER

PHILLIP HELBIG
Thomas-Mann-Str. 9,
D-63477 Maintal, Germany



The magnitude-distance relation for Type Ia supernovae is one of the key pieces of evidence supporting the cosmological concordance model. The resulting constraints on the cosmological parameters are often derived under the idealized assumption that the universe is perfectly homogeneous on small scales. Since we know that this is not the case, what does this mean for constraints on cosmological parameters derived from the magnitude-distance relation for Type Ia supernovae? And, conversely, what does the fact that these constraints, when small-scale homogeneity is assumed, agree with other constraints mean for the nature of dark matter?

1 Introduction and Background

In the last 20 years or so, cosmological observations have improved greatly and it also appears that the measured values are converging on the true values. Among the most important of these observations are those by the Supernova Cosmology Project [3,12,11,10,1,16] and the High-z Supernova Search Team [2,14,15] which provide joint constraints on λ_0 and Ω_0. Combined with other observations [9,13], these lead to quite well constrained values for the cosmological parameters [16]. Although the supernova data alone allow a relatively wide range of significantly different other models, the best-fitting values obtained from these observations using the current data are quite close to the better-constrained values using combinations of several observations without the supernova data, at least under the assumptions with which the former were calculated. However, since the m-z relation depends not only on λ_0 and Ω_0 (with H_0 as a scale factor) but also on the distribution of matter along and near the line of sight, conclusions drawn from the m-z relation for Type Ia supernovae depend on this matter distribution. Alternatively, such observations can perhaps tell us something about this distribution. Early on, the Supernova Cosmology Project [10] considered the effect of $\eta \neq 1$ on their results (see their fig. 8) and concluded that, at least in the 'interesting' region of the λ_0-Ω_0 parameter space, it had a negligible effect. With the larger number of supernovae now available, this is no longer the case.

Kayser, Helbig, & Schramm (KHS)[8] developed a general and practical method for calculating

cosmological distances in the case of a locally inhomogeneous universe. In this case, distances which depend on angular observables related to the propagation of radiation will differ from the homogeneous case because more or less convergence will change the angle involved. The basic idea is that one considers a universe which is homogeneous and isotropic on large scales, this determining the global dynamics via the Friedmann-Lemaître equation. Local inhomogeneities are modelled as clumps, where the extra matter in the clumps is taken from the surrounding matter; the assumption is that light propagates between the clumps.

KHS described the inhomogeneity *via* the parameter $0 \leq \eta \leq 1$, where η is ratio of the density inside the beam to the global density or, alternatively, the fraction of matter which is homogeneously distributed. η of course depends on the beam size. Since the beams of supernovae at cosmological distances are extremely thin objects, evidence for $\eta < 1$ should be most obvious in the m-z relation for Type Ia supernovae.

It was pointed out by Weinberg [17] that, roughly speaking, η must be 1 when averaged over all lines of sight. However, in practice lines of sight will probably avoid concentrations of matter, due to selection effects or design. If these selection effects do not exist, and if the sample is large enough, then the 'safety in numbers' effect [7] allows one to effectively assume $\eta = 1$ on average, even if it varies from one line of sight to another, with inhomogeneity merely increasing the dispersion, roughly linearly with redshift; see section 2.

2 Calculations, results and discussion

I have used the publicly available 'Union2.1' sample of supernova data [16] and calculated χ^2 and the associated probability following Amanullah *et al* [1] on a regularly-spaced grid in the λ_0-Ω_0-η parameter space. (More details on these calculations can be found in one of the papers related to this talk [5]; many more plots are available there and in the slides of my talk available at the conference website.) I have used the standard contour values 0.683, 0.954 and 0.997.

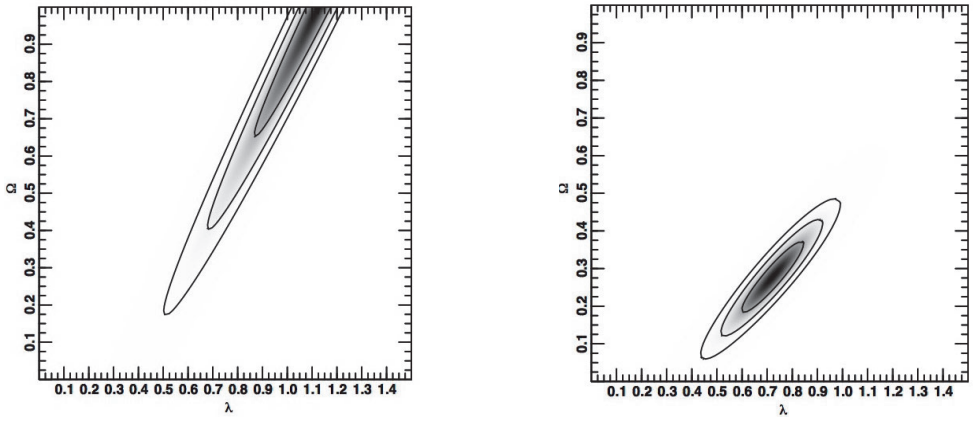


Figure 1 – *Left:* Two-dimensional probability distribution (PD) for $\eta = 0$. *Right:* The same for $\eta = 1$.

In all figures, the grey-scale corresponds to the probability.

Most discussion of the m-z relation for Type Ia supernovae has concentrated on two-dimensional contours, often *i.e.* with a δ-function prior on the nuisance parameters. Almost always, $\eta = 1$ is assumed. For comparison, in Fig. 1 I show constraints in the λ_0-Ω_0 plane for fixed values of η, namely 0 and 1.

Though little significance should be placed on variations in the probability within the innermost contour, it is remarkable that the maximum of the probability in Fig. 1 (right) is at

$\lambda_0 \approx 0.72$ and $\Omega_0 \approx 0.28$, *i.e.* at the values of the concordance model. (Note that when fewer supernova data were available, the best-fitting value was at much higher values of λ_0 and Ω_0 [4].) However, the best-fitting values for the (current) supernova data correspond to the concordance model only if one assumes $\eta \approx 1$. For $\eta = 0.455$ (not shown), the concordance model lies very near the 95.4 per cent contour, and for $\eta = 0$ it is even outside the 99.7 per cent contour. Thus, it is not possible to appreciably constrain η from the supernova data alone. However, the fact that the supernova data suggest the concordance model only for high values of η could be seen as evidence that $\eta \approx 1$.

A similar result is shown in Fig. 2 (left), where a flat universe ($\lambda_0 + \Omega_0 = 1$) has been assumed.

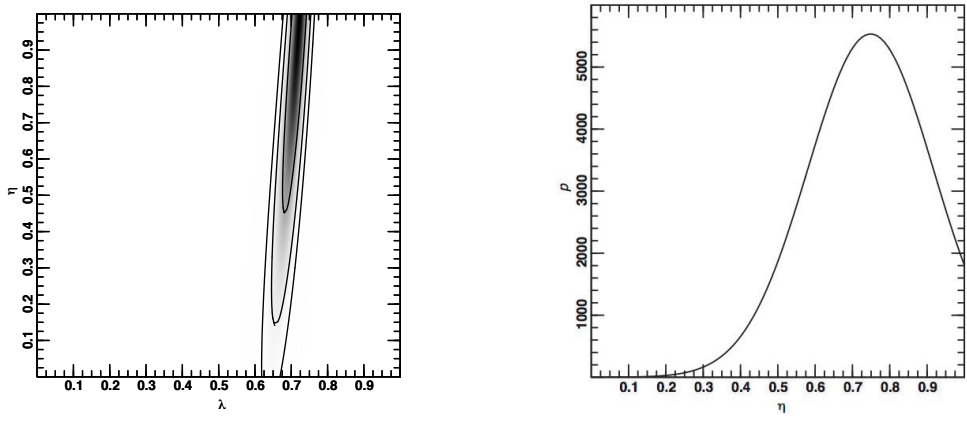


Figure 2 – *Left:* Two-dimensional PD for $k = 0$. *Right:* One-dimensional PD for the concordance model.

As in the other plots, λ_0 is reasonably well constrained, while η is quite weakly constrained. Note that the best-fitting value is for $\eta = 1$ and $\lambda_0 \approx 0.72$; in other words, again the best fit is for the concordance model with $\eta = 1$.

While the supernova data cannot usefully constrain η, the fact that they result in the concordance model if one assumes $\eta \approx 1$ suggests that $\eta \approx 1$. Since there are many cosmological tests completely independent of the supernova data, and also independent of the value of η, which suggest the concordance model, one can assume the concordance values for λ_0 and Ω_0 and calculate the probability of η from the supernova data with these additional constraints; this is shown in Fig. 2 (right).

What does it mean that $\eta \approx 1$? This could be due to the density along each line of sight being equal to the overall cosmological density, appropriately averaged along *each* line of sight, or to 'safety in numbers', with variation in the density along *all* lines of sight averaging out if the sample is large enough. In the former case, residuals and observational uncertainties should be proportional; in the latter case, the residuals should become larger, compared to the uncertainties, as redshift increases. Fig. 3 demonstrates that the quotient of residual and observational uncertainty does not show a trend with redshift. This indicates that the former scenario is more likely [6].

3 Conclusions

One might have thought that the increase in the number of data points since the first results of the Supernova Cosmology Project [10] would allow some sort of useful constraint to be placed on η from the supernova data without further assumptions. This is not the case. Even worse, if η is allowed to vary, then the conclusions about the cosmological model derived from the m-z relation

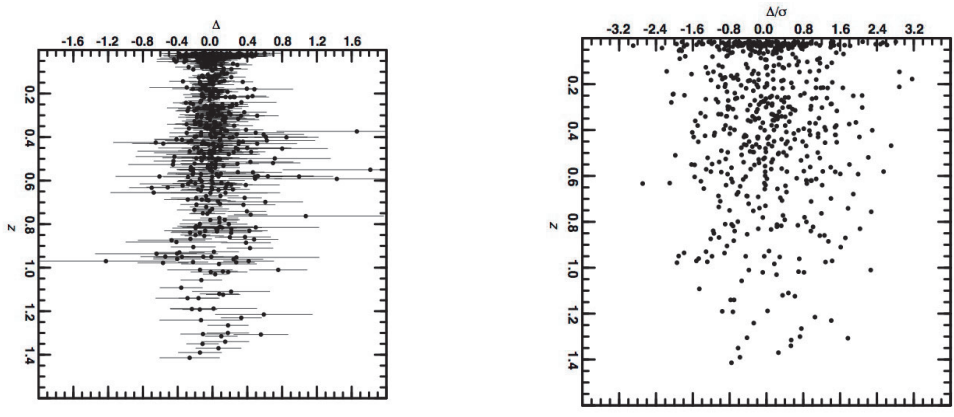


Figure 3 – *Left:* Residuals (points) and observational uncertainties (error bars). *Right:* Quotients of residuals and observational uncertainties.

for Type Ia supernovae are not as robust. However, current constraints from combinations of cosmological tests without using the supernova data determine the concordance model with $\lambda_0 \approx 0.7$ and $\Omega_0 \approx 0.3$ to rather high precision. It is thus perhaps more interesting to assume the concordance model and use the supernova data to constrain η, especially since η is otherwise difficult to measure. It is also extremely interesting that the supernova data have the best-fitting values for λ_0 and Ω_0 corresponding to those of the concordance model if and only if $\eta \approx 1$ is assumed. This could indicate that $\eta \approx 1$, which is somewhat surprising since the value of η as 'felt' by the supernova might be expected to be somewhat less, because the corresponding beams are extremely thin. The fact that even the supernova data 'want' $\eta \approx 1$ could indicate that dark matter is distributed extremely homogeneously.

References

1. R. Amanullah *et al*, *ApJ* 716, 712 (2010).
2. P. M. Garnavich *et al*, *ApJ* **493**, L53 (1998).
3. A. Goobar and S. Perlmutter, *ApJ* **450**, 14 (1995).
4. P. Helbig, *A&A* **350**, 1 (1999).
5. P. Helbig, *MNRAS* **451**, 2097 (2015).
6. P. Helbig, *MNRAS* **453**, 3975 (2015).
7. D. E. Holz and E. V. Linder, *ApJ* **631**, 678 (2005).
8. R. Kayser, P. Helbig, and T. Schramm, *A&A* **318**, 680 (1997).
9. E. Komatsu *et al*, *ApJS* **192**, 18 (2011).
10. S. Perlmutter *et al*, *ApJ* **517**, 565 (1999).
11. S. Perlmutter *et al*, *Nature* **391**, 51 (1998).
12. S. Perlmutter *et al*, *ApJ* **440**, L41 (1995).
13. *Planck* Collaboration, *A&A* **571**, A16 (2014).
14. A. G. Riess *et al*, *AJ* **116**, 1009 (1998).
15. A. G. Riess *et al*, *ApJ* **536**, 62 (2000).
16. N. Suzuki *et al*, *ApJ* **746**, 85 (2012).
17. S. Weinberg, *ApJ* **208**, L1 (1976).

New Solar metallicity measurements

Sunny Vagnozzi
The Oskar Klein Centre for Cosmoparticle Physics, Stockholm University, Sweden
NORDITA (Nordic Institute for Theoretical Physics), Stockholm, Sweden

In the past years, a systematic downward revision of the metallicity of the Sun has led to the "Solar composition problem", namely the disagreement between predictions of Standard Solar Models and inferences from helioseismology. Recent solar wind measurements of the abundance of metals in the Sun, however, favour once more a *high-Z* Sun. Because of possible residual fractionation, the derived value of the metallicity $Z_\odot = 0.0196$ actually represents a lower limit on the true metallicity of Sun. In this talk I discuss how these new measurements could bring us one step closer to solving the Solar composition problem.

1 The Standard Solar Model and helioseismology

Our Sun is a laboratory wherein we can test our understanding of the most disparate fields in physics and astronomy. Mathematically speaking, the Sun is described by the Standard Solar Model (SSM hereafter). In the SSM, our star is treated as a spherically symmetric quasi-static ball of gas within different states of ionisation, described by five basic quantities: matter density $\rho(r)$, pressure $P(r)$, temperature $T(r)$, luminosity $l(r)$, and mass $m(r)$. These quantities obey the four *stellar structure equations*:

$$\frac{\partial m}{\partial r} = 4\pi r^2 \rho \,, \tag{1}$$

$$\frac{\partial P}{\partial r} = -\frac{GM_r}{r^2}\rho \,, \tag{2}$$

$$\frac{\partial l}{\partial r} = 4\pi r^2 \epsilon(\rho, T, X_i) \,, \tag{3}$$

$$\frac{\partial T}{\partial r} = -\frac{GmT\rho}{r^2 P}\nabla \,, \tag{4}$$

where ϵ is the energy generation coefficient and the functional form of ∇ depends on the type of energy transport (radiative or convective). In the order above, the four equations describe respectively mass continuity, hydrostatic equilibrium, energy generation, and energy transport. To close the system, we furthermore need the equation of state (EoS), which relates the pressure to the mass density: $P = P(\rho, T, X_i)$, where X_i denotes the abundance of the ith chemical element present in the Sun. The photospheric composition of the Sun is currently, in mass, $\sim 75\%$ Hydrogen and $\sim 24\%$ Helium, with the remaining $\lesssim 2\%$ consisting of heavier elements, known as *metals*.

The above four equations are used as input, and a key input in particular is the detailed composition of the Sun. Furthermore, boundary conditions are required to constrain the problem: namely, the luminosity $l_\odot$, radius $R_\odot$, age $t_\odot$ and composition of the Sun, which are all

well known.[a] A one solar mass stellar model at age $t = 0$ is then evolved numerically up to the current age of the Sun, $t = t_\odot$. Two free parameters can then be adjusted in order to meet the required boundary conditions: the initial Helium abundance $Y_{\rm ini}$ and the mixing length parameter (which is used to model convection).

The outputs of the SSM can be compared with inferences from helioseismology (the study of the propagation of acoustic p-waves), which represent a key test of our understanding of the Sun. There are four main observables one can consider: the sound speed $u(r)$, the surface Helium abundance Y_s, the convective zone boundary (CZB) R_b (where the transition between radiative and convective energy transport occurs), and the Solar neutrino fluxes (Φ_{pp}, Φ_{Be}, Φ_B, $\Phi_{\rm CNO}$).

2 The Solar composition problem

The metallicity of the Sun, $Z_\odot$, i.e. the fraction of Solar mass residing in elements heavier than Helium, is not only a key input to the SSM, but also a fundamental diagnostic of the evolutionary history of our star. Therefore, it is of paramount importance to determine this quantity accurately. Up to 1998, the state-of-the-art was given by the measurements of Anders & Grevesse (AG89) [1] and Grevesse & Sauval (GS98) [2], which yielded metallicities of $Z_\odot = 0.0202$ and $Z_\odot = 0.0170$ respectively. Moreover, heavy element mixtures provided by AG89 and GS98 also yielded good agreement with inferences from helioseismology.

However, following 1998, a systematic downward revision of the Solar metallicity has degraded the agreement between SSM and helioseismology. In particular, the sets of abundances known as AGS05 [3] and AGSS09 [4] report a metallicity of $Z_\odot = 0.0122$ and $Z_\odot = 0.0133$ respectively. These revisions have completely spoilt the previous agreement between SSM and helioseismology, leading to what is now known as the "Solar composition problem" (see e.g. [5] for a review). The sound speed $u(r)$ is inferred to be $\sim 1\%$ lower than predicted at the bottom of the convective envelope (a discrepancy of about 10σ), whereas Y_s and R_b are approximately 7% lower and 1.5% higher than those deduced from helioseismology, which amount to discrepancies of approximately 6σ and 15σ respectively. Various solution to the problem have been proposed, including exotic energy transport due to captured dark matter (see e.g. [6]), but none appears compelling.

3 In situ solar wind measurements of metallicity

All of the heavy element abundances determinations listed above relied on the techniques of photospheric spectroscopy. Despite its broad use within the Solar physics community, the interpretation of such measurements is actually quite nontrivial. Sophisticated inversion techniques taking into account departures from local thermodynamic equilibrium, 3D structures, and radiative transport, and an accurate knowledge of atomic transition probabilities is required. Photospheric spectroscopy could be plagued by several systematics (e.g. line blending), but it is not clear up to what extent.

There is, nonetheless, a more direct way of measuring the metallicity of the Sun, through *in situ* collection of solar samples. Two current-time sampling techniques exist, which rely on the collection of energetic particles or solar wind samples. We will focus on the latter, i.e. *in situ* solar wind measurements. These types of measurements do not suffer from the difficulties discussed above for spectroscopy. Nonetheless, difficulties and possible systematics exist here too. For instance, fractionation processes can enhance or deplete the amount of certain ions depending on their ionization and transport histories. Collisional coupling and first ionization potential fractionation are among the most important processes at work in this direction.

Is it possible to turn this possible weakness into a strength? Fortunately the answer is yes! It has been extensively shown and recently definitely confirmed that fractionation processes

[a] With the likely exception of the composition of the Sun being uncertain, which is the topic of this talk.

are significantly reduced, if not completely absent, in solar wind emerging from Polar Coronal Holes (that is, polar regions near solar minimum) [7]. It is possible, and indeed likely, that an important systematic is still at play, namely that we cannot completely exclude a small amount of residual fractionation in these regions. However, it has been shown that any unaccounted residual fractionation would go in the direction of reducing the measured metallicity, and thus the derived metallicity $Z_\odot$ is actually a *lower limit* on the photospheric metallicity. In view of the recent downward revisions which have led to the "Solar composition problem", such a measurement can provide a very important cross-check to the values of metallicity obtained through spectroscopy.

4 New measurements: vSZ16

Very recently, Rüdi von Steiger and Thomas Zurbuchen have analysed data from the "Solar Wind Ion Composition Spectrometer" provided by the *Ulysses* mission [8] to reassess the abundance of heavy elements in the Sun [9]. Below we report such values (which we refer to as vSZ16), comparing them to the previous state-of-the-art given by AGSS09. The abundances are reported using the customary logarithmic abundance scale where the abundance of Hydrogen is set to be $\epsilon_H = 12.00$. The fractional variation in abundance for a given element i between vSZ16 and AGSS09 is thus given by $\delta Z_i = 10^{(\epsilon_{\mathrm{vSZ16},i} - \epsilon_{\mathrm{AGSS09},i})} - 1$. The total metallicity of the Sun is given by $Z_\odot = 0.0196 \pm 0.0014$.

Table 1: Elemental abundances in the vSZ16 and AGSS09 catalogues, and fractional variation between the two.

Element	$\epsilon_{\mathrm{AGSS09}}$	$\epsilon_{\mathrm{vSZ16}}$	δZ_i
C	8.43 ± 0.05	8.65 ± 0.08	0.66 ± 0.15
N	7.83 ± 0.05	7.97 ± 0.08	0.38 ± 0.08
O	8.69 ± 0.07	8.82 ± 0.11	0.35 ± 0.10
Ne	7.93 ± 0.10	7.79 ± 0.08	-0.28 ± 0.08
Mg	7.60 ± 0.04	7.85 ± 0.08	0.78 ± 0.16
Si	7.51 ± 0.03	7.82 ± 0.08	1.04 ± 0.21
S	7.12 ± 0.03	7.56 ± 0.08	1.75 ± 0.35
Fe	7.50 ± 0.04	7.73 ± 0.08	0.70 ± 0.15

5 Implications for the Solar composition problem

The changes in elemental abundances listed here directly affect the helioseismological observables previously described, which in turn has implications for the Solar composition problem. This occurs because varying the abundance of metals directly affects the radiative opacity of the Sun. This quantity describes the coupling between radiation and matter in the hot dense interior of the Sun. In [10], we worked out the response of three helioseismological observables to the change in metallicity: $u(r)$, Y_s and R_b. We did so by making use of the Linear Solar Model (LSM), an alternative to running fully-fledged nonlinear solar codes [11].

We find that broadly the variations of the helioseismological observables go in the right direction to address the Solar composition problem. In particular, the disagreement for Y_s is brought down to $\sim 1.3\sigma$, for R_b down to $\sim 0.6\sigma$, and for $u(r)$ down to $\sim 1.4\sigma$ (the sound speed profile is visually very much improved, see Figure 7 of [10]). As a note of caution, the large changes in the abundances of refractory elements (Mg, Si, S, Fe) leads to a large change in Y_s. In fact, its central value would appear to be in some tension with the required value (i.e. discrepant but in the opposite direction compared to AGSS09). However, the error bars at play are quite large (uncertainties from solar wind measurements are typically a factor of 2 or more larger than those from photospheric spectroscopy) and for this the agreement with helioseismology is improved.

Ultimately, neutrino fluxes would be necessary to discriminate between different abundances sets, or between proposed modifications to other input parameters for a fixed abundance set

(e.g. radiative opacity). An important diagnostic in this sense are the yet to be detected CNO neutrinos. The neutrino fluxes are highly sensitive to the metal composition of the Sun, in particular to that of the refractory elements. In [10], we estimated a $\sim$ 50% increase in the CNO neutrino fluxes with respect to baseline predictions, although a later study suggests that these numbers might have been underestimated [12], to the extent that current neutrino fluxes measurements or upper limits could pose a challenge to the vSZ16 abundances. Detailed studies are currently underway to resolve this controversy.

6 Conclusion

A step towards solving the Solar composition problem might be the realization that spectroscopy might be underestimating the true metallicity of the Sun. Indeed, this is what recent solar wind measurements suggest. The recent determinations by von Steiger & Zurbuchen provide a lower limit (due to possible residual fractionation) on the metallicity of the Sun of $Z_\odot = 0.0196$, thus preferring a *high-Z* Sun. In this talk I have discussed how these new measurements improve the agreement of three helioseismological observables with respect to previous predictions with *low-Z* abundances: sound speed, surface Helium abundance, and convective zone boundary. Ultimately, more precise measurements of solar neutrino fluxes should be able to pin down which is the correct set of abundances.

Before we can claim that the Solar composition problem has been truly solved, more accurate analyses of solar wind composition would be required to reduce the error bars at play, in order to check whether the improved agreement we determined still holds. But perhaps we are already moving towards a solution?

Acknowledgments

I wish to thank the organizers of the 51th Recontres de Moriond for giving me the opportunity of presenting this talk. I greatly benefited from discussions with Katherine Freese, Thomas Zurbuchen, Rüdi von Steiger, Mads Frandsen, Subir Sarkar, Ian Shoemaker, Piercarlo Bonifacio, Pat Scott, Aldo Serenelli and Francesco Villante in preparing this work. My research is supported by the Vetenskapsrådet (Swedish Research Council) through the Oskar Klein Centre. Part of this work was conducted at the Michigan Center for Theoretical Physics at the University of Michigan, Ann Arbor, which I thank for hospitality.

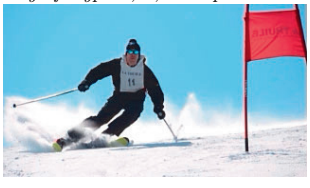
References

1. E. Anders and N. Grevesse, Geochim. Cosmochim. Acta **53** (1989) 197.
2. N. Grevesse and A. J. Sauval, Space Sci. Rev. **85** (1998) 161.
3. M. Asplund, N. Grevesse and J. Sauval, Nucl. Phys. A **777** (2006) 1
4. M. Asplund, N. Grevesse, A. J. Sauval and P. Scott, Ann. Rev. Astron. Astrophys. **47**, 481 (2009)
5. A. Serenelli, S. Basu, J. W. Ferguson and M. Asplund, Astrophys. J. **705** (2009) L123
6. M. T. Frandsen and S. Sarkar, Phys. Rev. Lett. **105** (2010) 011301
7. T. H. Zurbuchen, Annu. Rev. Astron. Astrophys. **45** (2007) 297
8. E. J. Smith *et al.*, Astron. Astrophys. Suppl. Ser. **92** (1992) 207
9. R. von Steiger and T. H. Zurbuchen, Astrophys. J. **816** (2016) 16
10. S. Vagnozzi, K. Freese and T. H. Zurbuchen, arXiv:1603.05960 [astro-ph.SR].
11. F. L. Villante and B. Ricci, Astrophys. J. **714** (2010) 944
12. A. Serenelli *et al.*, arXiv:1604.05318 [astro-ph.SR].

4. Theory

Generalised Dark Matter: Imprints on the CMB and mapping to non-perturbative models

Michael Kopp
Department of Physics, University of Cyprus, 1, Panepistimiou Street, 2109, Aglantzia, Cyprus



Dark Matter (DM) is a crucial component of the universe and is successfully modelled as a pressureless perfect fluid for calculations of the cosmic microwave background (CMB). With data from Planck it becomes possible to test generalisations of this model, searching for DM properties beyond the pressureless perfect fluid and thereby testing the CDM paradigm itself. Although there is no unique way to generalise the pressureless perfect fluid, the Generalised Dark Matter (GDM) model has proven useful in CMB applications. In this model, DM is an imperfect fluid with pressure and shear viscosity. We will present the GDM closure equations for pressure and shear that are parameterised by 3 new model parameters w, c_s^2 and $c_{\rm vis}^2$ and elucidate their physical meaning and main effects on the CMB.[1] This will shed light on our parameter constraints we obtain using Planck data, see also the contribution by D. Thomas. Assuming constant values we constrained those parameters $|w| < \mathcal{O}(10^{-3})$ and $c_s^2, c_{\rm vis}^2 < \mathcal{O}(10^{-6})$, both at the 99.7% CL using the CMB, finding no evidence for properties beyond the pressureless perfect fluid.[2] We will also discuss how several non-perturbative models can be related to GDM,[1] which will prove useful for extending the parameterisation to the non-linear regime of structure formation. These models include the non-equilibrium thermodynamics of Landau and Lifshitz, the so-called effective field theory of large scale structure and the effective field theory of fluids.

1 Generalized Dark matter

The evidence for Cold Dark Matter (CDM) has been mounting up for over 80 years [3] culminating in a precise measurement of its abundance to be $26 \pm 1\%$ of the total energy budget,[4] and spectacular demonstrations of its gravitational footprint and collisionless nature through observations of colliding galaxy clusters.[5] Many more independent astrophysical and cosmological observations created this concordant picture. In addition many extensions of the standard model of particle physics (SM), whose purpose was to solve problems within the SM, predict as byproducts the existence of particles, like axions, wimps or a sterile neutrino, which are perfect dark matter candidates. They are non-baryonic, electrically neutral and for most practical purposes cold and collisionless and therefore approximately described as pressureless perfect fluid,

$$T_c^{\mu\nu} = \rho_c u_c^\mu u_c^\nu \,. \tag{1}$$

On the other hand despite extensive searches [6,7] there is still no non-gravitational evidence for DM. We therefore should exploit all the available cosmological data to test the CDM paradigm by searching for properties beyond the perfect pressureless fluid. This requires modelling the DM component with a more general stress-energy-momentum-tensor

$$T_g^{\mu\nu} = \rho_g u_g^\mu u_g^\nu + P_g(g^{\mu\nu} + u_g^\mu u_g^\nu) + \Sigma_g^{\mu\nu} \,. \tag{2}$$

Although axions, wimps and sterile neutrinos can be reasonably well described as pressureless perfect fluid in the regime where linear perturbation theory applies, there are subtle differences and these manifest themselves as pressure P_g and shear $\Sigma_g^{\mu\nu}$.[8,9,10,11,12] Since there exist many more (and also more complicated) DM candidates,[13,14,15,16,17,18] and since there is no strong theoretical prior for any particular class of models, a phenomenological approach is best suited.

1.1 GDM definition

One such phenomenological model is the Generalised Dark Matter (GDM) model,[19] a specific ansatz for P_g and $\Sigma_g^{\mu\nu}$, with three parametric functions: *equation of state* w, *sound speed* c_s^2, and *viscosity* $c_{\rm vis}^2$. In more detail, this ansatz is for the GDM pressure and shear $P_g = \bar{P}_g + \bar{\rho}_g \Pi_g$, $\Sigma_{gj}^i = (\bar{\rho}_g + \bar{P}_g)\big(\vec{\nabla}^i\vec{\nabla}_j - \frac{1}{3}\vec{\nabla}^2\delta_j^i\big)\,\Sigma_g$, where Π_g and Σ_g are linear scalar perturbations of GDM pressure and shear and $\bar{P}_g$ the Friedmann-Robertson-Walker (FRW) background value of the GDM pressure. Hu postulated the following closure equations [19]

$$\bar{P}_g = w(a)\,\bar{\rho}_g \tag{3a}$$

$$\Pi_g = c_a^2(w)\,\delta_g + \big(c_s^2(a,k) - c_a^2(w)\big)\,\hat{\Delta}_g \tag{3b}$$

$$\dot{\Sigma}_g + 3\mathcal{H}\Sigma_g = \frac{4}{(1+w(a))} c_{\rm vis}^2(a,k)\,\hat{\Theta}_g \,, \tag{3c}$$

where $\hat{\Delta}_g = \delta_g|_{\text{rest frame}}$ and $\hat{\Theta}_g = \theta_g|_{\text{Newtonian}}$ are gauge invariant combinations, $\mathcal{H} = \dot{a}/a$, where a dot refers to a derivative w.r.t. conformal time τ, and $c_a^2 = w - \frac{1}{3}d\ln(1+w)/d\ln a$ is the *adiabatic sound speed*. The conservation equations $\nabla_\mu T_g^{\mu\nu} = 0$ give the remaining equations for the GDM background density $\bar{\rho}_g$ and density perturbation δ_g and as well as the GDM velocity perturbation θ_g. Together with the Einstein equation $G_{\mu\nu} = 8\pi G T_{\mu\nu}$, where $T^\mu{}_\nu = T_g{}^\mu{}_\nu + T_\Lambda{}^\mu{}_\nu + T_{\rm SM}{}^\mu{}_\nu + \dots$, is the total stress-energy-momentum tensor, the system of equations is closed. It should be noted that although the parameters c_s^2 and $c_{\rm vis}^2$ are allowed to depend on scale k, they are not allowed to depend on the particular solution. It is worth emphasising that the *non-adiabatic pressure*

$$\Pi_{\rm nad} \equiv \Pi_g - c_a^2\delta_g = \big(c_s^2(a,k) - c_a^2(w)\big)\,\hat{\Delta}_g \tag{4}$$

is algebraically related to the rest frame density perturbation $\hat{\Delta}_g$, while the Σ_g is dynamical and sourced by the Newtonian velocity perturbation $\hat{\Theta}_g$. We have investigated those choices implicit in (3), but refer the reader to our paper for more details.[1]

1.2 DM models encompassed by GDM

To get a feeling for the size and expected time dependence of those parameters, we compare in Fig. 1 two important cases. The dotted line shows the prediction for CDM by the effective field theory of large scale structure (EFTofLSS) [11] and the dashed line shows the upper bound for freely streaming warm dark matter. Note that while the former takes into account that even initially cold DM warms up through the backreaction of unresolved small scale non-linearities, the latter describes initially Maxwell-Boltzmann distributed warm dark matter without taking into account this backreaction. In these two cases $w \simeq c_s^2 \simeq c_{\rm vis}^2$, and it is interesting that the expectation for CDM comes close to the value of our upper bound (the constant line).

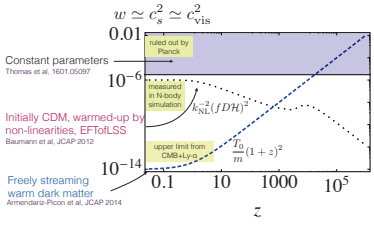


Figure 1 – Redshift evolution of GDM parameters for two physical DM models and the constant case.

1.3 GDM imprints on the CMB

The basic imprints of GDM on the CMB can be understood by expanding analytic solutions for $\bar{\rho}_g$ and the Newtonian potential $\hat{\Phi}$ (sourced only by GDM) in small $w, c_s^2, c_{\rm vis}^2 \ll 1$ giving [1]

$$a^3\bar{\rho}_g \propto \omega_g(1+3w\ln(1+z))\,, \qquad k_{\rm d}^{-1}(\tau) \simeq \tau\sqrt{c_s^2+\tfrac{8}{15}c_{\rm vis}^2}\,, \tag{5}$$

where $k_{\rm d}^{-1}$ is the scale below which the potential $\hat{\Phi}$ starts to decay. This explains most features in

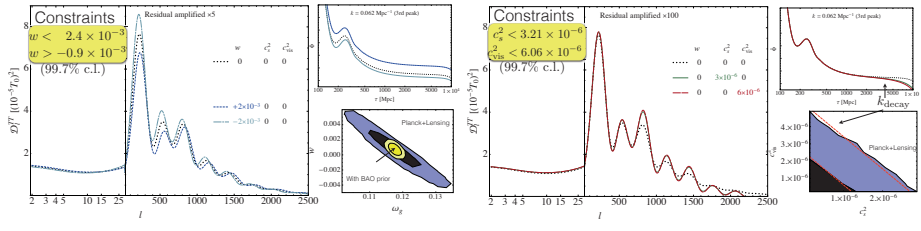
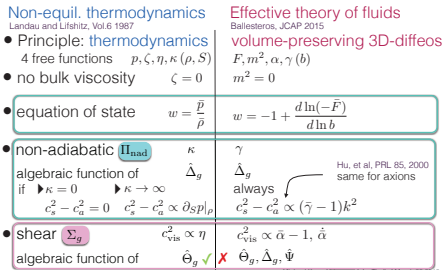


Figure 2 – Comparison of the effects of constant GDM parameter on the temperature power spectrum of the CMB, the potential evolution. Also shown are the constraints and important degeneracies.

the temperature power spectrum shown in Fig. 2, where we take the Planck best fit value for ω_g and the other standard parameters and switch on one GDM parameter with a size corresponding to our upper limits. The smaller upper plots show the effect on the evolution of a single k-mode of the potential $\hat{\Phi}$ and the contours show the results of our MCMC analysis confirming (5), which states that w, like ω_g, affect the freeze-out value of $\hat{\Phi}$ via matter-radiation equality and $c_s^2, c_{\rm vis}^2$ cause $\hat{\Phi}$ to decay below $k_{\rm d}^{-1}$, manifesting in a reduction of the lensing potential, amplifying slightly acoustic peaks and throughs. The yellow boxes in the left corners show our constraints.[2] Earlier studies only constrained one or two parameters.[20]

2 Non-pertubative Extensions

In order extend the GDM model into the non-linear regime of structure formation, necessary if we want to take into account the wealth of data that cannot be described by linear perturbation theory, we considered several models for imperfect fluids that are defined non-perturbatively. Here we focus on the non-equilibrium thermodynamics of Landau and Lifshitz (LL) [21] and the effective field theory of fluids (EFT) by Ballesteros.[22] Both theories use physical or mathematical principles to restrict the possible form of $T_g^{\mu\nu}$, Eq. (2), see the table below. In both causes the full $T_g^{\mu\nu}$ contains only a few free functions. To make the connection to GDM we to set to zero the bulk viscosity in both cases. The remaining free function κ and η for LL, as well as γ and α for EFT describe non-adiabatic pressure $\Pi_{\rm nad}$ and shear Σ_g.



While $\Pi_{\rm nad}$ in EFT is automatically of GDM form, although with a particular scale dependence, reminiscent of axions,[8] in LL $\Pi_{\rm nad}$ is in general dynamical. Nevertheless it is sourced by the particular density perturbation $\hat{\Delta}_g$. It can be made algebraic in two limits, either very large or very small heat conduction κ. In LL theory, the Σ_g is algebraically related to $\hat{\Theta}_g$, which gives a behaviour similar to Eq. 3c and connects the viscosity parameters η and $c_{\rm vis}^2$.

Acknowledgments

The research leading to these results has received funding from the European Research Council under the European Union's Seventh Framework Programme (FP7/2007-2013) / ERC Grant Agreement n. 617656 "Theories and Models of the Dark Sector: Dark Matter, Dark Energy and Gravity."

References

1. M. Kopp, C. Skordis, and D. B. Thomas. An extensive investigation of the Generalised Dark Matter model. *ArXiv: 1605.00649*, May 2016.
2. D. B. Thomas, M. Kopp, and C. Skordis. Constraining dark matter properties with Cosmic Microwave Background observations. *ArXiv: 1601.05097*, January 2016.
3. F. Zwicky. Die Rotverschiebung von extragalaktischen Nebeln. *Helvetica Physica Acta*, 6:110–127, 1933.
4. Planck Collaboration, P. A. R. Ade, N. Aghanim, M. Arnaud, et al. Planck 2015 results. XIII. Cosmological parameters. *ArXiv e-prints*, February 2015.
5. D. Clowe, M. Bradač, A. H. Gonzalez, et al. A Direct Empirical Proof of the Existence of Dark Matter. *ApJ*, 648:L109–L113, September 2006.
6. The CRESST Collaboration, F. Reindl, G. Angloher, A. Bento, et al. The CRESST Dark Matter Search - Status and Perspectives. *ArXiv e-prints*, September 2015.
7. LUX Collaboration, D. S. Akerib, H. M. Araújo, X. Bai, et al. Improved WIMP scattering limits from the LUX experiment. *ArXiv e-prints*, December 2015.
8. R. Hlozek, D. Grin, D. J. E. Marsh, and P. G. Ferreira. A search for ultralight axions using precision cosmological data. *Phys. Rev. D*, 91(10):103512, May 2015.
9. C. Armendariz-Picon and J. T. Neelakanta. How cold is cold dark matter? *JCAP*, 3:49, March 2014.
10. S. Hofmann, D. J. Schwarz, and H. Stöcker. Damping scales of neutralino cold dark matter. *Phys. Rev. D*, 64(8):083507, October 2001.
11. D. Baumann, A. Nicolis, L. Senatore, and M. Zaldarriaga. Cosmological non-linearities as an effective fluid. *JCAP*, 7:51, July 2012.
12. J. Lesgourgues and T. Tram. The Cosmic Linear Anisotropy Solving System (CLASS) IV: efficient implementation of non-cold relics. *JCAP*, 9:32, September 2011.
13. I. M. Oldengott, C. Rampf, and Y. Y. Y. Wong. Boltzmann hierarchy for interacting neutrinos I: formalism. *JCAP*, 4:16, April 2015.
14. R. Diamanti, E. Giusarma, O. Mena, et al. Dark radiation and interacting scenarios. *Phys. Rev. D*, 87(6):063509, March 2013.
15. C. Bœhm, A. Riazuelo, S. H. Hansen, and R. Schaeffer. Interacting dark matter disguised as warm dark matter. *Phys. Rev. D*, 66(8):083505, October 2002.
16. P. Serra, F. Zalamea, A. Cooray, et al. Constraints on neutrino-dark matter interactions from cosmic microwave background and large scale structure data. *Phys. Rev. D*, 81(4):043507, February 2010.
17. A. Pourtsidou, C. Skordis, and E. J. Copeland. Models of coupled dark matter to dark energy. *ArXiv e-prints*, July 2013.
18. Robert J. Scherrer. Purely kinetic k-essence as unified dark matter. *Phys. Rev. Lett.*, 93:011301, 2004.
19. Wayne Hu. Structure formation with generalized dark matter. *Astrophys.J.*, 506:485–494, 1998.
20. C. M. Müller. Cosmological bounds on the equation of state of dark matter. *Phys. Rev. D*, 71(4):047302, February 2005.
21. L. D. Landau and E. M. Lifshitz. *Fluid Mechanics, Second Edition: Volume 6 (Course of Theoretical Physics)*. Course of theoretical physics / by L. D. Landau and E. M. Lifshitz, Vol. 6. Butterworth-Heinemann, 2 edition, January 1987.
22. G. Ballesteros. The effective theory of fluids at NLO and implications for dark energy. *JCAP*, 3:1, March 2015.

The very best limits on cosmological magnetic fields

F. R. Urban
National Institute of Chemical Physics and Biophysics, Rävala 10
10143 Tallinn, Estonia

I introduce you to the very best limits on cosmological magnetic fields. The numbers: magnetic fields coherent across a Jeans' length (around 2.4 Mpc today), are bound to be weaker than about 1 nG (2σ statement), whereas for a field as wide as the entire observable Universe the number is approximately 0.5 nG. These limits are obtained from rotation measures data, and as such they do not depend on the epoch at which the fields were generated.

1 Why we care

The Universe is swamped with all sorts of magnetic fields (MF): planetary MFs, galactic MFs, cluster MFs, possibly void MFs, etc. [1,2]. Cosmological MFs (fields which imbue the entire Universe), on the other hand, remain elusive, but there is a whole world of physicists from different disciplines out there, ultra-high energy cosmic rays physics, structure formation, early and very early Universe theory, physics beyond the Standard Model, radio-astronomy, who would die to know more about them [3,4,5].

Cosmological MFs manifest themselves by rotating the plane of polarisation of electromagnetic waves propagating from far away sources to the Earth. Now, since we know that: (1) Faraday rotation measures (RM) of distant objects do not show any evolution with redshift z [6], and (2) cosmological MFs (cosmoMF) generate RMs as we move away from here [7,8], then (3) we can limit the strength of these cosmoMFs by comparing simulated and observed RMs distributions.

This contribution is based on my work with my collaborators Maxim Pshirkov and Peter Tinyakov [9].

2 The new method

Observations. The only formula we need to know is that of Faraday rotation: the plane of polarisation of a linearly polarised electromagnetic wave which moves through a magnetised plasma rotates by an angle φ proportional to the square of the wavelength λ: $\varphi = \mathrm{RM}\,\lambda^2$, where

$$\mathrm{RM} = 812 \int_D^0 \frac{n_\mathrm{e}(z) B_{||}(z)}{(1+z)^2} \left| \frac{\mathrm{d}l(z)}{\mathrm{d}z} \right| \mathrm{d}z \,. \tag{1}$$

Here n_e is the density of free electrons measured in cm^{-3}, $B_{||}$ is the component of the MF (in μG) parallel to the line of sight $l(z)$, and D is the distance to the source in kpc; here and everywhere the RM is measured in $\mathrm{rad}/\mathrm{m}^2$.

What do we know about those RMs? First, the data: the largest set of RM of extragalactic sources to date was compiled in [10] from the NRAO VLA Sky Survey (NVSS) data [11]. The total

number of observed sources was 37,543, of which 4002 have known redshifts [12]. These RMs consist of several contributions: we can split the observed RM as $\mathrm{RM_{obs}} = \mathrm{RM_{gal}} + \mathrm{RRM}$, where the first term comes from the regular MF of the Milky Way, and the second term stands for "residual RM": RM instrinsic to the source, measurement errors, turbulent galactic MF, and cosmoMF (xRRM) [13]. We massaged the data a bit to get the best grip on the redshift dependence, see [6] for all the tricks: after the massage we end up with a total of 2593 sources (our data points).

Simulations. Like we said, if there is a cosmoMF the xRRM systematically grows with redshift due to its accumulation along the line of sight. To compute this we need n_e, which we take from the observed Lyman-α forest distribution of neutral hydrogen absorption lines [14,15,7]. Next, since the conductivity of the Universe is extremely large, and since diffusion of the MF is inefficient at scales much larger than 1 AU, we can take a MF frozen into the plasma [16,17]. And then we run a simple code which spits out xRRM for a MF with strength B and coherence length l_c, the latter ranging from a tenth of the Jeans length λ_J to the Hubble size $1/H_0$.

These simulations can generate only the contribution from the cosmoMF, but in real life there is a mickle of other stuff we do not (want to) know, so here is the stratagem: we exploit the data at low redshifts to obtain information about these unsung, redshift-independent, heroes, since there the cosmoMF is subdominant there, and use it together with our simulated xRRM at high redshift. In practice the algorithm is: (i) split the Universe in two redshift bands; (ii) make a first RM batch by randomly picking RRMs from the low-z set; (iii) generate a second RM batch by simulating 100 xRRMs for each of the data sources of the high-z set; (iv) blindly pluck one value from each of the batches and incoherently (that is, each with its own sign) add them a bunch of times to generate the final theoretical |RRM| distribution; (v) compare with actual data by means of a Kolmogorov-Smirnov test, which yields a p-value for the statistical (in)compatibility of the two distributions.

3 The result

See the self-explanatory Fig. 1.

4 How we fare

Currently, the strongest upper limits on the strength of present-day cosmoMFs come from microwave background observations [18] and read $B \lesssim 2.8$ nG for a coherence length $l_c = 1$ Mpc — these limits apply only to primordial MFs, i.e., fields generated in the very early Universe. The limits coming RM data are looser [7,19]: λ_J-scale fields are bound by $B \lesssim 6$ nG. Our limits on the other hand read 1 nG (this is a 2σ statement) for $l_c = \lambda_J$, whereas $B \lesssim 0.5$ nG for the bloated field case, $l_c = 1/H_0$.

Conclusion: all in all, we win 😎

Acknowledgements. As always thanks to the organisers for their fantastic effort, and to Maxim and Peter for making a great team. This work was supported by IISN project No. 4.4502.13 and Belgian Science Policy under IAP VII/37; my participation in Moriond was supported by ERC grant IUT23-6.

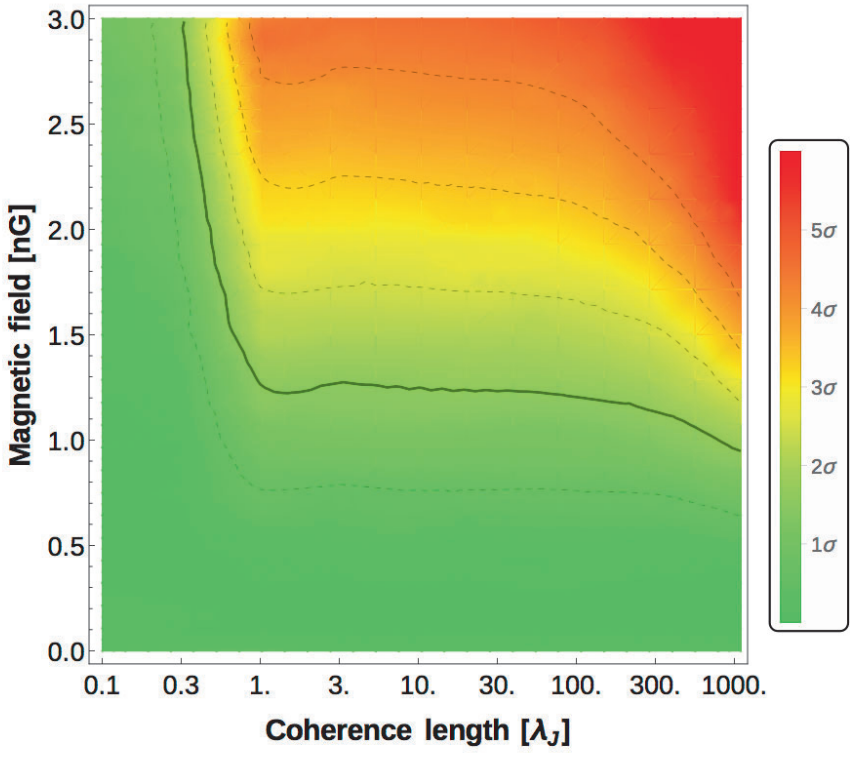


Figure 1 – Confidence interval contours obtained from the p-values of the Kolmogorov-Smirnov tests as a function of the MF reference strength (y-axis) and coherence length (x-axis).

References

1. J. P. Vallée, New Astron. Rev. **48** (2004) no.10, 763. doi:10.1016/j.newar.2004.03.017.
2. D. Ryu, D. R. G. Schleicher, R. A. Treumann, C. G. Tsagas and L. M. Widrow, Space Sci. Rev. **166** (2012) 1 doi:10.1007/s11214-011-9839-z [arXiv:1109.4055 [astro-ph.CO]].
3. O. Deligny, A. Letessier-Selvon and E. Parizot, Astropart. Phys. **21** (2004) 609 doi:10.1016/j.astropartphys.2004.04.012 [astro-ph/0303624].
4. L. M. Widrow, D. Ryu, D. R. G. Schleicher, K. Subramanian, C. G. Tsagas and R. A. Treumann, Space Sci. Rev. **166** (2012) 37 doi:10.1007/s11214-011-9833-5 [arXiv:1109.4052 [astro-ph.CO]].
5. R. Durrer and A. Neronov, Astron. Astrophys. Rev. **21** (2013) 62 doi:10.1007/s00159-013-0062-7 [arXiv:1303.7121 [astro-ph.CO]].
6. M. S. Pshirkov, P. G. Tinyakov and F. R. Urban, Mon. Not. Roy. Astron. Soc. **452** (2015) 2851 doi:10.1093/mnras/stv1273 [arXiv:1407.3909 [astro-ph.GA]].
7. P. Blasi, S. Burles and A. V. Olinto, Astrophys. J. **514** (1999) L79 doi:10.1086/311958 [astro-ph/9812487].
8. T. Akahori and D. Ryu, Astrophys. J. **738** (2011) 134 doi:10.1088/0004-637X/738/2/134 [arXiv:1107.0142 [astro-ph.CO]].
9. M. S. Pshirkov, P. G. Tinyakov and F. R. Urban, arXiv:1504.06546 [astro-ph.CO].
10. A. R. Taylor, J. M. Stil and C. Sunstrum, Astrophys. J. **702** (2009) 1230 doi:10.1088/0004-637X/702/2/1230.
11. J. J. Condon, W. D. Cotton, E. W. Greisen, Q. F. Yin, R. A. Perley, G. B. Taylor and J. J. Broderick, Astron. J. **115** (1998) 1693. doi:10.1086/300337.
12. A. M. Hammond, T. Robishaw and B. M. Gaensler, arXiv:1209.1438 [astro-ph.CO].
13. D. H. F. M. Schnitzeler, Mon. Not. Roy. Astron. Soc. **409** (2010) L97 doi:10.1111/j.1745-3933.2010.00957.x [arXiv:1011.0737 [astro-ph.GA]].
14. P. Coles and B. Jones, Mon. Not. Roy. Astron. Soc. **248** (1991) 1.
15. H. Bi and A. F. Davidsen, Astrophys. J. **479** (1997) 523 doi:10.1086/303908 [astro-ph/9611062].
16. L. Hollenstein, R. K. Jain and F. R. Urban, JCAP **1301** (2013) 013 doi:10.1088/1475-7516/2013/01/013 [arXiv:1208.6547 [astro-ph.CO]].
17. P. G. Tinyakov and F. R. Urban, arXiv:1309.2270 [astro-ph.CO].
18. P. A. R. Ade *et al.* [Planck Collaboration], arXiv:1502.01594 [astro-ph.CO].
19. P. P. Kronberg, M. L. Bernet, F. Miniati, S. J. Lilly, M. B. Short and D. M. Higdon, Astrophys. J. **676** (2008) 7079 doi:10.1086/527281 [arXiv:0712.0435 [astro-ph]].

Universal predictions of screened modified gravity on cluster scales

David F. Mota
Institute of Theoretical Astrophysics, University of Oslo, 0315 Oslo, Norway

We investigate the effects of modified gravity theories, in particular the symmetron and $f(R)$ gravity, have on the nonlinear regime of structure formation. In particular, we investigate on possible ways of detecting violations of the equivalence principle using the mass inferred via lensing methods versus mass inferred via dynamical methods.

1 Introduction

Scalar-tensor theories are an extension of General Relativity that include a scalar field φ to the standard Einstein-Hilbert Lagrangian. A general Lagrangian for the scalar field is

$$\mathcal{L} = -\frac{1}{2}\partial_\mu\varphi\partial_\nu\varphi - V(\varphi) + \beta(\varphi)T^\mu_\mu, \tag{1}$$

where $V(\varphi)$ is the self interacting potential, $\beta(\varphi)$ is a coupling function and T^μ_μ is the trace of the matter energy-momentum tensor. The scalar field gives rise to an additional *fifth force*, which can be quantified by $\gamma \equiv |\mathbf{F}_{\rm Fifth}|/|\mathbf{F}_{\rm N}|$, where $\mathbf{F}_{\rm N}$ is the Newtonian force. Experiments constrain $\gamma \ll 1$ in the Solar System. A screening mechanism with the aim to hide this field from local gravity experiments can be realised in two different ways:

Density dependent mass: If the mass of the field $m^2(\varphi)$ is large in dense environments, then the fifth force mediated by the scalar field is suppressed on scales above its Compton wavelength. On the other hand, in low density environments, the mass can be light and the scalar field mediates a long range fifth force. This is the so-called *Chameleon* screening [1];

Density dependent coupling: If the coupling to matter $\beta(\varphi)$ is small in the region of high density, the strength of the fifth force $\mathbf{F}_{\rm Fifth}$ is weak and the modifications to gravity are suppressed. On the other hand, in low density environments, the size of the fifth force can be of the same order as standard gravity. This idea is the so called Symmetron mechanism [2].

1.1 Chameleon-f(R) gravity

The Lagrangian for this theory is

$$S = \int {\rm d}^4x\sqrt{-g}\frac{1}{16\pi G}\Big(R + f(R)\Big) + S_m(g_{\mu\nu}, \psi_i), \tag{2}$$

We choose the Hu-Sawicki model [3] as a working example, which is given by

$$f(R) = -m^2\frac{c_1(R/m^2)^n}{c_2(R/m^2)^n + 1}, \tag{3}$$

where $m^2 = H_0^2\Omega_m$ is a mass scale and c_1, c_2 and n are model parameters. One recovers a ΛCDM expansion history by setting $c_1/c_2 = 6\Omega_\Lambda/\Omega_m$.

1.2 Symmetron

The Symmetron model [2] action is given by

$$S = \int \mathrm{d}x^4\sqrt{-g}\left[\frac{R}{16\pi G} - \frac{1}{2}(\partial\varphi)^2 - V(\varphi)\right] + S_m(\tilde{g}_{\mu\nu}, \psi). \tag{4}$$

The matter fields, ψ, couple to the Jordan frame metric $\tilde{g}_{\mu\nu}$ which relates to the Einstein frame metric $g_{\mu\nu}$, as $\tilde{g}_{\mu\nu} = A^2(\varphi)g_{\mu\nu}$. The coupling function $A(\varphi)$ is

$$A(\varphi) = 1 + \frac{1}{2}\left(\frac{\varphi}{M}\right)^2, \tag{5}$$

where M is a mass scale. The potential is taken to be

$$V(\varphi) = V_0 - \frac{1}{2}\mu^2\varphi^2 + \frac{1}{4}\lambda\varphi^4, \tag{6}$$

where the value of V_0 is determined by the condition that the model gives rise to the observed accelerated expansion of the Universe. The effective potential is given by

$$V_{\rm eff}(\varphi) = V_0 + \frac{1}{2}\left(\frac{\rho_m}{M^2} - \mu^2\right)\varphi^2 + \frac{1}{4}\lambda\varphi^4. \tag{7}$$

2 The Dynamical and Lensing Masses

A general prediction of Modified Gravity theories with screening mechanisms are violations of equivalence principle. The later can be measured by observing differences between the gravitational mass and the inertial mass of objects. In cosmology this can be tested via measurements of galaxy clusters masses. Astronomers infer the masses of galaxy clusters using lensing observations, and via dynamical methods. The former is a probe of the gravitational mass, while the later is a measure of the inertial mass. If differences between these two masses are found, that would be a smoking gun of modified gravity and screening mechanisms. In order to make predictions within the chamleon-f(R) and the symmetron gravity we need first to compute the Bardeen potentials. In the Jordan-frame we have

$$ds^2 = a^2(\eta)\left[-d\eta^2(1+2\Phi) + (1-2\Psi)d\vec{x}^2\right], \tag{8}$$

where $\Phi \simeq \Phi_N + \delta A(\phi)$, $\Psi \simeq \Phi_N - \delta A(\phi)$, with

$$\delta A(\phi) \equiv A(\phi) - 1 = \frac{1}{2}\left(\frac{\phi}{M}\right)^2.$$

The fifth-force potential is given by the difference in the above two potentials

$$\Phi_- = \frac{\Phi - \Psi}{2} = \delta A(\phi).$$

Lensing on the other hand is affected by the lensing potential

$$\Phi_+ = \frac{\Phi + \Psi}{2} = \Phi_N,$$

which satisfies the Poisson equation

$$\nabla^2\Phi_+ = 4\pi G a^2 \delta\rho_m. \tag{9}$$

This is the same equation as in GR since is conformally invariant and therefore photons are not affected by the fifth-force. The lensing mass is defined as

$$M_L = \frac{1}{4\pi G a^2}\int \nabla^2\Phi_+ dV. \tag{10}$$

which is the gravitational mass of the halo. It is determined from the simulations by counting the number of particles within a given radius. The dynamical mass $M_D(r)$ of a halo is defined as the mass contained within a radius r as inferred from the gravitational potential Φ, i.e.

$$M_D(r) = \frac{1}{4\pi G a^2} \int \nabla^2 \Phi dV, \tag{11}$$

where the integration is over the volume of the body out to radius r. Observationally, M_D can be determined from measurements of velocity dispersion of galaxies in clusters.

In GR the lensing mass is the same as the dynamical mass, but they can be significantly different in modified gravity. We follow [4] and define the relative difference

$$\Delta_M(r) = \frac{M_D}{M_L} - 1 = \frac{d\Phi_-/dr}{d\Phi_+/dr}. \tag{12}$$

This allows us to quantity the difference between the two masses in the simulations. In GR we have $\Delta_M \equiv 0$ while in the symmetron model Δ_M will vary depending on the mass of the halo and the environment it lies in. The theoretical maximum is achieved for small objects in a low-density environment where the screening is negligible and reads

$$\Delta_M^{\rm Max}(r) = 2\beta^2. \tag{13}$$

In Fig.1 we show $\Delta_M(r_{340})$ as a function of the halo mass in both high-density (purple circles) and low-density (blue circles) environments. This figure shows that GR is recovered for larger halos, independent of the environment. For low-mass halos we see a significant dispersion of Δ_M from 0 to the maximum value obtained in low-density environments for the same mass-ranges. This is because low-mass halos cannot efficiently screen themselves and must rely on the environment to get the screening. As expected, we see a clear trend that the small halos which are efficiently screened generally reside in high-density environments, while those which are less screened lie in low-density environments. Massive halos on the other hand can screen themselves efficiently and the environment only plays a small role in their total screening.

In Fig. (1) we show $\Delta_M(r)$ as a function of the distance r from the halo centre, for small and large halos in high and low density environments respectively. Again we see a large difference between large halos in dense environments and small halos in low density environments. The r-dependence of $\Delta_M(r)$ is seen to be rather weak in high density environments since the value of the scalar field inside the halo is mainly determined by the environment, while in low-density environments the value of the scalar field mainly depends on the mass of the halo, which leads to a stronger r-dependence.

Note also that in all the figures above the deviation from GR is stronger for higher symmetry-breaking redshift $z_{\rm SSB}$, and for larger values of the coupling β, which implies a stronger fifth-force and therefore a stronger effect.

3 Conclusions and Perspectives

The rise of a fifth force in modified gravity theories leads to a stronger clustering of matter. In order to find smoking guns of screening mechanisms we studied the environment dependence of the masses of dark matter halos in the symmetron modified gravity scenario. The potential governing the dynamics of the matter fields $(\Phi_- + \Phi_+)$ can differ significantly from the lensing potential Φ_+ in this model, which leads to a clear difference between the mass of the halo as obtained from dynamical measurements and that obtained from gravitational lensing. Such an effect found in the symmetron model can be significantly stronger than in $f(R)$ gravity. This signature, which is unique to modified gravity, can in practice be measured by combining dynamical (e.g. velocity dispersion) and lensing mass measurements of clusters of galaxies or

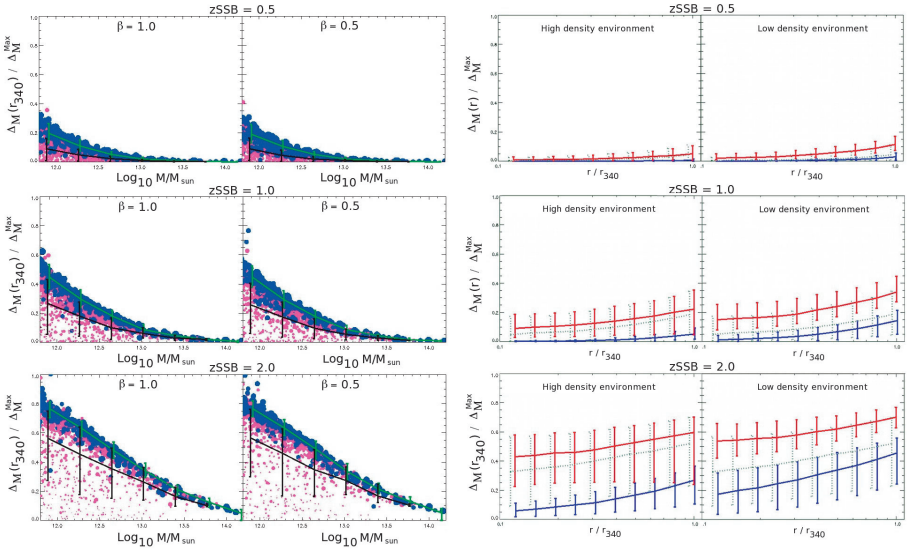


Figure 1 – Right: $\Delta_M(r_{340})/\Delta_M^{\rm Max}$ as a function of the halo lensing mass M_L for high density environments (purple) and low-density environments (blue) where $\Delta_M^{\rm Max} = 2\beta^2$. The error bars are 1σ. For the high-mass halos we recover GR independent of the environment as the effectiveness of the screening increases with mass. Left: $\Delta_M(r)/\Delta_M^{\rm Max}$ as a function of the rescaled halo radius r/r_{340}, where $\Delta_M^{\rm Max} = 2\beta^2$, for high and low density environments and small (red) and large (blue) halos. The error bars are 1σ.

even single galaxies. We find that the environmental dependence is strongest for small halos as very large halos are sufficiently massive to be able to screen themselves.

This discovered feature of environmental dependence also allows us, in principle, to distinguish between different modified gravity scenarios such as $f(R)$, more general chameleons, and the symmetron. In $f(R)$ the maximum fraction of the fifth-force to the Newtonian force in halos are around 30% while in chameleon/symmetron scenarios this fraction can be either smaller or larger, depending on the value of the coupling strength β.

Although the theoretical nature of screening mechanisms is different, we find common features in both the matter and the velocity properties. In particular, our findings suggest that one can classify them into three general regimes: 1) the fully screened regime where GR is recovered, 2) an unscreened regime where the strength of the fifth force is large, and, 3) a partially screened regime where screening occurs in the inner part of a halo, but the fifth force is active at larger radii. Any observable sensitive to this regimes and environments can be a future probe of screening mechanisms and modified gravity theories beyond General Relativity.

References

1. J. Khoury and A. Weltman, Phys. Rev. Lett. **93**, 171104 (2004)
2. K. Hinterbichler and J. Khoury, Phys. Rev. Lett. **104** (2010) 231301
3. W. Hu and I. Sawicki, Phys. Rev. D **76** (2007) 064004 [arXiv:0705.1158 [astro-ph]].
4. H. A. Winther, D. F. Mota and B. Li, Astrophys. J. **756** (2012) 166

Cosmology with vector distortion

Jose Beltrán Jiménez
CPT, Aix-Marseille Université, UMR 7332, 13288 Marseille, France.

We consider an extension of Weyl geometry with the most general connection linearly determined by a vector field. We discuss some of the geometrical properties within this framework and then we construct gravitational theories leading to an interesting class of vector-tensor theories with cosmological applications.

1 Introduction

The beauty of General Relativity (GR) resides in its geometrical interpretation as the curvature of the spacetime. A foundational property of GR is that the metric determines the entirely metric and affine structures of the spacetime. However, these two structures do not need to be related and, thus, if we decide to embrace the geometrical description of gravity, we are naturally led to considering the potential role of the neglected dof's contained in the connection. For the Einstein-Hilbert action, the connection is *dynamically* fixed to be metric compatible, but for more general gravitational theories, the inclusion of an arbitrary connection does lead to different physical effects [1]. These additional dof's are associated to the presence of torsion and/or non-metricity in the spacetime [2]. An intermediate approach is to consider only a constrained sector of the connection. A paradigmatic example of this is the Weyl geometry [3], where only the (vector) trace of the non-metricity is allowed. Aspects of Weyl geometry have been studied [4,5] and it represents a natural arena to formulate conformally invariant theories. We will introduce an extended version of this geometry and gravitational theories within this framework.

2 Extending Weyl geometry

Soon after Einstein formulated GR, Weyl considered an extension of its geometrical framework where the metric-compatibility condition was replaced by $\hat{\nabla}_\mu g_{\alpha\beta} = -2A_\mu g_{\alpha\beta}$ with A_μ some vector field. This condition is invariant under the Weyl rescaling $g_{\mu\nu} \to e^{2\Lambda(x)} g_{\mu\nu}$ together with $A_\mu \to A_\mu - \partial_\mu \Lambda(x)$ and we can easily solve for the connection as (assuming vanishing torsion)

$$\hat{\Gamma}^\alpha_{\beta\gamma} = \Gamma^\alpha_{\beta\gamma} - \left(A^\alpha g_{\beta\gamma} - 2A_{(\beta}\delta^\alpha_{\gamma)} \right) , \tag{1}$$

with $\Gamma^\alpha_{\beta\gamma}$ the usual Levi-Civita connection. This connection inherits the aforementioned Weyl symmetry and, therefore, the associated curvature tensor will also be invariant under such transformation. This Weyl connection can be naturally extended to the most general affine structure *linearly* determined by one single vector field and with no derivatives, which can be expressed as [6]

$$\hat{\Gamma}^\alpha_{\beta\gamma} = \Gamma^\alpha_{\beta\gamma} - b_1 A^\alpha g_{\beta\gamma} + b_2 \delta^\alpha_{(\beta} A_{\gamma)} + b_3 \delta^\alpha_{[\beta} A_{\gamma]} \tag{2}$$

with b_i some parameters. The non-Levi-Civita part of the connection is called *distortion* and, in this case, it carries both non-metricity and torsion. The metric (in-)compatibility condition in this case reads

$$\hat{\nabla}_\mu g_{\alpha\beta} = (b_3 - b_2) A_\mu g_{\alpha\beta} + (2b_1 - b_2 - b_3) A_{(\alpha} g_{\beta)\mu} \,. \tag{3}$$

For geometries with $2b_1 - b_2 - b_3 = 0$, this expression also remains invariant under a Weyl transformation so that they represent a generalization of Weyl geometry with a torsion component determined by the vector field. As we will discuss below, these geometries turn out to be special when constructing gravitational Lagrangians.

3 Gravitational theories

The curvature of the spacetime within the framework of geometries with vector distortion depends on the vector field and, thus, actions expressed in terms of curvature invariants will generically lead to theories with non-minimally coupled vector fields. Here we will consider two particularly interesting examples.

3.1 $f(\mathcal{R})$ theories

The Ricci scalar for the connection with vector distortion reads $\mathcal{R} = R - \beta_1 A^2 + \beta_2 \nabla \cdot A$, with $\beta_1 \equiv -3[4b_1^2 - 8b_1(b_2+b_3) + (b_2+b_3)^2]/4$ and $\beta_2 \equiv -3(2b_1+b_2+b_3)/2$. If we take a Lagrangian to be an arbitrary function of this Ricci scalar $\mathcal{L} = f(\mathcal{R})$, one can show that the vector is forced to be the gradient of a scalar so that only one dof will propagate. The Lagrangian for the resulting scalar can be written as [6]

$$\mathcal{L} = \varphi R + \frac{\beta_2^2}{4\beta_1 \varphi} \partial_\mu \varphi \partial^\mu \varphi - V(\varphi) \tag{4}$$

where $V(\varphi)$ is determined by the functional form of f. Here we can recognize the form of a Brans-Dicke scalar-tensor theory. In the special case of the generalized Weyl connection with $b_3 = 2b_1 - b_2$ we find $\beta_2^2 = 6\beta_1$ which corresponds to a non-propagating scalar field (resembling the usual results for $f(\mathcal{R})$ theories in the Palatini formalism). In the particular case of a quadratic function, the resulting Lagrangian can be written in the Einstein frame as

$$\mathcal{L} = \frac{M_{pl}^2}{2} \tilde{R} - \frac{1}{2} \tilde{g}^{\mu\nu} \tilde{\phi}_{,\mu} \tilde{\phi}_{,\nu} - \frac{3}{4} M_{pl}^2 M^2 \left(1 - e^{-\sqrt{\frac{2}{3\alpha}} \frac{\tilde{\phi}}{M_{pl}}} \right)^2 , \tag{5}$$

with M^2 the new mass scale and $\alpha \equiv 1 - \beta_2^2/(6\beta_1)$. The potential for the scalar field defines a one-parameter family of potentials that generalize the Starobinsky inflationary model (which is recovered for $\alpha \to 1$). For arbitrary α, we obtain the so-called α-attractor parameterization that appears in classes of supergravity and superconformal inspired inflationary models [7]. This vector field formulation for the α-attractor model has also been considered within the context of modified gravity with auxiliary vector fields [8], but without the geometrical framework of connections with vector distortion.

3.2 More general Lagrangians

In the previous subsection we have discussed how general Lagrangians constructed out of the Ricci scalar lead to scalar-tensor theories. In order to obtain proper vector-tensor theories (which do not reduce to one scalar dof), it is necessary to include more general curvature invariants. Motivated by Gauss-Bonnet terms we can seek for terms quadratic in the curvature. We can thus consider the most general quadratic Lagrangian in the Riemann tensor. Since we want to recover a healthy theory for vanishing distortion, we will impose that it reduces to pure Gauss-Bonnet when $A_\mu = 0$. Once everything is expressed in terms of the Levi-Civita connection and

the vector field, the Lagrangian can be written as [6,10]

$$\mathcal{L}_{(2)} = -\frac{1}{4}F_{\mu\nu}F^{\mu\nu} + \xi A^2 \nabla\cdot A - \lambda A^4 - \beta G^{\mu\nu}A_\mu A_\nu + \gamma_1(\nabla\cdot A)^2 + (\gamma_2 A^2 + \gamma_3 \nabla\cdot A)R \quad (6)$$

with $F_{\mu\nu} = \partial_\mu A_\nu - \partial_\nu A_\mu$ and ξ, λ, β and γ_i some parameters that depend on the distortion parameters and the coefficients of the quadratic terms in the Lagrangian. The above Lagrangian propagates 4 dof's for the vector field, one of which will be affected by the Ostrogradski instability. In order to avoid it, we impose the conditions $\gamma_i = 0$, which (in dimensions higher than 3) uniquely determine the distortion coefficients to satisfy [10] $b_3 = 2b_1 - b_2$, i.e., only the generalized Weyl class will give rise to healthy theories. If we add the Einstein-Hilbert term for the distorted connection we will also generate a mass term for the vector so we finally find

$$\mathcal{L}_{(2)} = -\frac{1}{4}F_{\mu\nu}F^{\mu\nu} + \frac{1}{2}M^2A^2 - \lambda A^4 + \xi A^2\nabla\cdot A - \beta G^{\mu\nu}A_\mu A_\nu \quad (7)$$

which was already obtained within the context of pure Weyl geometry [5]. The first two terms simply represent the Proca lagrangian for a massive vector field and (for $\xi = \lambda = \beta = 0$) it was suggested [5] that they could be a natural vector dark matter candidate. Since the mass can be close to the Planck mass, the field will be very heavy and, thus, we can apply the isotropy theorem [11] so that the corresponding averaged energy-momentum tensor will be isotropic and will mimic a dust component. The ξ-term is a vector Galileon interaction, which is a healthy vector non-gauge invariant derivative self-interaction, and the β-term is a healthy non-minimal coupling for the vector field, both particular examples of more general classes [12]. The coupling to the Einstein tensor was explored as a potential mechanism to generate cosmic magnetic fields [13]. The vector-tensor theory described by (7) has been shown to have interesting cosmological applications [10]. It has isotropic de Sitter phases, bouncing/re-collapsing solutions, the possibility of self-tuning or singularities with divergent $\dot{H}$, but finite H and ρ. It was also shown that the coupling to the Einstein tensor generates an anomalous propagation speed for gravitational waves and, therefore, it is subject to the corresponding constraints from binary pulsars [14].

At cubic order, we can use the result by Horndeski [15] that the non-minimal coupling $L^{\mu\nu\alpha\beta}F_{\mu\nu}F_{\alpha\beta}$, with $L^{\mu\nu\alpha\beta} = -\frac{1}{2}\epsilon^{\ \mu\nu\rho\sigma}\epsilon^{\alpha\beta\gamma\delta}R_{\rho\sigma\gamma\delta}$ the double dual Riemann tensor leads to second order equations of motion. Thus, we can use this term for our connection with vector distortion to generate additional interactions, which can then be written as [6,10]

$$\begin{aligned}\mathcal{L}_{(3)} &= L^{\mu\nu\alpha\beta}F_{\mu\nu}F_{\alpha\beta} + 2(2b_1+b_2+b_3)\tilde{F}^{\mu\alpha}\tilde{F}^{\nu}{}_{\alpha}\nabla_\mu A_\nu \\ &\quad + \frac{1}{2}\Big[\Big(2b_1 - b_2 - b_3\Big)^2 A^2 g^{\mu\nu} - 2\Big(4b_1^2 + (b_2+b_3)^2\Big)A^\mu A^\nu\Big]F_{\mu\alpha}F_\nu{}^\alpha \ . \end{aligned} \quad (8)$$

In the first line we find the vector-tensor Horndeski interaction[15] and a healthy (non-gauge invariant) derivative self-interaction, while in the second line we have standard interactions for the vector field. The cosmology and stability of the Horndeski interaction has been studied [16], showing that its relevant effects typically come in associated with instabilities.

4 Conclusions

Geometries with vector distortion represent a suitable framework to formulate gravitational theories leading to interesting classes of vector-tensor theories. They can easily accommodate the α-attractor generalization of Starobinsky inflation with the vector field effectively describing a scalar field. More general actions lead to ghost-free non-gauge invariant derivative self-interactions for the vector which can support de Sitter solutions and, thus, be used as candidates for inflation and/or dark energy. The presence of bouncing/re-collapsing solutions also give a novel scenario to consider bouncing and/or ekpyrotic universes.

Acknowledgments

It is a pleasure to thank the organizers of the Rencontres de Moriond 2016 and their participants for a memorable week. I also acknowledge the financial support of A*MIDEX project (n ANR-11-IDEX-0001-02) funded by the Investissements dAvenir French Government program, managed by the French National Research Agency (ANR), MINECO (Spain) projects FIS2014-52837-P and Consolider-Ingenio MULTIDARK CSD2009-00064

References

1. G. J. Olmo, Int. J. Mod. Phys. D **20** (2011) 413 [arXiv:1101.3864 [gr-qc]]. S. Capozziello, T. Harko, T. S. Koivisto, F. S. N. Lobo and G. J. Olmo, Universe **1** (2015) no.2, 199 [arXiv:1508.04641 [gr-qc]].
2. R. T. Hammond, Rept. Prog. Phys. **65** (2002) 599. K. Krasnov, Class. Quant. Grav. **25** (2008) 025001 [gr-qc/0703002]. R. F. Sobreiro and V. J. Vasquez Otoya, Braz. J. Phys. **40** (2010) 370 [arXiv:0711.0020 [hep-th]]. V. Vitagliano, Class. Quant. Grav. **31** (2014) no.4, 045006 [arXiv:1308.1642 [gr-qc]]. J. Beltran Jimenez, A. Golovnev, M. Karciauskas and T. S. Koivisto, Phys. Rev. D **86** (2012) 084024 [arXiv:1201.4018 [gr-qc]].
3. E. Scholz, arXiv:1111.3220 [math.HO].
4. M. R. Tanhayi, S. Dengiz and B. Tekin, Phys. Rev. D **85** (2012) 064016 [arXiv:1201.5068 [hep-th]]. Z. Haghani, N. Khosravi and S. Shahidi, Class. Quant. Grav. **32** (2015) no.21, 215016 [arXiv:1410.2412 [gr-qc]].
5. J. Beltran Jimenez and T. S. Koivisto, Class. Quant. Grav. **31** (2014) 135002 [arXiv:1402.1846 [gr-qc]].
6. J. Beltran Jimenez and T. S. Koivisto, Phys. Lett. B **756** (2016) 400 [arXiv:1509.02476 [gr-qc]].
7. R. Kallosh, A. Linde and D. Roest, JHEP **1311** (2013) 198 [arXiv:1311.0472 [hep-th]].
8. M. Ozkan, Y. Pang and S. Tsujikawa, Phys. Rev. D **92** (2015) no.2, 023530 [arXiv:1502.06341 [astro-ph.CO]].
9. M. Ozkan and D. Roest, arXiv:1507.03603 [hep-th].
10. J. Beltran Jimenez, L. Heisenberg and T. S. Koivisto, JCAP **1604** (2016) no.04, 046 [arXiv:1602.07287 [hep-th]].
11. J. A. R. Cembranos, C. Hallabrin, A. L. Maroto and S. J. N. Jareno, Phys. Rev. D **86** (2012) 021301 doi:10.1103/PhysRevD.86.021301 [arXiv:1203.6221 [astro-ph.CO]]. J. A. R. Cembranos, A. L. Maroto and S. J. N. Jareo, Phys. Rev. D **87** (2013) no.4, 043523 [arXiv:1212.3201 [astro-ph.CO]]. J. A. R. Cembranos, A. L. Maroto and S. J. N. Jareo, JCAP **1403** (2014) 042 [arXiv:1311.1402 [gr-qc]].
12. G. Tasinato, JHEP **1404** (2014) 067 [arXiv:1402.6450 [hep-th]]. L. Heisenberg, JCAP **1405** (2014) 015 [arXiv:1402.7026 [hep-th]]. E. Allys, P. Peter and Y. Rodriguez, JCAP **1602** (2016) no.02, 004 [arXiv:1511.03101 [hep-th]]. J. Beltran Jimenez and L. Heisenberg, Phys. Lett. B **757** (2016) 405 [arXiv:1602.03410 [hep-th]].
13. J. Beltran Jimenez and A. L. Maroto, JCAP **1012** (2010) 025 [arXiv:1010.4513 [astro-ph.CO]].
14. J. Beltran Jimenez, F. Piazza and H. Velten, Phys. Rev. Lett. **116** (2016) no.6, 061101 [arXiv:1507.05047 [gr-qc]].
15. G. W. Horndeski, J. Math. Phys. **17** (1976) 1980.
16. J. D. Barrow, M. Thorsrud and K. Yamamoto, JHEP **1302** (2013) 146 [arXiv:1211.5403 [gr-qc]]. J. Beltran Jimenez, R. Durrer, L. Heisenberg and M. Thorsrud, JCAP **1310** (2013) 064 [arXiv:1308.1867 [hep-th]].

BUMPY INFLATION: SUBLEADING EFFECTS IN AXION INFLATION

Ivonne Zavala
Department of Physics, Swansea University, Swansea, SA2 8PP, UK

An attractive inflaton candidate is an axion slowly rolling down a flat potential protected by a perturbative shift symmetry. However, realisations of axion inflation within natural and monomial inflation have been disfavoured by observations and are difficult to embed in string theory. We show that subleading, but significant non-perturbative corrections to the axion potential can superimpose sharp cliffs and gentle plateaus into the potential, whose overall effect is to enhance the number of e-folds of inflation. Sufficient inflation is achieved for smaller field ranges compared to the potential without such corrections and the tensor-to-scalar ratio results un-observably small, but there is a large negative running of the spectral index. This brings both single-field chaotic and natural inflation in UV complete theories like string theory, back into the favoured region of current observations with distinctive signatures.

1 Introduction

The latest results from Planck and BICEP2/Keck [1] agree with the simplest inflationary scenario where a period of quasi exponential acceleration is driven by a single scalar field, slowly rolling down a very flat potential, whose quantum fluctuations seeded the large scale structures observed today. The conditions on the inflaton potential for a sufficiently long epoch of slow-roll inflation are:

$$\epsilon_V \equiv \frac{M_{Pl}^2}{2}\left(\frac{V'}{V}\right)^2 \ll 1, \qquad |\eta_V| \equiv M_{Pl}^2\frac{|V''|}{V} \ll 1\,. \tag{1}$$

The challenge in slow-roll inflation is that higher order corrections, encoded in higher dimensional operators, $\mathcal{O}_d = c_d V(\phi)(\phi/M_{Pl})^{d-4}$ generically steepen the potential and spoil the slow-roll conditions (1). Moreover, for even moderately large $\phi \gtrsim M_{Pl}$, Planck suppressed operators are dangerously large, and can prevent inflation from occurring at all.

Invoking a symmetry is an attractive possibility to prevent large quantum corrections. Such a symmetry is provided, for example, if the inflaton is an axion with a shift symmetry. When the symmetry is broken non-perturbatively to a discrete symmetry, the potential is sufficiently flat for slow-roll *natural inflation* [7], for large values of the symmetry breaking scale, or axion decay constant, $f \gtrsim 4M_{Pl}$, and requires super-Planckian field displacements. When the symmetry is broken, e.g. spontaneously, one has an axionic realisation of monomial inflation, whose attempted string theoretic embeddings are known as *axion monodromy* [8].

Axion models give vanilla natural or monomial inflation only to leading order. Whilst the effective potential is protected from dangerous perturbative corrections, non-perturbative effects like instantons give further contributions of the form $\sum_n \Lambda_n^4 \cos(n\phi/f)$, where Λ_n are mass scales. Then large and frequent modulations are introduced into the potential, trapping the inflaton in a local minimum before it reaches the global one, and obstructing large numbers of e-folds of slow-roll natural inflation [9]. On the other hand, when non-perturbative corrections correspond to

tiny, frequent superimposed features in the slow-roll potential, their impact on the background trajectory of the inflaton is negligible, whilst leaving only small imprints on the CMB such as a large, possibly oscillating running of the scalar spectral index [10].

Assuming slow-roll from the time the observed perturbations in the CMB exited the horizon up to the end of inflation, the amplitude of the tensor modes, encoded in the tensor-to-scalar ration, r, can be related to the inflaton field excursion via the Lyth bound [2] and the inflationary scale, giving

$$\frac{\Delta\phi}{M_{Pl}} \gtrsim 2 \times \left(\frac{r}{0.01}\right)^{1/2} , \qquad V_{inf}^{1/4} \simeq \left(\frac{r}{0.1}\right)^{1/4} \times 1.8 \times 10^{16} \text{ GeV} . \tag{2}$$

Therefore, an observation of primordial gravitational waves with $r \sim 10^{-1} - 10^{-2}$ would fix the scale of inflation to be around the GUT scale and the inflaton field range to be super-Planckian implying that inflation is highly sensitive to quantum gravity effects. UV completions of high scale/large field inflation via string theory are difficult, due to the proximity of the inflationary scale (2) and the string scale, which is typically $M_s \lesssim 10^{17}$ GeV for perturbative string theory. This proximity puts under pressure the validity of 4D effective field theory during inflation, where, in order to be able to neglect massive string excitations and Kaluza-Klein modes, a hierarchy $V_{inf}^{1/4} \lesssim M_{kk} \lesssim M_s \lesssim M_{Pl}$ is required [4,6], M_{kk} being the compactification scale.

Here we show that non-perturbative corrections to axion models of inflation not only allow inflation, but can even help it with important implications on the field ranges, the decay constant and cosmological predictions. We quote here the relevant measurements and bounds on the CMB observables from Planck 2015/BICEP2-Keck [1]. For the scalar perturbations, the Planck analysis gives (including the tensor perturbations at the pivot scale $k_* = 0.05\text{Mpc}^{-1}$ and 68%CL for Planck TT+lowP): $n_s = 0.9667 \pm 0.0066\,, \alpha_s \equiv dn_s/d\ln k = -0.0126^{+0.0098}_{-0.0087}\,, r < 0.07$ (at 95% CL).

2 Bumpy Chaotic Inflation

We consider the following axionic monomial potential with non-perturbative corrections [11,12]

$$V(\phi) = A + \frac{1}{2}m^2\phi^2 + \lambda\phi\cos\left(\frac{\phi}{f}\right) . \tag{3}$$

For $\lambda = A = 0$, we recover ϕ^2 inflation, which gives a field range of $\Delta\phi \sim 15\,M_{Pl}$, with a tensor to scalar ratio $r \sim 0.12$ and an inflationary scale of around the GUT scale (2). While it gives a consistent value for the spectral index $n_s \sim 0.966$, this model is basically excluded by the latest results on r.

We consider the interesting case $\lambda/f < m^2$. Taking e.g. $m^2/d^4 = 10\,M_{Pl}^2$, $f = 1/3\,M_{Pl}$, and $\lambda/d^4 = 3.3\,M_{Pl}^3$ (where we have scaled the parameters by $d^2 = 9.3 \times 10^{-8}$ to match the normalisation of scale perturbations $P_s \simeq 2.1 \times 10^{-9}$ and for convenience with the numerics, also $t \to t/d^2$). We draw the potential in Fig. 1, together with the corresponding smooth ϕ^2 model with $\lambda = 0$. One can now easily compute the CMB observables from the slow-roll parameters at horizon crossing for the pivot scale: $n_s = 1 - 4\epsilon + 4\delta\,, \alpha_s = -8\xi + 20\epsilon\delta - 8\epsilon^2\,, r = 16\epsilon$, where $\epsilon \equiv 2\frac{H'^2}{H^2}$, $\delta \equiv \frac{H''}{H}$, $\xi\frac{H'''H'}{H^2}$, H is the Hubble parameter and a prime denotes derivative with respect to the inflaton.

Assuming the pivot scale crossed the horizon at around $N_e \sim 55$ e-folds before the end of inflation yield the following values for the inflationary observables

$$n_s = 0.9667\,, \qquad r = 3.1 \times 10^{-5}\,, \qquad \alpha_s = -0.015\,, \tag{4}$$

in the ballpark of the Planck measurements and constraints given by Planck15. The field range for the bumpy model from horizon crossing to the end of inflation is $\Delta\phi \sim 3.2\,M_{Pl}$, and the scale of inflation at horizon crossing is $V_{inf}^{1/4} = 9.9 \times 10^{-4} M_{Pl}$. Thus, non-perturbative corrections can modify a large field monomial model of inflation to one with intermediate field range and

inflationary scale, making a consistent perturbative string theory realisation of the model possible. The distinctive signature of such a scenario is a suppressed tensor mode and a large negative running of the spectral index.

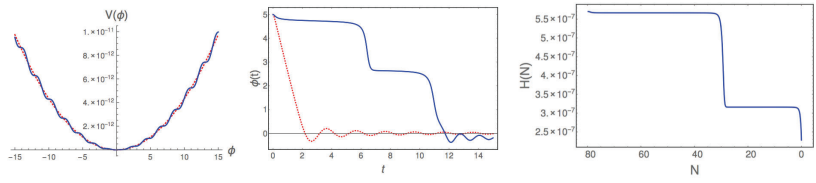


Figure 1 – Scalar potential (in Planck units) and inflaton's evolution in time for the smooth and bumpy chaotic model and Hubble parameter's evolution as a function of the number of e-folds N for the bumpy chaotic model.

3 Bumpy Natural Inflation

We now consider a single field modulated natural potential, which is generically predicted by string theory models:

$$V(\phi) = A + \Lambda^4 \left(1 + \cos\left(\frac{\phi}{f}\right)\right) + \tilde{\Lambda}^4 \left(1 + \cos\left(\frac{\phi}{\tilde{f}}\right)\right) \tag{5}$$

where $\tilde{\Lambda} < \Lambda$ and $\tilde{f} < f$ parameterise the bumps.

For example, choosing $\Lambda^4/d^4 = 1\, M_{Pl}^4$, $f = 1\, M_{Pl}$ and $\tilde{f} = 1/3\, M_{Pl}$, we tune $\tilde{\Lambda}^4/d^4 = 0.3329\, M_{Pl}^4$ (where now $d^2 = 9.1 \times 10^{-8}$) to ensure the turns in the potential are close to stationary points. The bumpy model again has a step-like shape, with steep regions connected by a plateau. The potential and scalar field's evolution for the smooth and bumpy models are given in Fig. 2 as well as the Hubble parameter's evolution as a function of the number of e-folds. Almost all the inflation proceeds in a slow-roll fashion, although there are large fluctuations in the slow-roll parameters when rolling down the steep slopes of the steps. Taking the pivot scale to cross the horizon at $N_e \sim 54$ e-folds before the end of inflation yield the following values for the cosmological observables:

$$n_s = 0.9677\,, \quad r = 3.5 \times 10^{-7}\,, \quad \alpha_s = -0.0025\,, \tag{6}$$

in agreement with the Planck measurements. As in the monomial model, tensor modes are undetectably small, whereas there is a large negative running of the spectral index. The field range from horizon crossing to the end of inflation is $\Delta\phi = 1.0\, M_{Pl}$ and the scale of inflation at horizon crossing is $V_{inf}^{1/4} = 3.2 \times 10^{-4} M_{Pl}$. We reiterate that non-perturbative corrections have made it possible to achieve single field, natural inflation with a Planckian axion decay constant, $f \sim M_{Pl}$, moderate field range and intermediate inflationary energy scale. Thus a consistent embedding in perturbative string theory becomes possible.

4 Conclusions

Axions provide an interesting class of inflationary models which are protected from dangerous perturbative corrections to the effective potential. Non-perturbative corrections typically introduce modulations into monomial and natural inflaton potentials. Whereas it was previously assumed that such bumps would either spoil slow-roll inflation [9] or produce negligible corrections to the slow-roll dynamics [8,10,11], we have seen that when the modulations take the form a series of steep cliffs and gentle plateaus, the large Hubble friction (or drag) and the sharp reduction

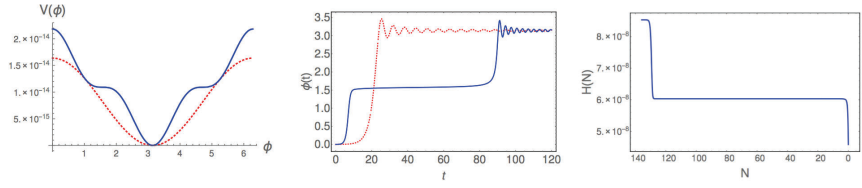


Figure 2 – Scalar potential and field evolution for the smooth and bumpy natural models and Hubble's parameter evolution as a function of the number of e-folds for the bumpy model. We use Planck units.

in acceleration at the end of the cliffs, cause the inflaton to roll slowly whenever it reaches a plateau. Hence, although slow-roll parameters have large fluctuations through the sharp cliffs, the plateaus provide regions of slow-roll that produce many e-folds of inflation.

Consequently, both single field monomial and natural inflation models can give sufficient e-folds for sub-Planckian axion decay constants, moderate field ranges and inflationary scales, when non-perturbative effects are included. This puts them back into the favoured region of current observations and the weakly coupled, supergravity limit of string theory. Such a scenario has distinctive signatures. In particular, the benchmark models considered here predict tensor modes 2-4 orders of magnitude below the projected bounds of future observations, $r \lesssim 10^{-3}$. Moreover, bumpy models also predict large, negative values for the running of the scalar spectral index over the scales probed by the CMB ($\alpha_s \approx -10^{-2}, -10^{-3}$, respectively), and small running of the running ($\beta_s \approx -10^{-4}, -10^{-5}$, respectively).

We considered simple potentials within effective field theory, and it would be important to understand whether the potentials and parameters emerging from string compactifications can fulfil the requisite tunings, such as for example in the models discussed in [12]. Also, a more detailed study of the inflationary observables would be very interesting, for example consequences of the running spectral index on all the scales probed by the CMB, and implications of the bumps for non-Gaussianities.

Acknowledgments.

I thank my collaborators on the topics discussed here, K. Kooner, N. Cabo-Bizet, O. Loaiza-Brito, S. Parameswaran and G. Tasinato.

References

1. **Planck Collaboration** Collaboration, P. Ade *et al.*, arXiv:1502.02114 [astro-ph.CO]. **BICEP2, Keck Array** Collaboration, P. Ade *et al.*, arXiv:1510.09217 [astro-ph.CO].
2. D. H. Lyth, *Phys.Rev.Lett.* **78** (1997) 1861–1863, arXiv:hep-ph/9606387 [hep-ph].
3. N. Arkani-Hamed et al. *JHEP* **06** (2007) 060, arXiv:hep-th/0601001 [hep-th].
4. K. Kooner, S. Parameswaran, and I. Zavala, arXiv:1509.07049 [hep-th].
5. S. Parameswaran et al. JCAP **1604** (2016) no.04, 008, arXiv:1602.02812.
6. S. Parameswaran and I. Zavala, to appear.
7. K. Freese, J. A. Frieman, and A. V. Olinto, *Phys. Rev. Lett.* **65** (1990) 3233–3236.
8. E. Silverstein et al. *Phys. Rev.* **D78** (2008) 106003, arXiv:0803.3085 [hep-th]. L. McAllister et al. *Phys. Rev.* **D82** (2010) 046003, arXiv:0808.0706 [hep-th].
9. T. Banks et al. *JCAP* **0306** (2003) 001, arXiv:hep-th/0303252 [hep-th].
10. T. Kobayashi et al. *JCAP* **1101** (2011) 026, arXiv:1011.3988 [astro-ph.CO].
11. R. Flauger et al. 1412.1814 [hep-th]; T. Kobayashi et al. 1510.08768 [hep-ph].
12. N.G. Cabo-Bizet, O. Loaiza-Brito and I. Zavala, to appear.

The Holiest Grail

P. Daniel Meerburg
CITA, University of Toronto, 60 St. George Street, Toronto, Canada

I will discuss to what degree the cosmic microwave background (CMB) can be used to constrain primordial non-Gaussianity involving one tensor and two scalar fluctuations, focusing on the correlation of one B-mode polarization fluctuation with two temperature fluctuations (BTT). In the simplest models of inflation, the tensor-scalar-scalar primordial bispectrum is non-vanishing and is of the same order in slow-roll parameters as the scalar-scalar-scalar bispectrum. I will show that constraints from an experiment like CMB-Stage IV using this observable are more than an order of magnitude better than those on the same primordial coupling obtained from temperature measurements alone. I will argue that B-mode non-Gaussianity opens up an as-yet-unexplored window into the early Universe, demonstrating that significant information on primordial physics remains to be harvested from CMB anisotropies. Specifically, if we measure any appreciable level of BTT correlation in the sky, its source is most likely not from inflation and as such can be used to directly test the inflationary paradigm.

1 Introduction

Our primordial Universe can be described by only 2 parameters; the amplitude A_s and tilt n_s of the power of initial fluctuations. Although beautiful in its simplicity, from a empirical point of view, it limits the amount of information we can hope to extract from the early Universe, which by itself is our only hope of ever probing energy scales way beyond the standard model of particle physics. Currently, our best best bet on further exploring the early Universe in search for other degrees of freedom is Cosmic Microwave Background polarization and Large Scale Structure. In this short note I will discuss a potentially very interesting observable that is sensitive to non-Gaussianities generated by the interaction between a single graviton and two scalars. The bispectrum associated with this interaction, leaves an imprint on the on the CMB in the temperature bispectrum [1]. However, similar to the tensor constraint derived from the TT power spectrum, the tensor contribution to the measured spectrum of fluctuations, has large cosmic variance from the scalar contribution. Therefore, we propose to correlate one B mode with tow T modes, i.e. $\langle BTT\rangle$. The replacement of one leg with a B mode, significantly lowers cosmic variance and allows us to constrain this type of interaction with increasing precision as B mode measurements improve.

2 Graviton-Scalar-Scalar Bispectrum

As a starting point we consider a primordial Universe with a single field driving an inflationary expansion (SFSR). For such model, the bispectrum of a graviton interacting with two scalars was first computed in [2] and is given by

$$\left\langle \zeta(\vec{k}_1)\zeta(\vec{k}_2)h^{\pm}(\vec{k}_3)\right\rangle = (2\pi)^3 F^{\pm 200}(\vec{k}_1,\vec{k}_2,\vec{k}_3)\delta\left(\sum_{n=1}^{3}\vec{k}_n\right), \tag{1}$$

where we have defined

$$F^{\pm 200}(\vec{k}_1,\vec{k}_2,\vec{k}_3) \;=\; \frac{H_*^4}{4M_{\rm pl}^4\epsilon_*} I(k_1,k_2,k_3) e^{\mp}_{ab}(\boldsymbol{k}_3)\boldsymbol{k}_1^a\boldsymbol{k}_2^b, \tag{2}$$

with

$$\mathcal{I}(k_1,k_2,k_3) \;=\; \frac{1}{k_1^3k_2^3k_3^3}\left(-k_t + \frac{k_1k_2+k_2k_3+k_1k_3}{k_t} + \frac{k_1k_2k_3}{k_t^2}\right). \tag{3}$$

The shape is specific for SFSR and can change if alternative models are considered. As a test-case we consider the shape above. It is very similar to a local shape. In a more general form, we define

$$\langle\zeta(\boldsymbol{k}_1)\zeta(\boldsymbol{k}_2)h^{\pm}(\boldsymbol{k}_3)\rangle \;=\; (2\pi)^3 16\pi^4 A_s^2\sqrt{r} f_{\rm NL}^{h\zeta\zeta}\delta^{(3)}\left(\sum_{n=1}^{3}\boldsymbol{k}_n\right)\mathcal{I}(k_1,k_2,k_3)e^{\mp}_{ab}(\boldsymbol{k}_3)\boldsymbol{k}_1^a\boldsymbol{k}_2^b, \tag{4}$$

For SFSR one can show that $f_{\rm NL}^{h\zeta\zeta} = \sqrt{r}/16$. $\mathcal{I}$ can be replaced by any shape that has is symmetric in k_1 and k_2. For a scale invariant spectrum of perturbations $\mathcal{I} \propto k^{-8}$.

Because tensors mostly affect transverse modes, a graviton-scalar-scalar bispectrum will get most of its contribution in the squeezed configuration (local-type). In projection, the signal in the CMB is maximized for large angle B-modes (ℓ_B) and small T modes (ℓ_T^1, ℓ_T^2). Because of the symmetry properties of the BTT correlation function, in the limit the T-modes are equal in length (i.e. when $\ell_T^1 = \ell_T^2$) the correlation function vanishes [3].

The flat-sky bispectrum can be computed through

$$\begin{aligned} B^{TTB}_{\boldsymbol{\ell}_1\boldsymbol{\ell}_2\boldsymbol{\ell}_3} \;=\; & 16\pi^2 A_s^2\sqrt{r} f_{\rm NL}^{h\zeta\zeta}(\boldsymbol{\ell}_1\times\boldsymbol{\ell}_3)\times\int dk_1^z dk_2^z\, \mathcal{I}\left(k_1^R,k_2^R,k_3^R\right) \\ & \Delta_T^{\zeta}(k_1^z,\ell_1)\Delta_T^{\zeta}(k_2^z,\ell_1)\Delta_P^{h}(k_3^z,\ell_3)\frac{\sqrt{2}k_3^z}{k_3^R\ell_3^2}\left[k_1^z(\boldsymbol{\ell}_2\cdot\boldsymbol{\ell}_3) - k_2^z(\boldsymbol{\ell}_1\cdot\boldsymbol{\ell}_3)\right], \end{aligned} \tag{5}$$

where the integrals over k_1^z, k_2^z run from $-\infty$ to $+\infty$, $k_3^z \equiv -(k_1^z+k_2^z)$, and $k_i^R \equiv \sqrt{(k_i^z)^2 + (\ell_i/D_R)^2}$, with $D_R = \tau_0 - \tau_R$, where τ_R is the conformal time at the peak of the CMB visibility function, and, for $X = T, P$ and $s = \zeta, h$,

$$\Delta_X^s(k_i^z,\ell_i) \equiv \int_0^{\tau_0}\frac{d\tau}{D^2}S_X^s(k_i^R)e^{-ik_z^i\tilde{D}}, \tag{6}$$

with $\tilde{D} = \tau - \tau_R$.

We have computed the $\langle BTT\rangle$ correlation function in the flat-sky limit $\ell_{\rm min} = 10$ in a Planck fiducial cosmology. We would again like to stress that the shape considered is a test-case; its predicted amplitude is too low to be observed (similar to the scalar bispectrum from SFSR).

3 Signal to Noise

In the flat-sky approximation the signal-to-noise ratio is given by the following integral over multipoles (rather than a discrete sum in the full-sky case) [4]:

$$\left(\frac{S}{N}\right)^2 = \frac{f_{\rm sky}}{4\pi^3}\int d^2\boldsymbol{\ell}_2\int d^2\boldsymbol{\ell}_3\frac{\left(B^{TTB}_{(-\boldsymbol{\ell}_2-\boldsymbol{\ell}_3),\boldsymbol{\ell}_2,\boldsymbol{\ell}_3}\right)^2}{\mathcal{C}^{TT}_{\ell_1}\mathcal{C}^{TT}_{\ell_2}\mathcal{C}^{BB}_{\ell_3}}, \tag{7}$$

where $\mathcal{C}_\ell = C_\ell + N_\ell$ with C_ℓ is the angular power spectrum, N_ℓ the noise, and we integrated out the $\boldsymbol{\ell}_1$ direction.

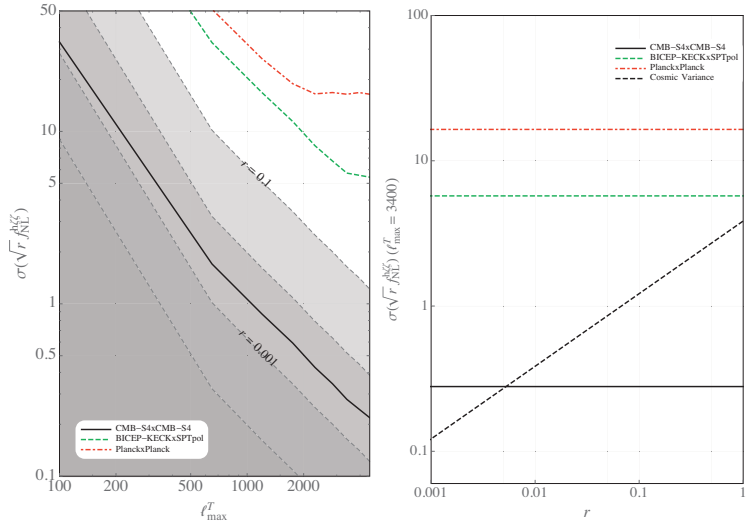


Figure 1 – Left: Forecasts for $\sigma(\sqrt{r} f^{h\zeta\zeta}_{\rm NL})$ for various CMB experiments as a function of $\ell_{\rm max}$. The colored lines present constraints when cosmic variance is negligible. The figure shows that cosmic variance would be subdominant for current and near future experiments if $r = 0.01$. For an experiment like CMB-Stage IV the total variance would be dominated by cosmic variance and not by instrumental noise unless $r \lesssim 0.001$ (with $\ell^T_{\rm max} = 4500$). Right: Forecasts for $\sigma(\sqrt{r} f^{h\zeta\zeta}_{\rm NL})$ for various CMB experiments. This figure illustrates that current experiments are all noise dominated for allowed values of r. CMB-Stage IV is comic variance dominated unless $r \lesssim 0.005$ (with $\ell^T_{\rm max} = 3400$). Cosmic variance limit can only be reduced if we consider more modes, i.e. by increasing $\ell^T_{\rm max}$).

The forecasted 1σ constraints on $\sqrt{r} f^{h\zeta\zeta}_{\rm NL}$ are plotted in Fig. 1 for several experiments including CMB-Stage IV. We assumed a noise dominated B-mode. If r is detected, the grey band indicates how the constraints are shifted. The plot should be compared to constraints from TTT on the same interaction, which $\sqrt{r} f^{h\zeta\zeta}_{\rm NL} \sim \mathcal{O}(10)$ [5]. CMB-Stage IV can improve those constraints by almost 2 orders of magnitude. Note that $\langle BTE \rangle$ and $\langle BEE \rangle$ should lead to similar constraints. Other combinations are expected to be worse (e.g. $\langle TEE \rangle$) since they are currently already cosmic variance dominated on large scales. Improvements can be achieved, but only from small angle T and E modes.

4 Discussion and Conclusion

We have explored the potential of the $\langle BTT \rangle$ bispectrum as probe of the early universe. The odd intrinsic parity of B-modes gives this bispectrum some properties which differ from that of the $\langle TTT \rangle$ bispectrum, but both are generically non-vanishing in a parity-conserving universe, and are sourced by primordial bispectra which are predicted to be of the same order in slow-roll parameters in single-field slow-roll inflation.

One advantage of the $\langle BTT \rangle$ bispectrum is that the signal suffers less from cosmic variance than its $\langle TTT \rangle$ counterpart for constraining the tensor-scalar-scalar bispectrum. Our analysis shows that with this observable it should be possible to constrain the level of non-Gaussianity to $\sigma(\sqrt{r} f^{h\zeta\zeta}_{\rm NL}) \sim \mathcal{O}(0.1) f^{-1/2}_{\rm sky}$.

We considered $\langle BTT \rangle$ bispectrum motivated by single-field slow-roll inflation, which maximizes when large-scale B modes are correlated with small-scale T modes. This shape has some experimental advantages, since a search for such a bispectrum could be performed, for instance, by cross-correlating a map of B-modes on large scales from a current or upcoming ground-based

CMB experiment with small-scale T fluctuations, such as those measured with the Planck satellite. On the other hand, it would be useful to consider other shapes for the $\langle BTT \rangle$ bispectrum, perhaps motivated by specific early-universe models.

We have not included possible contamination from dust, systematics, or lensing. Dust is a well-known contaminant in estimates of the $\langle BB \rangle$ power spectrum on large scales at the frequencies probed with ground-based experiments. Estimates of the $\langle BTT \rangle$ bispectrum will in principle be sensitive to correlations between large-scale dust polarization and small-scale dust intensity; while this may be less of an issue than in the power spectrum measure, this needs to be investigated in future work. Similarly, instrumental systematics which affect the measure of B on large scales should be decoupled from those that affect T on small scales, making this analysis less sensitive to systematics than the $\langle BB \rangle$ power spectrum. Finally, lensing converts E-mode polarization to B-mode polarization. As with measurements of the $\langle BB \rangle$ power spectrum, delensing to reduce effective noise from lensing needs to be performed when measuring the $\langle BTT \rangle$ bispectrum. In a universe with primordial gravitational waves, the $\langle BTT \rangle$ bispectrum will also contain a non-primordial signal on very large scales arising from correlations between B-modes from Thomson scattering after reionization and the curl mode of CMB lensing, which affects pairs of temperature modes. This is analogous to the scattered E-mode–lensing correlation induced by scalars in estimates of the $\langle ETT \rangle$ bispectrum [6].

We have focused on the $\langle BTT \rangle$ correlation function. However, other combinations sensitive to the coupling between scalars and tensors will add to the total signal-to-noise ratio. In particular, $\langle BEE \rangle$ and $\langle BTE \rangle$ are expected to have similar constraining power. In addition, similar to the use of E-modes for the scalar bispectrum, the B and E modes are projected through functions that have different nulls, which improves the mapping from the primordial space. In summary, the $\langle BTT \rangle$ bispectrum and other non-Gaussian correlations involving B-modes open up a new window into the early Universe. Ongoing and future CMB experiments will naturally make observations which allow us to carry out searches for and place non-trivial constraints on primordial tensor non-Gaussianity. While more theoretical work remains to discover the full value of B-mode non-Gaussianity, this new set of observables has the potential to be a very rich set of tools for probing primordial physics.

Acknowledgments

I would like to thank Joel Meyers, Alex van Engelen and Yacine Ali-Haimoud for their contribution to this work.

References

1. Maresuke Shiraishi, Shuichiro Yokoyama, Daisuke Nitta, Kiyotomo Ichiki, and Keitaro Takahashi. Analytic formulae of the cmb bispectra generated from non-gaussianity in the tensor and vector perturbations. *Phys. Rev. D*, 82:103505, Nov 2010.
2. J. Maldacena. Non-gaussian features of primordial fluctuations in single field inflationary models. *Journal of High Energy Physics*, 5:13, May 2003.
3. P. D. Meerburg, J. Meyers, A. van Engelen, and Y. Ali-Haïmoud. On CMB B-Mode Non-Gaussianity. *ArXiv e-prints*, March 2016.
4. Wayne Hu. Weak lensing of the cmb: A harmonic approach. *Phys. Rev. D*, 62:043007, Jul 2000.
5. Maresuke Shiraishi, Daisuke Nitta, Shuichiro Yokoyama, Kiyotomo Ichiki, and Keitaro Takahashi. CMB Bispectrum from Primordial Scalar, Vector and Tensor non-Gaussianities. *Prog. Theor. Phys.*, 125:795–813, 2011.
6. A. Lewis, A. Challinor, and D. Hanson. The shape of the CMB lensing bispectrum. *J. Cosm. Astropart. Phys.*, 3:018, March 2011.

PROBING INFLATION MODELS WITH GRAVITATIONAL WAVES

VALERIE DOMCKE
AstroParticule et Cosmologie (APC)/Paris Centre for Cosmological Physics, Université Paris Diderot

A direct detection of primordial gravitational waves is the ultimate probe for any inflation model. While current CMB bounds predict the generic scale-invariant spectrum to be below the reach of upcoming gravitational wave interferometers, this prospect may dramatically change if the inflaton is a pseudoscalar. In this case, a coupling to any abelian gauge field leads to a tachyonic instability for the latter and hence to a new source of gravitational waves, directly related to the dynamics of inflation. In this contribution we discuss how this setup enables the upcoming gravitational wave interferometers advanced LIGO/VIRGO and eLISA to probe the microphysics of inflation, distinguishing between different universality classes of single-field slow-roll inflation models. We find that the prime candidate for an early detection is a Starobinsky-like model.

1 Introduction

Unlike any other messenger, gravitational waves (GWs) can travel freely through the Universe, carrying information on times as early as cosmic inflation. During inflation, quantum fluctuations of the inflaton field and of the metric are stretched and become large-scale classical perturbations. GWs, corresponding to the metric fluctuations, carry the imprint of this very early stage of our universe, with a 1:1 correspondence between their frequency, the scale of the corresponding perturbation mode and the point in time when this mode exited the horizon during inflation. The frequency-dependence of the GW spectrum thus directly encodes the dynamics of cosmic inflation, i.e. can give us a time-resolved view of the microphysics (eg. the scalar potential) responsible for inflation.

Current indirect bounds on primordial GWs, obtained from bounds on the Cosmic Microwave Background (CMB) polarization, indicate that the nearly scale-invariant spectrum of the vacuum fluctuations during slow-roll inflation lies below the range of current and upcoming direct GW detectors. This picture may however change dramatically once interactions of the inflaton with other particles are taken into account [1]. To this end, we consider the generic coupling of a *pseudoscalar* inflaton ϕ to the field strength tensor $F_{\mu\nu}$ of an abelian gauge group,

$$\mathcal{L}_{\rm int} \sim \phi F_{\mu\nu}\tilde{F}^{\mu\nu}\,. \tag{1}$$

Such pseudoscalar (or 'axionic') flat directions, suitable for inflation, may be expected to be abundant at the high energy scales of cosmic inflation (for supergravity embeddings, see eg. [2,3]). As we will see, the presence of the interaction term (1) leads to a non-perturbative production of the gauge field during inflation [4], which provides an additional source of tensor perturbations, leading to a large enhancement of the resulting GW signal at small scales. In this contribution, we discuss how this enhancement will enable GW interferometers to probe different universality classes of inflation [5], classified by properties of the underlying scalar potential $V(\phi)$. This proceeding is based on work with Pierre Binétruy and Mauro Pieroni [6].

2 Pseudoscalar inflation

We consider a pseudoscalar ϕ coupled to $\mathcal{N}$ abelian gauge fields A^μ_a (see also [7] and refs therein),

$$\mathcal{L} = -\frac{1}{2}\partial_\mu\phi\partial^\mu\phi - \frac{1}{4}F^a_{\mu\nu}F^{\mu\nu}_a - V(\phi) - \frac{\alpha^a}{4\Lambda}\phi F^a_{\mu\nu}\tilde{F}^{\mu\nu}_a\,, \tag{2}$$

with $F^a_{\mu\nu}$ ($\tilde{F}^{\mu\nu}_a$) denoting the (dual) field-strength tensor, α/Λ parameterizing the coupling between the pseudoscalar and the gauge fields and $V(\phi)$ denoting the scalar potential driving inflation. The resulting equations of motion for the classical background fields read

$$\ddot{\phi} + 3H\dot{\phi} + \frac{\partial V}{\partial\phi} = \frac{\alpha}{\Lambda}\langle\vec{E}\vec{B}\rangle\,, \qquad \frac{d^2A^a_\pm(\tau,k)}{d\tau^2} + \left(k^2 \mp \frac{2\xi k}{\tau}\right)A^a_\pm(\tau,k) = 0\,, \tag{3}$$

with $\xi \equiv \alpha|\dot{\phi}|/(2\Lambda H)$. Here the second equation refers to the Fourier modes of the gauge field, $\vec{A}^a = \vec{e}_\pm A^a_\pm \exp(i\vec{k}\vec{x})$. The subscript $\pm$ denotes the two helicity modes of the massless gauge field. One of them (in our notation the A_+ mode) experiences a tachyonic instability, leading to an exponential growth of the low-momentum modes. If ξ is a slowly varying function in time, the two equations in (3) decouple and we can express the classical background gauge field as

$$A^a_+ \simeq \frac{1}{\sqrt{2k}}\left(\frac{k}{2\xi aH}\right)^{1/4} e^{\pi\xi - 2\sqrt{2\xi k/(aH)}}\,. \tag{4}$$

With this we find $\langle\vec{E}\vec{B}\rangle \simeq \mathcal{N}\cdot\,2.4\cdot10^{-4}H^4/\xi^4 e^{2\pi\xi}$. This acts an additional friction term in the slow-roll equation of motion for ϕ, which will overcome the Hubble friction term for sufficiently large values of ξ, thus modifying the background dynamics of inflation (and thus the predictions of a given inflation model, e.g. n_s and r). Note that $\xi \sim \dot{\phi}/H \sim \sqrt{\epsilon}$, with ϵ denoting the first slow-roll parameter of single-field inflation. In most single-field inflation models, ϵ is very small when the CMB scales exited the horizon (constrained by the CMB data) but increases monotonously to reach $\epsilon = 1$ at the end of inflation. Hence all effects sourced by the gauge fields are expected to be strongly suppressed at the CMB scales but can be very large at smaller scales, corresponding to perturbations mode which exited the horizon towards the end of inflation.

The gauge field background further modifies the equation of motion for the fluctuations of $\phi(t)$, leading to an additional contribution to the scalar power spectrum [8],

$$\Delta^2_s(k) = \Delta^2_s(k)_{\rm vac} + \Delta^2_s(k)_{\rm gauge} = \left(\frac{H^2}{2\pi|\dot{\phi}|}\right)^2 + \left(\frac{\alpha\langle\vec{E}\vec{B}\rangle/\sqrt{\mathcal{N}}}{3\beta H\dot{\phi}}\right)^2\,, \tag{5}$$

with $\beta \equiv 1 - 2\pi\xi\alpha\langle\vec{E}\vec{B}\rangle/(3\Lambda H\dot{\phi})$. At large values of ξ, this leads to an approximately scale invariant spectrum, $\Delta^2_s \simeq 1/(4\pi^2\mathcal{N}\xi^2)$.

Similarly, the gauge field background also provides an additional source for the tensor fluctuations, leading to an additional contribution to the GW spectrum

$$\Omega_{GW} = \frac{1}{12}\Omega_{R,0}\left(\frac{H}{\pi M_P}\right)^2\left(1 + 4.3\cdot10^{-7}\mathcal{N}\frac{H^2}{M_P^2\xi^6}e^{4\pi\xi}\right), \tag{6}$$

with $\Omega_{R,0} = 8.6\cdot10^{-5}$ denoting the radiation energy density today and $M_P = 2.4\cdot10^{18}$ GeV denoting the reduced Planck mass. Remarkably, the new contribution to the GW spectrum is maximally chiral, providing a powerful lever to distinguish it from other stochastic GW backgrounds.

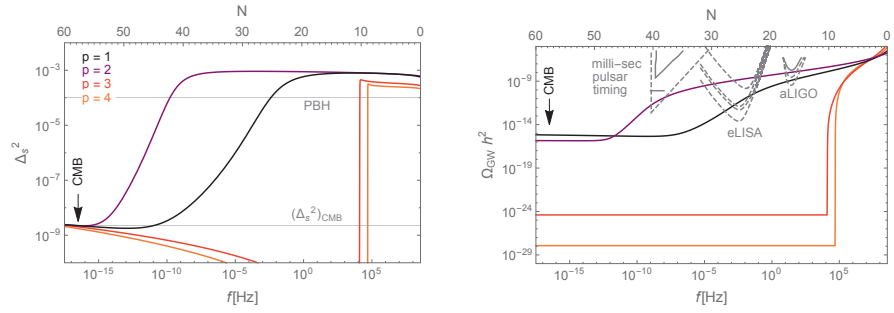


Figure 1 – Scalar and tensor power spectrum for different universality classes of inflation. For the scalar power spectrum, we show the CMB constraint as well as the PBH bound. For the tensor power spectrum, we indicate the sensitivity of some current and upcoming GW experiments.

3 Probing the microphysics of inflation

The impact of the gauge fields depends sensitively on the parameter ξ. As long as the gauge fields are subdominant in the equation of motion for ϕ, we have $\xi^2 \sim \epsilon = \dot{\phi}/(2H^2) \simeq \epsilon_V = (V'/V)^2/2$, i.e. the parameter ξ directly probes the scalar potential $V(\phi)$. Exploiting that the vast majority of single-field slow-roll inflation models may be parametrized by [5]

$$\epsilon_V \simeq \frac{\beta}{N^p} + \mathcal{O}(1/N^{p+1})\,, \tag{7}$$

with N denoting the number of e-folds ($N = -\int H dt$) elapsed since the end of inflation, we see that the predictions for pseudoscalar inflation can be phrased in terms of only three parameters: α/Λ, β and p. This allows us to systematically study the parameter space and to identify how future measurements may distinguish between different universality classes of inflation (different values of p) in this context.

Fig. 1 illustrates this for the scalar and tensor power spectrum, using four exemplary inflation models: quadratic chaotic inflation ($p = 1$), Starobinsky inflation ($p = 2$) and two implementations of hilltop inflation ($p = \{3, 4\}$) [9]. The two parameters β and α/Λ have been chosen to maximize the GW spectrum while obeying the CMB constraints. As can be easily understood from the ξ-dependence of the expressions above, a larger value of the parameter p implies suppression of the amplitude of the tensor fluctuations at CMB scales, but also a steeper increase of the spectrum towards higher frequencies. The parameter α/Λ governs the onset of the strong gauge field regime, i.e. increasing α/Λ shifts the strong increase in the spectrum to lower frequencies.[a] Note that both the scalar and tensor spectrum approach nearly universal values in the strong gauge field regime.[b]

From Fig. 1 we see that from the point of view of potential observations, the Starobinsky-type model with $p = 2$ is the most promising candidate. We thus turn to a more detailed study of the parameter space of this model, cf. Fig. 3. Here we in particular point out the powerful complementarity between CMB measurements and GW interferometers. Further important predictions of this setup are the production of primordial black holes [8], the predictions of excess radiation in form of gravitational waves contributing to the measurement of $N_{\rm eff}$ as well as the prediction of possibly observable excess μ-distortions in the CMB black body spectrum [10].

[a] The late rise in the hilltop models in Fig. 1 is due to CMB constraints on the spectral index n_s, which force α/Λ to be small in these models. Since $n_s \simeq 1 - p/N$ for $p > 1$, models with large value of p feature low values of n_s compared to the current Planck data, a situation which is aggravated in the presence of gauge fields due to the extra friction term.

[b] Both spectra obtain a $1/\mathcal{N}$ suppression in this regime if there is more than one abelian gauge group present. It should be noted that this regime of strong gauge fields is subject to a number of theoretical uncertainties.

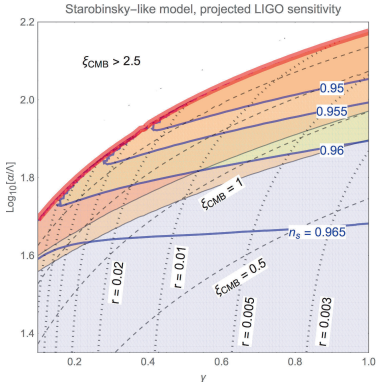


Figure 3 - Plot of the $(\alpha/\Lambda, \gamma)$ parameter space for the Starobinsky model,

$$V(\phi) = V_0 \left(1 - e^{-\gamma\phi}\right)^2 , \tag{8}$$

$(p = 2, \beta = 1/(2\gamma^2))$ with contour lines for the spectral index n_s (solid blue), the tensor-to-scalar ratio $r = \{0.003, 0.005, 0.1, 0.2, 0.3, \ldots\}$ (dotted) and $\xi_{\rm CMB} = \{0.5, 1, 1.5, \ldots\}$ (dashed). The white region in the top left corner is excluded due to the non-observation of non-gaussianities in the CMB. The orange shaded regions denote the projected sensitivity for advanced LIGO in the O2 and O5 run. The planned space-based interferometer eLISA will probe a similar region of the parameter space as LIGO, demonstrating the power of future multi-frequency GW analysis. See [6] for details.

4 Conclusion

If the inflaton is a pseudoscalar, its coupling to any abelian gauge field leads to a non-perturbative production of the latter during inflation. This in return modifies the inflationary dynamics by introducing an additional friction term, generically decreasing n_s and increasing r. Moreover, the scalar and tensor power spectra at high frequencies are strongly enhanced, leading to a wide spectrum of potentially observable features. In particular the GW spectrum, experimentally accessible over a very wide range of frequencies, can provide valuable information on the key parameters of the scalar potential driving inflation.

Acknowledgments

We acknowledge the financial support of the UnivEarthS Labex program at Sorbonne Paris Cité (ANR-10-LABX-0023 and ANR-11-IDEX-0005-02).

References

1. J. L. Cook and L. Sorbo, Phys. Rev. D **85**, 023534 (2012).
2. M. Kawasaki, M. Yamaguchi and T. Yanagida, Phys. Rev. Lett. **85**, 3572 (2000).
3. R. Kallosh and A. Linde, JCAP **1011**, 011 (2010), G. Dall'Agata and F. Zwirner, JHEP **1412**, 172 (2014), R. Kallosh and A. Linde, JCAP **1306**, 028 (2013), W. Buchmuller, V. Domcke and K. Kamada, Phys. Lett. B **726**, 467 (2013).
4. M. S. Turner and L. M. Widrow, Phys. Rev. D **37**, 2743 (1988), W. D. Garretson, G. B. Field and S. M. Carroll, Phys. Rev. D **46**, 5346 (1992), M. M. Anber and L. Sorbo, JCAP **0610**, 018 (2006).
5. V. Mukhanov, Eur. Phys. J. C **73**, 2486 (2013)
6. V. Domcke, M. Pieroni and P. Binetruy, arXiv:1603.01287 [astro-ph.CO].
7. M. M. Anber and L. Sorbo, Phys. Rev. D **81**, 043534 (2010), N. Barnaby, E. Pajer and M. Peloso, Phys. Rev. D **85**, 023525 (2012), N. Barnaby, R. Namba and M. Peloso, JCAP **1104**, 009 (2011), M. M. Anber and L. Sorbo, Phys. Rev. D **85**, 123537 (2012).
8. A. Linde, S. Mooij and E. Pajer, Phys. Rev. D **87**, no. 10, 103506 (2013)
9. A. D. Linde, Phys. Lett. B **129**, 177 (1983), A. A. Starobinsky, Phys. Lett. B **91**, 99 (1980), L. Boubekeur and D. H. Lyth, JCAP **0507**, 010 (2005).
10. P. D. Meerburg, R. Hloek, B. Hadzhiyska and J. Meyers, Phys. Rev. D **91**, no. 10, 103505 (2015), P. D. Meerburg and E. Pajer, JCAP **1302**, 017 (2013).

Gravitational Waves in the Early Universe from Gauge Field Production

Ido Ben-Dayan
Department of Physics, Ben-Gurion University, Beer-Sheva 84105, Israel

We demonstrate how observable gravitational waves (GW) signal on CMB scales can be produced in a bouncing cosmology from gauge field sources, thus generalizing earlier inflationary calculations. The GW spectrum is produced due to coupling between the scalar field dominating the energy density of the Universe and gauge fields, while not spoiling the background evolution. When the scalar is coupled only to $F\tilde{F}$ term, one helicity of the sourced GW spectrum is exponentially enhanced. The sourced spectrum is parametrically the square of the vacuum fluctuations spectrum, $\mathcal{P}_T^s \sim (\mathcal{P}_T^v)^2$, giving an even bluer spectrum than the standard vacuum one. In a companion paper we show that coupling the scalar also to F^2 term still enhances the spectrum and brings it arbitrarily close to scale invariance $n_T \geq 0$, allowing for GW observation on CMB scales, with distinct predictions compared to inflation.

1 Setup

A major motivation for considering a Bouncing Cosmology model is discarding the Big Bang singularity that is present in Cosmic Inflation [1]. This usually comes at a price of violating the Null Energy Condition (NEC) [2], and the absence of gravitational wave signal on CMB scales [3,4]. We shall show that coupling the scalar field that dominates the energy density of the Universe during the contraction to gauge fields, copiously produces gauge quanta and as a byproduct exponentially enhances GW production as well. This work is based on adapting previous inflationary analysis, [5,6,7,8], to bouncing cosmology.

We consider a slowly contracting Universe that is an exact solution to Einstein field equations in the spirit of ekpyrosis or the Pre Big Bang model [2,9]:

$$V = -V_1 e^{-\sqrt{2/p}\phi_1}, \quad a(\tau) = (-\tau/\tau_{end})^b, \quad -\infty < \tau \leq 0, \quad b = p/(1-p) \sim p \ll 1 \tag{1}$$

where τ is conformal time, and the scale factor is normalized to unity at the end of ekpyrosis. After ekpyrosis, there is a brief epoch of kinetic energy dominated contraction, bounce $\tau = 0$, kinetic energy dominated expansion and radiation domination of the Hot Big Bang. Consider coupling the 'bouncer' field ϕ_1 to gauge fields of the form:

$$\mathcal{S}_1 = \int d^4x\sqrt{-g}\left[\frac{M_p^2}{2}R - \frac{1}{2}(\partial\varphi_1)^2 - V(\varphi_1) - \frac{1}{4}F^{\mu\nu}F_{\mu\nu} - \frac{\alpha}{4f}\varphi_1\,\tilde{F}^{\mu\nu}\,F_{\mu\nu}\right] \tag{2}$$

Notice that the gauge group can be either the $U(1)_Y$ of the standard model, or a putative gauge group. These proceeding are largely based on [10], where interested readers should seek more details. More importantly, in [10], we also consider another model, where ϕ_1 is coupled both to F^2 and $F\tilde{F}$ term. In that model, not only is the amplitude of GW exponentially enhanced, but also its spectral tilt is controlled by the coupling between ϕ_1 and the gauge fields, thus allowing for a nearly scale invariant, slightly blue, GW spectrum with a definite helicity, that is observable

on CMB scales. Such a definite prediction is in stark contrast with the inflationary vacuum predictions that involve both GW helicities and a slightly red spectral tilt.

Consider $\hat{Q}_k = a\hat{h}_k$, where $\hat{h}_k$ is the tensor perturbation. Decomposing the spatial part of the metric $g_{ij} = a^2(\delta_{ij} + h_{ij})$, where the modes h_{ij} are transverse and traceless. Introducing the canonical modes:

$$\frac{M_p a}{2} h_{ij} = \int \frac{d^3k}{(2\pi)^{3/2}} \, \mathrm{e}^{i\vec{k}\cdot\vec{x}} \sum_{\lambda=\pm} \Pi_{ij,\lambda}\left(\hat{k}\right) Q_\lambda\left(\vec{k}\right) \quad , \quad \Pi_{ij,\lambda}\left(\hat{k}\right) = \epsilon_i^{(\lambda)}\left(\hat{k}\right) \epsilon_j^{(\lambda)}\left(\hat{k}\right) \tag{3}$$

where Q_λ is decomposed into vacuum and sourced fluctuations:

$$Q_k(\tau) = Q_{\vec{k}}^v(\tau) + Q_{\vec{k}}^s(\tau), \quad Q_k^v = b(\vec{k}) f_k(\tau) + b^\dagger(-\vec{k}) f_k^*(\tau), \quad \left[b(\vec{k}), b^\dagger(\vec{k}')\right] = \delta^{(3)}(\vec{k} - \vec{k}') \tag{4}$$

and we omitted the λ subscript for brevity and $f_k(\tau)$ are the mode functions whose solution is given in (6). The equation of motion for the tensor perturbation in the presence of a source is given by:

$$\left[\partial_\tau^2 + \left(k^2 - \frac{a''}{a}\right)\right] Q_\lambda\left(\tau, \vec{k}\right) = J_\lambda\left(\tau, \vec{k}\right) \tag{5}$$

The vacuum solution and the formal particular solution are:

$$f_k(\tau) = \frac{\sqrt{2\pi(-\tau)}}{M_{pl}} H^{(1)}_{1/2-b}(-k\tau) \tag{6}$$

$$Q_{\lambda,\mathrm{s}}\left(\tau, \vec{k}\right) = \int^\tau d\tau' G_k(\tau, \tau') \, J_\lambda\left(\tau', \vec{k}\right) \tag{7}$$

In the absence of coupling to gauge fields, there is no source term, $J_\lambda = 0$. The GW power spectrum generated by vacuum fluctuations is given by:

$$\mathcal{P}_T^v \simeq \frac{4}{\pi^2 M_{pl}^2 k_e^{2b}} k^{2+2b}, \tag{8}$$

which is scale invariant for inflation ($b = -1$) and very blue in a bouncing model ($b \ll 1$) and $k_e = -\tau_{end}$ is the last mode to exit the horizon and is a suitable pivot scale. Such a blue spectrum has to be unobservable by many orders of magnitude on CMB scales once BBN bounds and CMB constraints on N_{eff} are taken into account.

2 Gauge Field Production

Considering the Coulomb gauge $\hat{A}_0 = 0$, the 'electric' and 'magnetic' fields are $\hat{E}_i = -\frac{1}{a^2}\hat{A}_i'$, $\hat{B}_i = \frac{1}{a^2}\epsilon_{ijk}\partial_j \hat{A}_k$. Let us decompose the vector potential into modes:

$$\hat{A}_i(\tau, \vec{k}) = \sum_{\lambda=\pm} \epsilon_i^{(\lambda)}(\hat{k}) \tilde{A}_\lambda(\tau, k) \left[\hat{a}_\lambda(\vec{k}) + \hat{a}_\lambda^\dagger(-\vec{k})\right], \quad \left[a_\lambda(\vec{k}), a_{\lambda'}^\dagger(\vec{k}')\right] = \delta_{\lambda\lambda'}\delta^{(3)}(\vec{k} - \vec{k}') \tag{9}$$

where $\epsilon_i^{(\lambda)}$ are 'standard' circular polarization vectors[10]. The operators from (9) commute with the ones in (4). The coupling of φ_1 to gauge fields enhances the gauge field production and their amplitude is exponentially enhanced during horizon exit, such that $(8\xi)^{-1} < -k\tau < 2\xi$:

$$\left[\frac{\partial^2}{\partial\tau^2} + k^2 \pm \frac{2k\xi}{\tau}\right] A_\pm(\tau, k) = 0, \quad \xi = \alpha \frac{M_{pl}}{f} \frac{\sqrt{p}}{\sqrt{2}(1-p)} \tag{10}$$

$$\tilde{A}_+(\tau, k) \cong \frac{1}{\sqrt{2k}} \left(\frac{-k\tau}{2\xi}\right)^{1/4} e^{\pi\xi - 2\sqrt{-2\xi k\tau}} \tag{11}$$

Notice that only the + helicity is exponentially enhanced. The source term J_λ in (5) in terms of gauge fields is:

$$J_\lambda\left(\tau,\,\vec{k}\right)=\Pi^{*}_{ij,\lambda}\left(\hat{k}\right)\int\frac{d^3x}{(2\pi)^{3/2}}\,\mathrm{e}^{-i\vec{k}\cdot\vec{x}}\,\frac{a}{M_p}\,T_{ij}\left(\tau,\,\vec{x}\right)=-\frac{a^3}{M_{pl}}\Pi_{ij,\lambda}(\hat{k})\int\frac{d^3x}{(2\pi)^{3/2}}e^{-i\vec{k}\vec{x}}\left[\hat{E}_i\hat{E}_j+\hat{B}_i\hat{B}_j\right](x^i) \tag{12}$$

The parametric behavior of the different terms is therefore: $Q^s_\lambda\sim J_\lambda\sim\tilde{A}^2\sim e^{2\pi\xi}$. As a consequence, the sourced spectrum that is not correlated with the vacuum one, $\mathcal{P}_T=\mathcal{P}^v_T+\mathcal{P}^s_T$, will be exponentially enhanced $\mathcal{P}^s_T\sim(Q^s_\lambda)^2\sim e^{4\pi\xi}$. The reason there are no cross spectra is that the sourced spectrum comes from the ladder operators of the photons, while the vacuum spectrum is from the ladder operator of the gravitational waves. The production of gauge fields and GW as a byproduct, could backreact on the background geometry. To avoid a significant backreaction, the most stringent constraint on the Hubble parameter at the end of contraction is coming from the Friedmann equation:

$$\frac{H_{end}}{M_{pl}}\ll 146p^2\xi^{3/2}e^{-\pi\xi} \tag{13}$$

3 The GW Spectrum

To calculate the sourced GW spectrum we need the retarded Green's function (5,7). This can be done in general for FLRW cosmology:

$$G_{ret.}(\tau,\tau')=i\Theta(\tau-\tau')\frac{\pi}{4}\sqrt{\tau\tau'}\left[H^{(1)}_{1/2-b}(-k\tau)H^{(2)}_{1/2-b}(-k\tau')-H^{(1)}_{1/2-b}(-k\tau')H^{(2)}_{1/2-b}(-k\tau)\right] \tag{14}$$

A nice property of this Green's function is that it vanishes outside the horizon $-k\tau\ll 1$ in kinetic energy domination $b=1/2$, providing a natural mechanism for the shut down of GW production prior to the bounce. We can now write down the gravitational wave operator $\hat{h}_\lambda$ in terms of the gauge field operators:

$$\begin{aligned}\hat{h}_\lambda=-\frac{2}{M^2_{pl}a(\tau)}\int^\tau d\tau'\frac{G_k(\tau,\tau')}{a(\tau')}\int\frac{d^3p}{(2\pi)^{3/2}}P_\lambda(\vec{k},\vec{p},\vec{k}-\vec{p})\left\{\frac{2\xi}{-\tau'}\sqrt{p|\vec{k}-\vec{p}|}+p|\vec{k}-\vec{p}|\right\}\\ \times\tilde{A}_{\lambda'}(\tau',\vec{p})\tilde{A}_{\lambda'}(\tau',\vec{k}-\vec{p})\left[\hat{a}_{\lambda'}(\vec{p})+\hat{a}^\dagger_{\lambda'}(-\vec{p})\right]\left[\hat{a}_{\lambda'}(\vec{k}-\vec{p})+\hat{a}^\dagger_{\lambda'}(-\vec{k}+\vec{p})\right]\end{aligned} \tag{15}$$

with

$$|P_\lambda(\vec{k},\vec{p},\vec{k}-\vec{p})|^2=\frac{1}{16}\left(1+\lambda\frac{\vec{k}\cdot\vec{p}}{kp}\right)^2\left(1+\lambda\frac{k^2-\vec{k}\cdot\vec{p}}{k|\vec{k}-\vec{p}|}\right)^2 \tag{16}$$

and we have used definitions given in [10] for projection operators and the exact functional form of J_λ. Let us evaluate the dimensionless sourced tensor power spectrum according to $\mathcal{P}_\lambda(k)\delta_{\lambda\lambda'}\delta(\vec{k}+\vec{k}')\equiv\frac{k^3}{2\pi^2}\left\langle\hat{h}_\lambda(\vec{k})\hat{h}_{\lambda'}(\vec{k}')\right\rangle$. After performing the time integration, and considering the dominant contributions outside the horizon, we arrive at:

$$\left\langle\hat{h}_\lambda(\vec{k})\hat{h}_{\lambda'}(\vec{k}')\right\rangle=\frac{e^{4\pi\xi}k^{1+4b}}{2^7\xi^2M^4_{pl}k_e^{4b}}\int\frac{d\cos\theta dqq^2}{(2\pi)^2}\sqrt{q|\hat{k}-\vec{q}|}\frac{(1\pm\cos\theta)^2\left(1-q\cos\theta\pm\sqrt{1-2q\cos\theta+q^2}\right)^2}{(1-2q\cos\theta+q^2)\left(\sqrt{q}+\sqrt{|\hat{k}-\vec{q}|}\right)^6} \tag{17}$$

where $\vec{q}=\vec{p}/|k|$ is the dimensionless momentum. Since the momentum integral is diverging linearly, it will be dominated by the UV cut-off, H_{end}. Considering the dominant contribution of the large $q\gg 1$ limit:

$$\int\frac{d\cos\theta dqq^2}{(2\pi)^2}\sqrt{q|\hat{k}-\vec{q}|}\frac{(1\pm\cos\theta)^2\left(1-q\cos\theta\pm\sqrt{1-2q\cos\theta+q^2}\right)^2}{(1-2q\cos\theta+q^2)\left(\sqrt{q}+\sqrt{|\hat{k}-\vec{q}|}\right)^6}\simeq\frac{q_{UV}}{30(2\pi)^2}=\frac{H_{end}}{30(2\pi)^2k} \tag{18}$$

Hence the sourced contribution to the power spectrum is:

$$\mathcal{P}_T^s = \frac{e^{4\pi\xi}}{2^7\xi^2 30(2\pi)^2 2\pi^2}\frac{k^{3+4b}H_{end}}{M_{pl}^4 k_e^{4b}} \tag{19}$$

Notice, that this is the spectrum of the + helicity. The − helicity is not enhanced and will therefore give a negligible contribution to the overall GW spectrum. Comparing the above spectrum with the vacuum one for $k_e = -\tau_{end}, b = 1/50$, shows that the sourced spectrum dominates for $\xi \geq 3.1$. However, as we can immediately see, the resulting spectrum is even more blue than the vacuum one. In the inflationary case $\mathcal{P}_s \sim \mathcal{P}_{vac}^2$ and naively this repeats itself here. The main difference is that here we had a sharp cut-off H_{end} instead of integrating to infinite wave-number k. Hence, instead of getting k^{4+4b} dependence, we got, $H_{end}k^{3+4b}$, which is still bluer than the vacuum one, and as such, will still be unobservable at CMB scales.

In the companion paper [10], we also analyze another coupling

$$\mathcal{L} \supset a_2^{2n} e^{-2n\varphi_1/a_1}\left\{\frac{1}{4}F^{\mu\nu}F_{\mu\nu} - \frac{\gamma}{4}\tilde{F}^{\mu\nu}F_{\mu\nu}\right\}, \tag{20}$$

with $\xi = -\gamma n$ and show that the final sourced spectrum for $-2 < n < -5/4$ is given by:

$$\mathcal{P}_T^s(n_T \ll 1) \simeq \frac{11.1}{256\pi^6 n_T}\frac{e^{4\pi\xi}}{b^4\xi^6}\left(\frac{H_{end}}{M_{pl}}\right)^4\left(\frac{k}{H_{end}}\right)^{4(2+n)}, \tag{21}$$

with $n_T = 4(2+n)$, allowing for a blue spectrum, arbitrarily close to scale invariant. Furthermore, there is an identical spectrum, due to a 'duality" in the lagrangian, given by $n \to -1-n, \xi \to \xi$, that then corresponds to $1/4 < n < 1$. Hence, we have a proof of concept of observable GW on CMB scales in a bouncing cosmology.

Acknowledgments

I thank Jean-Luc Lehners, Marco Peloso and Lorenzo Sorbo for discussions and correspondence. Furthermore, I thank the 50th 'Rencontres de Moriond' Cosmology session committee for its financial support and the opportunity to participate in the conference and its proceedings.

References

1. A. Borde, A. H. Guth and A. Vilenkin, Phys. Rev. Lett. **90**, 151301 (2003) [gr-qc/0110012].
2. J. L. Lehners, Adv. Astron. **2010**, 903907 (2010) [arXiv:1001.3125 [hep-th]].
3. R. Brustein, M. Gasperini, M. Giovannini and G. Veneziano, Phys. Lett. B **361**, 45 (1995) [hep-th/9507017].
4. L. A. Boyle, P. J. Steinhardt and N. Turok, Phys. Rev. D **69**, 127302 (2004) [hep-th/0307170].
5. N. Barnaby and M. Peloso, Phys. Rev. Lett. **106**, 181301 (2011) [arXiv:1011.1500 [hep-ph]].
6. L. Sorbo, JCAP **1106**, 003 (2011) [arXiv:1101.1525 [astro-ph.CO]].
7. N. Barnaby, R. Namba and M. Peloso, JCAP **1104**, 009 (2011) [arXiv:1102.4333 [astro-ph.CO]].
8. C. Caprini and L. Sorbo, JCAP **1410**, no. 10, 056 (2014) [arXiv:1407.2809 [astro-ph.CO]].
9. M. Gasperini and G. Veneziano, Phys. Rept. **373**, 1 (2003) [hep-th/0207130].
10. I. Ben-Dayan, arXiv:1604.07899 [astro-ph.CO].
11. P. D. Meerburg, R. Hlozek, B. Hadzhiyska and J. Meyers, Phys. Rev. D **91**, no. 10, 103505 (2015) [arXiv:1502.00302 [astro-ph.CO]].

Statistical Decoupling of Lagrangian Fluid Parcel in Newtonian Cosmology

Xin Wang
Canadian Institute for Theoretical Astrophysics, 60 St. George St., Toronto, ON, M5H 3H8, Canada

Here we introduce a novel method for studying the Lagrangian dynamics of a single fluid element within a self-gravitational matter field. In Newtonian cosmology, the non-local tidal force complicates the theoretical investigation of the non-linear evolution of various cosmic objects, e.g. dark matter halos, since a fluid parcel with given initial density and shape may evolve differently depending on their environments. The statistical solution we provide here could decouple this environmental dependence. After deriving the probability distribution evolution equation of fluid variables, our method produces a set of closed ordinary differential equations whose solution is uniquely determined by the initial condition of the fluid element. Mathematically, it corresponds to the projected characteristic curve of the transport equation of the density-weighted probability density function. Physically, these trajectories describe the mean evolution averaged over all environments by substituting the tidal tensor with its conditional average.

1 Introduction

The large-scale structure of the Universe encodes valuable information of various physical processes including primordial physics, non-linear gravitational dynamics, and late-time baryonic galaxy formation. Recent developments in non-linear perturbation theory (PT) promise a very accurate estimation of the matter clustering in the weakly non-linear regime. In the deeply non-linear region, however, PT performs poorly. Alternatively, one could try to decouple the evolution of highly non-linear objects, e.g. dark matter halos, from their surroundings and study separately. This approach leads to phenomenological theory like the halo model[1]. In such model, these viralized halos provide the environment for most of the observed galaxies [1]; connect the statistical properties of galaxies with their spatial and size distribution.

However, the analytical investigation of these highly non-linear objects has been complicated by one intrinsic property of the Newtonian gravity – the non-locality, which means that the gravitational effect felt by a single element is determined by the matter distributed in the entire Universe, and that the whole field has be to taken into account for realistic modeling. Therefore, two proto-halos with exact the same initial density and shape might evolve into very different states cased by their distinct environments. To address these issues, we are going to present a statistical method that is well developed in turbulence, known as the probability density function (PDF) based method [2], where the key ingredient is the evolution of one-point PDF.

2 Lagrangian Dynamics of Cosmic Fluid

In the Newtonian cosmology, the gravitational instability of the large-scale structure is described by the fluid conservation equation of density contrast δ_ρ and peculiar velocity $\mathbf{u}$. Before shell-crossing, they satisfy the continuity and Eulerian equations respectively. In Lagrangian fluid

dynamics, these two equations are

$$\begin{aligned}
\frac{d}{d\tau}\delta_\rho &= -(1+\delta_\rho)\theta, \\
\frac{d}{d\tau}\theta &= -\left[\mathcal{H}(\tau)\theta + \frac{1}{3}\theta^2 + \sigma^{ij}\sigma_{ij}\right] - 4\pi G_N\bar{\rho}a^2\delta_\rho, \\
\frac{d}{d\tau}\sigma_{ij} &= -\left[\mathcal{H}(\tau)\sigma_{ij} + \frac{2}{3}\theta\sigma_{ij} + \sigma_{ik}\sigma^k_j - \frac{1}{3}\sigma_{mn}\sigma^{mn}\delta^K_{ij}\right] - \varepsilon_{ij},
\end{aligned} \tag{1}$$

where the total derivative $d/d\tau = \partial/\partial\tau + \mathbf{u}\cdot\nabla$, θ is the velocity divergence, σ_{ij} is the velocity shear tensor. Because of the Poisson equation, the peculiar tidal tensor at location $\mathbf{x}$ is an integral over the entire space

$$\varepsilon_{ij}(\mathbf{x}) = G_N\bar{\rho}a^2\int d^3x'\left[\frac{\delta^K_{ij}}{r^3} - 3\frac{r_i r_j}{r^5}\right]\delta_\rho(\mathbf{x}'), \tag{2}$$

which would also vary depending on the specific spatial location. To simplify the formalism, we would like to group all dynamical variables as $\boldsymbol{\psi} = \{\delta_\rho, \theta, \sigma_{ij}\}$, so that Equation (1) could simply be expressed as

$$\frac{d}{d\tau}\boldsymbol{\psi}(\tau) = \boldsymbol{\chi}[\boldsymbol{\psi}, \varepsilon_{ij}], \tag{3}$$

where $\boldsymbol{\chi}[\boldsymbol{\psi}, \varepsilon_{ij}]$ is the function depends on $\boldsymbol{\psi}$ and ε_{ij}.

3 The Evolution of Probability Density Function and the Mean Trajectory

Assume we could follow all fluid particles in a self-gravitational system, and we would like to consider the probability of a random selected parcel (e.g. originally located at some Lagrangian position $\mathbf{q}$) whose dynamical variables $\boldsymbol{\psi}$ at time τ equals $\boldsymbol{\Psi}$. In the following, the capitalized $\boldsymbol{\Psi}$ denotes the sample space variable corresponding to $\boldsymbol{\psi}$, i.e. $\boldsymbol{\Psi} = \{\Delta_\rho, \Theta, \Sigma_{ij}\}$. Initially, the resulting probability density function is simply Gaussian. As the dynamical system evolves following equation (3), the PDF will then change gradually. In the following, we will term it the Lagrangian PDF ($\mathcal{P}_L(\boldsymbol{\Psi};\tau)$, since the underlying dynamics is in the Lagrangian sense. For a single realization (or a randomly selected particle in the system), the probability density function, i.e. the fine-grained PDF ($\mathcal{P}^f_L$), could simply be written as Dirac-δ function [2,3]

$$\mathcal{P}^f_L(\boldsymbol{\Psi};\tau) = \delta_D\left[\boldsymbol{\psi}(\tau) - \boldsymbol{\Psi}\right] \tag{4}$$

since the probability of finding the dynamical variable $\boldsymbol{\psi} = \boldsymbol{\Psi}$ at τ will only be non-zero at the value determined by the dynamical equation (3). Now let us take an ensemble of particles, e.g. all particles in the system. By definition, this fine-grained PDF then relates to $\mathcal{P}_L(\boldsymbol{\Psi};\tau)$ by taking the ensemble average $\langle\cdot\rangle_L$ associated with $\mathcal{P}_L(\boldsymbol{\Psi};\tau)$

$$\langle P^f_L(\boldsymbol{\Psi};\tau)\rangle_L = \int d\boldsymbol{\Psi}' P_L(\boldsymbol{\Psi}';\tau)\delta_D(\boldsymbol{\Psi}' - \boldsymbol{\Psi}) = P_L(\boldsymbol{\Psi};\tau). \tag{5}$$

Practically, at any given time τ, $\langle\cdot\rangle_L$ is achieved by averaging over all fluid particles following the Lagrangian dynamical system from some initial distribution.

The evolution equation of $\mathcal{P}_L(\boldsymbol{\Psi};\tau)$ could then be derived simply by taking the time derivatives of equation (5),

$$\begin{aligned}
\frac{\partial}{\partial\tau}\mathcal{P}_L(\boldsymbol{\Psi};\tau) &= \left\langle\frac{\partial}{\partial\tau}\mathcal{P}^f_L(\boldsymbol{\Psi};\tau)\right\rangle_L = \left\langle\frac{d\psi_\alpha}{d\tau}\left[\frac{\partial}{\partial\psi_\alpha}\delta_D(\boldsymbol{\psi}(\tau) - \boldsymbol{\Psi})\right]\right\rangle_L \\
&= -\left\langle\chi_\alpha\left[\frac{\partial}{\partial\Psi_\alpha}P^f_L(\boldsymbol{\Psi};\tau)\right]\right\rangle_L = -\frac{\partial}{\partial\Psi_\alpha}\left\langle\chi_\alpha\mathcal{P}^f_L(\boldsymbol{\Psi};\tau)\right\rangle_L.
\end{aligned} \tag{6}$$

Here, we have changed the derivative variable from ψ_α to Ψ_α, since $\partial\delta_D(\boldsymbol{\psi}-\boldsymbol{\Psi})/\partial\psi_\alpha = -\partial\delta_D(\boldsymbol{\psi}-\boldsymbol{\Psi})/\partial\Psi_\alpha$. And we have also substituted the dynamical equation $d\psi_\alpha/d\tau = \chi_\alpha$. In the last equality, the partial derivative with respect to the sample space variable $\partial/\partial\Psi_\alpha$ has been taken out of the average, since it commutes with both random variables as well as the average operation $\langle\cdot\rangle_L$. Before proceeding, we first notice that, the right hand side of equation (1), $\boldsymbol{\chi}[\boldsymbol{\psi}, \varepsilon_{ij}]$, depends not only on $\boldsymbol{\psi}$ but also on another random variable, specifically the tidal tensor ε_{ij}. Therefore, the ensemble average $\langle\chi_\alpha \mathcal{P}_L^f(\boldsymbol{\Psi};\tau)\rangle_L$ should be performed regarding the joint PDF $\mathcal{P}_L(\boldsymbol{\Psi}, \boldsymbol{X};\tau)$, where $\boldsymbol{X}$ is the sample space variable corresponding to $\boldsymbol{\chi}$. This leads to $\langle\chi_\alpha \mathcal{P}_L^f(\boldsymbol{\Psi};\tau)\rangle_L = \langle\chi_\alpha|\boldsymbol{\Psi};\tau\rangle_L \mathcal{P}_L(\boldsymbol{\Psi};\tau)$, where we have expressed the joint PDF by the product of $\mathcal{P}_L(\boldsymbol{\Psi};\tau)$ and the conditional PDF $\mathcal{P}_L(\boldsymbol{X}|\boldsymbol{\Psi};\tau) = \mathcal{P}_L(\boldsymbol{X}|\boldsymbol{\psi}=\boldsymbol{\Psi};\tau)$. Finally, we show that the evolution of $\mathcal{P}_L(\boldsymbol{\Psi};\tau)$ is simply described by the conservation equation in multidimensional parameter space $\boldsymbol{\Psi}$

$$\frac{\partial}{\partial\tau}\mathcal{P}_L(\boldsymbol{\Psi};\tau) + \frac{\partial}{\partial\Psi_\alpha}\left[\langle\chi_\alpha|\boldsymbol{\Psi};\tau\rangle_L \mathcal{P}_L(\boldsymbol{\Psi};\tau)\right] = 0, \tag{7}$$

with the convective coefficients characterised by the conditional average $\langle\boldsymbol{\chi}|\boldsymbol{\Psi};\tau\rangle_L$.

Intuitively, the evolution equation (7) would encode valuable dynamical information about the Lagrangian evolution of fluid elements, since the only reason that could distort the shape of PDF in the parameter space of $\boldsymbol{\Psi}$ is because there are genuine particles moved to that region. As a linear partial differential equation (PDE), one of the standard analytical methods to solve this equation is the method of characteristics. With this method, the solution to equation (7) is represented as the surface fabricated by the union of characteristic curves, which are defined as the integral curves of the vector field determined by the coefficients of the PDE. For our purpose, however, instead of the full solution, we are mostly interested in its projection to the dynamical variable space of $\boldsymbol{\Psi}$. Following the standard procedure, the projected characteristic trajectory is expressed as

$$\frac{d}{d\tau}\boldsymbol{\Psi}(\tau) = \langle\boldsymbol{\chi}|\boldsymbol{\Psi};\tau\rangle_L. \tag{8}$$

This ordinary differential equation resembles the full dynamical system (3) except for the additional operation of average conditional on the value of dynamical variables $\boldsymbol{\Psi}$ at time τ. Therefore, it would eliminate the dependence on extra degree of freedom other than $\boldsymbol{\Psi}$, and the trajectory then becomes localized. In the right panel of Figure 1, we schematically illustrate the procedure.

Since the only extra term in $\boldsymbol{\chi}$ is the tidal tensor ε_{ij}, after the conditional average, there will be no modification needed for most part of equation (1) except for the evolution of velocity shear

$$\frac{d}{d\tau}\Sigma_{ij} + \mathcal{H}(\tau)\Sigma_{ij} + \frac{2}{3}\Theta\Sigma_{ij} + \Sigma_{ik}\Sigma^k_j - \frac{1}{3}\Sigma_{mn}\Sigma^{mn}\delta^K_{ij} = -\langle\varepsilon_{ij}|\boldsymbol{\Psi};\tau\rangle_L. \tag{9}$$

Therefore, at any given time τ, our solution is obtained by averaging over environmental tidal effects among all fluid elements with the same value of density, velocity divergence and velocity shear. So this procedure would produce a mean effective fluid element whose trajectory in $\boldsymbol{\psi}$ space is integrated along the conditional averaged change rate of shear tensor. Interestingly, if one takes the equation (8) as the original system, and repeats procedures, one would get the exact same $\mathcal{P}_L$ evolution equation (7). That is to say, although the dynamical behavior of a genuine fluid element is very different from the effective particles that described by equation (8), their one-point statistical will always be identical.

For Gaussian field, it is straightforward to show that the conditional average is simply linearly proportional to $\boldsymbol{\Psi}$,

$$\langle\varepsilon_{ij}|\boldsymbol{\Psi};\tau\rangle = \xi^{\varepsilon\psi}_{ij,\alpha}\left(\xi^{\psi\psi}\right)^{-1}_{\alpha\beta}\Psi_\beta = 4\pi G_N\bar{\rho}a^2\left(\frac{\sigma^2_{\delta\theta}}{\sigma^2_{\theta\theta}}\right)\Sigma_{ij}. \tag{10}$$

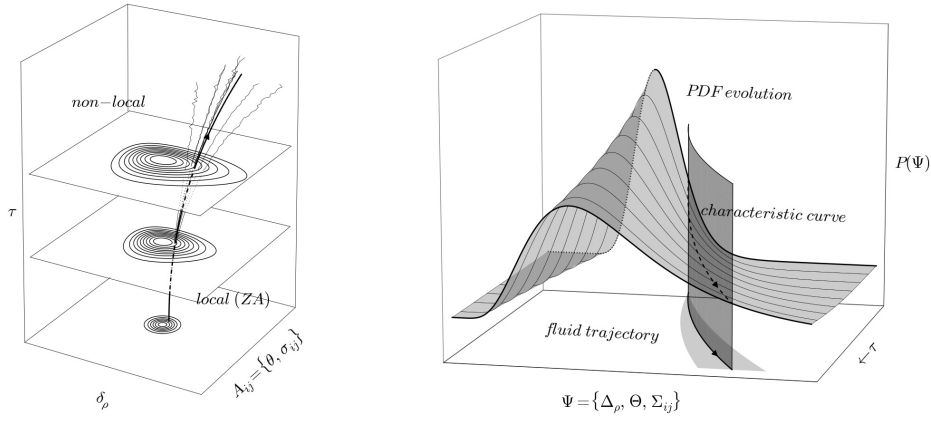


Figure 1 – (*Left*): The Lagrangian evolution of fluid elements in the parameter space of $\boldsymbol{\psi}=\{\delta_\rho,\theta,\sigma_{ij}\}$. Contours corresponds to the evolution of one-point probability density function, from Gaussian to some skewed distribution. At early stage, the evolution is fully described by Zel'dovich approximation, therefore is uniquely determined by initial condition $\boldsymbol{\psi}(\tau_i)$. However, after entering into non-linear regime, the tidal tensor will not be a simple deterministic function of $\boldsymbol{\psi}$ locally, and therefore will deviate from and spread around local solutions. (*Right*): Schematics of the PDF based method for deriving the mean trajectory in the parameter space of dynamical variables $\boldsymbol{\Psi}=\{\Delta_\rho,\Theta,\Sigma_{ij}\}$. The characteristic curves of the PDF evolution equation is then projected back into the dynamical space $\boldsymbol{\Psi}$.

where $\left(\xi^{\psi\psi}\right)^{-1}_{\alpha\beta}$ is the component of the inverse covariance matrix between $\boldsymbol{\psi}$, $\sigma^2_{\delta\theta}$ ($\sigma^2_{\theta\theta}$) is the variance between δ and θ (θ and θ). For weakly non-Gaussian field, we could also show that

$$\langle\varepsilon_{ij}|\boldsymbol{\Psi}\rangle \;=\; \langle\varepsilon_{ij}|\boldsymbol{\Psi}\rangle_G+\frac{1}{2}\xi^{(\varepsilon-\sigma)\psi\psi}_{ij,\alpha\beta}(\xi^{\psi\psi})^{-1}_{\alpha\delta}\;(\xi^{\psi\psi})^{-1}_{\beta\lambda}\Psi_\delta\Psi_\lambda \tag{11}$$

In general, the conditional average of the tidal tensor could be written as some function of dynamical variables $\boldsymbol{\Psi}$, i.e.

$$\langle\varepsilon_{ij}|\boldsymbol{\Psi};\tau\rangle=\mathscr{F}_{ij}(\boldsymbol{\Psi};\tau). \tag{12}$$

It is clear that the function $\mathscr{F}_{ij}$ would be symmetric and traceless on spatial coordinates. And the coefficients of its Tylor series would depend on the statistics of the field.

4 Conclusion

Here we presented a statistical method for decoupling the intrinsically non-local Lagrangian evolution of a fluid element from a self-gravitational random field in Newtonian cosmology. The method will be very useful for understanding the non-linear evolution of dark matter halos as well as other cosmic web morphologies.

References

1. A. Cooray and R. Sheth, Physics Reports **372**, 1 (2002)
2. S. B. Pope, Progress in Energy and Combustion Science, 1985, 11, 119
3. X. Wang and A. Szalay, *ApJ* **820**, 30 (2016).

Constraints On Gravity from CMB data: an Effective Field Theory approach

V. SALVATELLI
Aix Marseille Université, Centre du Physique Thorique, UMR 7332, 13288 Marseille, France.

We use the Effective Eield Theory of Dark Energy formalism to constrain dark energy models belonging to the *Horndeski* class with the recent Planck 2015 CMB data. We disentangle in our analysis the constraining power of data from that of the theory, by considering different set of viability conditions. We find that such criteria severely restrict the allowed parameter space. As a result we confirm that no theory performs better than ΛCDM when CMB data alone are analysed. Indeed any healthy dark energy model belonging to the large class here considered can reproduce the best-fitting phenomenological behaviours reported in previous studies [3].

1 Introduction

Understanding the origin of the present acceleration of the universe is one of the key challenge for cosmology. Recent progress in the analysis of the Cosmic Microwave Background [1] has significantly strengthen the case for the so called ΛCDM model. Although a pletora of different and more complex dark energy scenarios, where the acceleration is produced by time varying dark energy fluid or modifications in the action of the gravitational field, still survive the comparison with data. Particularly, the fact that the measurements of structure formation consistently seems to point towards a lower growth rate than expected in the ΛCDM model [2,3] leaves opened the tantalizing possibility that non-standard gravity emerges on cosmological scale. Furthermore, large-scale surveys as EUCLID and LSST, will soon provide an incredible large amount of data with enough sensitivity to discriminate modified gravity effects on cosmological scales, making the exploration of modified gravity even more crucial and timely.

In this context, it has became clear that individuating an efficient and widely-shared strategy for exploring the space of dark energy theories is essential to advance in the dark energy quest. Here we propose to describe deviations from the standard scenario in terms of "constitutive parameters" of alternative gravitational theories. This is made possible by the *effective field theory of dark energy* (EFT of DE) formalism, that allows to describe all dark energy and modified gravity models that contain one additional scalar degree of freedom in a unified language [4,5].

Particularly we use EFT of DE to explore which modified gravity models are compatible with current CMB data. Our goal is twofold. On the one hand, we want to single out specific MG models, in the Horndeski class, that are compatible with data and assess whether these models are more likely than the standard picture. On the other hand we want to disentangle in our analyses the constraining power of data from that of the theory, highlighting which portion of the parameter space is excluded not because of tension with observations, but because no healthy physical model is allowed there.

The paper is organised as follows. In Section 2 we recall the main elements of the EFT formalism and we describe the parametrization we adopt. In Section 3 we present the results in the space of parameters in the space of observables. In Section 5 we draw our conclusions.

2 Theory and Methodology

The EFT of dark energy allows to describe a vaste range of dark energy models by using a limited number of time dependent couplings [4,5]. Here we focus on the large class of Horndeski theories. Upon use of the Friedmann equations, the relevant couplings can be reduced to a minimal set of independent functions. While there is now a consensus on the power and the advantages of this formalism, there is no universal agreement on the conventions for the coupling functions yet. Here we use those of [6], that maintain a more direct link with the underlying theories. We parametrize the time behaviour of the coupling functions with the following expansion:

$$\mu(x) = (1-x)\left[p_1 + p_1^{(1)}\left(x - \Omega_m^0\right)\right] H(x)\,, \tag{1}$$

$$\mu_3(x) = (1-x)\left[p_3 + p_3^{(1)}\left(x - \Omega_m^0\right)\right] H(x)\,, \tag{2}$$

$$\epsilon_4(x) = (1-x)\left[p_4 + p_4^{(1)}\left(x - \Omega_m^0\right)\right]\,, \tag{3}$$

where the p_i are order-one coefficients that we want to constrain with our analysis and x is the fractional matter density of the background at each time. We set to zero the function $\mu_2(t)$, which only affects the sound speed of the scalar fluctuations. Requiring no early dark energy imposes an additional constraint between the p_i parameters, such that $p_1^{(1)}$ is not a free parameter [6]. One of the main advantages of the EFT formalism is the possibility of treating cosmological perturbations independently of the expansion history. We fix the background to that of a spatially flat ΛCDM model in this analysis.

2.1 Viability conditions

The theory that we are describing contains one scalar and two tensor degrees of freedom. In this work we consider three main viability conditions:

$$\begin{aligned} \text{stable}: &\quad \text{absence of ghosts and gradient instabilities,} \\ \text{stable} \;\&\; c_s < 1: &\quad \text{the above } \textit{and} \text{ scalar propagation speed not superluminal ,} \\ \text{stable} \;\&\; c_s < 1 \;\&\; c_T < 1: &\quad \text{the above } \textit{and} \text{ tensor propagation speed not superluminal.} \end{aligned}$$

2.2 Method of analysis and data

The aim of the analysis is to simultaneously evaluate the constrains on the six standard cosmological parameters that define a flat universe with a ΛCDM background history plus the p_i coefficients that encode the modified gravity effects, as described in (1)-(3).

Instead of solving the full set of linear perturbation equations for the couplings, we encode the modifications of gravity in two functions of the time, $\mu_{\rm MG} = G_{\rm eff}/G_N$ and $\gamma_{\rm MG} = \Psi/\Phi$, following the approach implemented in the MGCAMB code [7] and feeding the code with the EFT expressions of $\mu_{\rm MG}$ and $\gamma_{\rm MG}$ that have been derived and discussed in [6]. This method has the remarkable advantage of allowing a simpler numerical implementation while keeping a clear mapping between the μ_{MG}-γ_{MG} functions and the underlying EFT theory.

We use in this analysis the most recent CMB data from the Planck experiment [8]. In particular we include in our dataset the temperature high-l power spectra (PlikTT likelihood), the temperature and polarization spectra at low-l and the lensing from the CMB trispectrum.

We consider two different extensions of the standard model. The *3D*-Model, that corresponds to a minimal extension with one free parameter for every non-minimal coupling. And the *5D*-Model that, by adding a term in the Taylor expansion (1)-(3) of the coupling functions, gives more freedom to the functional space.

3 Constraints on EFT operators

In Fig. 1 and 2 we present constraints on the minimal EFT extension of the standard model of cosmology (*3D model*). The most prominent feature visible in the one-dimensional posteriors of p_1, p_3 and p_4 in Fig 1 is that the theoretical requirement of subluminality (for both scalar and tensor modes) significantly narrows the posterior interval of the EFT parameters. The theoretical viability conditions are thus powerful instruments that complement and increase the discriminatory power of data. Specifically, the main effect of the subluminality prior on p_1 and p_4 parameters is a reduction of the distribution width around the null value, while the net effect on p_3 is instead to shift it towards lower values, corresponding to no modified gravity signals.

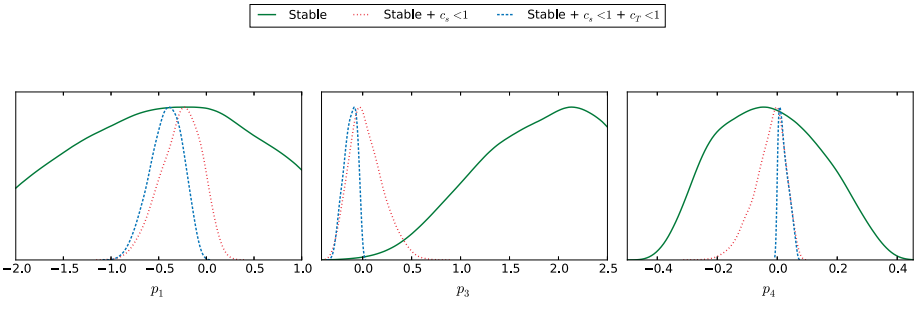


Figure 1 – Planck constraints on the *3D*-model: marginalised PDF for the EFT parameters p_1, p_3 and p_4.

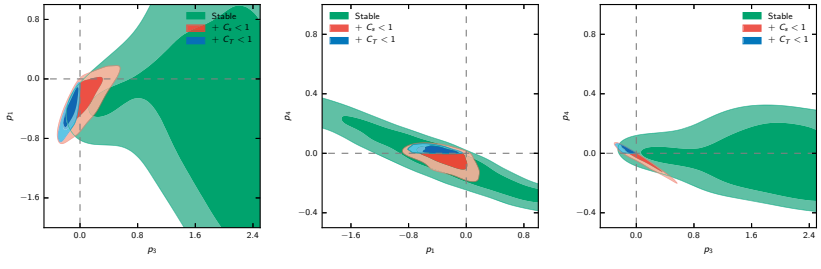


Figure 2 – Planck constraints on the *3D*-model: marginalised 2D PDF at 68% and 95% c.l. of EFT parameters.

While the one dimensional PDF peaks at around zero for both p_3 and p_4, a negative value of p_1 is preferred under any viability conditions. Although the χ^2 value associated to the best fitting EFT model is not lower enough, with respect to the ΛCDM model, to claim any evidence of modified gravity.

The bi-dimensional projected posterior PDF of the *model 3D* parameters is shown in Fig. 2 for the three combinations of parameters. This picture shows that asking for subluminal velocities considerably narrows the confidence regions. Interestingly, the viability priors not only impose tighter constraints as compared to those derived from cosmological measurements alone, but they also compensate both the statistical insensitivity and the parameter degeneracy.

The absence of any $3D$-model EFT parameters performing better than ΛCDM, together with the above remarks on the statistical power of the viability constraints, suggest to extend our parameter space to the $5D$-model, by including one order more in the Taylor expansion in Eqs. (2) and (3). The main results of this analysis are displayed in Fig. 3.

As expected, EFT parameters are somewhat less constrained when the *5D* model is considered, since we are dealing with more degrees of freedom. Nevertheless, the contours in Fig. 3

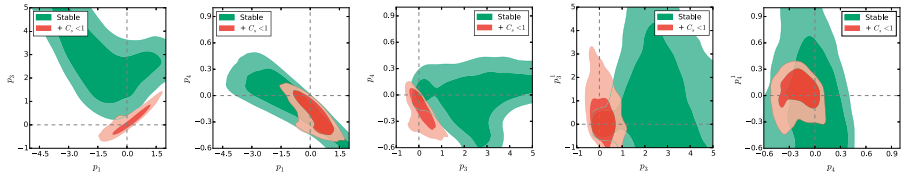


Figure 3 – Planck constraints on the *5D* model: 2D, marginalised, posterior PDF at 68% and 95% c.l. for the full set of EFT parameters contained in Eqs. (1) - (3).

show that the degeneracies between the 0th-order parameters are unaffected by the additional parameters. Also, no remarkable degeneracies are evident between the 0th-order parameters p_3, p_4 and the 1st-order parameters $p_3^{(1)}$, $p_4^{(1)}$. This implies that the *3D* model already catches the main features of the modifications of gravity. Additionally, the enlargement of the constraints completely washes out the indication of a preferred negative p_1. As a consequence, no signals of new physics emerge, also within this enlarged parameter space.

4 Constraints on cosmological observables

Constraining phenomenological quantities that are close to modified gravity observables is a complementary approach to the exploration in the space of the theories. We consider here the pair of functions $\mu_{\rm MG}(t)$ (the effective Newton constant) and $\gamma_{\rm MG}(t)$ (the gravitational slip). Any deviations from the unity of these functions, at any redshift, is notably considered a smoking gun for modified gravity. Interestingly, the Planck Collaboration recently highlighted a deviation from the standard value, at about 3 sigma, of both these functions at redshift $z = 0$ (see Fig. 14 of Ref. [3]) when combining CMB with low-redshift probes. Namely, values of $\mu_{\rm MG}(0)$ lower than 1 and values of $\gamma_{\rm MG}(0)$ higher than 1 seem to be preferred by this combination of probes.

Differently to the approach followed in [3], here, the expressions of $\mu_{\rm MG}$ and $\gamma_{\rm MG}$ are theoretically determined within the context of the EFT theory and they can be tracked back to underlying physical healthy theories.

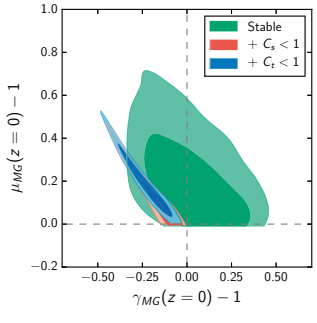


Figure 4 – 68 % and 95 % contour plots for the two parameters ($\mu_{\rm MG}$, $\gamma_{\rm MG}$) evaluated at the present time using the minimal parameterisation of the *3D* model.

The results of our analysis are presented in Fig. 4 and show the importance of not neglecting viability conditions in phenomenological constraints. First we note that there is no stable EFT model that lives in the portion of the space of observables characterised by a negative value of $\mu_{\rm MG} - 1$ today. More importantly, the best-fitting region arising by combining CMB and RSD and/or WL lays in the unstable region. That means that, even if confirmed by following exper-

iments, that signal do not corresponds to the effects of any viable Horndeski theory. Even more stringent conclusions emerge if subluminal propagation speed of scalar and tensor perturbations is required. In this case we find an additional tight constrain on the present value of $\gamma_{\rm MG}$ that is strictly lower than 1 in viable theories.

5 Conclusions

In this paper we extend the constraints on the EFT of DE formalism from Planck 2015 data. Particularly we show that theoretical viability conditions substantially reduces the allowed parameter space, tightly constraining the PDFs of the EFT parameters. Additionally we demonstrate that no healthy Horndeski theories can explain phenomenological results reported in [3].

Acknowledgments

We acknowledge the financial support of A*MIDEX project (no ANR-11-IDEX-0001-02).

References

1. P. A. R. Ade *et al.* [Planck Collaboration], "Planck 2015 results. XIII. Cosmological parameters," arXiv:1502.01589 [astro-ph.CO].
2. P. A. R. Ade *et al.* [Planck Collaboration], "Planck 2015 results. XXIV. Cosmology from Sunyaev-Zeldovich cluster counts," arXiv:1502.01597 [astro-ph.CO].
3. P. A. R. Ade *et al.* [Planck Collaboration], "Planck 2015 results. XIV. Dark energy and modified gravity," arXiv:1502.01590 [astro-ph.CO].
4. G. Gubitosi, F. Piazza and F. Vernizzi, "The Effective Field Theory of Dark Energy," JCAP **1302**, 032 (2013) [arXiv:1210.0201 [hep-th]].
5. J. K. Bloomfield, E. Flanagan, M. Park and S. Watson, "Dark energy or modified gravity? An effective field theory approach," JCAP **1308**, 010 (2013) [arXiv:1211.7054 [astro-ph.CO]].
6. L. Perenon, F. Piazza, C. Marinoni and L. Hui, "Phenomenology of dark energy: general features of large-scale perturbations," JCAP **1511**, no. 11, 029 (2015) [arXiv:1506.03047 [astro-ph.CO]].
7. A. Hojjati, L. Pogosian, G. Zhao, 'Testing gravity with CAMB and CosmoMC', JCAP **005**, 1108 (2011)
8. N. Aghanim *et al.* [Planck Collaboration], "Planck 2015 results. XI. CMB power spectra, likelihoods, and robustness of parameters," [arXiv:1507.02704 [astro-ph.CO]].









Cosmology of Massive Gravity and its Extensions

Kurt Hinterbichler

Department of Physics, Case Western Reserve University,
10900 Euclid Ave, Cleveland, OH 44106, USA

We review the status of the theory of dRGT massive gravity, and some of its extensions, as applied to cosmology and the cosmological constant problem.

1 Introduction

The cosmological constant problem [1,2] is a theoretical loose end in the description of the universe provided by the ΛCDM model of cosmology. One can categorize possible solutions on a spectrum ranging from conservative to radical. The multiverse/anthropic explanation sits on the conservative side, because in this case there is no new physics directly invoked to explain the acceleration; there is nothing to dark energy beyond a pure cosmological constant and its small value is explained anthropically via a selection effect within a dynamically populated multiverse of many possible values. The lack of any widely agreed upon compelling alternatives has driven many theorists to this conclusion. On the radical side, we have proposals which seek to change the rules of the game; perhaps effective field theory or quantum mechanics fundamentally fails at cosmological distances and something else is going on.

In between the two extremes, we have proposals which seek to address the problem by introducing new light degrees of freedom (they must be light so as to affect cosmology on large distances) without changing the standard rules of effective field theory. If we wish to maintain standard assumptions such as Lorentz invariance and locality,[a] then there is a list of representations (classified by Wigner and others) and we need only look at this list and decide what to add.

One representation in particular raises some questions – the massive spin-2 representation. General relativity describes the graviton as a massless spin-2, carrying two physical degrees of freedom. Is there any reason why the graviton could not live in the massive representation instead? What would physics look like if it did [b]?

There is a heuristic reason why we might think a small mass could help with the cosmic acceleration. The potential generated by a massless particle is the familiar Coulomb potential $\sim \frac{1}{r}$, but a massive particle instead generates a Yukawa potential $\sim \frac{1}{r}e^{-mr}$ which has an exponential

[a] These are assumptions which are well tested, but there is always the possibility that they may be violated cosmologically in the dark sector, and there are many interesting proposals along these directions, e.g. [3,4,5,6,7,8].

[b] The question of whether the graviton has a small mass falls into the class of natural "what if" questions which we believe are important to ask in their own right, regardless of whether they may help solve some outstanding problem or be tested observationally. If the whole massive gravity program fails for whatever theoretical or phenomenological reason, it is not a write-down, because we learn something about why the graviton must be massless. We learn more about what is by probing what could have been.

suppression kicking in at the length scale $\sim \frac{1}{m}$. If we imagine that this scale is very large, on the order of the Hubble scale today, $m \sim H$, then the force of a massive graviton would be weakened at these large scales and perhaps this could say something about the acceleration. Of course, this is a just a heuristic thought gleaned from the linear theory, and one should not try to take it too far. A proper treatment requires finding a fully non-linear theory and studying its cosmology.

2 Non-linear massive spin-2

A massive spin-2 has five degrees of freedom. The three degrees of freedom beyond the two of the massless graviton are the extra light modes we hope will be useful in explaining the current acceleration of the universe. The reason we may hope that this gives a better explanation than the cosmological constant is a symmetry reason: GR has a diffeomorphism symmetry which is broken in the massive theory. As the mass goes to zero, this symmetry is restored, so any quantum corrections to the mass (from e.g. heavy particles) should be proportional to the mass itself[c], and thus a small mass is technically natural.

It was long thought that a non-linear theory of a pure massive spin-2 could not be written down. This is primarily due to the Boulware-Deser ghost problem [11]: if one adds generic self-interaction terms to the linear [12] massive spin-2 theory, one finds that the non-linear theory propagates six physical degrees of freedom, as opposed to the desired 5 physical degrees of freedom. Around flat space, this extra degree of freedom is a non-issue: the theory is an effective field theory with a strong coupling scale $\Lambda_5 \sim (m^4 M_P)^{1/5}$, perturbatively the theory still has five degrees of freedom, and the ghost does not appear until one goes beyond this cutoff so one cannot say it is in the theory. The real problem is that one cannot say that any interesting non-linear solutions are in the theory [13,14,15]. If we attempt to find non-linear solutions (such as cosmological ones) and build an effective theory around them, the extra degree of freedom will generally appear as an additional scalar mode which has a wrong sign kinetic term and signals an instability in the background.

However, just because generic interactions have this issue, it does not mean that all interactions do, and in fact the renewed interest in massive gravity theories over the past few years is primarily due to the development of a theory with interactions that give a higher strong coupling scale and avoid this ghost issue. The theory was found by using modern effective field theory techniques to find interactions order by order [16], and then re-summing the result [17]. It is known as dRGT theory, after de Rham, Gabadadze and Tolley (see [18,19] for reviews). The action consists of the Einstein-Hilbert term plus a specific two parameter family of zero derivative potential terms,

$$S = \frac{M_P^2}{2} \int d^4x \sqrt{-g} \left[R[g] - \frac{m^2}{4} \sum_{n=0}^{3} \beta_n S_n \left(\sqrt{g^{-1}\eta} \right) \right] . \tag{1}$$

Here M_P is the usual Planck mass, m is the graviton mass, $\eta_{\mu\nu}$ is a fixed fiducial Minkowski metric upon which the theory is built, and $g_{\mu\nu}$ is the dynamical metric. S_n are the symmetric polynomials of the matrix square root $M^\mu_{\ \nu} \equiv \sqrt{g^{\mu\lambda}\eta_{\lambda\nu}}$, $S_n(M) = M^{[\mu_1}_{\ \ \mu_1} \cdots M^{\mu_n]}_{\ \ \mu_n}$. Of the 4 dimensionless coefficients $\beta_0, \cdots, \beta_3$, one combination should be tuned to allow a Minkowski solution and another combination is redundant with the graviton mass, leaving a two parameter family of interaction terms. The mass terms can be thought of as bi-metric generalizations of the cosmological constant, which can be given a geometric interpretation [20,21,22]. There are by now many proofs that the theory is ghost free [23,24,25,26].

[c] Diffeomorphism symmetry is a gauge symmetry, so the argument is more subtle than this, but the same conclusion bears out [9,10], for essentially the same reasons the mass of the W and Z bosons can be naturally small compared with the scale of electroweak symmetry breaking.

This theory is the unique way to add zero-derivative interaction terms to the Einstein-Hilbert action and maintain only 5 degrees of freedom (though there are other ways without using the Einstein-Hilbert term [27]). It is an effective field theory with a strong coupling scale $\Lambda_3 \sim (m^2 M_P)^{1/3}$, which is the highest possible strong coupling scale around Minkowski space for any theory of pure massive spin-2 build by adding zero-derivative interaction terms to Einstein-Hilbert [28,29]. Beyond this strong coupling scale, one finds unphysical effects such as superluminal propagation and breakdown of the Cauchy problem [30,31,32] in the classical theory. It is possible to dynamically reach these regions, so the main outstanding theoretical issue is UV completion: some new physics or strong coupling effects must kick in to complete the theory and determine what happens beyond this strong coupling scale.

3 Cosmological solutions of dRGT gravity

The general intuition is that massive gravity is a small deformation of GR, so the physics should be GR-like to the extent that the graviton mass is small. The number of degrees of freedom, however, is not continuous, and the way that physical continuity is achieved is through non-linearities which screen the extra degrees of freedom and cause them to decouple – the so-called Vainshtein mechanism [d] [35,36,37,38] (see [39] for a review). Around a source of mass M, there is a new distance scale $r_* \sim \left(\frac{M}{M_P}\right)^{1/3} \frac{1}{\Lambda_3}$, known as the Vainshtein radius, at which the non-linearities of the extra degrees of freedom start to become important (the non-linearities of GR do not become important until the much smaller Schwarzschild radius $r_s \sim \frac{M}{M_P^2}$). Inside the Vainshtein radius, the effects of the extra degrees of freedom are screened and physics looks like that of GR, whereas outside the Vainshtein radius the extra degrees of freedom are active and can give $\mathcal{O}(1)$ deviations from GR. Traditional tests of gravity, such as solar system tests, are all passed because these tests are performed well within the Vainshtein radius of the relevant gravitating body.

The intuition for cosmology is the following. Define an energy density associated with the graviton mass scale, $\rho_c \sim M_P^2 m^2$. Consider some sphere of matter of radius R and density ρ. The Vainshtein radius of this sphere of matter is $r_* \sim \left(\frac{\rho}{\rho_c}\right)^{1/3} R$. If $\rho \gg \rho_c$, then $r_* \gg R$ and the sphere of matter lies within its own Vainshtein radius and behaves as in GR. If $\rho \ll \rho_c$, then $r_* \ll R$ and the sphere of matter is larger than its own Vainshtein radius and experiences $\mathcal{O}(1)$ deviations from GR. Consider the very early universe, so that $H \gg m$ and $\rho \gg \rho_c$. Each Hubble patch of radius $1/H$ is well within its own Vainshtein radius and the universe behaves as in GR. In particular, all the physics of inflation, the CMB, etc. are unaffected. Now consider the far future universe, where $H \ll m$ and $\rho \ll \rho_c$. In this case each Hubble volume now lies outside its own Vainshtein radius so the behavior will be drastically different from GR. The crossover time occurs when $H \sim m$ and $\rho \sim \rho_c$. If we want the graviton to be explaining the current acceleration, the crossover should be happening about now.

When one tries to realize this quantitatively by solving the equations of motion of the action Eq.1 there are some immediate obstacles (see [40] for a review). The equations of motion for a standard flat FRW ansatz imply that the only solution for the scale factor $a(t)$ is a constant one: $\frac{d}{dt}a = 0$, so there are no flat FRW solutions other than Minkowski space (regardless of the presence of matter) [41]. Closed FRW solutions also do not exist, but open FRW solutions can be found, and they come in two branches: the normal branch and the self-accelerating branch. The normal branch is just Minkowski in a different slicing, but the self-accelerating branch is particularly interesting because the cosmology displays an acceleration with a scale $H \sim m$ set by the graviton mass, even in the absence of a bare cosmological constant [42,43,44,45,41,46,47]. However, upon studying perturbations, it is found that the scalar and vector modes around

[d] Non-linearities are essential for the operation of the Vainshtein mechanism; it does not work in the purely linear theory, which is why we have the van Dam-Veltman-Zakharov (vDVZ) discontinuity [33,34].

the self-accelerating solution have vanishing kinetic terms [48,49]. This does not mean that the solutions are inconsistent or ruled out, but rather they are infinitely strongly coupled, so standard perturbative techniques cannot be used.

There are other cosmological solutions that exhibit self-accelerating behavior with well-behaved perturbations, but which give up on the assumption of isotropy and have a preferred direction [50,51]. It is these solutions which are expected to be the relevant physical cosmological solutions. It seems that the massive theory prefers to be anisotropic, with the anisotropy becoming important only at late times, an interesting thing to consider given that observational constraints on anisotropies at the current Hubble scale may soon be tightened. At very late times, when $H \ll m$, we can imagine a universe composed of domains of size $\sim \frac{1}{m}$, each of which has its own randomly oriented preferred direction, but which taken together are isotropic on very large scales $\gg \frac{1}{m}$.

Studying the detailed phenomenology of these anisotropic solutions is difficult because almost all the standard analysis tools and codes used in cosmology assume homogeneity and isotropy from the outset. Because of this, little phenomenological work in this direction has been done so far, though progress can be made in certain limits [42,52].

4 Extensions of Massive Gravity

Most work on cosmology in massive theories has instead proceeded by attempting to keep the assumptions of homogeneity and isotropy and instead generalizing the theory so that it allows cosmological solutions. These approaches all involve adding more degrees of freedom, while retaining the essential feature of having a massive spin-2 degree of freedom.

One early attempt was to introduce a new scalar field ϕ and promote the mass term (and/or couplings) to be functions of the scalar, $m \to m(\phi)$, known as mass varying massive gravity [41,53]. In this case, flat cosmological solutions with stable perturbations can be found [54], though it is not quite surprising or convincing because there are now arbitrary free functions in the Lagrangian which can be chosen so that this is the case.

One can introduce a scalar in a way that does not also introduce free functions by demanding symmetry under a kind of scaling symmetry, resulting in a theory known as quasi-dilaton [55]. This theory has flat self-accelerating FRW solutions, but their perturbations are not completely stable and have other unusual features[54,56,57]. There is an extension of the quasi-dilaton obtained by adding derivative operators consistent with the scale symmetry [58]. This extension solves the issue with the unstable perturbations and appears to be the first example of a theory with a stable self-accelerating cosmological solution [59,60,61,62].

Another possibility is to couple galileon-like scalars to the theory in a way which respects the galileon shift symmetry [63] and preserves the absence of ghosts [64]. Geometrically, this is a natural thing to consider; the massive theory can be thought of as a sigma model from four-dimensional space time to some flat four-dimensional target space, and one gets the galileons by simply extending the dimensionality of the target space (coupling to gravity the brane constructions of [65,66,67,68,69]). The cosmological solutions and perturbations of this theory turn out to be very similar to those of pure dRGT theory; there are no flat FRW solutions and self-accelerating solutions have perturbations with vanishing kinetic terms [70,71]. An open question is whether stable non-isotropic solutions exist.

Massive gravity is formulated with a fixed reference metric, and this metric can be made arbitrary without re-introducing a ghost [72]. One can attempt to make this reference metric cosmological, but this runs into tensions between keeping perturbations stable and maintaining the Vainshtein mechanism [73]. A natural extension is to promote the background metric to a dynamical metric, adding a second Einstein-Hilbert term for it [74]. This preserves the ghost-freedom and strong coupling scale of the theory, resulting in an effective field theory describing a massless graviton and a massive graviton interacting with each other, for a total of seven

degrees of freedom. This is bi-metric gravity, and it is the extension which has received the most interest and analysis thus far (see [75,76,77] for reviews and further references).

The study of cosmological solutions and their phenomenology in bi-gravity has been an active area recently [e] [101,102,103,104,105,106,107,108,109,110,111,112,113,114,115,116,117,118,119,120,121]. Here we give only a brief summary of the current status. The cosmological solutions come in two branches. First there is the non-dynamical (or algebraic) branch, which is the cousin of the self-accelerating branch of the pure massive theory. On this branch, some of the perturbations have vanishing kinetic terms and so it is infinitely strongly coupled and not much can be done. Then there is the dynamical branch, which has several sub-branches. There is an "infinite" sub-branch where the ratio of scale factors of the two metrics becomes infinitely large at early times and decreases at later times, but in general the perturbations on this sub-branch are ghostly in both the scalar and tensor sectors. There is an "exotic" sub-branch which describes bouncing cosmologies and other unconventional solutions (about which perturbations seem to generically have pathologies). Then there is the "finite" sub-branch, which has received the most attention so far. In this sub-branch, there are self-accelerating solutions about which perturbations are healthy, with the exception of a scalar gradient instability which occurs at early times. By tuning (in a technically natural way [9]) the parameters of the theory, this instability can be pushed to unobservably early times, but then the cosmological signatures become indistinguishable from ΛCDM.

5 Conclusions

The trend seems to be that if a model does not have a limit that looks like GR, it gets ruled out, and if it does have a limit that looks like GR, it gets pushed into this limit and becomes observationally indistinguishable [f] from GR. Nevertheless, the fact that some of these models can explain acceleration without a cosmological constant is progress, even if it cannot at present be observationally distinguished from GR. It provides a different interpretation of the data and of the cosmological constant problem.

So does any of this solve the cosmological constant problem? Most would say that the answer, at present, is *no*, because it does not address the hard problem of why a large cosmological constant (from e.g. matter loops, phase transitions, bare CC, etc...) does not gravitate. For this more is needed. For instance, the idea of degravitation [122,123,124,125], that a condensate of massive gravitons can act as a high pass filter that effectively screens the effects of a cosmological constant. This seems to works at the linear level, but it has not been convincingly demonstrated in a complete and fully non-linear theory, and there are general arguments against it [126,127]. Though screening solutions can often be found (solutions in which the curvature is small despite a large bare cosmological constant), typical problems are that they do not possess a Vainshtein mechanism and thus run afoul of solar system tests [42], or are not robust in the presence of matter. There are, however, interesting proposals that make use of the essential structure of massive gravity [128,129], and there is the lingering possibility that a novel kind of gauge symmetry present in the so-called "partially massless" graviton may provide a symmetry that fixes the cosmological constant to the (already technically natural) small graviton mass, thereby providing a mechanism to keep the CC naturally small [130].

Given the more modest goal of providing an alternative mechanism to explain the cosmic acceleration, without a cosmological constant (that is, assuming some unknown mechanism sets the expected large cosmological constant to zero), then some of these theories offer a solution. This does not address the old cosmological constant problem of why the vacuum doesn't gravitate, but it reduces the problem to the form it took before the discovery of the cosmic acceleration.

[e] With two metrics, there is also the possibility for having non-trivial matter couplings, and there has been plenty of work exploring this possibility as well [78,79,80,81,82,83,84,85,86,87,88,89,90,91,92,93,94,95,96,97,98,99,100].

[f] By indistinguishable we mean indistinguishable given foreseeable technology. It is a different theory than GR, so it is of course in principle always distinguishable.

References

1. S. Weinberg, Rev. Mod. Phys. **61**, 1 (1989). doi:10.1103/RevModPhys.61.1
2. A. Padilla, arXiv:1502.05296 [hep-th].
3. S. L. Dubovsky, JHEP **0410**, 076 (2004) doi:10.1088/1126-6708/2004/10/076 [hep-th/0409124].
4. Z. Berezhiani, D. Comelli, F. Nesti and L. Pilo, Phys. Rev. Lett. **99**, 131101 (2007) doi:10.1103/PhysRevLett.99.131101 [hep-th/0703264 [HEP-TH]].
5. V. A. Rubakov and P. G. Tinyakov, Phys. Usp. **51**, 759 (2008) doi:10.1070/PU2008v051n08ABEH006600 [arXiv:0802.4379 [hep-th]].
6. D. Comelli, F. Nesti and L. Pilo, JHEP **1307**, 161 (2013) doi:10.1007/JHEP07(2013)161 [arXiv:1305.0236 [hep-th]].
7. M. Jaccard, M. Maggiore and E. Mitsou, Phys. Rev. D **88**, no. 4, 044033 (2013) doi:10.1103/PhysRevD.88.044033 [arXiv:1305.3034 [hep-th]].
8. A. De Felice and S. Mukohyama, Phys. Lett. B **752**, 302 (2016) doi:10.1016/j.physletb.2015.11.050 [arXiv:1506.01594 [hep-th]].
9. C. de Rham, G. Gabadadze, L. Heisenberg and D. Pirtskhalava, Phys. Rev. D **87**, no. 8, 085017 (2013) doi:10.1103/PhysRevD.87.085017 [arXiv:1212.4128].
10. C. de Rham, L. Heisenberg and R. H. Ribeiro, Phys. Rev. D **88**, 084058 (2013) doi:10.1103/PhysRevD.88.084058 [arXiv:1307.7169 [hep-th]].
11. D. G. Boulware and S. Deser, Phys. Rev. D **6**, 3368 (1972). doi:10.1103/PhysRevD.6.3368
12. M. Fierz and W. Pauli, Proc. Roy. Soc. Lond. A **173**, 211 (1939). doi:10.1098/rspa.1939.0140
13. N. Arkani-Hamed, H. Georgi and M. D. Schwartz, Annals Phys. **305**, 96 (2003) doi:10.1016/S0003-4916(03)00068-X [hep-th/0210184].
14. C. Deffayet and J. W. Rombouts, Phys. Rev. D **72**, 044003 (2005) doi:10.1103/PhysRevD.72.044003 [gr-qc/0505134].
15. P. Creminelli, A. Nicolis, M. Papucci and E. Trincherini, JHEP **0509**, 003 (2005) doi:10.1088/1126-6708/2005/09/003 [hep-th/0505147].
16. C. de Rham and G. Gabadadze, Phys. Rev. D **82**, 044020 (2010) doi:10.1103/PhysRevD.82.044020 [arXiv:1007.0443 [hep-th]].
17. C. de Rham, G. Gabadadze and A. J. Tolley, Phys. Rev. Lett. **106**, 231101 (2011) doi:10.1103/PhysRevLett.106.231101 [arXiv:1011.1232 [hep-th]].
18. K. Hinterbichler, Rev. Mod. Phys. **84**, 671 (2012) doi:10.1103/RevModPhys.84.671 [arXiv:1105.3735 [hep-th]].
19. C. de Rham, Living Rev. Rel. **17**, 7 (2014) doi:10.12942/lrr-2014-7 [arXiv:1401.4173 [hep-th]].
20. K. Hinterbichler and R. A. Rosen, JHEP **1207**, 047 (2012) doi:10.1007/JHEP07(2012)047 [arXiv:1203.5783 [hep-th]].
21. G. Gabadadze, K. Hinterbichler, D. Pirtskhalava and Y. Shang, Phys. Rev. D **88**, no. 8, 084003 (2013) doi:10.1103/PhysRevD.88.084003 [arXiv:1307.2245].
22. G. Goon, K. Hinterbichler, A. Joyce and M. Trodden, JHEP **1507**, 101 (2015) doi:10.1007/JHEP07(2015)101 [arXiv:1412.6098 [hep-th]].
23. S. F. Hassan and R. A. Rosen, Phys. Rev. Lett. **108**, 041101 (2012) doi:10.1103/PhysRevLett.108.041101 [arXiv:1106.3344 [hep-th]].
24. S. F. Hassan and R. A. Rosen, JHEP **1204**, 123 (2012) doi:10.1007/JHEP04(2012)123 [arXiv:1111.2070 [hep-th]].
25. M. Mirbabayi, Phys. Rev. D **86**, 084006 (2012) doi:10.1103/PhysRevD.86.084006 [arXiv:1112.1435 [hep-th]].
26. S. F. Hassan, A. Schmidt-May and M. von Strauss, Phys. Lett. B **715**, 335 (2012) doi:10.1016/j.physletb.2012.07.018 [arXiv:1203.5283 [hep-th]].
27. K. Hinterbichler, JHEP **1310**, 102 (2013) doi:10.1007/JHEP10(2013)102 [arXiv:1305.7227

[hep-th]].
28. M. D. Schwartz, Phys. Rev. D **68**, 024029 (2003) doi:10.1103/PhysRevD.68.024029 [hep-th/0303114].
29. C. Cheung and G. N. Remmen, JHEP **1604**, 002 (2016) doi:10.1007/JHEP04(2016)002 [arXiv:1601.04068 [hep-th]].
30. S. Deser and A. Waldron, Phys. Rev. Lett. **110**, no. 11, 111101 (2013) doi:10.1103/PhysRevLett.110.111101 [arXiv:1212.5835 [hep-th]].
31. R. Brito, A. Terrana, M. Johnson and V. Cardoso, Phys. Rev. D **90**, 124035 (2014) doi:10.1103/PhysRevD.90.124035 [arXiv:1409.0886 [hep-th]].
32. P. Motloch, W. Hu, A. Joyce and H. Motohashi, Phys. Rev. D **92**, no. 4, 044024 (2015) doi:10.1103/PhysRevD.92.044024 [arXiv:1505.03518 [hep-th]].
33. H. van Dam and M. J. G. Veltman, Nucl. Phys. B **22**, 397 (1970). doi:10.1016/0550-3213(70)90416-5
34. V. I. Zakharov, JETP Lett. **12**, 312 (1970) [Pisma Zh. Eksp. Teor. Fiz. **12**, 447 (1970)].
35. A. I. Vainshtein, Phys. Lett. B **39**, 393 (1972). doi:10.1016/0370-2693(72)90147-5
36. C. Deffayet, G. R. Dvali, G. Gabadadze and A. I. Vainshtein, Phys. Rev. D **65**, 044026 (2002) doi:10.1103/PhysRevD.65.044026 [hep-th/0106001].
37. E. Babichev, C. Deffayet and R. Ziour, Phys. Rev. Lett. **103**, 201102 (2009) doi:10.1103/PhysRevLett.103.201102 [arXiv:0907.4103 [gr-qc]].
38. E. Babichev, C. Deffayet and R. Ziour, Phys. Rev. D **82**, 104008 (2010) doi:10.1103/PhysRevD.82.104008 [arXiv:1007.4506 [gr-qc]].
39. E. Babichev and C. Deffayet, Class. Quant. Grav. **30**, 184001 (2013) doi:10.1088/0264-9381/30/18/184001 [arXiv:1304.7240 [gr-qc]].
40. A. De Felice, A. E. Gumrukcuoglu, C. Lin and S. Mukohyama, Class. Quant. Grav. **30**, 184004 (2013) doi:10.1088/0264-9381/30/18/184004 [arXiv:1304.0484 [hep-th]].
41. G. D'Amico, C. de Rham, S. Dubovsky, G. Gabadadze, D. Pirtskhalava and A. J. Tolley, Phys. Rev. D **84**, 124046 (2011) doi:10.1103/PhysRevD.84.124046 [arXiv:1108.5231 [hep-th]].
42. C. de Rham, G. Gabadadze, L. Heisenberg and D. Pirtskhalava, Phys. Rev. D **83**, 103516 (2011) doi:10.1103/PhysRevD.83.103516 [arXiv:1010.1780 [hep-th]].
43. K. Koyama, G. Niz and G. Tasinato, Phys. Rev. Lett. **107**, 131101 (2011) doi:10.1103/PhysRevLett.107.131101 [arXiv:1103.4708 [hep-th]].
44. T. M. Nieuwenhuizen, Phys. Rev. D **84**, 024038 (2011) doi:10.1103/PhysRevD.84.024038 [arXiv:1103.5912 [gr-qc]].
45. A. H. Chamseddine and M. S. Volkov, Phys. Lett. B **704**, 652 (2011) doi:10.1016/j.physletb.2011.09.085 [arXiv:1107.5504 [hep-th]].
46. A. E. Gumrukcuoglu, C. Lin and S. Mukohyama, JCAP **1111**, 030 (2011) doi:10.1088/1475-7516/2011/11/030 [arXiv:1109.3845 [hep-th]].
47. L. Berezhiani, G. Chkareuli, C. de Rham, G. Gabadadze and A. J. Tolley, Phys. Rev. D **85**, 044024 (2012) doi:10.1103/PhysRevD.85.044024 [arXiv:1111.3613 [hep-th]].
48. A. E. Gumrukcuoglu, C. Lin and S. Mukohyama, JCAP **1203**, 006 (2012) doi:10.1088/1475-7516/2012/03/006 [arXiv:1111.4107 [hep-th]].
49. A. De Felice, A. E. Gumrukcuoglu and S. Mukohyama, Phys. Rev. Lett. **109**, 171101 (2012) doi:10.1103/PhysRevLett.109.171101 [arXiv:1206.2080 [hep-th]].
50. A. E. Gumrukcuoglu, C. Lin and S. Mukohyama, Phys. Lett. B **717**, 295 (2012) doi:10.1016/j.physletb.2012.09.049 [arXiv:1206.2723 [hep-th]].
51. A. De Felice, A. E. Gumrukcuoglu, C. Lin and S. Mukohyama, JCAP **1305**, 035 (2013) doi:10.1088/1475-7516/2013/05/035 [arXiv:1303.4154 [hep-th]].
52. D. Spolyar, M. Sahln and J. Silk, Phys. Rev. Lett. **111**, no. 24, 241103 (2013) doi:10.1103/PhysRevLett.111.241103 [arXiv:1304.5239 [astro-ph.CO]].
53. Q. G. Huang, Y. S. Piao and S. Y. Zhou, Phys. Rev. D **86**, 124014 (2012)

doi:10.1103/PhysRevD.86.124014 [arXiv:1206.5678 [hep-th]].
54. A. E. Gumrukcuoglu, K. Hinterbichler, C. Lin, S. Mukohyama and M. Trodden, Phys. Rev. D **88**, no. 2, 024023 (2013) doi:10.1103/PhysRevD.88.024023 [arXiv:1304.0449 [hep-th]].
55. G. D'Amico, G. Gabadadze, L. Hui and D. Pirtskhalava, Phys. Rev. D **87**, 064037 (2013) doi:10.1103/PhysRevD.87.064037 [arXiv:1206.4253 [hep-th]].
56. G. D'Amico, G. Gabadadze, L. Hui and D. Pirtskhalava, Class. Quant. Grav. **30**, 184005 (2013) doi:10.1088/0264-9381/30/18/184005 [arXiv:1304.0723 [hep-th]].
57. S. Anselmi, D. Lpez Nacir and G. D. Starkman, Phys. Rev. D **92**, no. 8, 084033 (2015) doi:10.1103/PhysRevD.92.084033 [arXiv:1506.01000 [astro-ph.CO]].
58. A. De Felice and S. Mukohyama, Phys. Lett. B **728**, 622 (2014) doi:10.1016/j.physletb.2013.12.041 [arXiv:1306.5502 [hep-th]].
59. G. Gabadadze, R. Kimura and D. Pirtskhalava, Phys. Rev. D **90**, no. 2, 024029 (2014) doi:10.1103/PhysRevD.90.024029 [arXiv:1401.5403 [hep-th]].
60. T. Kahniashvili, A. Kar, G. Lavrelashvili, N. Agarwal, L. Heisenberg and A. Kosowsky, Phys. Rev. D **91**, no. 4, 041301 (2015) doi:10.1103/PhysRevD.91.041301 [arXiv:1412.4300 [astro-ph.CO]].
61. H. Motohashi and W. Hu, Phys. Rev. D **90**, no. 10, 104008 (2014) doi:10.1103/PhysRevD.90.104008 [arXiv:1408.4813 [hep-th]].
62. L. Heisenberg, JCAP **1504**, no. 04, 010 (2015) doi:10.1088/1475-7516/2015/04/010 [arXiv:1501.07796 [hep-th]].
63. G. Gabadadze, K. Hinterbichler, J. Khoury, D. Pirtskhalava and M. Trodden, Phys. Rev. D **86**, 124004 (2012) doi:10.1103/PhysRevD.86.124004 [arXiv:1208.5773 [hep-th]].
64. M. Andrews, G. Goon, K. Hinterbichler, J. Stokes and M. Trodden, Phys. Rev. Lett. **111**, no. 6, 061107 (2013) doi:10.1103/PhysRevLett.111.061107 [arXiv:1303.1177 [hep-th]].
65. C. de Rham and A. J. Tolley, JCAP **1005**, 015 (2010) doi:10.1088/1475-7516/2010/05/015 [arXiv:1003.5917 [hep-th]].
66. K. Hinterbichler, M. Trodden and D. Wesley, Phys. Rev. D **82**, 124018 (2010) doi:10.1103/PhysRevD.82.124018 [arXiv:1008.1305 [hep-th]].
67. G. Goon, K. Hinterbichler and M. Trodden, Phys. Rev. Lett. **106**, 231102 (2011) doi:10.1103/PhysRevLett.106.231102 [arXiv:1103.6029 [hep-th]].
68. G. Goon, K. Hinterbichler and M. Trodden, JCAP **1107**, 017 (2011) doi:10.1088/1475-7516/2011/07/017 [arXiv:1103.5745 [hep-th]].
69. C. Burrage, C. de Rham and L. Heisenberg, JCAP **1105**, 025 (2011) doi:10.1088/1475-7516/2011/05/025 [arXiv:1104.0155 [hep-th]].
70. M. Andrews, K. Hinterbichler, J. Stokes and M. Trodden, Class. Quant. Grav. **30**, 184006 (2013) doi:10.1088/0264-9381/30/18/184006 [arXiv:1306.5743 [hep-th]].
71. G. Goon, A. E. Gumrukcuoglu, K. Hinterbichler, S. Mukohyama and M. Trodden, JCAP **1408**, no. 08, 008 (2014) doi:10.1088/1475-7516/2014/08/008 [arXiv:1402.5424 [hep-th]].
72. S. F. Hassan, R. A. Rosen and A. Schmidt-May, JHEP **1202**, 026 (2012) doi:10.1007/JHEP02(2012)026 [arXiv:1109.3230 [hep-th]].
73. M. Fasiello and A. J. Tolley, JCAP **1211**, 035 (2012) doi:10.1088/1475-7516/2012/11/035 [arXiv:1206.3852 [hep-th]].
74. S. F. Hassan and R. A. Rosen, JHEP **1202**, 126 (2012) doi:10.1007/JHEP02(2012)126 [arXiv:1109.3515 [hep-th]].
75. A. Schmidt-May and M. von Strauss, J. Phys. A **49**, no. 18, 183001 (2016) doi:10.1088/1751-8113/49/18/183001 [arXiv:1512.00021 [hep-th]].
76. P. Bull *et al.*, Phys. Dark Univ. **12**, 56 (2016) doi:10.1016/j.dark.2016.02.001 [arXiv:1512.05356 [astro-ph.CO]].
77. A. R. Solomon, arXiv:1508.06859 [gr-qc].
78. S. F. Hassan, A. Schmidt-May and M. von Strauss, JHEP **1305**, 086 (2013) doi:10.1007/JHEP05(2013)086 [arXiv:1208.1515 [hep-th]].

79. Y. Akrami, T. S. Koivisto, D. F. Mota and M. Sandstad, JCAP **1310**, 046 (2013) doi:10.1088/1475-7516/2013/10/046 [arXiv:1306.0004 [hep-th]].
80. C. de Rham, L. Heisenberg and R. H. Ribeiro, Class. Quant. Grav. **32**, 035022 (2015) doi:10.1088/0264-9381/32/3/035022 [arXiv:1408.1678 [hep-th]].
81. J. Noller and S. Melville, JCAP **1501**, 003 (2015) doi:10.1088/1475-7516/2015/01/003 [arXiv:1408.5131 [hep-th]].
82. S. F. Hassan, M. Kocic and A. Schmidt-May, arXiv:1409.1909 [hep-th].
83. C. de Rham, L. Heisenberg and R. H. Ribeiro, Phys. Rev. D **90**, 124042 (2014) doi:10.1103/PhysRevD.90.124042 [arXiv:1409.3834 [hep-th]].
84. V. O. Soloviev, arXiv:1410.0048 [hep-th].
85. Y. Akrami, T. S. Koivisto and A. R. Solomon, Gen. Rel. Grav. **47**, 1838 (2015) doi:10.1007/s10714-014-1838-4 [arXiv:1404.0006 [gr-qc]].
86. A. R. Solomon, J. Enander, Y. Akrami, T. S. Koivisto, F. Knnig and E. Mrtsell, JCAP **1504**, no. 04, 027 (2015) doi:10.1088/1475-7516/2015/04/027 [arXiv:1409.8300 [astro-ph.CO]].
87. X. Gao and D. Yoshida, Phys. Rev. D **92**, no. 4, 044057 (2015) doi:10.1103/PhysRevD.92.044057 [arXiv:1412.8471 [hep-th]].
88. Y. Yamashita, A. De Felice and T. Tanaka, Int. J. Mod. Phys. D **23**, 1443003 (2014) doi:10.1142/S0218271814430032 [arXiv:1408.0487 [hep-th]].
89. A. Emir Gumrukcuoglu, L. Heisenberg and S. Mukohyama, JCAP **1502**, 022 (2015) doi:10.1088/1475-7516/2015/02/022 [arXiv:1409.7260 [hep-th]].
90. L. Heisenberg, Class. Quant. Grav. **32**, no. 10, 105011 (2015) doi:10.1088/0264-9381/32/10/105011 [arXiv:1410.4239 [hep-th]].
91. J. Enander, A. R. Solomon, Y. Akrami and E. Mortsell, JCAP **1501**, 006 (2015) doi:10.1088/1475-7516/2015/01/006 [arXiv:1409.2860 [astro-ph.CO]].
92. A. Schmidt-May, JCAP **1501**, 039 (2015) doi:10.1088/1475-7516/2015/01/039 [arXiv:1409.3146 [gr-qc]].
93. A. E. Gumrukcuoglu, L. Heisenberg, S. Mukohyama and N. Tanahashi, JCAP **1504**, no. 04, 008 (2015) doi:10.1088/1475-7516/2015/04/008 [arXiv:1501.02790 [hep-th]].
94. D. Comelli, M. Crisostomi, K. Koyama, L. Pilo and G. Tasinato, JCAP **1504**, 026 (2015) doi:10.1088/1475-7516/2015/04/026 [arXiv:1501.00864 [hep-th]].
95. K. Hinterbichler and R. A. Rosen, Phys. Rev. D **92**, no. 2, 024030 (2015) doi:10.1103/PhysRevD.92.024030 [arXiv:1503.06796 [hep-th]].
96. L. Heisenberg and A. Refregier, arXiv:1604.07306 [gr-qc].
97. S. Melville and J. Noller, JHEP **1601**, 094 (2016) doi:10.1007/JHEP01(2016)094 [arXiv:1511.01485 [hep-th]].
98. M. Lagos and J. Noller, JCAP **1601**, no. 01, 023 (2016) doi:10.1088/1475-7516/2016/01/023 [arXiv:1508.05864 [gr-qc]].
99. L. Heisenberg, Phys. Rev. D **92**, 023525 (2015) doi:10.1103/PhysRevD.92.023525 [arXiv:1505.02966 [hep-th]].
100. Q. G. Huang, R. H. Ribeiro, Y. H. Xing, K. C. Zhang and S. Y. Zhou, Phys. Lett. B **748**, 356 (2015) [Phys. Lett. B **748**, 356 (2015)] doi:10.1016/j.physletb.2015.07.003 [arXiv:1505.02616 [hep-th]].
101. M. von Strauss, A. Schmidt-May, J. Enander, E. Mortsell and S. F. Hassan, JCAP **1203**, 042 (2012) doi:10.1088/1475-7516/2012/03/042 [arXiv:1111.1655 [gr-qc]].
102. M. S. Volkov, JHEP **1201**, 035 (2012) doi:10.1007/JHEP01(2012)035 [arXiv:1110.6153 [hep-th]].
103. D. Comelli, M. Crisostomi, F. Nesti and L. Pilo, JHEP **1203**, 067 (2012) Erratum: [JHEP **1206**, 020 (2012)] doi:10.1007/JHEP06(2012)020, 10.1007/JHEP03(2012)067 [arXiv:1111.1983 [hep-th]].
104. M. S. Volkov, Phys. Rev. D **86**, 061502 (2012) doi:10.1103/PhysRevD.86.061502

[arXiv:1205.5713 [hep-th]].
105. D. Comelli, M. Crisostomi and L. Pilo, JHEP **1206**, 085 (2012) doi:10.1007/JHEP06(2012)085 [arXiv:1202.1986 [hep-th]].
106. M. Berg, I. Buchberger, J. Enander, E. Mortsell and S. Sjors, JCAP **1212**, 021 (2012) doi:10.1088/1475-7516/2012/12/021 [arXiv:1206.3496 [gr-qc]].
107. Y. Akrami, T. S. Koivisto and M. Sandstad, JHEP **1303**, 099 (2013) doi:10.1007/JHEP03(2013)099 [arXiv:1209.0457 [astro-ph.CO]].
108. M. S. Volkov, Class. Quant. Grav. **30**, 184009 (2013) doi:10.1088/0264-9381/30/18/184009 [arXiv:1304.0238 [hep-th]].
109. Y. Akrami, T. S. Koivisto and M. Sandstad, arXiv:1302.5268 [astro-ph.CO].
110. A. R. Solomon, Y. Akrami and T. S. Koivisto, JCAP **1410**, 066 (2014) doi:10.1088/1475-7516/2014/10/066 [arXiv:1404.4061 [astro-ph.CO]].
111. F. Koennig, Y. Akrami, L. Amendola, M. Motta and A. R. Solomon, Phys. Rev. D **90**, 124014 (2014) doi:10.1103/PhysRevD.90.124014 [arXiv:1407.4331 [astro-ph.CO]].
112. S. F. Hassan, A. Schmidt-May and M. von Strauss, Int. J. Mod. Phys. D **23**, no. 13, 1443002 (2014) doi:10.1142/S0218271814430020 [arXiv:1407.2772 [hep-th]].
113. A. De Felice, A. E. Gumrukcuoglu, S. Mukohyama, N. Tanahashi and T. Tanaka, JCAP **1406**, 037 (2014) doi:10.1088/1475-7516/2014/06/037 [arXiv:1404.0008 [hep-th]].
114. G. Cusin, R. Durrer, P. Guarato and M. Motta, JCAP **1505**, no. 05, 030 (2015) doi:10.1088/1475-7516/2015/05/030 [arXiv:1412.5979 [astro-ph.CO]].
115. J. Enander, Y. Akrami, E. Mrtsell, M. Renneby and A. R. Solomon, Phys. Rev. D **91**, 084046 (2015) doi:10.1103/PhysRevD.91.084046 [arXiv:1501.02140 [astro-ph.CO]].
116. G. Cusin, R. Durrer, P. Guarato and M. Motta, JCAP **1604**, no. 04, 051 (2016) doi:10.1088/1475-7516/2016/04/051 [arXiv:1512.02131 [astro-ph.CO]].
117. H. Nersisyan, Y. Akrami and L. Amendola, Phys. Rev. D **92**, no. 10, 104034 (2015) doi:10.1103/PhysRevD.92.104034 [arXiv:1502.03988 [gr-qc]].
118. F. Knnig, Phys. Rev. D **91**, 104019 (2015) doi:10.1103/PhysRevD.91.104019 [arXiv:1503.07436 [astro-ph.CO]].
119. L. Amendola, F. Knnig, M. Martinelli, V. Pettorino and M. Zumalacarregui, JCAP **1505**, 052 (2015) doi:10.1088/1475-7516/2015/05/052 [arXiv:1503.02490 [astro-ph.CO]].
120. K. Aoki, K. i. Maeda and R. Namba, Phys. Rev. D **92**, no. 4, 044054 (2015) doi:10.1103/PhysRevD.92.044054 [arXiv:1506.04543 [hep-th]].
121. Y. Akrami, S. F. Hassan, F. Knnig, A. Schmidt-May and A. R. Solomon, Phys. Lett. B **748**, 37 (2015) doi:10.1016/j.physletb.2015.06.062 [arXiv:1503.07521 [gr-qc]].
122. G. Dvali, G. Gabadadze and M. Shifman, hep-th/0208096.
123. G. Dvali, G. Gabadadze and M. Shifman, Phys. Rev. D **67**, 044020 (2003) doi:10.1103/PhysRevD.67.044020 [hep-th/0202174].
124. N. Arkani-Hamed, S. Dimopoulos, G. Dvali and G. Gabadadze, hep-th/0209227.
125. G. Dvali, S. Hofmann and J. Khoury, Phys. Rev. D **76**, 084006 (2007) doi:10.1103/PhysRevD.76.084006 [hep-th/0703027 [HEP-TH]].
126. J. Polchinski, hep-th/0603249.
127. R. Bousso, Gen. Rel. Grav. **40**, 607 (2008) doi:10.1007/s10714-007-0557-5 [arXiv:0708.4231 [hep-th]].
128. G. Gabadadze, Phys. Lett. B **739**, 263 (2014) doi:10.1016/j.physletb.2014.10.064 [arXiv:1406.6701 [hep-th]].
129. G. Gabadadze and S. Yu, arXiv:1510.07943 [hep-th].
130. C. de Rham, K. Hinterbichler, R. A. Rosen and A. J. Tolley, Phys. Rev. D **88**, no. 2, 024003 (2013) doi:10.1103/PhysRevD.88.024003 [arXiv:1302.0025 [hep-th]].

Living with ghosts in Hořava–Lifshitz gravity

Sabir Ramazanov
Gran Sasso Science Institute (INFN), Viale Francesco Crispi 7, I-67100 L'Aquila, Italy

It is believed that the projectable version of the Hořava–Lifshitz gravity becomes strongly coupled at unacceptably low scale, and, therefore, is phenomenologically non-viable. We argue that the scale of the strong coupling can be as high as ~ 10 TeV in the branch of the model with ghost instabilities at low energies.

1 Introduction and Summary

Power counting renormalizability of gravity can be achieved by the price of sacrificing Lorentz symmetry at high energies [1]. So, in the Hořava-Lifshitz (HL) model, one assigns different scaling dimensions to the time, t, and spatial coordinates, $\mathbf{x}$, in the ultraviolet (UV),

$$\mathbf{x} \to b^{-1}\mathbf{x}\,, \qquad t \to b^{-z}t\,, \tag{1}$$

where z is the so-called critical exponent. The scaling (1) fixes the high energy dispersion relation for the graviton to be of the form $\omega^2 = \frac{\mathbf{p}^{2z}}{M_{UV}^{2(z-1)}}$, where ω denotes the energy and $\mathbf{p}$ the momentum; M_{UV} is the scale of the UV physics in the HL model. Consequently, the behaviour of the propagators changes in the UV, potentially eliminating the divergence of the loop integrals. Power-counting renormalizable gravity corresponds to the value $z = 3$ in 4 dimensions.

Even pushing M_{UV} to very high values, Lorentz breaking effects may strongly affect low energy physics. The reason is that abandoning Lorentz symmetry, one typically excites extra degrees of freedom, which then propagate at the arbitrary scale. This may lead to the problem with recovering General Relativity (GR) in the infrared limit (IR). In particular, the lapse is a dynamical field, which exhibits the gradient instability [2]. Properly tuning the relevant model parameter, one can tame the instability,—unfortunately by the price of having an unacceptably low strong coupling scale.

There is, however, a version of the model (not the unique one, though), where this problem is absent—the so called projectable HL gravity. There one entertains the possibility that the lapse can be set to unity, i.e., $N = 1$. The reason why this scenario is important is twofold. First, it is the only version of the HL gravity which has been renormalized so far [4]. Second, it has quite a rich phenomenology. In particular, this model provides a candidate for the Dark Matter [5].

Still, the model of interest appears to be problematic in the infrared limit (IR). Compared to GR, there is an extra degree of freedom in the scalar sector of the model, i.e., the potential Ψ [1,?]. This degree of freedom is characterized by the constant sound speed squared c_s^2. Depending on the sign of the quantity c_s^2, the field Ψ is either a tachyon ($c_s^2 < 0$) or a ghost ($c_s^2 > 0$). The former branch of the projectable HL gravity is ruled out on the phenomenological grounds.

At the same time, the latter is viable in a wide range of the sound speed values [6], though the viability is achieved by the price of the perturbative renormalizability of the model.

2 Low energy action

The action for the IR limit of the projectable HL gravity is given by [1],

$$S_{IR} = S_{GR} + \int d^3x dt \sqrt{\gamma} N \left[\frac{\Sigma}{2} \left(\frac{1}{N^2} - 1 \right) - \frac{\lambda - 1}{16\pi G} K^2 \right] . \tag{2}$$

Here S_{GR} denotes the GR action, Σ is the Lagrange multiplier, enforcing the projectability condition $N = 1$, and λ is the dimensionless parameter. This we assume to be close to zero, i.e., $|\lambda - 1| \ll 1$. Otherwise, one would immediately compromise the consistency with GR tests at large distances.

Note that the model (2) can be interpreted as GR supplemented by the ' (imperfect) fluid'. The field Σ plays the role of the energy density of the 'fluid', while its sound speed squared is given by [1],

$$c_s^2 = \frac{1 - \lambda}{3\lambda - 1} .$$

Some properties of this 'fluid' have been discussed in Ref. [7] in the context of the mimetic matter scenario. In particular, it could be a promising candidate for the Dark Matter.

In the presence of the 'fluid', the potential Ψ becomes a dynamical degree of freedom. At the linear level, its properties can be deduced from the following action [1,3],

$$\delta_2 S_{IR} = \frac{1}{8\pi G} \int d^4x \left(-\frac{1}{c_s^2} \dot{\Psi}^2 - \Psi \Delta \Psi \right) . \tag{3}$$

We see that for $c_s^2 < 0$/ $c_s^2 > 0$ the field Ψ suffers from gradient/ghost instabilities.

Another issue with the IR limit of the projectable HL gravity is a finite scale of the strong coupling, which crucially relies on the sound speed c_s [3],

$$\Lambda_p \sim |c_s|^{3/2} M_{Pl} . \tag{4}$$

At higher scales, the corrections to the effective action, cubic in the field Ψ, become of the same order as the quadratic ones, and one loses the control upon the perturbative expansion.

The presence of the cutoff (4) poses a severe problem for the branch of the model with gradient instabilities in the IR. Naively, one could tame these instabilities by tuning the sound speed to be extremely small. However, this would result into an unacceptably small scale of the strong coupling, i.e., $\Lambda_p \ll 10^{-3}$ eV—in conflict with the sub-mm tests of the Newton's law. The situation seems to be more plausible in the branch with the ghost instabilities, as we will see shorly.

3 Vacuum decay

Lorentz-invariant models containing ghosts are non-viable, as they lead to an instantaneous destabilization of the vacuum. The situation is different in the Lorentz-violating theories, given that there is a finite cutoff Λ_p on the *spatial* momenta [8]. This is the case of the projectable HL gravity, where the strong coupling is understood as the cutoff on the ghosts momenta. Note that this way of stabilizing the vacuum immediately compromises the perturbative renormalizability of gravity—the original goal of the HL model. Following Ref. [6], we ignore this problem and focus on the phenomenological viability of the model.

We will be primarily interested in the process with two photons in the final state. This is argued to be the most relevant one in Ref. [8].

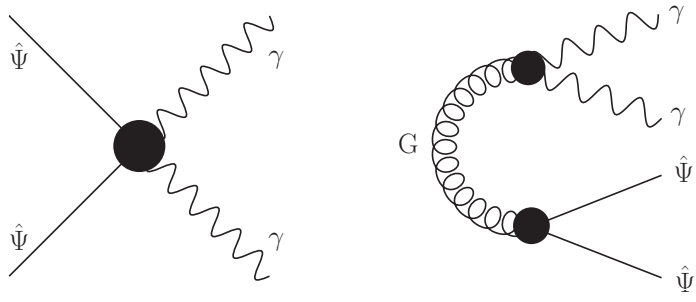


Figure 1 – Two diagrams of the vacuum decay into a pair of photons (the wiggly lines labelled by 'γ') and a pair of ghosts (the straight lines labelled by '$\hat{\Psi}$'). Despite the presence of the direct coupling of ghosts to the matter (the diagram on the left), the main contribution to the vacuum decay rate comes from the diagram on the right involving an exchange by the graviton (the springy line labelled by 'G').

It is described by the diagrams pictured in Fig. 1.

The diagram on the right, i.e., the one involving an exchange by the graviton, gives the main contribution to the decay rate of the vacuum estimated by [6],

$$\Gamma \sim c_s^{17} M_{Pl}^4 \, .$$

The concentration of the photons produced by this mechanism during the life time of the Universe t_0 is given by $n \sim \Gamma \cdot t_0$. The latter should not exceed the measured flux F in the range of energies corresponding to the X-rays and gamma-ray bursts [9],

$$F \sim 10 \cdot \frac{\text{keV}}{\text{s} \cdot \text{cm}^2 \cdot \text{sr} \cdot E_{ph}} \, .$$

where E_{ph} is the energy of the photon. We obtain [6],

$$c_s^2 \lesssim 10^{-20} \qquad \Lambda_p \lesssim 10 \text{ TeV} \, . \tag{5}$$

We see that in the ghost unstable branch of the projectable HL gravity, the scale of the strong scaling is allowed to be as large as $\sim$ TeV, in a comfortable agreement with GR tests.

References

1. P. Hořava, Phys. Rev. D **79** (2009) 084008.
2. D. Blas, O. Pujolas and S. Sibiryakov, JHEP **0910** (2009) 029.
3. D. Blas, O. Pujolas and S. Sibiryakov, JHEP **1104** (2011) 018;
   K. Koyama and F. Arroja, JHEP **1003** (2010) 061.
4. A. O. Barvinsky, D. Blas, M. Herrero-Valea, S. M. Sibiryakov and C. F. Steinwachs, Phys. Rev. D **93** (2016) no.6, 064022.
5. S. Mukohyama, Phys. Rev. D **80** (2009) 064005.
6. S. Ramazanov, F. Arroja, M. Celoria, S. Matarrese, L. Pilo; arXiv:1601.05405 [hep-th].
7. A. H. Chamseddine and V. Mukhanov, JHEP **1311** (2013) 135;
   A. H. Chamseddine, V. Mukhanov and A. Vikman, JCAP **1406** (2014) 017.
   F. Capela and S. Ramazanov, JCAP **1504** (2015) 051;
   L. Mirzagholi and A. Vikman, JCAP **1506** (2015) 028;
   S. Ramazanov, JCAP **12** (2015) 007.
8. J. M. Cline, S. Jeon and G. D. Moore, Phys. Rev. D **70** (2004) 043543.
9. P. Sreekumar *et al.* [EGRET Collaboration], Astrophys. J. **494** (1998) 523.


RENCONTRES DE VIGNORY
50
SPADEL
Converse


SPADEL


SPADEL


SPADEL

Cosmological constraints on Lorentz Invariance violation in gravity and dark matter

Mikhail M. Ivanov
FSB/IPHYS/LPPC, École Polytechnique Fédérale de Lausanne, Lausanne, Switzerland
Faculty of Physics, Moscow State University, Moscow, Russia
Institute for Nuclear Research of the Russian Academy of Sciences, Moscow, Russia

This brief contribution is devoted to phenomenological consequences of deviations from Lorentz invariance in gravity and dark matter. We will discuss main effects on cosmological observables and current constraints derived from astrophysical and cosmological data.

1 Introduction

Lorentz invariance (LI) has been playing a key role in our understanding of gravity over many decades. LI is a cornerstone of General Relativity (GR), the gravity theory whose predictions were verified at various scales. Besides, deviations from LI were tightly constrained in the sector of Standard Model (SM) particles[1]. Yet there are reasons to place LI under scrutiny. First, the constraints on Lorentz Invariance violation (LV) are much weaker or even do not exist for other sectors, e.g. the Dark sector. Second, theories without Lorentz invariance can have much better quantum behaviour than GR (e.g. Hořava gravity [2,3]). Furthermore, abandoning LI leads to curios theoretical models which may address the mysteries of dark matter, dark energy, and inflation. These reasons naturally pose the question: to what extent observational data support the belief that LI is a fundamental symmetry of Nature valid in all sectors? In this short note we will outline how this symmetry can be tested with cosmology.

2 Gravity theory without Lorentz invariance

The common way to parametrize generic effects of LV in gravity is to introduce a unit time-like vector field u_μ ("aether") that breaks local LI of GR down to the subgroup of rotations. This program yields the Einstein-aether theory[4],

$$S_{[EH]} + S_{[u]} = -\frac{1}{16\pi G_0}\int d^4x\sqrt{-g}\Big[R + K^{\mu\nu}{}_{\sigma\rho}\nabla_\mu u^\sigma \nabla_\nu u^\rho + l(u_\mu u^\mu - 1)\Big]\,, \tag{1}$$

$$K^{\mu\nu}{}_{\sigma\rho} = c_1 g^{\mu\nu}g_{\sigma\rho} + c_2\delta^\mu_\sigma\delta^\nu_\rho + c_3\delta^\mu_\rho\delta^\nu_\sigma + c_4 u^\mu u^\nu g_{\sigma\rho}\,. \tag{2}$$

The dimensionless parameters c_i characterize the deviation from GR and will be referred to as LV parameters. The scale G_0 controls the gravitational interaction, and is related to the Newton's gravitational constant through the LV parameters. Requiring that Minkowski space be a background with stable perturbations implies certain inequalities for the LV parameters[5]. Another set of constraints comes from the absence of gravitational Cherenkov radiation[6]. A variant of Einstein-aether gravity can be obtained by restricting the aether to be hypersurface-orthogonal, i.e.,

$$u_\mu \equiv \partial_\mu\varphi/\sqrt{\partial^\nu\varphi\partial_\nu\varphi}\,. \tag{3}$$

In this case the action (1) corresponds to the so-called khronometric model [7], the low-energy limit of Hořava gravity [3]. The restriction (3) implies that c_i are not independent, and the number of free LV parameters can be reduced to just three,

$$\lambda \equiv c_2\,, \quad \beta = c_3 + c_1\,, \quad \alpha = c_1 + c_4\,. \tag{4}$$

In fact, Einstein-aether gravity and khronometric gravity have completely similar tensor and scalar sectors which are characterised by these three parameters. The difference between the two theories appears only at the level of vector perturbations, whose impact, however, is negligible in cosmology for most of the parameter space [8]. Thus, for our purposes the Einstein-aether and khronometric gravity are almost identical and will be discussed in parallel in what follows.

The rest of fields in the Universe may also couple to u_μ through all possible covariant operators. For the SM sector, one has strong constraints that make this coupling negligible for any astrophysical observable [1]. Regarding dark matter (DM), the effect of a vector u^μ on a pressureless perfect fluid can be summarized in the following *macroscopic* action[9]

$$S_{[DM-u]} = m \int d^4x\sqrt{-g}\, n\, F(v_\mu u^\mu)\,, \tag{5}$$

where m is the mass of DM particles, n is their number density, and v_μ is their four-velocity. The function $F(v_\mu u^\mu)$ parameterizes the interaction between the DM fluid and u^μ. One can show that all the effects of LV in DM are encapsulated by a single parameter Y. It is instructive to write down the energy-momentum tensor generated by the action (5),

$$T^{[DM-u]}_{\mu\nu} = \rho_{[DM]} v_\mu v_\nu - Y \rho_{[DM]} (u^\lambda v_\lambda) v_\mu v_\nu + Y \rho_{[DM]} (u^\lambda v_\lambda) u_\mu u_\nu\,. \tag{6}$$

One can also consider the coupling of the aether to the dark energy[10] or inflaton[8,11] sectors. These interesting scenarios, however, are beyond the scope of this note. In what follows, we assume that the recent accelerated expansion of the universe is driven by the usual cosmological constant.

3 Astrophysical bounds

Even though the aether does not couple directly to SM, it alters the gravitational interactions in the Solar system. These effects are summarized in two PPN parameters α_1^{PPN} and α_2^{PPN} depending on α, β and λ[5]. These parameters are bounded as $|\alpha_2^{PPN}| < 10^{-7}$ and $|\alpha_1^{PPN}| < 10^{-4}$ [12], which impose two conditions of the same order of magnitude on the LV parameters. These bounds are very strong and, if imposed, exclude any observable consequences in cosmology. However, these bounds can be avoided for a special choice of parameters, which is different in khronometric and Einatein-aether gravity[a],

$$\alpha = 2\beta\,, \qquad \textit{khronometric}\,, \tag{7}$$

$$\alpha = -\beta - 3\lambda\,, \quad \textit{Einstein-aether}\,, \tag{8}$$

since then $\alpha_1^{PPN} = \alpha_2^{PPN} = 0$.

In either case, the Solar system tests do not completely constrain (1). LV gravity modifies the dynamics of relativistic binaries by changing the orbits (strong PPN parameters) and the properties of gravitational radiation. Using data from binary pulsar systems one can constrain the LV parameters at the level[13]

$$|\alpha, \beta, \lambda| < 0.01\,. \tag{9}$$

The parameter β controlling the propagation of gravity waves has recently been constrained from the direct observation of the GW150914 event[14],

$$\beta < 0.6\,. \tag{10}$$

[a] This difference arises due to vector polarisations, which contribute to the PPN parameters.

4 Effects on cosmology and observational bounds

It is customary to assume that the preferred frame aligns at late times with the cosmic microwave background (CMB) frame. This is a suitable assumption because this situation is dynamically stable in case of misalignment between the two frames [15]. At the homogeneous and isotropic level, the only effect of LV on cosmology is a difference between the gravitational constants appearing in Friedman and Poisson equations,

$$\Upsilon \equiv G_{Poisson}/G_{Friedman} - 1 = (\alpha + \beta + 3\lambda)/2 + O(\alpha^2)\,. \tag{11}$$

This is true even if LV in DM (5) is considered. Phenomenological consequences are richer once one considers cosmological perturbations[16,17]. One can identify the following effects that modify the power spectra of CMB temperature fluctuations and *linear* perturbations of matter,

1. **Enhanced gravity.** Thus effect is caused by the difference between $G_{Friedman}$ and $G_{Poisson}$ and it modifies the gravitational interaction for *all* species entering the Poisson equation. In particular, it leads to the enhanced growth rate of matter perturbations with respect to ΛCDM,

$$\delta_{[DM]} \sim \delta_{[B]} \sim a(\tau)^{1+\frac{3}{5}\Upsilon}\,, \tag{12}$$

where $a(\tau)$ is the scale factor. For CMB, this effect boosts the Integrated Sachs-Wolfe contribution (ISW), and changes the amplitude and the phase of acoustic oscillations. This induces the enhancement of the CMB power spectrum at large scales and modifies the pattern of acoustic peaks. The accelerated growth of perturbations (12) also enhances the amplitude of the matter power spectrum (MPS) and changes its slope. The parameter Υ accidentally vanishes in Einstein-aether gravity once the PPN bound (8) is imposed. Thus, the effect of enhanced gravity is viable only in the khronometric theory.

2. **Gravitational slip.** Another generic effect of LV in gravity is the appearance of an extra contribution to the anisotropic stress, which produces the difference between two gravitational potentials in the Newton gauge. This increases the viscosity of cosmic fluid and damps out perturbations of all species. The effect on CMB and MPS is an overall suppression, which, however, can be compensated by rescaling the amplitude of initial perturbations. This degeneracy implies that gravitational sleep should be less constrained from the data.

3. **Scale-dependent enhancement of dark matter clustering.** This effect is related to LV in dark matter and arises due to the violation of the equivalence principle in this sector. Remarkably, there appears an analogue of the chameleon mechanism in this case. The modes shorter than the characteristic "screening" scale $k_Y \sim H_0\sqrt{Y/a(\tau)\alpha}$ (H_0 is the Hubble rate today) experience the accelerated growth of density fluctuations,

$$\delta_{[DM]} \sim a(\tau)^{1+\kappa}\,, \quad \kappa = \frac{3}{5}\frac{\Omega_{dm}}{\Omega_{dm}+\Omega_b}Y + O(Y^2)\,, \tag{13}$$

while for the modes larger than k_Y the effect of LV in DM is screened and they evolve as in ΛCDM. This results in boosted ISW in CMB, and the scale-dependent enhancement of the matter power spectrum. We emphasize that, even if the effects of $Y \neq 0$ can be large, they may be completely screened at linear scales.

The discussed above effects were constrained using a combination of LSS observations and CMB data [16]. The constraints on the LV parameters in gravity and dark matter appeared to be very similar for Einstein-aether and khronometric gravity, and are given by (at 95% CL),

$$\alpha \;< 1.1\times 10^{-3}\,, \quad (\beta+\lambda)/\alpha < 55\,, \quad Y < 0.029\,, \qquad \textit{khronometric}\,, \tag{14}$$

$$\alpha \;< 5.0\times 10^{-3}\,, \quad (\beta+\lambda)/\alpha < 240\,, \quad Y < 0.028\,, \qquad \textit{Einstein-aether}\,. \tag{15}$$

If one assumes LI in the sector of DM ($Y \equiv 0$), then the constraints are quite different for Einstein-aether and khronometric gravity[16,17,18]. For the khronometric theory one obtains,

essentially, the same constraints on LV parameters in gravity as above. In the Einstein-aether model the effect of enhanced gravity disappears and we are left only with gravitational slip which is partially degenerate with the amplitude of the primordial power spectrum. This makes the bounds on Einstein-aether gravity degrade by one order of magnitude with respect to khronometric gravity,

$$\alpha \ < 1.8 \times 10^{-3}\,, \quad (\beta+\lambda)/\alpha < 91\,, \qquad \textit{khronometric}\,, \tag{16}$$

$$\alpha \ < 1.0 \times 10^{-2}\,, \quad (\beta+\lambda)/\alpha < 430\,, \qquad \textit{Einstein-aether}\,. \tag{17}$$

We point out that so far all cosmological constraints were derived using the CMB and linear MPS data (in fact, the bounds presented above are saturated already with the CMB data). We expect to obtain much better bounds once the non-linear dynamics at short scales (less than 10 Mpc) is taken into account, e.g. along the lines of [19].

LV in DM can also be constrained from observations of virialized objects, such as DM halos[9]. In fact, in addition to the violation of the equivalence principle, LV in DM generates velocity-dependent interactions, which are negligible in cosmology but might affect the dynamics of galaxies and galaxy clusters. These interactions can be relevant only for fast ($v_h^2 > \alpha/Y$) and small enough DM halos $R_h < \sqrt{Y\,\rho_{halo} G_0/\alpha}$ (ρ_{halo} is the halo density). For halos with larger radii all the effects of LV are eliminated by the screening mechanism.

To sum up, theories without Lorentz invariance provide us with an interesting framework to test modified gravity models and better understand the role of the Lorentz symmetry. These theories yield peculiar phenomenological effects, which can be examined with cosmological data. The cosmological constraints obtained so far bound LV in gravity at the sub-percent level, and are competitive with those derived from astrophysical test. The bounds on LV in DM were put at the percent level. More studies are required in order to understand the non-linear effects that will allow to test Lorentz invariance to a new level of precision with upcoming surveys.

Acknowledgments

This work was supported by the Swiss National Science Foundation and the RFBR grant 14-02-00894.

References

1. S. Liberati, *Class. Quant. Grav.* **30**, 133001 (2013), arXiv:1304.5795 [gr-qc].
2. A. O. Barvinsky, *et al*, *Phys. Rev.* D **93**, 064022 (2016), arXiv:1512.02250 [hep-th].
3. P. Hořava, *Phys. Rev.* D **79**, 084008 (2009), arXiv:0901.3775 [hep-th].
4. T. Jacobson and D. Mattingly, *Phys. Rev.* D **104**, 024028 (2001), gr-qc/0007031.
5. D. Blas, E. Lim, *Int. J. Mod. Phys.* D **23**, 1443009 (2015) arXiv:1412.4828 [gr-qc].
6. G. D. Moore, A. E. Nelson, *JHEP* **0109**, 023 (2001) hep-ph/0106220.
7. D. Blas, *et al. Phys. Rev. Lett.* **104**, 181302 (2010), arXiv:0909.3525 [hep-th].
8. C. Armendariz-Picon, *et al.* JCAP **1007** 010 (2010) arXiv:1003.1283 [astro-ph.CO].
9. D. Blas, *et al. JCAP* **1210** 057 (2012), arXiv:1209.0464 [astro-ph.CO].
10. D. Blas and S. Sibiryakov, *JCAP* **1107** 026 (2011), arXiv:1104.3579 [hep-th].
11. M. M. Ivanov and S. Sibiryakov, *JCAP* **1405** 045 (2014), arXiv:1402.4964 [astro-ph.CO].
12. C. M. Will, *Living Rev. Rel.* **9**, 3 (2006) gr-qc/0510072.
13. K. Yagi, *et al. Phys. Rev.* D **89**, 084067 (2014) arXiv:1311.7144 [gr-qc].
14. D. Blas, *et al*, arXiv:1602.04188 [gr-qc].
15. I. Carruthers, T. Jacobson, *Phys. Rev.* D **83**, 024034 (2011) arXiv:1011.6466 [gr-qc].
16. B. Audren *et al*, *JCAP* **1503** 016 (2015), arXiv:1410.6514 [astro-ph.CO].
17. B. Audren *et al*, *JCAP* **1308** 039 (2013), arXiv:1305.0009 [astro-ph.CO].
18. N. Frusciante, *et al*, *Phys. Dark Univ.* **13**, 7 (2016) arXiv:1508.01787 [astro-ph.CO].
19. D. Blas, *et al*, arXiv:1512.05807 [astro-ph.CO].

FINE-STRUCTURE CONSTANT CONSTRAINTS ON DARK ENERGY AND THE WEAK EQUIVALENCE PRINCIPLE

C.J.A.P. MARTINS, A.C.O. LEITE, A.M.M. PINHO, R.F.C. ALVES, P. CARREIRA, M.C. FERREIRA, A. GUSART, J. LÓPEZ, M. PINO, C.I.S.A. ROCHA, M. VON WIETERSHEIM
Centro de Astrofísica da U. Porto and IA-Porto, Rua das Estrelas s/n, 4150-762 Porto, Portugal

The observational evidence for the recent acceleration of the universe demonstrates that canonical theories of cosmology and particle physics are incomplete (and possibly incorrect) and that new physics is waiting to be discovered. The most fundamental task for the next generation of astrophysical facilities is to search for, identify and ultimately characterise this new physics. Here we provide a brief summary of the CAUP Dark Side team's recent work, consolidating the science case for using astrophysical tests of the stability of fundamental couplings as direct probes of cosmology and fundamental physics. In particular we show that recent measurements already provide competitive constraints on dark energy an on Weak Equivalence Principle violations, and we discuss the road ahead for this field.

1 Introduction

We know (from the LHC) that fundamental scalar fields are among Nature's building blocks, and that fundamental couplings run with energy. These fields will naturally couple to the rest of the model, unless there is a currently unknown principle to suppress them. In a cosmological context, couplings can therefore roll in time and ramble in space.

It follows that such couplings will lead to potentially observable long-range forces and variations of what are usually called fundamental constants [1]. These measurements (whether they are detections or null results) constrain fundamental physics and cosmology, as we will presently show. In particular, this ensures a quantifiable 'minimum guaranteed science' for forthcoming experiments, enabling detailed studies and optimisation of possible observational strategies.

It's worthy of note that we have no 'theory of constants': we don't know what role they play in physical theories, how many are fundamental, and so on (and yet they determine properties of atoms, cells and the universe). Therefore we also have no compelling reason to assume that they are constant—but if they vary, all the physics we know is incomplete.

A detection of varying dimensionless couplings would be revolutionary: *inter alia* it would immediately imply a violation of the Einstein Equivalence Principle (meaning that gravity is not a purely geometric phenomenon) and the existence of a fifth force of nature. On the other hand, improved null results are important and very useful. The simple way to see this is to note that the natural scale for the cosmological evolution of a dynamical scalar field would be the Hubble time, but current bounds are already about six orders of magnitude stronger than this, thereby ruling out many otherwise viable models.

This naturally leads to the question of how low in sensitivity should one go (until either a detection is found or one gives up and stipulates that there is no variation). Dark energy provides an enlightening analogy. If a scalar field is responsible for the dark energy, we would expect its equation of state—more rigorously, the dynamically relevant parameter $(1 + w)$—to

be of order unity, but observationally we know it to be less than about 10^{-1}. But if this is not of order unity, there is no known natural scale for the variation: either there is some fine-tuning or a new (currently unknown) symmetry forces it to be zero. Now, the same argument can be made for the relative variation of the fine-structure constant, $\Delta\alpha/\alpha$, the only difference being that this is observationally known to be less than 10^{-5}.

As we will discuss in the following section, the sensitivity of current measurements is typically at the few parts per million (ppm) level. So if no variations are found at this level is it worth pushing on? Certainly yes. The reason is akin to the CP Problem in QCD: a parameter naively of order unity is known to be less than 10^{-10} leading to the postulate of the Peccei-Quinn symmetry [2] and axions. A sufficiently tight bound on α will indicate either that there are no dynamical fields in cosmology or the presence of a new symmetry to suppress the couplings—whose existence would be as significant as that of the original field.

2 Observational status

Astrophysical tests of the stability of fundamental couplings through high-resolution spectroscopy of absorption systems along the line of sight of bright quasars have experienced very significant developments, including gains in sensitivity, over the past five years.

The dataset studied by *Webb et al.* [3] includes 293 archival absorbers, and the nominal weighted mean for the relative variation of α has a systematic uncertainty at the 2 ppm level, but it is known that the systematic uncertainties for each system are typically of order 9 ppm. On the other hand, there are currently 11 dedicated measurements (summarised in Ferreira & Martins [4]), mostly from a UVES Large Program [5,6,7], for which the nominal weighted mean is

$$\frac{\Delta\alpha}{\alpha} = 0.37 \pm 0.94\, ppm\,, \tag{1}$$

with more measurements expected imminently. However, the Large Program collaboration has also identified an irreducible systematics floor of 1ppm, which is intrinsic to all currently available spectrographs and can only be beaten by using more stable ones.

The analysis of *Webb et al.* indicates a statistical evidence at more than four sigma for a spatial dipole in the values of α. It's unclear if this is a pure spatial dipole or has some dependence of lookback time—the data is not good enough to distinguish between the two scenarios. In any case, the recent dataset of dedicated measurements, although small in number, has tight measurements and therefore has some impact in these scenarios [8]: specifically, the allowed dipole amplitude is reduced by 20%, and the direction of the dipole on the sky is also further constrained. It is still not possible to distinguish between a pure spatial dipole and one with a further redshift dependence.

A joint analysis of all existing optical/UV and radio/mm data is also interesting [4]: in particular, it reveals inconsistencies at the one to two sigma level between the optical and the radio measurements. This is especially true for data deep in the matter era. This should be clarified with APEX and ALMA, which have the capability of carrying out, in the radio/mm, measurements at the same high redshifts that are currently probed by optical/UV spectrographs such as UVES (and will soon be probed by ESPRESSO [9]). We note that considering all currently available data the best-fit for $\Delta\alpha/\alpha$ is -2ppm (at the two sigma level), though this is not statistically significant given the aforementioned systematics floor. Nevertheless, the possibility of a different behaviour in the matter and acceleration epochs is something that deserves additional observational exploration.

3 Fundamental cosmology

Recent cosmological observations suggest that the universe is dominated by an energy component whose gravitational behaviour is similar to that of a cosmological constant. A dynamical scalar

field is (arguably) a more natural explanation. Such a field must be slow-rolling (which is mandatory for $p < 0$) and dominate at low z. Standard methods (type Ia supernovas, etc) are known to be of limited use as dark energy probes[10,11], since the relevant cosmological parameters are hidden behind two integrals. Moreover, since the field is slow-rolling when dynamically important, a convincing detection of $w(z)$ will be tough at low z. Instead we must probe the deep matter era, where the scalar field dynamics is presumably fastest.

Fundamental couplings ideally probe the field dynamics beyond the domination regime, with the advantage that for the simplest models the relevant cosmological parameters are hidden behind only one integral—and in some specific classes of models the relation is even more direct. Thus astrophysical facilities such as ALMA, ESPRESSO and ELT-HIRES will map dark energy well into the matter era[9,12]—out to $z \sim 4$ and possibly beyond.

In the simplest class of models where the same scalar degree of freedom is responsible for the dark energy and (through a coupling to the electromagnetic sector) the varying α, the latter's evolution is parametrically determined. Specifically, for a quintessence-type field we have

$$\frac{\Delta\alpha}{\alpha}(z) = \zeta \int_0^z \sqrt{3\Omega_\phi(z')[1+w_\phi(z')]}\frac{dz'}{1+z'}\,, \tag{2}$$

where $w_\phi(z)$ is the dark energy equation of state, $\Omega_\phi(z)$ the fraction of the universe's energy density in this component, and ζ is the field coupling.

Current QSO, atomic clock[13] and background cosmology[14,15] data strongly constrains these models[16,17,18]. For example, taking the simple assumption of a constant equation of state[16] the 1D marginalised constraints are

$$|\zeta| < 5 \times 10^{-6}\,, \quad (95.4\%CL) \tag{3}$$

$$|1 + w_0| < 0.06\,, \quad (99.7\%CL)\,. \tag{4}$$

For comparison, with 12 ESPRESSO GTO measurements (see Ana Catarina Leite's contribution) one expects improvements by a factor 1.5 (assuming that there are no variations) or a detection of a non-zero coupling ζ assuming a variation that saturates current bounds.

Given the aforementioned parametric relation, these results are mildly dependent on the underlying fiducial model[17,18]. For example if we assume the CPL parameterisation we obtain weaker 1D marginalised constraints on the present-day dark energy equation of state

$$1 + w_0 = 0.00^{+0.15}_{-0.05}\,, \quad (99.7\%CL) \tag{5}$$

(and no significant constraint on the equation of state slope w_a), but correspondingly stronger constraints on the coupling

$$\zeta = (1 \pm 3) \times 10^{-6}\,, \quad (95.4\%CL)\,. \tag{6}$$

In these models the scalar field will inevitably couple to nucleons (through the a dependence of their masses) and therefore will also lead to violations of the Weak Equivalence Principle[19,20,21]. Depending on the dark energy model considered, this leads to a bound on the Eotvos parameter[17,18].

$$\eta < (2-4) \times 10^{-14}\,, \quad (95.4\%CL)\,. \tag{7}$$

These are one order of magnitude stronger than the current direct bounds, coming from torsion balance and lunar laser ranging experiments, but testable by the MICROSCOPE satellite). On the other hand, in models where dark energy and the α variation are due to different physical processes, the WEP bound is somewhat weaker, typically $\eta < (5-10)\times 10^{-14}$. Forthcoming high-resolution ultra-stable spectrographs will keep providing competitive constraints: ESPRESSO can reach a sensitivity on η of few x 10^{-16} (that is, better than MICROSCOPE) while ELT-HIRES can reach 10^{-18} similar to that of the proposed STEP.

4 Outlook

The observational evidence for the acceleration of the universe demonstrates that canonical theories of cosmology and particle physics are incomplete, if not incorrect. Precision astrophysical spectroscopy provides an optimal probe of the (still unknown) new physics. Currently it is clear that dimensionless fundamental couplings are stable at the 10^{-5} level. This is already a tight constraint: it is stronger than the Cassini bound, and it leads to the best available constraints on Weak Equivalence Principle violations.

Things are currently unclear at the ppm level, but significant improvements are coming. New dedicated instruments (ESPRESSO imminently, and ELT-HIRES in the next decade) will lead to a new generation of precision consistency tests of the standard model and enable a characterisation of new physics. Our work demonstrates their competitive 'guaranteed science' implications for dark energy and fundamental physics. They will also deliver a unique value of complementarity, redundancy, and synergies with other facilities (including ALMA, Euclid and SKA), that are currently being explored in more detail.

Acknowledgements

This work was done in the context of project PTDC/FIS/111725/2009 (FCT, Portugal). CJM is supported by an FCT Research Professorship, contract reference IF/00064/2012, funded by FCT/MCTES (Portugal) and POPH/FSE (EC). ACL is supported by an FCT fellowship (PD/BD/113746/2015) under the FCT PD Program PhD::SPACE (PD/00040/2012) and by the Gulbenkian Foundation through *Programa de Estímulo à Investigação* 2014, grant number 2148613525. AG, JL, MP and MVW were supported by the *Joves i Ciència* program of Fundació Catalunya–La Pedrera.

References

1. S.M. Carroll, *Phys. Rev. Lett.* **81**, 3067 (1998).
2. R.D. Peccei and H.R. Quinn, *Phys. Rev. Lett.* **38**, 1440 (1977).
3. J.K. Webb *et al.*, *Phys. Rev. Lett.* **107**, 191101 (2011).
4. M.C. Ferreira and C.J.A.P. Martins, *Phys. Rev.* D **91**, 124032 (2015).
5. P. Molaro *et al.*, A. & A. **555**, A681 (2013).
6. H. Rahmani *et al.*, M.N.R.A.S. **435**, 861 (2013).
7. T.M. Evans *et al.*, M.N.R.A.S. **445**, 128 (2014).
8. A.M.M. Pinho and C.J.A.P. Martins, *Phys. Lett.* B **756**, 121 (2016).
9. A.C.O. Leite and C.J.A.P. Martins, *Phys. Rev.* D **91**, 103519 (2015).
10. I. Maor, R. Brustein and P.J. Steinhardt, *Phys. Rev. Lett.* **86**, 6 (2001).
11. A. Upadhye, M. Ishak and P.J. Steinhardt, *Phys. Rev.* D **72**, 063501 (2005).
12. L. Amendola *et al.*, *Phys. Rev.* D **86**, 063515 (2012).
13. T. Rosenband *et al.*, Science **319**, 1808 (2008).
14. N. Suzuki *et al.*, Astrophys. J. **746**, 85 (2012).
15. O. Farooq and B. Ratra, Astrophys. J.. **766**, L7 (2013).
16. C.J.A.P. Martins and A.M.M. Pinho, *Phys. Rev.* D **91**, 103501 (2015).
17. C.J.A.P. Martins *et al.*, J.C.A.P. **1508**, 047 (2015).
18. C.J.A.P. Martins *et al.*, *Phys. Rev.* D **93**, 023506 (2016).
19. G. Dvali and M. Zaldarriaga, *Phys. Rev. Lett.* **88**, 091303 (2002).
20. T. Chiba and K. Kohri, Prog. Theor. Phys. **107**, 631 (2002).
21. J.-P. Uzan, Living Rev. Rel. **14**, 2 (2011).

EXPECTATION OF LEPTON HIERARCHY AND ABSOLUTE NEUTRINO MASSES IN A MICROSCOPIC COSMOLOGICAL MODEL

VO VAN THUAN
Vietnam Atomic Energy Institute (VINATOM)
59 Ly Thuong Kiet street, Hoan Kiem district, Hanoi, Vietnam
Email : *vvthuan@vinatom.gov.vn*

Based on time-space symmetry, a microscopic bi-cylindrical geometrical dynamics is proposed for a direct link between general relativity and quantum mechanics. In particular, Klein-Gordon-Fock equation is proved as a dual wave-like representation of the exponential geodesic solution of Einstein gravitational equation which serves a basis to formulate a microscopic cosmological model of quantum substances. Extending time-like curvatures up to higher orders within 3D hyper-spherical surfaces allows to solve the problem of mass hierarchy of charged leptons under a strict constraint of three generations. A spontaneous breaking of time-space symmetry leads to a very large mass hierarchy between heavy-lepton and neutrino sectors. Experimental verification of predicted absolute neutrino masses is available.

1 A duality of Einstein gravitational equation

Investigation is carried out on a time-space symmetrical "lightcone" $dt_k^2 = dx_l^2$ embedded in an ideal 6D flat time-space $\{t_k \mid x_l\}$, where $k, l = 1 \div 3$ are summation indexes [1]. Here natural units ($\hbar = c = 1$) are used unless it needs an explicit quantum dimension. For fluctuations including curved rotation and linear translation a symmetrical $\{3T, 3X\}$ bi-cylindrical geometry is introduced originally. Then assuming that due to interaction of a Higgs-like potential the time-space symmetry is spontaneously broken, leading to formation of energy-momentum. In the result, the bi-cylindrical geometry is getting asymmetrical, as shown in [2]. In observing an individual fermion elementary particle, e.g. a free lepton with (pseudo-)spins $\vec{\tau}$ and $\vec{s}$, its projections τ_k or $s_l = \pm 1/2$ can be fixed on the longitudinal axes of $\{t_k\}$ and $\{x_l\}$, respectively, leading to a cylindrical dynamical model. Being embedded in 6D-lightcone, cylindrical variables $\{\psi, \varphi\}$ are getting functions of linear coordinates $\{t_k, x_l\}$ and two 3D-local affine parameters t_0 and x_n which are introduced in according to projection of (pseudo-)spins $\vec{\tau}$ and $\vec{s}$, respectively. Applying the symmetrical bi-cylindrical geometry to orthonormal subspaces of 3D-time and 3D-space, the corresponding gravitational equation in $\{3T, 3X\}$-vacuum reads:

$$R_i^m - \frac{1}{2}\delta_i^m R = -\delta_i^m \Lambda, \tag{1}$$

When cosmological constant is vanished ($\Lambda = 0$), time-space symmetry is getting absolute and Equation (1) would be separated into two independent 3D sub-equations.
As $\psi = \psi(y)$ and $\varphi = \varphi(y)$, it is assumed that the Hubble law of the cosmological expansion is applied for the bi-cylindrical model of microscopic space-time: $\frac{\partial \psi}{\partial y} = v_y = H_y \psi$. Therefore: $\left[\frac{\partial y}{\partial \psi}\right] = \frac{1}{H_y \psi}$, where v_y is expansion rate proportional to the "microscopic scale factor" ψ and H_y is a "microscopic Hubble constant"; $y \equiv \{t, z\} \equiv \{t_0, t_3, x_n, x_3\} \in \{t_i, x_j\}$. As $\{i, j\}$ are

summation indexes of curved coordinates then $\{t_i\}$ and $\{x_j\}$ are explicitly embedded in 3D-time or in 3D-space, correspondingly. Equation $R^{\psi}_{\psi} = 0$ is a solution of (1), in which the acceleration term in 3D-time is enhanced strongly due to interaction with a Higgs-like potential V_T of a time-like "cosmological constant" Λ_T, leading to an asymmetrical bi-geodesic equation:

$$\frac{\partial^2\psi}{\partial t^2} - \frac{\partial^2\psi}{\partial {x_j}^2} = \left[\Lambda_T - \left(\frac{\partial\varphi}{\partial x_n}\right)^2_{even} - \Lambda_L\right]\psi. \tag{2}$$

where $\Lambda_L \equiv \left(\frac{\partial\varphi}{\partial x^L_n}\right)^2$ is a small space-like P-odd "cosmological constant" caused by the global weak interaction leading to the left-handed space. Being originated from Einstein gravitational equation (1), Equation (2) describes the microscopic cosmological evolution of time-space curvatures by its exponential solution $\psi = \psi_0 e^{\pm\varphi} = \psi_0 e^{\pm(\Omega t + k_j x_j)}$.
On other side, as variables $\{y\}$ can turn as well as $\{y\} \leftrightarrow \{iy\}$ then Equation (2) leads to a wave-like representation with $\psi_w \equiv \psi(y \to iy) \sim e^{i\varphi} = e^{i(\Omega t - k_j x_j)}$, namely:

$$-\frac{\partial^2\psi}{\partial t^2} + \frac{\partial^2\psi}{\partial {x_j}^2} = \left[\left(\frac{\partial\varphi}{\partial t^+_0}\right)^2 - B_e(k_n.\mu_e)^2_{even} - \left(\frac{\partial\varphi}{\partial x^L_n}\right)^2\right]\psi. \tag{3}$$

where B_e is a calibration factor and μ_e is magnetic dipole moment of charged lepton; its orientation correlates with spin vector $\vec{s}$ and being P-even value. The transformation from the exponential solution to the wave-like one is realized by replacing variables: $t \to -it$ and $x_j \to ix_j$, as well as of their corresponding covariant derivatives. This procedure is equivalent to transformation from an external observation to an internal investigation [2]. Really, in quantum mechanics the phase velocity is superluminal as $v_{phase} = \frac{dx_j}{dt} = \frac{\Omega}{k_j} = \frac{E}{p_j} > c$. Rescaling with Planck constant by implementing quantum dynamical operators $\frac{\partial}{\partial t} \to \hat{E} = i\hbar\frac{\partial}{\partial t}$; $\frac{\partial}{\partial x_j} \to \hat{p_j} = -i\hbar\frac{\partial}{\partial x_j}$ and making the functional parameter ψ of a scale of Compton length, a generalized Klein-Gordon-Fock equation is to be formulated explicitly from Representation (3) as:

$$-\hbar^2\frac{\partial^2\psi}{\partial t^2} + \hbar^2\frac{\partial^2\psi}{\partial x^2_j} - m^2\psi = 0, \tag{4}$$

where the square mass term m consists of the following components: $m^2 = m_0^2 - m_s^2 - m_L^2$. Except the rest mass m_0, the P-even contribution m_s is linked with an external curvature of spinning in 3D-space and a small non-zero mass factor $m_L \ll m_s$ which proves a tiny internal curvature of our realistic 3D-space. In general, Equation (4) is reminiscent of the squared Dirac equation of lepton. In duality to the wave-like equation (4), the geodesic equation (2) in a homogeneity condition being equivalent to de Sitter-like solutions can serve for modeling Hubble expansion in the microscopic time-space. In analogue to the standard model of macroscopic cosmology, a microscopic cosmological model is proposed to solve the mass hierarchy problem of leptons [3].

2 Charged lepton hierarchy in a microscopic cosmological model

In 4D space-time we assume [3] that all charged leptons are to involve in the same basic time-like cylindrical geodesic evolution with an internal curvature of the time-like circle $S_1(\varphi^+)$, where $\varphi^+ = \varphi({t_0}^+)$ is azimuth rotation in the plane $\{t_1, t_2\}$ about t_3 and the sign + means an evolution toward the future. This universal feature determines the common properties of all charged lepton generations, except their mass hierarchy. Developing higher orders of curvature, a generalized 3D time-like spherical system is considered, which is described by nautical angles $\{\varphi^+, \theta_T, \gamma_T\}$, where θ_T is a zenith in the plane $\{t_1, t_3\}$ and γ_T is another zenith in the orthogonal plane $\{t_2, t_3\}$. In 4D space-time an electron is seen oscillating along a line-segment of the time-like amplitude Φ, formulating one-dimensional comoving "volume": $V_1(\varphi^+) = \Phi = \psi.T$, where T

is the time-like Lagrange radius. As homogeneous solutions of Equation (2) recall a time-like de-Sitter solution, the microscopic cosmological model is applied to the 3D time-like sphere, considering Φ as the time-like microscopic Hubble radius and ψ as the time-like scale factor. The highest order curvatures C_n of $n-$hyper spherical surfaces are $C_n \sim \psi^{-n}$. For electron the energy density is: $\rho_1 = \epsilon_0/\psi$; where ϵ_0 is a universal lepton energy factor, then its mass is as:

$$m_e = \rho_1 V_1 = \rho_1 \Phi = \epsilon_0 . T = \epsilon_0 . W_1; \tag{5}$$

For muon and tauon except the common φ^+ evolution, there are additional hyper-spherical ED-curvatures. "Comoving volumes" $V_n(\Phi)$ with a fixed Φ are calculated:

$$V_n(\Phi) = \int_0^{\Phi} S_{n-1}(v)dv = S_{n-1}(\Phi) \int_0^{\Phi} dv = V_1 S_{n-1}. \tag{6}$$

Energy density of n-hyper spherical configuration can be expressed as: $\rho_n = \rho_1/\psi^{n-1}$and the mass of $n-$dimensional configuration reads:

$$m_n = \rho_n . V_n(\Phi) = (\rho_1/\psi^{n-1}) V_1 S_{n-1} = W_1 \rho_{n-1} S_{n-1}. \tag{7}$$

The value W_n is n-dimensional time-like Lagrange "volume" of particle. The simplest additional S_{n-1} configurations are: $[S_1(\theta_T) + S_1(\gamma_T)]$ and $S_2(\theta_T, \gamma_T)$ respectively, then:

$$m_\mu = W_1 \rho_1 [S_1(\theta_T) + S_1(\gamma_T)] = \epsilon_0 4\pi . T^2 = \epsilon_0 . W_2; \tag{8}$$

$$m_\tau = W_1 \rho_2 S_2(\theta_T, \gamma_T) = \epsilon_0 4\pi . T^3 = \epsilon_0 . W_3. \tag{9}$$

In the first order of approximation, using experimental masses of electron and muon for determining $\epsilon_0 = 31.0\ keV$ and $T = 16.5$, the mass of tau-lepton is predicted [3]:

$$m_e : m_\mu : m_\tau = 1 : 207.4 : 3421.5 = 0.511 : 106.0 : 1748.4\ (MeV). \tag{10}$$

3 Heavy lepton-neutrino hierarchy and absolute masses of neutrinos

Assuming neutrinos are time-space symmetrical partners of charged leptons, they are to be almost free in 3D-time ($\Lambda_T = 0$ except a CPV-residue) and weakly curved in 3D-space. Replacing: $\Lambda_L \to \Lambda_\nu \sim \Lambda_L$, $t \equiv t_3$, $x_j \to x_j^\nu \approx x_l$, from geodesics (2) an equation for neutrino reads:

$$-\frac{\partial^2 \psi_\nu}{\partial t_3^2} + \frac{\partial^2 \psi_\nu}{\partial {x_j^\nu}^2} = -\left(\Lambda - \Lambda_\nu\right) \psi_\nu \approx \Lambda_\nu \psi_\nu. \tag{11}$$

Here the cosmological constant $\Lambda = (\frac{\partial \varphi_\nu}{\partial t_0})^2_{CPV} \sim \delta {d_\nu}^2$ is introduced as a super-weak CPV term due to a tiny electrical dipole moment δd_ν of neutrino. However, if $\Lambda_L > 0$, rescaling (11) by conventional quantum operators leads to a formal "wave-like representation" of the quantum equation for a time-like lepton with an imaginary mass $i.m_\nu$ (adjusted by $m_{CPV} \ll m_\nu$):

$$-\hbar^2 \frac{\partial^2 \psi_\nu}{\partial t_3^2} + \hbar^2 \frac{\partial^2 \psi_\nu}{\partial x_l^2} \approx -(m_\nu^2 - m_{CPV}^2)\psi_\nu. \tag{12}$$

In effect, because neutrino mass $m_\nu \sim \sqrt{\Lambda_L}$ is too small, Equation (11) governs transmission of microscopic gravitational waves almost with the speed of light ($v = c$) carrying out a very weak space-like curvature characterized by ψ_ν. From another side, in symmetry to the charged leptons, Equation (11) in its "homogeneity condition" (without time-like variation) has a "space-like" de-Sitter solution in the microscopic cosmological model. Discussing on the mass eigenstates ν_n with absolute masses m_1, m_2 and m_3 but not the mixing eigenstates $(\nu_e, \nu_\mu, \nu_\tau)$, we achieve the normal ordering of mass hierarchy, where ν_1 is the lightest neutrino with a basic space-like

Table 1: Calculation of neutrino masses based on oscillation data.

Neutrino (ν_n)	ν_1	ν_2	ν_3
Density ρ_ν	ϵ_ν/ψ_ν	ϵ_ν/ψ_ν^2	ϵ_ν/ψ_ν^3
Comoving volume, V_ν	Φ_ν	$4\pi\Phi_\nu^2$	$4\pi\Phi_\nu^3$
Formula of m_n	$\epsilon_\nu X_\nu$	$\epsilon_\nu 4\pi X_\nu^2$	$\epsilon_\nu 4\pi X_\nu^3$
$Exp-tal\ \Delta m^2, eV^2$	$\Delta m_{31}^2 - \Delta m_{32}^2$ $= (1.0 \pm 7.0).10^{-5}$ $= \Delta m_{21}^{*\,2} \supset \Delta m_{21}^2$	$\Delta m_{21}^2 =$ 7.50×10^{-5} $(\pm 2.3\%)$	$\Delta m_{31}^2 =$ 2.46×10^{-3} $(\pm 1.9\%)$
a. *Calculated* m_n, eV $X_\nu = 5.728;$ $\epsilon_\nu = 2.10 \times 10^{-5} eV$	1.20×10^{-4}	8.66×10^{-3} $(\pm 1.2\%)$ $(*)$	4.96×10^{-2} $(\pm 1.0\%)$ $(*)$
b. *Calculated* m_n, eV $X_\nu = 6.774;$ $\epsilon_\nu^* = 1.27 \times 10^{-5} eV$	8.60×10^{-5}	7.32×10^{-3}	4.96×10^{-2} $(\pm 1.0\%)$ $(*)$
$\Delta_{ab} \equiv$ **(a-b)/(a+b)**, (%)	17%	9%	$(*)$

cylindrical curvature, ν_2 has additional S_1-curvatures and the heaviest ν_3 has an additional S_2-curvature. Accordingly, we derive formulas of masses, introducing ϵ_ν as neutrino energy factor and $X_\nu = \Phi_\nu/\psi_\nu$ as the microscopic space-like Lagrange radius (Φ_ν and ψ_ν are microscopic Hubble length and scale factor, respectively). In principle, based on "experimental masses" m_3 and m_2 (estimated by square roots of oscillation data Δm^2) for determining ϵ_ν and X_ν, then the lightest m_1 is calculated (Case **a**). Alternatively, due to a strong time-space asymmetry after a Higgs-like breaking symmetry, ϵ_ν can be fixed prior by ϵ_0 through a ratio of Fermi and fine-structure constants: $\epsilon_\nu \to \epsilon_\nu^* \approx (G_F m_e^2/\alpha)\epsilon_0$ then from "experimental mass" m_3 one can determine Lagrange radius X_ν, which are used for prediction of m_1 and m_2 (Case **b**). The results are summarized in Table 1, where the sign $(*)$ means a calibration by m_3 or m_2.

Conclusions of the model for neutrinos: i/ Being time-like substances and not able to observe directly, neutrinos in mass-eigenstates can not travel with $v < c$, but due to their tiny absolute masses the observable mixing eigenstates are transmitted almost as luxons ($v \approx c$). In the result, the helicity of mass-eigenstates is fixed, while their lepton numbers are not conserved strictly (due to CPV term) as the appearances of Majorana neutrinos; ii/ The fact that energy factors ϵ_0 and ϵ_ν^* are well correlated through a huge scale roughly nine orders of $G_F m_e^2/\alpha$ shows up an argument for a possible time-space partnership between charged leptons and neutrinos, but on another side, it serves a mechanism for a strong heavy lepton-neutrino hierarchy; iii/ The absolute masses of three neutrino generations qualitatively fit the normal ordering of hierarchy; iv/ However, it needs to improve precision of experimental values Δm_{31}^2 and $|\Delta m_{32}^2|$ at least by an order to confirm the mass hierarchy ordering before going to a quantitative proof of the predicted lightest mass m_1. It opens an opportunity for experimental verification of the model.

Acknowledgments

The author thanks the National foundation for science and technology development (NAFOSTED) and the Rencontres de Moriond for support to his participation in the Conference.

References

1. Vo Van Thuan, Communications in Physics **25**, 247 (2015). *arXiv:1507.00251[gr-qc]*2015.
2. Vo Van Thuan, *arXiv:1604.05164v2[physics.gen-ph]*2016.
3. Vo Van Thuan, *arXiv:1510.04126[physics.gen-ph]*2015.

RANDALL-SUNDRUM VS. HOLOGRAPHIC BRANEWORLD

NEVEN BILIC
Division of Theoretical Physics, Rudjer Bošković Institute, Bijenička 54, Zagreb, Croatia



A mapping between two braneworld cosmologies – Randall-Sundrum and holographic – is explicitly constructed. The cosmologies are governed by the appropriate modified Friedman equations. A relationship between the corresponding Hubble rates is established.

1 Introduction

Braneworld cosmology is based on the scenario in which matter is confined on a brane moving in the higher dimensional bulk with only gravity allowed to propagate in the bulk. We will consider two types of braneworlds in an AdS_5 bulk. In a holographic braneworld a 3-brane is located at the boundary of the asymptotic AdS_5 . The cosmology is governed by matter on the brane in addition to the boundary CFT. In the second Randall-Sundrum (RSII) model [?] a 3-brane is located at a finite distance from the boundary of AdS_5.

A cosmology on the brane is obtained by allowing the brane to move in the bulk. Equivalently, the brane is kept fixed at $z = z_{\rm br}$ while making the metric in the bulk time dependent. The time dependent spacetime may be regarded as a z foliation of the bulk with an FRW cosmology on each z slice. In particular, at $z = z_{\rm br}$ we have the RSII cosmology and, at z=0, the holographic cosmology. The Friedmann equation on the brane is modified

$$H^2 + \frac{\kappa}{a^2} = \frac{8\pi G_{\rm N}}{3}\rho + \left(\frac{4\pi G_{\rm N}\ell}{3}\right)\rho^2 + \frac{\mu\ell^2}{a^4}, \qquad (1)$$

where ℓ is the AdS_5 curvature radius, H is the Hubble rate and μ is a parameter. By introducing the boundary in AdS_5 at $z = z_{\rm br}$ instead of $z = 0$, the RSII model is conjectured to be dual to a cutoff CFT coupled to gravity, with $z = z_{\rm br}$ providing the IR cutoff. This conjecture then reduces to the standard AdS/CFT duality as the boundary is pushed off to $z = 0$. In the original RSII model one assumes the Z_2 symmetry, so the region $0 < z \leq z_{\rm br}$ is identified with $z_{\rm br} \leq z < \infty$, with the observer brane at the fixed point $z = z_{\rm br}$. Hence, the braneworld is sitting between two patches of AdS_5, one on either side, and is therefore dubbed "two sided". In contrast, in the "one-sided" RSII model the region $0 \leq z \leq z_{\rm br}$ is simply cut off so the bulk is the section of spacetime $z_{\rm br} \leq z < \infty$.

The variation of the action yields Einstein's equations on the boundary [?]

$$R_{\mu\nu} - \frac{1}{2} R g_{\mu\nu} = 8\pi G_{\rm N} (\gamma \langle T^{\rm CFT}_{\mu\nu} \rangle + T^{\rm matt}_{\mu\nu}), \tag{2}$$

where $T^{\rm matt}_{\mu\nu}$ and $T^{\rm CFT}_{\mu\nu}$ are the energy-momentum tensors associated respectively with matter on the holographic brane and the CFT on the boundary. The parameter γ takes on the value 1 and 2 for the 1-sided and 2-sided RSII model, respectively. According to the AdS/CFT prescription, the expectation value $\langle T^{\rm CFT}_{\mu\nu} \rangle$ is obtained by functionally differentiating the renormalized on-shell bulk gravitational action with respect to the boundary metric [?]. From (**??**) one derives the Friedmann equation at the boundary

$$\mathcal{H}_0^2 = \frac{\ell^2}{4} \left(\mathcal{H}_0^4 + \frac{4\mu}{a_0^4} \right) + \frac{8\pi G_{\rm N}}{3} \rho_0. \tag{3}$$

where $\mathcal{H}_0^2 = H_0^2 + \kappa / a_0^2$ and $H_0 = \dot{a}_0 / a_0$ is the Hubble rate at the holographic boundary.

A map between z-cosmology and $z = 0$-cosmology can be constructed using [?]

$$a^2 = a_0^2 \left[\left(1 - \frac{\mathcal{H}_0^2 z^2}{4} \right)^2 + \frac{1}{4} \frac{\mu z^4}{a_0^4} \right], \quad n = \frac{\dot{a}}{\dot{a}_0}. \tag{4}$$

The map is schematically illustrated as

$$\begin{array}{ccc} d\tau^2 - a_0^2 d\Omega_\kappa^2 & \xrightarrow{\tau \to \tilde{\tau}} & (1/n^2) d\tilde{\tau}^2 - a_0^2 d\Omega_\kappa^2 \\ \Big\downarrow z & & \Big\downarrow z \\ n^2 d\tau^2 - a^2 d\Omega_\kappa^2 & \xrightarrow[\tau \to \tilde{\tau}]{} & d\tilde{\tau}^2 - a^2 d\Omega_\kappa^2 \end{array}$$

where τ and $\tilde{\tau}$ are the holographic and RSII synchronous times, respectively. There is a clear distinction between the maps involving 1-sided and 2-sided versions of the RSII model [?]. In the 2-sided map the low-density regime on the RSII brane corresponds to the high negative energy density on the holographic brane. The low density regime can be made simultaneous only in the 1-sided RSII. It is conceivable that we live in a braneworld with emergent cosmology. That is, dark energy and dark matter could be emergent phenomena induced by what happens on the primary braneworld. For example, suppose our universe is a one-sided RSII braneworld the cosmology of which is emergent in parallel with the primary holographic cosmology. If ρ_0 describes matter with the equation of state satisfying $3p_0 + \rho_0 > 0$, as for, e.g., CDM, we will have an asymptotically de Sitter universe on the RSII brane. If we choose ℓ so that the cosmological constant Λ fits the observed value, the quadratic term will be comparable with the linear term today but will strongly dominate in the past and hence will spoil the standard cosmology. However, the standard ΛCDM cosmology could be recovered by including a negative constant term in ρ_0 and fine tune it to cancel Λ up to a small phenomenologically acceptable contribution.

Acknowledgments

This work has been supported by the Croatian Science Foundation, Project No. IP-2014-09-9582.

References

1. L. Randall and R. Sundrum, *Phys. Rev. Lett.* **83**, 4690 (1999).
2. N. Bilic, *Phys. Rev.* D **93**, 066010 (2016)
3. S. de Haro, S. N. Solodukhin and K. Skenderis, *Commun. Math. Phys.* **217**, 595 (2001))
4. P. S. Apostolopoulos, G. Siopsis and N. Tetradis, *Phys. Rev. Lett.* **102**, 151301 (2009)

Running vacuum versus the ΛCDM

Adrià Gómez-Valent [a, b], Joan Solà [a], and Javier de Cruz Pérez [a]
Departament de Física Quàntica i Astrofísica, Univ. de Barcelona, Av. Diagonal 647, E-08028 Barcelona, Catalonia, Spain



It is well-known that a constant Λ-term is a traditional building block of the concordance ΛCDM model. We show that this assumption is not necessarily the optimal one from the phenomenological point of view. The class of running vacuum models, with a possible running of the gravitational coupling G, are capable to fit the overall cosmological data SNIa+BAO+H(z)+LSS+BBN+CMB better than the ΛCDM, namely at a level of $\sim 3\sigma$ and with Akaike and Bayesian information criteria supporting a strong level of statistical evidence on this fact. Here we report on the results of such analysis.

1 A brief introduction to Running Vacuum Models (RVM's)

Some theoretical works point out that the dynamical nature of the vacuum could be described by QFT in curved space-time (see the lengthy and comprehensive review [1] and references therein). In such proposal, the following ansatz for the β-function of Λ is used:

$$\frac{d\,\Lambda}{d\ln\mu} = \frac{1}{16\pi^2}\left[\sum_i C_i\mu^2 + D_i\frac{\mu^4}{M_i^2} + ...\right] \to \Lambda(H) = C_0 + C_H H^2 + C_{\dot{H}}\dot{H} + ... \qquad (1)$$

where in the second formula we identify the energy scale μ^2 with a linear combination of H^2 and $\dot{H}$. Notice that there is no conflict at all with the Cosmological Principle, provided $\rho_\Lambda = \rho_\Lambda(H)$ is homogeneous and fully respects the general covariance. By virtue of the Bianchi identity, the covariant conservation of the full momentum tensor must be satisfied,

$$\nabla^\mu(GT_{\mu 0}) = 0 \to \frac{d}{dt}\left[G(\rho_m + \rho_r + \rho_\Lambda)\right] + 3GH\sum_{i=m,r}(\rho_i + p_i) = 0\,. \qquad (2)$$

Thus, Λ can vary if: (i) there exists an energy exchange between the vacuum and matter sectors: A-type models [2,3]; (ii) the gravitational coupling G is also dynamical and matter is covariantly conserved: G-type models [3,4]; (iii) (i)+(ii). Each of these scenarios gives rise to different background, linear and non-linear dynamics. One of the most striking features of these

[a] E-mail: adriagova@ecm.ub.edu, sola@ecm.ub.edu, decruz@ecm.ub.edu .
[b] Speaker.

Table 1: Best-fit values for the ΛCDM and RVM's. 663 data points: SNIa+BAO+H(z)+LSS+BBN+CMB.

Model	h	ω_b	n_s	Ω_m	$\nu_{eff} = \nu - \alpha$	χ^2/dof	ΔAIC	ΔBIC
ΛCDM	0.689 ± 0.004	0.02248 ± 0.00013	0.971 ± 0.004	0.300 ± 0.005	-	639.49/659	-	-
G1	0.676 ± 0.006	0.02243 ± 0.00014	0.969 ± 0.004	0.298 ± 0.004	0.0009 ± 0.0003	622.14/658	15.35	10.85
G2	0.676 ± 0.006	0.02242 ± 0.00014	0.968 ± 0.004	0.298 ± 0.004	0.0011 ± 0.0003	621.85/658	15.64	11.13
A1	0.676 ± 0.006	0.02244 ± 0.00013	0.969 ± 0.004	0.298 ± 0.004	0.0009 ± 0.0003	621.95/658	15.54	11.03
A2	0.680 ± 0.005	0.02240 ± 0.00014	0.968 ± 0.004	0.299 ± 0.005	0.0012 ± 0.0004	622.76/658	14.73	10.23

kind of models is that they are able to connect the primordial inflationary and the current accelerated phases of the Universe [5]. After the inflationary epoch, the vacuum energy in the current Universe can be effectively described by $\rho_\Lambda(H, \dot{H}) = \frac{3}{8\pi G}\left(c_0 + \nu H^2 + \frac{2}{3}\alpha\dot{H}\right)$, since the higher derivative contributions become totally negligible. The values of the two dimensionless parameters ν and α govern the running of the vacuum energy density and they are theoretically expected to be in the range $10^{-6} - 10^{-3}$, depending on the extensions of the SM of Particle Physics and the predicted particle multiplicities in each of these extensions. Plugging ρ_Λ in the Friedmann and the pressure equations, we can obtain the main background cosmological functions [2,3,4].

2 Akaike and Bayesian information criteria

AIC and BIC are model selection criteria [6]. They read, AIC= $\chi^2_{min}+2n$ and BIC=$\chi^2_{min}+n\ \ln N$, where χ^2_{min} is the minimum of the χ^2 function, N is the number of data points and n the number of free parameters that enter the fit. AIC and BIC allow us to compare models with a different number of free parameters that have been fitted with the same data set, strongly penalizing the use of extra dof. To test the effectiveness of a given RVM (versus the ΛCDM) for describing the overall data, we evaluate the pairwise differences ΔAIC (ΔBIC) with respect to the model that carries smaller value of AIC (BIC), in this case the RVM. The larger these differences the higher is the evidence against the model with larger value of ΔAIC (ΔBIC). For ΔAIC and/or ΔBIC above 10, one speaks of "very strong evidence". According to both criteria, the results of Table 1 show that the ΛCDM appears very strongly disfavored as compared to the RVM's. Hence, the RVM's emerge as serious alternative candidates for the description of our expanding Universe[3,4]. The dynamical character of the vacuum energy density in them seems to be firmly supported by the current cosmological data, in which the absence of vacuum dynamics is excluded at $\sim 3\sigma$.

Acknowledgments

A. Gómez-Valent acknowledges the Quantum Physics and Astrophysics Department of the Univ. of Barcelona, which has made possible his attendance to the 51st Rencontres de Moriond.

References

1. Solà, J., J. Phys. Conf. Ser. 453 (2013) 012015.
2. Gómez-Valent, A., Solà, J., & Basilakos, S., JCAP 01 (2015) 004; Gómez-Valent, A., & Solà, J., MNRAS 448 (2015) 2810.
3. Solà, J., Gómez-Valent, A., & de Cruz Pérez J., arXiv:1602.02103.
4. Solà, J., Gómez-Valent, A., & de Cruz Pérez J., ApJ 811 (2015) L14.
5. Solà, J., & Gómez-Valent, A., Int.J.Mod.Phys. D24 (2015) 1541003.
6. Burnham, K.P., & Anderson, D.R., *Model selection and multimodel inference* (Springer, New York, 2002); Sugiura, N., Communications in Statistics A, Theory and Methods, 7 (1978) 13.

GENERAL FEATURES OF SINGLE-SCALAR FIELD DARK ENERGY MODELS

L. PERENON
Aix-Marseille Université, CNRS, CPT, UMR 7332, 13288 Marseille, France.
Université de Toulon, CNRS, CPT, UMR 7332, 83957 La Garde, France.

We present a systematic study of modified gravity (MG) models containing a single scalar field non-minimally coupled to the metric. Despite a large parameter space, exploiting the effective field theory of dark energy (EFT of DE) formulation and imposing simple physical constraints such as stability conditions and (sub-)luminal propagation of perturbations, we arrive at a number of generic predictions about the large scale structures.

The goal of this work, in collaboration with F. Piazza, C. Marinoni and L. Hui [1], is to study the predictability of MG theories aiming at challenging the standard ΛCDM explanation of cosmic acceleration. We use the EFT of DE [2] for it has established a common formalism to describe the widest set of MG theories, those adding a single extra scalar degree of freedom to the Einstein-Hilbert action.

Such a unifying description enables MG theories to be parametrized in a common framework in terms of structural functions of time, describing how matter perturbations evolve in the universe. The requirements needed to fully describe an EFT model can be reduced to two constants and three functions of time $\left\{\Omega_m^0,\ w,\ \mu(t),\ \mu_3(t),\ \epsilon_4(t)\right\}$. The three functions are non-minimal couplings, once "turned on" they enable the description theories in the Horndeski class: μ is the Brans-Dicke (*BD*) non-minimal coupling, adding μ_3 models the cubic galileon (*H3*) term and ϵ_4 encodes the 4 and 5 Horndeski (*H45*) Lagrangians. In parallel, the EFT of DE allows one to independently set the background expansion, *i.e* the Hubble rate. This reduces to fixing the two constants, the present fractional matter density of non-relativistic matter in the perfect fluid approximation Ω_m^0 and the background DE equation of state parameter w [3]. They are set by the latest constraints [4] to reproduce a flat ΛCDM background, thus respectively ~ 0.3 and -1.

Another asset of the EFT of DE is to provide a clear and common means of assessing if theories are pathological or not, *i.e* whether they suffer from ghost or gradient instabilities. The main purposes of this work is to show that despite large degrees of freedom, definite features common to all healthy —stable and with no superluminal propagation of scalar and tensor modes— EFT models arise within the vast Horndeski class. We show this by expanding the non-minimal coupling functions in power series up to second order in the reduced matter density, x, used as time variable. An overall $(1-x)$ pre-factor ensures the vanishing of the couplings at early times, hence recovering general relativity. We randomly generate the coefficients of the expansions until we obtain 10^4 healthy *BD*, *H3* and *H45* theories.

At the linear level and under certain conditions, non-standard gravitational scenarios result in time dependent modifications of the Newton's constant G_{eff} and of the gravitational slip pa-

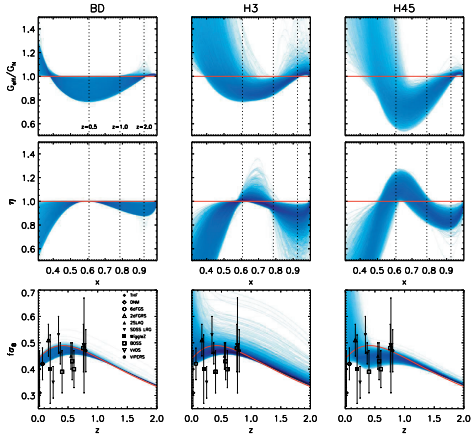


Figure 1 – The behaviour of $G_{\rm eff}/G_{\rm N}$ (first row), η (second row) as a function of the reduced matter density x and the redshift evolution of $f\sigma_8$ (third row) are shown for 10^4 randomly generated viable EFT models (*BD*, *H3*, *H45*). The dotted vertical lines identify, from left to right, the cosmic epochs $z = 0.5$, $z = 1$ and $z = 2$. The thick red line represents the ΛCDM prediction. The density of curves passing through a region is shown by the levels of blue.

rameter η. The requirement of a healthy theory leads to bounded evolutions and generic features in these quantities. For instance, as is it shown in fig. 1, the curves of $G_{\rm eff}/G_{\rm N}$ display a characteristic *S-shape*, an alternation, stronger gravity at early times, weaker gravity at intermediate redshifs and stronger gravity again today. Two competing effects are at play: the matter density entering the perturbations of an EFT model is not the same as that of the background x and being generally smaller it lowers the gravitational coupling; the contribution of the extra scalar field is attractive (healthy spin-0 field) which enhances the gravitational coupling.

The effective Newton constant acts as a source term in the growth of matter perturbations. An observable of the large scale structures such as the growth function $f\sigma_8$ can be effectively used to constrain MG. As it is shown in fig. 1, its sensitivity to $G_{\rm eff}$ translates into having almost all models displaying lower growth than ΛCDM at $0.5 \lesssim z \lesssim 1$ and always predicting stronger growth for $z > 1.5$. The *H3* and *H45* cases, exhibiting more freedom, can introduce a few models deviating strongly from the ΛCDM reference however they are statistically insignificant.

Complementing this analysis with η highlights more definite features and enhances the discriminating power. For *BD* theories, one can show analytically that $\eta \leqslant 1$ always holds. When going to *H3* and *H45*, a distinctive shape is still seen, η is always smaller than unity at any redshifts except in the window $0.5 \lesssim z \lesssim 1$.

We are now exploring, Perenon *et al.* in prep., the impact on the universality of our results when changing the background DE equation of state and changing the asymptotic behaviour of the non-minimal couplings (early dark energy). We are also investigating the link between self-acceleration and the production of weaker gravity.

References

1. L. Perenon, F. Piazza, C. Marinoni and L. Hui, JCAP **1511**, no. 11, 029 (2015) doi:10.1088/1475-7516/2015/11/029 [arXiv:1506.03047 [astro-ph.CO]].
2. G. Gubitosi, F. Piazza and F. Vernizzi, JCAP **1302**, 032 (2013) [arXiv:1210.0201 [hep-th]].
3. F. Piazza, H. Steigerwald and C. Marinoni, JCAP **1405**, 043 (2014) [arXiv:1312.6111 [astro-ph.CO]].
4. P. A. R. Ade *et al.* [Planck Collaboration], [arXiv:1502.01589 [astro-ph.CO]].

UNDER PRESSURE: CONSTRAINING EXTENSIONS OF COLD DARK MATTER

D.B. THOMAS
Department of Physics, University of Cyprus, 1 Panepistimiou Street, 2109 Aglantzia, Nicosia, Cyprus

We present the results of arXiv:1601.05097, where an MCMC analysis of the Planck CMB data is used to put constraints on the Generalised Dark Matter (GDM) parameters, w, c_s^2 and $c_{\rm vis}^2$. These parameters generalise the Cold Dark Matter component of the ΛCDM model.

1 What is GDM?

In the standard ΛCDM cosmological model, the Cold Dark Matter is a crucial component. It is described as a non-interacting initially pressureless perfect fluid, making it an extremely simple system to model physically. However, although the CDM model is consistent with cosmological observations, no dark matter candidate has been found experimentally. Moreover, many physical models of dark matter are not as idealised as the pure CDM model. Thus, it seems timely, with the precision cosmological data currently available, to examine constraints on departures from this idealised model. Here, we are interested in constraining the properties of dark matter by modelling it beyond a simple pressureless perfect fluid. We parameterise the extensions to CDM according to the Generalised Dark Matter (GDM) model [1].

The GDM parameterisation naturally arises in more realistic models; in [2] we study the relation of GDM to other models as well as examining more closely the physical effects and the interpretation of GDM. In GDM, the pressureless perfect fluid of CDM is extended to have a (background) isotropic pressure $\bar{P}_g$, a pressure perturbation Π_g and a shear perturbation Σ_g. These are controlled by three parameters that are all zero for the CDM case: the equation of state w, sound speed c_s^2 and viscosity $c_{\rm vis}^2$.

The equations governing the GDM take the following form, with bars denoting background quantities,

$$\dot{\bar{\rho}}_g = -3\mathcal{H}(1+w)\bar{\rho}_g w = \frac{\bar{P}_g}{\bar{\rho}_g} \qquad \dot{\delta}_g = 3\mathcal{H}\left(w\delta_g - \Pi_g\right) - (1+w)\left(\tfrac{1}{2}\dot{h} - \nabla^2\theta_g\right) \tag{1}$$

$$\dot{\theta}_g = (3c_a^2 - 1)\mathcal{H}\theta_g + \tfrac{\Pi_g}{1+w} + \tfrac{2}{3}\nabla^2\Sigma_g \qquad \dot{\Sigma}_g = -3\mathcal{H}\Sigma_g + \tfrac{4}{(1+w)}c_{\rm vis}^2\left(\theta_g - \tfrac{1}{2}\dot{\nu}\right) \tag{2}$$

$$\Pi_g = c_s^2\delta_g + 3\mathcal{H}(1+w)(c_s^2 - c_a^2)\theta_g. \tag{3}$$

Note that here we are working in conformal time in the synchronous gauge and considering scalar perturbations only; h and ν are the two scalar metric perturbations in this gauge.

For the present work we consider only constant equation of state w such that the adiabatic sound speed $c_a^2 = w$. In general, the sound speed c_s^2 causes oscillations in the density perturbation δ_g below the Jeans length, although if c_s^2 and $c_{\rm vis}^2$ become comparable in size then there are no sound waves. For convenience, we refer to c_s^2 as the sound speed, although this is only true for $c_s^2 \gg c_{\rm vis}^2$. The viscosity $c_{\rm vis}^2$ damps the density perturbations. For details of the model and investigations into which physical models map to GDM, see [1,2].

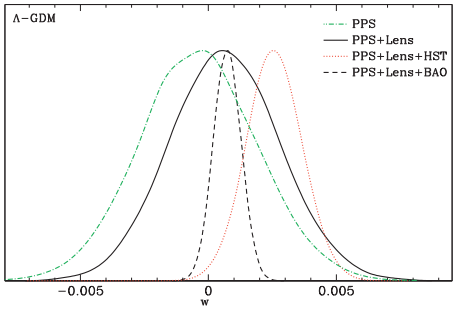


Figure 1 – The 1d posteriors for the w parameter within the Λ-GDM model. The green (dot-dashed) curve is for the Planck Power Spectrum (PPS) dataset, the black (solid) curve is for the combination of PPS and Planck lensing (Lens), the red (dotted) curve is for the combination of the PPS and Lens datasets with the addition of the HST prior and the blue (dashed) curve is for the PPS, Lens and BAO dataset combination.

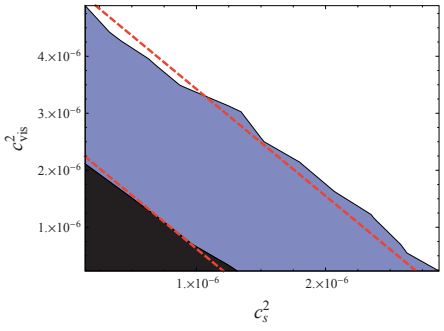


Figure 2 – The 68% and 95% confidence interval contours for $c^2_{\rm vis}$ and c^2_s, showing the strong negative correlation between these parameters. These contours are for PPS + Lens data. The red (dashed) lines denote lines of constant $c^2_s + \frac{8}{15}c^2_{\rm vis}$, showing that the degeneracy is well fit by the $k_{\rm dec}$ parameter (see Key Results).

2 MCMC analysis of the Planck data

In [3] we performed an MCMC analysis of the Planck data using the MontePython code [4] attached to our modified version of the Boltzmann code CLASS [5]. We considered two of models: the Λ-wDM model where CDM is replaced with GDM but only the equation of state w is non-zero, and the Λ-GDM model where all three GDM parameters are included. In addition, we assume that all three GDM parameters take constant values, i.e. have no time or space dependence.

The main dataset that we used was the Planck 2015 data release [6] of the CMB anisotropies. We used the full (temperature and polarisation) low-l likelihood and the full TT, EE and TE high-l likelihood. The combination of the high-l and low-l likelihoods will be referred as Planck Power Spectrum (PPS). We ran further chains that included the Planck lensing potential likelihood in addition, and found that this made a significant difference to the constraints on c^2_s and $c^2_{\rm vis}$.

Finally, we investigated the effect of including datasets that constrain the expansion history, notably the HST key project [7] and Baryon Acoustic Oscillation (BAO) data [8,9].

3 Key Results

- Strong constraints on w, c^2_s and $c^2_{\rm vis}$, see table 1
- BAO and/or HST data contribute significantly to constraints on background parameters
- CMB lensing data contributes significantly to constraints on perturbative parameters
- Minimal degeneracy between background (Ω_g,w) and perturbative (c^2_s,$c^2_{\rm vis}$) parameters
- Degeneracy between c^2_s and $c^2_{\rm vis}$: potential begins to decay at scale $k^{-1}_{dec}(\eta) = \eta\sqrt{c^2_s + \frac{8}{15}c^2_{\rm vis}}$

Table 1: Constraints on the GDM parameters for the two models and different combinations of experiments.

	Λ-wDM		Λ-GDM					
	$10^2 w$		$10^2 w$		$10^6 c_s^2$, upper bound		$10^6 c_{\rm vis}^2$, upper bound	
Likelihoods	95%	99.7%	95%	99.7%	95%	99.7%	95%	99.7%
PPS (Planck TT+Pol.)	$0.007^{+0.463}_{-0.466}$	$0.007^{+0.676}_{-0.673}$	$-0.040^{+0.473}_{-0.468}$	$-0.040^{+0.700}_{-0.701}$	3.31	6.31	5.70	11.3
PPS + Lens	$0.087^{+0.439}_{-0.448}$	$0.087^{+0.662}_{-0.648}$	$0.066^{+0.434}_{-0.427}$	$0.066^{+0.654}_{-0.642}$	1.92	3.44	3.27	5.99
PPS + Lens + HST	$0.256^{+0.217}_{-0.217}$	$0.256^{+0.322}_{-0.323}$	$0.259^{+0.216}_{-0.218}$	$0.259^{+0.321}_{-0.326}$	1.87	3.38	3.11	5.56
PPS + Lens + BAO	$0.063^{+0.108}_{-0.112}$	$0.063^{+0.163}_{-0.164}$	$0.074^{+0.111}_{-0.110}$	$0.074^{+0.164}_{-0.163}$	1.91	3.21	3.30	6.06

References

1. Wayne Hu. Structure formation with generalized dark matter. *Astrophys.J.*, 506:485–494, 1998.
2. M. Kopp, and et al. An extensive investigation of the Generalised Dark Matter model. *ArXiv e-prints*, May 2016.
3. D. B. Thomas, and et al. Constraining dark matter properties with Cosmic Microwave Background observations. *ArXiv e-prints*, January 2016.
4. B. Audren, and et al. Conservative constraints on early cosmology with MONTE PYTHON. *JCAP*, 2, February 2013.
5. Julien Lesgourgues. The Cosmic Linear Anisotropy Solving System (CLASS) I: Overview. *ArXiv e-prints*, 2011.
6. Planck Collaboration, N. Aghanim, and et al. Planck 2015 results. XI. CMB power spectra, likelihoods, and robustness of parameters. *ArXiv e-prints*, July 2015.
7. A. G. Riess, and et al. A 3% Solution: Determination of the Hubble Constant with the Hubble Space Telescope and Wide Field Camera 3. *ApJ*, 730:119, April 2011.
8. L. Anderson, and et al. The clustering of galaxies in the SDSS-III Baryon Oscillation Spectroscopic Survey: baryon acoustic oscillations in the Data Releases 10 and 11 Galaxy samples. *MNRAS*, 441:24–62, June 2014.
9. F. Beutler, and et al. The 6dF Galaxy Survey: baryon acoustic oscillations and the local Hubble constant. *MNRAS*, 416:3017–3032, October 2011.


GÉNÉPY









THE ACCELERATION OF THE MOON AND THE UNIVERSE

Göran Henriksson
Department of Physics and Astronomy, Uppsala University, Box 516, SE-751 20 Uppsala[a]



In 2015, I determined the margins of error in my new calibration of the lunar sidereal secular acceleration, -30.128 ± 0.0035 arcseconds/century^2($''/cy^2$), based on 33 ancient total solar eclipses. The lunar secular acceleration, from the Lunar Laser Range (LLR) measurements, $-25.856 \pm 0.003''/cy^2$, must be corrected for relativistic effects, $-3.604''/cy^2$, in the Earth-Moon-system to get the lunar secular acceleration, $-29.460''/cy^2$. The difference between this value and my new calibration, $-0.668 \pm 0.0046''/cy^2$, corresponds to the cosmological acceleration predicted by Dvali et al. in a modified theory of gravity with the mass of the graviton $1.306 \pm 0.009x10 - 56$grams.

1 Lunar sidereal secular acceleration in longitude from ancient total solar eclipses

In 1985 the author finished a computer program for calculation of ancient solar eclipses based on the theory for the motion of the sun and the moon by Carl Schoch[1], but with modern values for the astronomical constants. Schoch calibrated his lunar sidereal secular acceleration, -29.68 arcseconds/century^2($''/cy^2$), from a conjunction between the bright star Spica and the moon in 283 BC, and from an analysis of total solar eclipses dating back to 600 BC.

However, Schoch had a third-order term in the formula for the lunar longitude, introduced by Simon Newcomb. In 2011, I decided to eliminate this non-physical term and to optimise the physical value for the lunar sidereal secular acceleration. This value must give the same result as in the earlier successful calculations according to Schoch's original formula. A search started for the value of the lunar sidereal secular acceleration that gave the maximum sum of the magnitudes for 33 total, or almost total, solar eclipses between 878 AD and 3653 BC.

The new value for the lunar sidereal secular acceleration, $-30.128 \pm 0.0035''/cy^2$, gives an even better agreement with the ancient observations than the original formula[2]. It is valid at least during the last 5650 years with a timing error of less than two minutes.

2 The tidal acceleration of Moon from Lunar Laser Range (LLR) measurements

Among the scientific instruments onboard Apollo 11, which performed the first landing on the moon on 20 July 1969, there was a reflecting prism. There are now five reflecting prisms on the surface of the moon, the last arrived in 1973. An American and a French research team

[a] goran.henriksson@physics.uu.se

have performed parallel investigations. In the weighted mean I gave the value by Chapront et al[3], $-25.858 \pm 0.003''/cy^2$, weight three because its numerical value should be three times more accurate than $-25.85''/cy^2$ by Williams et al.[4] as this value has only two decimals and with no error estimate. The weighted mean of the lunar secular acceleration from the LLR-measurements in the Earth-Moon inertial system is: $-25.856 \pm 0.003''/cy^2$.

3 Relativistic effects in the Earth-Moon system according to Nordtvedt

In my earlier papers[5,6,2] I have used the precession of the geodesic by the Sun, $-1.92''/cy^2$, published by Nordtvedt[7]. In another paper,[8] he made a complete formula, to four decimal precision, for the relativistic effects in the Earth-Moon-system including also the Solar tidal acceleration and the precession of the geodesic by the Earth[9]. I have calculated these effects with four decimals to avoid rounding effects. They are, $-1.9189, +0.1177$ and $-0.0006''/cy^2$ respectively. The total relativistic effect on the lunar secular acceleration in longitude is $2x - 1.8018''/cy^2 = -3.6036/cy^2$.

4 The Radius of Crossover and the Mass of the Graviton

If the LLR measurements is corrected for the relativistic effect, $-3.6036''/cy^2$, we get the lunar secular acceleration, $-29.6938 \pm 0.003''/cy^2$. If this value is subtracted from the observed lunar sidereal secular acceleration $-30.128 \pm 0.0035''/cy^2$, by Henriksson, we get $-0.6685''/cy^2$ with total uncertainty $\pm 0.0046''/cy^2$. Dvali et al.[10] predicted in their theory for modified gravity an additional cosmological precession of the Earth-Moon-system. I have calculated this effect as $-0.5227''/cy^2$, from their formulas in chapter 3, with the radius of crossover, $rc = 6Gpc$ (1.85 x 1028 cm). If the observed additional acceleration, $-0.6685 \pm 0.0046''/cy^2$, is interpreted as the cosmological precession, the corresponding radius of crossover is 4.69 Gpc or 15.3 billion light years. The Age of the Universe is 13.8 billion years and the radius of the Universe is 46.5 billion light years. This means that the acceleration of the Universe started 4.54 billion years after Big Bang. According to chapter 4[10], the mass of the graviton $mg = 1/rc$. After converting units it is found that the mass of the graviton is $1.306 \pm 0.009x10 - 56$ grams. The massive graviton is 5-dimensional and needs a 5D space, but within distances $< rc$, a 4D theory is sufficient. For distances $> rc$, the gravitons begin to leak to the 5th dimension and the gravitational forces between the galaxies are weakened resulting in the observed acceleration of the Universe. The sign of the cosmological acceleration is negative which means that we find ourselves in the standard cosmological branch.

Acknowledgments

I am grateful to Dr. Andreas Korn for his critical reading of my text and to the Department. of Physics and Astronomy of Uppsala University for the financial support of my participation in the Rencontres de Moriond 2016.

References

1. C. Schoch, Astronomische Abhandlungen, Ergänzungs-hefte zu den Astronomischen Nachrichten, Band 8 B2 (1931). (World Scientific, Singapore, 1988)
2. G. Henriksson, Lunar secular acceleration supports a modified theory for gravity, Proceedings of the 49th Rencontres de Moriond, La Thuile, March 22-29 (2014)
3. J. Chapront, M. Chapront-Touz and G. Francou. A new determination of lunar orbital parameters, precession constant and tidal acceleration from LLR measurements. Astron. Astrophys. 387, 700-709 (2002)
4. J.G. Williams, D.H. Boggs and W.M. Folkner, DE421 Lunar orbit, Physical Librations, and Surface Coordinates. IOM 335-JW,DB,WF-20080314-001, March 14 (2008)
5. G. Henriksson, Astronomical Society of the Pacific, Conference Series 409, 166 (2009)
6. G. Henriksson, Journal of Cosmology 9, 2259 (2010)
7. K. Nordtvedt, Physics Today, May 1996, 49:5, 29 (1996)
8. K. Nordtvedt, The Relativistic Orbit Observables in Lunar Laser Ranging. ICARUS 114, 51-62.(1995)
9. A. Einstein, Annalen der Physik 49 (1916)
10. G. Dvali, A. Gruzinov, and M. Zaldarriaga, Phys. Rev. D, 68, Issue 2, id. 024012 (2003)

Bianchi type V viscous fluid dark energy cosmological model with gauge function

B. Mishra
Department of Mathematics,Birla Institute of Technology and Science-Pilani, Hyderabad Campus,Hyderabad-500078, INDIA, [a]

We have investigated Bianchi type V space-time in scale invariant theory with dark energy. The matter field is considered in the form of viscous fluid. The field equations for scale invariant theory has been solved by applying a variation law for generalized Hubble's parameter [Berman [7]]. The gauge function depends on time coordinate only (Dirac gauge). The cosmological model is constructed, its physical and kinematical properties are discussed.

1 Introduction

Another modification of Einstein's theory of gravitation is the scale invariant theory of gravitation proposed by Wesson [28,29]. This is one of the prominent alternative theory. In this theory, the Einstein field equations have been written in a scale dependent way by using the conformal or scale transformation as:

$$\bar{g_{ij}} = \beta^2(x^k) g_{ij}. \tag{1}$$

where the gauge function β, in its most general formulation, is a function of all space-time coordinates. Thus, using the conformal transformation of the type given by (1), Wesson [28,29] transforms the usual Einstein field equations into

$$G_{ij} + 2\frac{\beta_{;ij}}{\beta} - 4\frac{\beta_{,i}\beta_{,j}}{\beta^2} + (g^{ab}\frac{\beta_{,a}\beta_{,b}}{\beta^2} - 2g^{ab}\frac{\beta_{;ij}}{\beta})g_{ij} + \Lambda_0\beta^2 g_{ij} = -T_{ij}. \tag{2}$$

where $G_{ij} \equiv R_{ij} - \frac{1}{2}Rg_{ij}$. Semicolon and comma respectively denote covariant differentiation with respect to g_{ij} and partial differentiation with respect to coordinates. G_{ij} is the conventional Einstein tensor involving g_{ij}. R_{ij} is the Ricci tensor, and R is the Ricci scalar. The cosmological term Λg_{ij} of Einstein theory is now transformed to $\Lambda_0\beta^2 g_{ij}$ in scale invariant theory with dimensionless cosmological constant Λ_0. G is the Newtonian gravitational parameter. T_{ij} is the energy momentum tensor of the matter field. It is worthy to note that no independent equation for β exists in this theory. In this theory, Beesham [4,5,6], Mohanty and Daud [16], Mohanty and Mishra [17,18], Mishra [11,12], Mishra and Sahoo [13,14,15] have investigated several aspects of scale invariant theory.

Cosmic observations from supernovae [Riess et al.[23]; Perlmutter et al.[22]], cosmic microwave background (CMB) radiation [Spergel et al.[26]; Komatsu et al.[10]], large scale structure (LSS) [Tegmark et al.[27]; Seljak et al.[25]], baryon acoustic oscillations (BAO) [Eisenstein et al.[8]] and weak lensing [Jain and Taylor[9]] have implied that the expansion of the universe is accelerating at the present stage. The latest data sets coming from astrophysics and cosmological observations such as CMB and supernovae survey indicate that the energy budget of the universe is the following:

[a] bivudutta@yahoo.com

74 percent dark energy, 22 percent dark matter and 4 percent ordinary baryonic matter [Riess et al.[24]; Eisenstein et al.[8]; Astier et al.[2]; Spergel et al.[26]]. Nojiri and Odintsov[19,20,21], Bamba et al.[3] have developed the cosmological reconstruction method in terms of cosmological time.

2 Field equations for Bianchi Type V metric

Here we consider Bianchi type V space-time with a Dirac gauge function $\beta = \beta(ct)$ of the form

$$ds_W^2 = \beta^2(-dt^2 + A^2dx^2 + e^{2\alpha x}(B^2dy^2 + C^2dz^2)). \tag{3}$$

The metric potentials A, B and C are functions of t only. c is the velocity of light. ds_W^2 represents the intervals in Wesson theory. Further, $x^i, i = 1, 2, 3, 4$ respectively denote for x,y,z and t only. The energy momentum tensor T_{ij} in eqn. (2) in gravitational units $G = c = 1$ is the combination of viscous fluid $T_{ij}^{(vis)}$ and dark energy fluid $T_{ij}^{(de)}$, which can be expressed as

$$T_{ij}^{(vis)} = (\rho + \bar{p})u_iu_j + \bar{p}g_{ij} = diag[-\rho, p, p, p]. \tag{4}$$

where $\bar{p} = p - \xi u^i_{;i}$, and

$$\begin{aligned} T_{ij}^{(de)} &= diag[-\rho^{de}), p_x^{(de)}, p_y^{(de)}, p_z^{(de)}] \\ &= diag[-1, \omega_x, \omega_y, \omega_z]\rho^{(de)} \\ &= diag[-1, (\omega + \delta), (\omega + \gamma), (\omega + \eta)]\rho^{(de)}. \end{aligned} \tag{5}$$

The skewness parameters δ, γ, and η are the deviations from ω on x, y and z axes respectively. Hence, for the metric (3) and energy momentum tensor (4) and (5), the field equations for scale invariant theory (2) yield the following equations:

$$\frac{\ddot{B}}{B} + \frac{\ddot{C}}{C} + \frac{\dot{B}\dot{C}}{BC} - \frac{\alpha^2}{A^2} + 2\frac{\dot{\beta}}{\beta}\left(\frac{\dot{B}}{B} + \frac{\dot{C}}{C}\right) + 2\frac{\ddot{\beta}}{\beta} - \frac{\dot{\beta}^2}{\beta^2} + \Lambda_0\beta^2 = -p + 3\Xi H - (\omega + \delta)\rho^{(de)}. \tag{6}$$

$$\frac{\ddot{A}}{A} + \frac{\ddot{C}}{C} + \frac{\dot{A}\dot{C}}{AC} - \frac{\alpha^2}{A^2} + 2\frac{\dot{\beta}}{\beta}\left(\frac{\dot{A}}{A} + \frac{\dot{C}}{C}\right) + 2\frac{\ddot{\beta}}{\beta} - \frac{\dot{\beta}^2}{\beta^2} + \Lambda_0\beta^2 = -p + 3\Xi H - (\omega + \gamma)\rho^{(de)}. \tag{7}$$

$$\frac{\ddot{A}}{A} + \frac{\ddot{B}}{B} + \frac{\dot{A}\dot{B}}{AB} - \frac{\alpha^2}{A^2} + 2\frac{\dot{\beta}}{\beta}\left(\frac{\dot{A}}{A} + \frac{\dot{B}}{B}\right) + 2\frac{\ddot{\beta}}{\beta} - \frac{\dot{\beta}}{\beta^2} + \Lambda_0\beta^2 = -p + 3\Xi H - (\omega + \eta)\rho^{(de)}. \tag{8}$$

$$\frac{\dot{A}\dot{B}}{AB} + \frac{\dot{B}\dot{C}}{BC} + \frac{\dot{C}\dot{A}}{CA} - 3\frac{\alpha^2}{A^2} + 2\frac{\dot{\beta}}{\beta}\left(\frac{\dot{A}}{A} + \frac{\dot{B}}{B} + \frac{\dot{C}}{C}\right) + 3\frac{\dot{\beta}^2}{\beta^2} + \Lambda_0\beta^2 = \rho + \rho^{(de)}. \tag{9}$$

$$2\frac{\dot{A}}{A} - \frac{\dot{B}}{B} - \frac{\dot{C}}{C} = 0. \tag{10}$$

The over dot on a field variable denotes exact differentiation with respect to time t. We conserve the energy momentum tensors of the two sources separately. The energy conservation equation for the viscous fluid $T^{(vis)ij}_{;j} = 0$ and dark energy $T^{(de)ij}_{;j} = 0$ components respectively defined as $\dot{\rho} + 3(\bar{p} + \rho)H = 0$ and $\dot{\rho}^{(de)} + 3\rho^{(de)}(\omega + 1)H + \rho^{(de)}(\delta H_1 + \gamma H_2 + \eta H_3) = 0$. Then we split the conservation of energy momentum tensor of the dark energy into two parts [Akarsu and Kilinc [1]]. One corresponds to the deviations of equation of state (EoS) parameter and the other is the deviation free part. This can be expressed as:

$$\dot{\rho}^{(de)} + 3\rho^{(de)}(\omega + 1)H = 0 \tag{11}$$

$$\rho^{(de)}(\delta H_x + \gamma H_y + \eta H_z) = 0 \tag{12}$$

Now, the behaviour of ρ^{de} is controlled by deviation free part of EoS parameter of dark energy but deviations will affect ρ^{de} indirectly. For a physically viable model of the universe consistent with observations, the choice of skewness parameters are quite arbitrary. However, we consider the skewness parameters δ, γ and η be functions of cosmic time.

3 Solutions of the field equations

In the field eqns.(6)-(9), number of unknowns exceeds the number of equations. In order to obtain explicit exact solution, we need additional constraints relating to the unknowns. With the help of special law of variations proposed by Berman [7], which yields constant deceleration parameter of the models of the universe, we will solve the system of equations. The constant deceleration parameter model for defined as

$$q = -\frac{R\ddot{R}}{\dot{R}^2} = constant \tag{13}$$

where $R = (ABC)^{\frac{1}{3}}$. Hence, eqn.(13) yields the solution

$$R = \left(R_0^{(1+q)} + (1+q)(t-t_0)\right)^{\frac{1}{1+q}} \tag{14}$$

where R_0 is the integration constant and taken as 1 and $1+q>0$. Again using the physical condition that the shear scalar σ is proportional to scalar expansion θ, we take

$$B = C^m \tag{15}$$

where m is constant. With the help of eqns.(10), (14) and (15), we obtain the expression for the metric potentials as $A = R, B = C^m = R^{\frac{2m}{m+1}}$. We also consider $\beta = \beta(t) = \frac{1}{t}$ and express the directional Hubble parameter in terms of the mean Hubble parameter H as $H_x = H$, $H_y = \left(\frac{2m}{m+1}\right)H$, $H_z = \left(\frac{2}{m+1}\right)H$. Now,eqns. (6), (7), (8) and (12) yields the following

$$\gamma\rho^{de} = -\left(\frac{1-m}{1+m}\right)\left(\frac{m+5}{3(m+1)}\right)\left(\frac{\ddot{R}}{R} + 2\frac{\dot{R}^2}{R^2} - \frac{2}{t}\frac{\dot{R}}{R}\right) \tag{16}$$

$$\eta\rho^{de} = \left(\frac{1-m}{1+m}\right)\left(\frac{1+5m}{3(m+1}\right)\left(\frac{\ddot{R}}{R} + 2\frac{\dot{R}^2}{R^2} - \frac{2}{t}\frac{\dot{R}}{R}\right) \tag{17}$$

$$\delta\rho^{de} = \left(\frac{1-m}{1+m}\right)\left(\frac{2(m-1)}{3(m+1}\right)\left(\frac{\ddot{R}}{R} + 2\frac{\dot{R}^2}{R^2} - \frac{2}{t}\frac{\dot{R}}{R}\right) \tag{18}$$

We use the barotropic bulk viscus pressure and fluid relation $\bar{p} = \epsilon\rho$, where ϵ is a constant. Then the energy density ρ can be obtained as

$$\rho = \frac{\rho_0}{(ABC)^{1+\epsilon}} = \frac{\rho_0}{R^{3(1+\epsilon)}} \tag{19}$$

Subsequently, the energy density for dark energy component can be found as

$$\rho^{de} = \left(\frac{2(m^2+4m+1)}{(m+1)^2}\right)\frac{\dot{R}^2}{R^2} - 3\frac{\alpha^2}{R^2} - \frac{6}{t}.\frac{\dot{R}}{R} + \frac{3+\Lambda_0}{t^2} - \frac{\rho_0}{R^{3(1+\epsilon)}} \tag{20}$$

Now, Using eqn. (20), eqns. (16)-(18) reduces to

$$\gamma = -\frac{\left(\frac{1-m}{1+m}\right)\left(\frac{m+5}{3(m+1)}\right)\left(\frac{\ddot{R}}{R}+2\frac{\dot{R}^2}{R^2}-\frac{2}{t}\frac{\dot{R}}{R}\right)}{\left(\frac{2(m^2+4m+1)}{(m+1)^2}\right)\frac{\dot{R}^2}{R^2}-3\frac{\alpha^2}{R^2}-\frac{6}{t}.\frac{\dot{R}}{R}+\frac{3+\Lambda_0}{t^2}-\frac{\rho_0}{R^{3(1+\epsilon)}}} \tag{21}$$

$$\eta = \frac{\left(\frac{1-m}{1+m}\right)\left(\frac{1+5m}{3(m+1)}\right)\left(\frac{\ddot{R}}{R}+2\frac{\dot{R}^2}{R^2}-\frac{2}{t}\frac{\dot{R}}{R}\right)}{\left(\frac{2(m^2+4m+1)}{(m+1)^2}\right)\frac{\dot{R}^2}{R^2}-3\frac{\alpha^2}{R^2}-\frac{6}{t}.\frac{\dot{R}}{R}+\frac{3+\Lambda_0}{t^2}-\frac{\rho_0}{R^{3(1+\epsilon)}}} \tag{22}$$

$$\delta = \frac{\left(\frac{1-m}{1+m}\right)\left(\frac{2(m-1)}{3(m+1)}\right)\left(\frac{\ddot{R}}{R}+2\frac{\dot{R}^2}{R^2}-\frac{2}{t}\frac{\dot{R}}{R}\right)}{\left(\frac{2(m^2+4m+1)}{(m+1)^2}\right)\frac{\dot{R}^2}{R^2}-3\frac{\alpha^2}{R^2}-\frac{6}{t}.\frac{\dot{R}}{R}+\frac{3+\Lambda_0}{t^2}-\frac{\rho_0}{R^{3(1+\epsilon)}}} \tag{23}$$

Moreover, the EOS parameter ω is obtained as

$$\omega = \frac{-\frac{2}{3}\left(\frac{m^2+4m+1}{(1+m)^2}\right)\left(2\frac{\ddot{R}}{R}+\frac{\dot{R}^2}{R^2}-\frac{2}{t}2\frac{\dot{R}}{R}\right)-\frac{\alpha^2}{R^2}+\frac{3+\Lambda_0}{t^2}-\frac{\epsilon\rho_0}{R^{3(1+\epsilon)}}}{\left(\frac{2(m^2+4m+1)}{(m+1)^2}\right)\frac{\dot{R}^2}{R^2}-3\frac{\alpha^2}{R^2}-\frac{6}{t}.\frac{\dot{R}}{R}+\frac{3+\Lambda_0}{t^2}-\frac{\rho_0}{R^{3(1+\epsilon)}}} \tag{24}$$

4 Some Physical and Kinematical properties of the Model

In this section, we have investigated some physical behaviour of the constructed model. The scalar expansion of the model, $\theta = \frac{A_4}{A}+\frac{B_4}{B}+\frac{C_4}{C} = 3\left[1+(1+q)(t-t_0)\right]^{-1}$, which indicates that the scalar expansion remains constant for $t=0$; however for large value of t, the expansion decreases. The spatial volume found to be, $V = R^3 = ABC = \left[1+(1+q)(t-t_0)\right]^{\frac{1}{1+q}}$. It is observed that the spatial volume is unity at $t=t_0$ and it increases as t increases. Thus, the universe starts evolving with unit volume at $t=t_0$ and expands with cosmic time t. Also, for $1+q>0$, the universe is expanding. The shear scalar, $\sigma^2 = \frac{1}{2}\left(\Sigma H_i^2-\frac{1}{3}\theta^2\right) = \left(\frac{m-1}{m+1}\right)^2\left[1+(1+q)(t-t_0)\right]^{-2}$ becomes constant for large value of t. Therefore the shape of the universe remains unchanged during evolution. Moreover, $\frac{\sigma^2}{\theta^2}$ turns out to be a constant, the model does not approach isotropy for large value of t. However, for $m=1$, the model becomes isotropic.

The generalized mean Hubble's parameter H is $H = \frac{1}{3}(H_x+H_y+H_z) = \left[1+(1+q)(t-t_0)\right]^{-1}$. The Hubble's parameter is unity at $t=t_0$. The rate of expansion is accelerated or decelerated depends on the signature of the parameter. However, as $1+q>0$, the model indicates acceleration. The average anisotropy parameter is calculated as $A_m = \frac{4}{3}\Sigma\left(\frac{\Delta H_i}{H}\right)^2 = \frac{2}{3}\left(\frac{m-1}{m+1}\right)^2$. Now, the mean anisotropic parameter is uniform throughout the evolution of the universe since A_m is constant. The energy density, $\rho(t) = \frac{\rho_0}{R^{3(1+\epsilon)}} = \frac{\rho_0}{[Q(t)]^{\frac{3(1+\epsilon)}{1+q}}}$, vanishes for large t,where $Q(t) = [1+(1+q)(t-t_0)]$. The EoS parameter ω, obtained as

$$\omega = \frac{-\frac{2}{3}\left(\frac{m^2+4m+1}{(1+m)^2}\right)\left(\frac{1-2q}{[Q(t)]^2}-\frac{4}{t[Q(t)]}\right)-\frac{\alpha^2}{[Q(t)]^{\frac{2}{1+q}}}+\frac{3+\Lambda_0}{t^2}-\frac{\epsilon\rho_0}{[Q(t)]^{\frac{3(1+\epsilon)}{1+q}}}}{\left(\frac{2(m^2+4m+1)}{(m+1)^2}\right)\frac{1}{[Q(t)]^2}-3\frac{\alpha^2}{[Q(t)]^{\frac{2}{1+q}}}-\frac{6}{t[Q(t)]}+\frac{3+\Lambda_0}{t^2}-\frac{\rho_0}{[Q(t)]^{\frac{3(1+\epsilon)}{1+q}}}}$$

It is observed that δ and γ are functions of time t. Moreover, δ and γ never diverges as t vanishes.

5 Conclusions

In this paper, we have investigated Bianchi type V dark energy cosmological models with variable EoS parameter in scale invariant theory of gravitation. In the constructed model, it is observed that the dark energy model in scale invariant theory is consistent with the recent observations of Type Ia supernovae. The EoS parameters and skewness parameter turn out to be functions of cosmic time t. This study is significant, because dark energy is the best candidate to explain the cosmic acceleration in the general and alternative theories of gravitation.

Acknowledgement

BM acknowledge SERB-DST, New Delhi, India for financial support to carry out the Research project[No. SR/S4/MS:815/13].

References

1. Akarsu, O., Kilinc, C.B.: Gen. Rel Grav. **42**, 119 (2010).
2. Astier, P., et al.: Astron. Astrophys. **447**, 31 (2006).
3. Bamba, K., et al.: Astrophys Space Sci. **342**, 155 (2012).
4. Beesham, A.: Clasic. Quant. Grav. **3**, 481(1986a).
5. Beesham, A.: Astophys. Space Sci. **119**, 415(1986b).
6. Beesham, A.: Clasic. Quant. Grav. **3**, 1027(1986c).
7. Bermann, M.S.: Nuovo Cimento B**74**, 182(1983).
8. Eisenstein, D.J., et al.: (SDSS) Astron. J. **633**, 560 (2005).
9. Jain, B., Taylor, A.: Phys. Rev. Lett.**91**, 141302 (2003).
10. Komatsu, E., et al.: The Astrophys J. **180**,330 (2009).
11. Mishra, B.: Chinese. Phys. Lett.**21(12)**, 2359(2004).
12. Mishra, B.: Turk. J. Phys. **32**, 357(2008).
13. Mishra, B., Sahoo, P.K.: Int. J. pure and Appl. Maths.**80(4)**, 535(2012a).
14. Mishra, B., Sahoo, P.K.: Int. J. Theo. Phys.**51(2)**, 399(2012b).
15. Mishra, B., Sahoo, P.K.: Astrophys. Space Sci.**349**, 491(2014).
16. Mohanty, G., Daud, S.M.: Theo. Appl. Mechanics**23**, 115(1997).
17. Mohanty, G., Mishra, B.: Czech. J. Phys**51**, 525(2002).
18. Mohanty, G., Mishra, B.: Astrophys. Space Sci.**283**, 67(2003).
19. Nojiri,S., Odintsov, S.D.: Phys. Rev.D **68**, 123512 (2003).
20. Nojiri, S., Odintsov, S.D.: Phys. Rev. D. **72**, 023003 (2005).
21. Nojiri, S., Odintsov, S.D.: Phys. Rep.**505**, 59 (2011).
22. Perlmutter, S., et al.: Astrophys. J. **517**, 565 (1999).
23. Riess, A.G., et al.: Astron. J. **116**, 1009 (1998) .
24. Riess, A.G., et al. :(Supernova Search Team): Astron. J. **607**, 665 (2004).
25. Seljak, U., et al.: Phys Rev. D **71**,103515 (2005).
26. Spergel, D.N., et al.: (WMAP) Astrophys. J. Suppl. Ser. **170**,3771 (2007).
27. Tegmark, M., et al.: Phys Rev. D **69**,103510 (2004).
28. Wesson, P.S.: Astron. Astrophys.**102**, 45 (1981a).
29. Wesson, P.S.: Mon. Not. R. Astro. Soc.**39**, 429 (1981b).


Ale House
QUALITY
ALES

STATIC AND OSCILLATING UNIVERSES

J. KEHAYIAS
Department of Physics & Astronomy, Vanderbilt University,
PMB 401807, 2301 Vanderbilt Place,
Nashville, TN 37235-1807, United States

This contribution is based on work[1] in collaboration with Robert Scherrer, as well as earlier work[2] with Anthony Aguirre. We consider static and oscillating cosmological solutions in General Relativity with a single barotropic fluid. A barotropic fluid has the general equation of state $p = f(\rho)$, where p is the pressure and ρ is the energy density. We provide examples and derive conditions for these solutions. This work extends and generalizes earlier studies on such cosmological solutions. These solutions generally have various instabilities, such as tunneling to zero size or being sensitive to quantum fluctuations. In addition, we find a classical instability (a "no-go") for oscillating solutions due to a negative squared sound speed.

1 Introduction and Summary

While our current understanding of the universe indicates we live in a time of accelerated expansion, it is possible that a static or oscillating state may have played a role in the past, or will in the future. Additionally, while such cosmological solutions of General Relativity (GR) are interesting in their own right, they potentially address some deep questions in cosmology. For instance, the question of initial conditions and a "beginning of time." A static solution is also the past asymptotic state of the universe in the "emergent universe" inflationary scenario[3 4], which can avoid a quantum gravity era, has no horizon problem, and other attractive features.

However, these types of solutions generically have instabilities, both classical and quantum. One generic problem is the possibility to tunnel to zero size[5]. Often these cosmologies require precise tunings, and are thus susceptible to quantum fluctuations[2] spoiling this delicate balance.

In work[1] with Robert Scherrer we look at a very general class of models, ones with a single barotropic fluid, with equation of state $p = f(\rho)$. This encapsulates many different models previously considered in the literature (such as Chaplygin gas models); our results generalize and extend previous work. We derive conditions for static and oscillating solutions and find that classically stable static solutions exist, while oscillating solutions have a general classical instability. However, the static solutions have quantum mechanical instabilities as well.

2 Solutions and Instabilities

We consider a single barotropic fluid in an isotropic and homogeneous universe. There is a static solution, with $\dot{a} = \ddot{a} = 0$, at a specific density, ρ_*, scale factor, a_*, and equation of state parameter $w = -1/3$. They are related by

$$\rho_* = \frac{3k}{a_*^2}, \tag{1}$$

where k is the curvature, required to be $+1$ here. The condition for stability is

$$\frac{\mathrm{d}w}{\mathrm{d}a} > 0 \qquad \Rightarrow \qquad \frac{\mathrm{d}p}{\mathrm{d}\rho} < -1/3. \tag{2}$$

An example of such a (classically) stable static solution can be found in the generalized Chaplygin gas model[6] with equation of state $p = -A/\rho^{\alpha}$.

The static solutions, although classically stable, can suffer from quantum instabilities. Using the Wheeler-DeWitt equation, we see that the generalized Chaplygin gas model (as an example) has a minimum at $a = 0$. Even without such a minimum, the tunneling rate to zero size cannot generically be made to vanish[7], and thus the solution is unstable. Furthermore, the precise tuning required for static models in general will be spoiled by quantum fluctuations[2], and they cannot be long-lived.

Besides small oscillations about the static solution, we can look for more general oscillating possibilities. Such a solution has to satisfy eq. (1) at the minimum and maximum for a, as well as $\ddot{a} > 0$ ($\ddot{a} < 0$) at the minimum (maximum). If w is a monotonic function of a, then this requires

$$\frac{\mathrm{d}w}{\mathrm{d}a} > 0 \qquad \equiv \qquad \frac{\mathrm{d}p}{\mathrm{d}\rho} < \frac{p}{\rho}, \tag{3}$$

during both the contracting and expanding phases. If w is always negative this can be written as

$$\frac{\mathrm{d}\ln p}{\mathrm{d}\ln \rho} > 1. \tag{4}$$

Again, the generalized Chaplygin gas has such an oscillating solution.

However, there is an instability for the oscillating solutions: for a perfect fluid, perturbation growth is unstable when the sound speed $c_{\mathrm{s}}^2 \equiv \mathrm{d}p\,/\,\mathrm{d}\rho < 0$. The requirements above immediately lead to c_{s}^2 being necessarily negative. Thus we have a "no-go" theorem: a single (perfect) barotropic fluid, along with positive curvature, cannot have a stable oscillating solution.

While we can construct both static and oscillating solutions with a single barotropic fluid, the instabilities one usually finds for such solutions in GR persist here as well. Indeed, it appears very difficult (impossible?) to find stable and well-behaved eternal cosmologies. Whether this is a true feature of GR, or gravity more generally, is still being explored.

Acknowledgments

The author was supported in part by the United States Department of Energy (DE-SC0011981).

References

1. John Kehayias and Robert J. Scherrer. Oscillating and Static Universes from a Single Barotropic Fluid. *JCAP*, 1512(12):015, 2015.
2. Anthony Aguirre and John Kehayias. Quantum Instability of the Emergent Universe. *Phys.Rev.*, D88:103504, 2013.
3. George F.R. Ellis and Roy Maartens. The emergent universe: Inflationary cosmology with no singularity. *Class.Quant.Grav.*, 21:223–232, 2004.
4. George F.R. Ellis, Jeff Murugan, and Christos G. Tsagas. The Emergent universe: An Explicit construction. *Class.Quant.Grav.*, 21:233–250, 2004.
5. Audrey T. Mithani and Alexander Vilenkin. Collapse of simple harmonic universe. *JCAP*, 1201:028, 2012.
6. M. C. Bento, O. Bertolami, and A. A. Sen. Generalized Chaplygin gas, accelerated expansion and dark energy matter unification. *Phys. Rev.*, D66:043507, 2002.
7. Audrey T. Mithani and Alexander Vilenkin. Stabilizing oscillating universes against quantum decay. *JCAP*, 1507(07):010, 2015.

5.
Neutrinos and Cosmology

CONSTRAINTS ON NEUTRINO MASSES WITH LYMAN-α FOREST POWER SPECTRUM

Ch. YÈCHE
CEA-Saclay, Irfu F-91191 Gif-sur-Yvette, France



We present constraints on neutrino masses in the case of the ΛCDMν and ΛWDM models, using the one-dimensional Lyα-forest power spectrum measured the Baryon Oscillation Spectroscopic Survey (BOSS) of the Sloan Digital Sky Survey (SDSS-III), complemented by Planck 2015 Cosmic Microwave Background (CMB) data. Fitting Lyα data alone leads to cosmological parameters in excellent agreement with the values derived independently from CMB data, except for a weak tension on the scalar index n_s. Combining BOSS Lyα with Planck CMB constrains the sum of neutrino masses to $\sum m_\nu < 0.12$ eV (95% C.L.) including all identified systematic uncertainties. In the case of ΛWDM model, we issue the tightest bounds to date on pure dark matter particles: $m_X \gtrsim 4.35\,\mathrm{keV}$ (95% C.L.) for early decoupled thermal relics and its corresponding bound for a non-resonantly produced right-handed neutrino $m_s \gtrsim 26.4\,\mathrm{keV}$ (95% C.L.).

1 Introduction

The flux power spectrum of the Lyman-α (Lyα) forest in quasar absorption spectra is a powerful tool to study clustering in the Universe, at redshifts $\sim 2-4$. Compared to a model derived from a set of dedicated hydrodynamical simulations, the Lyα-flux power spectrum can provide valuable information on the formation of structures and their evolution. Furthermore, by probing scales down to a few Mpc, the 1D flux power spectrum is also sensitive to neutrino masses through the suppression of power on small scales that neutrinos induce because they become non-relativistic at small redshift and they therefore free-stream during most of the history of structure formation. We here use the 1D Lyα flux power spectrum measured by [1] with the DR9 release of BOSS quasar data , and a grid of 36 hydrodynamical simulations having a resolution equivalent to 3×3072^3 particles in a $(100\ h^{-1}\ \mathrm{Mpc})^3$ box [2, 3], to constrain both cosmology and the sum of the neutrino masses $\sum m_\nu$.

Cosmic Microwave Background (CMB) can also constrain $\sum m_\nu$. In the standard thermal history of the Universe, massless neutrinos have a temperature corresponding to ~ 0.17 eV at the epoch of last scattering. This temperature sets the range of masses for which neutrinos start to have an appreciable effect on the CMB power spectrum to $\sum m_\nu > 3 \times 0.17 = 0.51$ eV. Below this mass, the neutrinos are still relativistic at recombination and have no impact on the

primary CMB anisotropies. The latest limit on $\sum m_\nu$ from CMB data alone is at the level of 0.7 eV [4].

Lyα data alone have sensitivity to $\sum m_\nu$ at the level of about 1 eV due to the fact that the scales probed by Lyα forests are in the region where the ratio of the power spectra for massive to massless neutrinos is quite flat. However, a tight constraint on $\sum m_\nu$ can be obtained by combining CMB data, which probe the initial power spectrum unaffected by $\sum m_\nu$, and Lyα data, which probe the suppressed power spectrum. Thus, Lyα measures the power spectrum level, defined by σ_8 and Ω_m, CMB provides the correlations between these parameters and $\sum m_\nu$, and the joint use of these two probes significantly improves the constraint on $\sum m_\nu$ compared to what either probe alone can achieve.

In the case of ΛWDM models, when traveling, massive particles can interfere with the gravitational collapse of structures. This manifests in a step-like suppression in the matter power spectrum at scales above $\sim 0.01(\mathrm{km/s})^{-1}$ for particles of a few keV. These particles have a free-streaming scale which falls below the Mpc range and within the region probed by the Lyα forests of distant high redshift quasars. Lyα forest data therefore provide again an ideal tool to study keV-range WDM and give constraints on the lower-bound mass of early decoupled thermal relics.

2 Data, Simulations and Methodology

As our large-scale structure probe, we use the 1D Lyα-flux power spectrum measurement [1] from the first release of BOSS quasar data. The data consist of a sample of 13 821 spectra selected from the larger sample of about 60 000 quasar spectra of the SDSS-III/BOSS DR9 [5, 6] on the basis of their high quality, high signal-to-noise ratio and good spectral resolution ($< 85\,\mathrm{km\ s^{-1}}$ on average over a quasar forest). We use 12 redshift bins, spanning the range $2.1 < z < 4.5$, as shown on Fig. 1. We do the analysis on 420 Lyα data points, consisting of 12 redshift bins and 35 k bins.

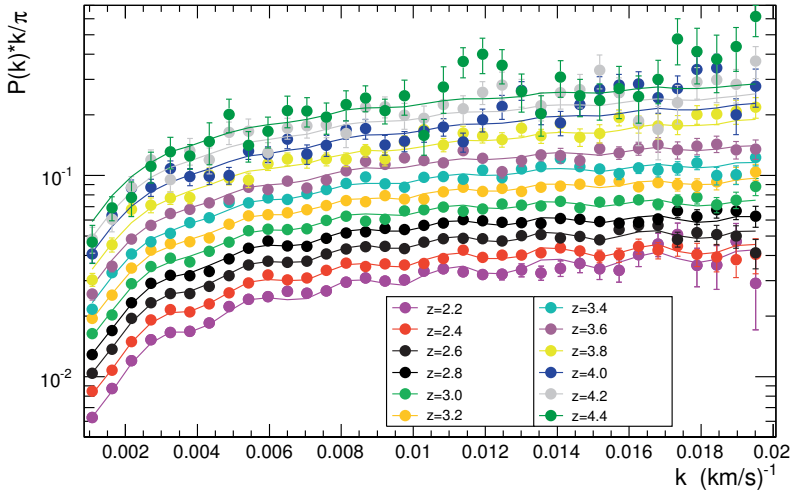


Figure 1 – *1D Lyα forest power spectrum from the SDSS-III/BOSS DR9 data. The solid curves show the best-fit model when considering Lyα data alone. The oscillations arise from Lyα-Si III correlations, which occur at a wavelength separation $\Delta\lambda = 9.2\AA$.*

The cosmic microwave background (CMB) data and results we use, are described in the 2015 Planck cosmological parameters paper [4]. In our analysis [7], we consider several subsets of Planck data and we obtain very similar results for the different configurations. Therefore, in this proceeding, we focus on the base configuration, denoted 'TT+lowP' as in [4] which uses the TT spectra at low and high multipoles and the polarization information up to multipoles $\ell = 29$ ('lowP').

The cosmological interpretation of the Lyα power spectrum measurement is obtained by comparison to a set of full hydrodynamical cosmological simulations that were produced specifically for that purpose (see Fig. 2). The methodology and technical framework for these simulations are presented in [2], while all issues concerning the inclusion of neutrinos in the pipeline and their impact on the power spectrum are described in detail in [3]. The neutrinos, considered as three degenerate species, are globally introduced as a third particle type, in addition to cold dark matter and baryons. The simulations were run using `CAMB` to compute the transfer functions and linear power spectra at $z = 30$, then `2LPT` (second-order Lagrangian Perturbation Theory) to compute the initial displacement of the particles, and finally `GADGET-3` [8] for the hydrodynamical processing. Using a splicing technique [2], we infer the flux power spectrum of an equivalent ($L = 100\,h^{-1}$ Mpc, $N = 3072$) simulation from a combination of three lesser ones: a scaled-down (25, 768) to provide high resolution on small scales, a large-box low-resolution (100, 768) for large scales, and a small-box low-resolution (25, 192) which bridges the preceding two at intermediate scales.

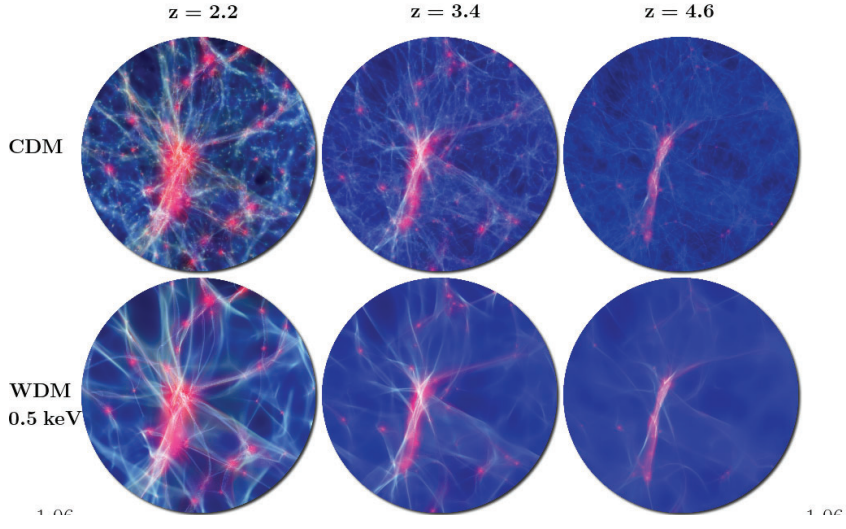


Figure 2 – *Visual inspection of the baryon gas density and temperature (encoded in intensity and color respectively), at $z = 2.5$, at $z = 3.4$ and at $z = 4.6$ for CDM (top panels) and for DM particle masses of 0.5 keV (bottom panels). Panels are 8 h^{-1}* Mpc *across in comoving coordinates.*

The ΛWDM analysis described in [9] shares a similar strategy. We just use two particle types, baryons and dark matter instead of three types. We explore two pure ΛWDM models with $m_X = 2.5$ and 5 keV thermal relics implemented using the neutrino mass degeneracy parameters in CAMB to encode $\Delta N_{\rm eff} \propto (T/T_\nu)^4$, which models the impact of any massive particle with temperature T coupled to photons prior to standard neutrino decoupling.

By varying the input parameters (cosmological and astrophysical parameters, total neutrino mass or inverse of thermal relic mass) around a central model chosen to be in agreement with the latest Planck results [4], the simulations were used to derive a second-order Taylor expansion,

including cross-terms, around the central model. Finally, we minimize a likelihood built around three categories of parameters which are floated. The first category describes the cosmological model assuming a flat Universe. The second category models the astrophysics within the IGM, and the relationship between the gas temperature and its density. The purpose of the third category (nuisance parameters) is to describe the imperfections of our measurement of the 1D power spectrum. This likelihood allows us to compare the measurement to the power spectrum predicted from the hydrodynamical simulations described above.

3 Results for ΛCDMν

The maximization of the likelihood with the Lyα data, imposing a Gaussian constraint $H_0 = 67.4 \pm 1.4$ gives a best-fit value of $\sum m_\nu$, the sum of the neutrino masses equal to 0.41 eV and compatible with 0 at about 1σ as described in[7]. The upper bound on $\sum m_\nu$ is thus 1.1 eV (95% C.L.). The cosmological parameters $\sigma_8 = 0.830 \pm 0.032$ and $\Omega_m = 0.293 \pm 0.013$ are in excellent agreement with the values derived independently from CMB data [4]. We observe a weak tension at the 2.3 σ level on the scalar index, $n_s = 0.939 \pm 0.010$. The fitted values of the astrophysical and nuisance parameters are all well within the expected range. The 2D constraints in the $n_s - \sigma_8$, $\sum m_\nu - \Omega_m$ and $\sum m_\nu - \sigma_8$ planes are shown as the red contours in Fig. 3. The neutrino mass is correlated to σ_8 (-48%), n_s (48%) and Ω_m (52%). Correlations between all other cosmological parameters have smaller amplitudes.

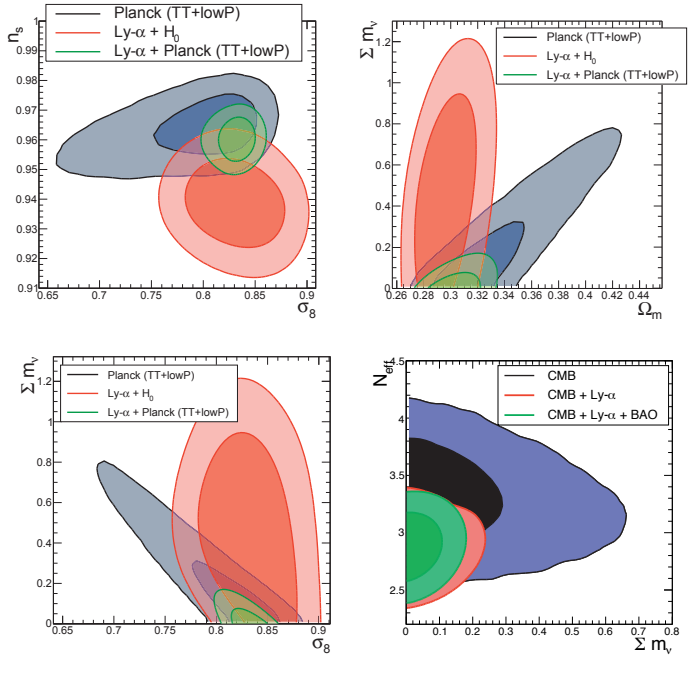


Figure 3 – **Unclockwise from top left:** *2D confidence level contours for the* $(\Omega_m, \sum m_\nu)$, (σ_8, n_s) *and* $(\sigma_8, \sum m_\nu)$ *cosmological parameters (see full description in [7]). The 68% and 95% confidence contours are obtained for the BOSS Ly*α *data with a Gaussian constraint* $H_0 = 67.4 \pm 1.4$ km s^{-1} Mpc^{-1}*, for the Planck 2015 data (TT+lowP) and for the combination of BOSS Ly*α *and Planck 2015.* **Bottom left** *2D confidence level contours for the* $(\sum m_\nu, N_{eff})$ *cosmological parameters for the CMB (Planck 2013, ACT, SPT and WMAP polarization) alone, then adding BOSS Ly*α *and finally BAO (see full description in [10]).*

Then we combine the Lyα likelihood (imposing no constraint on H_0) with the likelihood of Planck 2015 data. We constrain $\sum m_\nu$ to be less than 0.12 eV (at 95% C.L.) from Lyα and Planck TT+lowP, closer to to the inverted-hierarchy lower bound of 0.10 eV than current CMB-based limits. For comparison, Planck (TT+lowP) alone constrains the sum of the neutrino masses to $\sum m_\nu < 0.72\ eV$ and Planck (TT+lowP) with BAO measurements to $\sum m_\nu < 0.21$ eV.

In addition, with Ly-α data we can constrain the effective number of neutrino species, $N_{\rm eff}$, as described in a similar analysis [10]. Fig. 3-bottom-left summarizes the main results of our fitting procedure for the values of $N_{\rm eff}$ and $\sum m_\nu$, derived by combining CMB (Planck 2013 + ACT + SPT + WMAP polarization as defined in [11], blue contours) with Lyα forest data (red contours), or by further adding BAO information (green contours). Specifically, we obtain $N_{\rm eff} = 2.91^{+0.21}_{-0.22}$ (95% CL) and $\sum m_\nu < 0.15$ eV (95% C.L.) in the first case, and $N_{\rm eff} = 2.88 \pm 0.20$ (95% C.L.) and $\sum m_\nu < 0.14$ eV (95% C.L.) in the second. These tight constraints on $N_{\rm eff}$ exclude the possibility of a sterile neutrino thermalized with active neutrinos – or more generally of any decoupled relativistic relic with $\Delta N_{\rm eff} \simeq 1$ - at significance of over 5 σ, implying that there is no need for exotic neutrino physics in the concordance ΛCDM model. These results are fully consistent with the latest constraints reported by Planck 2015 [4].

4 Results for ΛCDMν with n_s running

The small tension between the values of n_s preferred by Lyα or Planck data motivates a combined fit allowing n_s to vary with scale. We thus introduce $\mathrm{d}n_s/\mathrm{d}\ln k$ by using the corresponding Planck chains and adapting the Lyα likelihood to include a running of n_s (see details in [7]). We choose a pivot scale $k_0 = 0.05\ \mathrm{Mpc}^{-1}$, the same as in the analyses led by the Planck collaboration in order to allow direct comparisons. The scalar mode power spectrum is then parameterized by a power law with

$$P_s = \left(\frac{k}{k_0}\right)^{n_s - 1 + \frac{1}{2}\mathrm{d}n_s/\mathrm{d}\ln k \ln(k/k_0)} . \quad (1)$$

The pivot scale k_0 is approximately in the middle of the logarithmic range of the scales probed by Planck. The Lyα forests cover scales ranging from $\sim 0.07\ \mathrm{Mpc}^{-1}$ to $\sim 1.7\ \mathrm{Mpc}^{-1}$, with a pivot near $k_{Ly\alpha} \sim 0.7\ \mathrm{Mpc}^{-1}$. The constraint that we can derive on the running index $\mathrm{d}n_s/\mathrm{d}\ln k$ comes mostly from the different levels of the power spectra at the CMB and Lyα pivot scales k_0 and $k_{Ly\alpha}$.

On the theoretical side, the simplest inflationary models predict that the running of the spectral index should be of second order in inflationary slow-roll parameters and therefore small, $|\mathrm{d}n_s/\mathrm{d}\ln k| \sim (n_s - 1)^2 \sim 10^{-3}$ [12]. Nevertheless, it is possible to accommodate a larger scale dependence of n_s, by adjusting the third derivative in the inflaton potential, for instance. On the experimental side, recent CMB experiments have a mixed history of null-results and a-few-sigma detections of running of the scalar index. The final 9-year WMAP analysis found no evidence of running using WMAP alone, with $\mathrm{d}n_s/\mathrm{d}\ln k = -0.019 \pm 0.025$ at 68% CL, while the combination of WMAP data with the first data releases from ACT and SPT found a negative running at nearly the 2σ level with $\mathrm{d}n_s/\mathrm{d}\ln k = -0.022 \pm 0.012$ [13]. The Planck 2015 results, while roughly consistent with zero running of the scalar spectral index, indicate a $\sim 1\sigma$ preference for negative running, $\mathrm{d}n_s/\mathrm{d}\ln k = -0.0084 \pm 0.0082$.

Allowing a running of n_s improves the fit χ^2 by ~ 10 compared to the results obtained for the same set of data but without running and it gives $n_s = 0.960 \pm 0.004$ at CMB pivot, k_0 and $\mathrm{d}n_s/\mathrm{d}\ln k = -0.0149^{+0.0050}_{-0.0048}$. This is driven by the fact that a negative running of order 10^{-2} is favored both by Planck data alone, and by the tension on n_s between Planck and Lyα data sets. The corresponding 2D contours are illustrated in figure 4, left plot.

As the global χ^2 is clearly improved by letting $\mathrm{d}n_s/\mathrm{d}\ln k$ free, it is interesting to study the impact of this extra parameter on the determination of $\sum m_\nu$ in the base ΛCDMν model with running. As shown on the right plot of the figure 4, the correlation between $\mathrm{d}n_s/\mathrm{d}\ln k$ and

$\sum m_\nu$ is small. By adding this free parameter, $\mathrm{d}n_s/\mathrm{d}\ln k$ we obtain a limit $\sum m_\nu < 0.19$ eV (95% C.L.) which is less constraining limit as expected. However, if we add the BAO data, we recover the constraint without the additional free parameter, $\sum m_\nu < 0.12$ eV (95% C.L.).

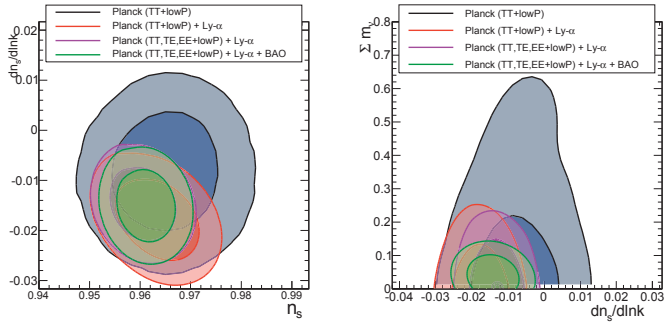


Figure 4 – *Constraints on the scalar spectral index n_s, the running $\mathrm{d}n_s/\mathrm{d}\ln k$, and $\sum m_\nu$. 68% and 95% confidence contours obtained for four combinations – Planck 2015 TT+lowP data alone, then adding BOSS Lyα, high-ℓ polarization from Planck (TE and EE) and finally BAO data.*

5 Results for ΛWDM cosmology

The likelihood used in the case of ΛWDM cosmology is quite similar to the likelihood described in the Sec. 3. The analysis is fully detailed in in [9]. Combining the Ly-α forest data with the expansion rate value of $H_0 = 67.3 \pm 1.0$ km s^{-1} Mpc^{-1} issued by the Planck 2015 [4], we obtain the most stringent lower limit on WDM mass to date, set at $m_X > 4.35$ keV for thermal relics.

Our work distinguishes itself from those of our predecessors [14, 15, 16] in a sharpened understanding of the systematics related to our numerical simulations and in the usage of a significantly larger sample of medium-resolution quasar spectra (SDSS-III) than previously (SDSS-I). Our QSO sample includes over four times as many medium-resolution spectra than previous SDSS studies, with all spectra selected for their high signal-to-noise ratio and good quality, and overall it includes more objects in the highest redshift bins. As the damping of small-scale perturbations due to free-streaming is more prominent at higher redshifts, the bounds on WDM particle mass are better constrained at higher redshifts. For instance, dropping the two highest redshift bins from our sample issues $m_X > 3.1$ keV, which is illustrative of their significance.

Finally, to obtain a constraint on the sterile neutrino mass, we consider a non resonantly production in which no lepton asymmetry is required. Using the Dodelson-Widrow [17] mechanism, in which the sterile neutrinos are produced by oscillations with the active neutrinos in a seesaw mechanism in the early Universe ($T \sim 100$ MeV for keV masses), we can derive a limit on non-resonantly-produced sterile neutrinos $m_s \gtrsim 26.4$ keV (95% C.L.). as shown on Fig. 5.

The work described in [9] focuses on early decoupled thermal relics (such as gravitinos for instance) and neutrinos produced in a Dodelson-Widrow mechanism, and allows us to set the strongest bounds on their mass. Other models with resonantly-produced sterile neutrino[16, 18] (which have been recently suggested as a plausible origin of the 3.55 keV line observed in the X-ray spectrum of galaxy clusters [19, 20]), will be investigated in a forthcoming study.

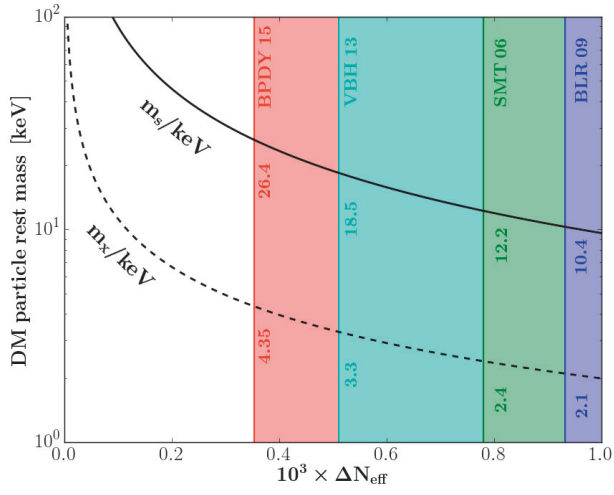


Figure 5 – Relation between $\Delta N_{\rm eff} \propto (T/T_\nu)^4$ and dark matter particle mass in the thermal relic (dotted line) and Dodelson-Widrow [17] sterile neutrino (solid line) cases. The dark matter lower-bound mass obtained by our analysis [9], labelled 'BPDY15' and previous works are illustrated by the solid black vertical lines: BLR09 [16], SMT06 [15] and VBH08 [14].

Acknowledgments

This work was done in collaboration with Nathalie Palanque-Delabrouille and Julien Baur. The author thanks Julien Lesgourgues, Graziano Rossi and Matteo Viel for their precious feedback and input, as well as Volker Springel for making `GADGET-3` available to our team. He acknowledges PRACE (Partnership for Advanced Computing in Europe) for awarding us access to resource curie-thin and curie-xlarge nodes based in France at TGCC, under allocation numbers 2010PA2777, 2014102371 and 2012071264.

References

[1] Palanque-Delabrouille, N., C. Yèche, A. Borde, et al. The one-dimensional Ly-alpha forest power spectrum from BOSS. *A. & A.*, 559:A85, 2013. `arXiv:1306.5896`.

[2] Borde, A., N. Palanque-Delabrouille, G. Rossi, et al. New approach for precise computation of Lyman-α forest power spectrum with hydrodynamical simulations. *JCAP*, 7:005, 2014. `arXiv:1401.6472`.

[3] Rossi, G., N. Palanque-Delabrouille, A. Borde, et al. Suite of hydrodynamical simulations for the Lyman-α forest with massive neutrinos. *A & A*, 567:A79, 2014. `arXiv:1401.6464`.

[4] Planck Collaboration, P. A. R. Ade, N. Aghanim, et al. Planck 2015 results. XIII. Cosmological parameters. *ArXiv:1502.01589*, 2015. `arXiv:1502.01589`.

[5] Ahn, C. P., R. Alexandroff, C. Allende Prieto, et al. The Ninth Data Release of the Sloan Digital Sky Survey: First Spectroscopic Data from the SDSS-III Baryon Oscillation Spectroscopic Survey. *ApJS*, 203:21, 2012. `arXiv:1207.7137`.

[6] Dawson, K. S., D. J. Schlegel, C. P. Ahn, et al. The Baryon Oscillation Spectroscopic Survey of SDSS-III. *The Astronomical Journal*, 145:10, 2013. arXiv:1208.0022.

[7] Palanque-Delabrouille, N., C. Yèche, J. Baur, et al. Neutrino masses and cosmology with Lyman-alpha forest power spectrum. *JCAP*, 11:011, 2015. arXiv:1506.05976.

[8] Springel, V., N. Yoshida, and S. D. White. GADGET: a code for collisionless and gasdynamical cosmological simulations. *New Astronomy*, 6:79–117, 2001. arXiv:astro-ph/0003162.

[9] Baur, J., N. Palanque-Delabrouille, C. Yèche, et al. Lyman-alpha Forests cool Warm Dark Matter. *ArXiv:1512.01981*, 2015. arXiv:1512.01981.

[10] Rossi, G., C. Yèche, N. Palanque-Delabrouille, et al. Constraints on dark radiation from cosmological probes. *Phys. Rev. D*, 92:063505, 2015. arXiv:1412.6763.

[11] Planck Collaboration, P. A. R. Ade, N. Aghanim, et al. Planck 2013 results. XVI. Cosmological parameters. 2013. arXiv:1303.5076.

[12] Kosowsky, A. and M. S. Turner. CBR anisotropy and the running of the scalar spectral index. *Phys. Rev. D*, 52:1739, 1995. astro-ph/9504071.

[13] Hinshaw, G., D. Larson, E. Komatsu, et al. Nine-year Wilkinson Microwave Anisotropy Probe (WMAP) Observations: Cosmological Parameter Results. *The Astrophysical Journal Supplement Series*, 208:19, 2013. arXiv:astro-ph.CO/1212.5226.

[14] Viel, M., G. D. Becker, J. S. Bolton, et al. How Cold Is Cold Dark Matter? Small-Scales Constraints from the Flux Power Spectrum of the High-Redshift Lyman-α Forest. *Phys. Rev. Lett.*, 100:041304, 2008. arXiv:0709.0131.

[15] Seljak, U., A. Makarov, P. McDonald, et al. Can Sterile Neutrinos Be the Dark Matter? *Phys. Rev. Lett.*, 97:191303, 2006. astro-ph/0602430.

[16] Boyarsky, A., J. Lesgourgues, O. Ruchayskiy, et al. Lyman-α constraints on warm and on warm-plus-cold dark matter models. *JCAP*, 5:12, 2009. arXiv:0812.0010.

[17] Dodelson, S. and L. M. Widrow. Sterile neutrinos as dark matter. *Phys. Rev. Lett.*, 72: 17–20, 1994. hep-ph/9303287.

[18] Boyarsky, A., J. Lesgourgues, O. Ruchayskiy, et al. Realistic Sterile Neutrino Dark Matter with KeV Mass does not Contradict Cosmological Bounds. *Physical Review Letters*, 102: 201304, 2009. arXiv:hep-ph/0812.3256.

[19] Bulbul, E., M. Markevitch, A. Foster, et al. Detection of an Unidentified Emission Line in the Stacked X-Ray Spectrum of Galaxy Clusters. *ApJ*, 789:13, 2014. arXiv:1402.2301.

[20] Boyarsky, A., O. Ruchayskiy, D. Iakubovskyi, et al. Unidentified Line in X-Ray Spectra of the Andromeda Galaxy and Perseus Galaxy Cluster. *Physical Review Letters*, 113:251301, 2014. arXiv:1402.4119.

COSMIC NEUTRINOS AND OTHER LIGHT RELICS

JOEL MEYERS
Canadian Institute for Theoretical Astrophysics, Toronto, ON M5S 3H8, Canada

Cosmological measurements of the radiation density in the early universe can be used as a sensitive probe of physics beyond the standard model. Observations of primordial light element abundances have long been used to place non-trivial constraints on models of new physics and to inform our understanding of the thermal history to the first few minutes of our present phase of expansion. Precision measurements of the angular power spectrum of the cosmic microwave background temperature and polarization will drastically improve our measurement of the cosmic radiation density over the next decade. These improved measurements will either uncover new physics or place much more stringent constraints on physics beyond the standard model, while pushing our understanding of the early universe to much earlier times.

1 Introduction

The primordial light element abundances and the angular power spectrum of the cosmic microwave background (CMB) are sensitive to the total radiation density that was present in the early universe, usually parametrized through a quantity $N_{\rm eff}$. In the standard models of particle physics and cosmology, the value of $N_{\rm eff}$ measures the total energy density of cosmic neutrinos. In more general models, however, $N_{\rm eff}$ receives contributions from all forms of relativistic species apart from photons present in the early universe. This means that $N_{\rm eff}$ can be used as a sensitive probe of physics beyond the standard model. The next generation of CMB experiments will drastically improve our constraints on $N_{\rm eff}$, opening a characteristically new regime in the cosmological search for new physics.

The quantity $N_{\rm eff}$ is typically defined as the ratio of the energy density of all dark radiation (that is all radiation except photons) to that of photons [1]

$$N_{\rm eff} = \frac{8}{7}\left(\frac{11}{4}\right)^{4/3}\frac{\rho_X}{\rho_\gamma}\,. \tag{1}$$

The standard model predicts $N_{\rm eff} = 3.046$ [2].

2 Observational Signatures

2.1 Primordial Light Element Abundances

The process by which light elements form in the early universe, known as big bang nucleosynthesis (BBN), is affected by the presence of dark radiation due to its impact on the expansion rate. For example, an increase in $N_{\rm eff}$ tends to produce a higher helium-4 abundance through the following chain of events: for higher radiation density, the expansion rate is higher, which implies that the temperature drops more quickly with time, leading to a higher neutron-to-proton

freeze-out ratio and less time for free neutron decay, thus leaving a higher number density of neutrons surviving when the universe cools sufficiently for the formation of helium nuclei, thereby producing more helium-4 than in the standard scenario [1,3,4].

Astrophysical measurements of the primordial helium-4 abundance have for a long time provided the best constraint on $N_{\rm eff}$, though recently improved measurements of the primordial deuterium abundance have become competitive with those of helium-4 [5,4]. The current best measurement of $N_{\rm eff}$ from primordial abundances is [4]

$$N_{\rm eff}^{\rm BBN} = 3.28 \pm 0.28\,, \tag{2}$$

which is fully consistent with the predictions of the standard model.

2.2 Cosmic Microwave Background

Dark radiation impacts the angular power spectrum of the CMB in a number of ways. The most prominent observational signature is the effect of increased damping in the presence of higher radiation density [6]. Perturbations in free-streaming radiation (such as cosmic neutrinos) also lead to shifts in the amplitude and phase of acoustic peaks which approach constants at small angular scales [7,8]. The phase shift is of particular interest, since it is not degenerate with other cosmological parameters and will become increasingly important in driving future constraints on $N_{\rm eff}$ [8]. Furthermore, since the phase shift is only sourced by free-streaming radiation, measurements of the CMB can also be used to distinguish the nature of dark radiation [9,10,11,8]. The phase shift has recently been isolated and detected in the Planck temperature data [12].

Measurements from the Planck satellite using both temperature and polarization currently provide the best constraint on $N_{\rm eff}$, giving [13]

$$N_{\rm eff}^{\rm CMB} = 3.04 \pm 0.18\,. \tag{3}$$

We see that this measurement is consistent with the prediction of the standard model and also with the measurements of primordial abundances.

Future measurements of the CMB, in particular from a ground-based CMB Stage-IV experiment, are expected to improve on the current constraints on $N_{\rm eff}$ by about an order of magnitude [14,15]. The phase shift of the acoustic peaks will play an increasingly important role in these constraints [8]. The E-mode polarization power spectrum has sharper acoustic peaks than that of the temperature power spectrum, thus leading a more accurate measurement of the phase shift and $N_{\rm eff}$. Since gravitational lensing of the CMB tends to smooth out acoustic peaks, delensing which sharpens peaks can improve the constraints on $N_{\rm eff}$ [8,16].

2.3 Complementarity

Measurements of $N_{\rm eff}$ from the CMB are now more precise than those from primordial abundance observations, though these should be viewed as complementary rather than competing probes. The two measurements are sensitive to different aspects of the radiation content of the universe (since for example the primordial abundances depend weakly on the distribution function of active neutrinos [17]), and so combining these measurements provides a more comprehensive picture than either alone. Furthermore, these two measurements are sensitive to the radiation energy density at different times in the cosmic history, thereby allowing constraints on the evolution of the radiation density and the thermal history of the universe [18,19,20,21,22].

The CMB is also directly sensitive to the primordial helium abundance through its effect on the damping tail. Such constraints from CMB Stage-IV will be more precise and much less sensitive to astrophysical systematics than the current best observations of primordial helium [15,8].

3 Theoretical Targets

Precise measurements of $N_{\rm eff}$ naturally place constraints on many extensions of standard model physics. This includes for example gravitational waves [23,24,25], dark photons [26,27,28], sterile neutrinos [29,30,31], and many more [19,32].

Perhaps one of the most compelling motivations for studying $N_{\rm eff}$ is that all light thermal relics contribute to $N_{\rm eff}$ at a level which is determined by the spin and decoupling temperature alone [33,11]. The minimum contribution from a thermal relic which decoupled after the QCD phase transition is roughly $\Delta N_{\rm eff} \sim 0.3$ which is the regime currently probed by the Planck observations. The measurements of CMB Stage-IV will be sensitive to light relics which decoupled at much earlier times and higher temperatures. Light thermal relics with essentially arbitrarily high decoupling temperature always [a] produce $\Delta N_{\rm eff} \geq 0.027$ [33,11]. A CMB experiment which reaches this level of sensitivity will therefore either detect new physics, or rule out the existence of new light thermal relics, a conclusion which would have extremely far reaching consequences for particle physics [34].

Measurements of $N_{\rm eff}$ therefore allow the CMB to be used as a window onto particle physics at energies much higher than are accessible by other means. The next decade of CMB observations will thus be an extremely exciting period for cosmologists and particle physicists alike.

Acknowledgments

Thanks to Daniel Baumann, Dan Green, Alex van Engelen, and Benjamin Wallisch for their contributions to the research which forms the basis of this article.

References

1. Steven Weinberg. *Cosmology*. 2008.
2. Gianpiero Mangano, Gennaro Miele, Sergio Pastor, Teguayco Pinto, Ofelia Pisanti, and Pasquale D. Serpico. Relic neutrino decoupling including flavor oscillations. *Nucl. Phys.*, B729:221–234, 2005.
3. K. A. Olive et al. Review of Particle Physics. *Chin. Phys.*, C38:090001, 2014.
4. Richard H. Cyburt, Brian D. Fields, Keith A. Olive, and Tsung-Han Yeh. Big Bang Nucleosynthesis: 2015. *Rev. Mod. Phys.*, 88:015004, 2016.
5. Ryan Cooke, Max Pettini, Regina A. Jorgenson, Michael T. Murphy, and Charles C. Steidel. Precision measures of the primordial abundance of deuterium. *Astrophys. J.*, 781(1):31, 2014.
6. Zhen Hou, Ryan Keisler, Lloyd Knox, Marius Millea, and Christian Reichardt. How Massless Neutrinos Affect the Cosmic Microwave Background Damping Tail. *Phys. Rev.*, D87:083008, 2013.
7. Sergei Bashinsky and Uros Seljak. Neutrino perturbations in CMB anisotropy and matter clustering. *Phys. Rev.*, D69:083002, 2004.
8. Daniel Baumann, Daniel Green, Joel Meyers, and Benjamin Wallisch. Phases of New Physics in the CMB. *JCAP*, 1601:007, 2016.
9. Nicole F. Bell, Elena Pierpaoli, and Kris Sigurdson. Cosmological signatures of interacting neutrinos. *Phys. Rev.*, D73:063523, 2006.
10. Alexander Friedland, Kathryn M. Zurek, and Sergei Bashinsky. Constraining Models of Neutrino Mass and Neutrino Interactions with the Planck Satellite. 2007.
11. Zackaria Chacko, Yanou Cui, Sungwoo Hong, and Takemichi Okui. Hidden dark matter sector, dark radiation, and the CMB. *Phys. Rev.*, D92:055033, 2015.

[a] This conclusion can be avoided if a large number of dark sector species decay into standard model particles after the decoupling of the dark radiation, thereby diluting its relic abundance.

12. Brent Follin, Lloyd Knox, Marius Millea, and Zhen Pan. First Detection of the Acoustic Oscillation Phase Shift Expected from the Cosmic Neutrino Background. *Phys. Rev. Lett.*, 115(9):091301, 2015.
13. P. A. R. Ade et al. Planck 2015 results. XIII. Cosmological parameters. 2015.
14. K. N. Abazajian et al. Neutrino Physics from the Cosmic Microwave Background and Large Scale Structure. *Astropart. Phys.*, 63:66–80, 2015.
15. W. L. K. Wu, J. Errard, C. Dvorkin, C. L. Kuo, A. T. Lee, P. McDonald, A. Slosar, and O. Zahn. A Guide to Designing Future Ground-based Cosmic Microwave Background Experiments. *Astrophys. J.*, 788:138, 2014.
16. Daniel Green, Joel Meyers, and Alexander van Engelen. An All-Orders Approach to Delensing, 2016.
17. Pasquale Dario Serpico, S. Esposito, F. Iocco, G. Mangano, G. Miele, and O. Pisanti. Nuclear reaction network for primordial nucleosynthesis: A Detailed analysis of rates, uncertainties and light nuclei yields. *JCAP*, 0412:010, 2004.
18. Willy Fischler and Joel Meyers. Dark Radiation Emerging After Big Bang Nucleosynthesis? *Phys. Rev.*, D83:063520, 2011.
19. Davide Cadamuro, Steen Hannestad, Georg Raffelt, and Javier Redondo. Cosmological bounds on sub-MeV mass axions. *JCAP*, 1102:003, 2011.
20. Justin L. Menestrina and Robert J. Scherrer. Dark Radiation from Particle Decays during Big Bang Nucleosynthesis. *Phys. Rev.*, D85:047301, 2012.
21. Dan Hooper, Farinaldo S. Queiroz, and Nickolay Y. Gnedin. Non-Thermal Dark Matter Mimicking An Additional Neutrino Species In The Early Universe. *Phys. Rev.*, D85:063513, 2012.
22. Marius Millea, Lloyd Knox, and Brian Fields. New Bounds for Axions and Axion-Like Particles with keV-GeV Masses. *Phys. Rev.*, D92(2):023010, 2015.
23. Latham A. Boyle and Alessandra Buonanno. Relating gravitational wave constraints from primordial nucleosynthesis, pulsar timing, laser interferometers, and the CMB: Implications for the early Universe. *Phys. Rev.*, D78:043531, 2008.
24. Andrew Stewart and Robert Brandenberger. Observational Constraints on Theories with a Blue Spectrum of Tensor Modes. *JCAP*, 0808:012, 2008.
25. P. Daniel Meerburg, Renee Hlozek, Boryana Hadzhiyska, and Joel Meyers. Multiwavelength constraints on the inflationary consistency relation. *Phys. Rev.*, D91(10):103505, 2015.
26. Lotty Ackerman, Matthew R. Buckley, Sean M. Carroll, and Marc Kamionkowski. Dark Matter and Dark Radiation. *Phys. Rev.*, D79:023519, 2009. [,277(2008)].
27. David E. Kaplan, Gordan Z. Krnjaic, Keith R. Rehermann, and Christopher M. Wells. Dark Atoms: Asymmetry and Direct Detection. *JCAP*, 1110:011, 2011.
28. Francis-Yan Cyr-Racine and Kris Sigurdson. Cosmology of atomic dark matter. *Phys. Rev.*, D87(10):103515, 2013.
29. Kevork Abazajian, George M. Fuller, and Mitesh Patel. Sterile neutrino hot, warm, and cold dark matter. *Phys. Rev.*, D64:023501, 2001.
30. Alessandro Strumia and Francesco Vissani. Neutrino masses and mixings and... 2006.
31. Alexey Boyarsky, Oleg Ruchayskiy, and Mikhail Shaposhnikov. The Role of sterile neutrinos in cosmology and astrophysics. *Ann. Rev. Nucl. Part. Sci.*, 59:191–214, 2009.
32. Steven Weinberg. Goldstone Bosons as Fractional Cosmic Neutrinos. *Phys. Rev. Lett.*, 110(24):241301, 2013.
33. Christopher Brust, David E. Kaplan, and Matthew T. Walters. New Light Species and the CMB. *JHEP*, 12:058, 2013.
34. Daniel Baumann, Daniel Green, and Benjamin Wallisch. A New Target for Cosmic Axion Searches. 2016.

INTERPLAY BETWEEN COSMOLOGY AND LABORATORY EXPERIMENTS: TWO EXAMPLES FROM NEUTRINO PHYSICS

M. GERBINO
The Oskar Klein Centre for Cosmoparticle Physics,
Department of Physics, Stockholm University, AlbaNova, and
The Nordic Institute for Theoretical Physics, Roslagstullsbacken 23,
SE 106 91 Stockholm, Sweden

We present here two examples of the interplay between cosmology and laboratory searches within the framework of neutrino physics. We firstly discuss the constraints on the neutrino mass scale coming from a combination of cosmological and laboratory measurements. Finally, we investigate the viability of a model involving the decay of a MeV sterile neutrino population as a solution to the "Lithium problem" in light of cosmological and laboratory probes.

1 Introduction

Neutrino physics is one of the most exiciting arena for future research in cosmology. Even though we know from oscillation experiments that neutrinos do have masses, we still fail in assessing the neutrino mass scale. Cosmological probes[1] such as Cosmic Microwave Background (CMB) and Large Scale Structures (LSS) currently provide the tightest upper bounds on the total neutrino mass M_ν[2]. Additional avenues aiming to experimentally probe the absolute scale of neutrino masses are related to laboratory physics, such as direct measurements, studying the kinematics of β decay[3], and searches for neutrinoless double β decay ($0\nu2\beta$)[4]. The former approaches have the advantage of being model-independent. On the other hand, if $0\nu2\beta$ decay, i.e., the double β decay of nuclei, in which no neutrinos are present in the final state. was observed, it would guarantee that neutrinos have a non-vanishing Majorana mass; if not, we can still place upper limits on the mass scale, under the assumption that neutrinos are Majorana particles. These two approaches should be considered as complementary to the cosmological measurements, as each of them presents its own advantages and probe slightly different quantities related to the neutrino masses. Combining them in the framework of bayesian statistics also allows to propagate correctly the uncertainty coming from our imprecise knowledge of the appropriate nuclear matrix elements (NME) relevant for $0\nu2\beta$ searches[5].

Combining cosmology and laboratory experiment is also relevant for assesing the feasibility of cosmological model, such as the one recently proposed[6] as a solution to the "Lithium problem", i.e. the disagreement between the theoretical abundance predicted for primordial ^{7}Li and the value inferred by astrophysical measurements. In the context of Big Bang Nucleosynthesis (BBN), ^{7}Li is mainly produced via the β-decay of ^{7}Be[7]. Hence, the proposed solution advocates the decay of a primordial MeV sterile neutrino population right after BBN as the ignition of an electromagnetic cascade responsible for the photodisintegration of the primordial berillium and consequently the inhibition of lithium production. The sterile neutrino decay, being a source of energy injection and extra relativistic species, affects CMB in several ways [8], so that it can be employed to test the model. Moreover, the mixing angles θ_α between the sterile species

and the three active neutrino families ($\alpha = e$, μ, τ respectively) are constrained by laboratory searches, using different techniques (accelerators, observation of neutrinos produced in final states of decays, $0\nu2\beta$ decays). The fact that the model proposed not only solves the "Lithium problem", but is also able to fit both cosmological data and laboratory bounds makes it worth to be investigated in further details.

2 Results from the two analysis

We start discussing constraints on neutrino mass scale. We employ a combination of oscillation, cosmological, kinematic and $0\nu2\beta$ data in order to constrain the following quantities: the sum of the three neutrino masses $M_\nu \equiv \sum_i m_i$, the effective neutrino mass $m_\beta^2 \equiv \sum_i |U_{ei}|^2 m_i^2$ and the Majorana mass $m_{\beta\beta} \equiv |\sum_i U_{ei}^2 m_i|$, where U is the neutrino mixing matrix and m_i (i = 1, 2, 3) are the masses of the neutrino mass eigenstates. We discuss separetly the two different scenarios of normal hierarchy (NH) and inverted hierarchy (IH) and consider 3 different combination of datasets, corresponding to "current", "forthcoming" (i.e. expected within next 5 years) and "next-generation" results. Since we do not expect dramatic improvements with respect to the current limits from oscillation measurements, all the combinations include the most updated information from oscillation experiments[9] . The "current" dataset includes results from the Planck 2015 release for cosmology[10], and GERDA-I for $0\nu2\beta$ searches[11]. The "forthcoming" dataset include the same cosmological data as the previous dataset, GERDA-II (upgrade of GERDA-I), and KATRIN [12] for kinematic measurements. The "next generation I (II)" dataset includes Euclid, nEXO without (with) Ba tagging and HOLMES[13]. For future data, we have to assume fiducial values of the parameters: in the case of the forthcoming dataset, we take the best estimates from the combination of oscillations and Planck2015. For the "next-generation" case, we assume $M_\nu = 0.1\,\mathrm{eV}$ and estimate m_β and $m_{\beta\beta}$ from the combination of Euclid and oscillation parameters. In order to account for the uncertainty related to nuclear modeling, we compute $m_{\beta\beta}$ using fiducial values of nuclear matrix elements (NME), and then rescale it by a factor ξ^2.

We present our results for M_ν in Fig. 1, both in the case where ξ^2 is fixed to 1 (which recovers our fiducial values) and when ξ^2 is marginalized over; results for the remaining parameters are discussed in[14]. The low mass region is excluded by the oscillation data. Limits provided by the present dataset are independent of whether nuclear uncertainties are marginalized over: present constraints are dominated by the cosmological limit on M_ν, so that they are not affected by uncertainties in nuclear modeling. Forthcoming datasets yield similar constraints for the mass parameters: the upgraded sensitivity of GERDA-II and the inclusion of KATRIN provide a marginal improvement to the cosmological plus oscillations data combination. Substantial differences arise for next-generation experiments. In this case, cosmological observations and $0\nu2\beta$ searches have comparable constraining power, and the nuclear uncertainties have a dramatic impact in deriving parameter constraints. Marginal evidence at 95% CL for non-minimal mass parameters can be highlighted in the case of normal hierarchy, even when a factor 2 uncertainty in nuclear modeling is taken into account.

We now move to consider a non-thermal BBN possible solution to the Lithium problem[6]. We analyse the possibility that ^{7}Be is detroyed by photons released by the decay of a MeV sterile neutrino population, leading to a deployment of the final ^{7}Li abundance. The energy range involved in this process is narrow: we require that the released energy does not affect the well constrained primordial abundance of deuterium D ($E_{\gamma,max} = 2.2\,\mathrm{MeV}$); the minimum energy allowed is the photodisintegration threshold for ^{7}Be ($E_{\gamma,min} = 1.6\,\mathrm{MeV}$). We consider both cases of a Dirac and of a Majorana sterile neutrino, since decay rates for given mass and mixing angles between sterile and active species are different in the two cases; moreover, some of the laboratory limits that we use to constrain mixing angles only apply if the sterile neutrino is a Majorana particle. The total rates for the three main decaying channels of the sterile neutrinos

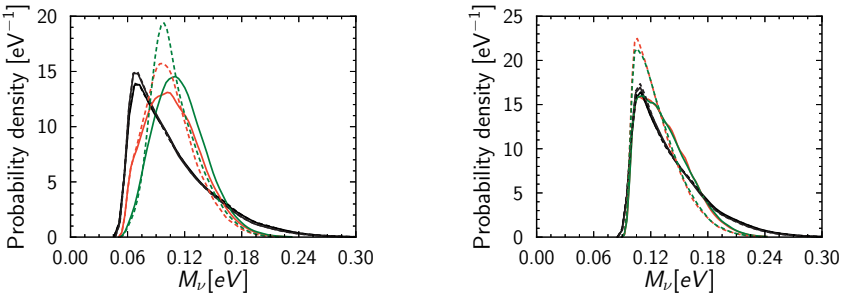


Figure 1 – One-dimensional posterior probability for M_ν in the case of NH (left) and IH (right) for "current" (black), "forthcoming" (blue) and "next-generation I(II)" (red and green respectively) combination of datasets. Dashed curves correspond to fixed value of NME, solid curves are marginalized over NME uncertainties[14].

are detailed in[15]. What we want to stress here is that the final products of the sterile neutrino decays affect cosmological observables: photons can change light element abundances through photodisintegration; electromagnetic decay products induce spectral distortions and modify the entropy of the cosmic plasma; light neutrinos increase the energy density of relativistic species, changing the value of $N_{\rm eff}$. As a result, we can use CMB data to constrain the parameter space of the model under consideration. In particular, we employ the Planck 2015 data[16] both in temperature and polarization and the limits on the μ-type spectral distorsion from COBE-FIRAS[17] as our CMB dataset. We also combine direct astrophysical observations of lithium and deuterium abundances[18], and laboratory bounds on the mixing angles θ_α[19]. Given the preliminary nature of our results, we prefer to discuss them following a qualitative approach. A thourough investigation will be performed in[20]. Our results are summarized in the left panel of Fig.2. We show the predicted abundance of primordial lithium at the end of BBN (red dotted curve) and at the last scattering surface (blue dash-dotted curve), along with the abundance of berillium at the end of BBN, as a function of the baryon-to-photon ratio η (or equivalently as a funtion of the baryon density parameter $\Omega_b h^2$). The vertical band is the 1σ limit on $\Omega_b h^2$ from Planck 2015 data. As shown by the figure, lithium is mainly produced at the end of BBN, by converting berillium. In the standard BBN scenario, the value inferred theoretically is at odd with astrophysical measurements, reported as the horizontal band: the blue curve is roughly three times higher than the 1σ experimental bounds. However, if one considers a non-thermal BBN process as the model depicted above, the predicted abundance of lithium is then represented by the black solid line. For the value of $\Omega_b h^2$ prefered by Planck, the agreement between atrophysical constraint on ^{7}Li and theoretical prediction is astonishing.

We have shown that the model can accomodate expected values and astrophysical measurements. We need to show to what extent this model is prefered or at least not rejected by cosmological and laboratory probes. In the right panel of Fig.2, we report the one-dimensional posterior probability for the mixing angles θ_α for the combination of dataset listed above and for the Majorana scenario, as an example of our results. These limits are perfectly in agreement with laboratory bounds, telling us that the model is physically viable. If we further compare the difference between the χ^2 of the bestfit model with the standard ΛCDM bestfit χ^2, we see that the addition of a decaying MeV sterile neutrino does not alter the CMB bestfit, so that the non-thermal BBN process is also viable from the cosmological point of view. On the other hand, the improvement of the χ^2 computed for astrophysical abundances is of course dramatic.

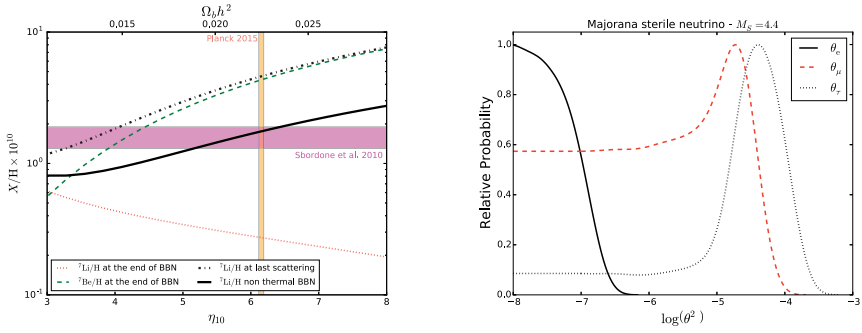


Figure 2 – *Left*: Primordial abundances of berillium and lithium as a function of the baryon density, see text for details. *Right*: One-dimensional posterior probability for θ_α for the combination of Planck, COBE, astrophysical and laboratory datasets when assuming a Majorana $M_s = 4.4$ MeV sterile neutrino (preliminary results).

3 Conclusions

We have shown the importance of combining information coming from cosmology and laboratory physics when investigating neutrino properties. A joint analysis of CMB, LSS, oscillation, kinematic and $0\nu2\beta$ measurements is extremely timing. Laboratory searches also represent a valuable probe for assessing the viability of non-standard cosmological model, such as the non-thermal BBN solution to the "Lithium problem", in addition to CMB constraints.

Acknowledgments

In collaboration with M.Lattanzi, A.Melchiorri, L.Pagano and L.Salvati. M.G. is supported by the Vetenskapsrådet (Swedish Research Council) and "Avvio alla Ricerca" (Univ. "Sapienza").

References

1. J. Lesgourgues and S. Pastor, Phys. Rept. **429**, 307 (2006).
2. P. A. R. Ade *et al.* [Planck Collaboration], arXiv:1502.01589 [astro-ph.CO].
3. G. Drexlin *et al*, Adv. High Energy Phys. **2013**, 293986 (2013).
4. O. Cremonesi and M. Pavan, Adv. High Energy Phys. **2014**, 951432 (2014).
5. S. Dell'Oro *et al* Advances in High Energy Physics, Volume 2016 (2016), Article ID 2162659
6. V. Poulin and P. D. Serpico, Phys. Rev. Lett. **114** (2015) 9, 091101
7. R. H. Cyburt *et al* arXiv:1505.01076 [astro-ph.CO].
8. H. Ishida *et al* Phys. Rev. D **90** (2014) 8, 083519; J. Chluba and R. A. Sunyaev, Mon. Not. Roy. Astron. Soc. **419** (2012) 1294
9. D. V. Forero *et al* Phys. Rev. D **90**, 093006 (2014).
10. P. A. R. Ade *et al.* [Planck Collaboration], arXiv:1502.01589 [astro-ph.CO].
11. M. Agostini *et al.* [GERDA Collaboration], Phys. Rev. Lett. **111**, 122503 (2013).
12. A. Osipowicz *et al.* [KATRIN Collaboration], hep-ex/0109033.
13. R. Laureijs *et al.* (Euclid collaboration), arXiv:1110.3193 [astro-ph.CO]; `https://www-project.slac.stanford.edu/exo/`; B. Alpert *et al* [HOLMES Collaboration], arXiv:1412.5060 [physics.ins-det].
14. M. Gerbino *et al* Phys. Rev. D **93**, no. 3, 033001 (2016)
15. D. Gorbunov and M. Shaposhnikov, JHEP **0710**, 015 (2007) Erratum: [JHEP **1311**, 101 (2013)]
16. N. Aghanim *et al.* [Planck Collaboration], [arXiv:1507.02704 [astro-ph.CO]].
17. D. J. Fixsen *et al* Astrophys. J. **473** (1996) 576
18. Sbordone *et al* A&A, 522, A26; R. Cooke *et al* Astrophys. J. **781** (2014) 1, 31
19. G. Gelmini *et al* JCAP **0810** (2008) 029 J. C. Helo *et al* Phys. Rev. D **84** (2011) 053008
20. L.Pagano *et al*, in preparation.

6.
Clusters

High angular resolution SZ observations with NIKA and NIKA2

B. Comis[1], R. Adam[1,2], P. Ade[3], P. André[4], M. Arnaud[4] I. Bartalucci[4], A. Beelen[5], A. Benoît[6], A. Bideaud[3], N. Billot[7], O. Bourrion[1], M. Calvo[6], A. Catalano[1], G. Coiffard[9], F.-X. Désert[10], S. Doyle[3], J. Goupy[6], C. Kramer[7] G. Lagache[8] S. Leclercq[9] J. F. Macías-Pérez[1], P. Mauskopf[3,11], F. Mayet[1], A. Monfardini[6], F. Pajot[5], E. Pascale[3], L. Perotto[1], E. Pointecouteau[12] G. Pisano[3], N. Ponthieu[10], G. W. Pratt[4] V. Revéret[4], A. Ritacco[1], L. Rodriguez[4], C. Romero[9], F. Ruppin[1], G. Savini[13], K. Schuster[9], A. Sievers[7], S. Triqueneaux[6], C. Tucker[3], R. Zylka[9]

[1] *Laboratoire de Physique Subatomique et de Cosmologie, Université Grenoble Alpes, CNRS/IN2P3, 53, avenue des Martyrs, Grenoble, France*

[2] *Laboratoire Lagrange, Université Côte d'Azur, Observatoire de la Côte d'Azur, CNRS, Blvd de l'Observatoire, CS 34229, 06304 Nice cedex 4, France*

[3] *Astronomy Instrumentation Group, University of Cardiff, UK*

[4] *Laboratoire AIM, CEA/IRFU, CNRS/INSU, Université Paris Diderot, CEA-Saclay, 91191 Gif-Sur-Yvette, France*

[5] *Institut d'Astrophysique Spatiale (IAS), CNRS and Université Paris Sud, Orsay, France*

[6] *Institut Néel, CNRS and Université Grenoble Alpes, France*

[7] *Institut de RadioAstronomie Millimétrique (IRAM), Granada, Spain*

[8] *Aix Marseille Université, CNRS, LAM (Laboratoire d'Astrophysique de Marseille) UMR 7326, 13388, Marseille, France*

[9] *Institut de RadioAstronomie Millimétrique (IRAM), Grenoble, France*

[10] *Institut de Planétologie et d'Astrophysique de Grenoble (IPAG), CNRS and Université de Grenoble, France*

[11] *School of Earth and Space Exploration and Department of Physics, Arizona State University, Tempe, AZ 85287*

[12] *Université de Toulouse, UPS-OMP, Institut de Recherche en Astrophysique et Planétologie (IRAP), Toulouse, France*

[13] *University College London, Department of Physics and Astronomy, Gower Street, London WC1E 6BT, UK*

NIKA2 (New IRAM KID Arrays) is a dual band (150 and 260 GHz) imaging camera based on Kinetic Inductance Detectors (KIDs) and designed to work at the IRAM 30 m telescope (Pico Veleta, Spain). Built on the experience of the NIKA prototype, NIKA2 has been installed at the 30 m focal plane in October 2015 and the commissioning phase is now ongoing. Through the thermal Sunyaev-Zeldovich (tSZ) effect, NIKA2 will image the ionized gas residing in clusters of galaxies with a resolution of 12 and 18 arcsec FWHM (at 150 and 260 GHz, respectively). We report on the recent tSZ measurements with the NIKA camera and discuss the future objectives for the NIKA2 SZ large Program, 300h of observation dedicated to SZ science. With this program we intend to perform a high angular resolution follow-up of a cosmologically-representative sample of clusters belonging to SZ catalogues, with redshift $\geq$ 0.5. The main output of the program will be the study of the redshift evolution of the cluster pressure profile as well as that of the scaling laws relating the cluster global properties.

1 Introduction

Clusters of galaxies are the largest gravitationally bound structures observable in our Universe. They represent the last step of the hierarchical structure formation process and so their number

and distribution as a function of mass and redshift can provide an excellent tool for cosmology. Being complementary to purely geometric probes and observables of the primordial Universe, clusters can provide tight constraints on the matter content and distribution within our Universe but also on the origin of its accelerated expansion. However, to do cosmology with clusters, we must be able to translate the direct observables, used to detect and count them, into precise mass estimates. The accuracy and the precision of the total mass estimates will in fact directly impact the robustness of the derived cosmological constraints.

Clusters of galaxies are mainly ($\sim$ 80%) constituted of dark matter, while most of the baryons are in the form of a hot ionized gas, the so-called intra-cluster medium (ICM). Then, cluster total masses can be measured through their gravitational effect, through the gravitational lensing, or by using their baryonic components as a tracer of the total mass distribution. In particular, the observables related to their main baryonic component, the ICM, have been proven to be a good proxy of the cluster total mass. Given its temperature (10^6 - 10^8 K) and density (10^{-4} - 10^{-2} cm^{-3}) this gas is responsible for the Bremsstrahlung X-ray emission, but it also produces a secondary anisotropy of the Cosmic Microwave Background (CMB), which is the thermal Sunyaev-Zel'dovich (tSZ) effect. The tSZ effect is a distortion of the black body CMB spectrum produced by the inverse Compton interaction of CMB photons with the hot electrons of the ICM [17,18,19]. This interaction produces a unique spectral signature, with a decreased and increased CMB intensity at frequencies respectively lower and higher than 217 GHz. While the frequency behavior is, at first order, specific of the effect, the amplitude of the signal, given by the Comptonization parameter y, is instead related to the cluster thermal energy content, and then to its mass, being proportional to the integral of the gas pressure along the line of sight ($y = \sigma_{\rm T}/m_{\rm e}c^2 \int P_{\rm e} dl$, with m_e the electron mass, c the light speed, σ_T the electron Thomson scattering cross-section). A third interesting point about SZ is that, since we are dealing with a spectral deformation, it is not affected by the dilution with redshift. Making it particularly well adapted to detect clusters at higher z where their number and distribution is the most sensitive to the underlying cosmology.

During the last decade, the first cluster derived cosmological constraints were obtained, initially mainly using X-ray data and more recently also with tSZ. In fact, during the last years, thanks to survey dedicated experiments like Planck [14], ACT [11] and SPT [6], we rapidly went from the first SZ-discovered clusters [16] to SZ-selected cluster catalogs containing more than thousand of sources, enabling to estimate cosmological parameters (σ_8, Ω_m). However these results have shown tension with those derived from primary CMB anisotropies. Anyway, in order to interpret further this tension and an eventual cosmological explanation for it, we must control any possible systematic. On CMB side the tension has been reduced by the latest Planck constraints on the optical depth of reionization [13], while on the cluster side we need to further explore the presence and the amplitude of astrophysical systematics that might be introduced by an incomplete knowledge of the details of cluster physics and the different assumption made. Indeed, at present, tSZ derived cosmological constraints lay on several assumptions. These are the assumption of hydrostatic equilibrium between the gas and the overall cluster potential well and the self-similarity of the cluster population. Furthermore we also extrapolate up to intermediate redshift ($\sim$ 0.5) and beyond the calibration of cluster properties that have been obtained observationally in the local universe ($\sim$ 0.2). In order to make clusters a tool for precision cosmology we still need precise calibrations of the mass-observable relation as a function of redshift, mass and morphology, taking into account also how the details of the cluster internal structure affect the global cluster properties used as mass proxies. And for this we must enrich tSZ observations with high angular resolution, which are among the scientific goals of the NIKA and NIKA2 camera, observing at 150 and 260 GHz.

2 From NIKA to NIKA2

The New-IRAM-KIDs-array is a project dedicated to the construction of a dual-band camera customly developed to work at the focal plane of the IRAM 30 m telescope. Located at Pico Veleta, in the Spanish Sierra Nevada, at 2850 m above the sea level, this telescope is one of the two facilities operated by the Institut de Radioastonimie Millimetrique, IRAM, which observes from a site particularly adapted for mm wave astronomy. It is a single dish telescope with a primary mirror with a diameter of 30 m, representing one of the largest and most sensitive to observe at mm wavelength. The size of the primary dish results in a diffraction limited resolution of 17 and 10 arcsec for the 150 and 260 GHz bands respectively. Thus, in order to fully sample the 6.5 arcmin correct Field of View (FoV), a photometric camera for this telescope needs arrays containing hundred of pixels. This is why NIKA uses KIDs, kinetic inductance detectors. Being naturally multi-plexable in the frequency domain, this kind of detectors represents an interesting alternative to the more traditional technologies used at these wavelengths, in the perspective of building arrays with a very large number of detectors. KIDs are printed circuits brought to work at a temperature well below the one at which the material they are made up of become superconductive. They act like superconductive RLC resonators, characterized by a given resonance frequency. The photons that reach the detector break cooper pairs, and so change the kinetic inductance of the system. This variation in the properties of the circuit results in a change in the resonance frequency, which is propositional to the incoming optical power. This is why, with a single transmission line, we can monitor the resonance frequencies of a large number of pixels, the number being limited only by the bandwidth of the readout electronics.

The project started in 2008, building a pathfinder, NIKA [12], for the final instrument, NIKA2. NIKA has worked at the focal plane of the 30 m until august 2015. In its final configuration [10], it counted a total of 356 pixels split over the two bands. The prototype was not able to completely fill the whole FoV of the instrument, but has been a successful experience, used for technical campaigns and also for three observational campaigns open to the scientific community, with proposals from external users. However the most important point is that NIKA has shown state-of-the-art detector performances, which has been a key step for the approval of the NIKA2 project as the camera of choice to be the resident photometric instrument of the IRAM 30 m telescope, for at least the next decade. NIKA2 (New IRAM KID Array 2)[9] is a camera based upon kilo-pixel arrays of Kinetic Inductance Detectors. So it fills the entire field of view of the telescope. With a factor ten in the total number of detectors and two arrays at 1.15 mm, allowing us to measure the linear polarization of the incoming light, NIKA2 has been built thanks to the know-how from the experience gained with the prototype. However, it is a completely new instrument, whose development has implied changes at all levels, from the detector arrays themselves all the way up to the optical chain of the 30 m telescope (all the components of the optical chain that follow the secondary mirror have been replaced). The NIKA2 pixels are based on Hilbert type LEKID that can efficiently absorb both polarization, the selection of the direction of the polarisation is done with a wire grid. The NIKA2 cryostat is precooled to $\sim$5 K by two Pulse Tubes (PT) working in parallel. A closed-cycle dilution refrigerator is then used to reach the base working temperature of about 150 mK, which is achieved after 5 days. The system, which is completely cryogen free and can be fully remote controlled, can then be kept cold indefinitely. The multiplexed readout of KID is achieved using dedicated electronics boards called NIKELv15 [8]. These board can excite and readout up to 400 pixels over a 500 MHz bandwidth. The camera has been permanently installed at the IRAM 30 m telescope in October 2015. And its commissioning phase is on-going to made accessible to the scientific community at the end of 2016, after a one-year commissioning period.

3 NIKA tSZ pilot study

NIKA2 SZ capabilities have been demonstrated through an SZ pilot study conducted with its pathfinder, NIKA. In the context of this pilot study we have mapped the SZ signal in the direction of six clusters of galaxies (Fig. 1), validating the KIDs capabilities when dealing with such a faint and diffuse signal [3,1], even at high redshift [2], with complex morphologies [4] and at the level of detection of the Planck catalogue of SZ sources [15].

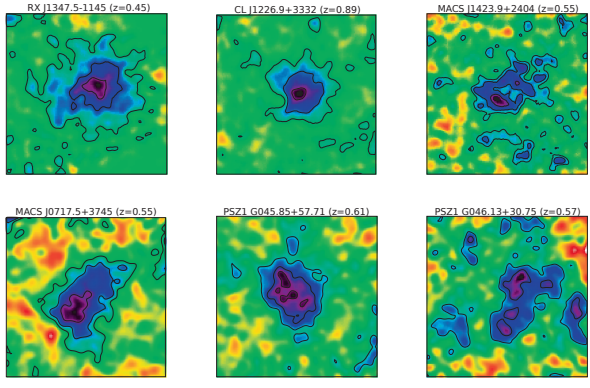


Figure 1 – Raw (no point source and foreground removal) 4 arcmin × 4 arcmin tSZ NIKA maps, obtained at 150 GHz for a sample of six clusters, whose name and redshift are provided in the titles.

3.1 Well-known cluster - RX J1347.5-1145

In November 2012, RX J1347.5-1145 was identified as the ideal test target. This cluster is one of the most extensively studied, located at intermediate redshift ($z = 0.451$). It represented a particularly well-suited candidate for the NIKA 5th run, being both compact and strong enough for the prototype FoV and sensitivity. Furthermore, this cluster is a perfect illustration of the complementarity of tSZ effect and X-ray signals: initially thought to be a well-relaxed (cool-core) object according to its first X-ray data, later tSZ observations showed a substructure located at ~ 20 arcsec from the center towards the SE region, interpreted as a hotter, over-pressured component resulting from a merging event. The non-trivial morphology makes this cluster an ideal target to validate NIKA capabilities of probing the details of ICM physics. The 140 GHz tSZ map, shown in Fig. 1, was obtained with a total observing time of 5h 47min and by using the highest frequency band for a dual-band decorrelation of the atmospheric noise [3]. In order to extract the signal from the shock, produced by the ongoing merger, we have modeled the relaxed component by considering a generalized Navarro, Frenk and White pressure profile centered at the X-ray position of the system. The model represents well the northern part of the tSZ map while the southern side cannot be explained without including an overpressure component, that is known to be due to the merging of a sub-cluster. This result has allowed us to prove that KIDs arrays are competitive detectors for millimeter wave astronomy, also for the observation of galaxy clusters via the tSZ effect, and that NIKA is able to recover the details of the energy distribution of the gas within clusters, by mapping their tSZ signal.

3.2 High-z cluster - CL J1226.9+3332

CL J1226.9+3332 is a hot and massive cluster, located at $z = 0.89$, that has been chosen to show the tSZ mapping capabilities of NIKA in observing high redshift objects [2]. With an overall

effective observing time of 7.8 hours, NIKA has provided the first resolved observation of this cluster at these frequencies, as Fig. 1 and 2 illustrate. The cluster signal is detected in the two bands, with a higher significance at 150 GHz, as expected, since at this frequency the signal is higher. The maps obtained for this cluster point out a further interesting point of the simultaneous dual-band capability. In the case of RX J1347.5-1145, the highest-frequency channel was used to build a template to remove the atmosphere contamination. This dual-band decorrelation approach has the advantage to enable the recovering the large-scale signal. Given the smaller angular size of CL J1226.9+3332, a single band common-mode decorrelation is instead used, and the dual band information has provided the detection of a sub-millimeter point source at 260 GHz, 30 arcsec away from the cluster center (Fig. 2, left panel). This source also partially compensates the tSZ decrement at 150 GHz (Fig. 1). The dual-band capability of NIKA has permitted to account for such contaminant and then to produce a robust reconstruction of the tSZ morphology (Fig. 2, right panel). These observations can then be used to reconstruct the pressure profile over a wide range of angular scales (from $\sim$ 20 up to $\sim$ 200 arcsec) and cluster typical scales (from 0.1 r_{500} up to r_{500}, r_{500} being the radius at which the cluster mean density is equal to 500 times the critical density of the Universe, at the cluster redshift). The reconstructed tSZ map of CL J1226.9+3332 has been used to constrain its pressure distribution, as well as the thermodynamics of the ICM gas by combining it with X-ray data.

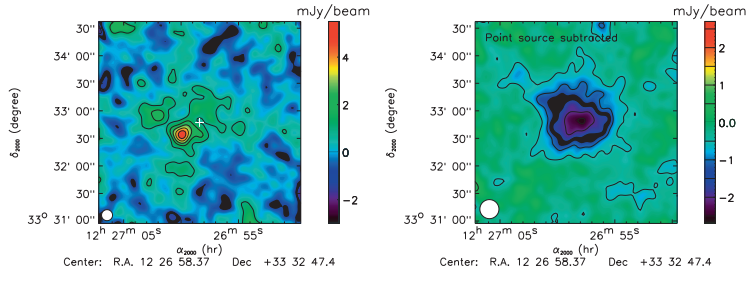


Figure 2 – NIKA maps of CL J1226.9+3332 at 260 GHz (left), and at 150 GHz after the subtraction of the contaminating point source (right). Contours are multiples of 3 σ. The bottom left white circles represent the FWHM of the native beams (12.0 and 18.2 arcsecond), although the displayed images are smoothed with an extra 10 arcsec FWHM Gaussian. The white cross on the 260 GHz map indicates the position of the X-ray center.

3.3 Relaxed cluster - MACS J1423.8+2404

MACS J1423.8+2404 has been chosen to test the observation of relaxed clusters as well as the impact of point sources contamination on the reconstruction of the pressure distribution with NIKA[1]. One of the main challenges in observing relaxed clusters is that they often host a strong central radio source, which can significantly compensate the tSZ decrement. Furthermore, in the context of high angular resolution tSZ observations, in general the removal of the contamination from point sources will be one of the main challenges. Galaxy clusters are in fact crowded environment, containing galaxies that can host radio sources or a significant amount of dust. Finally, clusters at intermediate redshift provide optimal lenses, which can magnify sub-millimeter background galaxies, in addition to the possible presence of foreground contaminating sources. In Fig. 3 we show a multi-wavelength view of MACS J1423.8+2404, as well as the NIKA maps at 150 and 260 GHz. In the 4 $\times$ 4 arcmin^2 field around MACS J1423.8+2404, 19 point sources have been identified and ancillary sub-millimeter (*Herschel*) and radio (SZA, OVRO/BIMA, VLA and NVSS). The target was detected by NIKA at 150 GHz (4.5 σ) in only 1.47 hours and the ring-like shape at 150 GHz (Fig. 1) shows evidence for the presence of a contaminating central radio source, as expected. But this cluster also hosts sub-millimeter point sources, two of

which are also detected on the NIKA 260 GHz map (Fig. 3, upper right panel). Previous radio observations have been used to extrapolate the fluxes to the NIKA bands, while sub-millimeter sources have been extrapolated by modeling their SED with a gray-body spectrum, obtained complementing the NIKA data with those from the *Herschel* satellite. The bottom left panel of Fig. 3 shows the 150 GHz map after point source subtraction. The results obtained for this cluster allow us to show that, if external data at complementary wavelengths are available, point sources contamination can be estimated and subtracted from the NIKA tSZ map. Nevertheless, the presence of a point source at the cluster center, without strong priors on its flux, can severely limit our ability to constrain the inner pressure profile and the cluster morphology. However, the resolved nature of the NIKA observations allows the large-scale pressure distribution to be almost unaffected by the presence of point source. The NIKA tSZ data have been combined also with the Planck ones, as well as with the X-ray observations obtained both with Chandra and XMM-Newton The comparison with X-ray only data shows good agreement for the pressure (Fig. 3, bottom right panel), temperature, and entropy profiles, all indicating that MACS J1423.8+2404 is a dynamically relaxed cool-core system. The tSZ-X joint analysis conducted on this cluster has also shown that the quality of the NIKA tSZ mapping enables to finally use the tSZ and X-ray complementarity to constrain the temperature and entropy profiles of galaxy clusters independently from X-ray spectroscopy, using density and pressure profiles. Moving to high redshift, X-ray observations become time expensive and high-quality X-ray mapping becomes challenging because of redshift dimming. In this context, the results we have obtained on this cluster show that we are able to constrain the ICM thermodynamics with a good accuracy by combining resolved NIKA tSZ observations and X-ray mapping.

4 NIKA2 tSZ large program

On the basis of the success of the NIKA tSZ pilot study, 300 hours of the NIKA2 telescope guaranteed time have been assigned to develop an *SZ Large Program*. The main objective of this program is to obtain high resolution tSZ observations for a representative sample of clusters at intermediate and high redshift ($z > 0.5$), to study the evolution of the cluster physical properties across cosmic times. At present, cluster derived cosmological constraints are in fact limited by our understanding of the impact of the details of cluster astrophysics and this kind of study is then mandatory to make clusters a competitive probe for the future challenges of precision cosmology. NIKA2 (Sect. 2) is well adapted for high angular resolution follow-up observations of SZ clusters, because of its large number of high sensitive detectors observing at two frequency bands (150 and 260 GHz), its large field of view (6.5 arcmin) and the resolution allowed by a 30 m telescope.

With this camera, we intend to observe a large (~ 50) and cosmologically representative sample of clusters of galaxies, with redshift ≥ 0.5. The main output of the program will be the study of the redshift evolution of the cluster pressure profiles and of the scaling laws relating cluster direct observables (i.e. the integrated Compton parameter, Y) to their total masses (M_{tot}). This can be achieved with NIKA2 tSZ observations and by combining them with ancillary data, including X-rays and optical observations, leading to significant improvements on the use of clusters of galaxies to draw cosmological constraints. Our target selection strategy is mainly driven by the need of an homogeneous coverage in SZ flux. Especially when dealing with SZ, a flux-selected subset of the cluster population can be considered as representative of a sample and not biased towards a given morphology. Such a sample is then adapted to the goals of our large program: derive relations that can be applicable to the whole cluster population, achieving a good global characterization of the cluster population and an improved control of systematics due to cluster astrophysics, up to high-z. Our selection criterion follows in fact the approach adopted to build the REXCESS [7] sample, an XMM-Newton large program dedicated to the in-depth study of a representative sample of 33 clusters ($0.055 < z < 0.183$) that has been used

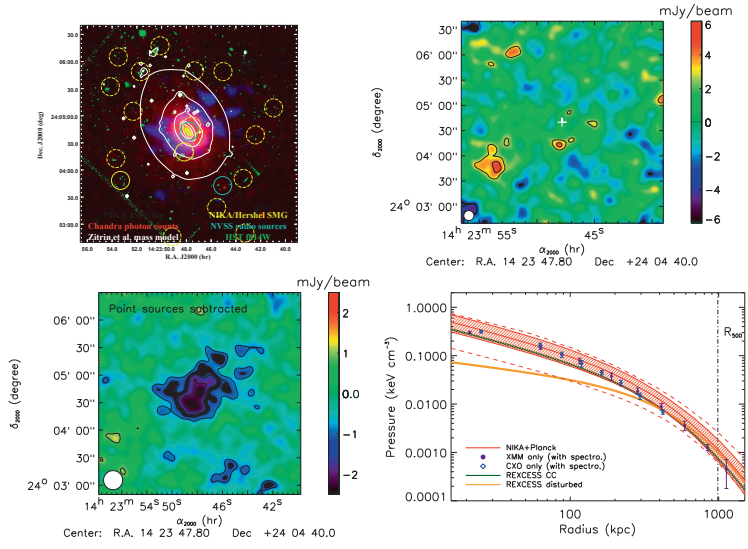


Figure 3 – **Upper left:** Composite multi-wavelength image of MACS J1423.8+2404. In blue the NIKA 150 GHz map (tSZ signal). In red the Chandra photon counts (tracing the electronic density). In green the Hubble Space Telescope data. The surface mass distribution model is shown by the white contours while the yellow circles correspond to millimeter sources locations obtained with the NIKA 260 GHz channel (solid line) and identified using *Herschel* (dashed-line). The cyan circles show the radio point sources present in the field (VLA). **Upper right:** NIKA 260 GHz map, the white cross indicates the X-ray center. **Bottom left:** NIKA 150 GHz map after point source subtraction. **Bottom right:** In red the NIKA constraints on the deprojected pressure radial profile of MACS J1423.8+2404. The Chandra and XMM-Newton only measurements are respectively shown with blue diamonds and purple dots. The green and orange solid lines respectively allows also comparison with the universal cluster pressure profiles of cool core and morphologically disturbed clusters, as obtained with REXCESS, a representative sample of nearby X-ray clusters.

to build the universal pressure profile for the ICM [5].

In order to fulfill this goal within the total available observing time, 300 hours, we have considered the following target selection criteria:

- clusters belonging to SZ selected samples (already existing tSZ based cluster samples from Planck and ACT) for which we already have the redshift information and estimates of the total tSZ flux (to add a further constrain at large angular scale);
- z > 0.5, to which the NIKA2 FoV is the most adapted;
- dec > -11, to ensure observability of the sources from the Pico Veleta site.

The overall observation time has been distributed among the different clusters of the sample taking into account the need of having a homogeneous quality of the maps, at a given characteristic radius, for the whole sample.

5 Conclusions

At present, cluster derived cosmological constraints are limited by our understanding of the impact of the details of cluster astrophysics. The development of precision cosmology with clusters requires high angular resolution and multi-probe studies (X-ray, tSZ, lensing, optical) up to high redshift. On the SZ side what must be done is to continue enriching catalogs up

to high z, but also to calibrate the properties of the cluster population at the different epochs: without these tools in our hands we cannot fully exploit catalogues, and we will remain limited by astrophysical systematics.

With NIKA2, a kilo-pixel KIDs based camera installed at the focal plane of the IRAM 30 m telescope, we will produce high-angular resolution ($\sim$ 20 arcsec) tSZ maps of a representative sample of clusters, belonging SZ selected catalogues and located at $z > 0.5$. The NIKA2 tSZ capabilities have been demonstrated through a pilot study, conducted with its pathfinder, NIKA. Between 2012 and 2014 NIKA has observed six clusters, providing excellent results up to high redshift ($z \sim 0.9$) and at the level of detection of the Planck catalogue of SZ sources.

The NIKA2 tSZ Large Program will spend 300 hours of telescope time observing a statistically significant ($\sim$ 50), representative sample of clusters of galaxies at intermediate and high redshift The angular resolution of the system will enable a detailed examination of cluster morphology through the tSZ effect. This will enable the study of the calibration of the SZ flux as a mass proxy, its evolution with redshift and cluster dynamics, the redshift evolution of the universal cluster pressure profiles, as well as deviations from its mean behavior due to cluster complex astrophysics and thermodynamical history. This kind of study is mandatory to achieve cluster derived precision cosmology.

Acknowledgments

We would like to thank the IRAM staff for their support during the campaigns. The NIKA dilution cryostat has been designed and built at the Institut Néel. In particular, we acknowledge the crucial contribution of the Cryogenics Group, and in particular Gregory Garde, Henri Rodenas, Jean Paul Leggeri, Philippe Camus. This work has been partially funded by the Foundation Nanoscience Grenoble, the LabEx FOCUS ANR-11-LABX-0013 and the ANR under the contracts "MKIDS", "NIKA" and ANR-15-CE31-0017. This work has benefited from the support of the European Research Council Advanced Grant ORISTARS under the European Union's Seventh Framework Programme (Grant Agreement no. 291294). We acknowledge fundings from the ENIGMASS French LabEx (R. A., F. R. and B. C.), the CNES post-doctoral fellowship program (R. A.), the CNES doctoral fellowship program (A. R.) and the FOCUS French LabEx doctoral fellowship program (A. R.).

References

1. R. Adam, B. Comis, J. F. Macías-Pérez *et al*, A&A **586**, A122 (2016).
2. R. Adam, B. Comis, I. Bartalucci *et al*, A&A **576**, A12 (2015).
3. R. Adam *et al*, A&A **569**, A66 (2014).
4. R. Adam *et al, in preparation.*
5. M. Arnaud *et al*, A&A **517**, A92 (2010).
6. L. E. Bleem *et al*, ApJS **216**, 2 (2015).
7. H. Böhringer *et al*, A&A **469**, 363 (2007).
8. O. Bourrion *et al*, JINST **7**, 7014 (2012).
9. M. Calvo *et al*, JLTP , arXiv:1601.02774 (2016).
10. A. Catalano, N. Ponthieu, M. Calvo & NIKA Collaboration, A&A **569**, A9 (2014).
11. M. Hasselfield *et al*, JCAP **07**, 008 (2013).
12. A. Monfardini *et al*, ApJS **194**, 24 (2011).
13. Planck Collaboration XIII, submitted to A&A , arXiv:1502.01589 (2015)
14. Planck Collaboration XXIX, A&A **571**, A29 (2014).
15. F. Ruppin *et al*, *in preparation.*
16. Z. Staniszewski *et al*, The Astrophysical Journal **701**, 32 (2009).
17. R. A. Sunyaev & Y. B. Zel'dovich, Comments Astrophys. Space Phys. **2**, 66 (1970).
18. R. A. Sunyaev & Y. B. Zel'dovich, Comments Astrophys. Space Phys. **4**, 173 (1972).
19. R. A. Sunyaev & Y. B. Zel'dovich, ARA&A **18**, 537 (1980).

THERMAL SUNYAEV ZEL'DOVICH EFFECT FROM HIGH REDSHIFT ($z > 2$) STRUCTURES

LOÏC VERDIER
Commissariat à l'énergie Atomique (CEA), Centre CEA de Saclay, 91191 Gif-sur-Yvette, France

We present the detection of a significant thermal Sunyaev-Zeld'ovich (tSZ) signal in high redshift structures by combining Planck observations with the Baryon Oscillation Spectroscopic Survey quasar catalogue. We first extract the flux from the Planck sky maps at the quasars' position with a matched filter. This flux is dominated by an emission from dust particles, probably lying inside the quasars themselves. In order to obtain the possible sub-dominant tSZ signal we develop an enhanced multifrequency matched filter which is able to separate tSZ from dust. With this tool, we extract a tSZ signal of $\overline{Y}_{500} = (10.86 \pm 1.46) \times 10^{-6}\mathrm{arcmin}^2$ (7σ detection) from structures in the redshift range $2.5 < z < 4$ [1]. It is currently difficult to interpret the origin of this signal. It could come from proto-clusters hosting the quasars or from the feedback of the quasars themselves.

1 Introduction : detecting the hot gas at high redshift

The baryonic matter in the densest regions of the Universe starts to be ionized at $z \simeq 9$ due to the presence of early stars and/or early quasars. The full ionization is reached at $z \simeq 6$. The hot ionized resulting gas could be detected by Bremsstrahlung X-ray emission or by the inverse Compton scattering of the CMB photons, the thermal Sunyaev Zeld'ovich (tSZ) effect, for far-infrared radiation. These two effects have been intensively used to detect individual structure like galaxy clusters which are the combination of a dark matter halo, galaxies (from tens to several thousands) and a virialized hot gas. For example, the Planck cluster catalogue was constructed from significant tSZ sources in the Planck maps [2]. Clusters counts from this kind of catalogue allow to constrain cosmological parameters.

However, the hot gas has only been detected in low-redshift galaxy clusters, up to $z \sim 2$ for the X-ray emission and up to $z \sim 1.9$ for the tSZ effect. Higher-redshift galaxy clusters and proto-clusters (the progenitors of the galaxies clusters) are too faint to be detected individually in X-ray or tSZ. So, a big part of the story of the formation of hot gas structures is still unveiled.

To detect the tSZ effect from the gas in these higher-redshift structures, a statistical approach is required. We need an independent tracers of the matter overdensities to proceed. For each position given by the tracer, we extract a signal with a proper filter on millimeter flux maps. In order to increase the signal-to-noise ratio and get a significant signal, we work with the average signal on the whole tracer population.

We employ here the final version of the non-polarized Planck sky maps (2015) [3]. We restrain our analysis to the following 7 frequencies : 70 GHz, 100 GHz, 143 GHz, 217 GHz, 343 GHz, 545 GHz and 857 GHz. Each sky maps is cut into 504 small tangential patches. We will extract our signal on these patches. Our tracers are the quasars from the SDSS-DR12 BOSS catalogue [4]. This catalogue contains 297 301 quasars. We removed the quasars lying in the region where the dust emission dominates in the Planck maps in order to avoid foreground contamination.

2 Monofrequency filtering

The first step of the analysis is dedicated to the extraction of the flux at the quasars'position at each frequency to build the average spectra and identify the nature of the signal. First of all, we assume we can write the flux from the Planck map at the frequency ν as the sum of a flux from a structure plus some noise:

$$m_\nu(\vec{x}) = F_\nu \cdot \tau_\nu(\vec{x} - \vec{x_0}) + n_\nu(\vec{x}) \tag{1}$$

with $m_\nu(\vec{x})$, the Planck map at the position on the sky $\vec{x} = (RA, DEC)$, F_ν the flux from the structure (quasar and hot gas), $\vec{x_0}$ the quasar's position, $\tau_\nu(\vec{x})$ the spatial profile of the cluster (convolved with the Planck beam) and $n_\nu(\vec{x})$ the instrumental and astrophysical noise. We suppose the noise to be stationary, so the following estimator of the flux is unbiased [5]:

$$\hat{F_\nu} = \int m_\nu(\vec{k})\phi_\nu(k)e^{-2\pi i k x_0}d\vec{k} \tag{2}$$

with $m_\nu(\vec{k})$ the Fourier transform of the Planck maps and $\phi_\nu(k) \propto \tau_\nu(k)/P_\nu(k)$, the matched filter. $\tau_\nu(k)$ is the Fourier transform of the profile and $P(k)$ the power spectrum of the noise in the Planck maps. For one quasar, the flux $\hat{F_\nu}$ is not significantly detected. We have to work with the average flux $< \hat{F_\nu} >$ on the whole quasar population. This leads to the figure 1. Our signal appears to be dominated by a modified black body spectrum which is the signature of a dust emission. If we perform the same analysis at random positions on the sky, our signal is compatible with zero confirming that the signal at the quasars' position is associated to structures hosting the quasars or to the quasars themselves.

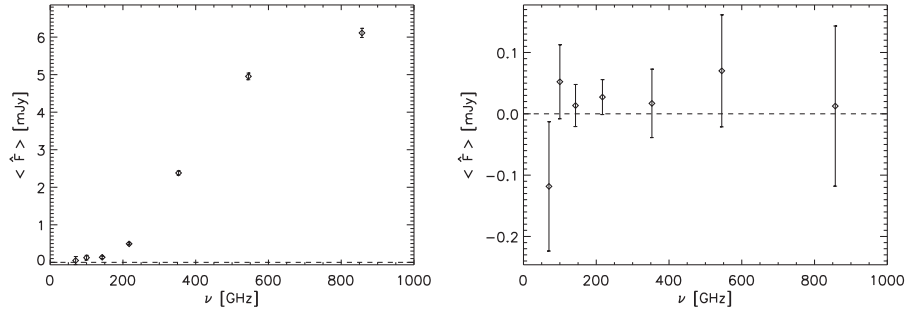


Figure 1 – Evolution of the average flux with the Planck frequencies for structures at the quasars' position (left) or at random positions (right).

3 Multifrequency filtering

3.1 Extraction of the tSZ component at low frequencies

Our signal is dominated by dust emission, at least at high frequencies. So we restrain here our analysis to the 100 GHz and 143 GHz Planck maps and we assume the tSZ signal to be dominant:

$$F_\nu = y \cdot tSZ(\nu) \tag{3}$$

with $tSZ(\nu)$ the spectral signature of the tSZ effect which does not depend on the redshift of the object and y the Compton parameter. For each quasar, we extract $\hat{y}$ employing a multifrequency matched filter (MMF) combining the data at several frequencies with respect to the spectrum

of the signal, here $tSZ(\nu)$. This filter could be seen as a combination of the mono-frequency matched filters ϕ_ν. The MMF has been intensively used for extracting tSZ emission and for building the Planck cluster catalogue [6]. After the extraction, we convert y into the intrinsic Compton parameter $Y_{500} = y \cdot E^{-2/3}(z) \cdot \left(\frac{D_A(z)^2}{500\mathrm{Mpc}}\right)$ with $D_A(z)$ the angular distance. For a low-redshift virialized cluster, Y_{500} only depends on M_{500} the total mass (baryon + dark matter) of the cluster so $Y_{500} = f(M_{500})$. If the gas is non-virialized, this relation is not valid.

We split our SDSS-DR12 catalogue into redshift bin of size $\Delta z = 0.5$ and we obtain the evolution with redshift of the average estimated Compton parameter $< \hat{y} >$ and the average estimated intrinsic Compton parameter $< \hat{Y}_{500} >$. These evolutions are presented in the left panel of the figure 2. We do not find a significant tSZ signal. The dust emission at low-frequency might compensate the tSZ signal which is negative for $\nu < 217\,\mathrm{GHz}$. So, we need the leverage arm at high frequencies for constraining and removing the dust emission.

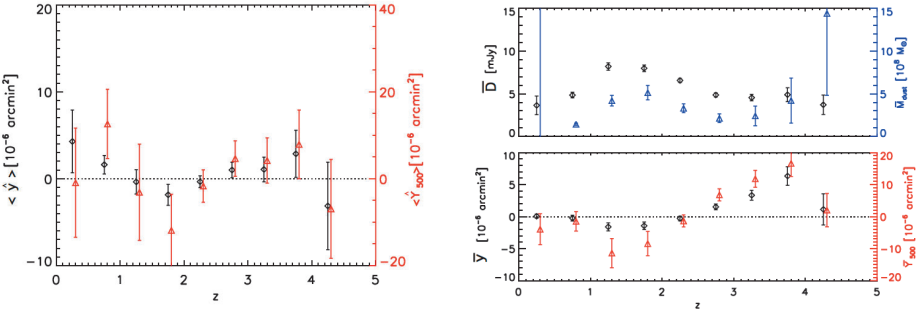


Figure 2 – *Left panel:* The evolution of the average Compton parameter (black diamond) and the intrinsic one (red triangle) with redshift for a low-frequency filtering assuming a tSZ emission alone. *Bottom right panel:* The evolution of the marginalized Compton parameter (black diamond) and the intrinsic one (red triangle) with redshift assuming a mixture of tSZ and dust emissions. *Top right panel:* The evolution of the marginalized dust amplitude (black diamond) and the dust mass (blue triangle) with redshift assuming a mixture of tSZ and dust emissions.

3.2 Extraction of the the dust and tSZ components

We work again with the 7 Planck frequencies spanning from 70 GHz to 857 GHz. Let us assume our signal to be the mixture of a dominant dust emission and a sub-dominant tSZ :

$$F_\nu = y \cdot tSZ(\nu) + D \cdot dust(\nu, \beta_d, T_d, z) \tag{4}$$

with D the amplitude of the dust emission and $dust(\nu, \beta_d, T_d, z)$ the dust spectrum. We assume this emission to be a grey body, the product of the black body with a power law: $dust(\nu, \beta_d, T_d, z) \propto \nu^{\beta_d} B_\nu(\frac{T_d}{1+z})$. In the contrary of $tSZ(\nu)$, the dust emission is not universal and depends on the redshift of the source. It also depends on two parameters, the slope of the power law β_d and the temperature T_d. These values are not well constraint for the dust so we let them free. The mass of the dust lying in the structure M_{dust} can be computed from D, with a general relation $M_{dust} = D \cdot g(\beta_d, T_d, z)$ [7]. In order to extract simultaneously the estimators $\hat{y}$ and $\hat{D}$, we built a multi-component MMF which is a linear combination of simple MMF assuming different spectrum for the different emissions, here $tSZ(\nu)$ and $dust(\nu, \beta_d, T_d, z)$.

We choose starting values for β_d and T_d and we extract $\hat{y}$ and $\hat{D}$ for each quasar. We compute the average values $< \hat{y} >_{\beta_d, T_d}$ and $< \hat{D} >_{\beta_d, T_d}$ on the whole quasar sample considered. We redo the same operation for different values of β_d and T_d, exploring the (β_d,T_d) plane. We marginalize $< \hat{y} >_{\beta_d, T_d}$ and $< \hat{D} >_{\beta_d, T_d}$ on β_d and T_d in order to obtain the following marginalized quantities $\overline{y}$ and $\overline{D}$. The same method is employed for computing the equivalent quantities $\overline{Y_{500}}$ and $\overline{M_{dust}}$.

Quasars with a counterpart in the FIRST (Faint Images of the Radio Sky at Twenty-Centimeters) survey are removed because they strongly contaminate the signal with a synchrotron emission at low-frequency. This emission might compensate the tSZ which is negative for $\nu < 217\,\mathrm{GHz}$. Results of the extraction for redshift bin of size $\Delta z = 0.5$ are presented in the right panel of the figure 2. The mass of the dust increases until $z \simeq 2$ and decreases after, following the star formation rate of galaxies [8] .

The intrinsic Compton parameter appears to be significant in the redshift range $2.5 < z < 4$. Its average value in this interval is $\overline{Y}_{500} = (10.86 \pm 1.46) \times 10^{-6}\mathrm{arcmin}^2$, a quantity significant at 7σ. Assuming a tSZ signal from virialized clusters and standard redshift evolution, we can estimate the mass of the galaxy clusters hosting the quasars, employing scaling laws. This lead to the average value of $1.71 \pm 0.13 h^{-1} 10^{13} \mathrm{M}_{\odot}$. It is compatible with clustering analysis of quasars done for SDSS-DR7, estimating the mass of the host clusters to be $1.41 \pm 0.6 h^{-1} 10^{13} \mathrm{M}_{\odot}$ [9].

4 Conclusion : interpretations of the tSZ signal

It is difficult to determine the origin of the tSZ-detected hot gas. It could be a virialized gas from young galaxy clusters, a gas ejected from quasars by feedback or a mixture of both. Additional constraints from other frequencies and a proper modeling of quasars feedback are required to interpret further the data. We investigate the X-ray counterpart of our tSZ signal in the ROSAT (Röntgensatellit) observations. We extract the average X-ray luminosity of the structures at the positions of the quasars in the redshift range $2.5 < z < 4$ and assuming scaling law for low-redshift galaxy clusters, we infer an equivalent tSZ signal of $\tilde{Y}_{500} = (51.4 \pm 4.6) \times 10^{-6}\mathrm{arcmin}^2$. It is 4 times stronger than the one estimated from Planck observations. If this discrepancy between the tSZ estimation and the X-ray one does not rule out completely the young cluster origin, it favors a feedback origin or at least a mixture of both.

The Atacama Cosmology Telescope (ACT) found a significant tSZ signal on ACT maps employing quasars from SDSS-DR10 as tracers [10]. Working with the galaxies from the Blanco Cosmology Survey and VISTA Hemisphere Survey as tracers ($z < 1.5$), the South Pole Telescope collaboration extracted also a significant tSZ signal in SPT maps [11]. Both studies favor the feedback interpretation.

Acknowledgments

I would like to thank the organizers of Les Rencontres de Moriond for the opportunity to present this study.

References

1. L. Verdier, J.-B. Melin, J. G. Bartlett, C. Magneville, N. Palanque-Delabrouille, and C. Yèche. *A&A*, 588:A61, Apr. 2016.
2. Planck Collaboration. *ArXiv e-prints*, Feb. 2015. 1502.01598.
3. Planck Collaboration. *ArXiv e-prints*, Feb. 2015. 1502.01587.
4. S. Alam et al. *ApJ Supplement*, 219:12, July 2015.
5. J. L. Sanz, D. Herranz, and E. Martínez-Gónzalez. *ApJ*, 552:484–492, May 2001.
6. J.-B. Melin, J. G. Bartlett, and J. Delabrouille. *A&A*, 459:341–352, Nov. 2006.
7. A. Beelen et al. *ApJ*, 642:694–701, May 2006.
8. P. Madau and M. Dickinson. *Annual Review of Astronomy and Astrophysics*, 52:415–486, Aug. 2014.
9. J. Richardson, Z. Zheng, S. Chatterjee, D. Nagai, and Y. Shen. *ApJ*, 755:30, Aug. 2012.
10. D. Crichton, M. B. Gralla, K. Hall, T. A. Marriage et al. *ArXiv e-prints*, Oct. 2015. 1510.05656.
11. A. Spacek, E. Scannapieco, S. Cohen, B. Joshi, and P. Mauskopf. *ApJ*, 819:128, Mar. 2016.

THE MASS ACCRETION RATE OF GALAXY CLUSTERS: A MEASURABLE QUANTITY

C. DE BONI

Institut d'Astrophysique Spatiale, CNRS (UMR8617) Université Paris-Sud 11, Bât. 121, F-91405 Orsay, France;
Dipartimento di Fisica, Università di Torino, via P. Giuria 1, I-10125 Torino, Italy;
Istituto Nazionale di Fisica Nucleare (INFN), Sezione di Torino, via P. Giuria 1, I-10125 Torino, Italy



We [1] are interested in investigating the growth of structures at the nonlinear scales of galaxy clusters from an observational perspective: we explore the possibility of measuring the mass accretion rate of galaxy clusters from their mass profile beyond the virial radius. We derive the accretion rate from the mass of a spherical shell whose infall velocity is extracted from N-body simulations. In the redshift range $z = [0, 2]$, our prescription returns an average mass accretion rate within $20 - 40\%$ of the average rate derived from the merger trees of dark matter haloes extracted from N-body simulations. Our result suggests that measuring the mean mass accretion rate of a sample of galaxy clusters is actually feasible, thus providing a new potential observational test of the cosmological and structure formation models.

1 The Mass Accretion History

The stochastic process of the mass accretion of dark matter halos is generally investigated with the identification of the merger trees of dark matter halos, enabling the study of the mass accretion history (MAH) and its derivative with respect to cosmic time, the mass accretion rate (MAR), as a function of redshift z. Here we explore the possibility of using the cluster mass profile at radii larger than the virial radius to estimate the MAR of galaxy clusters by measuring the mass of an infalling spherical shell surrounding the cluster. We compare the MAR estimated with our recipe with the MAR of dark matter halos derived from their halo merger trees obtained from the CoDECS suite of numerical simulations (www.marcobaldi.it/CoDECS) [2]. For each halo at $z = 0$ we build the MAH at $2R_{200}$. $2R_{200}$ roughly corresponds to the outermost radius reached by the accreted material in its first orbit around the cluster center, the so-called splashback radius $R_{\rm sp}$ [3].

2 The Spherical Infall Model

We aim to quantify the mass accretion rate (MAR) as the ratio between the mass of a spherical shell of thickness $\delta_s R_i$ and the time it takes to fall onto the halo. The thickness δ_s depends on the initial radius of the cluster R_i, on the infall time $t_{\rm inf}$, and on the initial infall velocity v_i. The infall radius $R_{\rm inf}$, i.e., the radius where the minimum of the radial velocity profile $v_{\rm rad}$ occurs, is between $2R_{200}$ and $3R_{200}$, independently of mass and redshift (Figure 1, left). We use $R_i = 2R_{200} \sim R_{\rm sp}$ as the radius at which we consider the infall to happen in our spherical infall prescription and $v_i \sim v_{\rm rad}(R_{\rm inf})$. For the infall time, which is the last parameter of the model, we choose $t_{\rm inf} = 10^9$ yr, similar to the dynamical time for the clusters of our analysis. Once R_i, $v_{\rm shell}$ and $t_{\rm inf}$ are specified, the model is completely determined. For each halo and for each progenitor at higher redshift, we evaluate the thickness δ_s of the infalling shell and its mass.

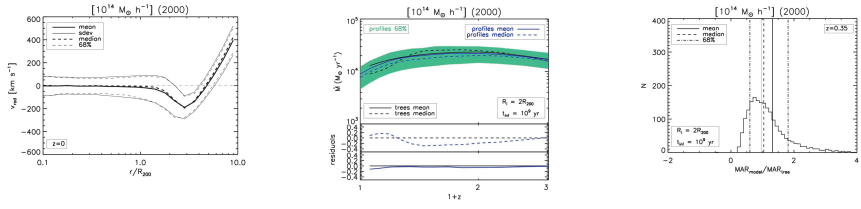


Figure 1 – Radial velocity profile at $z = 0$ (left), results of our spherical infall model and comparison with the MAR from merger trees (center) and histogram of the halo-by-halo ratio between the MAR from our spherical infall model and the MAR from the merger trees at $z = 0.35$ (right) for clusters of 10^{14} M$_\odot$ h^{-1}.

3 Results

The mean and median results from the merger trees lie within the region defined by the 68% range of the distribution of the MAR's obtained with our spherical infall prescription. The mean and median MAR from our prescription recover the merger tree results within 20% in the redshift range $z = [0, 2]$ for objects of 10^{14} M$_\odot$ h^{-1} (Figure 1, center). Despite our recipe was not conceived to completely capture all the features of the MAR derived by the complex merging process of individual halos, the average of the MAR of individual halos still is satisfactorily estimated by our recipe. The median value of the ratio between the MAR estimated with our recipe and the MAR derived from the merger tree for each individual halo is close to the ratio between the average MAR from our model and the average MAR from the merger trees (Figure 1, right). The final goal is to apply our spherical infall recipe to the clusters in the CIRS and HeCS catalogs whose outer mass profiles have already been measured with the caustic technique.

Acknowledgments

I thank my collaborators for allowing me to show results from our common projects. This work was partially supported by grants from Région Ile-de-France.

References

1. C. De Boni, A.L. Serra, A. Diaferio, C. Giocoli and M. Baldi, *Astrophys. J.* **818**, 188 (2016)
2. M. Baldi, *Mon. Not. R. Astron. Soc.* **422**, 1028 (2012)
3. S. More, B. Diemer and A.V. Kravtsov, *Astrophys. J.* **810**, 36 (2015)

Can dark energy explain the observed outflow in galaxy clusters?

M. Donnari[1,2], M. Arca-Sedda[1], M. Merafina[1]
[1] *Department of Physics, Sapienza University of Rome*
Piazzale Aldo Moro 5, I-00185 Rome, Italy

[2] *Department of Physics, Tor Vergata University of Rome*
Via O. Raimondo 18, I-00173 Rome, Italy

Recent observations of the Virgo cluster and the Local Group suggested that some galaxies are flowing out from their parent cluster. This may be the signature that dark energy (DE) acts significantly also on small cosmological scales. By means of direct N-body simulations we performed several simulations, in which the effect of DE and gravity are taken into account, aiming to determine whether DE can produce an outflow of galaxies compatible with observations. Comparing the different simulations, our results suggest that the observed outflow of galaxies is likely due to the local effect of DE.

1 Scientific context and numerical method

Recent observations of the local velocity field of the Local Group and the Virgo cluster, have revealed a linear velocity-distance relation of the outermost galaxies, properly referred to as Local Hubble Flow (LHF) [1, 2]. Following a non-Friedmann cosmology [3], we performed a series of direct N-body simulations of a galaxy cluster (composed by 240 galaxies) which suffers the anti-gravitational effect of DE, using a modified version of the direct N-body code `HiGPUs` [5]. We modelled also the Intra-Cluster Medium (ICM), limiting the study to its gravitational action, thus avoiding other effects. Nowdays there are still controversial opinions about the nature of the LHF. On large scales the Universe is homogeneous and the global Hubble constant is $H_0 \simeq 72$ km/s/Mpc. On the other hand, on small scales the Universe is inhomogeneous due to the presence of galaxies and clusters. Because of this, it is possible to define a local Hubble constant H_L, slightly different from the global one, H_0.

Each galaxies has been modelled according to the so-called γ-model and we put them in the space according to a King density profile. For DE, we take into account the ΛCDM model, by considering $\rho_\Lambda = 0.7 \times 10^{-29}$ g cm^{-3} [4] whereas for ICM we assume that its distribution is well represented by a modified β-model. In order to make our results as reliable as possible, we performed a single-particle (SP) simulation, in which each galaxy is represented as a point-like mass. This choice allowed us to simulate the evolution of the cluster up to $\simeq 30$ Gyr, since the computational time has been considerably reduced.

2 Results

We studied the trajectory of the outermost galaxies of the cluster founding that after a Hubble time the system lose around 10 % of its initial mass. Comparing MM4 and MM1 models (see left panel of Table 1), it is clear that the action of DE overtakes gravity, pushing the galaxy

away from the cluster. Even adding the gravitational effect of ICM, the galaxy still departs from its parent cluster, confirming that the gas gravitational field poorly affects the dynamics of the cluster. The correlation between the radial velocity and the distance from the cluster centre is a way to highlight the effect of DE on local volume by rougly estimate the value of H_L.

Table 1: Left: Physical processes considered in simulations and their evolutionary ages. Right: Values of H_L found from different models from both the best fit of the Hubble diagrams and the average for MM2 and SP models.

Model	Λ	ICM	$T_{ev}(Gyr)$
MM1	X		3.7
MM2	X	X	5.3
MM3		X	3.5
MM4			3.5
SP	X	X	30

Model	H_L (best fit) km/s/Mpc	H_L (average) km/s/Mpc
MM2	15.9 ± 5.3	22.0 ± 1.7
SP (5.3 Gyr)	20.8 ± 7.1	25.0 ± 4.4
SP (13.5 Gyr)	41.5 ± 4.4	44.0 ± 1.3
SP (30 Gyr)	61.1 ± 0.7	55.4 ± 0.7

In Fig. 1 is shown the Hubble diagram for MM4 model (left) in which the average of galaxies radial velocity is very close to zero, MM2 model (center) shortly after 5 Gyr. In this case is well visible the increasing of the outer galaxies radial velocity. In SP model (right) the evolution achieved the Hubble time, and the increasing of v_r is more evident.

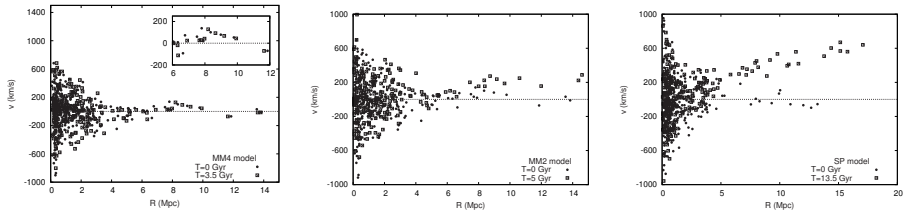


Figure 1 – Hubble diagrams of the cluster in MM4, MM2 and SP models. Dots represent the starting point wherease open squares represent the end of the simulation.

3 Conclusion

Our results suggest that a kind of LHF is possible only if DE contribution is take into account. The evaluation of the linear slope in the velocity-distance diagram, allows us to constraint the value of the local Hubble constant in the range $30 < H_L < 60$ km/s/Mpc. In the SP simulation we found that the averaged value of H_L increases in time and marks the evolutionary ages of the cluster, reaching a value of $H_L = 55.4 \pm 0.7$ km/s/Mpc at 30 Gyr. From the best fit of the Hubble diagram we obtain $H_L = 61.1 \pm 0.7$ km/s/Mpc. Hence, our results suggest that can be used for determining a rough estimate of the cluster dynamical age and, at the same time, they can be used for further testing different cosmological scenarios.

References

[1] I. D. Karachentsev *et al*, *A&A* **389**, 812 (2002).

[2] A. D. Chernin *et al*, *A&A* **520**, A104 (2010).

[3] A. D. Chernin, P. Teerikorpi and Y. V. Baryshev, *A&A* **456**, 13 (2006).

[4] Planck collaboration, P. A. R. Ade *et al*, *A&A* **520**, A104 (2010).

[5] R. Capuzzo-Dolcetta, M. Spera and D. Punzo, J. Co. Ph. **236**, 580 (2013).

7.
21 cm

Cosmology with the 21cm signal

M. G. Santos
Department of Physics, University of Western Cape, Cape Town 7535, South Africa
SKA South Africa, The Park, Park Road, Cape Town 7405, South Africa
CENTRA, Instituto Superior Técnico, Universidade de Lisboa, 1049-001 Lisboa, Portugal
E-mail: mariogrs@gmail.com

HI intensity mapping (IM) is a novel technique capable of mapping the large-scale structure of the Universe in three dimensions and delivering exquisite constraints on cosmology, by using HI as a biased tracer of the dark matter density field. This is achieved by measuring the intensity of the redshifted 21cm line over the sky in a range of redshifts without the requirement to resolve individual galaxies. Using this technique, the SKA will provide an unique (and transformational) window on Cosmology (from dark energy to Gravity and the primordial Universe). Moreover, a similar technique at higher redshifts (> 6) is being used to probe the Epoch of Reionization, when the first stars and galaxies formed.

1 Introduction

The cosmic microwave background (CMB) has been one of the main observational tools for cosmology in recent years. Although basically only giving 2-dimensional information, we were able to constrain the standard cosmological model with great accuracy [1]. This "high precision cosmology" is particularly true for the "vanilla" model with 6 parameters. More parameters or non-standard models can lead to degeneracies and limit the constraining power of the CMB (for instance the w_0/w_a non-flat model). The next step towards precision cosmology and exploring novel models will need to use extra information. In particular, due to its huge information content, measurements of the 3-dimensional large-scale structure of the Universe across cosmic time will be an invaluable tool. One of the most accessible methods to probe this is through large galaxy surveys to trace the underlying dark matter distribution. Several surveys are now under way or in preparation, such as BOSS (SDSS-III), DES, eBOSS, DESI, 4MOST, LSST, and the Euclid satellite. These surveys are based on imaging of a large number of galaxies at optical or near-infrared wavelengths combined with redshift information to provide a 3-dimensional position of the galaxies.

Galaxy surveys are threshold surveys in that they set a minimum flux above which galaxies can be individually detected. Instead we could consider measuring the integrated line emission of several galaxies in one angular pixel on the sky and for a given frequency resolution. For a reasonably large 3d pixel we expect to have several galaxies in each pixel so that their combined emission will provide a larger signal. Since Cosmology relies on scales much larger than galaxy sizes, using these large pixels should not affect the quality of the measurements. Moreover we can use statistical techniques, similar to those that have been applied for instance to CMB experiments, to measure quantities in the low signal to noise regime. By not requiring the detection of individual galaxies, the specification requirements imposed on the telescope will be much less demanding. This is what has been commonly called an "intensity mapping"

experiment. It is similar to what is being planned for experiments aimed at probing the Epoch of Reionization (at $z > 6$), such as the ones using the radio telescopes LOFAR, MWA and PAPER. By not requiring the detection of individual galaxies, the specification requirements imposed on the telescope will be much less demanding. This way, the intensity mapping technique transfers the problem to one of foreground cleaning: how to develop cleaning methods to remove everything that is not the HI signal at a given frequency [2,3,4]. This in turn also impacts on the calibration requirements of the instrument.

Several lines could be considered for intensity mapping: CO, CII, Lyman-α, H-α, etc. In this proceeding, we concentrate on the 21cm HI line. Although weaker than other lines, it has several advantages: Hydrogen is the most abundant element in the Universe and a good tracer of dark matter. It is observed at low radio frequencies and so it has very little contaminants from other lines at low redshifts. Moreover, because observations are done at long wavelengths, radio telescopes have naturally low resolutions and large fields of view, which matches perfectly the requirements for intensity mapping (while at the same time, having naturally high frequency/redshift resolution). Telescopes probing the sky between a rest frequency of 1420 MHz and 250 MHz will be able to detect the signal up to redshift 5. In particular, we focus on what can be achieved with a large survey using phase 1 of the Square Kilometre Array [5].

2 The HI signal

After reionization, most neutral hydrogen will be found in dense systems inside galaxies, e.g. Damped Lyman-alpha Absorbers (DLAs). In terms of the brightness temperature, the average signal over the sky can be written as:

$$\overline{T}_b(z) \approx 566h \left(\frac{H_0}{H(z)}\right) \left(\frac{\Omega_{\rm HI}(z)}{0.003}\right) (1+z)^2 \ \mu{\rm K}, \tag{1}$$

where the neutral hydrogen density fraction is given by

$$\Omega_{\rm HI}(z) \equiv (1+z)^{-3} \rho_{\rm HI}(z)/\rho_{c,0}, \tag{2}$$

$\rho_{\rm HI}(z)$ is the proper HI density and $\rho_{c,0}$ the critical density of the Universe at redshift zero. Figure 1 shows constraints on $\Omega_{\rm HI}(z)$ from different experiments. For a recent summary of observed trends we refer to Padmanabhan et al.[6].

Assuming the signal is linear with respect to the underlying dark matter fluctuations, the total brightness temperature at a given position on the sky and frequency will be

$$T_b(\nu, \Omega) \approx \overline{T}_b(z) \Big[1 + b_{\rm HI}\delta_m(z) - \frac{1}{H(z)}\frac{dv}{ds}\Big]. \tag{3}$$

The signal will then be completely specified once we find a prescription for the HI density and bias function ($b_{\rm HI}$). This can be obtained by making use of the halo mass function, $\frac{dn}{dM}$ and halo bias, while relying on a model for the amount of HI mass in a dark matter halo of mass M, e.g. $M_{\rm HI}(M)$.

For the mass function, we decided to consider a simple power law:

$$M_{\rm HI}(M) = AM^{\alpha}, \tag{4}$$

which is independent of redshift. We found that a value of $\alpha \sim 0.6$ fits both the low z and high z data reasonably well. This can be seen in figure 1 (left), that shows the $\Omega_{\rm HI}(z)$ measurements and the evolution obtained from this model (solid line). The constant A is normalised to the results from Switzer et al. [8] at $z \sim 0.8$. The right panel shows the redshift evolution for both the linear and power law model of the temperature multiplied by the bias, which is the figure of merit for the strength of the power spectrum used in the forecasts.

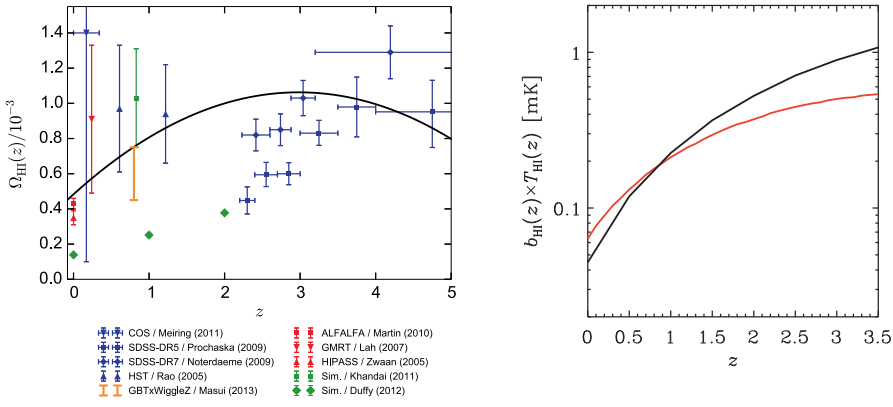


Figure 1 – Left: Current constraints on the HI density fraction as a function of redshift, partially based on the compilation in Duffy et al.[7]. DLA observations are shown in blue, cross-correlations in orange, other observations in red, and simulations in green. The thick black line shows $\Omega_{\rm HI}(z)$ from the fiducial model power law used throughout this chapter. Right: Evolution of the brightness temperature times bias with redshift for the linear (red curve) and our fiducial power-law model (blue).

3 Current and planned experiments

First attempts at using intensity mapping have been promising, but have highlighted the challenge of calibration and foreground subtraction. The Effelsberg-Bonn survey [9] has produced a data cube covering redshifts out to $z = 0.07$, while the Green Bank Telescope (GBT) has produced the first (tentative) detection of the cosmological signal through IM by cross-correlating with the WiggleZ redshift survey [10,8,11]. As probes to constrain cosmological parameters these measurements are, as yet, ineffective, but they do point the way to a promising future.

We can basically divide the intensity mapping experiments into two types: single dish surveys and interferometers. In single dish surveys (e.g. using auto-correlations) each pointing of the telescope gives us one single pixel on the sky (though more dishes or feeds can be used to increase the field of view). This has the advantage of giving us the large scale modes by scanning the sky. Since brightness temperature is independent of dish size we can achieve the same sensitivity with a smaller dish although that will in turn limit the angular resolution of the experiment (a 30 arc min resolution at $z \sim 1$ would require a dish of about 50 m in diameter). One example is the GBT telescope as described above. BINGO [12] is a proposed 40m multi-receiver single-dish telescope to be situated in South America and aimed at detecting the HI signal at $z \sim 0.3$.

Interferometers basically measure the Fourier transform modes of the sky. They have the advantage of easily providing high angular resolution as well being less sensitive to systematics that can plague the auto-correlation power. On the other hand, the minimum angular scale they can probe is set by their shortest baseline which can be a problem when probing the BAO scales. One example of a purpose built interferometer for intensity mapping is CHIME, a proposed array, aimed at detecting BAO at $z \sim 1$, made up of 20×100m cylinders, based in British Columbia, Canada. TIANLAI, set in China, follows a similar approach. A different setup is used in HIRAX, to be set in South Africa: an interferometer with about 1,000 highly packed 6m dishes.

The next generation of large dish arrays can also potentially be exploited for HI intensity mapping measurements. Such is the case of MeerKAT and ASKAP. However, these interferometers do not provide enough baselines on the scales of interest (5m to 80m) so that their

sensitivity to BAO will be small. The option is to use instead the auto-correlation information from each dish, e.g. make a survey using the array in single dish mode. The large number of dishes available with these telescopes will guarantee a large survey speed for probing the HI signal. The great example of this approach will be SKA1, the first phase of the SKA telescope, to be built in 2018. An HI intensity mapping survey will turn SKA phase 1 into a state of the art cosmological probe. In particular, the huge volume available with such a survey will surpass any other large experiment such as Euclid or LSST. In the following sections I will summarise what can be achieved with SKA1, assuming 133 15m dishes plus 64 13.5m MeerKAT dishes, a band 2 from 950 MHz to 1420 MHz ($0 < z < 0.5$) and a band 1 from 350 MHz to 1050 MHz ($0.35 < z < 3.06$) and a survey size of 25,000 deg^2 over 10,000 hours.

4 High precision cosmology with an SKA1-MID HI intensity mapping survey

Surveys of large-scale structure are a rich source of information about the geometry and expansion history of the Universe. The baryon acoustic oscillations (BAO) are a preferred clustering scale imprinted in the galaxy distribution, originating from the time when photons and baryonic matter were coupled together in the early Universe. By using them as a statistical 'standard ruler', one can obtain constraints on the expansion rate, $H(z)$, and (angular) distance-redshift relation, $D_A(z)$, as functions of redshift, as has been done successfully with recent large galaxy redshift surveys such as BOSS and WiggleZ. Measuring these functions is vital for testing theories of dark energy which seek to explain the apparent acceleration of the cosmic expansion, as they constrain its equation of state, $w = P/\rho$, and thus its physical properties. Shedding light on the behaviour of dark energy – especially whether w deviates from -1 and whether it varies in time – is one of the foremost problems in cosmology.

Intensity mapping (IM) has a few major advantages over conventional galaxy surveys for this task. IM surveys can map a substantial fraction of the sky with low angular resolution in a short period of time. Combined with the wide bandwidths of modern radio receivers, this makes it possible to cover extremely large survey volumes and redshift ranges in a relatively short time, helping to beat down sample variance. Figure 2 (left) summarises the expected constraints from the SKA HI IM surveys for the BAO scale at $k \sim 0.074$ Mpc^{-1}. Although the real power of the SKA1 IM survey will be on very large scales, we see that even at BAO scales, SKA1-MID present constraints not far from Euclid while only using a ~ 2 year survey (the full Euclid requires about 5 years). In fact, as shown in Bull [13], the high sensitivity of the SKA1 survey at low redshifts will allow it to surpass contemporary spectroscopic galaxy surveys such as DESI and Euclid in terms of constraints on modified gravity parameters. This is aided by the ability of an SKA1 IM survey to achieve sub-1% measurements of $f\sigma_8$, where $f(z)$ is the linear growth rate, which can be measured from the degree of anisotropy of the redshift-space correlation function (or power spectrum). The growth rate is directly related to the strength of gravity, and so is an extremely useful tool for probing possible deviations from general relativity that have been invoked as an alternative to dark energy to explain cosmic acceleration (see Figure 2 - right).

5 Probing very large scales with a SKA1 HI intensity mapping survey

The study of the Universe on ultra-large scales is one of the major science cases for the SKA. On ultra-large cosmic scales, two key effects become significant: primordial non-Gaussianity and relativistic corrections to cosmological observables. Moreover, if late-time acceleration is driven not by dark energy but by modifications to general relativity, then such modifications should become apparent near and above the horizon scale. As a result, the SKA is forecast to deliver transformational constraints on non-Gaussianity and to probe gravity on super-horizon scales for the first time. Figure 3 (left) summarises the expected constraints from the SKA HI IM surveys for a very large scale, past the equality peak at $k \sim 0.01$ Mpc^{-1}. We see the huge

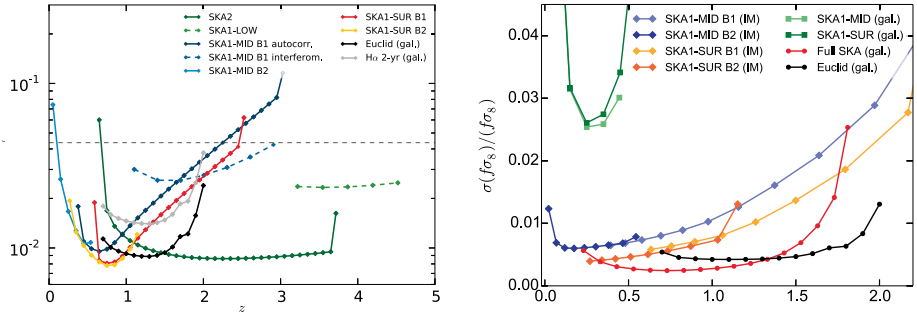


Figure 2 – *Left:* Constraints (noise over signal) from SKA HI IM surveys for BAO scales ($k \sim 0.074$ Mpc^{-1}) as a function of redshift. Dashed line shows the BAO detection threshold. The lower green curve shows what would be expected from a SKA2 IM survey (in interferometer mode) optimised for high-z. The grey curve shows what can be expected for a two-year H_α galaxy survey with similar depth as Euclid but over a smaller sky area. *Right:* Predicted constraints from SKA on the unparameterized growth function $f\sigma_8$ from the SKA1 (galaxy and IM) and the SKA2 galaxy survey, compared with predicted constraints coming from the Euclid galaxy survey. Both constraints include Planck+BOSS priors.

constraining power of these surveys (see Camera et al. [14] for a more in depth discussion).

In Camera et al. [15], an analysis is given of the constraining power of IM surveys over non-Gaussianity, showing that errors on $f_{\rm NL}$ can be taken down towards $\sigma_{f_{\rm NL}} \lesssim 3$ with SKA1, which is more than three times better than the current constraint from Planck. In terms of testing Einstein's theory of general relativity on horizon scales, one of the most interesting effects is the correction to the standard Newtonian approximation for the observed galaxy overdensity. It turns out that these relativistic corrections are very hard to detect using IM (although the same is true for other single tracers) due to cosmic variance. The way forward is the use of the multi-tracer technique. By combining an HI IM survey from SKA1 with a galaxy survey such as from Euclid or LSST, it is possible to obtain exquisite constraints on these large scale relativistic corrections as well as primordial non-Gaussianity [16] (Figure 3 - right). Moreover, these novel cross-correlation between different surveys will give a better handle on systematics and foreground issues.

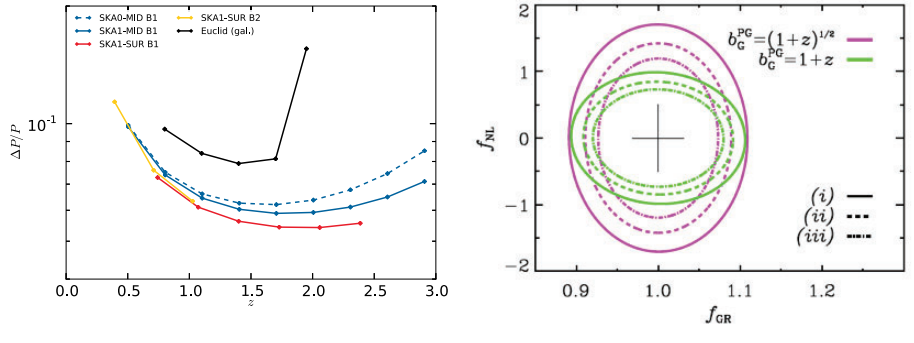


Figure 3 – *Left:* Constraints (noise over signal) from SKA HI IM surveys for large scales, past the equality peak ($k \sim 0.01$ Mpc^{-1}) as a function of redshift. A value below 1 would imply a detection. Dashed line indicates what can be achieved with SKA0 (50% of SKA1) which is quite similar to SKA1. *Right:* Joint constrains on primordial non-Gaussianity and relativistic corrections by combining an HI IM survey with a LSST type survey using the multi-tracer technique and assuming two different types of galaxy bias.

6 Foregrounds and Technical challenges

One of the most important challenges facing HI intensity mapping is the presence of foregrounds (both galactic and extra-galactic) with amplitudes several orders of magnitude larger than the signal to be measured. Because the frequency structure as well as other statistical properties of the foregrounds are significantly different from those of the cosmological signal, it is not unreasonable to hope that they can be successfully subtracted [17,18,19,20,21,22,23,24,25,26,27,28,29]. Although a lot of work in terms of simulations and testing cleaning techniques has already been done, we still face huge challenges ahead, in particular if we want to use this signal for high precision cosmology. Increasingly realistic large simulations should be developed to try to test the limitations of the intensity mapping measurements. This should include as many instrumental effects as possible in order to account for possible contamination from the calibration process. Ultimately, we will need to start analysing real data in order to improve and build up our knowledge towards the SKA.

The problem of foregrounds has been addressed in the literature mainly within the EoR regime. The different algorithms that have been proposed to date can be classified into *blind* [21,8,30] and *non-blind* [31,29,32] methods, depending on the kind of assumptions made about the nature of the foregrounds (e.g. whether only generic properties such as spectral smoothness and degree of correlation are assumed or whether a more intimate knowledge of the foreground statistics is required). The poor observational constraints on the foregrounds in the relevant range of frequencies justifies considering the use of blind methods. Recently, Wolz et al. [28] studied the effectiveness of independent component analysis (in particular the implementation of FastICA [33]) for intensity mapping. By propagating the foreground removal residuals into the cosmological analysis, they showed that, while foreground cleaning may induce a residual bias on large angular scales, which could prevent a full analysis based on the shape of the temperature power spectrum, robust features like the BAO scale should remain unaffected. This result is reasonable: most relevant foregrounds are (fortunately) exceptionally smooth and therefore it should be possible to distinguish them from the much "noisier" cosmological signal. Any foreground residual will probably be dominated by galactic synchrotron emmission, which is most relevant on large angular scales.

With regards to calibrating single dish experiments, this is a source of major concern. Major systematic effects to be tackled are spillover and sidelobe pickup as well as gain drifts. Again, these are issues that have been tackled successfully in the analysis of CMB data although novel approaches can be envisaged. So, for example, the BINGO experiment [12] propose to use a partially illuminated aperture and a fixed single dish, minimising the problems that arise from moving parts. Another intriguing possibility is, for a cluster of single dishes working in autocorrelation mode, to use the cross correlation data for calibrating off known sources. This means that in principle, calibrating the gains should be straightforward using the interferometer data since the high resolution will allow access to a good sky model.

7 Conclusions

HI intensity mapping is set to become a leading cosmology probe during this decade. One of the key instruments that can be used for this purpose is phase I of the SKA. A large sky survey with this telescope (in total power array) should be able to provide stringent constraints on the nature of dark energy, modified gravity models and the curvature of the Universe. Moreover, it will open up the possibility to probe BAO at high redshifts as well as ultra-large scales, beyond the horizon size, which can be used to constrain effects such as primordial non-Gaussianity or potential deviations from large-scale homogeneity and isotropy. The combination of this signal with galaxy surveys using the multi-tracer technique will provide revolutionary constraints on non-Gaussianity and relativistic corrections on large scales.

Several challenges will have to be overcome, however, if we want to use IM for cosmological

purposes. In particular, cleaning of the huge foreground contamination, removal of any systematic effects and calibration of the system. Foreground cleaning methods have already been tested with relative success taking advantage of the foreground smoothness across frequency but novel methods need to be explored in order to deal with more complex foregrounds. Other contaminants, such as some instrumental noise bias that shows up in the auto-correlation signal, can in principle be dealt with the same methods. Ultimately, we should deal with the cleaning of the signal and the map making at the same time. This will require even more sophisticated statistical analysis methods and it will be crucial to take on such an enterprise in the next few years in order to take full advantage of this novel observational window for cosmology.

Acknowledgments

MGS acknowledges support by the South African Square Kilometre Array Project, the National Research Foundation and FCT grant PTDC/FIS-AST/2194/2012.

References

1. Planck Collaboration. Planck 2013 results. XVI. Cosmological parameters. *ArXiv e-prints*, March 2013.
2. D. Alonso, P. G. Ferreira, and M. G. Santos. Fast simulations for intensity mapping experiments. *MNRAS*, 444:3183–3197, November 2014.
3. D. Alonso, P. Bull, P. G. Ferreira, and M. G. Santos. Blind foreground subtraction for intensity mapping experiments. *MNRAS*, 447:400–416, February 2015.
4. L. Wolz et al. Foreground subtraction in Intensity Mapping. In *Advancing Astrophysics with the Square Kilometre Array*, page PoS (AASKA14) 032, 2014.
5. Robert Braun, Tyler Bourke, James A Green, Evan Keane, and Jeff Wagg. Advancing Astrophysics with the Square Kilometre Array. *PoS*, AASKA14:174, 2015.
6. H. Padmanabhan, T. R. Choudhury, and A. Refregier. Theoretical and observational constraints on the HI intensity power spectrum. *ArXiv e-prints*, July 2014.
7. A. R. Duffy, S. T. Kay, R. A. Battye, et al. Modelling neutral hydrogen in galaxies using cosmological hydrodynamical simulations. *MNRAS*, 420:2799–2818, March 2012.
8. E. R. Switzer, K. W. Masui, K. Bandura, L.-M. Calin, T.-C. Chang, X.-L. Chen, Y.-C. Li, Y.-W. Liao, A. Natarajan, U.-L. Pen, J. B. Peterson, J. R. Shaw, and T. C. Voytek. Determination of z ˜ 0.8 neutral hydrogen fluctuations using the 21 cm intensity mapping autocorrelation. *MNRAS*, 434:L46–L50, July 2013.
9. J. Kerp, B. Winkel, N. Ben Bekhti, L. Flöer, and P. M. W. Kalberla. The Effelsberg Bonn H I Survey (EBHIS). *Astronomische Nachrichten*, 332:637, July 2011.
10. Tzu-Ching Chang, Ue-Li Pen, Kevin Bandura, and Jeffrey B. Peterson. Hydrogen 21-cm Intensity Mapping at redshift 0.8. *Nature*, 466:463–465, 2010.
11. K. W. Masui et al. Measurement of 21 cm Brightness Fluctuations at z ˜ 0.8 in Cross-correlation. *Ap. J. L.*, 763:L20, January 2013.
12. R. A. Battye, I. W. A. Browne, C. Dickinson, G. Heron, B. Maffei, and A. Pourtsidou. HI intensity mapping: a single dish approach. *MNRAS*, 434:1239–1256, September 2013.
13. P. Bull. Extending Cosmological Tests of General Relativity with the Square Kilometre Array. *ApJ*, 817:26, January 2016.
14. S. Camera, A. Raccanelli, P. Bull, D. Bertacca, X. Chen, P. Ferreira, M. Kunz, R. Maartens, Y. Mao, M. Santos, P. R. Shapiro, M. Viel, and Y. Xu. Cosmology on the Largest Scales with the SKA. *Advancing Astrophysics with the Square Kilometre Array (AASKA14)*, page 25, 2015.
15. S. Camera, M. G. Santos, P. G. Ferreira, and L. Ferramacho. Cosmology on Ultralarge Scales with Intensity Mapping of the Neutral Hydrogen 21 cm Emission: Limits on Pri-

mordial Non-Gaussianity. *Phys.Rev.Lett.*, 111(17):171302, October 2013.
16. J. Fonseca, S. Camera, M. G. Santos, and R. Maartens. Hunting Down Horizon-scale Effects with Multi-wavelength Surveys. *ApJ*, 812:L22, October 2015.
17. T. Di Matteo, R. Perna, T. Abel, and M. J. Rees. Radio Foregrounds for the 21 Centimeter Tomography of the Neutral Intergalactic Medium at High Redshifts. *ApJ*, 564:576–580, January 2002.
18. S. P. Oh and K. J. Mack. Foregrounds for 21-cm observations of neutral gas at high redshift. *MNRAS*, 346:871–877, December 2003.
19. M. G. Santos, A. Cooray, and L. Knox. Multifrequency Analysis of 21 Centimeter Fluctuations from the Era of Reionization. *ApJ*, 625:575–587, June 2005.
20. M. F. Morales, J. D. Bowman, and J. N. Hewitt. Improving Foreground Subtraction in Statistical Observations of 21 cm Emission from the Epoch of Reionization. *ApJ*, 648:767–773, September 2006.
21. X. Wang, M. Tegmark, M. G. Santos, and L. Knox. 21 cm Tomography with Foregrounds. *ApJ*, 650:529–537, October 2006.
22. L. Gleser, A. Nusser, and A. J. Benson. Decontamination of cosmological 21-cm maps. *MNRAS*, 391:383–398, November 2008.
23. V. Jelić et al. Foreground simulations for the LOFAR-epoch of reionization experiment. *MNRAS*, 389:1319–1335, September 2008.
24. G. Bernardi, A. G. de Bruyn, M. A. Brentjens, B. Ciardi, G. Harker, V. Jelić, L. V. E. Koopmans, P. Labropoulos, A. Offringa, V. N. Pandey, J. Schaye, R. M. Thomas, S. Yatawatta, and S. Zaroubi. Foregrounds for observations of the cosmological 21 cm line. I. First Westerbork measurements of Galactic emission at 150 MHz in a low latitude field. *A & A*, 500:965–979, June 2009.
25. G. Bernardi, A. G. de Bruyn, G. Harker, M. A. Brentjens, B. Ciardi, V. Jelić, L. V. E. Koopmans, P. Labropoulos, A. Offringa, V. N. Pandey, J. Schaye, R. M. Thomas, S. Yatawatta, and S. Zaroubi. Foregrounds for observations of the cosmological 21 cm line. II. Westerbork observations of the fields around 3C 196 and the North Celestial Pole. *A & A*, 522:A67, November 2010.
26. V. Jelić, S. Zaroubi, P. Labropoulos, G. Bernardi, A. G. de Bruyn, and L. V. E. Koopmans. Realistic simulations of the Galactic polarized foreground: consequences for 21-cm reionization detection experiments. *MNRAS*, 409:1647–1659, December 2010.
27. D. F. Moore, J. E. Aguirre, A. R. Parsons, D. C. Jacobs, and J. C. Pober. The Effects of Polarized Foregrounds on 21 cm Epoch of Reionization Power Spectrum Measurements. *ApJ*, 769:154, June 2013.
28. L. Wolz, F. B. Abdalla, C. Blake, J. R. Shaw, E. Chapman, and S. Rawlings. The effect of foreground subtraction on cosmological measurements from intensity mapping. *MNRAS*, 441:3271–3283, July 2014.
29. J. R. Shaw, K. Sigurdson, U.-L. Pen, A. Stebbins, and M. Sitwell. All-sky Interferometry with Spherical Harmonic Transit Telescopes. *ApJ*, 781:57, February 2013.
30. E. Chapman, F. B. Abdalla, G. Harker, V. Jelić, P. Labropoulos, S. Zaroubi, M. A. Brentjens, A. G. de Bruyn, and L. V. E. Koopmans. Foreground removal using FASTICA: a showcase of LOFAR-EoR. *MNRAS*, 423:2518–2532, July 2012.
31. A. Liu and M. Tegmark. A method for 21 cm power spectrum estimation in the presence of foregrounds. *PRD*, 83(10):103006, May 2011.
32. J. R. Shaw, K. Sigurdson, M. Sitwell, A. Stebbins, and U.-L. Pen. Coaxing Cosmic 21cm Fluctuations from the Polarized Sky using m-mode Analysis. *ArXiv e-prints*, January 2014.
33. A. Hyvärinen. Fast and robust fixed-point algorithm for independent component analysis. *IEEE Trans. on Neural Network*, 10(3):626–634, 1999.

Tianlai: a 21cm radio telescope array for BAO and dark energy, status and progress

Fengquan Wu[1], Yougang Wang[1], Juyong Zhang[2], Huli Shi[1], and Xuelei Chen[1]
[1]*National Astronomical Observatories, Chinese Academy of Sciences, 20A Datun Road, Chaoyang District, Beijing, China*

[2]*Hangzhou Dianzhi University, Hangzhou, China,*

The Tianlai project is a 21cm intensity mapping experiment dedicated to the survey of the neutral hydrogen in the Universe below redshift 3. Through this survey, one could probe the large-scale structure and detect baryon acoustic oscillation (BAO) features to constrain dark energy models. The construction of the Tianlai cylinder and dish pathfinder arrays have been completed at the end of 2015, the two arrays are now undergoing the commissioning process.

1 Introduction

The 21cm radio emission comes from the transition between the two levels of the hydrogen 1s ground state, slightly split by the interaction between the electron spin and the nuclear spin. The splitting is known as hyperfine structure. As the neutral hydrogen constitutes about 3/4 of the baryonic matter in the Universe, these 21cm emissions provide a very useful tool to probe the universe. Radio observations usually suffer the problem of low angular resolution, but it has been proposed that the large-scale structure of the universe can be surveyed without resolving individual galaxies[1,2]. The hydrogen distribution follows cosmic density field on large scales, so the 21cm intensity fluctuations can be used to measure the power spectrum of matter fluctuations. From the power spectrum of matter fluctuations, one could detect the baryon acoustic oscillation (BAO) wiggles. The BAO wiggles could provide a "standard ruler" for distance measurement in cosmology and help us to understand the acceleration of the Universe and the nature of dark energy which causes such acceleration.

The Tianlai project is a pathfinder for testing the basic principles and key technologies of 21cm intensity mapping[3,4]. The project is an international effort with participants from China, France, the USA and Canada. Telescopes are built in a radio very quiet site in Balikun, Xinjiang, China[5], consist of 3 cylinders(15m wide and 40 m long) and 16 dishes(6m diameter) at present. A forecast for the capability of the cylinder array in constraining dark energy parameters and primordial non-Gaussianity can be found in Xu et al. (2015) [6].

2 Status and Progress

The construction of the Tianlai cylinder and dish pathfinder arrays (see Fig.1: left panel) have been completed at the end of 2015, the two arrays are now undergoing the commissioning process. The cylinder array includes three adjacent 15m long 40m wide cylindrical reflectors oriented in the North-South direction, equipped with 96 dual linear-polarization feeds(see Fig.1: right panel). These feeds could be moved freely along the guide rail. This allows people to

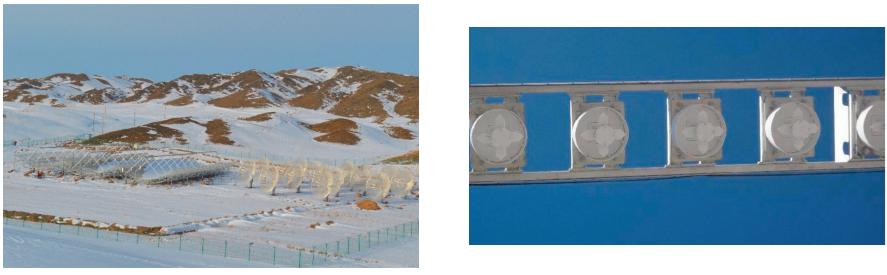


Figure 1 – Left: Tianlai cylinder array and dish array. Right: feeds on cylinder antenna.

change the separation between the feeds flexibly. Next to the cylinder array, there is also a dish pathfinder array, with 16 dishes of 6m diameter, each equipped with a dual linear-polarization feed. These dishes are equipped with electronically controlled motor drives in the altitude-azimuth mount, which allow us to steer the dishes to point to almost any desirable directions above the horizon.

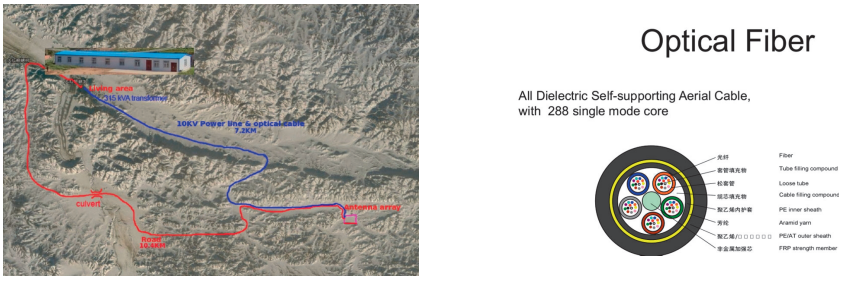


Figure 2 – Left:map of living area and antenna site. Right: sketch of optical fiber with 288 cores.

The antenna arrays are located in a sparsely populated area, shielded by hills and accessible only through a dirt trail. To avoid self-inflicted radio frequency interferences (RFI), the station house is built at the Hongliuxia village, which is about 8 km away as the crow flies. The array are connected with the station house by a 288-core optical fibre cable for signal transportation and a 10kV power line for electricity. (see Fig.2).

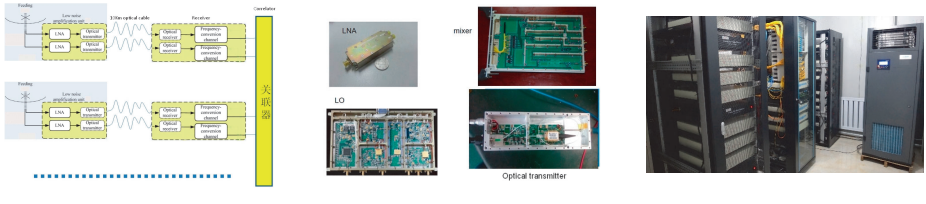


Figure 3 – RF analog system. Left: schematic of analog system. Center: LNA, mixer, LO and optical transmitter. Right: analog-system room.

The density evolution of the Universe is very sensitive to the dark energy below redshift 2.5. This redshift range corresponds to frequency of 400-1420MHz for 21cm emission. Therefore, the Tianlai array receivers are designed to have broad band response (400-1500MHz), and there is a replaceable bandpass filter in front of receiver which has 100 MHz bandwidth and very high rectangle coefficient(30dB:3dB <2). This enables us to switch the observation frequency easily. A schematic of the RF analog system is shown in Fig.3. The incoming radio wave is focused

by the cylinder reflector, picked up by the feed, and amplified by the low noise amplifier (LNA) mounted on the back of the feed can. The LNA is design to have low noise temperature (about 35K at room temperature) and wide operating frequency range(400-1500MHz). Then through the 3-layer shielded radio frequency (RF) cable, RF signal is sent to the optical transmitter under the antenna. Via optical transmitter, RF signal is converted to optical signal, which is then transmitted to the station house via optical fiber. In the RF analog system room in the station house, the optical signal is converted back to the RF electric signal, then in the mixer the RF signal is converted to the intermediate frequency (IF) band. Finally, the IF signal is sent to digital system in the next room through bulkhead connectors between the analog and digital systems (Fig.4 Right panel).



Figure 4 – Digital system(Left) and bulkhead connectors between analog and digital system(Right).

The digital backend system (Fig.4) has 200 signal channels, and it consists of three subsystems: (1) the analog to digital converter (ADC) and FPGA, which perform an fast Fourier transform (FFT) of the time series data and send the frequency domain data to a switch board; (2) the switch board system, with a rapidIO switch which connects the FPGA acquisition system and the DSP correlation system, the data of the same frequency but from different input channels are collected in the same unit for cross-correlation computation; (3) the DSP computing boards which computes the correlations. The sampling rate of the system is 250MSPS, with 14 bits sampling length.

The calibration system is very important, especially for the phase difference induced in the transmission of the data. The absolute calibration could be done by celestial calibration sources. We develop a set of relative calibration system by using the noise source controlled by the correlator. A schematic diagram for the noise source calibration system could be found in Fig.5.

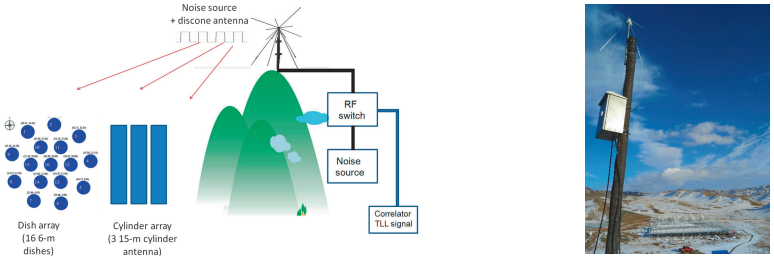


Figure 5 – Schematic diagram for noise source calibration system(Left) and calibration antenna on the hill beside the antenna array(Right).

3 Conclusion

The Tianlai pathfinder has both a cylinder array, with 3 north-south oriented cylinders of 15m wide, 40m long, and also a 16 dish array, with 6m dishes, which are dedicated to study new technique for 21cm intensity mapping. In the future the cylinder array may be expanded to $100m^2$ and thousands of receiver units. The construction of the Tianlai cylinder and dish pathfinder arrays have been completed by the end of 2015, the two arrays are now undergoing the commissioning process. A lot of adjustments and tests will be made during this year. Formal observation will probably start at the end of 2016, and may last a few years while we try to collect and analyse the data. By running this small experiment, we will be able to identify possible problems, make improvements, and try various methods of data analysis. Hopefully, the results of this experiment will pave the way for precision measurement of dark energy using radio observations.

Acknowledgments

This work is supported by the Ministry of Science and Technology of China through the 863 project (2012AA121701), by the Chinese Academy of Sciences through the Repair and Procurement program, the Strategic Priority Research Program XDB09000000, by the John Templeton Foundation and the NSFC grant 11473044.

References

1. T. Chang, U. Pen, J. B. Peterson, P. McDonald, Baryon Acoustic Oscillation Intensity Mapping of Dark Energy, Physical Review Letters 100, 1303(2008)
2. J.B. Peterson, et al., 2009, 21 cm Intensity Mapping, White Paper for the Astro2010 Astronomy Decadal Review, arxiv:0902.3091
3. Xuelei Chen., 2012, 090008The Tianlai project: a 21cm cosmology experiment090009, International Journal of Physics Conference Series, 12, 256, proceeding of the 2nd Galileo-Xu Guangqi Meeting (2009)070302 arxiv:1212.6278
4. Xuelei Chen at. al. Tianlai: A 21cm intensity Mapping Experiment, Proceedings of the XXXIst URSI General Assembly and Scientific Symposium
5. Fengquan Wu at. al. Site Selection for the Tianlai experiment, Proceedings of the XXXIst URSI General Assembly and Scientific Symposium
6. Xu Y., Wang X., Chen X., Forecasts on the Dark Energy and Primordial Non-Gaussianity Observations with the Tianlai Cylinder Array, ApJ, 798, 40 (2015)

Update on the BINGO 21cm intensity mapping experiment[a]

Richard Battye, Ian Browne, Tianyue Chen, Clive Dickinson, Stuart Harper, Lucas Olivari, Michael Peel, Mathieu Remazeilles, Sambit Roychowdhury, Peter Wilkinson
Jodrell Bank Centre for Astrophysics, School of Physics and Astronomy, University of Manchester, Oxford Road, Manchester M13 9PL, U.K.

Elcio Abdalla, Raul Abramo, Elisa Ferreira
Departamento de Física Matematica, Instituto de Física, Universidade de São Paulo, Rua do Matão 1371, São Paulo, Brazil

Alex Wuensche, Thyrso Villela
Divisão de Astrofísica, INPE, São Jose dos Campos - SP, Brazil

Manuel Caldas, Gonzalo Tancredi
Departamento Astronomia, Facultad de Ciencias, Universidad de la Republica, Igua 5225, 11400 Montevideo, Uruguay

Alexander Refregier, Christian Monstein
Institute for Astronomy, Department of Physics, ETH Zurich, Wolfgang Pauli Strasse 27, 8093 Zurich, Switzerland

Filipe Abdalla
Department of Physics and Astronomy, University College London, Gower St, London WC1E 6BT, U.K.

Alkistis Pourtsidou
Institute of Cosmology and Gravitation, University of Portsmouth, Dennis Sciama Building, Burnaby Road, Portsmouth P01 3FX, U.K.

Bruno Maffei
Institut d'Astrophysique Spatiale, Universite Paris Sud, 91405 Orsay Cedex, France

Giampaolo Pisano
School of Physics and Astronomy, Cardiff University, Queens Building, The Parade, Cardiff CF24 3AA, U.K.

Yin-Zhe Ma
School of Chemistry and Physics, University of KwaZulu-Natal, Westville Campus, Private Bag X54001, Durban 4000, South Africa

21cm intensity mapping is a novel approach aimed at measuring the power spectrum of density fluctuations and deducing cosmological information, notably from the Baryonic Acoustic Oscillations (BAO). We give an update on the progress of BAO from Integrated Neutral Gas Observations (BINGO) which is a single dish intensity mapping project. First we explain the basic ideas behind intensity mapping concept before updating the instrument design for BINGO. We also outline the survey we plan to make and its projected science output including estimates of cosmological parameters.

[a]We dedicate this update to the memory of our friend and colleague Prof Richard Davis OBE who passed away on 4th May 2016. He already played a role in the early stages of the development of the BINGO project and we were looking forward to benefiting from his technical wisdom as part of the project.

1 Introduction

The estimation of cosmological parameters from the anisotropies of the Cosmic Microwave Background (CMB) within the standard ΛCDM model is now a mature subject [1]. However, very tight constraints are limited to the flat 6 parameter model; if the model is extended to include, for example, the dark energy equation of state parameter $w = P_{\rm de}/\rho_{\rm de}$ then the angular diameter degeneracy leads to only weak constraints on w and increased error-bars on the other 6 parameters. In order to rectify this situation CMB data are often combined with a probe of Large-Scale Structure (LSS) and the most popular example is the use of the Baryonic Acoustic Oscillations [2] (BAOs) in the matter power spectrum deduced by performing galaxy redshift surveys in the optical waveband. The results of the BAO measurements are compatible with the CMB data from the *Planck* satellite and hence lead to tight constraints on any extension of the standard model. This is contrary to a number of other LSS probes [3] such as weak lensing, clusters counts and redshift space distortions.

In coming years the BAOs will be measured with increasing precision and over a wide redshift range by deep redshift surveys such as that which will be performed as part of the DESI project [4]. The BAOs are expected to be a relatively clean probe of cosmology, but at the level of precision probed by future experiments this cannot be guaranteed. It is important to contemplate performing similar surveys in other wavebands and, for example, it has been suggested that spectroscopic surveys using the redshifted 21cm line of neutral hydrogen can be carried out by the SKA [5]. This will require the significant collecting area of the SKA to detect high redshift galaxies due to the long lifetime of the spin-flip transition responsible for the line.

2 21cm intensity mapping

Observations made by a radio telescope are diffraction limited in the plane perpendicular to the line-of-sight and hence a telescope with a diameter of 10s of meters will have resolution $\sim 1\,$deg, but a spectral resolution of $\sim 1\,$MHz around an observation frequency of $\sim 1\,$GHz is easily achievable. Such a telescope will be unable to detect the 21cm signal from anything but the most closeby galaxies. However, there will be an overall integrated signal due to the combined effect of all galaxies within the beam, and this will vary from position to position on the sky. If this signal can be extracted from the much brighter continuum emission then processing it will allow an estimate of the matter power spectrum and techniques similar to those used in the optical can be used to extract cosmological information such as the BAO scale. This is the basic idea of 21cm intensity mapping [6,7].

In order to estimate the size of the signal consider a cell of the Universe corresponding to $(30\,{\rm arcmin})^2 \times 1\,{\rm MHz}$ observed at a frequency of 1 GHz, which corresponds to $z \sim 0.4$. The volume of the cell is $(8h^{-1}\,{\rm Mpc})^3$, such a region will contain an average of $\sim 10^{10}\,M_\odot$ neutral hydrogen and the r.m.s. variance in the density on such scales is $\sigma_8 \approx 1$. The average brightness temperature is $\sim 100\,\mu$K and such a signal could be detected with a radio telescope with instantaneous sensitivity on a bandwidth of 1 MHz of $\sim 50\,{\rm mK\,s^{1/2}}$ in 2-3 days of integration suggesting that the detection of such a signal over a significant portion of the sky would be possible in around a year observing.

In fig.1 we plot the expected 3D power spectrum as a function of wavenumber, k, for a redshift bin defined by frequencies $960 - 1260\,$MHz. We also present the BAO signal, highlighted by the ratio of the actual 3D power spectrum and one which is smooth, against wavenumber k. The amplitude of the signal is compatible with our earlier estimate and we see that the BAO signal is localised in the range $k = 0.02\,h^{-1}\,{\rm Mpc}$ to $0.2\,h^{-1}\,{\rm Mpc}$.

A number of dedicated projects have been proposed to detect this signal. These include interferometers such as CHIME [8] and TIANLAI [9], and also single dishes with multiple feedhorns such as BINGO (which stands for BAO from Integrated Neutral Gas Observations). The two approaches are complementary since interferometers are typically targeted at high redshifts

($z \sim 0.8$), while single dishes are more suited to lower redshift ($z \sim 0.3$) - the reason being that it can become prohibitively expensive to achieve the resolution necessary to resolve the BAO scale at higher redshifts (lower frequencies) using a single dish. Ultimately it might be possible to perform an intensity mapping survey using the SKA using both interferometric and single dish modes and such a survey could be competitive with the *Euclid* satellite [10].

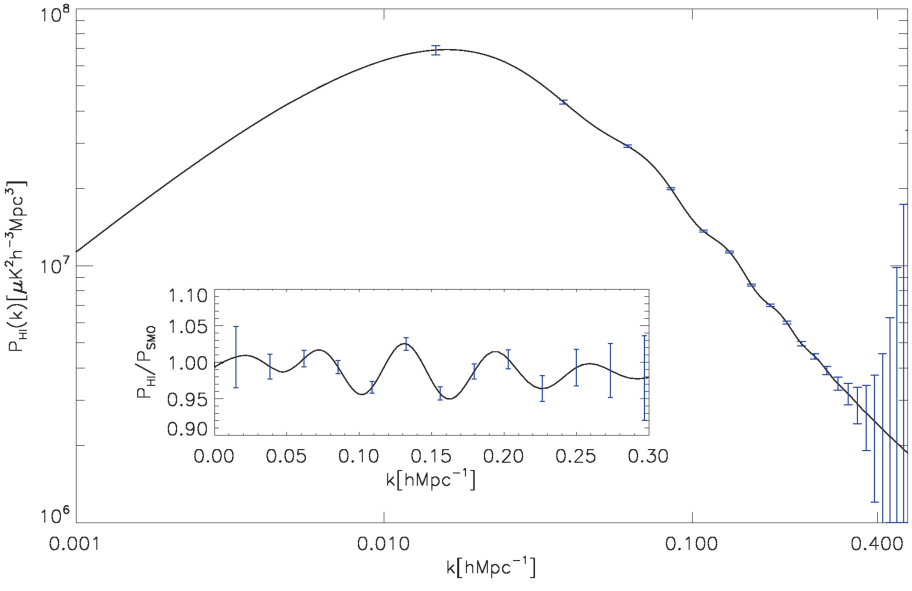


Figure 1 – The HI power spectrum, $P_{\rm HI}(k)$, versus wavenumber, k, at $z = 0.28$ - corresponding to the centre frequency of BINGO - along with projected errors on the reconstruction from the proposed BINGO survey with 50 feedhorns and 1 year of on-source integration time covering 2000 deg^2. Included as an inset is the power spectrum divided by a "smooth spectrum" to isolate the BAOs.

3 Updated BINGO concept

The basic idea of BINGO was discussed in the conference proceedings of the 2012 Moriond Cosmology meeting [11] and the single dish idea for intensity mapping has been studied in detail [12]. In this contribution we present an update of the design and the projected science output.

3.1 New optical design and basic telescope/survey parameters

The underlying concept behind the project is to provide a simple, clean and cheap approach to 21cm intensity mapping. We will build on the experience of measuring the anisotropies in the Cosmic Microwave Background (CMB) which has many similarities, although measurements of the CMB are at much higher frequencies and foregrounds are likely to be much more of a problem in the case of intensity mapping.

Originally we suggested [11,12] using a "cliff" telescope with a static dish at the bottom of a cliff of height ~ 100 m and a focal ratio ~ 3 in order to accommodate a large focal plane array with very little aberration at the edges. This would have been located at the top of the cliff which would allow the very heavy horns required to be supported by the cliff rather than an expensive mechanical structure. Unfortunately we were unable to find an appropriately sized cliff at the optimum latitude $\sim \pm(30 - 40)^\circ$ and therefore we have decided to evolve our

the design to have two dishes of comparable size with one acting as a secondary - the so-called Crossed-Dragone/Compact Range Antenna design often used in CMB polarization experiments. The basic optical design, which is more compact than the original one, is illustrated in fig. 2.

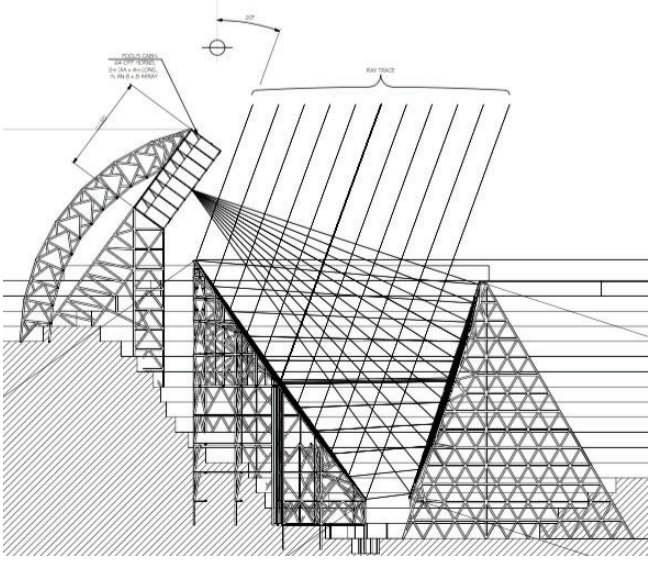


Figure 2 – Basic optical design of the BINGO telescope from side-on with a draft sketch of the mechanical structure. On the left is the focal plane array with rays focussed on a single pixel and on the right is the secondary mirror that has diameter $\sim 40\,\mathrm{m}$ which focusses the rays from the the primary mirror of diameter $\sim 48\,\mathrm{m}$.The primary is in the middle and this reflects the rays from the sky onto the secondary mirror.

The BINGO telescope will comprise of two static dishes surfaced with wire mesh, each with a diameter of around 40 m. They will be significantly under-illuminated (∼25 m) in order to suppress sibe-lobes and the beam will have a full-width-half-maximum (FWHM) of $\theta_{\mathrm{FWHM}} \approx 40\,\mathrm{arcmin}$ at an observing frequency of 1 GHz corresponding to a wavelength of $\lambda \approx 30\,\mathrm{cm}$. The telescope structure and the focal plane array of $\approx 50-100$ horns - will be supported by the sides of a quarry (see discussion of the site below). The receiver system will be a pseudo-correlation design in order to suppress the $1/f$ noise and achieve a "knee" frequency of $\sim 1\,\mathrm{mHz}$ over a bandwidth of 1 MHz. The output of each receiver chain will be the difference between the signal received from a main horn pointing at the dish and a reference horn which will point directly at the South Celestial Pole (SCP). There will need to be as many reference horns as main horns, and each will have a beam size $\sim 25\,\mathrm{deg}$. The overall system temperature, T_{sys}, of this uncooled system, built from "off-the-shelf" RF components, will be $\approx 50\,\mathrm{K}$ and have an overall instantaneous bandwidth of $\Delta f_{\mathrm{inst}} = 300\,\mathrm{MHz}$ from $f_{\mathrm{obs}} = 960\,\mathrm{MHz}$ to 1260 MHz corresponding to a redshift range of $z \approx 0.13 - 0.48$. The basic properties of the telescope are presented in table 1.

The telescope will be located at latitude $\approx -32°$ and perform a drift scan survey at declination $\approx -15°$. The receivers will be arranged so as to create an instantaneous field of view with a width of 15 deg in the direction perpendicular to the scan and up to 15 deg in the direction of the scan dependent on the number of horns. This will facilitate a survey of $15\,\mathrm{deg} \times 360\cos(15°)\,\mathrm{deg}$. The reference horns will point at the SCP, which will provide a constant signal with a similar spectrum to the rest of the sky enabling a good balancing of the pseudo-correlation system that will lead to cancellation of the $1/f$ noise. Any residual drifts in the receiver baseline will be removed by a combination of calibration and component separation techniques, for example, using

Principal Component Analysis [13] (PCA) or Generalised Needlet Internal Linear Combination [14] (GNILC).

Table 1: Summary of proposed BINGO telescope parameters

Main reflector diameter	40 m
Illuminated diameter	25 m
Angular resolution FWHM for observing at 1 GHz)	$\sim$ 40 arcmin
Number of feeds	50-100
System temperature	$\approx$ 50 K
Instantaneous field of view (dependent on number of horns)	15 deg $\times$ 15 deg
Frequency range	960 MHz to 1260 MHz
Number of frequency channels	$\geq$300

3.2 Foam horns

The BINGO design is extremely simple but there is one significant practical hurdle that needs to be overcome. The horns will be extremely large - they will need to have a diameter of $\sim$ 1.7 m and a length of $\sim$ 4.5 m and hence each horn would weigh around $\sim$ 2 tonnes if made from a conventional metal design. The focal plane array of 50-100 horns would be prohibitively expensive and require an extremely solid - and hence expensive structure - to mount them.

In order to overcome this problem we have designed corrugated horns made from foam that are coated with copper tape, which will be significantly lighter and less expensive. These horns are made of sheets of foam that are $\sim$ 2.5 cm thick which have an appropriate sized circular hole cut in them and copper tape stuck on. The sheets are then compressed together in order for the horn to have good electrical conduction. In fig. 3 we show a 124-element horn and the measured polar-diagram for the beam profile compared to a theoretical profile. The agreement between the measurement and theory is excellent in the high-signal-to-noise region for the measurements around the main beam and the side-lobes are also satisfactorily reproduced within the measurement accuracy. Note also that the sidelobes are reduced by -40dB relative to the main beam.

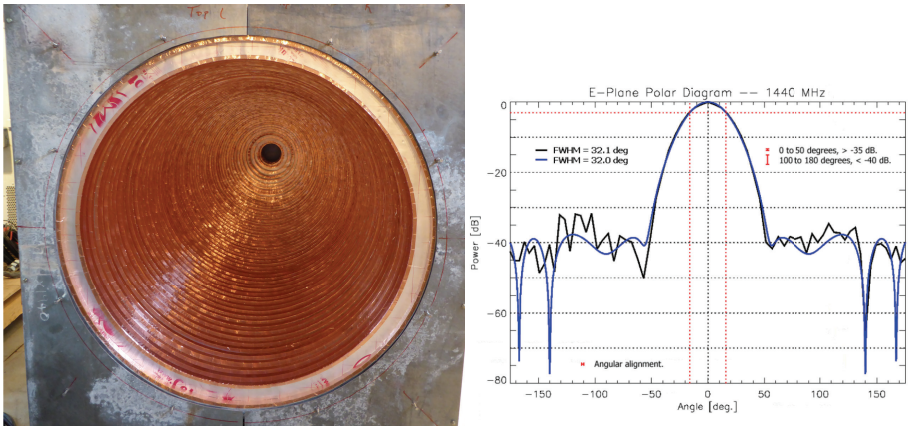


Figure 3 – On the left is a picture looking down the throat of the large foam based horn described in the text and on the right is the polar diagram of the horn [15]. Notice the good agreement, at least for the main beam between the measured beam and the theoretical prediction. Each indentation is a foam sheet covered with copper tape.

3.3 Site in Northern Uruguay

We have selected a site in Northern Uruguay close to the small town of Minas Corales. It will be in the Castrillon quarry - a dis-used gold mine that is well-matched to the BINGO optics being $\approx 50\,\mathrm{m}$ deep and $\approx 40\,\mathrm{m}$ wide, with a $\approx 45^\circ$ slope at one end, orientated close to N-S (see fig. 4). The main advantage of the site is the low population density of the area resulting in low levels of Radio Frequency Interference (RFI). Initial RFI tests in 2013 have shown that the $960 - 1260\,\mathrm{MHz}$ band is relatively clean at the site. We also have support from the mining company and the local community.

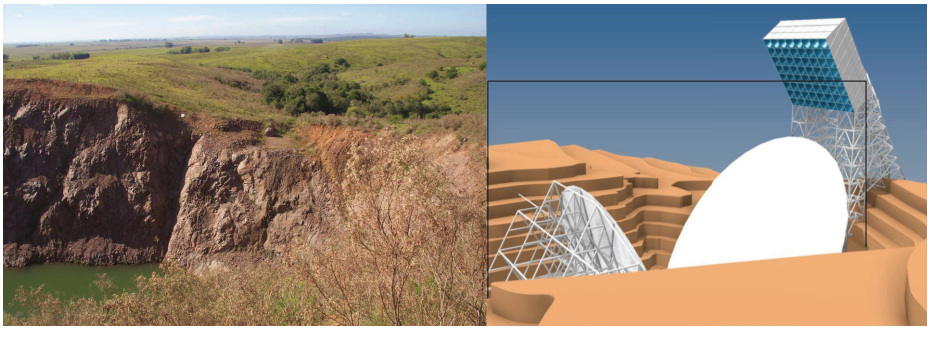


Figure 4 – On the left is a picture of the Castrillon quarry which is the proposed site of the BINGO telescope. On the right is an engineering drawing of the telescope with primary, secondary and focal plane array of horns in position. The black box in the right hand figure is approximately the plane of the picture on the left.

3.4 Project status and timeline

A proposal has been submitted to FAPESP, the São Paulo regional funding agency, to cover a significant fraction of the capital costs and it is in the final stages of being approved subject to (i) the successful construction of a full proto-type receiver chain including a full-scale horn, (ii) a design study of the telescope structure, and (iii) support is forthcoming from the other relevant funding agencies.

Phase 1 of the project which involves fulfilling the criteria (i)-(iii) is underway and will be completed by the middle of 2017. It is hoped that phase 2 of the project - the construction of the telescope within the Castrillon quarry - will take place during 2017-2018. The aim is to start science operations toward the end of 2018 and to take data for at least 4 years.

4 Projected science output and component separation

The main goal of BINGO is a measurement of the BAO scale in the redshift range $z = 0.13 - 0.48$ and the design has been optimised for this [12]. The choice of 40 arcmin resolution was chosen in order to achieve the best constraint on the BAO scale, k_A without getting into the situation where any improvement in the constraint leads to a significant the extra cost due to the increased resolution. Using a thermal noise dominated survey with 50 horns and 1 year of on-source integration time covering $\approx 2000\,\mathrm{deg}^2$, it was shown that a constraint of $\delta k_\mathrm{A}/k_\mathrm{A} \approx 0.025$ could be achieved. With an increased number of horns, that might be possible subject to cost, it should be possible to do somewhat better than this.

We have simulated the reconstruction of the power spectrum and the expected cosmological parameter estimation from the proposed BINGO survey in conjunction with information coming from the CMB observations made by *Planck*. Projected errorbars on the power spectrum for the survey described above are included in fig. 1. CMB observations by themselves cannot constrain the equation of state of dark energy, w, but we find that a combination of *Planck* and BINGO can constrain $\Delta w \approx 0.1$.

In addition to the measurement of BAOs there are many other interesting scientific goals that will be pursued as part of the BINGO project.

- *Neutrino masses:* The shape of the matter spectrum is sensitive to the masses of the neutrinos. If there is no significant scale dependent bias between the HI power spectrum and the underlying matter power spectrum then it will be possible to measure the sum of the masses of the neutrinos, $\sum m_\nu$, using BINGO observations.

- *Redshift space distortions:* Redshift space distortions can can be extracted from the 21cm intensity mapping signal by splitting the power spectrum into components which is perpendicular and parallel to the line-of-sight. It has been shown that such observations have the capacity to distinguish between different models of modified gravity [16]. Observations made by the BINGO telescope will be able to probe such models.

- *Cross-correlation with optical redshift surveys:* It should be possible to cross-correlate the 21cm intensity mapping survey provided by BINGO with the redshift survey provided by the Dark Energy Survey. We have estimated that there will be $\sim 800\,\mathrm{deg}^2$ of overlap between the two surveys. This should lead to additional constraints on the origin of cosmic acceleration [18].

- *Fast Radio Bursts (FRBs):* The Fast Radio Burst (FRB) phenomenon is arguably the most exciting and unexpected astronomical discovery so far this century [17]. BINGO with its multiple beams giving wide instantaneous sky coverage will be a great engine for FRB discovery. At present less than 20 examples are known and BINGO with suitable digital processing should be able to find them at a rate of tens per year. In order to achieve this, the BINGO telescope will need to be fitted with additional "backend" electronics needed to achieve a higher time resolution than necessary for intensity mapping. In an ambitious third phase of BINGO, small outrigger telescopes could be added in order to measure real-time accurate positions for FRBs to enable optical identification of their hosts, a step essential to distinguish between the many proposed explanations of the origin of FRBs.

- *Galactic science:* By virtue of the drift scan strategy the BINGO survey will cross the Galactic plane. Regions where the Galactic emission is particularly high will be excluded from the cosmological analyses, but they will provide interesting information on the nature of the this Galactic emission which will be combined with the observations, for example, from the *Planck* satellite to provide an improved model of the galaxy. Interesting information that could be gleaned from this will include line emission from the radio-recombination lines (RRLs) due to the ionised gas in the Galactic plane [19].

Acknowledgments

We would like to thank Adrian Galtress for his work on the mechanical design of the BINGO telescope and the engineering drawings presented in fig. 4.

References

1. Planck Collaboration, arXiv:1502.01589
2. A.J. Cuesta *et al*, arXiv:1509.06371
3. R.A. Battye, T. Charnock, A. Moss, *Phys. Rev.* D **91**, 103508 (2014)
4. J. Guy, in these proceedings
5. F. Abdalla, S. Rawlings, Mon. Not. Roy. Ast. Soc. **360**, 27 (2005)
6. R.A. Battye, R.D. Davies, J. Weller, Mon. Not. Roy. Ast. Soc. **355**, 1339 (2004)
7. T.-C. Chang *et al*, *Phys. Rev. Lett.* **100**, 091303 (2008)
8. K. Bandura *et al*, Proc. SPIE Int. Soc. Opt. Eng. **9145**, 22 (2014)
9. X. Chen, Int. J. Mod. Phys. Conf. Ser. **12**, 256 (2013)
10. P. Bull *et al*, Astrophysical Journal **803**, 21 (2015)
11. R.A. Battye *et al* in the Proceedings of the XLVIIth Rencontres de Moriond Ed. E. Auge, J. Dumarchez and J. Tran Thanh Van (2012), arXiv:1209.1041
12. R.A. Battye *et al*, Mon. Not. Roy. Ast. Soc. **434**, 1239 (2013)
13. M.-A. Bigot-Sazy *et al*, Mon. Not. Roy. Ast. Soc. **454**, 2154 (2015)
14. L. Olivari *et al*, Mon. Not. Roy. Ast. Soc. **456**, 2749 (2015)
15. A. Colclough, MSc Thesis, University of Manchester (2015)
16. A. Hall, C Bonvin, A. Challinor, *Phys. Rev.* D **87**, 064026 (2015)
17. D. Lorimer *et al*, Science **318**, 777 (2007)
18. A. Pourtsidou, D. Bacon, R. Crittenden, *Phys. Rev.* D **92**, 103506 (2015)
19. M.I.R Alves *et al*, Mon. Not. Roy. Ast. Soc. **405**, 1654 (2010)

Simulated Effects of $1/f$ Noise on an SKA Intensity Mapping Survey

Stuart E. Harper, Clive Dickinson, Richard Battye, Lucas Olivari
Jodrell Bank Centre for Astrophysics, School of Physics and Astronomy, University of Manchester, Alan Turing Building,Manchester M13 9PL, England

It has been proposed recently that the SKA1-MID could be used to conduct an HI intensity mapping survey that could rival upcoming Stage IV dark energy surveys. However, measuring the weak HI signal is expected to be very challenging due to contaminations such as residual Galactic emission, RFI, and instrumental $1/f$ noise. Modelling the effects of these contaminants on the cosmological HI signal requires numerical end-to-end simulations. Here we present how $1/f$ noise within the receiver can double the effective uncertainty of an SKA-like survey to HI on large angular scales ($\ell < 50$).

1 Introduction

It has long been considered that the 21 cm spin-flip transition of neutral hydrogen (HI) could be used as a tracer of large-scale structure (LSS) throughout the Universe. However, the low surface brightness of HI emission has meant that only a small number of individual galaxies have been surveyed at low redshifts.[1,2] A way forward for HI cosmology is to use a technique called intensity mapping (IM);[3] which measures the total integrated HI signal within voxels that contain many individual galaxies. IM is not limited to detecting HI emission from each independent galaxy, but instead treats the HI signal as a continuous field.

The SKA1-MID as an array of single dishes could perform an IM survey with sensitivities to LSS comparable to Euclid-like Stage IV dark energy surveys.[4,5] However, the HI signal is weak relative to other foreground emissions making HI emission challenging to isolate.[6] In particular, the difficulties associated with IM surveys have been recently highlighted by GBT observations.[7] Therefore it is likely IM surveys will not be sensitivity limited, but instead limited by systematic effects. Modeling these effects requires end-to-end simulations. Here, we present a preliminary discussion of the effect of $1/f$ noise on the recovery of the observed HI power spectrum for an SKA-like IM survey.

2 Simulations

The setup of the simulated SKA1-MID survey was designed to be similar to that described in Bull et al. 2015.[4] There are 180 dishes with a system temperature of 44 K, a frequency range of $350 - 1050$ MHz, and a frequency resolution of 35 MHz. The survey full-width half-maximum is 0.8 degrees. The specific observing strategy is continuous azimuthal rotation at a single fixed elevation of 50 degrees, and a total observing time of 30 days.

The simulated observed sky was created by combining maps of the cosmological HI signal, Galactic continuum foregrounds and $1/f$ instrumental noise. A `CAMB`-generated matter power spectrum was used to deduce the projected HI angular power spectra for each redshift slice.[3] The amplitude of Galactic foreground emission from synchrotron radiation was calculated using the reprocessed Haslam 408 MHz map,[8] and spectral indicies measured between 408 MHz and 2.3 GHz.[9] Free-free emission was simulated using a combined all-sky Hα map.[10]

The $1/f$ noise maps were created from binning time-ordered data (TOD) produced from the Fourier transform of a $1/f$ noise spectrum.[6,11] 90 noise map realisations were made at knee frequencies ($\nu_{\rm k}$) 0.1, 1, and 10 Hz. Figure 1 shows the survey area coverage and the relative brightnesses of the foregrounds, $1/f$ noise, and HI signal for a specific realisation. The $1/f$ noise model induces more power on longer timescales but these timescales contain little sky information. Therefore, filtering was applied to the TOD on timescales equal to the period of each azimuthal scan ring.

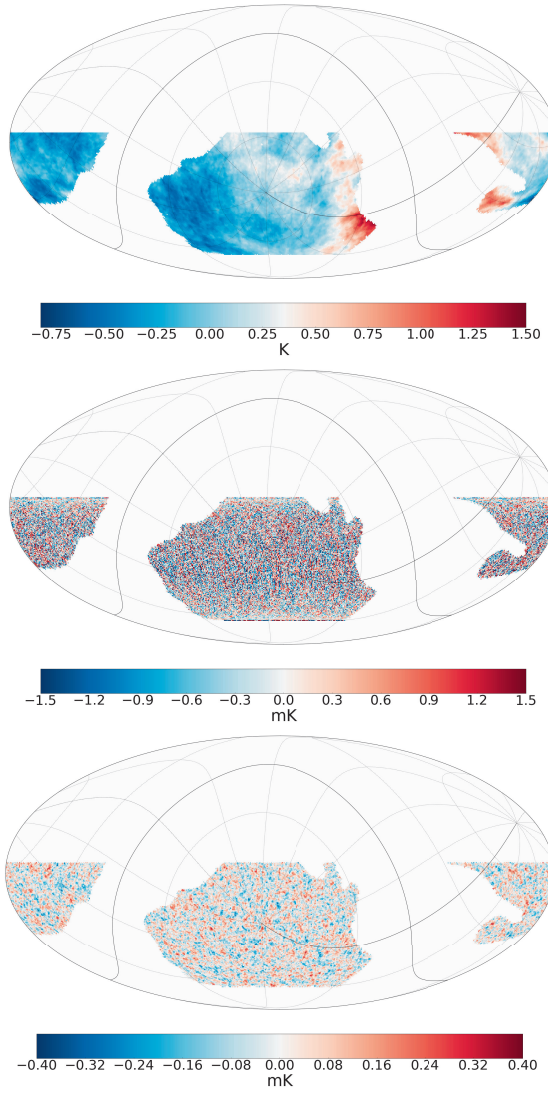


Figure 1 – Molleweide projections of the simulated sky at one frequency in the celestial frame overlaid with graticules in the Galactic coordinate frame. Note that the strip appears incomplete due to masking of the Galactic plane. The amplitude of the spatial brightness variations of the foregrounds (*top*, K) and $1/f$ noise (*middle*, mK) here dominate the cosmological HI signal (*bottom*, mK) by orders of magnitude.

It was found that $1/f$ noise with a perfectly flat frequency (bandpass) response could be trivially removed using blind component separation methods such as principle component analysis (PCA). However, in reality the frequency response of $1/f$ noise is not expected to be flat. Therefore a toy bandpass model with a 15 per cent smooth variation in gain at low and high frequencies was used to simulate the $1/f$ noise frequency response. Another interesting effect tested by the simulations were two bandpass calibration models. One model assumed perfect calibration with zero uncertainty in frequency space, and the other applied a 5 per cent Gaussian uncertainty to each frequency channel.

The input HI maps were recovered by performing PCA based blind foreground removal. The recovered HI power spectra were then calculated using `PolSpice`[12], accounting for incomplete sky coverage. Two figures-of-merit were used to determine the robustness of the recovered spectra (C_ℓ^k). First, the absolute mean fractional bias in the power spectrum defined as

$$b_\nu = \left| \left\langle \frac{C_\ell^{k,\nu} - C_\ell^{0,\nu}}{C_\ell^{\rm HI}} \right\rangle \right|, \tag{1}$$

where $C_\ell^{k,\nu}$ is the recovered power spectrum for a knee frequency k, $C_\ell^{0,\nu}$ is the recovered power spectrum for data with zero knee frequency, and $C_\ell^{\rm HI}$ is the measured power spectrum of the input HI map. Figure 2 shows the resulting bias for both perfect and 5 % bandpass calibration errors. In both cases the additional bias due to $1/f$ noise is always less than a few per cent across all ℓ with a slightly higher bias on large-scales, shown also in Table 1.

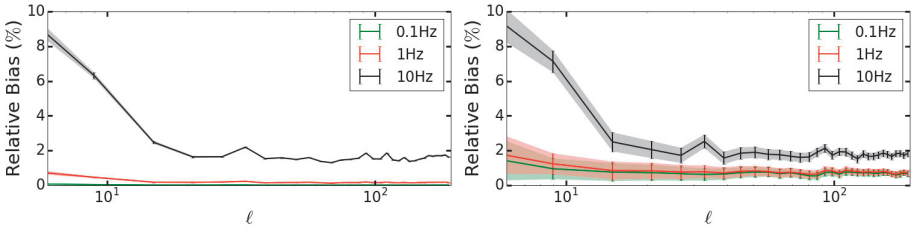


Figure 2 – Magnitude of the bias in the estimation of the power spectrum due to $1/f$ noise. *Left*: Perfect calibration across bandpass. *Right*: 5% Gaussian calibration error across bandpass.

Table 1: The measured bias in C_ℓ as a percentage due to $1/f$ noise for calibration uncertainties ($\sigma_{\rm cal}$) of 0 and 5 per cent over three ranges of ℓ for three knee frequencies ($\nu_{\rm k}$) of 0.1, 1, and 10 Hz.

ℓ		$0-10$		$10-50$		$50-190$	
$\sigma_{\rm cal}$		0%	5%	0%	5%	0%	5%
$\nu_{\rm k}$ (Hz)	0.1	0.04	1.0	0.018	0.7	0.016	0.7
	1	0.46	1.2	0.18	0.8	0.162	0.8
	10	6.3	7.1	1.85	2.0	1.56	1.8

The second figure-of-merit is the ratio of the additional uncertainty on each recovered C_ℓ due to the $1/f$ noise (σ_c) over the expected white-noise level (σ_w) defined as, $r_\nu = \sigma_c/\sigma_w$. Figure 3 and Table 2 show the additional uncertainties assuming 0 % and 5 % frequency calibration errors. The increase at low-ℓ when there is no calibration errors is small, less than 20 per cent for all knee frequencies and all ℓ. However, the $1/f$ noise combined with a calibration error of 5 % effectively doubles the noise level of the survey even for the smallest knee frequency of 0.1 Hz.

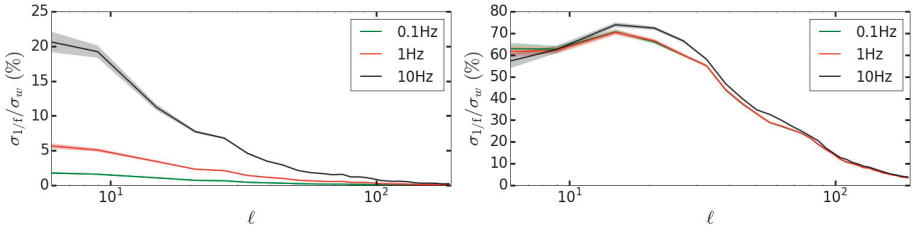


Figure 3 – Ratio of the additional noise on each C_ℓ due to $1/f$ noise over the calculated white-noise from the simulated SKA survey. *Left*: Perfect bandpass calibration. *Right*: 5% Gaussian calibration error across bandpass.

Table 2: The increase in uncertainty on each C_ℓ as a percentage due to $1/f$ noise over the expected uncertainty from white-noise. For each range of ℓ results based on perfect and 5% calibration uncertainties are presented.

ℓ		0-10		10-50		50-190	
$\sigma_{\rm cal}$		0%	5%	0%	5%	0%	5%
$\nu_{\rm k}$ (Hz)	0.1	1.6	62	0.59	55	0.090	13
	1	5.1	62	1.90	56	0.285	13
	10	19.2	63	6.1	60	0.80	14

3 Discussion

The results presented in Section 2 indicate that just $1/f$ receiver noise combined with a 5 % calibration error can almost half the sensitivity of an SKA-like survey to large-scales ($\ell < 50.$). However, the results of Section 2 are dependent upon the complexity of the frequency response of the $1/f$ noise. In reality the $1/f$ noise is expected to be more complex in frequency than the toy model assumed here, which could lead to large increases in the bias and uncertainty due to $1/f$ noise. Further, the calibration errors are unlikely to have a Gaussian distribution but will have skewed or correlated errors. For more details see Harper et al. 2016 (*in prep.*). The effects of component separation on the results also require future investigation, as other techniques will yield different results to those of the PCA method. Finally, it should be pointed out that the complexity of real observations, due to other systematics such as standing waves or RFI, will further increase the bias and uncertainty in the HI power spectra.

References

1. M. A. Zwaan, M. J. Meyer, L. Staveley-Smith, et al. MNRAS, 359:L30–L34, May 2005.
2. A. M. Martin, E. Papastergis, R. Giovanelli, et al. ApJ, 723:1359–1374, November 2010.
3. R. A. Battye, I. W. A. Browne, C. Dickinson, et al. MNRAS, 434:1239–1256, September 2013.
4. P. Bull, P. G. Ferreira, P. Patel, et al. ApJ, 803:21, April 2015.
5. M. Santos, P. Bull, D. Alonso, et al. AASKA14, 19, 2015.
6. M.-A. Bigot-Sazy, C. Dickinson, R. A. Battye, et al. MNRAS, 454:3240–3253, December 2015.
7. L. Wolz, C. Blake, F. B. Abdalla, et al. ArXiv e-prints, October 2015.
8. M. Remazeilles, C. Dickinson, A. J. Banday, et al. MNRAS, 451:4311–4327, August 2015.
9. P. Platania, C. Burigana, D. Maino, et al. A&A, 410:847–863, November 2003.
10. C. Dickinson, R. D. Davies, and R. J. Davis. MNRAS, 341:369–384, May 2003.
11. M. Seiffert, A. Mennella, C. Burigana, et al. A&A, 391:1185–1197, September 2002.
12. I. Szapudi, S. Prunet, D. Pogosyan, et al. ApJ, 548:L115–L118, February 2001.

The Multi-Tracer Technique To Detect Horizon-Scale Effects

Stefano Camera
Jodrell Bank Centre for Astrophysics, School of Physics, and Astronomy, The University of Manchester
Alan Turing Building, Oxford Road, Manchester M13 9PL, UK



The opportunity of measuring various effects occurring on the largest cosmic scales have recently drawn an increasing attention, thanks also to the strong effort that will lead to next-generation cosmological experiments such as the *Euclid* satellite, the Large Synoptic Survey Telescope, and the Square Kilometre Array. Such experiments will probe enormous volumes of the Universe, allowing us to have a glimpse at scales near and beyond the cosmological horizon. The study of perturbations on those scales is extremely interesting, because their evolution is fully linear, and we can safely neglect baryonic effects occurring on much smaller scales. Through probes of ultra-large scales we can learn a lot about gravity, inflation and the early Universe. Unfortunately, measurements of such long-wavelength modes are hampered by the poor statistical sampling usually referred to as 'cosmic variance'. Here, we shall briefly review the so-called 'multi-tracer' technique, which will enables us to overcome cosmic variance by comparing the relative clustering of different tracers of the underlying cosmic structure. We shall discuss the most recent results and also illustrate how an incorrect treatment of horizon-scale effects may lead to a seriously biased reconstruction of cosmological parameters.

1 Horizon-Scale Cosmology

Constraints on properties and evolution of density fluctuations on extremely large scales, near and beyond the Hubble horizon $H^{-1}(z)$, will greatly improve our understanding of gravity, inflation and the physics of the early Universe [see e.g. 1, 2]. Hitherto, the study of the physics occurring on those scales has remained confined in a rather small niche, mostly because of the impossibility of performing measurements that could corroborate theoretical findings. However, the next decade will see a revolution in this respect, mostly thanks to forthcoming observational campaigns like the European Space Agency's flagship, the *Euclid* satellite [3, 4],[a] and the Large Synoptic Survey Telescope (LSST),[b] at optical/near-infrared wavelengths, or the various surveys envisaged for the Square Kilometre Array [5, 6, 7, 8],[c] at radio frequencies.

[a] `http://www.euclid-ec.org`
[b] `http://www.lsst.org`
[c] `https://www.skatelescope.org`

1.1 *Relativistic Corrections*

A crucial point that has to be emphasised is that, when we observe galaxies, we do not really have access to a Universe 'cube', but we rather see sources on the past light-cone. This means that we cannot simply perform a three-dimensional Fourier analysis of source number counts to get the power spectrum of density fluctuations. Instead, the correct procedure is to take such light-cone projection effects into account via e.g. full-sky angular power spectrum tomography or spherical Bessel-Fourier decomposition [9, 10, 11]. (Similar considerations can be made concerning redshift-space analyses [e.g. 12].) This procedure leads to general relativistic (GR) corrections to the standard linear power spectrum. The observed galaxy number counts contain not only the well-known Kaiser redshift-space distortions (RSDs), but also further GR contributions from gravitational redshift, lensing convergence, Doppler terms, Sach-Wolfe (SW) and integrated SW (ISW) terms, and a time-delay term.

On sub-Hubble scales, terms other than RSDs and lensing are typically negligible. However, on scales near and beyond the horizon, the other purely GR terms become increasingly important. This is one of the reasons why cosmology on horizon scales is so promising to deepen our knowledge of gravity. On the one hand, if we measure such purely GR effects, we will have a further confirmation of the validity of Einstein's theory of gravity in a régime extremely far from where we have accurate tests of it. On the other hand, deviations from the GR prediction on ultra-large scales will be a strong hint in favour of an explanation of the present-day cosmic acceleration in terms of modified gravity effects [see e.g. 13].

1.2 *Primordial Non-Gaussianity*

A small amount of non-Gaussianity in the primordial distribution of density fluctuations is predicted in many scenarios of inflation [e.g. 14]. We can parameterise through an overall amplitude, $f_{\rm NL}$, such primordial non-Gaussianity (PNG) in Bardeen's gauge invariant potential Φ, as the sum of a linear Gaussian term ϕ and a quadratic correction [15], namely $\Phi = \phi + f_{\rm NL}(\phi^2 - \langle\phi^2\rangle)$. A non-Gaussian distribution of primordial density perturbations cannot be fully described by a power spectrum. In this case, we also need higher-order moments such as the bispectrum, andc. In particular, different models of inflation give rise to different bispectrum shapes, thus making the study of PNG valuable for obtaining a deeper knowledge of the physics of inflation.

So far, the best way to probe PNG has relied upon measurements of the cosmic microwave background (CMB) temperature anisotropy bispectrum [see 16, for the most recent results]. However, it has been demonstrated that PNG also induces an additional, peculiar scale and redshift dependence in a biased tracer of the underlying matter distribution [e.g. 17]. For the sake of simplicity, we shall limit ourselves to the most well-studied type of PNG, which is referred to as 'local' type. The modification $\Delta b(z,k)$ it causes to the Gaussian large-scale bias b of a biased tracer is $\Delta b(z,k) \propto 3[b(z)-1]f_{\rm NL}/[k^2T(k)D(z)]$, where $b(z)$ is assumed scale-independent, $T(k)$ is the transfer function, $D(z)$ is the linear growth factor of density perturbations (normalised to unity today), and the proportionality depends on other standard cosmological parameters. Clearly, the effect of local-type PNG on the power spectrum grows on large scales because of the k^{-2} term.

2 Accessing the Largest Scales

Until recently, measurements of horizon-scale effects have been out of reach even for the most advanced cosmological experiments. On the one hand, the CMB is, practically speaking, a single slice in redshift. This implies that the reconstructed power spectrum of its temperature (or polarisation) anisotropies is a two-dimensional quantity, with much fewer large-scale modes than any three-dimensional probe [see also 18]. On the other hand, the matter power

spectrum reconstructed from spectroscopic surveys [e.g. 19] relies on computing correlations between three-dimensional positions of a large number of galaxies. However, it is hard to reach high-significance detections both over large areas of the sky and at high redshifts. Hence, state-of-the-art spectroscopic surveys reach at most modes $k_{\rm min} \simeq 0.01h\,{\rm Mpc}^{-1}$, making it unfeasible to put constraints on large-scale effects such as PNG that are competitive with those from the CMB. Prospects for next-generation surveys like *Euclid* or the SKA look certainly better [e.g. 20, 21], but probably not enough to put a final word on PNG.

A newly proposed, promising approach is represented by mapping the intensity of the unresolved neutral hydrogen (HI), which is expected mostly to reside in galaxies after the end of reionisation [e.g. 7].[d] Such 'intensity mapping' will allow us to obtain CMB-like maps of the HI distribution over the redshift range $0 \lesssim z \lesssim 4$, highly valuable for PNG and GR effects [22, 23].

2.1 The Multi-Tracer Technique

The multi-tracer (MT) technique is a different approach to the problem of accessing the largest cosmic scales [24]. Instead of observing larger and larger volumes to lessen the repercussions of cosmic variance, we try to bypass it directly. MT involves a comparison between the relative clustering of different tracers of the underlying cosmic structure. It is based on the fact that on large, linear scales, the dark matter haloes are biased but not stochastic tracers of dark matter. (In other words, on large scales the stochastic quantity is the distribution of matter fluctuations itself, whereas the bias is deterministic.) Then, if what we are interested in is measuring quantities that have a peculiar impact on the clustering of biased tracers of the cosmic structure, by comparing various tracers with different biases we have in a sense access to different realisation of the bias field [see 25, for a comprehensive discussion].

In Fig. 1 we illustrate the great potential of the MT technique by showing the forecast marginal errors on $f_{\rm GR}$ (solid) and $f_{\rm NL}$ (dashed) as a function of the noise level for two single-tracer surveys: a phase 1 SKA HI intensity mapping survey (IM, blue); and a *Euclid*-like photometric galaxy survey (PG, red); as well as their combined MT analysis (black) [see 26, for details]. Here, $f_{\rm GR}$ is a fudge factor parameterising all the terms in the angular power spectrum of number counts other than standard Newtonian fluctuations and RSDs. We multiply the noise of both intensity mapping and galaxy number counts by an overall amplitude and let it vary from 0 to 1, where 0 means a noiseless experiment and 1 is the real setting. It is straightforward to see that, as we remove noise, single tracers soon reach the cosmic variance limited plateau, while MT keeps improving.

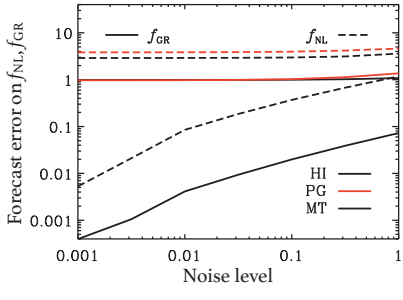


Figure 1 – Forecast 1σ marginal error on $f_{\rm GR}$ (solid) and $f_{\rm NL}$ (dashed) vs noise level for SKA phase 1 intensity mapping (blue), *Euclid*-like photo-z galaxies (red) and MT (black) [from 26].

[d] See also: M.G. Santos; R. Battye; S. Harper; and L. Olivari in this volume 'Moriond 2016 – Cosmology'.

3 Ultra-Large Scales Matter

Lastly, we show that, albeit horizon-scale effects such as GR corrections or PNG are largely sub-dominant with respect to the standard terms included in a power spectrum analysis, it will be very important for next-generation cosmological experiments to include them in their analysis pipeline, if we do not want to bias the reconstruction of cosmological parameters. First, we can note that the large scales where PNG is stronger are the very same on which GR corrections become significant. Therefore, one needs to incorporate the GR corrections in theoretical analysis in order to make accurate (and non-biased) predictions and estimates of PNG. To illustrate this, the left panel of Fig. 2 show with a dashed, blue ellipse the 1σ confidence region forecast for an SKA HI galaxy survey on the estimation of $f_{\rm NL}$ (on abscissas, the amplitude of the primordial power spectrum, A_s) [27]. Here, the true input value for the parameters is indicated by the red dot, and GR corrections have been thoroughly neglected in the analysis (i.e. $f_{\rm GR} = 0$). In other words, an incorrect treatment of GR corrections will lead to a spurious measurement of PNG due to the fact that the two signals have a similar impact on the power spectrum on large scales.

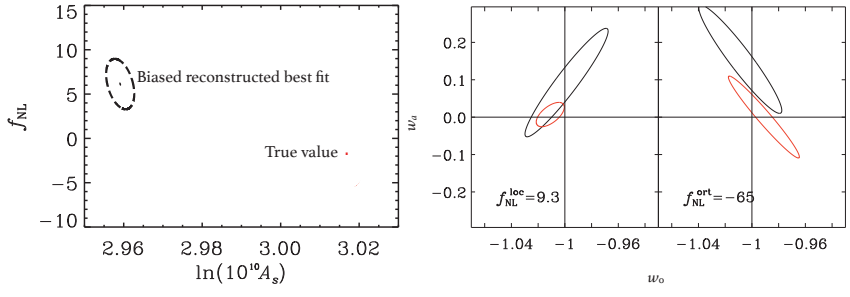


Figure 2 – Biased 1σ error contours on cosmological parameters due to incorrect modelling of horizon-scale effects. *Leftmost panel:* Spurious estimation of $f_{\rm NL}$ by an SKA HI galaxy survey caused by neglecting GR corrections in the analysis [from 27]. *Rightmost panel:* Spurious estimation of dynamical dark energy by a *Euclid*-like spectroscopic galaxy survey cause by not accounting for non-zero local-type (left panel) or orthogonal-type (right panel) PNG, with (red) and without (black) priors from *Planck* [from 28].

The right panel of Fig. 2 considers a similar scenario, but in this case the experimental set up is a *Euclid*-like spectroscopic galaxy survey, on the axes are the dark energy equation-of-state parameters $\{w_0, w_a\}$, and the horizon-scale effect that has been neglected to the purpose of showing its impact is PNG [see 28, for more details]. In particular, the left panel refers to local-type PNG, whilst the right panel is for PNG of the orthogonal-type. The central crosses indicate the fiducial value in the concordance ΛCDM model. It is important to note that the fiducial values for $f_{\rm NL}$ quoted in the plot are well within $1-2\sigma$ bounds from *Planck* [16]. Black ellipses are obtained with *Euclid*-like data alone, whereas red contours include priors from *Planck*. Clearly, the bias on the estimated value of $\{w_0, w_a\}$ is much smaller than in the previous case. However, let us emphasise that dark energy is not significant on ultra-large scales only. This means that even for measuring standard cosmological parameters—more, parameters that are the most targeted by forthcoming surveys—it is of primary importance to account for horizon-scale effects correctly, either we will get very accurate but biased results that may undermine the quality of envisaged scientific products of future cosmological experiments.

Acknowledgments

The author wishes to thank his collaborators, for allowing him to show results from common projects, and the organisers, for granting him the possibility to present his work. The author is

supported by ERC Starting Grant No. 280127.

References

[1] S. Camera, A. Raccanelli, Phil Bull et al. *PoS*, AASKA14:025, 2015.

[2] P. Bull et al. *Phys. Dark Univ.*, 12:56–99, 2016.

[3] R. Laureijs et al. *ESA-SRE*, 12, 2011.

[4] L. Amendola et al. *Living Rev. Rel.*, 16:6, 2013.

[5] F. Batoni Abdalla, P. Bull, S. Camera et al. *PoS*, AASKA14:017, 2015.

[6] M. Jarvis, D. Bacon, C. Blake, M.L. Brown et al. *PoS*, AASKA14:018, 2015.

[7] M. Santos, P. Bull, D. Alonso, S. Camera et al. *PoS*, AASKA14:019, 2015.

[8] M.L. Brown, D.J. Bacon, S. Camera et al. *PoS*, AASKA14:023, 2015.

[9] J. Yoo. *Phys. Rev.*, D82:083508, 2010.

[10] C. Bonvin & R. Durrer. *Phys. Rev.*, D84:063505, 2011.

[11] Anthony Challinor & Antony Lewis. *Phys. Rev.*, D84:043516, 2011.

[12] D. Bertacca, R. Maartens, A. Raccanelli & C. Clarkson. *JCAP*, 1210:025, 2012.

[13] T. Clifton, P.G. Ferreira, A. Padilla & C. Skordis. *Phys. Rept.*, 513:1–189, 2012.

[14] N. Bartolo, E. Komatsu, S. Matarrese & A. Riotto. *Phys. Rept.*, 402:103–266, 2004.

[15] L. Verde, L.-M. Wang, A. Heavens & M. Kamionkowski. *Mon. Not. Roy. Astron. Soc.*, 313:L141–L147, 2000.

[16] P.A.R. Ade et al. *eprint arXiv:1502.01592*, 2015.

[17] S. Matarrese & L. Verde. *Astrophys. J.*, 677:L77–L80, 2008.

[18] D. Scott, D. Contreras, A. Narimani & Y.-Z. Ma. 2016.

[19] L. Anderson et al. *Mon. Not. Roy. Astron. Soc.*, 441(1):24–62, 2014.

[20] C. Fedeli, C. Carbone, L. Moscardini & A. Cimatti. *Mon. Not. Roy. Astron. Soc.*, 414:1545–1559, 2011.

[21] S. Camera, M.G. Santos & R. Maartens. *Mon. Not. Roy. Astron. Soc.*, 448:1035, 2015.

[22] S. Camera, M.G. Santos, P. Ferreira & L. Ferramacho. *Phys. Rev. Lett.*, 111:171302, 2013.

[23] D. Alonso, P. Bull, P.G. Ferreira, R. Maartens & M.G. Santos. 2015.

[24] U. Seljak. *Phys. Rev. Lett.*, 102:021302, 2009.

[25] L.R. Abramo & K.E. Leonard. *Mon. Not. Roy. Astron. Soc.*, 432:318–326, 2013.

[26] J. Fonseca, S. Camera, M.G. Santos & R. Maartens. *Astrophys. J.*, 812(2):L22, 2015.

[27] S. Camera, R. Maartens & M.G. Santos. *Mon. Not. Roy. Astron. Soc.*, 451:L80, 2015.

[28] S. Camera, C. Carbone, C. Fedeli & L. Moscardini. *Phys. Rev.*, D91(4):043533, 2015.


RENCONTRES DE MORIOND
50


CHAMPAGNE
Rencontres de Moriond
50





HI INTENSITY MAPPING: EXTRACTING THE 21 CM SIGNAL IN THE PRESENCE OF FOREGROUNDS

L. C. OLIVARI
Jodrell Bank Centre for Astrophysics, Alan Turing Building, School of Physics and Astronomy, The University of Manchester, Oxford Road, Manchester, M13 9PL, U.K.

HI intensity mapping is a new observational technique to map fluctuations in the large-scale structure of matter using the 21 cm emission line of atomic hydrogen (HI). Sensitive HI intensity mapping experiments have the potential to detect Baryon Acoustic Oscillations (BAO) at low redshifts ($z \leq 1$), which can be used to constrain the properties of dark energy. Observations of the HI signal will be contaminated by instrumental noise and by astrophysical foregrounds, such as Galactic synchrotron emission, which is at least four orders of magnitude brighter than the HI signal. We study the ability of the Generalized Needlet Internal Linear Combination (GNILC) method to subtract radio foregrounds and to recover the cosmological HI signal. For simulated radio observations including HI emission, Galactic synchrotron, Galactic free-free, radio sources and 0.05 mK thermal noise, we find that the GNILC method can reconstruct the HI power spectrum for multipoles $30 < \ell < 150$ with 6% accuracy on 50% of the sky for a redshift $z \sim 0.25$.

1 Introduction

Intensity mapping is the study of the large-scale fluctuations in the intensity of a given spectral line, in particular the 21 cm line of the neutral hydrogen, emitted by a number of unresolved objects. It has been suggested that the HI intensity field can be used to measure the power spectrum as a function of redshift [1]. The main advantage of HI intensity mapping, compared to the optical surveys of galaxies, is that a large sky volume is achieved within a relatively short observing time. This type of radio survey can then be used to measure the Baryon Acoustic Oscillations (BAO), which can be used to constraint the properties of the dark energy, the mysterious component that drives the accelerated expansion of the Universe.

The success of any HI intensity mapping experiment strongly depends on our ability to subtract the astrophysical contaminations that will be present in the observed HI signal. At $\nu = 1$ GHz, the most relevant foregrounds are the Galactic emission, mostly synchrotron radiation, and the background emission of extra-galactic point sources. These emissions are at least four orders of magnitude larger, $T_b \sim 10$ K, than the HI signal, $T_b \sim 1$ mK. The high spectral resolution offered by any HI intensity mapping experiment allows us to use the frequency information of the observed data. As the foregrounds spectra are expected to be smooth, we can approximate them by a power-law in the frequency range of interest. This property can then be used to separate the HI signal from any other signal correlated in frequency [2].

In this work, we describe the application of the Generalized Needlet Internal Linear Combination (GNILC) [3,4] as a non-parametric component separation technique for HI intensity mapping experiments. In general, the GNILC method can extract the emission of a multidimensional component (spatially correlated components) from the observed data. Here we review the performance of the GNILC method for a single-dish HI intensity mapping experiment in low

redshifts and make a brief discussion on how component separation connects to cosmology.

2 GNILC

The GNILC method can be divided into two main steps. First, using a prior on the HI power spectrum, we determine the local signal to noise ratio and perform a constrained Principal Component Analysis (PCA) of the data to determine the effective dimension of the HI subspace. Second, we perform a multimensional ILC filter within the HI subspace and reconstruct the HI signal. In the constrained PCA step, the number of principal components of the observation covariance matrix is estimated locally both in space and in angular scale, which is done by using a wavelet (needlet) decomposition of the observations. We also use a statistical information criterion (AIC) [5] to make the selection of the principal components of the observation covariance matrix.

The steps of the GNILC method can be summarized as follows:

1) To isolate the different ranges of angular scales, we first define a set of needlet windows in harmonic space. These needlet windows work as band-pass filters. The spherical harmonic coefficients $a_{\ell m}$ of the observed frequency maps are then band-pass filtered by the needlet windows. We then produce one observed map for each needlet scale j.

2) For each needlet scale j, we compute the data covariance matrix, at pixel p, of a pair of frequencies a and b as

$$\hat{\mathbf{R}}_{ab}(p) = \sum_{p' \in \mathcal{D}(p)} \mathbf{x}_a(p') \mathbf{x}_b^T(p'), \tag{1}$$

where $\mathcal{D}$ is a domain of pixels centred around the pixel p.

3) For each needlet scale j, we also compute the HI emission covariance matrix by using HI maps $\mathbf{y}$ simulated from a theoretical prior on the HI angular power spectrum, exactly like Eq. 1.

4) We diagonalize the transformed data covariance matrix, $\hat{\mathbf{R}}_{\rm HI}^{-1/2} \hat{\mathbf{R}} \hat{\mathbf{R}}_{\rm HI}^{-1/2}$, as

$$\hat{\mathbf{R}}_{\rm HI}^{-1/2} \hat{\mathbf{R}}(m) \hat{\mathbf{R}}_{\rm HI}^{-1/2} = \mathbf{U}_N \mathbf{D}_N \mathbf{U}_N^T + \mathbf{U}_S \mathbf{U}_S^T, \tag{2}$$

where D_N collects the m largest eigenvalues as selected by the minimization of AIC [4], $\mathbf{U}_N$ the corresponding eigenvectors, and $\mathbf{U}_S$ the $(n_{\rm ch} - m)$ eigenvectors related to the HI emission subspace.

5) For each needlet scale j, we apply an $(n_{\rm ch} - m)$-dimensional ILC filter to the observed data,

$$\hat{\mathbf{s}}^{(j)} = \hat{\mathbf{S}} (\hat{\mathbf{S}}^T \hat{\mathbf{R}}^{-1} \hat{\mathbf{S}})^{-1} \hat{\mathbf{S}}^T \hat{\mathbf{R}}^{-1} \mathbf{x}^{(j)}, \tag{3}$$

where the estimated mixing matrix is given by $\hat{\mathbf{S}} = \hat{\mathbf{R}}_{\rm HI}^{1/2} \mathbf{U}_S$.

6) Finally, we synthesize the reconstructed needlet HI maps $\hat{\mathbf{s}}^{(j)}$ as follows: the maps are transformed to spherical harmonic space, their harmonic coefficients are again band-pass filtered by the respective needlet window and the filtered harmonic coefficients are transformed back to maps in real space. This operation gives one reconstructed HI maps per needlet scale. These maps are then added to give, for each frequency channel, the complete reconstructed HI map.

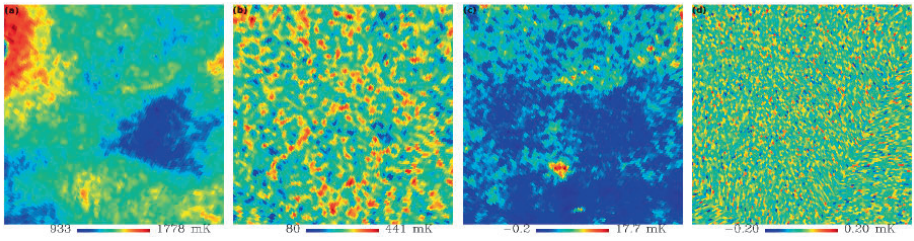


Figure 1 – Maps of four simulated signals covering a $50^\circ \times 50^\circ$ patch of the sky: (a) Galactic synchrotron, (b) extragalactic point sources, (c) Galactic free-free, (d) and thermal noise. The maps are centred at Galactic coordinates $(120^\circ, -60^\circ)$ and observed at 1117.5 MHz (redshift $z \sim 0.3$).

3 Simulation

To test our component separation method we perform a simulation of the observed sky that is expected for a standard HI intensity mapping experiment. For our simulation, we consider the bandwidth of the BINGO experiment [6]: 960 to 1260 MHz. This bandwidth corresponds to a redshift range of 0.13 to 0.48. The frequency channels are chosen to be equally spaced in the given bandwidth. The number of frequency channels is chosen to be 20.

Our astrophysical sky is given by the HI emission, synchrotron radiation with spatially variable spectral index, extragalactic radio point sources, free-free radiation, and thermal noise with an amplitude of 0.05 mK per pixel. Figure 1 shows some maps of the components of the simulated sky at 1117.5 MHz. The temperature scale is in mK.

We use a Galactic mask to cover the area of the sky where the synchrotron emission of our Galaxy is brightest. Our Galactic mask is given by the product of two masks: a $\pm 20^\circ$ latitude mask and a mask designed to cover the Galactic emission with brightness temperatures larger than the threshold of 30 K at 408 MHz. This mask gives 51% of sky coverage.

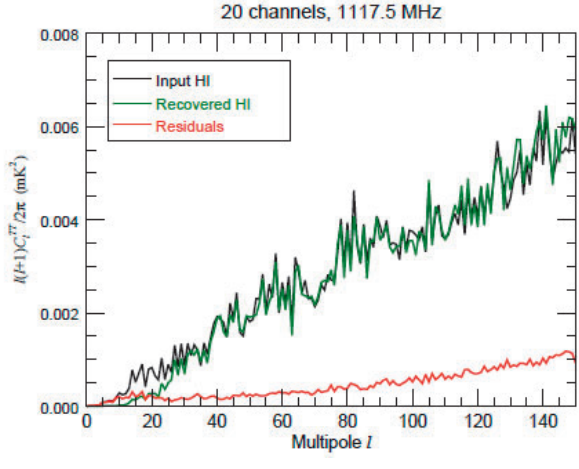


Figure 2 – Result on simulation (HI, synchrotron with spatially variable spectral index, point sources, free-free, and thermal noise): power spectra, $\ell(\ell+1)C_\ell/2\pi$, of the simulated HI signal (black), the recovered HI signal (green), and the residual signal (red) at frequency 1117.5 MHz with 20 frequency channels.

After applying the GNILC method to our simulated maps, we obtain an average normalized absolute difference between the input HI power spectrum, C_ℓ^S, and the reconstructed HI power

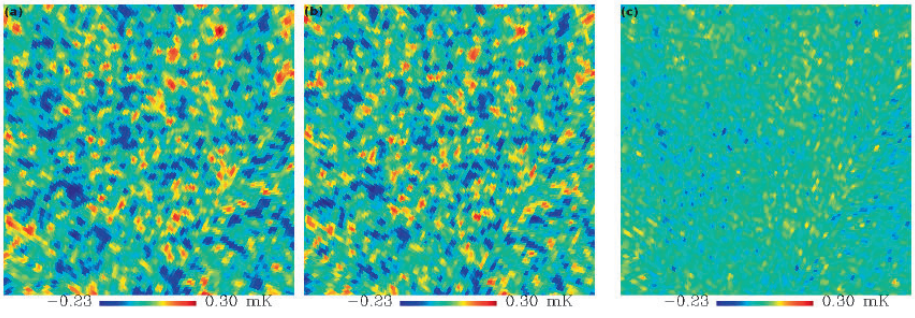


Figure 3 – Maps covering a $50^\circ \times 50^\circ$ patch of the sky with three different signals: (a) input HI, (b) GNILC reconstructed HI, and (c) residuals. The maps are centred at Galactic coordinates $(120^\circ, -60^\circ)$ and observed at 1117.5 MHz (redshift $z \sim 0.3$).

spectrum, C_ℓ^R, of the HI signal that is around 6.1% for multipoles in the range between 30 and 150. Figure 2 shows the power spectra of the recovered HI signal, the input HI signal, and the residual map (recovered HI signal minus input HI signal) for our simulation with 20 frequency channels. Figure 3 shows the input HI signal, the reconstructed HI signal and the residual contamination at 1117.5 MHz. These maps are shown with an angular resolution of 40 arcmin. We see that, after cleaning foregrounds and thermal noise of the observed signal, the GNILC method is able to reconstruct the temperature fluctuations of the HI signal with a r.m.s residual equals to 0.04 mK at this $50^\circ \times 50^\circ$ patch of the sky.

4 Cosmology and Component Separation

Once we have a set of reconstructed HI maps, we can use these maps to calculate the angular power spectra that are needed to study the large-scale properties of the Universe and thus constraint the cosmological parameters of the particular cosmology being studied. As any component separation method always loses some HI power, we may have as a consequence a bias in the power spectra. This bias in the power spectra may leads to a bias in some cosmological parameters (e.g. optical depth and Hubble parameter). A careful analysis of the effect of component separation in the cosmological parameters is then necessary; this analysis is being done by the present author and soon will be available in the literature [7].

Acknowledgements

LCO acknowledges funding from CNPq, Conselho Nacional de Desenvolvimento Cientifico e Tecnologico - Brazil.

References

1. J. B. Peterson *et al* in Astronomy, Vol. 2010, astro2010: The Astronomy and Astrophysics Decadal Survey, p. 234 (2009).
2. R. Ansari *et al*, A&A **540**, A129 (2012).
3. M. Remazeilles *et al*, MNRAS **418**, 467 (2011).
4. L. C. Olivari *et al*, MNRAS **456**, 27490 (2016).
5. H. Akaike in IEEE Transactions on Automatic Control, 19, 716 (1974).
6. R. A. Battye. *et al*, MNRAS **434**, 1239 (2013).
7. L. C. Olivari *et al* in preparation.

THE QUEST FOR DUSTY PRIMEVAL GALAXIES

C. MANCUSO, A. LAPI, L. DANESE
SISSA-ISAS, Via Bonomea 265, 34136, Trieste, Italy



We use the continuity equation approach and the star-formation timescales typical of the 'main sequence' galaxies to probe the bright end of the SFR functions, constituted by a galaxy population featuring large star formation rates (SFRs) $\psi \geq 10^2\, M_\odot\ \mathrm{yr}^{-1}$ in heavily dust-obscured conditions. It turned to be the high-redshift counterpart of the dusty star-forming population already surveyed for $z \leq 3$ in the far-IR band by the *Herschel* space observatory. After having validated our approach against many different observables, we worked out predictions, namely number counts and redshift distributions, taking into account also galaxy-scale gravitational lensing. Since our analyses highlighted that UV-dust corrected luminosity functions are not capable to reproduce the number densities of galaxies, we aimed the predictions to existing and upcoming (sub-)mm and radio observations, showing that complementing them with current UV surveys, they will be able to observationally reconstruct the bright end of the tomographic SFR functions out to $z \leq 8$.

1 Aims and Methods

The history of star formation in massive galaxies (the host of high-redshift quasars) is a fundamental problem in galaxy evolution.

We address two important issues: is star formation in galaxies mainly regulated by in-situ processes or by merging? How does the presence of dust affect the statistics of the star formation rate in galaxies at high redshift $z \geq 3$?

To cast light on these issues (see Fig.1), we built up the SFR functions in the range $z \sim$ 0-10. For $z \leq 3$ we fitted a Schechter function to the UV data for SFRs $\psi \leq 30\ M_\odot$/yr and to the far-IR data for SFRs $\psi \leq 100\ M_\odot$/yr. We have imposed that at $z \geq$ the UV-inferred SFR function is representative of the intrinsic one, since we expect small attenuation by dust due to the short age of the Universe.

This allows us to set the redshift evolution of the Schechter parameters to work out predictions for the SFR function over the whole redshift range.

We checked the SFR functions obtained against observed number counts and z-distributions at different wavelengths finding good agreement (see Fig.2 for an example); we furthermore exploited the continuity equation approach and the 'main sequence' star formation timescales

to reproduce the stellar mass function of active, star-forming galaxies at $z \geq 4$ (see Fig.3,left panel). We also computed average relationships between stellar vs halo mass via the abundance matching technique and worked out two different methods to study such galaxies at high-z .

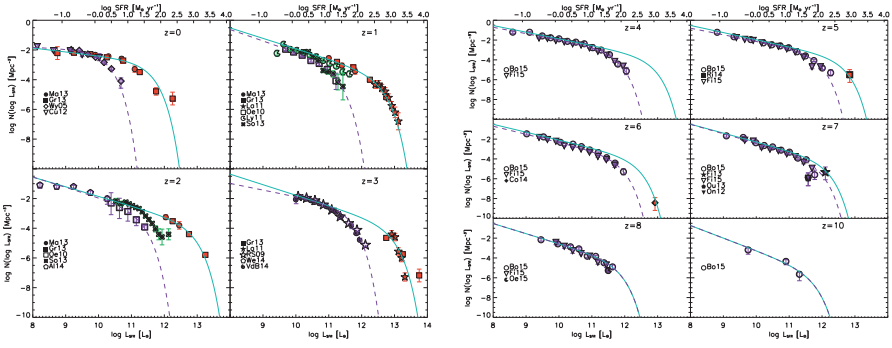


Figure 1 – The SFR function at redshifts $z \approx 0-3$(left panel) and at redshifts $z \approx 4-10$ (right panel). Solid cyan lines illustrate our fits to the intrinsic (IR+UV) SFR functions, while violet dashed lines refer to the UV-inferred SFR functions. For the references of the data see Mancuso *et al.* [1]

2 Main Results

Our analysis highlights that:

- the buildup of stars and black holes in galaxies occurs via in-situ processes, with mergers playing a marginal role at least for stellar masses $\leq 3 \times 10^{11} M_{\odot}$ and BH masses $\leq 10^{9} M_{\odot}$ (see Fig.3,right panel).
- we designed an observational strategy to hunt dusty star-forming galaxies at $z \geq 4$ based on a color preselection in the far -IR or (sub)-mm band (see Fig. 4, left panel).
- to probe the bright end of the SFR functions we computed the expected number counts and z-distributions of dusty star- forming galaxies (see Figs.5,6).
- we investigated the nature of UV-selected galaxies at $z \geq 4$ finding their attenuation to be in strong excess with respect to the commonly used one, which is based on the β-IRX relation(see Fig.4, right panel); we propose an attenuation proportional to $\psi^{0.25}$.
- we propose the combination of current UV surveys with (sub)-mm and radio upcoming facilities (ALMA, NIKA2, SKA) to definitely probe the bright end of the SFR functions at $z \geq 4$.

References

1. Mancuso, C., Lapi, A., Shi, J., et al. (2016), Apj accepted, airxiv:1604.02507

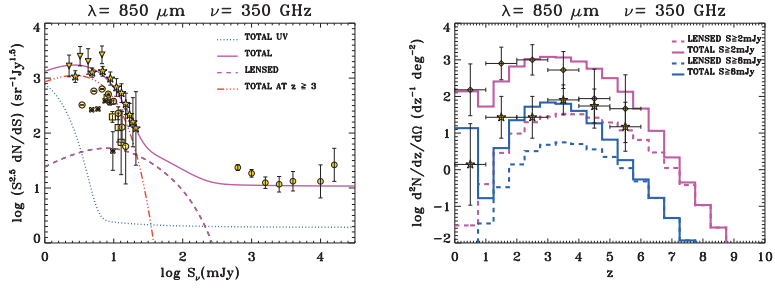


Figure 2 – Euclidean-normalized differential number counts at 850μm (left panel) and redshift distributions (right panel) for the same wavelenght. In the left panel magenta lines refer to the counts derived from our intrinsic SFR function; the contribution to the total counts (solid) from strongly lensed galaxies (dashed) is highlighted. The triple dot-dashed red line is the contribution to unlensed counts from galaxies at $z \geq 3$. The blue dotted line refers to the counts derived from the UV-inferred SFR function. For the references of the data see Mancuso *et al.* [1]

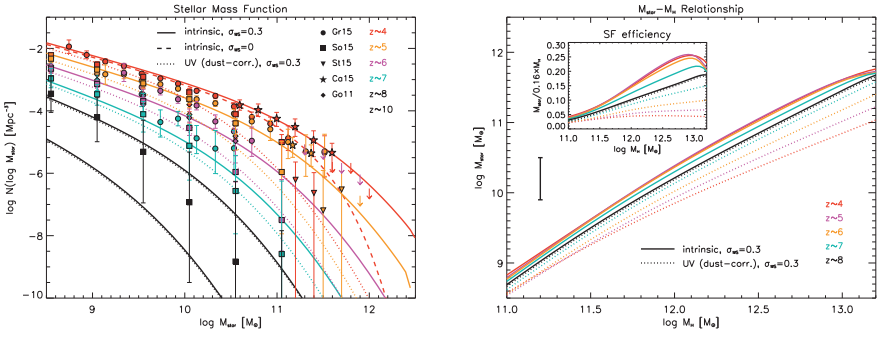


Figure 3 – Left panel: the stellar mass function at redshifts $z \approx 4-10$ (color-coded), obtained via the continuity equation from the intrinsic (solid) or UV-inferred (dotted) SFR function and a scatter of $\sigma_{\rm MS} \approx 0.3$ dex around the median main sequence relationship; at $z \approx 4$ the outcome from the intrinsic SFR function with $\sigma_{\rm MS} \approx 0$ is highlighted by the dashed red line. For the references of the data see Mancuso *et al.* [1]. Right panel: the relationship $M_\star - M_{\rm H}$ between stellar mass and host halo mass as derived from the abundance matching of the halo mass function to the $M_\star$ derived from the intrinsic SFR function (solid lines) or to the SFR function inferred from (dust-corrected) UV data (dotted lines). The inset illustrates the corresponding star-formation efficiency, i.e., the stellar to baryon fraction $M_\star/0.16 \times M_{\rm H}$ vs. the halo mass. In both top panels, the error bars represent the typical uncertainty.

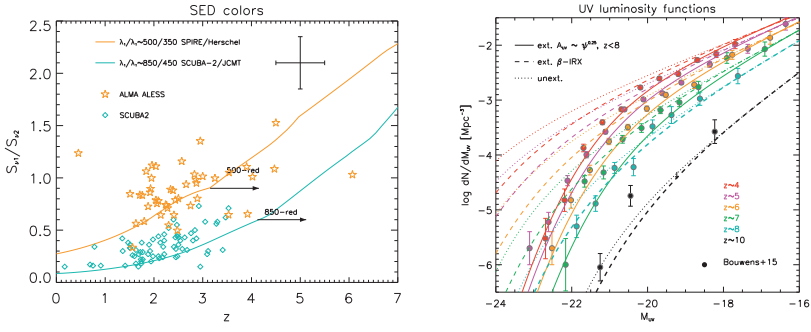


Figure 4 – left panel:SED colors $S_{\nu,1}/S_{\nu,2}$ as a function of redshift, exploited for *Herschel* and *SCUBA-2* preselection of dusty primeval galaxies; different lines refer to 500/350 (orange) and 850/450 (cyan) colors. Arrows indicate the redshift ranges where red galaxies are preferentially located. In the upper right corner the typical data uncertainty on the median is reported. For the references of the data see Mancuso *et al.* [1]. right panel:UV luminosity function at different redshift $z \approx 4-10$ (color-coded), as reconstructed from our intrinsic SFR function by not correcting for dust extinction (dotted lines), correcting via the standard $\beta_{\rm UV}$-IRX relation (dashed lines), and via the simple relationship $A_{\rm UV} = \psi^{0.25}$ (solid lines) with a scatter of 1 mag at given ψ (for $z < 8$). Data points (circles) are from Bouwens et al. (2015).

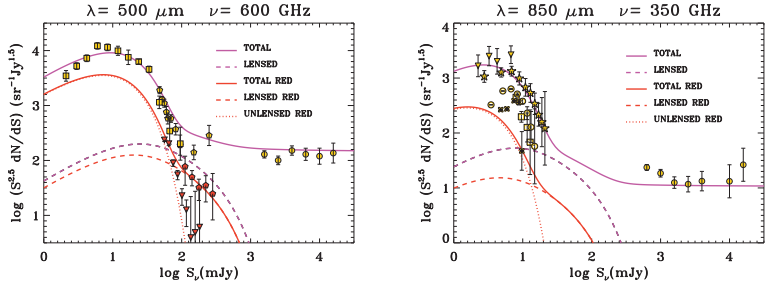


Figure 5 – Euclidean-normalized differential number counts at 500 and 850 μm. Magenta lines refer to the counts derived from our intrinsic SFR function; the contribution to the total counts (solid) from strongly lensed galaxies (dashed) is highlighted. The counts of red galaxies are illustrated in red, with the solid lines referring to the total, the dotted lines to unlensed counts and the dashed lines to the gravitationally lensed sources. For the references of the data see Mancuso *et al.* [1].

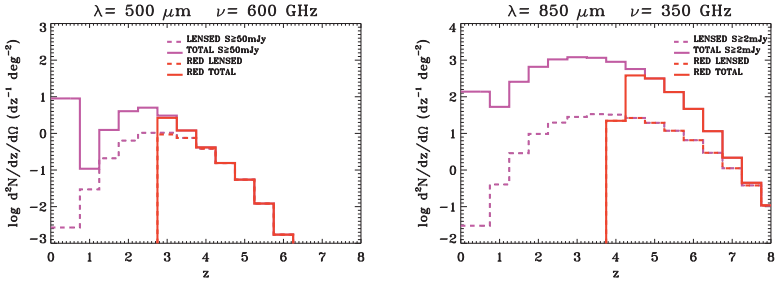


Figure 6 – Redshift distributions at 500 (top panel) and 850 μm (bottom panel). At 500 μm magenta lines refer to the *Herschel* limiting flux of $\approx$ 50 mJy, with the contribution to the total (solid) from strong galaxy-scale gravitational lensing (dashed) highlighted; the same for red sources is shown in red. At 850 μm the magenta lines refer to a limiting flux of 2 mJy (again red lines refer to red sources).

8.
Others

STUDY OF BIG BANG NUCLEOSYNTHESIS DEEP UNDERGROUND

C. GUSTAVINO (for the LUNA collaboration)

Department of Physics, University of Rome "Sapienza", P.le A. Moro 2, Rome, Italy

The good accuracy of elemental abundances inferred from astronomical observations and the high precision of the baryon density measured by CMB experiments suggest a renewed study of several nuclear reactions of the BBN chain, to improve constraints on cosmology and particle physics. It will be shown that the ongoing study of the $D(p,\gamma)^3He$ reaction at BBN energies with the underground LUNA accelerator is of primary importance to improve the constraints on the existence of "dark radiation" and to measure the baryon density with accuracy comparable to the one derived from CMB data.

1 BBN and nuclear astrophysics at LUNA

In the standard scenario, the primordial abundance of elements created during the Big Bang Nucleosynthesis (BBN) only depends on the baryon density Ω_b, on the dynamics of particle physics and on nuclear astrophysics, i.e. cross sections of nuclear reactions of BBN chain. Presently the uncertainty of BBN predictions mainly depends on the knowledge of cross sections of BBN nuclear processes, because particle physics is known with extraordinary accuracy and recent CMB data provide the value of Ω_b at percent level [1]. Therefore, in the present precision era of cosmology, it is highly desirable to improve the knowledge BBN nuclear processes, in order to constrain cosmology and particle physics through the comparison of elemental abundances inferred from astronomical observations with the ones calculated with BBN theory. At BBN energies the cross sections are very low because of the coulomb barrier between interacting charged nuclei. Therefore it is convenient, if not essential, to perform measurements deep underground to reduce the background induced by cosmic rays. LUNA (Laboratory for Underground Nuclear Astrophysics) at LNGS ("Laboratori Nazionali del Gran Sasso", Italy) is the workd's only underground accelerator of ion devoted to nuclear astrophysics measurements. The Gran Sasso mountain provides a huge reduction of background induced by cosmic rays, making possible measurements of nuclear cross sections at energies well below the Coulomb barrier. The key reactions $d(p,\gamma)^3He$ and $d(^3He,p)^4He$ has been studied with the previous 50 kV accelerator [3,4], while the cross sections of $^3He(^4He,\gamma)^7Be$ and $D(^4He,\gamma)^6Li$ processes have been measured by means the present LUNA400 facility [5,6]. This four reactions are particularly important to calculate the abundance of deuterium, ^3He, ^7Li and ^6Li respectively. As an Example, LUNA has measured for the first time the cross section of the $D(^4He,\gamma)^6Li$ reaction at BBN energy, making the calculation of ^6Li abundance much more reliable because no more based on extrapolations of data taken at higher energies [6].

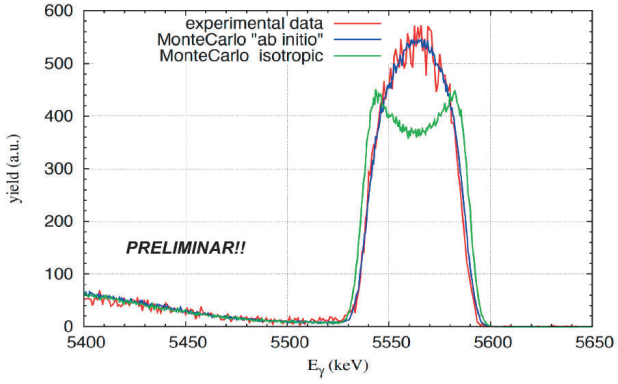


Figure 1 – Simulated spectra of the $D(p,\gamma)^3He$ reaction, assuming isotropic (green) and "ab initio" (blue) angular distribution at $E_{cm} = 112.5$ keV. The LUNA experimental data (red) are also shown. Data have been normalized to remark the close agreement with the "ab initio" angular distribution of emitted photons.

2 The $d(p,\gamma)^3He$ at LUNA

Presently the primordial deuterium abundance extracted from direct observations $(D/H)_{obs}$ [2] is more accurate with respect the calculated value $(D/H)_{BBN}$. The uncertainty of $(D/H)_{BBN}$ is mainly due to the paucity of data at BBN energies of the deuterium-burning reaction $d(p,\gamma)^3He$[7]. In fact, in the BBN energy region, the measurements have a large error (about 9%) and differs from the theoretical "ab initio" calculation of about 20%. Therefore a renewed measurement is necessary to improve the BBN calculation accuracy. The goal of the ongoing LUNA measurement is to measure the cross section at $40 < E_{cm} < 266$ with 3% accuracy. Such a measurement allows to measure Ω_b with a precision comparable to the one obtained by the PLANCK collaboration [1]. As the deuterium abundance relative to hydrogen also depends on the expansion rate of universe, the comparison of $(D/H)_{BBN}$ with $(D/H)_{obs}$ allows to constrain the existence of "dark radiation", i.e. the existence of extra relativistic particles (only photons and 3 neutrino families account for the early universe expansion in the ΛCDM model) [7]. Finally, the total and differential cross section measurements allows the comparison of data with theoretical "ab initio" nuclear calculations. A preliminary comparison of data with "ab initio" angular distribution and the isotropic one is shown is shown in fig.1. Data taking will last about 8 months from now.

References

1. PLANCK collaboration: arXiv:1502.01589v2 [astro-ph.CO] 6 Feb 2015.
2. R. Cooke *et al*, ApJ. **781**, 31, (2014).
3. C. Casella *et al*, Nuclear Physics A **706** 203-216. (2002).
4. H. Costantini *et al*, Phys. Lett. B **482** 430-49 (2000).
5. F. Confortola *et al*, Phys. Rev. C **75**, 065803 (2007).
6. M. Anders *et al*, PRL **113**, 042501 (2014).
7. E. Di Valentino *et al.*, Phys. Rev. D **90**, 023543 (2014).

NONLINEAR ELECTRODYNAMICS CONTRIBUTING TO A MINIMUM VACUUM ENERGY, *COSMOLOGICAL CONSTANT*, ALLOWED IN EARLY UNIVERSE COSMOLOGY

A.W. BECKWITH
College of Physics, Chongqing University Huxi Campus
No. 55 Daxuechen Nanlu, Shapingba District, Chongqing 401331
Chongqing, P.R. China, 400014

This summary of results poses the question of a minimum cosmological constant, i.e. vacuum energy at the start of the cosmological evolution from a near singularity. We pose this comparing formalism of a minimum time length, and compare that with a minimum time length at the start of cosmological space-time evolution. Thus, we use a minimum time length as a way of specifying a magnetic field dependence of the cosmological constant. The presented results are a summary of results in JHEPGC, and reference the JHEPGC article. The cited results use the idea of a magnetic monopole charge to start with.

1 Introduction

We use a minimum magnetic monopole charge[1] as given by

$$e = \frac{m}{4\pi nc^2 \cdot (\Delta t)^2} \ln \frac{\xi_{\rm init}}{\xi_{\rm final}} = e_{\rm E\&M} \sim \sqrt{\frac{B^2 \cdot r_{\rm min}}{\mu_0 \cdot \left[1 - 2 \cdot \frac{B^2 \cdot r_{\rm min}}{c} \cdot X_0\left(\frac{B_c}{B}\right)\right]}}. \tag{1}$$

Eq. (1) has a deeper meaning. Not only is there a net *magnetic* monopole charge, as given in Eq. (1), there is a minimum nonzero E and M *energy density,* as given by either $\xi_{\rm init}$ or $\xi_{\rm final}$ for an emergent *magnetic monopole* charge from an initial space-time configuration. This energy density value will lead to a first-order minimum upper time step, which we characterize as

$$(\Delta t)^2 = \frac{m}{4\pi nc^2 \cdot e} \ln \frac{\xi_{\rm init}}{\xi_{\rm final}} \sim \sqrt{\frac{B^2 \cdot r_{\rm min}}{\mu_0 \cdot e^2 \cdot \left[1 - 2 \cdot \frac{B^2 \cdot r_{\rm min}}{c} \cdot X_0\left(\frac{B_c}{B}\right)\right]}}. \tag{2}$$

We present the minimum time step above, citing a JHEPGC article.[1] and we will then go to the issue of the vacuum energy next. Here, the function given above is explained in Beckwith[1] with the minimum radius assumed to be of the order of Planck length, and a minimum magnetic field given in the cited article. Next, we link this above to the vacuum energy.

2 Vacuum Energy as Given in Terms of Minimum Time Step (Planck Time)

Begin with the starting point, from Beckwith,[1] of

$$(\Delta t)^2 = \frac{m_e}{2nc^2 \cdot e} \ln \frac{\xi_{\rm init}}{\xi_{\rm final}} \xrightarrow{\omega \to \text{small}} t^2_{\rm Planck} \propto \left(5.39 \times 10^{-44}\right)^2 \sec^2$$
$$\xrightarrow{\omega \to \text{much larger}} \# \cdot t^2_{\rm planck} > \left(5.39 \times 10^{-44}\right)^2 \sec^2. \tag{3}$$

That is, for low frequency, we have a collapse to the Planck time frequency value, whereas the minimum time step rises as frequency, ω, rises. Furthermore, Eq. (3) is formed in a way independent of a changing vacuum energy, as given by[1]

$$\Lambda(t) \sim (H_{\text{inflation}})^2 . \tag{4}$$

This may tie into a massive graviton mass, as given by the author, as a spin off of massive gravitons given in[1]

$$m_{\text{g}}^2 = \frac{\widetilde{\kappa} \cdot \Lambda_{\max} \cdot c^4}{48 \cdot h \cdot \pi \cdot G}. \tag{5}$$

Note the time step is then independent upon elementary arguments as to massive graviton mass.

3 Conclusion: GW Generation Due to the Thermal Output of Plasma Burning

The easiest case to consider is, if the Λ is not overly large, and the initial scale factor, $a(t)$, is small, then we have[1]

$$t \sim \frac{2}{\sqrt{3\Lambda}} \cdot \left[a(t) \cdot \sqrt{\frac{\Lambda}{8\pi G\rho}} - \frac{a^3(t)}{2.3} \left(\frac{\Lambda}{8\pi G\rho} \right)^{\frac{3}{2}} + HOT \right]. \tag{6}$$

Then, we are looking at a minimum vacuum energy of

$$\Lambda \sim \frac{8\pi G\rho_{\text{galaxies}}}{a^2(t)} \cdot \left[1 - \sqrt{\frac{3}{4}} \frac{m^2 \mu_0 \omega}{e^2 a(t)} \sqrt{8\pi G\rho_{\text{galaxies}}} \cdot 10^{2\widetilde{\beta}} \right] \tag{7}$$

Here, $a(t_{\text{initial}}) \sim 10^{-30}$ is very small, but we are also assuming an ultra low ρ_{galaxies} and ω, and small m.

Acknowledgments

This work is supported in part by National Nature Science Foundation of China grant No. 11375279.

References

1. A. Beckwith, J. High Energy Phys. Gravity Cosmol. **2**, 25 (2016). doi:10.4236/jhepgc.2016.21003

UNITED NATURE OF DARK ENERGY AND LOW ENERGY NUCLEAR REACTIONS

Mikhail Ja. Ivanov
Central Institute of Aviation Motors, Moscow, 111116, Russia



United nature of Dark Energy (DE) and Low Energy Nuclear Reactions (LENR) is considered and experimentally confirmed. Integral semi empirical and differential LENR simulations based on the analysis of the mass excess for the initial and destination of burning products are proposed. We consider also the external Space Thermostat (ST) with $T = 2.73K$, which contains DE and Dark Matter (DM) and presents all its parameters.

1 DM and DE modeling

The nature of DE and LENR is determined by the Planck-Einstein-de Broglie "state equation"

$$E = mc^2 = h\nu = kT, \tag{1}$$

where h and k - the Planck and Boltzmann constants. If we know the medium temperature T and the perturbation velocity c this ratio allows calculating the particle mass $m = kT/c^2$ of medium, in which thermal energy processes is developed. The relation (1) gives also the space particle mass, when the free cosmic temperature $T = 2.73K$ (the temperature of Cosmic Microwave Background- CMB). The presence of these nonzero mass particles in physical vacuum was specified in [1,2] and it was identified with massive particles of DM. The same way we are modeling of DE [3].

Considering concentration n and multiplying (1) on n we can write $n \cdot mc^2 = n \cdot kT$ and go to

$$p \approx \rho c^2 = nkT. \tag{2}$$

Here $\rho = n \cdot m$ - density, p - positive pressure (not negative). The relation (2) is one of the known mathematical forms of Avogadro's law. The relations (1) and (2) may be used for typical answers so to what comprises about 96% of the Universe content (i.e., what and why over 70% of the mass-energy content of the Universe is in form of the unknown vacuum DE, over 20% of mass is in form of the mysterious DM). These relations also are the base of our particle thermodynamics[3].

2 LENR modeling

We presents integral and differential models of LENR[4], based on an analysis of mass excess (1) of an initial and ended combustion products and application of Avogadro's law (2). Heat processes in generators by the Filimonenko - Fleischmann - Pons type[5] (based on the electrolysis of heavy water using cathode with palladium) and in generators by the Rossi-Parhomov type[6] (based on changes in the isotopic composition of a mixture of hydride lithium and nickel powders when heated up to temperatures of 1300-1500 K) are analysed. Common change of the isotopic component composition for these generators was described in accordance with typical items of classical nuclear physics and our DE nature simulation. The developed model allows recommending other combinations of substances for similar heat generators with the comparative assessments of their thermal efficiency. In order to validate our theoretical approaches of DE and LENR studies special physical experiments were fulfilled and presented in detail for discussion[4].

3 Space Thermostat

In heat problems the thermostat is called greater thermodynamic system, in which the number of particles far exceeds the number of particles of a studied system with her in thermal contact[7]. In our case as such external Space Thermostat (ST) we take CMB with known temperature $T = 2.73K$ and with certain massive particles $m = kT/c^2 = 5.6 \cdot 10 - 40kg = 3 \cdot 10 - 4eV$ (holders and carriers of thermal radiation [1,2,3]). Any investigated system we naturally believe in the thermal contact with the ST. Applying the law of evenly distributed energy on freedom degrees, we show that each electromagnetic oscillation have an average energy kT. Thus we demonstrate applicability of the relation (1) and implement the fundamental question to thermodynamic views in relativistic and quantum mechanics in case their equity if there is the ST - CMB. The presence of the ST introduces important adjustments in the general equations of a dynamic system motion. Look at some consequences of the existence of the ST and, above all, the question of the applicability of the Noether theorem. Noether's theorem takes place only for dissipative less isolate systems. In our case with the ST presence we have no possibility to use Noether's theorem. The same situation is with Lagrangian and Hamiltonian mechanics. The requirement of invariance of the Lagrangian for local gauge transformations is the original principle of all modern physics theories of a microcosm. The particle and gauge theories should be changed.

4 Conclusions

United nature of Dark Energy and Low Energy Nuclear Reactions has been demonstrated. This nature is a moving kinetic energy of ST particles at temperature $T = 2.73K$.

The Universe presents itself the greatest Space Thermostat with the nonzero temperature, which has thermal contact with any studied system.

The Noether theorem, the formalism by Lagrange and by Hamilton can?t be right in such type dissipative systems. Therefore the particle and gauge theories should be modified. Linearization of initial conservation laws of mass, momentum and energy for medium motion gives wavelet quantum mechanics and relativistic approximation (with curve space and curve time).

References

1. Ivanov M.Ja. Thermodynamically compatible conservation laws in the model of heat conduction radiating gas. J. of Comp. Math. and Math. Phys. 51(1), 2011, pp. 133-142.
2. Ivanov M.Ja., Mamaev V.K. Hidden mass boson. J. Modern Phys. 3(8), 2012, pp. 686 - 693.
3. Ivanov M.Ja. Space Energy. "Energy Conservation", In Tech, 2012, DOI:10-5772/52493.
4. Ivanov M.Ja., Mamaev V.K. LENR theory and application to aerospace power plant. Space Propulsion, Proc. of the V-th International Conference, 2-6 May 2016, Rome, Italy.
5. Fleischmann M., Pons S. Electrochemically induced nuclear fusion of deuterium. J. of Electroanalytical Chemistry and Interfacial Electrochemistry, 261 (2 A), 1989.
6. Focardi S., Rossi A. A new energy source from nuclear fusion. J. of Nuclear Phys. 28 Feb. 2010.
7. Louis de Broglie. Introduction a la theorie des particules. Gauthier-Villars, Paris, 1961.

THE APPARENT MOTIONS OF THE EXTRAGALACTIC SOURCES IMAGES DUE TO ASTROMETRIC GRAVITATIONAL MICROLENSING IN THE GALAXY: A ROLE OF THE DM SUBSTRUCTURE

E. Fedorova,V. I. Zhdanov,A.N.Alexandrov[1], A. Del Popolo[2,3,4]
Astronomical Observatory of National Taras Shevchenko University of Kiev, Observatorna 3, 04053 Kiev, Ukraine

Dipartimento di Fisica e Astronomia, University of Catania, Viale A.Doria 6, 95125, Catania, Italy

INFN sezione di Catania, via S.Sofia, 95123 Catania, Italy

International Institute of Physics, Universidade Federal do Rio Grande do Norte, 59012-970, Natal, Brazil

The gravitational field of Galactic masses causes visual dragging of the extragalactic sources images, which is essentially different in case of discrete and continuous matter distribution. Dark matter substructures also can contribute to this effect. We estimate this image motion within the latest model of the Galactic mass distribution and consider the contribution of dark matter (DM) in the dragging effect within cold DM model.

1 Introduction

During the last decade, our representations about the fine DM structure, often referred to as clumps [1,4], were progressing significantly. These substructures of DM have contribute to observed gravitational microlensing statistics.It has been pointed out[9,11] that the astrometric microlensing of the extragalactic source image, besides a stochastic component, is accompanied with a systematic motion on the sky, which depends upon bulk velocity of microlensing stars. The typical velocity of the motion remains nonzero even for a homogeneous distribution of microlensing masses, provided they have a non-zero collective (average) velocity. Here we reconsider the visual effect of the gravitational image motion (GIM) of extragalactic sources due to the field of the Galaxy matter, taking into account both the results of numerical simulations of DM substructure [6,7,8], and the updated model of the matter distribution in the Galaxy [2,3]. This effect can reach up to $\sim$ microarsecond, like the accuracy reachable with such missions as GAIA (http://www.esa.int/esaSC/120377_index_0_m.html) and RadioAstron (www.asc.rssi.ru/radioastron). In the first section we briefly describe the weak microlensing equations used. The recent Galaxy model, used in the calculations, is described in the second section. In the third one we describe our results and draw our conclusions.

2 Gravitational microlensing equations

Here we calculate the GIM effect due to continuous and discrete density distribution in the same way as in [10], using the following formula for the deflection angle in the framework of weak-lensing

approximation $r >> (mz)^{1/2}$ by the microlens with a mass M, $m = GM/c^2$:

$$\vec{\Psi} = -2k_{\rm ds} m \mathbf{r} F(r)(1 + z \cdot (z^2 + r^2)^{-1/2}), \quad (1)$$

where z is a distance from the observer to the microlensing mass, $\mathbf{r}$ is an impact radius-vector, $r = |\mathbf{r}|$ is an impact parameter, for the observer at the space origin ($\mathbf{r}$,z). The function F(r) depend on the microlens properties, i.e. $F(r) = 1/r^2$ for point masses (used for the stellar component), $r_a^{\alpha-2}/r^\alpha$ for cusped CDM clumps and $1/(r^2 + r_s^2)$ for cored SIDM clumps [4] . Then, for the microlens velocity $\mathbf{V}_p = (\mathbf{v}, w)$ (here w is the velocity projection onto the line-of-the-sight, and two-dimensional vector $\mathbf{v}$ is a transversal part of the velocity), the GIM effect due to this microlens $m\mathbf{U}$ (in radians per a unit of time), is:

$$\mathbf{U} = \frac{d\mathbf{\Psi}}{mdt} = -2\mathbf{v}F(r)\left(1 + \frac{z}{\sqrt{z^2+r^2}}\right) + 2\mathbf{r}\left\{F'(r)\,\frac{(\mathbf{r}\cdot\mathbf{v})}{r}\cdot[1 + \frac{z}{\sqrt{z^2+r^2}}] - F(r)\,\frac{w\mathbf{r} - z\mathbf{v}/2}{(z^2+r^2)^{3/2}}\right\}. \quad (2)$$

To calculate the average GIM effect in the Galaxy, this formula was integrated alike as in [10].

3 The Galaxy model

In our calculations we have used the Galaxy model consisting of five components:

1. the bulge, supposed to be ellipsoidal, with the density profile
   $\rho_B(R) = \frac{M_{bulge}}{2\pi R_h^3 q\kappa}[\frac{r^2+z^2/q^2}{R_b^2}]^\gamma \exp(-\frac{r^2+z^2/q^2}{R_h^2})$ and the rotational curve
   $V_B^2(r) = \frac{GM_{bulge}}{r}[1 - \exp(-1.867r)\,[1 + 1.543r + 0.1898r^2 + ...]$,
   where κ=54.1, mass $M_{bulge} = (1.3 \pm 0.5) \cdot 10^{10} M_\odot$, R_h=1.9 kpc, R_b=1 kpc,
   ellipticity q=0.6, and steepness γ=1.8 [3];

2. the thick and thin disks, with the density profile $\rho_{disk}(r,z) = \frac{M_{disk}}{4\pi R_d^2 H}\exp(-\frac{r}{R_d} - \frac{|z|}{H})$,
   the rotational curves $V_{disk}^2 = GM_{disk}\left(\frac{1}{r} - (\frac{1}{R_{disk}} + \frac{1}{r})\exp\left[-\frac{r}{R_{disk}}\right]\right)$, and parameters of the thin disk M=1.7·$10^9 M_\odot$, R=2.5±0.5 kpc, and thickness 0.18 kpc, and of the thick one: M=1.2·$10^8 M_\odot$, R=2.5±0.5 kpc, and the thickness 1 kpc [3];

3. the stellar and dark matter haloes, with the spherically-symmetrical Einasto density profile: $\rho_{halo}(R) = \frac{M_{halo}}{4\pi R_{halo}^3 K_{halo}}\exp(-\frac{2}{\alpha}[\frac{r}{R_{halo}}]^\alpha)$ and rotational curves
   $V_{Halo}^2 = \frac{4\pi G M_{DM}}{3R_{DM}^3} r^3 \exp\left(-\frac{2}{\alpha}\left[\frac{r}{R_S}\right]^\alpha\right)\left(1 + \frac{2}{\alpha+3}\left[\frac{r}{R_S}\right]^\alpha\right)$.
   The parameters of the stellar halo are M=5·$10^9 M_\odot$, R=22.2 kpc and α=2.2, and of the Dark matter halo: M=$10^{12} M_\odot$, R=20 kpc, and α=0.17 [2,3].

4 The results and conclusions

For the observer at the Galactic center the maximum GIM constitute 3.5·10^{-8}arcsec/year. The dependency of the dragging effect from the inclination angle for an observer at the center of the Galaxy is shown on the left panel of the Fig.1.

The GIM effect in the Galactic plane for the observer moving with the Sun is shown on the right panel of the Fig.1. Cored SIDM structures give the same effect as the point masses, even if the density of a clump is quite low (the maximum effect in the direction of the Galaxy centre reaches 1.6*10^{-7} arcsec/year). The effect of CDM clumps is slightly higher (1.8*10^{-7} arcsec/year). In the same time, in comparison with our previous result [10], the updated model of the mass distribution with the Milky Way give us wider angular area where the GIM effect is

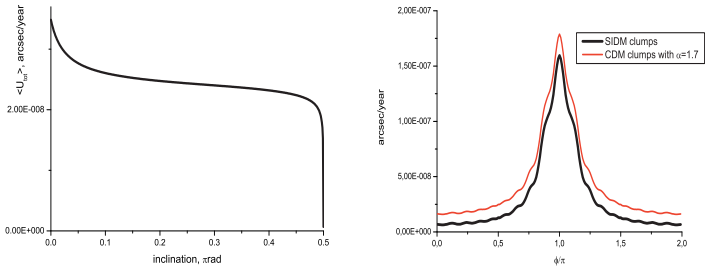


Figure 1 – The GIM for the observer at the Galactic center, dependence from the inclination angle (left panel) and for the observer in the Solar System, dependence from the azimuth angle $\phi = \pi$ is a direction onto the Galaxy center (right panel).

considerable (i.e., greater than 10^{-7} arcsec/year) , namely 0.85π-1.15π vs. 0.94π-1.06π. For the WDM models (no DM clumps[7]) the GIM is lower than for CDM and SIDM ones. But, anycase, for the observer in the Solar System the GIM in the Galactic plane can reach more than 10^{-7} arcsec/year. This small value, however, contribute to the errors of observations of extragalactic objects. Practically, today this effect is on the limit of the existing accuracy, however in the high-accuracy observations like GAIA or RadioAstron it should be taken into account for the extragalactic sources close the Galactic plane.

References

1. R. Aloisio, P. Blasi, A.V. Olinto, AJ **601**, 47 (2004).
2. N. Bernel, S. Palomarez-Ruis, astro-ph arxiv: 1103.2377.
3. V.F. Cardone, M. Sereno A&A **438**, 545 (2005).
4. E. Fedorova et al. MNRAS **457:4**, 4147 (2016).
5. M. Sazhin, V. Zharov, A. Volynkin, T. Kalinina MNRAS **300**, 287 (1998).
6. A. Schneider, L. Krauss, B. Moore Phys.Rev.D **82**, 063525 (2010).
7. A. Schneider, R.E. Smith, A. Macci, B. Moore, MNRAS **424**, 684 (2012).
8. M. Vogelsberger et al. MNRAS **423**, 3740 (2012).
9. V.Zhdanov, A.Alexandrov, E.Fedorova, V.Sliusar In: Dark energy and dark matter of the universe/Ed. V. Shulga. Vol. 2: Dark matter: Astrophysical aspects of the problem/K.: Akademperiodyka(2014).
10. V.I. Zhdanov, E. Fedorova, A.N. Alexandrov, KFNT **20**, 422 (2004).
11. V.I.Zhdanov, V.V.Zhdanova, A&A **299**, 321 (1995).


RENCONTRES DE MORIOND
50
N-Z

Authors Index

Alexandrov, A.	The apparent motions of the extragalactic sources images due to astrometric gravitational microlensing in the galaxy: a role of the DM substructure	353
Alves, R.	Fine-structure constant constraints on dark energy and the Weak Equivalence Principle	241
Arca-Sedda, M.	Formation and evolution of heavy sub-structures in the centre of galaxy clusters: the local effect of dark energy	137
Arca-Sedda, M.	Can dark energy explain the observed outflow in galaxy clusters?	303
Banerji, R.	Beam systematics in CMB polarisation measurements	77
Battye, R.	Update on the BINGO 21cm intensity mapping experiment	81
Battye, R.	Simulated Effects of $1/f$ Noise on an SKA Intensity Mapping Survey	327
Bautista, J .	BAO Correlations at $z = 23$ with SDSS DR12 Lyman-alpha forests	319
Beckwith, A.	Non Linear electrodynamics and a minimum vacuum energy(a cosmological constantant) allowed in Early Universe cosmology	85
Beltrán Jiménez, J.	Cosmology with vector distortion	349
Ben-Dayan, I.	Gravitational Waves in the Early Universe from Gauge Field Production	193
Bielewicz, P.	Testing significance of the large angular scale CMB anomalies using Planck data	209
Bilic, N.	Randall-Sundrum vs holographic braneworld	11
Bischoff, C.	Measurements of degree-scale B-mode polarization with BICEP2, KECK ARRAY, and BICEP3	249
Blanchard, A.	On the dark contents of the Universe: a Euclid survey approach	117
Boehm, V.	A bias to CMB lensing from the bispectrum of large-scale structure	19
Bonnivard, V.	Dark matter distribution and indirect detection in dwarf spheroidal galaxies	153
Brunner, J.	Directional detection of Dark Matter with the MIcro-tpc MAtrix of Chambers	165
Busto, J.	Directional detection of Dark Matter with the MIcro-tpc MAtrix of Chambers	165
Camera, S.	The Multi-Tracer Technique To Detect Horizon-Scale Effects	331
Carreira, P.	Fine-structure constant constraints on dark energy and the Weak Equivalence Principle	241
Chen, X.	Tianlai: a 21cm radio telescope array for BAO and dark energy, status and progress	315
Colas, P.	Directional detection of Dark Matter with the MIcro-tpc MAtrix of Chambers	165
Collis Olivari, L.	HI intensity mapping: extracting the 21 cm signal in the presence of foregrounds	337
Combet, C.	Dark matter distribution and indirect detection in dwarf spheroidal galaxies	153
Comis, B.	High angular resolution SZ observations with NIKA and NIKA2	289
Corre, D.	Dark Energy constraints from the ESPRESSO Fundamental Physics GTO	121
Couturier, C.	Directional detection of Dark Matter with the MIcro-tpc MAtrix of Chambers	165
Cruz Pérez, J.	Running vacuum versus the ΛCDM	251
D'Alessandro, G.	Instrumentation development for spectroscopic observation of the Cosmic Microwave Background	27
Danese, L.	The quest for Dusty Primeval Galaxies	341
Davini, S.	The DarkSide program at LNGS	157
De Boni, C.	The mass accretion rate of galaxy clusters: a measurable quantity	301
Del popolo, A.	The apparent motions of the extragalactic sources images due to astrometric gravitational microlensing in the galaxy: a role of the DM substructure	353
Di Giovanni, A.	The XENON1T Dark Matter experiment	53
Dickinson, C.	CMB foregrounds - A brief overview	141
Dickinson, C.	Simulated Effects of $1/f$ Noise on an SKA Intensity Mapping Survey	327
Domcke, V.	Probing inflation models with gravitational waves	205
Donnari, M.	Can dark energy explain the observed outflow in galaxy clusters?	303
Donnari, M.	Formation and evolution of heavy sub-structures in the centre of galaxy clusters: the local effect of dark energy	137
du Mas des Bourboux, H.	Quasar-Lyman α Forest Cross-Correlation from SDSS-III BOSS survey: Baryon Acoustic Oscillations	91
Errard, J.	Future CMB polarization observatory in the presence of foregrounds and gravitational lensing: the Simons Array	43
Fabbian, G.	Multiple lensing of CMB anisotropies	71
Fedorova, E.	The apparent motions of the extragalactic sources images due to astrometric gravitational microlensing in the galaxy: a role of the DM substructure	353
Ferreira, M.	Fine-structure constant constraints on dark energy and the Weak Equivalence Principle	241
Fouchez, D.	Directional detection of Dark Matter with the MIcro-tpc MAtrix of Chambers	165

Gómez-Valent, A.	Running vacuum versus the ΛCDM	251
Galli, S.	Planck results 2015	3
Gangler, E.	SUGAR : when spectra help standardizing supernovae	113
Gerbino, M.	Interplay between cosmology and laboratory experiments: two examples from neutrino physics	283
Gil-Marìn, H.	Constraining cosmological parameters using BOSS data: Power Spectrum and Bispectrum	95
Giomataris, I.	Directional detection of Dark Matter with the MIcro-tpc MAtrix of Chambers	165
Guillaudin, O.	Directional detection of Dark Matter with the MIcro-tpc MAtrix of Chambers	165
Gusart, A.	Fine-structure constant constraints on dark energy and the Weak Equivalence Principle	241
Gustavino, C.	Study of Big Bang Nucleosynthesis deep underground	347
Guy, J.	The Dark Energy Spectroscopic Instrument	103
Harper, S.	Simulated Effects of $1/f$ Noise on an SKA Intensity Mapping Survey	327
Harrison, I.	Weak Lensing with the Square Kilometre Array	125
Helbig, P.	The magnitude-redshift relation for type IA supernovae, locally inhomogeneous cosmological models, and the nature of dark matter	171
Henriksson, G.	The acceleration of the Moon and the Universe	259
Henrot-Versille, S.	The Hillipop likelihood and the $A_{\rm L}$ parameter using Planck data	7
Hinterbichler, K.	Cosmology of Massive Gravity and its Extensions	223
Ivanov, M.	Cosmological constraints on Lorentz Invariance violation in gravity and dark matter	351
Ivanov, M.	United Nature of Dark Energy and Low Energy Nuclear Reactions	237
Kehayias, J.	Static and Oscillating Universes	267
Kopp, M.	Generalised Dark Matter: Imprints on the CMB and mapping to non-perturbative models	181
Léget, P-F.	SUGAR : when spectra help standardizing supernovae	113
López, J.	Fine-structure constant constraints on dark energy and the Weak Equivalence Principle	241
Lamine, B.	On the dark contents of the Universe: a Euclid survey approach	117
Lapi. A.	The quest for Dusty Primeval Galaxies	341
Laurent, P.	Measuring BAO scale with quasar clustering in EBOSS	99
Lefranc, V.	Dark matter search in the inner Galactic Centre halo with HESS	149
Leite, A.	Dark Energy constraints from the ESPRESSO Fundamental Physics GTO	121
Leite, A.	Fine-structure constant constraints on dark energy and the Weak Equivalence Principle	241
Liu, J.	Constraining Multiplicative Bias in CFHTLenS Weak Lensing Shear Data	67
Mancuso, C.	The quest for Dusty Primeval Galaxies	341
Martins, C.	Fine-structure constant constraints on dark energy and the Weak Equivalence Principle	241
Martins, C.	Dark Energy constraints from the ESPRESSO Fundamental Physics GTO	121
Maurin, D.	Dark matter distribution and indirect detection in dwarf spheroidal galaxies	153
Meerburg, P.	The holiest grail	201
Merafina, M.	Formation and evolution of heavy sub-structures in the centre of galaxy clusters: the local effect of dark energy	137
Merafina, M.	Can dark energy explain the observed outflow in galaxy clusters?	303
Meyers, J.	Cosmic Neutrinos and Other Light Relics	279
Mishra, B.	Bianchi type V viscous fluid dark energy cosmological model with gauge function	261
Molaro, P.	Dark Energy constraints from the ESPRESSO Fundamental Physics GTO	121
Moncelsi, L.	SPIDER: Probing The Dawn Of Time From Above The Clouds	47
Mota, D.	Universal predictions of screened modified gravity on cluster scales	189
Moulin, E.	Dark matter search in the inner Galactic Centre halo with HESS	149
Naraghi, F.	Directional detection of Dark Matter with the MIcro-tpc MAtrix of Chambers	165
Ntelis, P.	The Homogeneity Scale of the Universe	129
Olivari, L.	Simulated Effects of $1/f$ Noise on an SKA Intensity Mapping Survey	327
Pagano, D.	The weak equivalence principle with antimatter: the AEgIS experiment at CERN	161
Peloton, J.	Data analysis and cosmological results from the first observational campaigns of the POLARBEAR experiment	35
Perenon, L.	General features of single-scalar field dark energy models	253
Pinho, A.	Fine-structure constant constraints on dark energy and the Weak Equivalence Principle	241
Pino, M.	Fine-structure constant constraints on dark energy and the Weak Equivalence Principle	241

Racine, B.	Cosmological Parameters from CMB Maps without Likelihood Approximation	15
Ramazanov, S.	Living with ghosts in Hořava–Lifshitz gravity	233
Riffard, Q.	Directional detection of Dark Matter with the MIcro-tpc MAtrix of Chambers	165
Rocha, C.	Fine-structure constant constraints on dark energy and the Weak Equivalence Principle	241
Roman, M.	Local environment of SNLS5 Type IA supernovæ	109
Rossi, G.	Constraining $N_{\rm eff}$ with the Lyman-α Forest	135
Salvatelli, V.	Constraints On Gravity from CMB data: an Effective Field Theory approach	217
Santos, D.	Directional detection of Dark Matter with the MIcro-tpc MAtrix of Chambers	165
Santos, M.	Cosmology with the 21cm signal	307
Schmittfull, M.	A bias to CMB lensing from the bispectrum of large-scale structure	19
Sherwin, B. D.	A bias to CMB lensing from the bispectrum of large-scale structure	19
Shi, H.	Tianlai: a 21cm radio telescope array for BAO and dark energy, status and progress	315
Solà, J.	Running vacuum versus the ΛCDM	251
Stolpovskiy, M.	QUBIC experiment	31
Tao, C.	Directional detection of Dark Matter with the MIcro-tpc MAtrix of Chambers	165
Thomas, D.	Under Pressure: constraining extensions of cold dark matter	255
Tutusaus Lleixa, I.	On the dark contents of the Universe: a Euclid survey approach	117
Urban, F.	The very best limits on cosmological magnetic fields	185
Vagnozzi, S.	New Solar metallicity measurements	175
Vansyngel, F.	Simulating the polarised galaxy	63
Verdier, L.	Thermal Sunyaev Zel'dovich effect from high redshift ($z > 2$) structures	297
von Wietersheim, M.	Fine-structure constant constraints on dark energy and the Weak Equivalence Principle	241
VoVan, T.	Expectation of lepton hierarchy and absolute neutrino masses in a microscopic cosmological model	245
Wang, X.	Statistical Decoupling of Lagrangian Fluid Parcel in Newtonian Cosmology	213
Wang, Y.	Tianlai: a 21cm radio telescope array for BAO and dark energy, status and progress	315
Wu, F.	Tianlai: a 21cm radio telescope array for BAO and dark energy, status and progress	315
Yèche, C.	Constraints on the neutrino mass from the Lyman-α forest power spectrum	271
Zavala, I.	Bumpy Inflation: Subleading Effects in Axion Inflation	197
Zhang, J.	Tianlai: a 21cm radio telescope array for BAO and dark energy, status and progress	315
Zhdanov, I.	The apparent motions of the extragalactic sources images due to astrometric gravitational microlensing in the galaxy: a role of the DM substructure	353

List of Participants

Family Name	First Name	Institution	Country	Email
Aghanim	Nabila	IAS	France	nabila.aghanim@ias.u-psud.fr
Antilogus	Pierre	LPNHE	France	P.Antilogus@in2p3.fr
Arca Sedda	Manuel	Università la Sapienza	Italy	m.arcasedda@gmail.com
Astier	Pierre	LPNHE	France	pierre.astier@in2p3.fr
Austermann	Jason	Nat. Institute of Standards and Tech.	USA	jea@nist.gov
Babichev	Eugeny	LPT Orsay	France	eugeny.babichev@th.u-psud.fr
Baldauf	Tobias	Institute for Advanced Study	USA	t.baldauf@tbaweb.de
Banerji	Ranajoy	APC	France	banerji@apc.in2p3.fr
Battye	Richard	Jodrell Bank Centre for Astrophysics	UK	Richard.Battye@manchester.ac.uk
Baur	Julien	CEA Saclay / Irfu	France	julien.baur@cea.fr
Bautista	Julian	University of Utah	USA	bautista@astro.utah.edu
Beckwith	Andrew	Chongqing University	China	rwill9955b@gmail.com
Beltran Jimenez	Jose	CPT	France	jose.beltran@cpt.univ-mrs.fr
Ben-Dayan	Ido	Ben Gurion University	Israel	ido.bendayan@gmail.com
Bender	Amy	Argonne National Lab.	USA	abender@anl.gov
Bertucci	Bruna	University of Perugia / INFN	Italy	Bruna.bertucci@pg.infn.it
Betoule	Marc	LPNHE	France	marc.betoule@lpnhe.in2p3.fr
Bianchini	Federico	SISSA	Italy	fbianchini@sissa.it
Bielewicz	Paweł	Nicolaus Copernicus Astronomical Ctr	Poland	pbielew@camk.edu.pl
Bilić	Nevenko	Ruđer Bošković Institute	Croatia	bilic@irb.hr
Bischoff	Colin	Harvard-Smithonian Center Astroph.	USA	cbischoff@cfa.harvard.edu
Blanchard	Alain	IRAP	France	alain.blanchard@irap.omp.eu
Blas	Diego	CERN - TH	Switzerland	diego.blas@cern.ch
Boehm	Vanessa	MPI Astrophysics	Germany	vboehm@mpa-garching.mpg.de
Bolejko	Krzysztof	The University of Sydney	Australia	krzysztof.bolejko@sydney.edu.au
Bongard	Sébastien	LPNHE	France	sebastien.bongard@lpnhe.in2p3.fr
Burgess	Cliff	Perimeter Institute	Canada	cburgess@pitp.ca
Camera	Stefano	Jodrell Bank Centre for Astrophysics	UK	stefano.camera@manchester.ac.uk
Campigotto	Marta	Università di Torino	Italy	martacostanza.campigotto@to.infn.it
Chun	Eung Jin	KIAS	South Korea	ejchun@kias.re.kr
Collis Olivari	Lucas	Jodrell Bank Centre for Astrophysics	UK	lucas.olivari@postgrad.manchester.ac.uk
Combet	Céline	LPSC	France	celine.combet@lpsc.in2p3.fr
Comis	Barbara	LPSC	France	barbara.comis@lpsc.in2p3.fr
Couturier	Camille	LPSC	France	ccouturi@lpsc.in2p3.fr
Creminelli	Paolo	ICTP	Italy	creminel@ictp.it
D'Alessandro	Giuseppe	Università la Sapienza	Italy	giuseppe.dalessandro@roma1.infn.it
D'Amico	Guido	CERN	Switzerland	damico.guido@gmail.com
Davini	Stefano	Gran Sasso Science Institute	Italy	stefano.davini@gssi.infn.it
De Boni	Cristiano	IAS	France	cristiano.deboni@ias.u-psud.fr
de Haan	Tijmen	UC Berkeley	USA	tijmen@berkeley.edu
Di Giovanni	Adriano	New York University	UAE	adriano.digiovanni@nyu.edu
Dickinson	Clive	Jodrell Bank Centre for Astrophysics	UK	Clive.Dickinson@manchester.ac.uk
Domazet	Silvije	Ruđer Bošković Institute	Croatia	sdomazet@irb.hr
Domcke	Valerie	APC	France	valerie.domcke@apc.univ-paris7.fr
Donnari	Martina	Università la Sapienza	Italy	donnari.m@gmail.com
Doux	Cyrille	APC	France	cdoux@apc.in2p3.fr
du Mas des Bourboux	Hélion	CEA Saclay	France	Helion.du-Mas-des-Bourboux@cea.fr
Duivenvoorden	Adri	Oskar Klein Centre	Sweden	adri.duivenvoorden@fysik.su.se
Dumarchez	Jacques	LPNHE	France	jacques.dumarchez@cern.ch
Errard	Josquin	ILP - LPNHE	France	josquin.errard@gmail.com
Fabbian	Giulio	SISSA	Italy	gfabbian@sissa.it

Falco Martina	Università di Torino	Italy	mafalco@unito.it
Fedorova Elena	Astronomical Observatory	Ukraine	efedorova@ukr.net
Galli Silvia	IAP	France	gallis@iap.fr
Gangler Emmanuel	LPC Clermont-Ferrand	France	gangler@clermont.in2p3.fr
Gerbino Martina	Oskar Klein Center	Sweden	marti.gerbino@gmail.com
Gil Marin Hector	LPNHE	France	hector.gilmarin@lpnhe.in2p3.fr
Gómez-Valent Adriá	Institute of Cosmos Science	Spain	adriagova@ecm.ub.edu
Gudmundsson Jon	Oskar Klein Center	Sweden	jegudmunds@gmail.com
Gustavino Carlo	INFN	Italy	carlo.gustavino@roma1.infn.it
Guy Julien	LPNHE	France	guy@lpnhe.in2p3.fr
Guyonnet Augustin	LPNHE	France	guyonnet@lpnhe.in2p3.fr
Hamann Jan	Sydney Institute for Astronomy	Australia	jan.hamann@sydney.edu.au
Harper Stuart	Jodrell Bank Centre for Astrophysics	UK	stuart.harper@manchester.ac.uk
Harrison Ian	Jodrell Bank Centre for Astrophysics	UK	ian.harrison-2@manchester.ac.uk
Helbig Phillip		Germany	helbig@astro.multivax.de
Henriksson Göran	Dep. Physics and Astronomy	Sweden	goran.henriksson@physics.uu.se
Henrot-Versillé Sophie	LAL	France	versille@lal.in2p3.fr
Hinterbichler Kurt	Perimeter Institute	Canada	khinterbichler@perimeterinstitute.ca
Hoyle Ben	Ludwig Maximilian University	Germany	benhoyle1212@gmail.com
Hwang Jai-chan	Kyungpook National University	South Korea	jchan@knu.ac.kr
Ivanov Mikhail	Central Institute of Aviation Motors	Russia	mikhivan@yandex.ru
Ivanov Mikhail	EPFL	Switzerland	mikhail.ivanov@epfl.ch
Jacobs David	University of Cape Town	South Africa	dmj15@case.edu
Kehayias John	Vanderbilt University	USA	john.kehayias@vanderbilt.edu
Khlopov Maxim	APC	France	khlopov@apc.in2p3.fr
Kopp Michael	University of Cyprus	Cyprus	kopp.michael@ucy.ac.cy
Kubik Bogna	IPN Lyon	France	bkubik@ipnl.in2p3.fr
Lapi Andrea	SISSA	Italy	lapi@sissa.it
Laurent Pierre	CEA Saclay	France	pierre.laurent@cea.fr
Le Breton Remy	LPNHE	France	remy.lebreton@lpnhe.in2p3.fr
Le Goff Jean-Marc	CEA Saclay / Irfu	France	jmlegoff@cea.fr
Le Guillou Laurent	LPNHE	France	llg@lpnhe.in2p3.fr
Le Jeune Maude	APC	France	lejeune@apc.in2p3.fr
Leclercq Florent	Institute of Cosmology & Gravitation	UK	florent.leclercq@polytechnique.org
Lefranc Valentin	CEA / Irfu	France	valentin.lefranc@cea.fr
Leite Ana Catarina	Centro de Astrofísica	Portugal	Ana.Leite@astro.up.pt
Lewis Antony	University of Sussex	UK	antony@cosmologist.info
Liu Jia	Columbia University	USA	jia@astro.columbia.edu
Lopez Nacir Diana	CERN - TH	Switzerland	diana.laura.lopez.nacir@cern.ch
Lozanov Kaloian	Institute of Astronomy	UK	kd309@cam.ac.uk
Mancuso Claudia	SISSA	Italy	cmancuso@sissa.it
Martins Carlos	Centro de Astrofísica	Portugal	carlos.martins@astro.up.pt
Meerburg Pieter	CITA	Canada	meerburg@cita.utoronto.ca
Meyers Joel	CITA	Canada	jmeyers@cita.utoronto.ca
Millea Marius	Institut Lagrange	France	mariusmillea@gmail.com
Mishra Bivudutta	Department of Mathematics	India	bivudutta@gmail.com
Moncelsi Lorenzo	Caltech	USA	moncelsi@caltech.edu
Mota David F.	University of Oslo	Norway	mota@astro.uio.no
Nadathur Seshadri	Institute of Cosmology & Gravitation	UK	seshadri.nadathur@port.ac.uk
Niemack Michael	Cornell University	USA	niemack@cornell.edu
Noh Hyerim	Astronomy and Space Science Institute	South Korea	hr@kasi.re.kr
Notari Alessio	Universitat de Barcelona	Spain	notarialessio@gmail.com

Ntelis Pierros	APC	France	pntelis@apc.in2p3.fr
Pagano Davide	Università degli Studi	Italy	davide.pagano@unibs.it
Peloton Julien	University of Sussex	UK	j.peloton@sussex.ac.uk
Perdereau Olivier	LAL	France	perdereau@lal.in2p3.fr
Perenon Louis	CPT	France	louis.perenon@cpt.univ-mrs.fr
Piazza Federico	CPT	France	fedosquare@gmail.com
Puddu Roberto	Università la Sapienza	Italy	roberto.puddu@roma1.infn.it
Quartin Miguel	Universidade Federal	Brazil	mquartin@if.ufrj.br
Racine Benjamin	Institute of Theoretical Physics	Norway	racinebenjamin@gmail.com
Ramazanov Sabir	Gran Sasso Science Institute	Italy	sabir.ramazanov@gssi.infn.it
Roman Matthieu	LPNHE	France	matthieu.roman@lpnhe.in2p3.fr
Rossi Graziano	Sejong University	South Korea	graziano@kias.re.kr
Sakr Ziad	IRAP	France	zsakr@irap.omp.eu
Salvatelli Valentina	CPT	France	Valentina.Salvatelli@cpt.univ-mrs.fr
Santos Mario	University of Western Cape	South Africa	mariogrs@gmail.com
Sathyaprakash B.S.	Cardiff University	UK	B.Sathyaprakash@astro.cf.ac.uk
Schael Stefan	I. Physikaliches Institut RWTH	Germany	schael@physik.rwth-aachen.de
Sibiryakov Sergey	CERN / EPFL / INR-RAS	Switzerland	Sergey.Sibiryakov@cern.ch
Simonovic Marko	Institute for Advanced Study	USA	markos@ias.edu
Simonyan Ani	IPNO	France	simonyan@ipno.in2p3.fr
Sliwa Krzysztof	Tufts University	USA	krzysztof.sliwa@tufts.edu
Soares-Santos Marcelle	Fermilab	USA	marcelle@fnal.gov
Spolyar Douglas	Stockholm University	Sweden	dspolyar@gmail.com
Stolpovskiy Mikhail	APC	France	mikhail.stolpovskiy@apc.univ-paris7.fr
Story Kyle	Stanford / KIPAC	USA	kstory@stanford.edu
Thomas Daniel	University of Cyprus	Cyprus	daniel.b.thomas@port.ac.uk
Traini Alessandro	APC	France	alessandro.traini@apc.univ-paris7.fr
Trevisan Gabriele	NYU	USA	gt989@nyu.edu
Trott Michael	Niels Bohr Institute	Denmark	michael.trott@cern.ch
Tutusaus Lleixa Isaac	IRAP	France	isaac.tutusaus@irap.omp.eu
Urban Federico	NICPB	Estonia	federico.urban@kbfi.ee
Vagnozzi Sunny	Oskar Klein Centre	Sweden	sunny.vagnozzi@fysik.su.se
Vansyngel Flavien	IAS	France	flavien.vansyngel@ias.u-psud.fr
Vargas-Magaña Mariana	UNAM	Mexico	mmarianav@gmail.com
Verdier Loïc	CEA Saclay	France	loic.verdier@cea.fr
Vernizzi Filippo	CEA Saclay / IPhT	France	filippo.vernizzi@cea.fr
Vieira José	University of Sussex	UK	J.Pinto-Vieira@sussex.ac.uk
Vikman Alexander	Institute of Physics	Czech Rep.	vikman@fzu.cz
Vo Van Thuan	VINATOM	Vietnam	vvthuan@vinatom.gov.vn
von der Linden Anja	Stony Brook University	USA	anja.vonderlinden@stonybrook.edu
Wang Xin	CITA	Canada	xwang@cita.utoronto.ca
Weller Jochen	Ludwig-Maximilians University	Germany	jochen.weller@usm.lmu.de
Whittaker Lee	University of Manchester	UK	lee.whittaker@manchester.ac.uk
Wu Fengquan	National Astronomical Observatories	China	wufq@bao.ac.cn
Yamaguchi Masahide	Tokyo Institute of Technology	Japan	gucci@phys.titech.ac.jp
Yeche Christophe	CEA Saclay / Irfu	France	christophe.yeche@cea.fr
Zavala Ivonne	Swansea University	UK	e.i.zavalacarrasco@swansea.ac.uk

Dépôt légal : octobre 2016
Achevé d'imprimer : octobre 2016
COPYMÉDIA
www.copy-media.net
Avenue de Guitayne - 33610 CANÉJAN